The Dissertation Committee for Kimberly Grau Talley
certifies that this is the approved version of the following dissertation:

Assessment and Strengthening of ASR and DEF Affected Concrete Bridge Columns

Committee:

_____
John E. Breen, Supervisor

_____
Kevin J. Folliard

_____
James O. Jirsa

_____
Maria G. Juenger

_____
Harovel G. Wheat

Assessment and Strengthening of ASR and DEF Affected Concrete Bridge Columns

by

Kimberly Grau Talley, B.S., M.S.E.

Dissertation

Presented to the Faculty of the Graduate School of

the University of Texas at Austin

in Partial Fulfillment

of the Requirements

for the Degree of

Doctor of Philosophy

The University of Texas at Austin

August 2009

To my husband, Austin, who has believed in me, even when I've doubted myself.

Acknowledgements

There are so many people to thank for their kind assistance during the course of my doctoral studies that I cannot list them all, but know that I greatly appreciated your help!

I want to thank my advisor, Dr. John E. Breen, for his guidance and support throughout my research and writing of this dissertation. I also wish to thank my committee for their insight and helpful suggestions during the research process.

For their financial support of my graduate studies, I would like to thank the National Science Foundation Graduate Research Fellowship Program, the University of Texas at Austin Thrust 2000 Fellowship Program, and the Austin Chapter of the American Association of University Women. I also wish to thank Jose Arrellaga, Matthew Price, Ensoft Inc. and Cervenka Consulting for their generous assistance with the computer modeling system.

I want to thank the staff of the Ferguson Structural Engineering Laboratory who have always been so friendly and helpful. Many thanks to In Sung Kim for his guidance and assistance in my FRP repair. There have been many friends at FSEL to share concerns and celebrations, with a special thank you going to Catherine Hovell, Jason Stith, and Daniel Williams. To my family and friends, thank you for your love, support, and patience with this dissertation process. To Austin, thank you for your love, enthusiasm, and belief in me.

Assessment and Strengthening of ASR and DEF Affected Concrete Bridge Columns

Publication No._____

Kimberly Grau Talley, Ph.D.
The University of Texas at Austin, 2009

Supervisor: John E. Breen

Alkali silica reaction (ASR) and delayed ettringite formation (DEF) are two causes of concrete deterioration. Both mechanisms cause expansion of concrete and thus extensive cracking. Most previous research on ASR and DEF focused on understanding the material science of the mechanisms. This dissertation adds to the smaller body of knowledge about ASR/DEF's effect on the structural behavior of reinforced concrete columns. It compares the structural performance of ASR/DEF affected concrete columns to mechanically cracked columns, evaluates the relative performance of four different concrete repair methods for strengthening damaged columns, and describes how to model pre-existing cracks in the finite element program ATENA.

Previous research on scaled columns used mechanically cracked concrete as an approximation of ASR/DEF cracking damage. These earlier column tests, by Kapitan, were compared to two columns affected by ASR/DEF. Due to a deficiency in original design of the actual columns modeled, all of these scaled column specimens failed in bearing during testing under biaxial bending. The ASR/DEF affected columns exhibited nearly identical performance (including bearing capacity) as Kapitan's control specimen.

Thus, with over one percent expansion due to ASR/DEF, there was no reduction in bearing capacity for these columns.

Based on the bearing failure observed in these scaled column specimens, concrete repairs were designed to increase confinement of the column capital to address the bearing capacity deficiency. A series of bearing specimens was constructed, externally reinforced using four different strengthening schemes, and load tested. From this bearing specimen series, both an external post-tensioned repair and a concrete jacketing repair performed well beyond their designed capacities and are recommended for bearing zone confinement repair of similar ASR/DEF affected concrete columns.

Further, this dissertation presents how Kapitan's scaled column results were modeled using ATENA (a reinforced concrete finite element program). A technique for modeling the mechanical cracking was developed for ATENA. Once calibrated, a parametric study used the model to find that a 0.17-inch wide through-section crack in the scaled columnd (5/8 inches in the field) was the threshold that reduced capacity of the scaled column to the factored design load.

Table of Contents

Table of Figures

Table of Tables

CHAPTER 1
Introduction

1.1 BACKGROUND

The elevated sections of Interstate Highways 10 and 35 in downtown San Antonio, Texas are known as the San Antonio Y. Deterioration in the form of extensive vertical cracking of some bridge columns was noted during routine inspections by the bridge owner, the Texas Department of Transportation (TxDOT). This deterioration was brought to the attention of researchers at the University of Texas at Austin (UT) who examined concrete core samples that revealed some columns were affected primarily by delayed ettringite formation (DEF)[1-3]. Other deterioration was caused primarily by alkali silica reaction (ASR) or a combination of the two mechanisms[1-3]. Both ASR and DEF are mechanisms that cause expansion of concrete, which leads to extensive cracking[1-3]. As a structure suffering primarily from DEF had hitherto not been reported in the literature, the materials research team was very interested in examining the structure[1]. ASR affected structures had previously been reported worldwide[46,50,58,60,62-64,68-70]. TxDOT was primarily concerned with the public safety. Thus, TxDOT wanted a method of evaluating the affected columns and recommendations for future action. As a result of this situation, TxDOT sponsored research studies at the UT Center for Transportation Research (CTR) to determine the effect of ASR and DEF on the capacity of the columns, likelihood of future deterioration, and remediation recommendations[1].

Much of the research at CTR and in published research had focused on understanding the mechanisms driving ASR and DEF and on developing test procedures for prevention or diagnosis of these mechanisms[2,4-40]. Of this research, ASR had received more attention than DEF. The uneven weighting of research is likely because ASR had been more commonly diagnosed as the primary cause of deterioration, often with DEF playing a secondary role[1,3,20,38,41]. Additionally, while there had been extensive research to

determine the influence of ASR on material properties of concrete, there had been much less on research in ASR's influence on the strength of reinforced concrete members, and practically no research on the effects of DEF on those structural properties[10,22,37,38,42-52].

Previous research at the Ferguson Structural Engineering Laboratory (FSEL) found that the affected columns of the San Antonio Y had a deficiency in their design for bearing[3]. Fortunately, core tests indicated that the actual concrete compressive strength was substantially greater than the assumed design strength. Therefore, this design deficiency did not affect the current load rating of the columns[3]. In addition, a preliminary study on the effects of column capacity versus induced crack width gave the indication that the reduction of capacity due to column cracking was mitigated by the excess concrete strength observed in several of the deteriorated columns[3]. Not all of the columns in the San Antonio Y may have as much excess, however. Thus, a possible repair technique to improve bearing capacity and, as a result, the capacity of the columns was desired to have on hand in case a column with less excess concrete compressive strength showed signs of distress.

This research study had three main components: scaled column specimens, bearing specimens, and computer modeling.

The scaled column specimens were identical to the specimens used in Kapitan's column series except these columns were cast with ASR susceptible concrete and heat treated to trigger DEF. The heat treating involved preheating the concrete materials and tenting the concrete during initial curing. To add to the heat of a July day in Central Texas, two propane heaters increased the temperature under the tent in order to raise the internal concrete temperature. As both ASR and DEF require moisture to cause concrete expansion, a moisture retention system was developed for the column specimens' exposure period. This system involved soaker hoses wrapped around the columns' tops and felt-backed plastic wrapped around the columns (including the hoses). Water was

applied four times a day, regulated by an automatic timer, and the plastic wrapping prevented evaporation. Further, the columns were axially post-tensioned (with scaled dead and live load) during exposure in order to obtain distributed vertical cracking similar to that observed in the San Antonio Y columns. The specimen scale was set by Kapitan's earlier work to a ratio of 1/3.67, which corresponds to a number three reinforcing bar in the laboratory representing a number eleven reinforcing bar in the field. These two columns complemented the series by Kapitan. They were used to correlate ASR/DEF cracking and behavior to the behavior measured in Kapitan's mechanically cracked specimens.

Based on the bearing failure observed in the scaled column specimens, concrete repairs were designed to increase confinement of the column capital to address the bearing capacity deficiency. The bearing specimens examined the ability of four different repair techniques to confine the column capital and thus improve the bearing strength of the columns. Packing straps, a fiber reinforced polymer wrap, external post-tensioning, and concrete jacketing were the repairs studied. These repairs were applied to bearing specimens that replicated the column capital (top sixteen inches) of the scaled column series. The original intent of the specimens was to repair ASR/DEF caused cracking damage. For that goal, the specimens were cast with ASR susceptible concrete and heat treated to trigger DEF. Due to the size of these specimens the heat treating was able to include the materials and formwork heating overnight in an oven prior to placing. The specimens were then cast within and remained in the oven overnight. A different moisture system was used for these specimens than the one used for the scaled column specimens. This alternate system proved to be less effective than the scaled column specimen's system. The bearing specimens were axially post-tensioned with the same load as the scaled column specimens, but then placed above a pool of water and tented. The intent of this system was to create a warm, high-humidity environment. The axial post-tensioning was in place to cause any cracking to have vertical orientation. As there was no significant expansion of these specimens during their exposure period, the bearing

specimens were mechanically cracked with splitting wedges (0.1-inch wide cracks) prior to repair. The repairs were designed to provide lateral confinement sufficient to add a vertical load capacity corresponding to 25% of the maximum axial load carried by Kapitan's control scaled column specimen.

ATENA, a commercially available finite element program designed specifically to model reinforced concrete behavior, was used to model Kapitan's results. The model used the same scale as Kapitan (1/3.67) in order to directly compare results. Once calibrated to Kapitan's control specimen, the model was used in a parametric study to determine the maximum vertical through-section crack width that the column could have and still carry the factored design load.

1.2 OBJECTIVES

This dissertation had the following objectives:

- Calibrate the computer program ATENA using results from previous research on mechanically cracked columns.
- Make predictions of column capacity, using the calibrated model, for a variety of initial crack widths.
- Correlate previous research on crack width versus column capacity to the capacity of columns with ASR/DEF deterioration.
- Evaluate the relative effectiveness of different repair methods for strengthening the bearing performance of cracked bridge columns.
- Recommend a repair method for increasing bearing capacity with consideration for ease of application, approximate cost of repairs, and aesthetic impact.

1.3 ORGANIZATION

Chapter 2 of this dissertation gives detailed background to the project history, ASR, DEF, previous research involving structural behavior of ASR/DEF affected concrete, and column repair techniques. Chapter 3 describes the scaled column specimens, including

previous work and the ASR/DEF affected scaled column specimens. Chapter 4 illustrates the design, exposure, repair, and test set-up of the bearing specimens. Chapter 5 explains the computer model used and findings from the parametric study. Chapter 6 presents the results from the scaled column specimen tests and Chapter 7, similarly, presents the bearing specimen repair test results. As well, these chapters will include data from the monitoring of both the scaled column and the bearing specimens, respectively. Chapter 8 describes recommendations based upon the results, summarizes the research detailed within this dissertation, and presents final conclusions.

CHAPTER 2
Background

2.1 PROJECT HISTORY

The bulk of the San Antonio Y was constructed in 1986-1987[3]. Some of the bridge columns in this section of highway began cracking as early as the mid 1990s[2]. The location of the columns under consideration is shown in Figure 2.1. Petrographic investigation of the bridge elements in 1996 had not shown evidence of ASR or DEF[2,53]. In 2003 additional petrographic investigation showed signs of DEF in one of the affected columns[7]. As a result of this finding, Dr. Kevin Folliard, of UT, was contacted by TxDOT to investigate the cracking and to suggest a course of action to manage the structure[1,2]. The initial focus of the research program was to investigate the material cause of the cracking. However, as the bridge owner also wanted a methodology to assess the column capacities, a structural portion of the research program was also defined[1]. This dissertation is part of the structural aspect of the project.

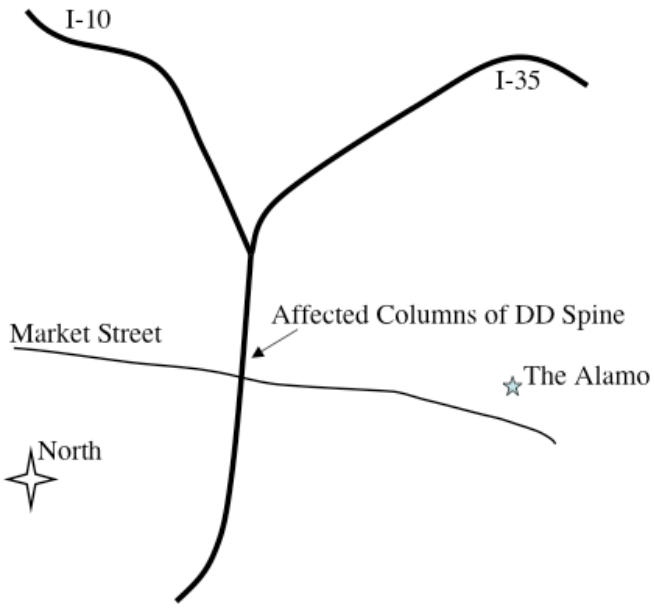

Figure 2.1: General Location of Affected Columns in DD-Spine, San Antonio Y[1-3]

The bridge column DD7, which was the typical column for the DD-spine, had a cross sectional area of thirty (30) square feet[54]. Such a large cross section resulted in mass concrete pours that, in combination with the high cement levels (eight sacks or more) and Type III cement likely used, produced high curing temperatures of the fresh concrete[1,2,7]. Further anecdotal evidence, as reported in Williams' thesis, from TxDOT personnel indicated that the curing temperature was so high it caused the formwork to warp[2]. Additionally, testing at CTR found that the concrete contained ASR reactive aggregates[1,2]. The high heat of hydration set the stage for DEF, as further explained in section 2.3. The reactive aggregates in the concrete created the possibility of the later onset of ASR, which is discussed in section 2.2. Drainpipes, which provided the storm water runoff for the bridge deck, also ran through the center of the column cross sections[2]. With a combination of leaking bridge joints, possibly clogged and leaking drainpipes, and environmental exposure at the edge of the bridge, the columns received regular wetting[2]. In Figure 2.2 discoloration of column DD6 due to water from the deck joint is easily seen, as well as the DEF induced cracking of the concrete. The availability of moisture is a key need to drive the reactions of either DEF or ASR[1,2].

Figure 2.2: DEF Induced Damage in DD6[55]

In the materials investigation, numerous core samples were tested to measure the possibility of future expansion in the columns from either ASR or DEF[1,2]. These core tests to indicate future expansion potential were run by placing the concrete cylinders in ideal environments for the acceleration of either ASR or DEF mechanism. For instance, concrete cores tested for ASR induced expansions were placed in alkaline rich water-based solutions. This solution ensured there was an unending supply of alkaline ions in the pore solution as well as moisture for expansion of the gel reaction product. In a field structure, the alkali content is supplied from the cement in the concrete. Thus, there is a finite amount of alkali ions that would be supplied to the pore solution. As well, field structures typically do not have uninterrupted access to essentially an inexhaustible moisture supply. These differences between laboratory and field conditions mean that a field structure may never reach the expansions predicted by the laboratory tests. Instead, the tests served as a worst-case scenario for the structure, not a prediction of future behavior on a scaled timetable. Figure 2.3 and Figure 2.4 show the results of the tests, which indicated that some of the columns could still expand considerably. The results from these expansion tests also showed the wide variation in susceptibility to future expansions in concrete cores from the same bridge project. Williams reported that the high heats of hydration during construction, which resulted in the warping of formwork, were combated by adding fly ash to some concrete batches. This changing mixture could explain the difference in adjacent columns' susceptibility. For an in-depth description of the tests run on the cores and the theory behind these standardized tests, please refer to Williams 2005 thesis. Column DD7 showed a great potential for future expansion from either ASR or DEF. It is important to note that these tests do not indicate that the concrete will definitely expand to the levels measured. Instead, the tests indicate the maximum levels to which the concrete could expand if all the factors were in place for that expansion to occur. Thus, these tests give a worst-case scenario estimate[1,2].

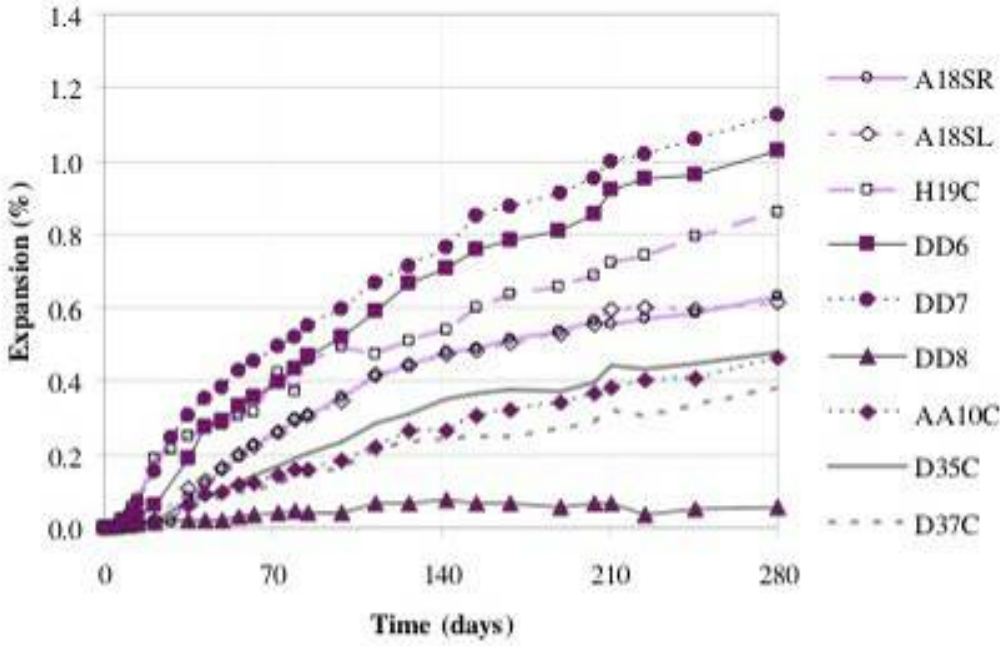

Figure 2.3: ASR Expansion in Cores from San Antonio Y[2]

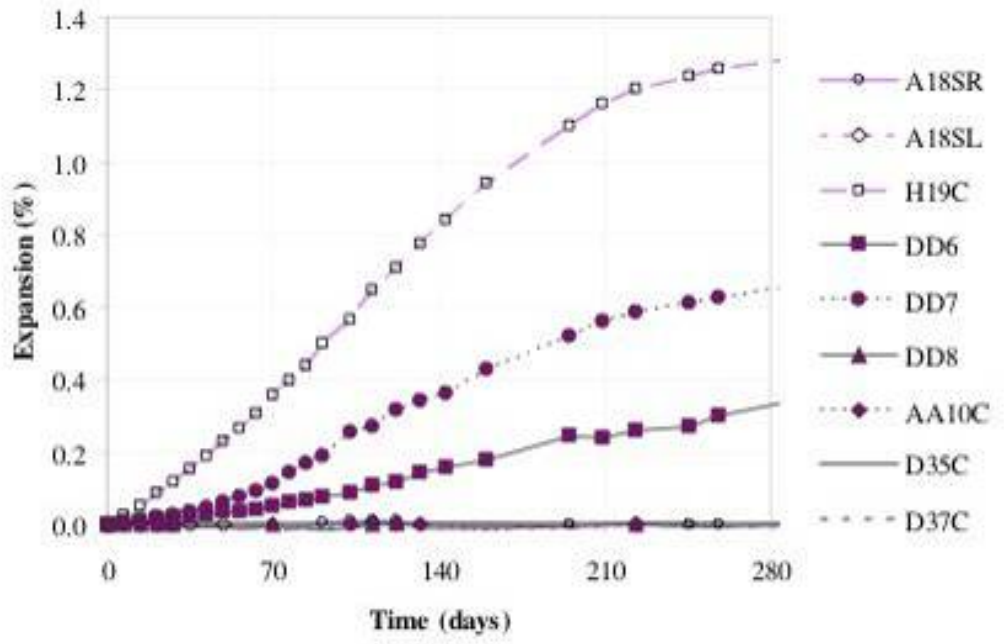

Figure 2.4: DEF Expansion in Cores from San Antonio Y[2]

Petrographic investigation looks for evidence of deterioration at the microscopic level[2]. From this investigation, the petrographer can assign a damage rating to the concrete. The damage rating assigns points to each sample based upon the presence and extent of deterioration elements, such as micro-cracking and ASR gel. A rating of fifty or greater indicates that the concrete is extensively deteriorated[2]. The damage levels found for the San Antonio Y samples are listed in Table 2.1[1,2]. A rating of zero indicates no damage and values less than fifty indicate there are some deterioration indications present but the concrete is still largely undamaged. Williams' 2005 thesis gave an excellent explanation of petrographic investigation including the preparation of samples and the workings of the scanning electron microscopes. For greater detail about petrographic investigation, the reader should refer to Williams.

Table 2.1: Damage Rating Indices for San Antonio Y[2]

Structural Element	Damage Rating Index
DD-6	69
DD-7	109
DD-8	37
H-19C	183

2.2 ALKALI SILICA REACTION (ASR)

2.2.1 Mechanism

The basic definition of ASR involves the formation of an expansive gel through the reaction of alkalies and silicates in concrete[4,8,10,37,38,40,41,56]. This gel, in the presence of sufficient moisture, expands and puts pressure on the surrounding cement paste and aggregates, which can lead to cracking[4,8-10,27,37,38,40,41,56]. Whether the gel absorbs water, takes in water through osmosis, or attracts moisture by electrically charged layers

surrounding the gel is a continuing topic of debate. However, the correlation between moisture presence and gel expansion is unquestioned[9,27,37,38,40,41]. Thus, in order for the reaction to occur, three conditions must be satisfied: the presence of reactive aggregate, a high level of alkalinity, and sufficient moisture. Without any of these three elements, the reaction cannot occur[2,4,8-10,27,37,38,40,41,56].

The alkalies involved in the reaction come predominantly from the cement in the concrete mixture, although they can also come from admixtures and mixing water[37,38,40,41]. Siliceous aggregates provide the silica in ASR[2,4,8-10,27,37,38,40,41]. The reactivity of the silicate depends on the type and structure of the silica phase. If the crystal structure is well ordered, such as quartz, then the aggregate is resistant to reaction. However, if the structure is highly disorganized and amorphous, such as opal, then the aggregate is reactive. Even at as low a concentration as 0.5%, opal can cause an aggregate to be reactive[37,38,40,41]. The reactivity of the aggregate is also affected by the level of alkalies present. At very high levels, the alkalies can attack well organized silica bonds. As well, highly reactive aggregates can react at relatively low levels of alkalies[37,40,41].

Figure 2.5 is a schematic of the ASR mechanism. As shown in the figure, a high level of alkaline ions in the pore solution will essentially attack the silica bonds in the aggregate and cause the silica to dissolve. This high level of alkalinity corresponds with a pH of 13.5 to 14[41]. When the silica goes into the concrete pore solution then it is able to react with the alkaline ions present in the solution. The chemical reaction between the silica and the alkali ions form an alkali-silica gel around the edge of the aggregate. With sufficient moisture present the gel expands and pushes against the surrounding concrete. The high localized pressure can result in micro-cracking of the concrete and, with additional time and moisture, cracking of the concrete that is visible to the unaided eye[40].

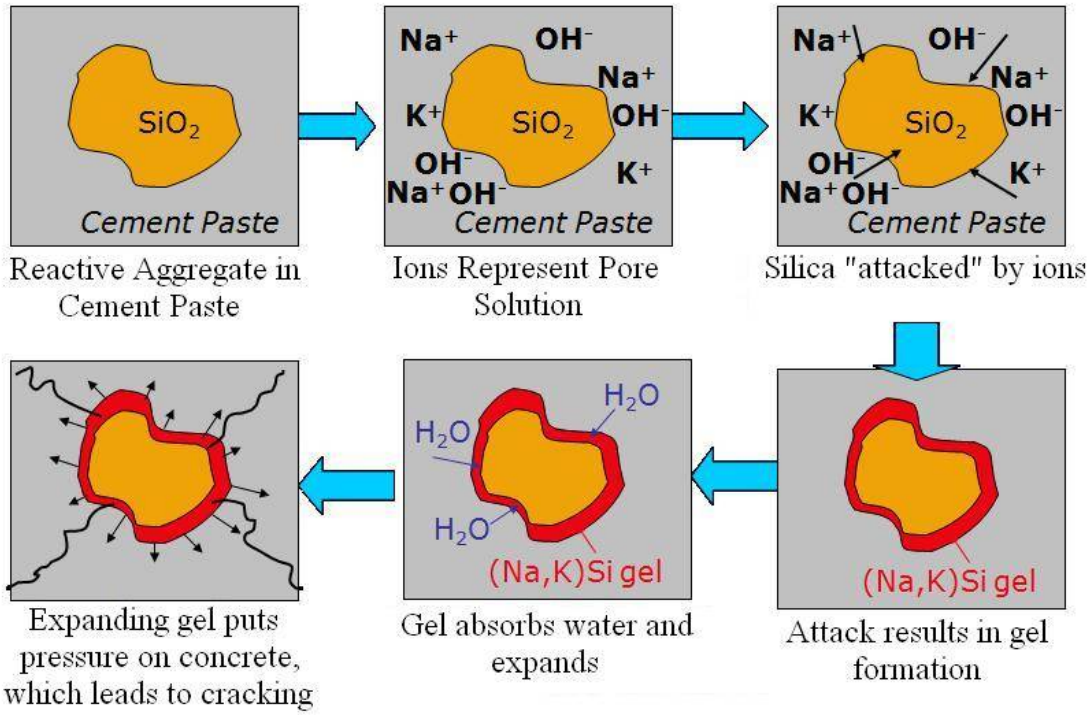

Figure 2.5: Schematic of ASR Mechanism[41]

Moisture plays a major role in ASR[2,4,8-10,27,37,38,40,41]. Without a sufficient level of moisture, the reaction does not proceed or the gel ceases to expand. Wetting and drying cycles can also create local concentrations of alkalies by causing the alkalies to migrate towards the drying surface of the concrete. Such a migration can trigger ASR in discrete portions of a concrete member that otherwise has too low a level of alkalies to react. ASR can initiate at a relative humidity of 80%[37,40]. Thus, even internal humidity from excess mix water can trigger ASR in otherwise dry environments if the moisture is trapped in the concrete[8,37,40].

Even a small amount of reinforcement can greatly reduce the expansion caused by ASR[37]. A reinforcing ratio of one percent can halve the expansion versus an unrestrained specimen[38]. For well anchored, three-dimensional reinforcing cages, the core of the concrete member is restrained, thus reducing the overall expansion of the

member[37,38,43,47,48,56,57]. The Institution of Structural Engineers (ISE) reports that the accelerated methods used in laboratory tests result in higher internal stresses than would be triggered by the same level of expansion achieved at a lower expansion rate[37]. As a result of this expansion rate dependent behavior, it is possible that the accelerated methods used in the laboratory result in an elevated worst case scenario values for reductions of material properties.

2.2.2 Effects on Material Properties

The micro- and macro-cracking of concrete due to ASR can greatly affect the engineering properties of the material. Research conducted to quantify these effects is summarized in Table 2.2 and in the following sections. In several research papers it was noted that ASR introduces a tremendous amount of variability in engineering material properties. This variability can be regional, due to local materials, or even within the same structure[37,57-59]. Beyond the trend of variability, a size effect was noted in studies that examined this variable. The trend noted was that ASR's deteriorating effects decreased with increasing size of specimen tested[44,49]. For example, Ahmed et al. found that their large reinforced specimens tested for bearing strength concentrically had only a 3% reduction from ASR damage. Smaller reinforced specimens tests in the same arrangement showed a 35% reduction in bearing strength due to ASR induced expansions. The larger specimens were eight times (800%) larger than the smaller specimens.

Table 2.2: Summary of Engineering Properties Affected by ASR

Property		Effect (up to)	Reference
Plain Concrete			
Compressive Strength	Unrestrained	60% loss, others report no significant loss	10, 37, 38, 45, 49-52
	Restrained	Depends on restraint level, can retain the majority of compressive strength	8, 37, 38, 49
Tensile Strength		40-80% loss (depends on test method)	37, 38, 45, 47, 52, 59
Elastic Modulus		80% loss (effect less with restraint)	10, 37, 38, 45, 49-51, 58
Bearing Strength		15-50% loss (depends on specimen size and eccentricity)	43
Reinforced Concrete			
Axial Strength		With adequate reinforcement no reduction, else 30% loss	8, 37, 49, 57, 60
Flexural Strength		25% loss at high expansion, else no reduction	10, 37, 45, 50
Shear Strength		With adequate shear reinforcement no reduction	37, 61
Bond Strength		No reduction if well restrained by stirrups, else 50% loss	37, 44
Bearing Strength		13-45% loss (depends on specimen size and eccentricity)	43

2.2.2.1 Compressive Strength

The compressive strength lost due to ASR caused expansion in concrete varies by experimental procedure and type of compression test performed. Cube compression tests tend to give higher strength values versus cylinder tests for the same concrete and expansion level[37,52,59]. Unrestrained concrete specimens and core samples have shown reductions in strength versus unaffected concrete of thirty five to sixty percent[37,38,49,50,52]. Other results, such as those from Monette et al., show that although the stiffness is decreased, the ASR affected concrete cylinders still achieve similar strengths to undamaged concrete cylinders[10,45]. These values are all from concrete without reinforcing or external restraint. With restraint, ASR's effect is lessened[38,47,49]. For instance, in tests by Takemura et al. concrete columns with well anchored reinforcement showed reductions in axial load capacity of one to twenty percent versus their undamaged concrete counterparts[49]. The Institution of Structural Engineering (ISE) cast doubts upon

Takemura's results in their ASR technical guidance publication in 1992, saying that the ASR acceleration methods used altered the concrete's engineering properties. The reduction in deterioration effect from ASR, however is still well recognized. In both the ISE's technical guidance paper and the Canadian Standards Association's (CSA) 2000 publication, "A864-00: Guide to the Evaluation and Management of Concrete Structures Affected by Alkali-Aggregate Reaction", the importance of well anchored three dimensional reinforcement was stressed. The restraint provided by the reinforcing results in an internal prestressing force as the core concrete attempts to expand[37,38,49]. This prestressing mitigates the loss of compressive strength and can lead to an increase in ductility of the concrete member in the short to moderate term[49]. With the long term effect of creep or yielding of the reinforcing steel, the prestressing effect is diminished and thus any enhancement of behavior it provides should not be relied upon indefinitely[38].

Additionally, there is some dissent in the literature was to whether the compressive strength of unrestrained concrete will continue to decrease with increasing expansion or if it will reach some minimum strength value that is maintained despite increased expansion. Clayton in a 1989 report, indicated that when the concrete shows macro-cracking at approximately 0.05% expansion it has reached its minimum compressive strength[52]. This assertion is marginally supported by the 1992 Guide by ISE. The guide compiled available test data on reduction of material properties for varying expansions caused by ASR. The compilation showed cylinder strength reductions to be the same at 0.25% and 0.50% expansion[37]. Concrete cube strength tests, however, continued to decline with increasing expansion. Thus, the table could suggest a maximum reduction of forty percent of twenty eight day strengths. However, the plateau did not occur until five times the expansion proposed by Clayton and is not supported at all by the cube tests[37]. Monette et al. in both a 2000 and a 2002 report showed no reduction in compressive strength of concrete cylinders affected by ASR[10,45]. These results would support the theory that cylinder strengths can plateau. Ono and Taguchi, in a 2000 paper,

report the gradual reduction in compressive strength of a field structure afflicted by ASR over the eleven years it was monitored[51]. The expansion level of this structure was not provided in the report for comparison with other results.

2.2.2.2 Tensile Strength

The measurement of concrete's tensile strength is very sensitive to the test procedure used[37,38,45,47,59]. For instance in a series of plain concrete specimens tested by Clayton, the tension methods used were split cylinder, beam in bending, and gas pressure tension tests. The results versus twenty eight day strengths for these tests were twenty-five, fifty, and eight percent reductions, respectively[52]. Thus, the reduction in tensile strength by ASR induced deterioration varies depending on expansion level and test procedure, giving wide ranging reductions of unrestrained concrete tensile strength[37,38,52]. This variation makes assessment of residual tensile strength challenging to determine with confidence. Similar to the compressive strength reductions, the deterioration effects are substantially reduced when the concrete is restrained[37,38].

2.2.2.3 Modulus of Elasticity

Unrestrained concrete's modulus of elasticity can be drastically reduced versus undamaged concrete: Tests showed a reduction of thirty to eighty percent[10,37,38,45,49-51,58]. In the case of reinforced concrete, ASR's effect is much less. Moduli of elasticity back calculated from load tests were one and a half to three times the moduli found from core samples[38,50,62,63]. This discrepancy is explained because the core samples are removed from the restraint of the system and thus have internal stresses released when they are removed from their original environment[50,64].

2.2.2.4 Bearing Strength

One study focused on the bearing strength behavior of ASR affected concrete[43]. Ahmed et al. varied reinforcement, size of specimen, and loading arrangement in their study. The loading arrangement varied by size of bearing area and eccentricity. The study reinforced the idea that a well secured three dimensional reinforcing cage restricts both the

expansion and effects of ASR, as the highly reinforced specimens carried the highest loads. Still, bearing strengths were reduced versus the identical control specimens thirteen to fifty percent[43]. The largest reductions were observed in plain concrete blocks. As well, the larger of the two specimens sizes showed less expansion and less reduction in performance due to ASR. Ahmed et al. conjecture that it was harder for moisture to reach the interior of the larger specimens thus reducing the expansion and impact of ASR[43]. The author proposes that the confinement of the surrounding concrete offered additional restraint to the core concrete versus the smaller specimens. Other findings include that increasing either bearing area or eccentricity decreases the effect of ASR. Specimens loaded at an eccentricity had lower ultimate loads than identical specimens with purely axial loading. The reductions due to ASR expansion, however, were less pronounced in the eccentric loading scenarios[43]. Implications from this research could be that large, well reinforced concrete members loaded eccentrically are less affected by ASR when considering structural capacity.

2.2.2.5 Flexural Strength

Several studies showed that although ASR can dramatically decrease the elastic modulus and tensile capacity of plain concrete specimens, the reaction has very little effect on the flexural capacity of reinforced concrete beams[10,37,45]. One such study, by Monette et al., examined reinforced concrete beams under three different exposure conditions: unloaded, under static load, and cyclic loading. All specimens were submersed in a heated alkaline rich bath during the exposure period. Loading during exposure resulted in decreased ASR expansion. Regardless of expansion level, which reached about 0.3%, all of the beams had similar ultimate failure loads. The load displacement behaviors of the ASR affected specimens were nearly identical to those of the control specimens. Thus, even though stiffness of ASR affected cylinders was much lower than the control cylinders, the ASR induced damage had little effect on the member stiffness[10,45]. This study also examined the relationship between a petrographic damage rating index and the measured impact of ASR on material properties. The ASR induced damage ratings from 100 to

200, which are greater than the damage ratings assigned to the San Antonio Y samples. The same petrographer assigned damage ratings to each set of samples. The Monette et al. study concluded that the damage rating index values corresponded to the elastic modulus loss, but no relationship could be established with the ultimate flexural load or the cylinders' compressive strengths[10].

2.2.2.6 Shear Strength

Studies have shown that with adequate shear reinforcing, there is no loss in shear strength for members affected with ASR[37,61]. The ISE stated in its summary of ASR research findings that so long as there is a 0.2% shear stirrup reinforcing ratio ($\rho_V = 0.002$) then ASR has no effect on shear capacity[3]. A more recent study at the University of Texas at Austin examined the potential effect of ASR or DEF on the shear capacity of bent caps[61]. This study used shear stirrup ratios of 0.15% and 0.31% ($\rho_V = 0.0015$ and $\rho_V = 0.0031$) and had expansions of up to 0.54% at the time of testing. These beams showed no reduction in shear capacity versus the non-reactive control beams[61]. That the shear reinforcing ratio of 0.15% also had sufficient capacity to overcome the detrimental effects of ASR/DEF deterioration would indicate that the ISE's value of 0.2% minimum shear stirrup reinforcing is somewhat conservative.

2.2.2.7 Loss of Bond and Delamination

Cracking induced by ASR can cause delamination of the cover concrete and loss of reinforcement bond. Cracks near the main reinforcing of a member that are wider than 0.3 mm can indicate delamination at the plane of reinforcement[37]. The loss of concrete cover can result in corrosion of the reinforcing steel or, in the case of stirrups with ninety degree hooks, loss of core confinement[41]. In the CSA's 2000 ASR management guide, it noted that a 0.6% expansion of the member can cause loss of bond[38]. Ahmed et al. examined the effect of ASR on the effectiveness of lap splices in reinforced concrete beams[44]. The specimens in this study reached expansions of 0.3 to 0.5%. The study found that for very short lap lengths, eight times the bar diameter or less, ASR had very

little influence as the insufficiency of the splice controlled the load carrying capacity. Once a lap length of twelve times the bar diameter was reached, the ASR affected specimens generally showed a twenty percent reduction in ultimate capacity versus the control specimens. The longest lap length tested was thirty two times the bar diameter, where the ASR damage caused an 18% reduction in strength compared with the control specimen[44].

2.2.2.8 Natural Corrosion Protection

ASR reduced the natural corrosion protection that concrete affords its reinforcing in two ways: cracking and reduction of internal pH. Cracks, especially wide cracks (>0.3 mm) can provide easy access for moisture, increase chloride ingress, and speed the rate of concrete carbonation[37]. In addition to the pH drop associated with carbonation, the reaction triggering ASR will also lower the pH of the concrete pore solution through the binding of alkaline ions in the reaction gel[37,38,41]. The loss of pH can trigger corrosion of the reinforcing steel. The naturally highly alkaline pore solution in concrete, with a pH of 13.2 or higher, typically protects reinforcement by creating a passive film over the surface of the bars[37,41,65]. With the drop in pH or when under attack from chloride ions, the passive film breaks down and the reinforcement becomes susceptible to corrosion[65]. The corrosion of the reinforcing steel reduces the steel cross sectional area, and thus the capacity of the reinforcing steel. Therefore, corrosion of reinforcing can lead to significant structural problems for reinforced concrete members[65].

2.3 DELAYED ETTRINGITE FORMATION (DEF)

2.3.1 Mechanism

Ettringite formation is a normal occurrence in the hydration of cement. As shown in Figure 2.6, ettringite, a needle-like crystal, forms and surrounds cement grains during the first few hours of hydration. Ettringite slows the hydration process and thus prevents flash set and increases the workability of the fresh concrete[11,41]. This early ettringite formation, also known as primary ettringite, helps provide early strength to the

concrete[36]. Ettringite formation in the first few days of hydration is a key feature of shrinkage compensating concretes[11].

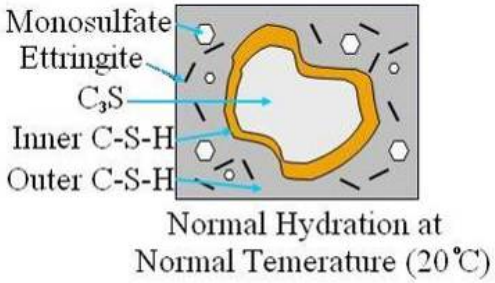

Figure 2.6: Ettringite Surrounding Cement Grain in Normal Hydration (sketch based on reference 41)

DEF, by definition, is ettringite formation that is delayed past the normal formation timeframe. This formation occurs months or years after concrete casting[4,11,36,41]. Figure 2.7 is a diagram of the basic DEF mechanism. In order for DEF to occur, the concrete must reach an internal temperature of at least 158 °F (70 °C) during the initial curing period[4,11,12,21,22,31-35,41,42,66]. At such elevated temperatures, two mechanisms occur to prevent primary ettringite formation. In one mechanism, the ettringite crystals that form are dissolved into incongruous pieces and are essentially trapped in the inner ring of calcium silicate hydrate (C-S-H), a cement reaction product formed around non-hydrated cement grains[4,11,35,41]. The other mechanism also involves C-S-H. The elevated temperatures cause the C-S-H rate of formation to significantly increase. During formation the C-S-H adsorbs sulfates and aluminates, the ettringite building blocks. The C-S-H formation thus prevents ettringite formation by depleting available reactants[4,21,31,34,35,66]. At this point, the stage is set for DEF, but its appearance will only occur if conditions are favorable. Favorable conditions include sufficient moisture in the concrete and diffusion of adsorbed reactants from the C-S-H[4,21,22,31,32,34,41,42].

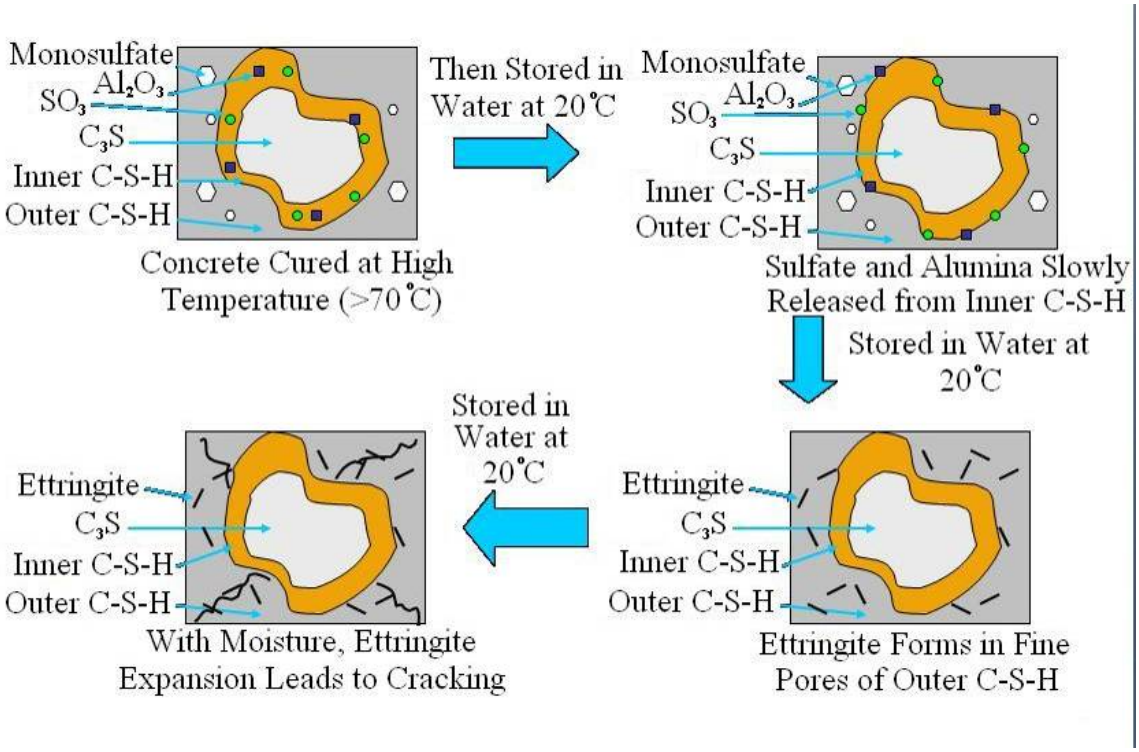

Figure 2.7: Basic DEF Mechanism

(sketch based on reference 41)

Moisture is needed in order to facilitate the diffusion of the reactants out of the C-S-H. Sulfates diffuse out of the C-S-H to try to reach equilibrium with the pore solution. When sulfates react with aluminates to form ettringite the sulfates are removed from the pore solution, which recreates the imbalance and triggers additional diffusion[4,21,22,31,32,34,41,42]. The exact mechanism governing the expansion created by DEF continues to be debated in the literature[4,12,35,41,66]. Two main theories have emerged from the discussion. One theory proposes that as the ettringite precipitates, it forms in available openings. These openings include gaps between aggregate and cement paste, air entrainment pores, and any cracking already present in the concrete. The theory postulates that as the crystals try to expand beyond the width of the openings, they apply pressure to the concrete matrix causing cracking[11,35,66]. The other main theory acknowledges that ettringite is an opportunistic crystal, which grows in these gaps but does not cause expansion there. Instead, the proponents of this other theory, propose that

many small ettringite crystals form dispersed throughout in the cement paste. These small crystals form in confined spaces and thus apply pressure on the surrounding paste from formation[20,21,32,35,66]. Brunetaud et al. proposed in 2004 that the mechanism is likely a combination of these two theories. The combined theory postulates that the diffused ettringite initiates cracking and the expanding larger crystals propagate the cracks[35].

As indicated by the diffuse ettringite group, not all ettringite that forms in concrete causes expansion and deterioration. In typical concrete, the crystal is merely opportunistic and forms where there are already voids and cracks in the concrete. Ettringite is trying to reach a low energy state by forming large crystals, and will conserve energy by growing in large openings before it creates its own space. As a result of this opportunistic quality, cracks full of ettringite crystals are often observed during petrographic investigation when other mechanisms are the primary cause of distress[20,32,41].

2.3.2 Effects on Material Properties

Research has focused on trying to understand the mechanism driving DEF rather than studying its effects on engineering material properties. This research focus is understandable in that learning how to treat the effect and prevent it in the future requires knowledge of the causes of the deterioration. As well, DEF has typically been a secondary reaction occurring in concrete members already affected by ASR. Thus, the concentration of research on the engineering material property effects has been on ASR's influence[3]. A few research papers on the effect of DEF have emerged, however, and their findings are summarized here.

Bergol et al. used ultrasonic pulse velocity and notched beam tests to correlate deterioration with the dynamic modulus and apparent fracture toughness of concrete, respectively. The researchers tested six different concrete mixture designs. Table 2.3 shows the composition of these mixtures, C1-C6, which varied the amount of tri-calcium aluminate and sulfate components. These two cement components are necessary to

develop DEF, however there is no established relationship between the amount of these ingredients and expansion level from DEF[4]. The specimens were steam-cured at 95 ^{o}C for twelve hours. In the results, the fracture toughness and ultrasonic pulse velocity values are only given versus time, as shown in Figure 2.8 and Figure 2.9 respectively, not expansion. Thus, while one can surmise that the deterioration should increase with time, the reader cannot see a clear trend in the correlation of material property as a measure of DEF onset. The researchers were examining whether monitoring dynamic modulus or fracture toughness would be a good indicator of affectation by DEF. It was expected that, with the onset and propagation of DEF, the resulting damage to the concrete would result in reduced toughness. The fracture toughness is a measure of the energy required to break the concrete. Thus, the researchers were expecting to see the fracture toughness values decrease with increasing DEF damage, although to differing amounts due to the differing cement chemistries. Instead, as Figure 2.8 shows, some specimens had increasing fracture toughness with time, while others decreased, and a few first decreased and then began to increase fracture toughness with time. The researchers thus concluded that DEF did not have a strong influence on fracture toughness. With increasing DEF induced damage it was also expected that the ultrasonic pulse velocities would decrease. However, the ultrasonic pulse velocity, which is used to calculate dynamic modulus, for several of the specimens decreased with time and then began to increase as shown in Figure 2.9. As well, two of the specimens, C2 and C5, showed steadily increasing values, which were not expected for concrete with DEF. The researchers concluded that the cracks were filled or began to self heal, which would result in an increase in the ultrasonic pulse velocity. Thus, they concluded that dynamic modulus test could yield misleading results[30].

Table 2.3: Cement Composition Variables (from ref. 30)

Specimen	C1	C2	C3	C4	C5	C6
SO_3 (%)	2.86	1.9	4.17	3.92	3.52	4.04
C_3A (%)	8.14	0.99	7.9	0.9	5.49	7.33

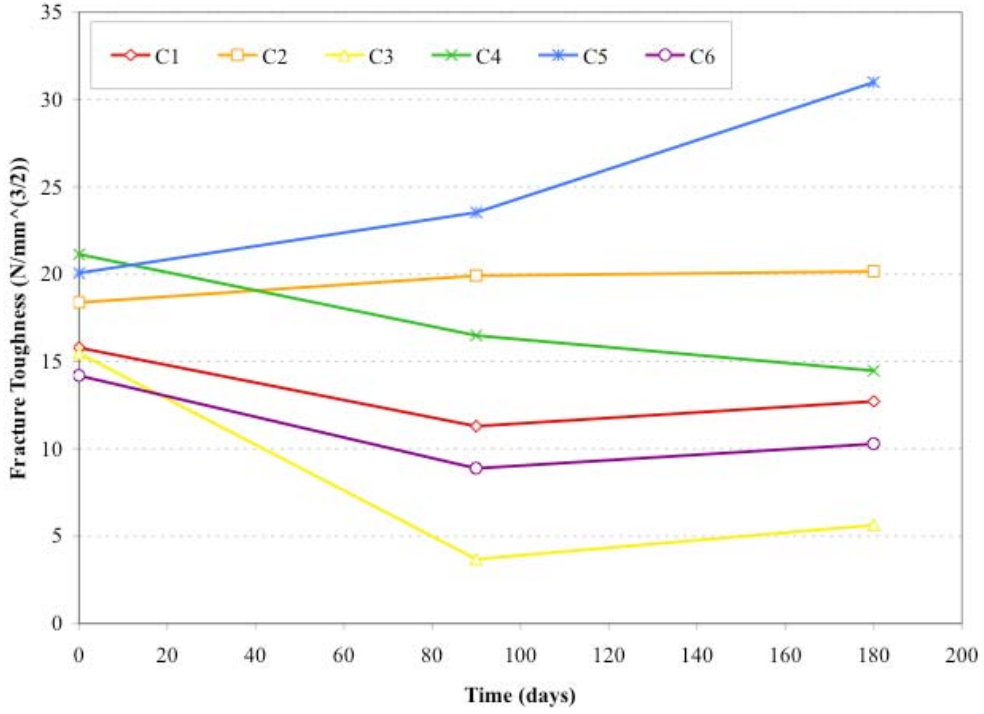

Figure 2.8: Apparent Fracture Toughness versus Time (from ref. 30)

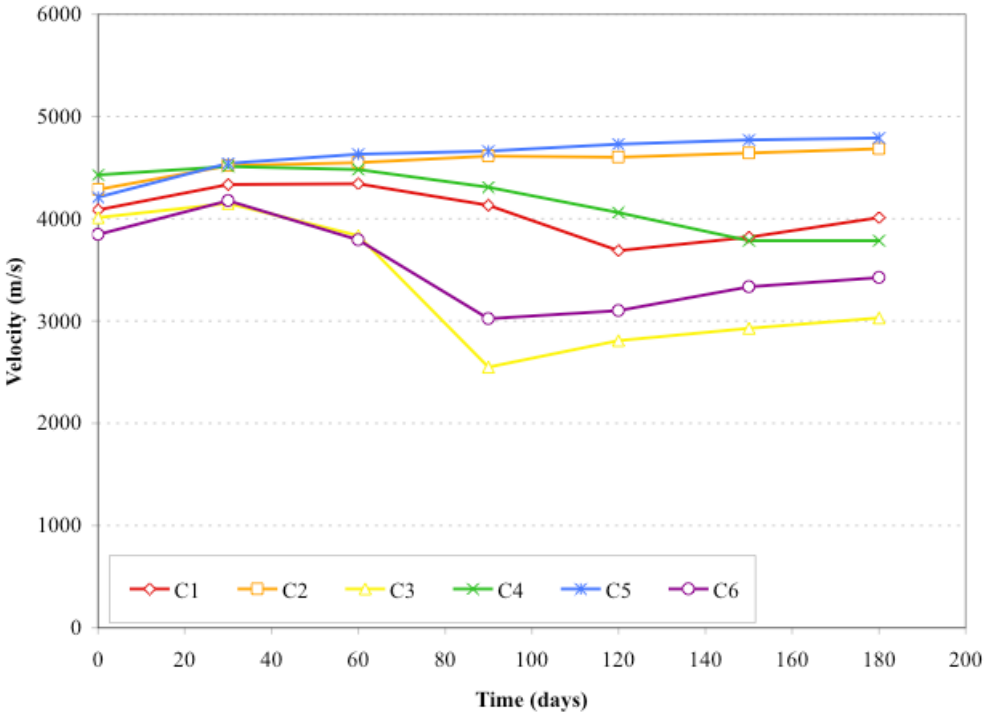

Figure 2.9: Transverse Ultrasonic Pulse Velocity versus Time (from ref 30)

Yan et al. were interested in the effects of restraint on the development of DEF. The researchers were driven by concerns that with massive concrete pours for foundations four or more meters thick in China, that the internal hear of hydration would certainly exceed the threshold value. Therefore, they wished to find if the concrete in the center of the foundations would be affected by the restraint and moisture restrictions offered by the surrounding concrete. As shown in Figure 2.10, specimens were cast between two steel plates, which were welded to a steel rod that ran through the center of the concrete. The steel plate system restrained the concrete longitudinally. The specimens, except for the control, were heat treated to a temperature profile observed in a massive concrete pour. As well as this heat treating, three moisture conditions were examined: sealing the concrete surface so that only internal humidity was available, a fog room offering high humidity, and under water. The results are shown in Figure 2.11 to Figure 2.13. Three specimens were initially cured in each of the three different moisture conditions. The specimens were then rearranged so that the long term exposure groupings of three specimens contain one specimen each from the initial groupings. The results are given in the initial curing groups. For example, Figure 2.11 shows the expansions of all the specimens that were initially cured with sealed surfaces. The legend in the figures indicates the long term curing conditions for each specimen. As a general trend observed in all figures, specimens with sealed edges in long term exposure shrank. These data points are marked with an "x." As well, regardless of initial curing condition, specimens stored underwater for long term exposure expanded. These underwater long term specimens are marked with triangles in all figures. The control specimen, which is marked with a square in all figures, was always exposed to a fog room environment. Therefore, the control cannot be used to compare with the sealed or submerged specimens. Without a control experiencing similar moisture conditions, one cannot isolate the effect of DEF in the system. The heat-treated specimens that were in the fog room for long term exposure showed little net expansion. These date points are marked with circles. After an initial expansion, peaking at approximately a month of exposure, these specimens shrank back to near their initial length. The control specimens, which

were also in a fog room exposure, experienced a very small, gradual expansion over the same time. Thus, for the high humidity environment, it would appear that sufficient restraint prevented significant DEF expansion. The researchers noted that although some specimens exceed four hundred microstrains, where one would expect to see cracking, no cracking was observed. Thus, the research team concluded that DEF does not always result in the destruction of affected structures[22].

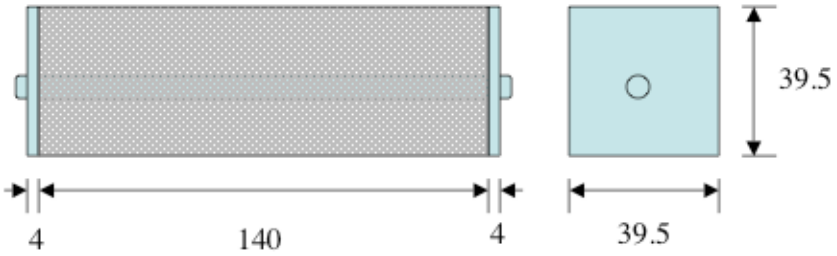

Figure 2.10: Restraint Arrangement (dimensions in millimeters)[22]

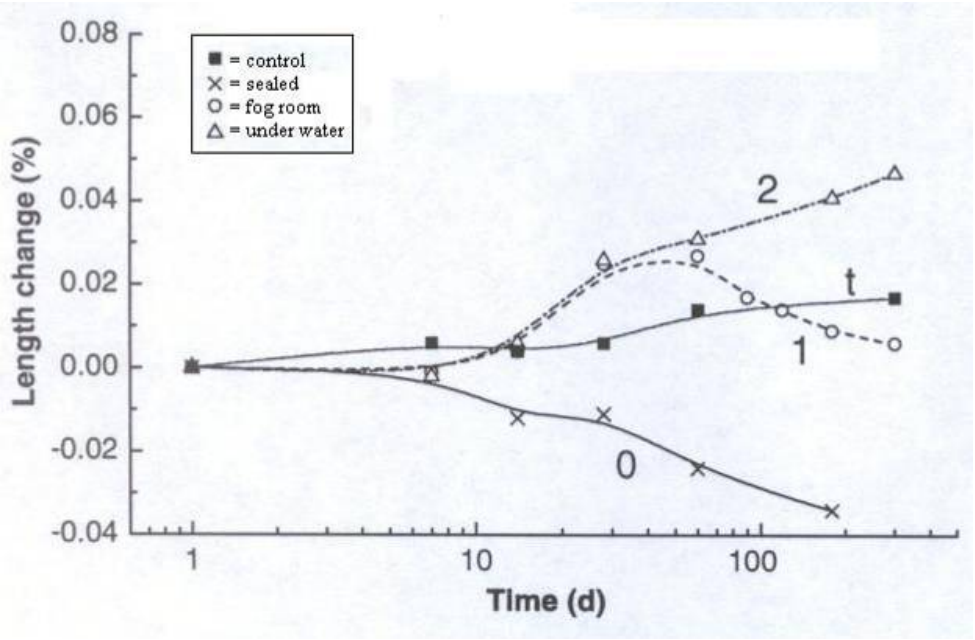

Figure 2.11: Initial Curing with Sealed Edges (from ref. 22)

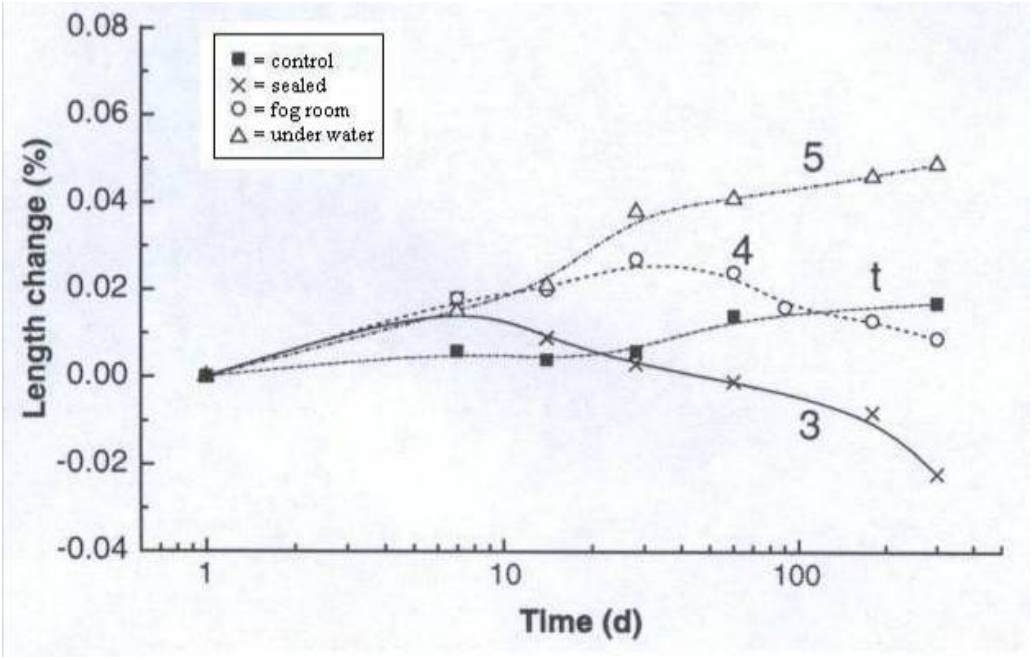

Figure 2.12: Initial Curing in Fog Room (from ref. 22)

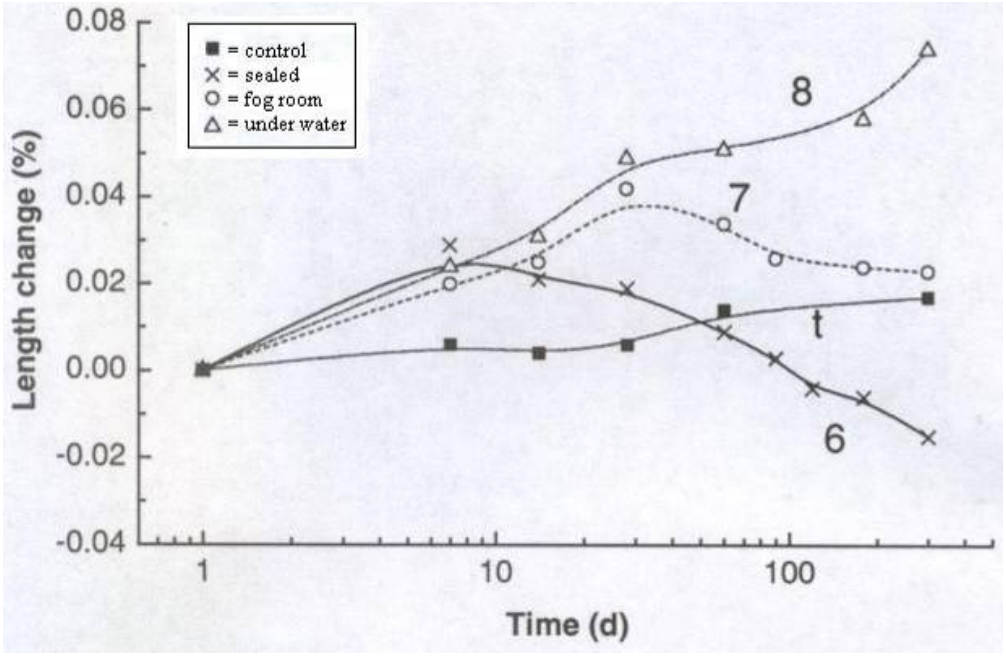

Figure 2.13: Intial Curing under Water (from ref. 22)

Zhang et al. heat treated mortar bars during curing in order to induce DEF. The research team wanted to study several effects of DEF including dynamic modulus and expansion. The specimens were suspended above water in order to be in a humid environment without leaching due to water contact. The dynamic modulus was determined by measuring the transverse resonance frequency of the mortar bars. For specimens showing at least 0.13% expansion, the dynamic modulus was reduced. As shown in Figure 2.14, over the 900 days of observation a 10-40% reduction in dynamic modulus was observed in DEF affected mortar bars. From the available results, the researchers developed a numerical correlation between expansion and reduction in dynamic modulus, which is shown in Figure 2.14[42].

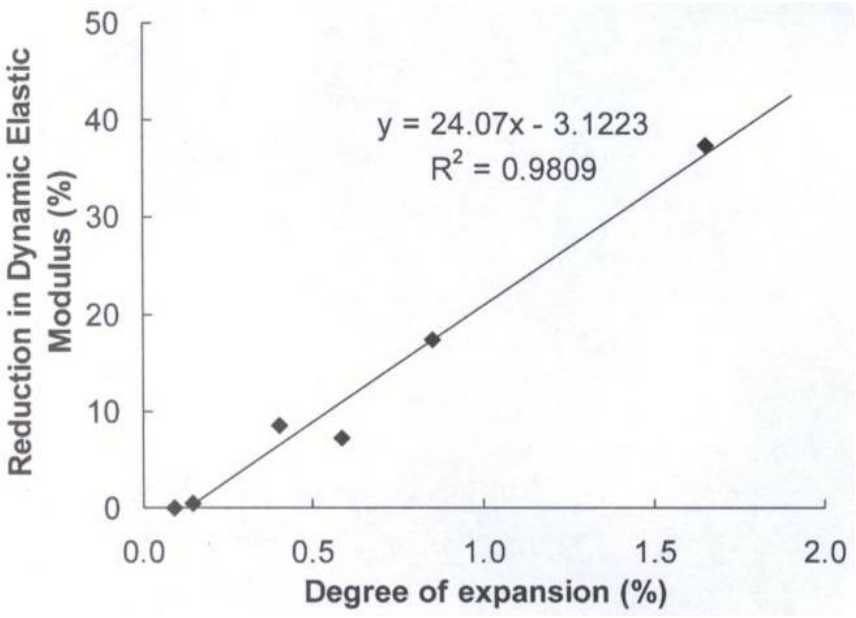

Figure 2.14: Relationship between Loss of Dynamic Modulus and Expansion in equation, y = % reduction in modulus and x = % expansion (from ref. 42)

These few research papers, while an important start, do not give a full picture of the potential effects of DEF. More research is needed in the area of engineering material properties of DEF affected concrete.

2.4 LOAD TESTING

A concrete bridge with ASR caused deterioration is not a unique phenomenon to the San Antonio Y[37,38,47,50,51,57,60,67]. Other countries have noticed ASR in bridge substructures and conducted analyses and load tests of the structures in order to ensure their continued ability to predict capacity. So long as the substructures still behaved elastically, their capacities could be predicted and checked against the loading requirements for the bridge. With this comparison available, bridge officials could determine whether the bridge could remain in service. As well, load testing a structure remains the ultimate determination of behavior. Measuring the structure's response to a given load and then its recovery once the load is removed gives the most accurate representation of the load capacity[8,38,50,56-58,60,62,64,67-69].

2.4.1 South African Experience

Figure 2.15 shows a bridge portal frame supporting a double-decker elevated highway in Johannesburg, South Africa constructed in 1963, which had cracked significantly in one corner by the late 1970s[63,68]. The portion showing the most cracking was not covered by the bridge deck and it also had an internal drain pipe. Through petrographic analysis it was determined that the cause of the deterioration was ASR. The bridge owner considered the level of cracking to be alarming the general public and sought recommendation as to repair or rebuild the structure. The investigators performed a load test to determine if the bridge was still behaving elastically. They used the results of their investigation to recommend further action on the maintenance of the bridge. Before the load test was conducted, cores of the concrete were taken from undamaged concrete in the frame and from the ASR affected area. Modulus of elasticity tests on the cores showed a reduction in stiffness in the ASR affected section compared to the undamaged concrete: 11 GPa and 32 GPa, respectively. The researchers chose an intermediate modulus value of 18 GPa for the analysis for the frame behavior under load. As well, the analysis considered both a best and worst case scenario for behavior of the joint. The best case scenario assumed that the joint would continue to fully transfer moments and

thus behave as a fixed joint. For the worst case it was assumed that the joint could transfer no moments and thus was modeled as a pinned joint. The analysis further assumed an elastic response from the bridge[62-64,68].

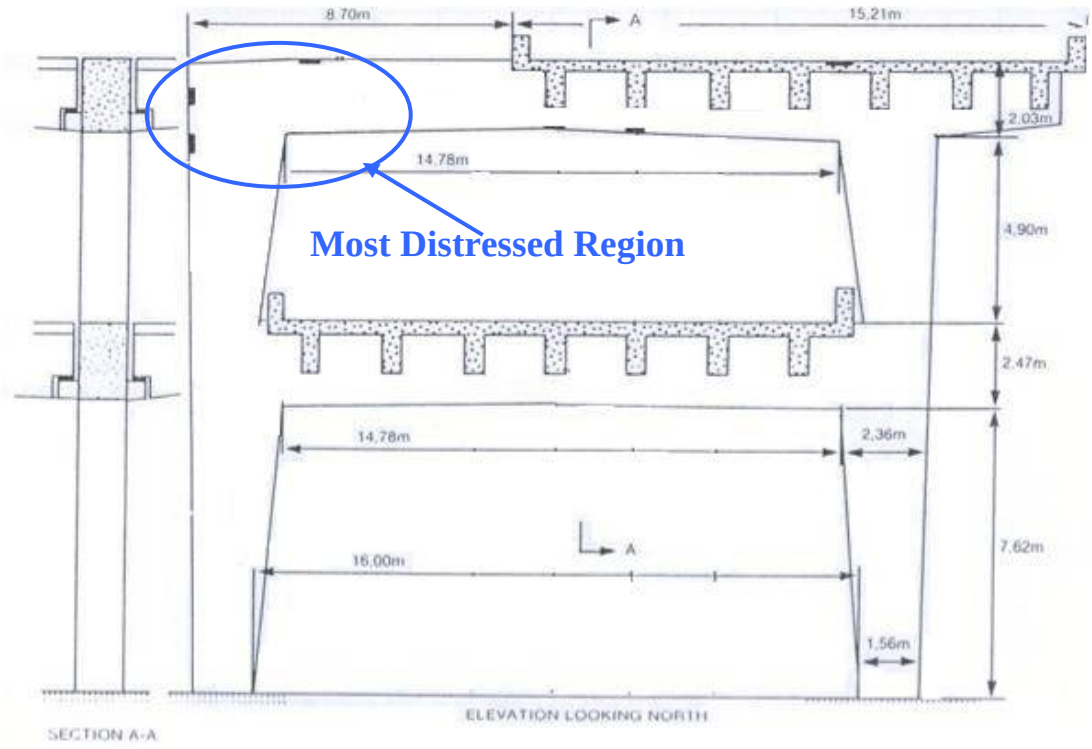

Figure 2.15: Johannesburg Portal Frame[64]

The load test involved filling the upper deck highway span that is supported by this portal frame with trucks filled to the legal limit. Only 84% of the design live load was reached as the span could hold no more trucks. During the test numerous values were measured including: deflections of the upper and lower decks, rotations of the frame, and both steel and concrete strains. These values were compared to the analysis predicted behavior. As well, the values were monitored during the load to watch for any non-linear behavior of the bridge[62-64,68].

From the results of the load test, it was found that the behavior of the bridge was still elastic. As well, the frame responded as a stiffer structure than was assumed in the

analysis. The frame was thus considered perfectly safe although it was recommended to reduce the moisture coming in contact with the concrete. This reduction was to be manifested by the closing of the internal drain and coating of the concrete[64]. The same frame underwent a second load test six years later to allay concerns about the continued safety of the frame. In the later test, the bridge again behaved elastically and with more stiffness than assumed in analysis. Compared with the first load test, the second test showed a slight amount of deterioration through reduction of stiffness in its response[62]. When back calculated from the load test result, the actual stiffness of the bridge during both tests indicated a modulus of 24GPa[63]. The researchers' conclusion was that although ASR can induce a considerable amount of cracks in the concrete, it does not significantly reduce the performance of the structure. This conclusion also notes that actual loads are typically far lower than design loads so that a slight reduction in capacity would not affect the structures ability to carry normal loads[62,64,69].

This deteriorated corner of the portal frame was demolished and rebuilt in 1991[68]. The bridge owner agreed that the testing showed there was adequate structural capacity in the frame. The owner was not eager to engage in long term monitoring of the frame and it was under pressure to act decisively in resolving the situation[63].

2.4.2 Japan – Hanshin Expressway

The substructure of the Hanshin Expressway more closely resembles the substructure of the San Antonio Y than does the South African portal frame previously discussed. Some of the Hanshin Expressway's column capitals of the single column supports exhibited pervasive map cracking in 1982, as shown in Figure 2.16. Core samples taken from undamaged concrete and the affected area showed that the concrete had lost 35% of its strength and 78% of its stiffness due to ASR induced cracking. This drastic reduction in the engineering properties of the concrete in the structure greatly concerned the bridge officials. An analysis of the predicted behavior of the columns and a subsequent load test were used to determine the ASR's effect on the structural behavior of the columns[50].

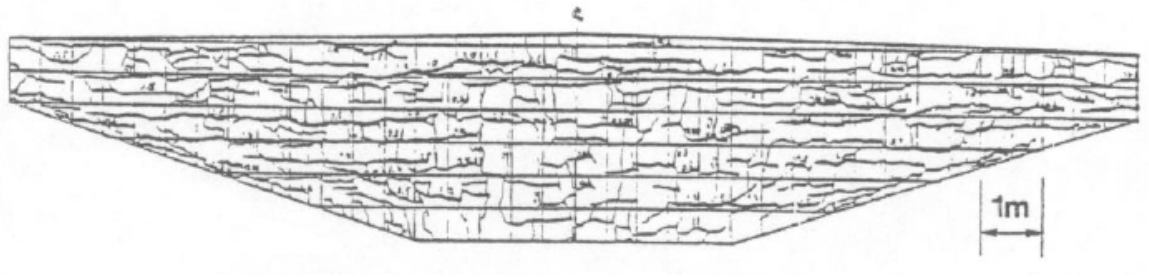

Figure 2.16: Cracked Column Capital from Hanshin Expressway[50]

As in the case in South Africa, the reduced stiffness and strength values were used in an elastic analysis of the bridge column. The subsequent load test was compared with the predicted values to determine the accuracy of the calculations. Both undamaged and ASR affected columns were analyzed and loaded. The measured deflections of both undamaged and ASR affected columns were very similar to the predicted behavior of the undamaged columns. As well, these difference in deflections between undamaged and ASR affected concrete varied less than 0.2 mm. Thus, the investigators concluded that although material properties measured from cores showed a considerable reduction in stiffness, the structure retained nearly all of its original stiffness. As well, they concluded that ASR caused mostly cosmetic damage. The columns were epoxy injected and then coated with a membrane to prevent additional moisture ingress. The sealing of the columns was intended to halt the introduction of additional water, which could further ASR induced expansion of the concrete or induce corrosion[50].

2.4.3 French Experience

The A26 highway in Northeast France, which was built in the 1970s, has 224 bridges, several of which are suffering from ASR. As a result, the bridge owner (SANEF) developed a management plan to assess the damage caused by the ASR and to investigate further remediation required. As it was standard practice to load test these highway bridges upon completion of construction, a baseline behavior during load testing is already on record. Thus, load testing an ASR affected structure can easily show deterioration compared to the baseline behavior. The load test results, along with the

predicted behavior from analysis and results from both petrographic examination and further expansion testing on concrete cores are used in making repair decisions. In the case study presented by Baillemont et al. in a 2000 paper, the bridge columns exhibited significant cracking from ASR induced expansion. This bridge appeared to be at the end of the expansion process, as the cores did not exhibit significant expansion during testing. As well, while the load test showed one area of the bridge with minor reduction in stiffness, less than 10%, the overall structural stiffness was very good. Thus, the bridge repair did not involve strengthening, but instead applying a coating to prevent further moisture ingress[60].

2.4.4 Other Load Testing Uses

2.4.4.1 Non-bridge Applications

Load testing of ASR affected structures has not been limited to bridge applications. For instance, Poole et al. reported testing an ASR affected column removed from a covered water reservoir, Wood et al. load tested affected parking decks, and Bae et al. tested affected foundations of high mast light poles[46,58,70]. The first two papers detailed load testing that had taken place in the UK and the third paper discussed load testing foundations in Houston, Texas (USA). From all of these load tests it was found that ASR induced damage caused cracking in the cover concrete, but did not significantly reduce the capacity of the sections.

2.4.4.2 ASR Management/Assessment Plans

The literature also finds numerous references to load testing as part of assessment and management plans for ASR affected structures. In additional to the French case discussed in section 2.4.3, several other countries are represented. A paper by Okada details the Japanese approach to assessment and management[71]. Wood et al. gives the perspective of a consulting engineering on the assessment and monitoring for structures in the UK[58]. Fournier et al. authored a publication by CANMET (Canada Centre for Mineral and Energy Technology) on the management of ASR affected structures in

Canada[8]. Additionally, AASHTO (American Association of State Highway and Transportation Officials) gives some guidance on assessment of the structural effects of deterioration in its general guide to load rating transportation bridges in the USA[72]. Some common themes emerge from the examination of these various plans. First, there is the need to establish that the distress observed, typically identified through routine inspections, is actually caused by ASR. After the cause of damage is determined, then an assessment of damage already caused to the structure is conducted, and often accelerated expansion tests on cores establish the likelihood of additional ASR caused damage. Analysis of the structure using material properties taken from the core samples is often verified by load testing. Load testing is used to definitively answer questions as to how the structural behavior has changed and if sufficient capacity remains[8,58,60,71]. As well, load testing is typically recommended when the engineer investigating the structure has reason to believe that the analytical model is not reporting the actual value[72]. The engineer may be led to this decision if the analytical model used an assumed concrete value that is suspected of being low, if secondary elements, such as concrete railings, are expected to contribute favorably to the structural stiffness, or if deterioration of the concrete makes the assumed concrete properties of the analysis inaccurate[72].

2.5 AASHTO LOAD CASES

Load cases are combinations of loads expected on a bridge at any given time. These expected loads include permanent loads such as self weight of the structure and the weight of pavements and guide rails. The design loads also considering changing loads, such as the weight of traffic and the force from wind blowing against the structure. The different prescribed load combinations detailed in building codes and design specifications are all calculated to determine which particular load case creates the greatest force, or demand, in the structure. This largest demand governs the design, as the designers want to insure that the structure can withstand this load case. The San Antonio Y was designed and constructed under the AASHTO 1983 Standard Specification for Highway Bridges[3]. Kapitan[3] identified the governing load case for the

columns investigated in this project to be AASHTO Load Case III with two lanes. During the design of the San Antonio Y, the designers considered transverse and longitudinal moments from the load case separately. They, however, did not consider the biaxial effect of the moments in these directions being applied at the same time[3]. AASHTO 1983 Load Case III is illustrated in Figure 2.17 through Figure 2.20. This load case considers a combination of dead loads (permanent loads) and live loads (moving traffic). The live load, as defined in the 1983 code, is either an individual truck load or a distributed lane load with a single concentrated load, as shown in Figure 2.17 and Figure 2.18 respectively, whichever creates the greatest load demand[73]. The truck load is idealized as a group of point loads representing the trucks axles. These loads are located along the deck wherever they will create the greatest demand. As well, Load Case III considers the effect of wind on the structure, wind on the traffic that is driving on the structure, centrifugal forces of traffic following a curve in the structure, and braking forces[3,73]. These forces create bending moments in the bridge column in both the transverse (perpendicular to the direction of traffic) and longitudinal (parallel to the direction of traffic) directions, as shown in Figure 2.19 and Figure 2.20, respectively. Although the original design for the San Antonio Y columns considered centrifugal forces, the section of highway investigated for this research program is straight and thus the centrifugal forces approach zero. This load case does not directly correspond to a specific load case under the current AASHTO specifications. The load case used for design most closely matches the 2005 AASHTO LRFD Strength V load case, which considers the same load components but with a slight variation in load factor[74]. As well, in the 2005 code, the live load is a combination of both the design truck and a distributed lane load[74]. The AASHTO Manual for Condition Evaluation and Load and Resistance Factor Rating (LRFR) of High Bridges only requires the Strength I be considered when evaluating an existing bridge's substructure. The load case of Strength I considers dead and live loads but neglects wind loads[72].

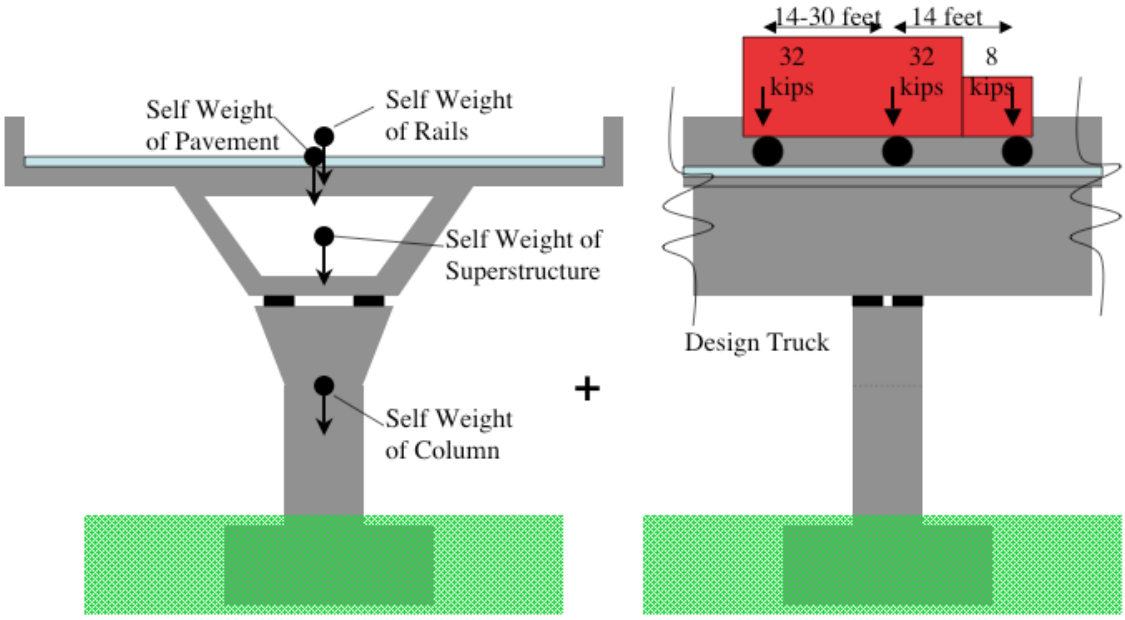

Figure 2.17: AASHTO Load Case III, Axial Load with Design Truck

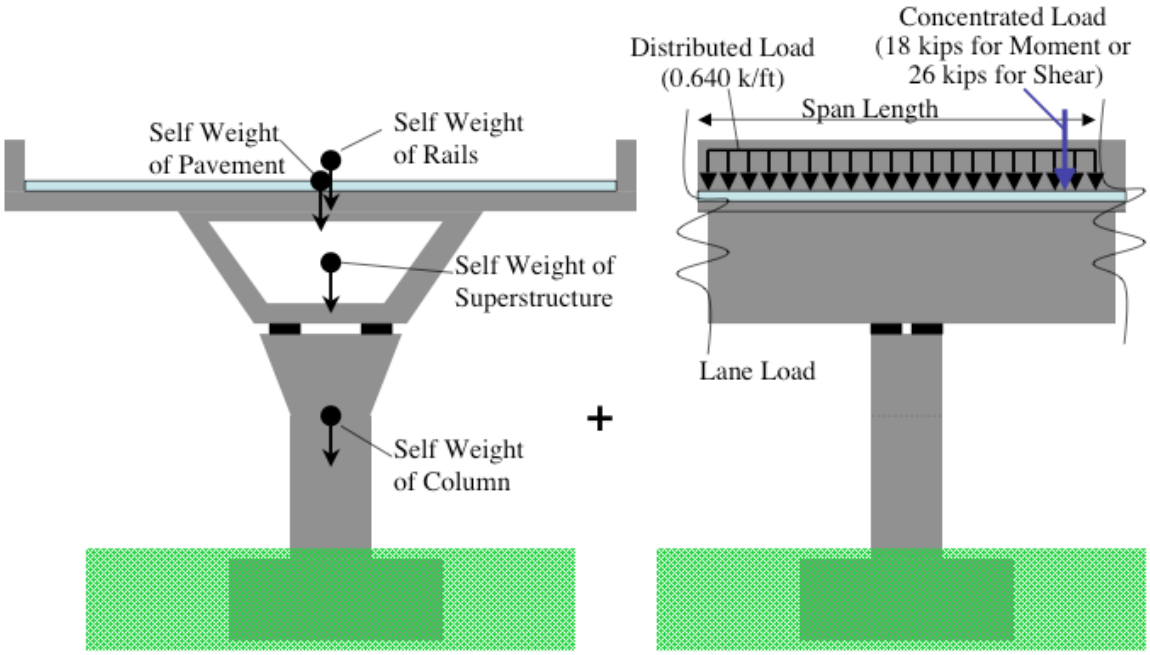

Figure 2.18: AASHTO Load Case III, Axial Load with Lane Load

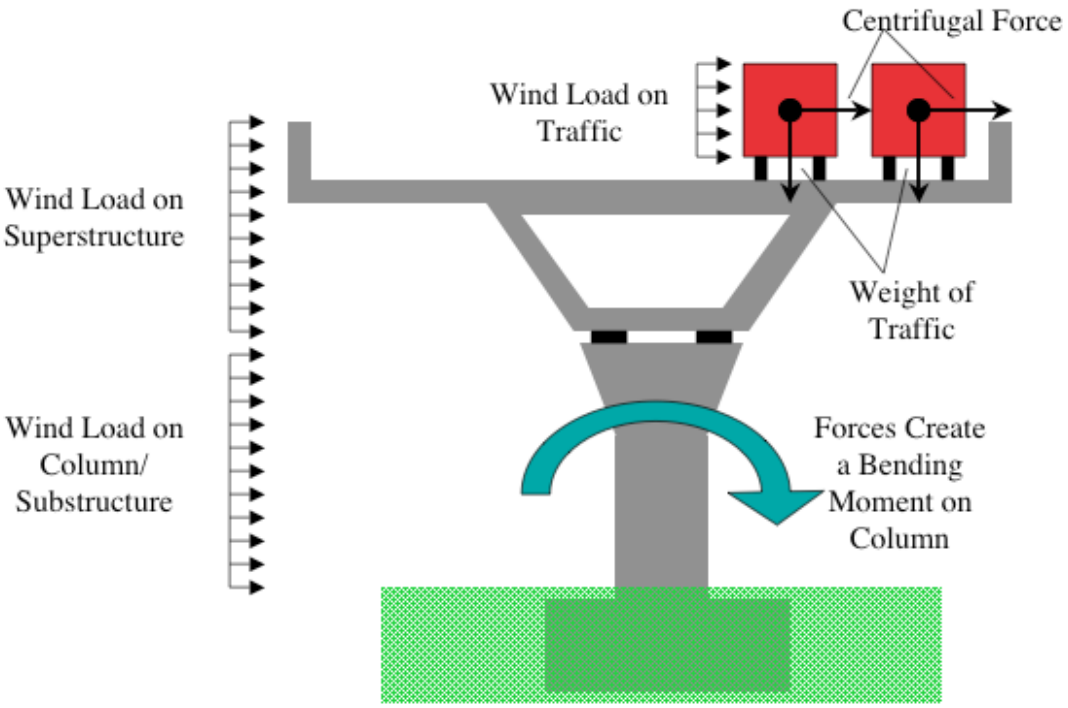

Figure 2.19: AASHTO Load Case III with Two Lanes, Transverse Moment

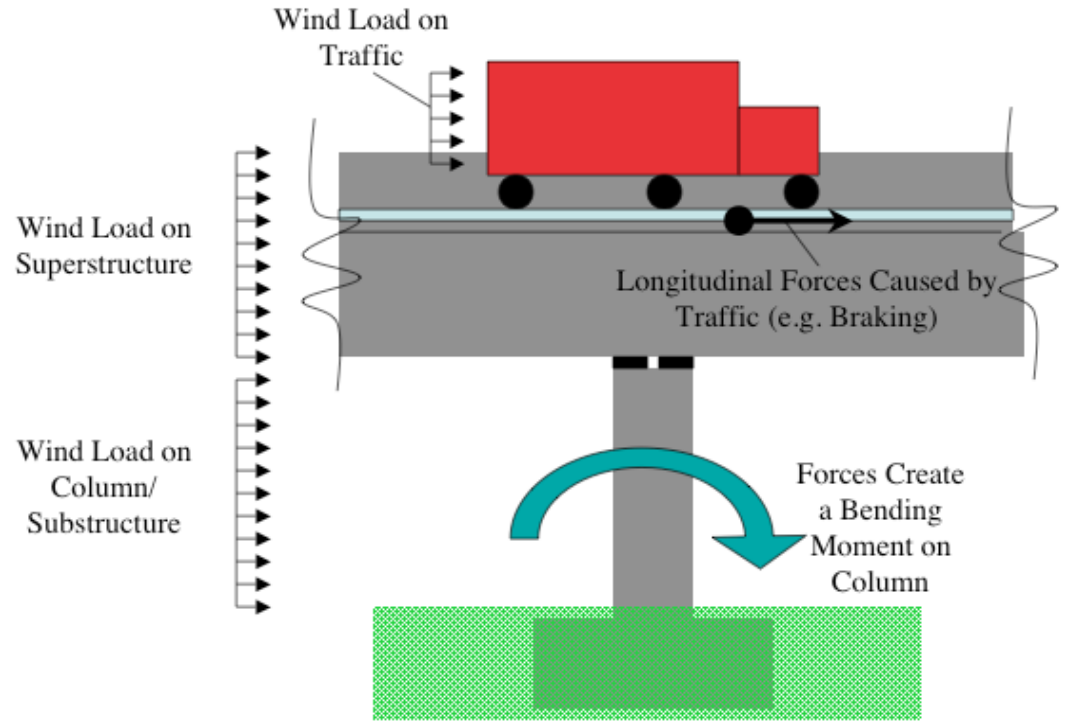

Figure 2.20: AASHTO Load Case III with Two Lanes, Longitudinal Moment

2.6 COLUMN REPAIR/STRENGTHENING

In order to increase the life expectancy of deteriorating bridge columns a repair or strengthening retrofit is often needed[8,75-90]. There can be many reasons that a repair is needed. These reasons include addressing a material defect or degradation (such as ASR/DEF attack), increased load demand on the structure, and seismic upgrades. For the case of columns, the driving need for the first two reasons is the increase of axial load. Seismic retrofit largely focuses on the need to increase ductility of the column in order to increase lateral displacement capacity[8,75-77,80,81,83-87]. This research program is centered on bridge columns with material degradation and therefore the repair literature reviewed focused on increased axial capacity from the repairs.

As the focus of repairs for this research study was to increase axial capacity, the repairs were designed for a specific capacity, as described in Chapter 4. The confinement provided by repairs intended to increase axial capacity can also suppress future ASR or DEF induced expansion. A study at the University of New Brunswick found that DEF expansion can be suppressed by 300-450 psi of confining pressure[5]. Research at the University of Texas at Austin suggests that similar levels of confinement can restrain ASR and DEF induced expansions[5]. This work was completed using steel fiber reinforced concrete and thus additional study is needed to quantify a threshold level of external condiment to provide adequate restraint to suppress ASR[5]. For an active repair, such as post-tensioning, inducing an average pressure of 450 psi should prevent future ASRDEF expansion. Passive repairs, which introduce confinement as the concrete expands, should be designed to achieve this threshold pressure with 0.04% expansion[5]. This level of expansion is viewed as the limit of acceptable expansion in concrete[5].

2.6.1 Packing Strap Repair

2.6.1.1 Description

Packing straps were developed for use in the shipping industry to hold freight to pallets[75]. These straps are commercially available. Figure 2.21 shows a packing strap applied to a concrete specimen for testing. The basic premise behind a packing strap is that a loop of thin metal (or in some cases plastic strapping) is looped around the item to be fastened, tightened, and then held in place with a clip. For this research project, the straps are used to provide lateral confinement of the column capital. After looping into place, the ends of the loop are overlapped and pulled to remove slack from the system. Packing straps can either be tightened with hand tools or mechanized tensioning tools. Hand tools, such as the tension tool shown in Figure 2.21, can get a snug-tight fit, while mechanized tightening can introduce additional force to the system by post-tensioning the strap before fastening the ends together. The overlapping strap is held in place with a crimped metal seal, which shows up orange against the black steel straps in Figure 2.21.

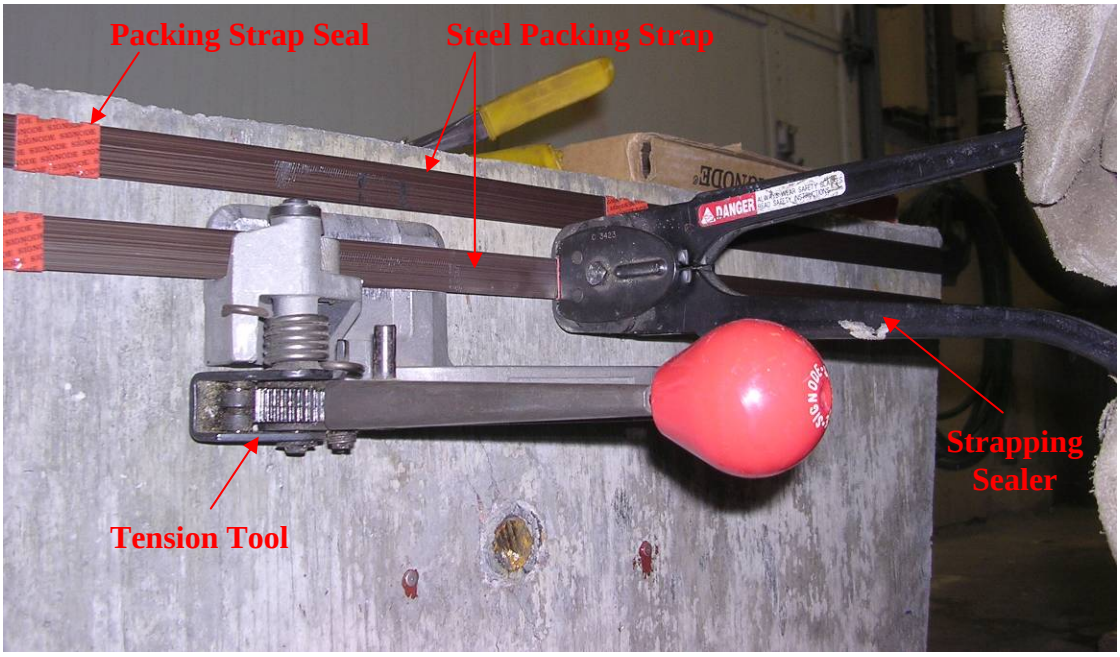

Figure 2.21: Steel Packing Straps Applied to Concrete

2.6.1.2 Previous Research

In a British study seeking a low cost repair method for increasing column ductility, Frangou et al. used commercial packing straps to provide external lateral reinforcement to columns[75]. The researchers specifically sought a low-cost, easy-to-install strengthening method. They were aware that many buildings owners would only voluntarily strengthen their buildings for seismic performance if the cost was relatively low[75]. The researchers decided to use commercial packing straps, which are designed to fasten freight to pallets for shipping. In Frangou et al.'s study, the steel packing straps were tested on both round and square concrete prisms, using different clear spacing of the straps[75]. The prisms were small scale plain concrete specimens (100 mm [3.94 inches] diameter by 200 mm [7.87 inches] tall cylinders and 100 mm [3.94 inches] squares by 200 mm [7.87 inches] tall rectangular prisms). These prism tests were used to establish the efficacy of using the packing straps to provide lateral confinement to the concrete. The improved axial capacity of the prisms, both square and round, is shown in Figure 2.22. The improvement can be seen by the data points having normalized values greater than one, where one represents the unconfined concrete prism's axial load.

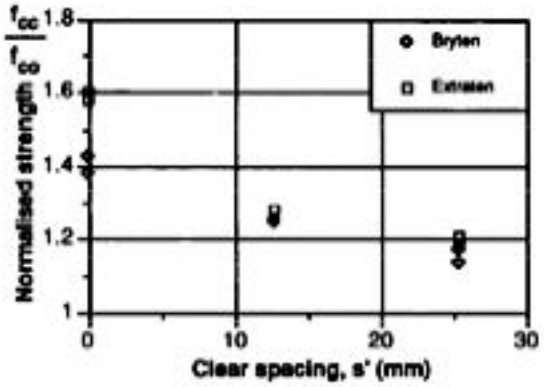

Figure 10 Normalized strength for cylindrical specimens confined with Bryten and Extraten metal strips for various spacing

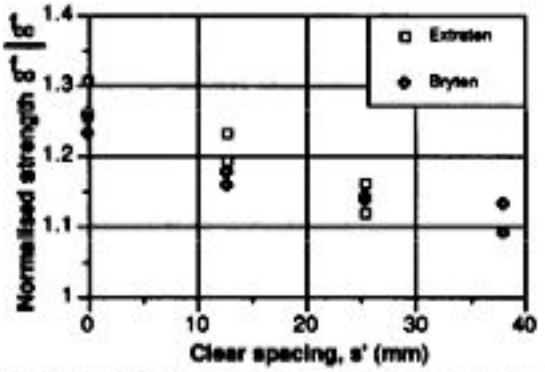

Figure 11 Normalized strength for prism specimens confined with Bryten and Extraten metal strips for various spacing

Figure 2.22: Frangou et al. Axial Capacity Results[75]

This repair method yielded encouraging results. As shown in Figure 2.22, the straps could increase the specimens' axial capacity by confining the concrete. With a capacity increase of 10-25% for square prisms, the packing straps proved their ability to increase the confinement of plain concrete in axial capacity even when the straps made 90^{o} bends[75]. Additionally, the researchers tested the performance of a beam whose shear reinforcement was made up in part or in total by these external packing straps. This test was intended to model a repair required when the existent shear stirrups in a beam are insufficient for the expected loads[75]. Significant increases in the beam specimens' ductile capacity after the application of external packing straps for shear stirrups are shown in Figure 2.23 (BC 2 is before the repair and BC 2R after repair). The excellent behavior of

the beam specimens would indicate that the packing straps could successfully take the place of shear reinforcement when it is inadequate in the member[75].

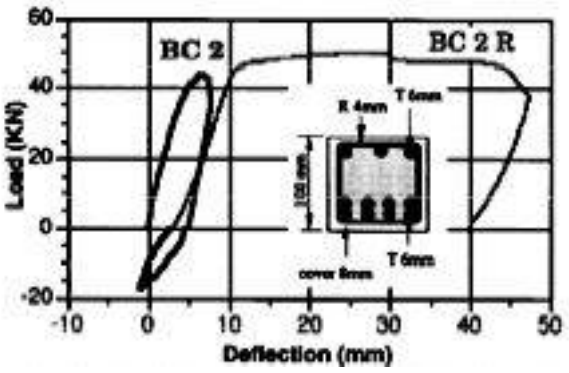

Figure 2.23: Frangou et al. Ductility in Bending Results[75]

2.6.1.3 Relevance

A packing strap repair is considered in this research study because it is easy to apply and has potential for increasing concrete confinement as shown in Frangou et al.'s research paper. As well, packing straps are fairly inexpensive and extremely easy to install with hand tools.

2.6.2 Fiber Reinforced Polymers

2.6.2.1 Description

A fiber reinforced polymer (FRP) repair takes the form of a fabric being impregnated with a polymer such as epoxy and applied to concrete[91,92]. The fiber used for this repair method is typically carbon, glass, or aramid fiber (Kevlar being the brand name)[77,79-81,83-87,93]. Figure 2.24 shows carbon fiber fabric before epoxy polymer saturation. For a detailed discussion of how the polymer works with the fiber fabric to create the new engineering properties of the resulting composite material, see Orton's dissertation[91]. Chapter 4 describes the application process for a carbon fiber reinforced polymer (CFRP) wrap, which was used in this research program. By orientating the wrap's fibers horizontally around the column capital, as shown in Figure 2.25, it provides lateral

confinement of the column capital[77,81,83,85-87]. FRP can be applied either before or after the polymer sets. Application prior to the polymer hardening is called a wet lay-up, and this method allows the wrap to be applied following the concrete surface[77,80,81,83-87,91-93]. The FRP wrap in Figure 2.25 used the wet lay-up method. For an after-hardening situation, the FRP is formed into flat sheets. These sheets are then attached to the member being repaired by epoxy, bolting, or some other fastening method[79,80,91,92].

Figure 2.24: Carbon Fiber Fabric

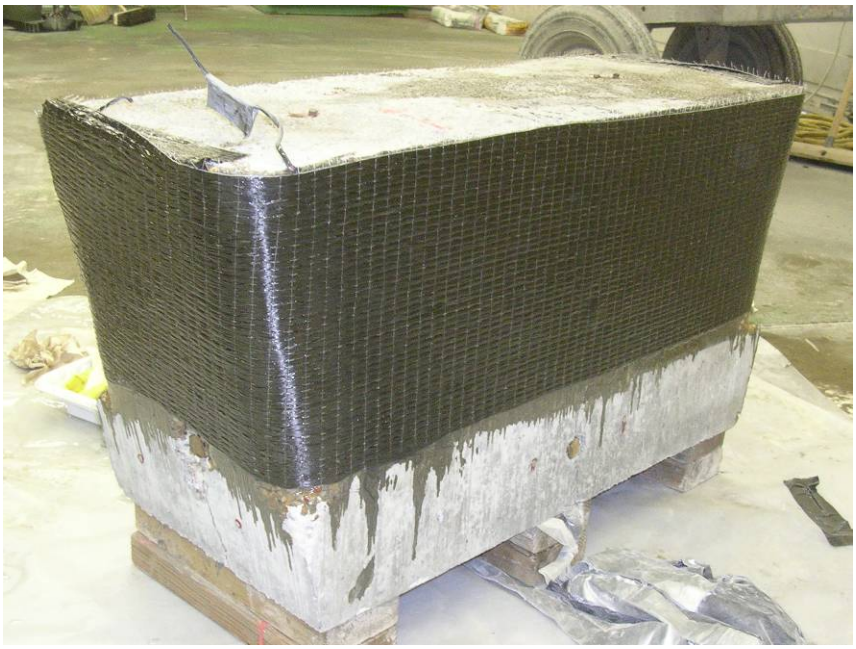

Figure 2.25: FRP Wrap Applied to Concrete Specimen

2.6.2.2 Previous Research

There is agreement in the literature that well anchored column wraps of FRP provide good confinement of the concrete core[77,80,81,83-87,91-93]. The anchorage noted is an overlap of the wrap, ranging from 4 inches [100 mm] to 6 inches [150 mm][83,93]. As noted in the introduction to the repair section, column repairs are desired for both increased in load carrying capacity and improved seismic performance[8,75-90]. FRP wraps are an increasingly popular seismic repair as the confined concrete exhibits superior ductility and lateral displacement over unconfined concrete columns[75,77,80,87]. This same confinement that improves seismic performance also enhances the axial load carrying capacity of columns[77,84]. Passive confinement methods, such as an FRP wrap, engage once the concrete column has begun to experience some damage such as micro-cracking and dilation under axial load[77,86,87]. It is when the concrete is thus beginning to expand laterally that the wrap exerts a confining pressure upon the concrete[77,86,87].

In CANMET's guide for managing structures with ASR, FRP wraps are listed as beneficial for repairs, as long as the wrap has sufficient confining strength to contain

future expansion from the continued reaction[8]. Pantazopoulou et al. and the same researchers in another paper by Lee et al. used FRP wraps to repair heavily corroded concrete columns showing a 28% improvement over the corroded control[81,85].

Through various research studies, general trends of FRP behavior have emerged. One such trend is that with increasing layers of wrap, the confining strength of the repair is increased[83,85,93]. This trend seems intuitive as more material has more capacity than less material of equal strength. Another trend is that a wrap repair is more effective on circular columns than square or rectangular columns[83,86]. For square or rectangular columns, the FRP wrap exerts a lower confining stress in the middle of the flat faces than it does around the curved corners[83]. Corners of the rectangular columns must be rounded to prevent locally high stresses at the corners causing premature failure[83,86,93]. As well, increasing the radius of corner improves the confinement and therefore axial capacity of the repaired columns[83].

For a representative example, in a study by Rochette and Labossiére, the researchers used round, square, and rectangular column specimens. For additional variables, the square and rectangular columns had their corners rounded to different radii. Further, the type of fiber and number of FRP layers used were also varied[83]. The results from this study indicate that regardless of the number of layers used or corner radii used on a square column, aramid fibers (also known by the brand name Kevlar) produced approximately a 20% increase in axial load carrying capacity versus the control[83]. Carbon fiber wrapped specimens showed much more variation in performance than did the aramid fiber. Yet, all carbon fiber wraps on circular or square specimens with rounded corners showed increased capacity versus the control (3-92% increases for square specimens and 60-75% increases for circular specimens)[83]. Increasing the corner radii, and thus decreasing the sharpness of bend in the fibers, resulted in increased performance in the carbon fiber wraps. For instance, the smallest radius, 5 mm (essentially a sharp corner), showed no improvement, whereas the largest radius, 38 mm [1.5 inches], had as much as a 92%

increase in capacity versus the control. As well, more layers of FRP resulted in higher loads[83]. For square specimens with a corner radius of 38 mm, three layers of CFRP resulted in a 20% increase in capacity versus the 92% increase from five layers of CFRP. There was some variation in the results (such as identical square specimens with a 25% difference in capacity), which could be from imperfections in the materials or application of the fibers.

2.6.2.3 Relevance

A FRP wrap was selected for use in this research program in order to consider a repair that would have little impact on the column profile. One of the desires of TxDOT, owner of the San Antonio Y bridge, was that the repair method have little visual impact as the deteriorating bride columns are located in a public parking lot. Thus, a repair that would have only minor impact on the aesthetic appearance of the structure was desirable. As well, previous research showed definite improvement in axial capacity can be achieved through this repair. Carbon fiber fabric was chosen for this program because it was readily available.

2.6.3 Column Jacketing

2.6.3.1 Description

A traditional method for addressing a column of insufficient strength or size is to surround it with additional material to carry the remaining load. This material can be either steel or concrete, and often takes the form of a jacket completely surrounding the column. These jackets help to confine the concrete and thus increase axial capacity and ductility[8,75-77,80,84,87]. Figure 2.26 shows a concrete jacket on a specimen. To apply a concrete jacket, the original concrete column surface needs to be roughened to increase bond with the new concrete placed within the jacket, as discussed in Chapter 4. A new steel reinforcing cage is then constructed around the existing column. The new concrete can then be applied through shotcreting or traditional formwork[76,80,89].

Figure 2.26: Concrete Jacket Repair on Specimen

2.6.3.2 Previous Research

Confining concrete with steel of concrete jackets are traditional methods for improving axial capacity[8,75-77,80,84,87]. Steel jacketing was also an early commonly used method for seismic retrofit[77,80,84,87]. Fukuyama et al. studied the effect of concrete and steel jackets on columns with extensive earthquake damage. The specimens tested used rubble for the concrete core buckled longitudinal bars[80]. Under cyclic loading, the concrete jacketed specimens showed a 62% increase in shear capacity over the control specimen. With both a concrete jacket and a steel jacket, one repaired specimen exhibited a 135% improvement. When applied to a undamaged column, the steel jacket alone caused a 31% improvement over the control[80]. Thus, both of these jacketing methods proved capable of confining a concrete column to improved ductility. As discussed previously, this confining ability also results in increased axial capacity[77].

Concrete jacketing has also been used to strengthen structures damaged by ASR[8,89]. In a study by Haddad et al., concrete jackets with various steel fiber configurations were tested on ASR-affected specimens. These jackets improved the beam specimens' shear

carrying capacity by 6-20% over the undamaged control and 20-35% improvement over the ASR damaged control[89]. The variation in result depended on the type of steel fiber used in the concrete jacket, with a mixture of hooked and brass coated steel fibers yielding the best results[89].

Ramirez published a study in 1996 in which several different traditional styles of column repairs were tested for their improvement of axial load capacity. The first series of repairs were trying to increase the axial load carrying capacity of the columns through full column repairs. The second series examined local repairs, as if the columns were cast with a large void, requiring repairs of local defects[75]. For the first specimen series, which strengthened the whole column, Ramirez focused on concrete jacketing and variations on using steel angles and plates to help transfer the load around the original column, as illustrated in Figure 2.27. In this figure, from left to right, the specimens are the concrete jacket with the new concrete highlighted in blue and the three steel angle variations: original, with grout for a tighter fit, and with a cross beam through the original concrete column. Concrete jacketing was found to be an effective method, with an increase of 60% over the control specimen in the three specimens tested[75]. These specimens were limited by the slab column connection these specimens, which were the source of failure in the concrete jacketed specimens[75]. Therefore, it is possible that the concrete jacket repairs could cause greater improvements in axial capacity than reported. The steel angle variations showed improved performance with an increasingly tight fit of the steel and the concrete column. Thus, when the concrete was tightly encapsulated by the steel plates and angles then it behaved as confined concrete, and was able to carry a higher load. The three specimens had a 50-90% improvement over the control column[75]. Ramirez did not list capacities for the local repairs, but reported that the concrete jacket and steel plate repairs were satisfactory[75].

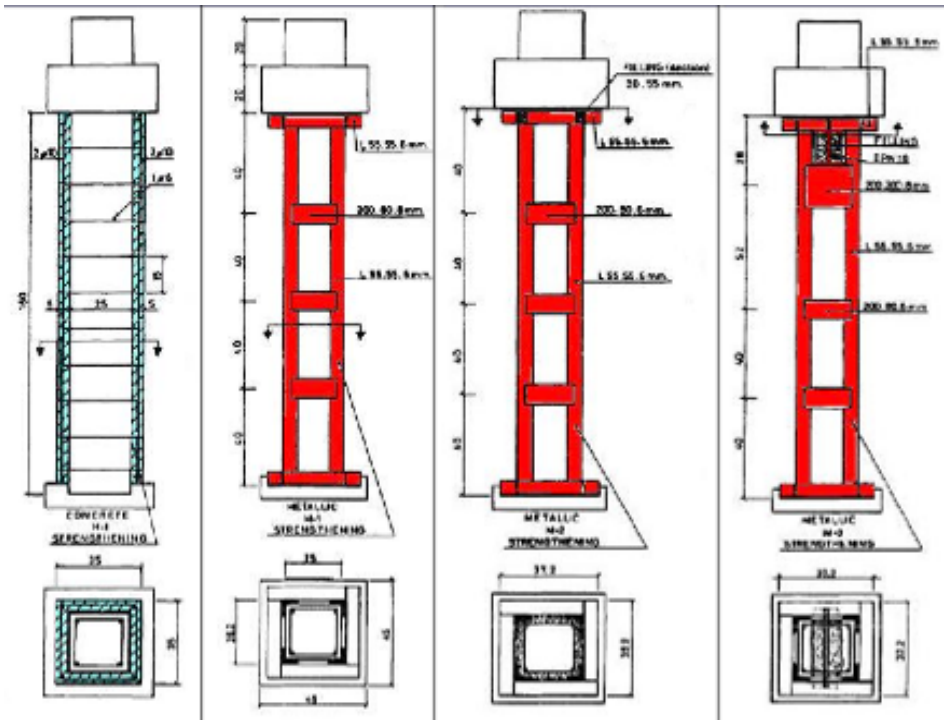

Figure 2.27: Ramirez's Full Column Repair Specimens[75]

2.6.3.3 Relevance

Concrete jacketing was selected for this research program because it is a traditional repair method. The author wanted to compare this traditional method's performance to the more recently developed repair methods being tested. As well, the materials used are relatively inexpensive[75]. Thus, with good performance, the lower cost would increase the overall ranking of this repair.

2.6.4 External Post-Tensioning

2.6.4.1 Description

In column repair, external post-tensioning is used to confine the concrete by clamping the cross section[8,78,82,84,88]. Figure 2.28 and Figure 2.29 are examples of post-tensioning used to repair column capitals. The "external" description indicates that the post-tensioning system is outside of the concrete column. This layout is easily achieved by using post-tensioning bars that run through steel angles, channels, or custom brace to

form a clamp. For a rectangular cross section, the post-tensioning needs to be applied in two directions in order to effectively confine the concrete, as shown in Figure 2.28. Figure 2.29 was a short-term emergency repair where additional restraint was needed only in one direction[90]. Post-tensioning is an active repair in that through its installation, the post-tensioning system applies force to the concrete[8,78,82,84,88]. Other repairs are considered passive as the concrete contained within those repairs has to shift (through internal expansion or from additional external load application) before they are engaged in restraining the concrete[77].

Figure 2.28: Column Capital Repaired with Post-Tensioning[94]

Figure 2.29: Post-tensioning Used for Temporary Repair[90]

2.6.4.2 Previous Research

Use of external post-tensioning as a repair for ASR affected concrete is often noted in the literature[8,78,84]. As the post-tensioning process actively creates a compressive stress in the concrete cross-section, it is able to suppress further ASR expansion[8,78,84]. Further, the added confinement of the cross section results in increased axial capacity of the concrete column[8,77,78,84]. Therefore, this repair is often noted for ASR affected concrete due to its dual ability to slow or prevent further deterioration while also strengthening the existing column[8,78,84].

From the previously discussed study of Ramirez et al., the steel jacketing repairs showed increased axial capacity with increasingly tight fits of the steel section[76]. A post-tensioned clamp, with its extremely tight fit to the concrete surface, should, following this logic, exhibit axial capacity improvement similar to Ramirez et al.'s specimen M2, which had a 65% improvement over the control[76].

Torii et al. studied the effect of confinement from a post-tensioned repair on ASR affected concrete columns. This study found that the confined cross section had an axial capacity of 25 MPa (3.6 ksi) versus the reinforced concrete control's capacity of 17 MPa (2.5 ksi)[84]. As well as showing this 47% improvement in axial capacity, the researchers

recommended the post-tensioning method for closing existing cracks and suppressing further ASR expansion[84].

2.6.4.3 Relevance

External post-tensioning was considered in this study because it can effectively clamp a rectangular section and provide lateral confinement. As well, this method was frequently recommended in the literature for its ability to suppress future expansion of the concrete from ASR while also confining the concrete to increased capacity.

CHAPTER 3

Scaled Column Specimens: Background and Methods

3.1 OVERVIEW

As mentioned in the background section, TXDOT was concerned about the structural capacity of several bridge columns due to premature material deterioration in the form of cracking. In order to get a rough estimate of capacity, the major cracking due to ASR/DEF damage was approximated using unaffected concrete that was damaged mechanically with splitting wedges. A series of four 1/3.67 scale bridge columns were constructed by Kapitan[3]. Two columns were tested undamaged to determine a baseline capacity. The remaining columns were then damaged using splitting wedges to open longitudinal cracks. Columns with three different crack widths were tested to find the influence of crack width upon the column behavior[3]. To complement these earlier column tests, two additional columns were constructed as part of this research project. The reinforcing and dimensions of the additional columns were identical to Kapitan's series, only these new columns were cast with ASR susceptible concrete and were heated during initial concrete curing to induce DEF type damage. Details of both Kapitan's column series and ASR/DEF column series are given in the subsequent sections.

Kapitan's scale column specimens were direct models of the field (prototype) column. In direct modeling theory, by keeping the material properties identical to those of the prototype, then the response of the model can be scaled directly to interpret as the response of the prototype[95]. While the applied axial load was reduced from the prototype to the model by a square of the scale factor, linear dimensions, including external dimensions, crack widths, and crack spacing were reduced directly with the scale factor[95]. Thus, for Kapitan's and subsequently the author's scaled specimens, the concrete and reinforcing properties were selected to match those of the prototype. By matching the material response to the prototype, then the model could directly scale the crack size by

the scale factor used to reduce the specimen dimensions[95]. For further discussion on the investigation of the prototype's material properties and direct modeling, see Kapitan.

3.2 KAPITAN'S COLUMN SERIES

3.2.1 Experiment Set-up/Goals

Jacob Kapitan, in his master's research at the University of Texas at Austin, built 1/3.67 scale models of the typical column used in the San Antonio Y[3]. The typical column specifically modeled was column DD7. Kapitan's goal was to determine the influence of cracking and crack width on the load carrying capacity of the column. For his experiment, Kapitan tested two columns that were undamaged for a baseline capacity value and subsequently tested columns that had normal concrete but were cracked mechanically. The cracks were induced using splitting wedges inserted in PVC voids through the concrete section. The undamaged specimens also contained the voids, but the voids were filled with reinforcing steel for testing in order to avoid crushing of the voids during loading. The splitting wedges were designed to split rock and thus could accommodate the strengths found in concrete[3]. Figure 3.1 shows one of the control columns, complete with filled voids, set up for testing.

Figure 3.1: Control Column Ready for Testing

The mechanical cracking was conducted because waiting for concrete to crack from ASR and/or DEF can take a considerable amount of time, even under accelerated laboratory conditions. In the field it can take 10-30 years or more for ASR/DEF cracking to appear[37,38,41]. The PVC void pattern was selected to mimic the cracking observed in the field. The columns showing distress in the DD spine of the San Antonio Y had the largest cracks running vertically down roughly the middle of each face of the columns, as shown in Figure 3.2. This arrangement led to speculation as to whether the cracks had

passed completely through the column and essentially cleaved the single large column into four adjacent slender columns. If these columns had separated into four pieces then only the transverse ties and friction along the fractured surface would be holding the columns together. Additionally, as the continued ASR/DEF induced expansion widened the cracks, it was possible that the transverse ties could yield and thus would be unable to effectively hold the column quarters in close contact. Therefore, the experiment was designed to induce cracks to pass through the cross section of the column and create this worst case scenario for the columns, as illustrated in Figure 3.3. Differing crack widths were used to examine their influence on the capacity of the column[3].

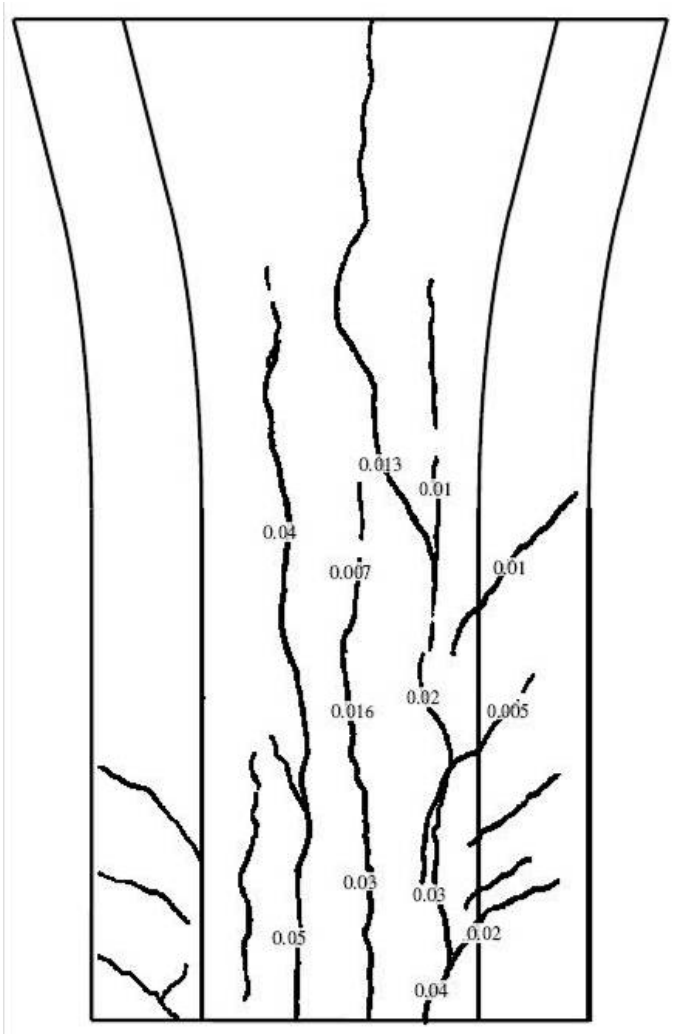

Figure 3.2: Crack Mapping of DD7 in San Antonio, TX (from ref. 2)
Widths are in Inches

Figure 3.3: Mechanically Induced Cracking (Cracks Marked in Green)

In one specimen Kapitan induced cracks that were the scaled size of the maximum crack width measured in the typical column being modeled, DD7. In the next specimen the crack size was the scaled equivalent of the largest crack width on DD6, a non-typical column adjacent to DD7. A final test used the scaled width of 175% the size of the largest crack observed in the field investigation.

3.2.2 Results

Kapitan predicted the load carrying capacity of the undamaged specimens prior to the first testing day. His prediction was based upon the axial-flexural capacity of the narrowest cross section under combined axial load and two-way bending. Axial load with biaxial bending was used as Kapitan found that load case to be the most critical loading from an evaluation of the design loading cases considered[3]. The critical scenario was AASHTO Load Case III with two lanes, which was illustrated in Chapter 2.

The undamaged specimens did not reach the predicted load because they did not fail in combined axial load and flexure. Instead, the concrete spalled and crushed under the most heavily loaded bearing pad, as shown in Figure 3.4. This phenomenon caused Kapitan to investigate the design calculations used for the bearing design of the columns. He found that the columns had only been designed for uniaxial bending. When the critical load case of axial load and biaxial bending was applied, the load under one of the bearing pads was substantially increased. Strut and tie modeling by Kapitan indicated that for this load case the top level of transverse steel in the column capital was subjected to far more load than it had been sized to carry[3].

Figure 3.4: Concrete Spalling and Crushing under Heavily Loaded Bearing Pad

As shown in Figure 3.5 and Table 3.1, the cracked specimens showed reductions in capacity compared to the results of the control specimen. Because of the bearing design deficiency, the biaxial load capacities were not near the original axial-flexural prediction. The loads were near the predicted bearing capacity, however. Even with this situation, Kapitan was able to determine the relative influence of the cracking. With wider cracks, the capacity decreased. However, the reduction was not large, up to 5%, for the first two levels of cracking, which correspond to the observed cracking in the field. The reduction only reached approximately 18% when the crack width was increased to 175% the size of the largest observed cracking width. This width would be equivalent to a crack width in the field columns of 0.3 inches.

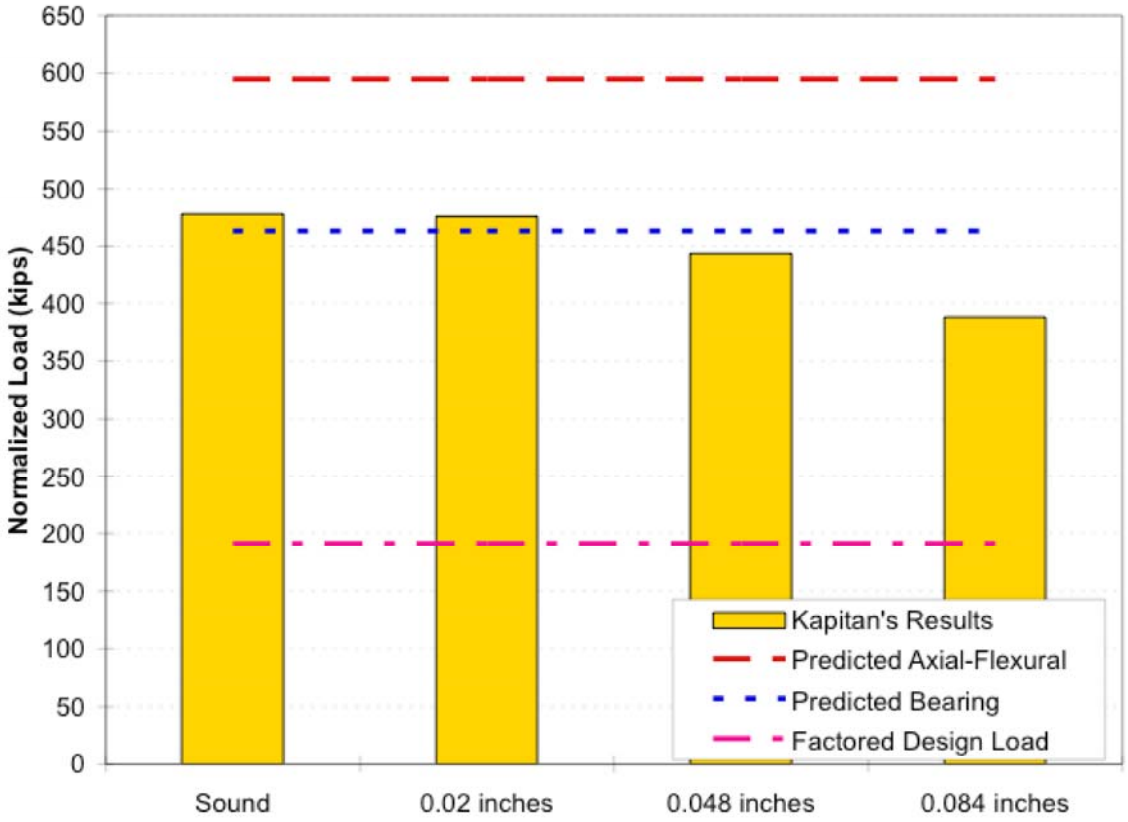

Figure 3.5: Summary of Kapitan's Results[3]

Table 3.1 : Crack Size and Load Relationship from Kapitan[3]

Specimen Crack Size (inches)	Corresponding Field Crack Size (inches)	Failure Load (kips)	% Less Than Control Specimen
Control – 0.0	0.0	478	0.0%
0.02	0.078	476	0.4%
0.048	0.177	451	5.6%
0.084	0.3	395	17.4%

Additionally, the column design used for all of the typical columns in this elevated highway was based upon the most demanding loads found in any section of the bridge. Thus, these columns had been designed to carry a wider and longer deck section, to be

taller and therefore more slender, and also to support a highway section that was curving and thus needing to resist significant centripetal forces. As the bridge column under investigation does not actually face as great of a load as that for which it was designed, it has considerable excess capacity, as evidenced in Figure 3.5. From these results, it was determined that DD7 was not in imminent danger of failing[3].

Because there are some columns in the bridge that are carrying loads that are closer to the design load and because those columns have the same bearing design deficiency, it was decided to further investigate a method to repair the columns to improve their bearing performance. Although the columns with higher load do not yet show signs of deterioration, they are also susceptible to future deterioration as they were constructed with similar concrete mixtures and construction practices. Thus the investigators desired to find an effective repair so that knowledge is available at the time when and if these columns begin to suffer from materials related deterioration. Further details of the specimen repair study are presented in Chapter 4.

3.3 ASR/DEF COLUMNS

3.3.1 Design

The reinforcing and physical dimensions of the columns were identical to that used in Kapitan's columns and are presented in Appendix A. Figure 3.6 shows the reinforcing cages used. The formwork used was the same as Kapitan's column series and is shown in Figure 3.7. In fact, Kapitan assisted with the construction of this column series prior to his graduation. Unlike Kapitan's column series however, there were no PVC voids in the ASR/DEF columns because the concrete cracking was from ASR/DEF expansion, not from splitting wedges. As well, the concrete used in construction was proportioned with materials known to be highly susceptible to ASR. These columns were also heat treated during initial concrete curing to induce susceptibility to DEF.

Figure 3.6: Reinforcing Cages used for ASR/DEF Columns

Figure 3.7: Formwork Set Up for ASR/DEF Columns[96]

3.3.2 Susceptible Concrete

The concrete mixture design and heat treatment were the major differences of these columns versus Kapitan's columns. The project team members involved in the materials investigation designed a concrete mixture that was highly reactive and thus very susceptible to ASR[96]. Both the fine and coarse aggregates selected were known to be reactive: Wright Materials manufactured sand and Texas Industries river gravel, respectively. In order to also have a highly alkaline pore solution to further increase the chances of inducing ASR, the mixture contained eight sacks of Type III cement, which is highly alkaline, and the concrete was further dosed with additional sodium hydroxide. To achieve strength similar to Kapitan's columns series and core samples from the field, a water-to-cementitious materials ratio of 0.45 was used. As well, super-plasticizer was added to increase the slump to approximately eight inches, which increased the workability of the concrete. Additionally, the columns were placed under a cover as

shown in Figure 3.8, tented, and then the air was heated with two kerosene powered heaters to subject the fresh concrete to an elevated temperature as shown in Figure 3.9. The internal temperature of the fresh concrete reached a maximum of approximately 210°F and was held around 200°F for over twelve hours, which is above the 158°F threshold needed to set the stage for DEF[96].

Figure 3.8: ASR/DEF Columns about to Receive Cover[96]

Figure 3.9: Heater used to Raise Temperature in Tent[96]

(Second Heater on the Other Side)

3.3.3 Instrumentation/Monitoring

In order to better compare any differences in behavior between Kapitan's column series and the ASR/DEF columns, the instrumentation pattern used by Kapitan was duplicated. As the region of interest in the columns turned out to be the bearing capacity and confinement at the top of the column, rather than the stresses resulting from a combined biaxial load failure mechanism, additional instrumentation was included at the top of the column.

3.3.3.1 Strain Meters

Although it is common practice to apply strain gauges to steel reinforcement and assume that the strain measured in that steel is the same as the strains in the adjacent concrete, there are times when researchers wish to know the strain behavior at a location in the concrete where there are no pieces of reinforcing steel. In the column design modeled, the longitudinal reinforcement is located along the perimeter of the column. Thus, to measure the strain in the center of the bulk concrete a different measurement method was required. The research team decided to use strain meters for the direct concrete strain measurement. The strain meter design was based upon the one developed by Stone at the University of Texas at Austin in 1980[97]. These strain meters were constructed from a core of aluminum bar stock that was threaded on the ends to allow the addition of a washer and nut. The large washers set the gauge length of four inches and were used to engage the concrete by transferring strain to the bar. A strain gauge was applied to the aluminum bar and several layers of moisture protection were utilized. Heat-shrink plastic tubing was the final layer used to create a bond breaking surface with the concrete so that the strain observed would be the average strain over the gauge length. Aluminum was selected for its similar modulus of elasticity to the concrete, which would help the meters measure small strains[97]. Figure 3.10 shows the upper level of strain meters and Figure 3.11 and Figure 3.12 show the strain meter locations in the upper and lower instrumentation layers, respectively. A schematic of the strain meter construction is presented in Appendix A.

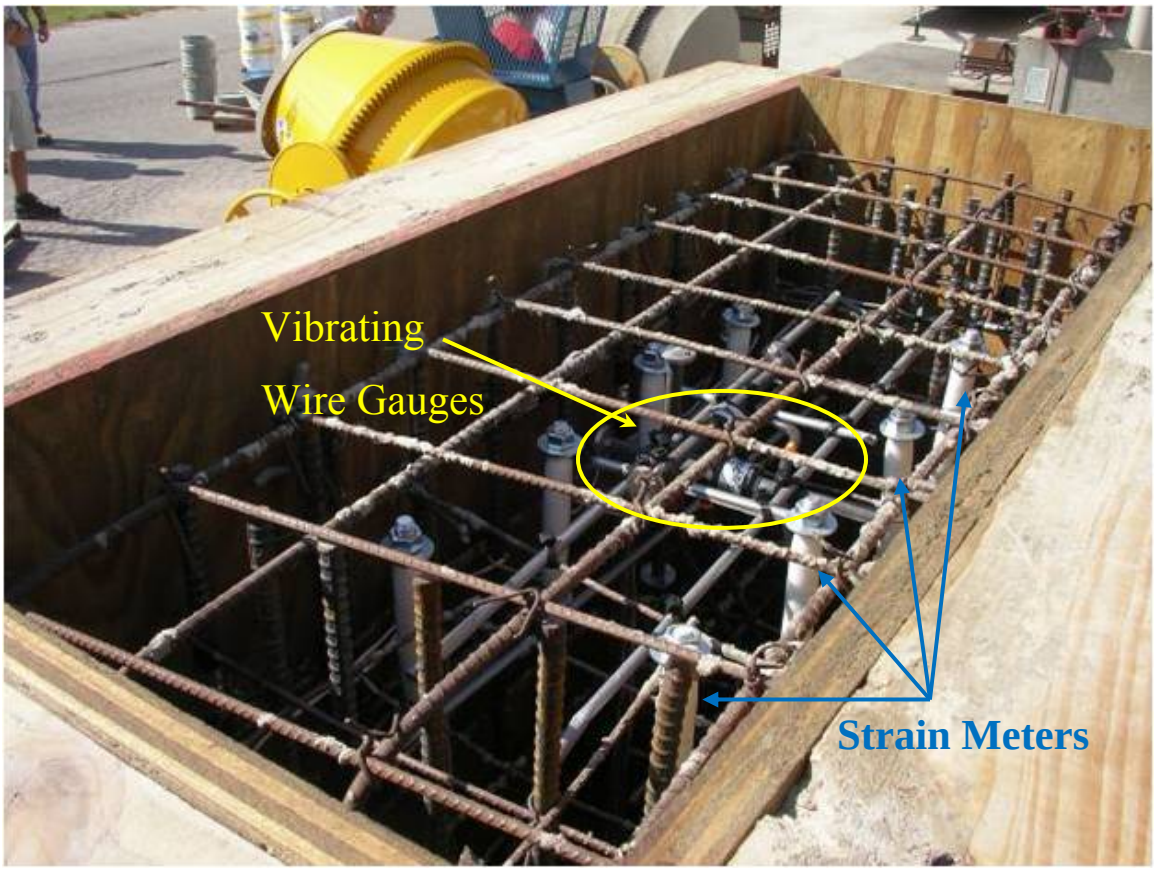

Figure 3.10: Strain Meters and Vibrating Wire Gauges in Position[96]

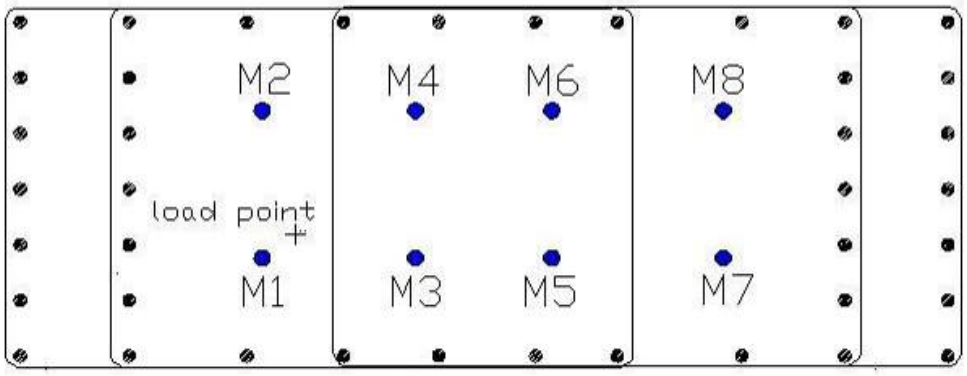

Figure 3.11: Strain Meter Locations in Upper Layer

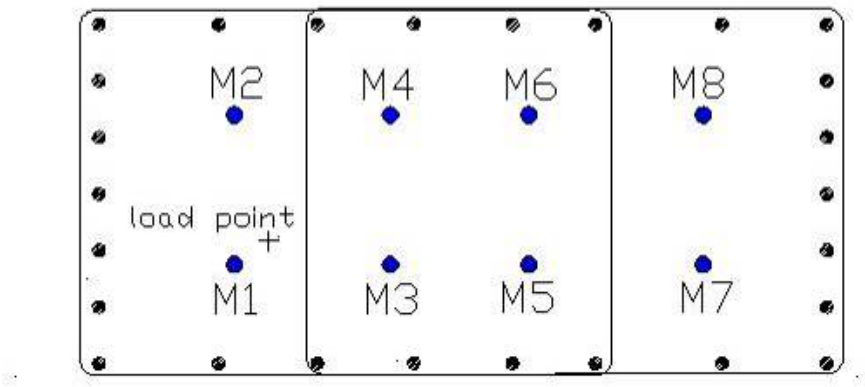

Figure 3.12: Strain Meter Locations in Lower Layer

3.3.3.2 Strain Gauges

Strain gauges were applied in two layers, as mentioned previously. One layer corresponded with Kapitan's strain gauge arrangement and the added layer was at the top layer of reinforcement. This top layer was included to gather information on the columns' behavior in biaxial bending and bearing failure. All transverse strain gauges and the upper and lower L1 longitudinal gauges were monitored during the columns' exposure period. The results of this monitoring program are in Chapter 6. Diagrams of the strain gauge locations are shown in Figure 3.13 and Figure 3.14. The strain gauge naming notation used indicates whether the strain gauge is monitoring transverse or longitudinal reinforcement. Labels beginning with a "T" designate transverse reinforcement gauges and "L" labels indicate longitudinal reinforcement gauges. The upper layer of strain gauges is shown on a reinforcing cage in Figure 3.15. Details about the type of strain gauges used are presented in Appendix A.

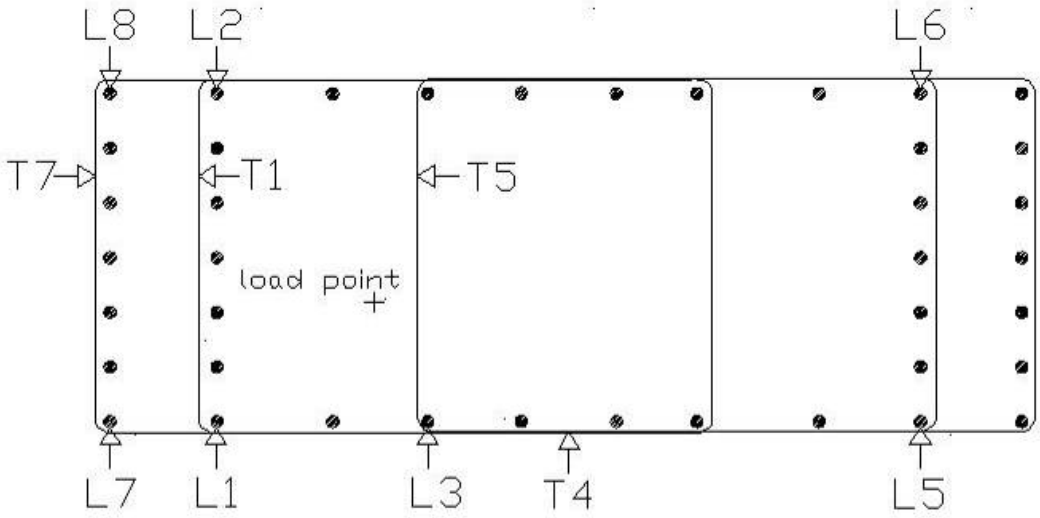

Figure 3.13: Strain Gauge Locations in Upper Layer

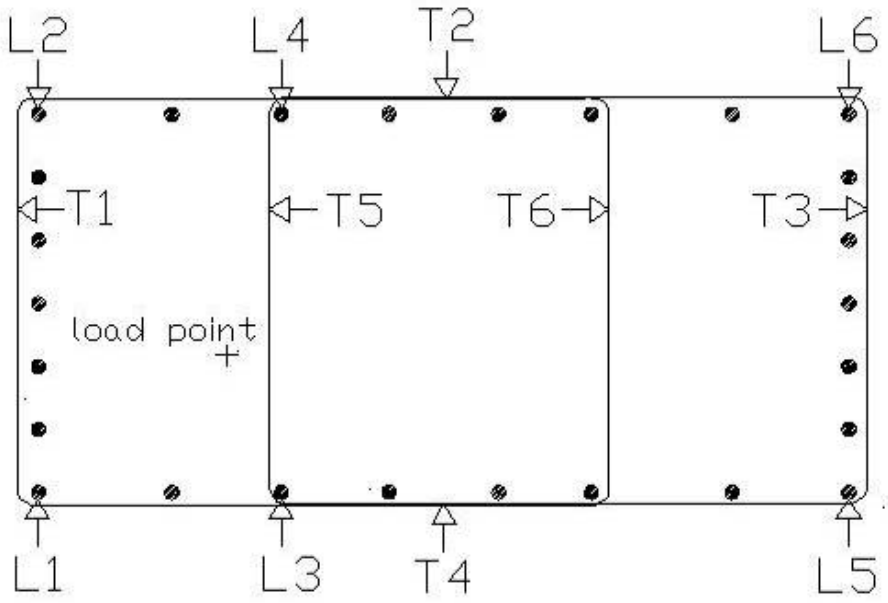

Figure 3.14: Strain Gauge Locations in Lower Layer

Figure 3.15: Strain Gauges of Upper Layer (Covered in Protective Foil Tape)

3.3.3.3 Demec Points

Demec monitoring points are small metal disks with an indent that are mounted on concrete or an embedded metal stud in concrete at a set gauge length. Figure 3.16 shows the demec points on ASR/DEF column B and a close-up view of one of the demec points mounted on an embedded stud. The expansion of the concrete at the surface is thus monitored by a demec gauge, which measures the change in distance between the two points versus the gauge length. The external expansion of the columns was monitored regularly.

Figure 3.16: Demec Points on Column (Left) and Close-up of Demec Point (Right)

3.3.3.4 Vibrating Wire Gauges

Vibrating wire gauges were also installed in the columns at the center of the bulk concrete cross section, at the top of the columns. The location of the strain meters is highlighted in Figure 3.10. These gauges were only used to monitor expansion of the concrete.

3.3.4 Exposure Conditions

3.3.4.1 Post-Tensioning

As ASR and DEF are naturally three dimensional expansions, without restraint the resulting cracking would have a map cracking pattern. This pattern would generally be evenly distributed throughout the concrete and the cracks would have random orientation. With restraint in the system, the cracks form along the direction of restraint as explained

in the background chapter. The researchers wished to induce ASR and/or DEF cracking in the model columns to as closely mimic the cracking in DD7 as possible. Thus, an axial load was needed to simulate the dead load in the bridge, creating axial restraint and longitudinal cracking. This axial load was added by using a post-tensioning system to load the column axially.

3.3.4.1.1 Lay-out

The aim of the post-tensioning arrangement was to provide a load equal to the scaled dead load from the bridge superstructure. Thus, the target post-tensioning load was 134 kips total axial load. This total load translates into 33.5 kips for each of the four post-tensioning bars used in the set-up as shown in Figure 3.17. Due to space limitations with the stressing chairs used in the post-tensioning process a wrench did not fit between the nuts on the post-tensioning bar and the stressing chairs. Therefore, the nuts were finger tightened and an overstress was added to the required stress needed for the 33.5 kip per bar loading. This overstress was intended to make up for seating loses anticipated from the finger tightened nuts. Details of the post-tensioning process are in Appendix A.

As seen in Figure 3.17, the post-tensioning bars clamp the column between two beams, which are located at the top and bottom of the system. A series of railroad springs were used to transfer the load so that any relaxation in the steel or creep in the concrete would not result in significant stress loss. The load is transferred from the springs to the column through a spreader beam and bearing pads, which are in the same arrangement as used by Kapitan.

Figure 3.17: Overview of the Post-Tensioning Arrangement

3.3.4.1.2 Spring Monitoring

During the exposure period, questions were raised as to whether the post-tensioning system might lose load and how to monitor the load in the system. The post-tensioning

system featured railroad springs to ensure there would always be substantial load in the system. For instance if the steel relaxed or the concrete compressed through creep, then the springs would continue to keep load in the system by expanding to fill any change in the component lengths. As all of the load carried by the column passed through the springs, the load was determined by measuring the spring height.

The spring constant was determined by using data from a different research project that loaded the railroad springs axially until all of the free height was removed. The average load for the three-spring set, which was used in the post-tensioning arrangement of this research project, was 40 kips. The free height, or difference in height between the loaded spring and a full loaded spring where the spring coils just touch, was determined from a railroad spring manufacturer's standard. This free height was 1.625 inches. Thus the spring constant, which was a value of the load required to compress a spring one unit of distance, was determined to be 24.6 kips/inch.

By measuring the distance between the channels sandwiching the springs at the north and south ends an average spring height was determined. Using the compressed distance, which was the difference between the unloaded and loaded spring heights, the spring constant and the number of springs it was determined that the axial load in the system was 190 kips. Thus, it appeared that the overstress values used in post-tensioning were conservative and the columns were experiencing the scaled load of dead load plus one live load. The spring heights were monitored approximately monthly.

3.3.4.2 Moist Environment

In order to provide a constant source of moisture to the concrete, a necessary ingredient in both ASR and DEF, a moist wrap was applied to the columns. The moisture was provided to the system by soaker hoses wrapped around the top of the columns. The soaker hoses were on an automatic timer to run for one minute, four times a day. Felt-backed plastic sheeting was wrapped around the columns to retain the moisture in

between soakings. The plastic was secured in place with wire loops at the base and top of the column as well as with nuts and washers threaded onto the embedded studs, which were present for the demec point expansion monitoring. Figure 3.18 shows the moist environment set-up.

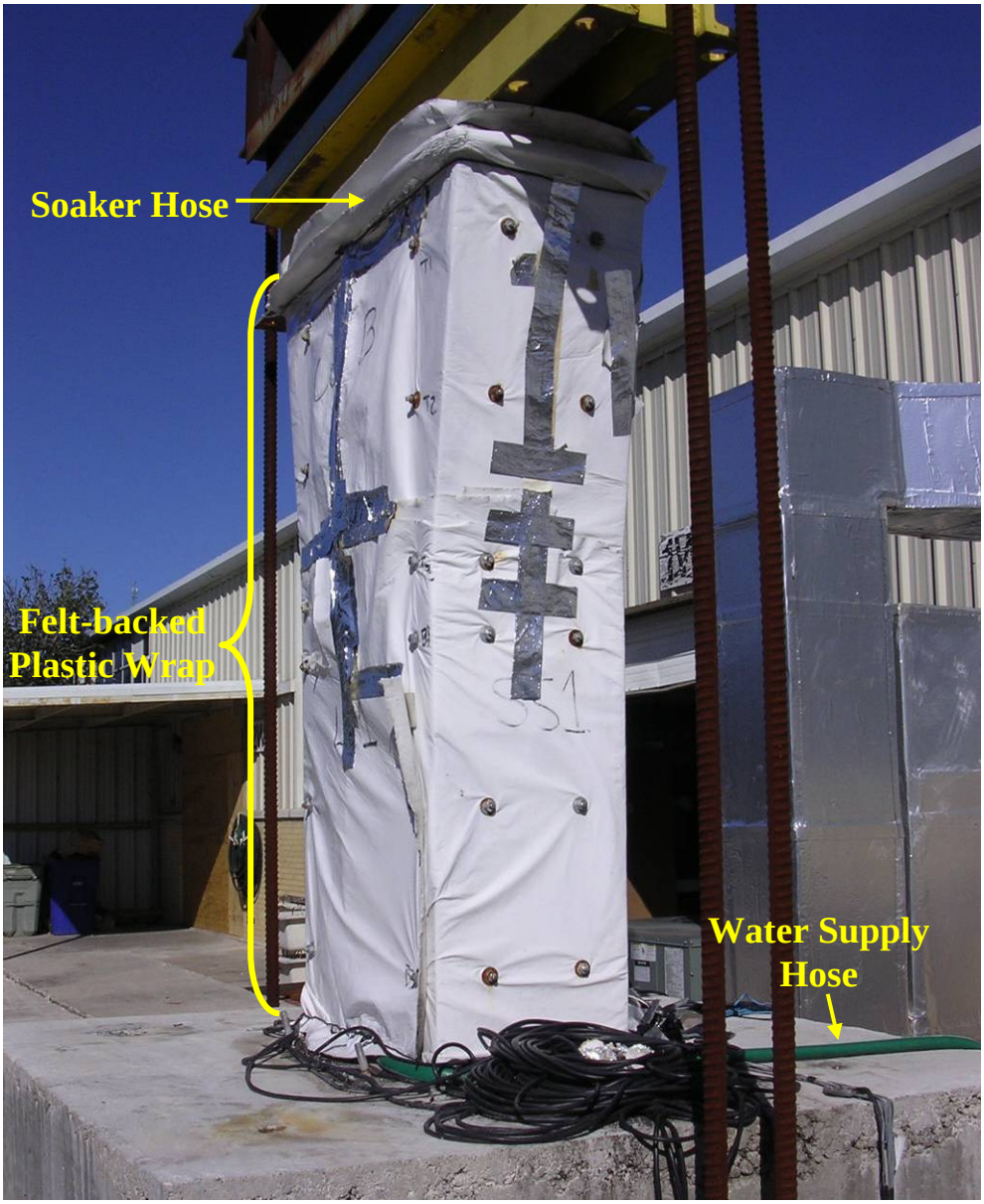

Figure 3.18: Moisture Retaining Wrap

3.3.5 Test Set-up

For testing of the columns, the same testing frame, loading ram, spreader beam and bearing pads as were used by Kapitan were employed. Figure 3.19 shows a close view of the loading ram and spreader beam arrangement and Figure 3.20 is an overview of the test set-up. As well, linear potentiometers were used to measure horizontal deflection of the column at the center of both long and short faces. The linear potentiometers were set up at the top, middle, and base of the column on each monitored face, as shown in Figure 3.21. This layout was intended to mimic the deflection monitoring system used by Kapitan. Exact locations of the instruments are found in diagrams in Appendix A.

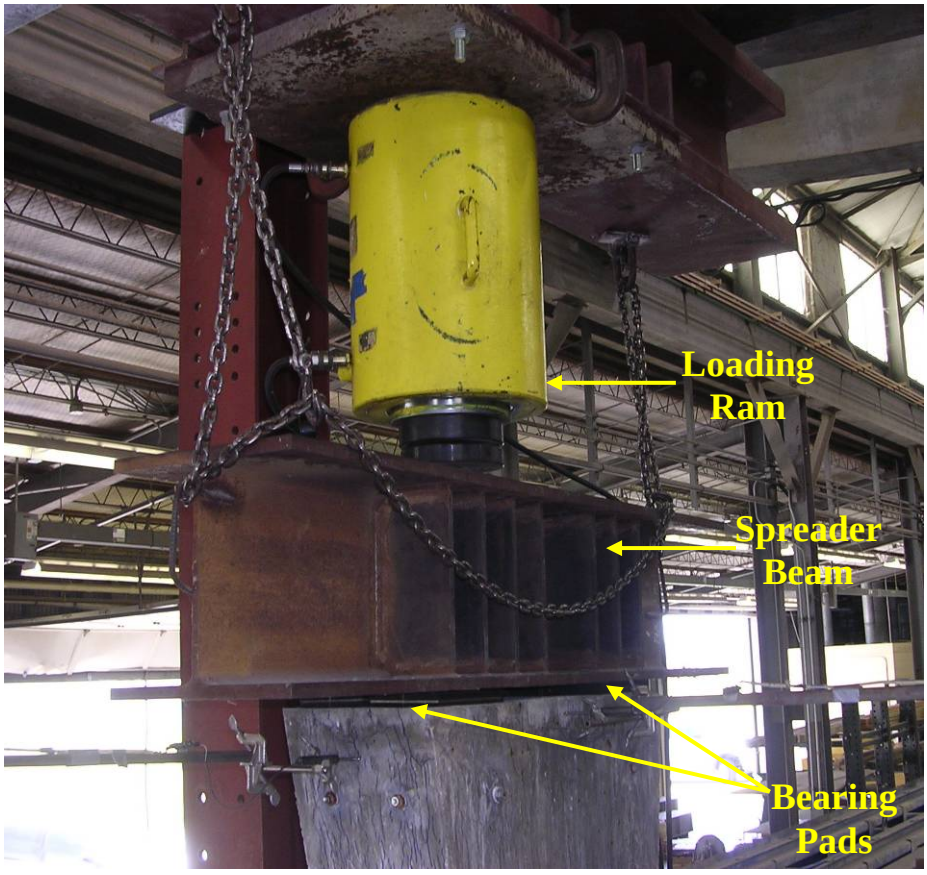

Figure 3.19: Spreader Beam and Loading Ram

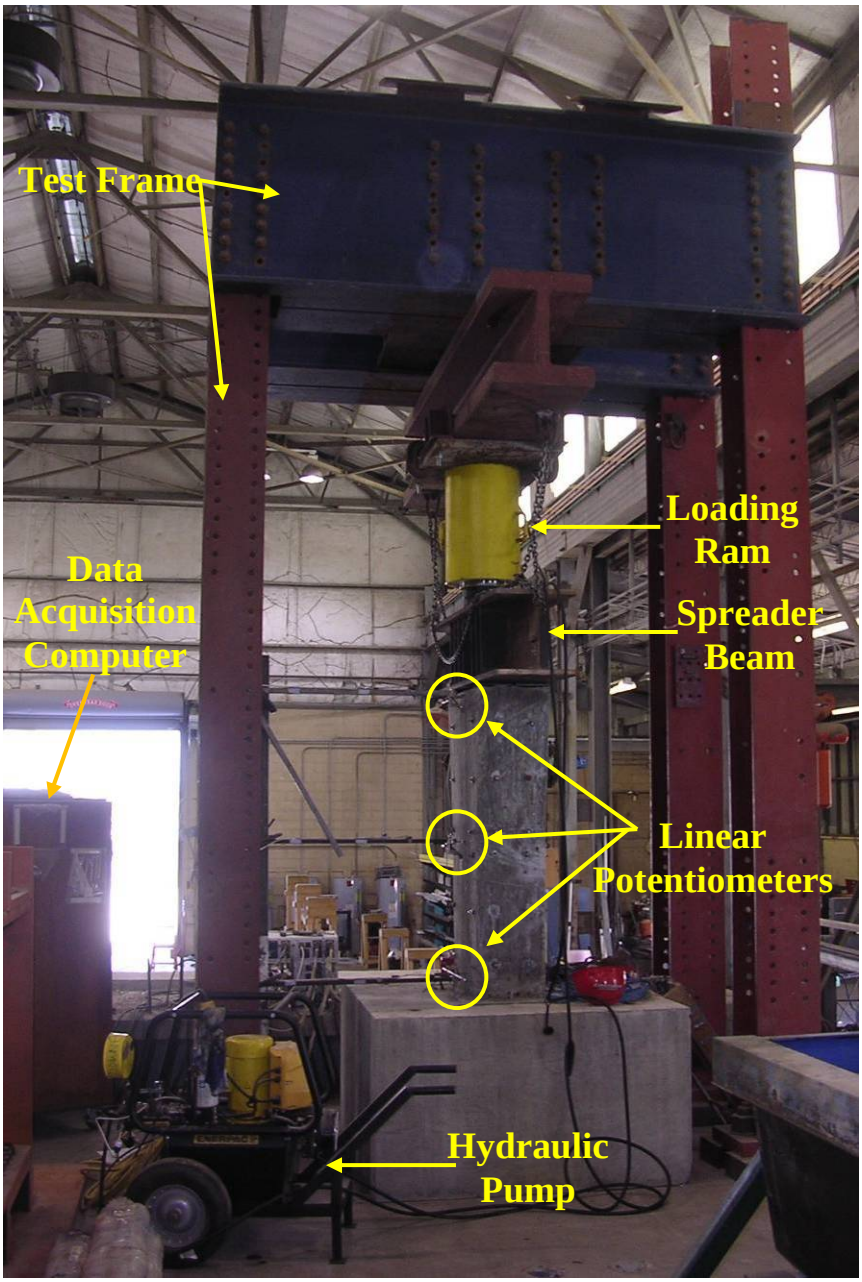

Figure 3.20: Overview of Test Set-up

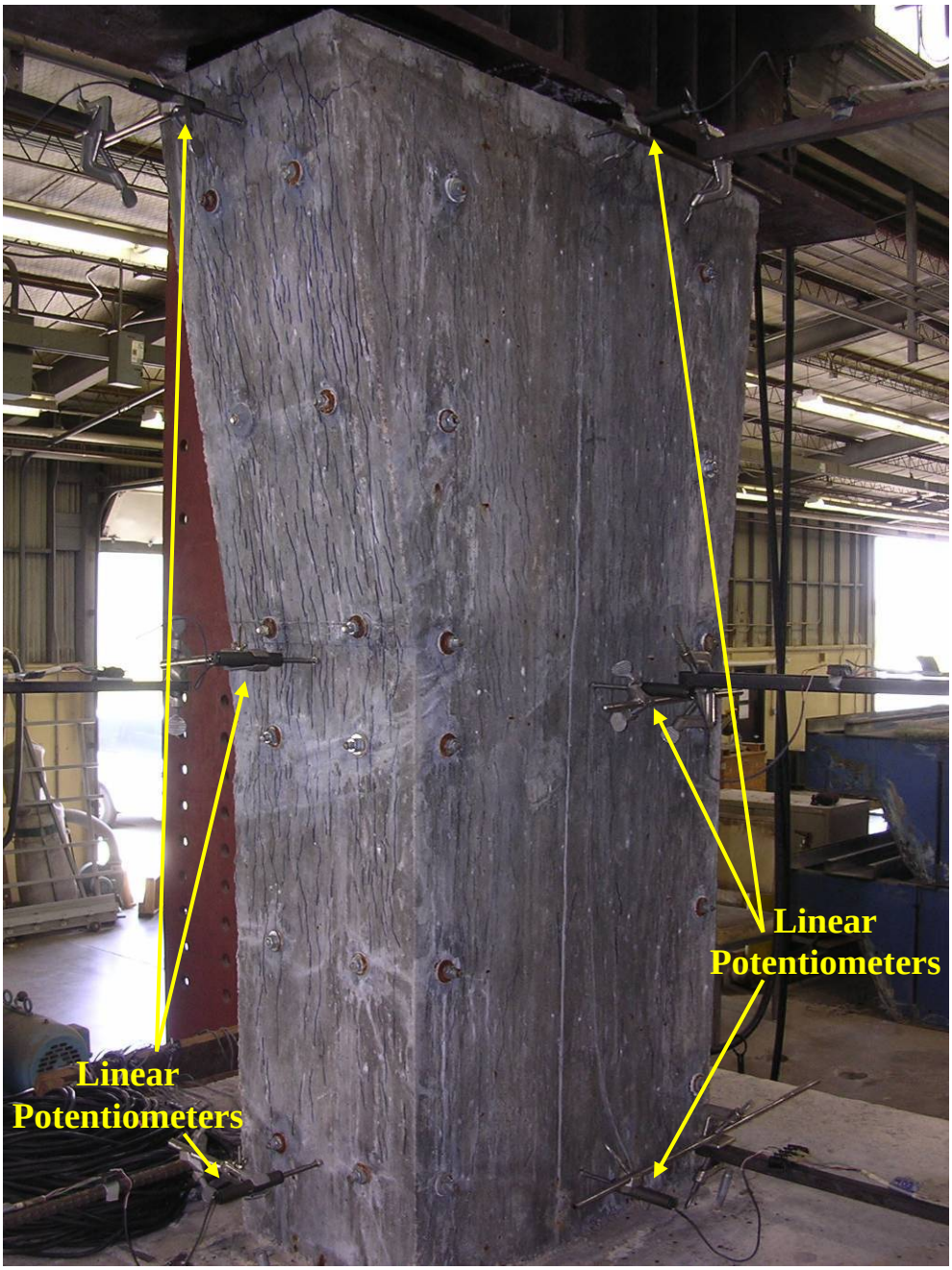

Figure 3.21: Linear Potentiometer Arrangement

CHAPTER 4
Bearing Specimens: Background and Methods

4.1 BACKGROUND

During the course of Kapitan's experimental program, the persistent bearing area failure mode of corner crushing raised concerns about the performance in the field of a bridge column affected by ASR/DEF. The repeated failure in the laboratory led to Kapitan's review of the original bearing area design. This review found that the bearing was not designed for biaxial bending. Instead, it had been designed assuming a less aggressive loading scenario, which only considered bearing in one plane[3]. As a result of this design assumption, the bearing pads had been designed such that the critical pad would carry 34% of the total axial load. In the worst case loading scenario modeled by Kapitan, AASHTO Load Case III with two lanes, the columns were subjected to biaxial bending and thus the critical pad carried 56% of the total axial load[3]. Thus, the difference in load cases considered led to a 56/34 = 1.65 or 65% increase in load on the critical bearing pad. Further, Kapitan used strut and tie modeling to calculate the load carried by the transverse reinforcing ties in the column capital[3]. Under the factored design load for AASHTO Case III with two lanes the ties were expected to carry 15 kips. However from their size, that load exceeds their maximum capacity of 11 kips. At the ultimate failure load observed during Kapitan's testing, the ties would be forced to transfer 37 kips, a value well over their expected strength[3].

From the experimental results that confirmed a crushing failure in the bearing area and the analysis of the bearing area deficiency in lateral reinforcement, it was decided to test various repairs that could reinforce the lateral tie capacity of the column capitals and thus increase the bearing performance. While the repairs were designed to address the bearing deficiency, the confinement provided by the repairs could also help suppress ASR/DEF expansion, as discussed in Chapter 2. Although the specific columns investigated by

Project 0-5218 had been shown to have excess capacity versus actual loads carried[3], there were columns in the San Antonio Y that may carry loads closer to their design capacity. If these columns were to begin to deteriorate due to ASR/DEF, already having adequate repair techniques documented would allow TxDOT to make timely and informed decisions to protect the public safety. This research completed well in advance avoids the situation of instigating a research program to find the answer at a time when the solution is imminently required.

4.2 DESIGN

As this series of specimens was intended to model the bearing behavior of the same columns as Kapitan's series, the same scale was used. It was determined to use the top sixteen inches of a Kapitan column, which models approximately the top five feet of the prototype column, in order to investigate bearing. Thus, the reinforcing layout is the same as the top sixteen inches of Kapitan and is shown in Figure 4.1 and detailed in Appendix B. As well, the formwork used was Kapitan's, only cut down to accommodate the new shorter specimens. The new formwork arrangement was designed to cast up to four specimens in series and is shown in Figure 4.2 with additional details presented in Appendix B.

Figure 4.1: Reinforcing Cage of Bearing Specimen

Figure 4.2: Formwork for Bearing Specimens

Due to the possibility that the concrete might not have cracked to desired levels for testing repairs in the timeline allowed for this research project, PVC pipes were cast into the column. As Kapitan did in his research, these pipes were used to create voids in the concrete section in order that splitting wedges could be inserted and used to mechanically crack the specimens. The splitting wedges were designed to cleave sections of stone by being inserted into core holes. The PVC pipes create the voids for the wedges so that no coring through the section, and likely damage to the reinforcing cage, was necessary. The PVC pipes are shown in the reinforcing cage in Figure 4.3 and a schematic of their spacing in a specimen is presented in Appendix B.

Figure 4.3: PVC Pipes in Reinforcing Cage

4.3 ASR/DEF CONCRETE AND CASTING CONDITIONS

The bearing specimens were cast with an ASR susceptible concrete mixture in order to attempt to instigate ASR or DEF. This concrete mixture, which is listed in Table 4.1, is the same one that was used to cast the ASR/DEF columns and reported in Section 3.3.2.

Table 4.1: Concrete Mixture Design per Bearing Specimen[98]

Component	Amount
Allentown Type III Cement	134 lb
Coarse Aggregate (TXI River Gravel)	295 lb
Fine Aggregate (Wright Materials Manufactured Sand)	198 lb
Water	60 lb
Super-plasticizer	13.4 oz
Sodium Hydroxide	527 g

In order to create the possibility of DEF damage, the casting temperature needed to be above 158 °F for at least six hours[32,33,42,66]. In order to reach these elevated temperatures the concrete was cast in a walk-in oven and heated overnight to raise the initial temperature of the concrete. As well, the formwork, reinforcing cages, and pre-measured materials for the concrete were assembled the day before in the walk-in oven used for curing and heated to 140 °F prior to concrete placement as shown in Figure 4.4. During casting the oven door was left open to accommodate the concrete placement. Figure 4.5 shows concrete placement in the oven. Thermocouples were located in the center and in one corner of each specimen so that the temperature profiles of the concrete were recorded. Although there was some difficulty with the monitoring program since the thermocouples were limited to a range of approximately 180 °F, the rest of the profile shows that they did reach and stay well above the required temperature for the specified time frame. Figure 4.6 shows a typical temperature profile for the initial curing of the concrete. All of the temperature profiles are shown in Appendix B.

Figure 4.4: Formwork, Reinforcing Cage, and Materials in Oven to Preheat

Figure 4.5: Placing concrete in a Walk-in Oven (Left), Vibrating Specimen (Right)[99]

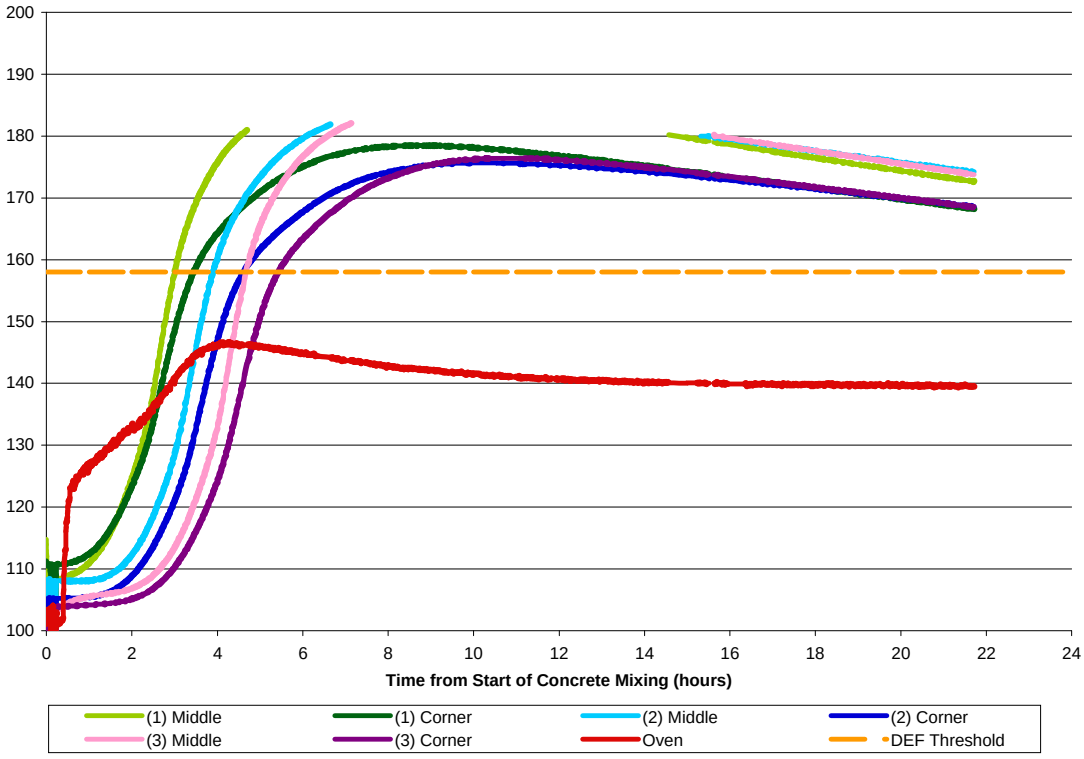

Figure 4.6: Temperature Profile for Bearing Specimens Cast July 10, 2007[98]

4.4 INSTRUMENTATION AND MONITORING

4.4.1 Strain Gauges

Strain gauges were applied to the reinforcing cages of the bearing specimens. As the goal of the repair was to improve the lateral confinement of the column capitals to improve the bearing capacity, every lateral tie was gauged at the top level of reinforcement. As well, four longitudinal bars were gauged in order to monitor axial loads in the specimen. The gauge locations are illustrated in Figure 4.7 and the gauges on the reinforcing cage are shown in Figure 4.8, where the gauges are covered in foil tape for protection. The strain gauge naming notation used indicates whether the strain gauge is monitoring transverse or longitudinal reinforcement. Labels beginning with a "T" designate transverse reinforcement gauges and "L" labels indicate longitudinal reinforcement gauges. Details about the type of strain gauges used are presented in Appendix B.

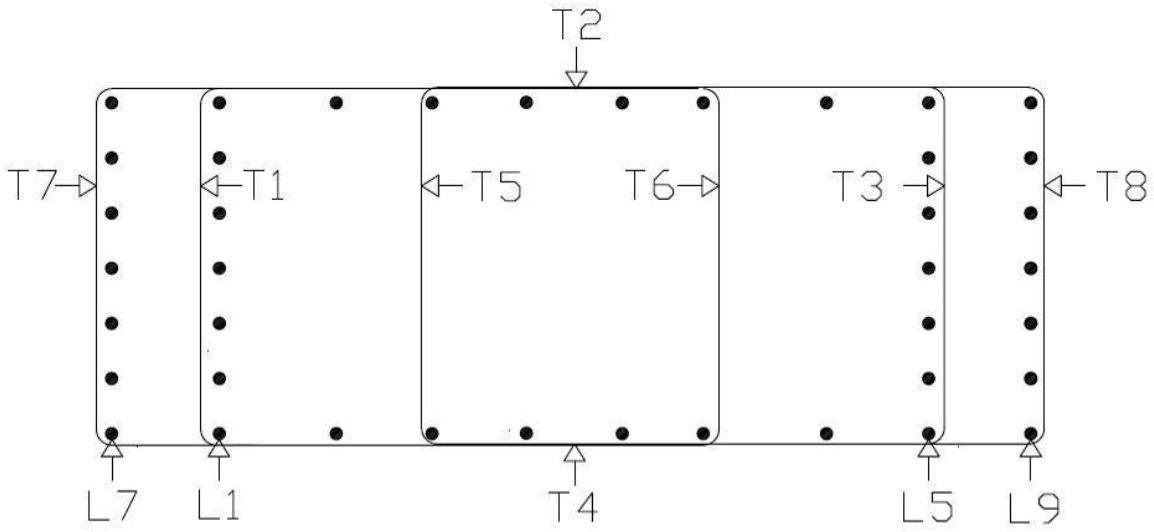

Figure 4.7: Strain Gauge Locations

Figure 4.8: Reinforcing Cage with Strain Gauges (Covered in Protective Foil Tape)

4.4.2 Demec Points

In order to measure external expansion of the specimens, half of them were instrumented with demec points. These points were spaced at six inches and were measured bi-weekly to monitor the expansion of the specimens. As the specimens were stacked two high for their exposure period, only the top blocks were instrumented due to accessibility limitations. The expansion plots are given in the results, Chapter 6. Figure 4.9 shows the demec points in the exposure set-up.

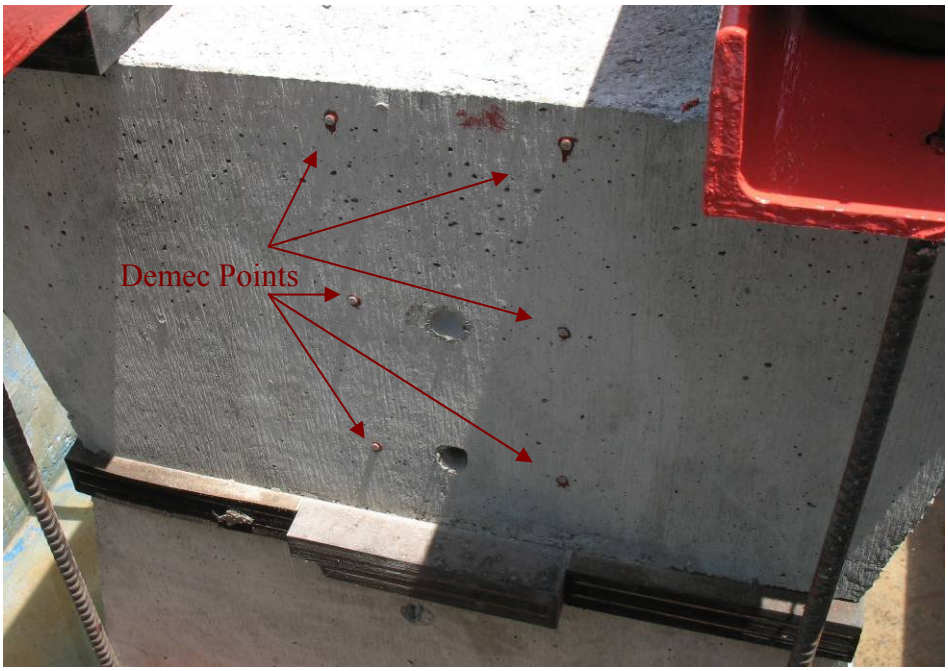

Figure 4.9: Demec Points on Specimen

4.5 EXPOSURE CONDITIONS

The exposure condition of the bearing specimens was designed to increase their likelihood of cracking in the required timeline and to cause the cracks orientation to simulate field conditions.

4.5.1 Post-Tensioning

The bearing specimens were stacked two high and then post-tensioned vertically in order to provide axial restraint to any expansion and thus induce longitudinal cracking. Figure 4.10 shows the blocks post-tensioned and in location for exposure. A schematic of the specimen layout, including casting date, is presented in Appendix B.

Figure 4.10: Post-Tensioned Specimens

4.5.2 Humid Environment

The researchers at CTR have enjoyed great success at triggering ASR in cylinders within a short period of time by suspending them above water at room temperature[100]. Thus, in trying to fulfill the goal of ASR/DEF cracking within four months for the purposes of the bearing specimens, it was decided to place the specimens above water in a humid environment. An existing exposure tank at FSEL was available for use. This tank was a good size to hold the five specimens stacks with room to move around them for the purpose of measuring the demec points. The specimens were raised up on blocks and the bottom of the tank flooded with approximately six inches of water as shown in Figure 4.11. The specimens and tank were then covered with black plastic to attract heat and help create a warm, moist environment as shown in Figure 4.12. To combat the falling

temperatures of autumn, submersible water heaters were added to the system to raise the water temperature and thus the air temperature around the columns through radiant heating via the water. The water heater arrangement is shown in Figure 4.13.

Figure 4.11: Water Flooding the Bottom of Exposure Tank

Figure 4.12: Black Plastic Covering Specimens

Figure 4.13: Water Heater Set-up

4.6 REPAIRS

As of mid-November 2007 the specimens were not showing signs of significant cracking due to ASR/DEF. As well, the expansion monitoring showed no significant expansion of the blocks at the time of destressing. From the numerous cracks observed in the ASR affected column specimens, it is likely that with a longer timeframe for exposure sufficient internal cracking could develop for testing. However, the time had come to begin repairing the specimens so that there would be sufficient time to test the repairs. Due to the lack of cracking, the PVC pipe created voids were used with splitting wedges to damage the specimens before repair. Figure 4.14 shows the splitting wedges in use to induce cracking. A damaged specimen and measuring of the crack width using demec points are shown in Figure 4.15. The specimens were cracked to an average width of 0.10 inches, which corresponds to the scaled crack width of 0.37 inches in the San Antonio Y. After mechanical cracking, the voids were filled with reinforcing bar to prevent crushing of the voids during testing. The level of cracking was chosen to be 120% of the maximum crack width used by Kapitan. The researchers anticipated that this level of cracking could cause a 25% reduction in capacity, which would allow a sufficient difference in performance between undamaged and damaged specimens to evaluate the effectiveness of the repairs. The demec measurements taken at the time of induced cracking are presented in Appendix B.

Figure 4.14: Splitting Wedges in Use to Damage Specimens

Figure 4.15: Damaged Specimen (Left), Measuring the Crack Width (Right)

All of the repair designs were based upon Kapitan's strut and tie modeling of the load demand on the transverse ties in the column capitals. The model was scaled to determine the lateral load required to make up for the 25% loss of axial load capacity. Kapitan's model considered all reinforcement in the top ten inches of the model column to contribute to the column capital's tie. Thus, the repairs were designed to carry 9.25 kips laterally and were restricted to the top ten inches of the bearing blocks. Calculation of

the repair load is presented in Appendix B. In order to verify that the design load level was appropriate the control blocks were tested first. One of these blocks was left undamaged to determine a baseline capacity. The other control block was cracked to the same average level of 0.10 inches as the repaired blocks. It was tested without repair to find the loss of capacity due to this level of damage. These tests were conducted first in the series as the difference in capacity was used to check if the repair design strength was appropriate to the specimens' as-built condition and concrete strength, so as to allow for the possible increase of the designed repair capacities prior to their application. Schematics and calculations of the repair designs are presented in Appendix B.

4.6.1 Concrete Jacketing

As steel provides significant tensile strength to reinforced concrete members, a reinforcing cage was designed to carry the entire additional lateral load for the concrete jacket repair. The repair jacket was designed to cover only the top ten inches of the specimen and the steel reinforcing bars were distributed throughout this depth to provide uniform confinement in the repaired region. Prior to application of the jacket repair, the specimen surfaces were intentionally roughened to increase bond between the existing and newly placed concretes. A sledge hammer was used to intentionally roughen the concrete surface by knocking off much of the specimens' sharp corners and pockmarking the flat surfaces. Figure 4.16 shows an example of the roughened surface. Due to the mobility of the specimens, the new reinforcing cages were constructed separately, as shown in Figure 4.17, and the specimens were then lowered into the cages. For a column in the field, the cage would have to be tied in its final position around the column. The formwork set up around the specimens is shown in Figure 4.18. As the concrete used to repair the bearing specimen had a small volume, commercially available bagged concrete mix was mixed at the laboratory and placed in the formwork. For this repair, the author used three sacks of eighty-pound size Quikrete 4000 psi concrete mix for each jacket. In less accessible applications of a concrete jacket, shotcrete could be simpler to implement than using traditional formwork. Shotcrete is a method of concrete application where the

fresh concrete is sprayed into position, in a manner similar to air brushing. The shotcrete requires a backing such as a single side of formwork, column, or another wall to apply[41,101]. Figure 4.19 shows the complete concrete jacket repair.

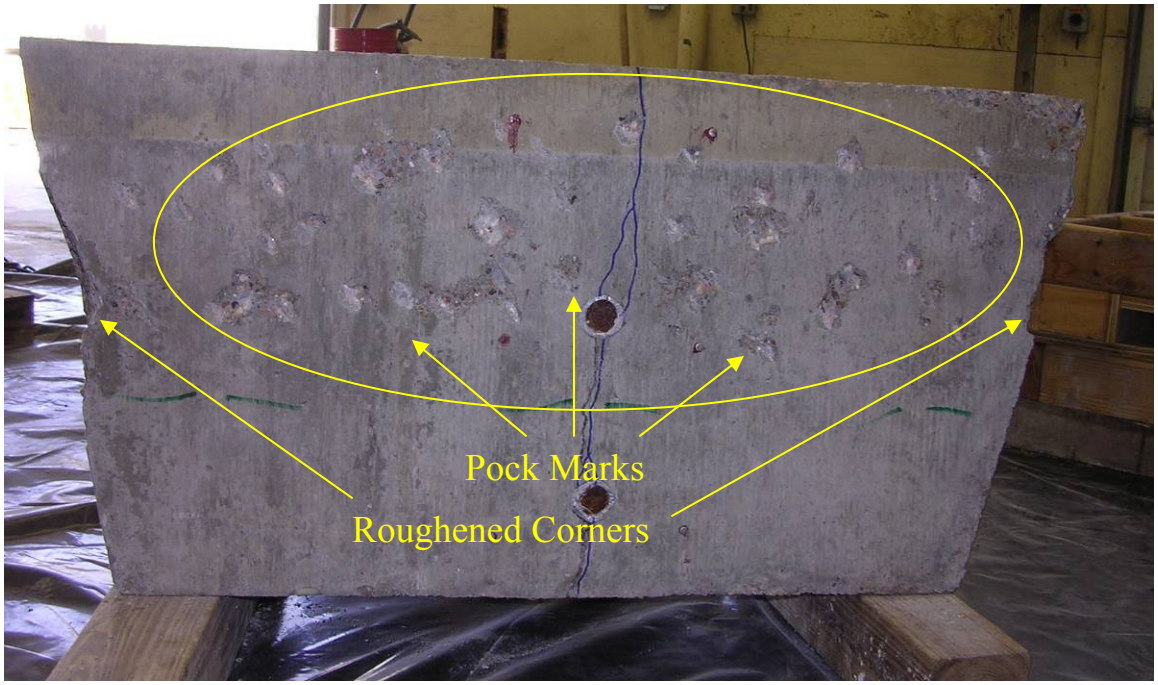

Figure 4.16: Intentionally Roughened Surface

Figure 4.17: Reinforcing Cage for Concrete Jacket Repair

Figure 4.18: Formwork Set Up for Placing Concrete

Figure 4.19: Concrete Jacket Repair

4.6.2 Post-Tensioning Clamp

The post-tensioning repair was intended to provide an alternative load path around the top of the column via post-tensioning bars and steel angles. In addition to adding lateral tensile capacity, the clamp further confined the concrete of the column. As shown in Ramirez[76], the tighter the fit of a steel repair to a concrete column, the better the performance. Thus, the bars were post-tensioned to the repair design load of 9.25 kips. The specimens were clamped in both the long and short directions. Two Power Team RH121 twelve ton rams were used to stress the post-tensioning bars. The rams were held away from the steel angles of the clamp by a stressing chair in order to allow tightening of the nut after the stress was applied. Figure 4.20 shows the tightening of the nut on the post-tensioning bar to lock in the stress. A Power Team Series P460 hand operated hydraulic pump, as shown in Figure 4.21, was used to apply the pressure needed to stress the bars. The pressure was checked using a dial gauge attached to the hydraulic system. The ram area was 2.76 in^2 so in order to apply 9.25 kips of force, the hydraulic pressure required was 9.25 k/2.76 in^2 = 3.35 ksi or 3350 psi. As the post-tensioning process was applying a load to the bearing block in its application, it was considered an active repair. The other repairs are considered passive in that they provided additional capacity, however it was not realized until the concrete was loaded and beginning to deform. Conversely, the post-tensioning provided the additional capacity for confinement even before the concrete is loaded. Figure 4.22 shows the complete post-tensioning repair.

Figure 4.20: Tightening the Post-Tensioning Nut

Figure 4.21: Hand Operated Hydraulic Pump

Figure 4.22: Post-Tensioning Repair

4.6.3 Packing Strap

This repair was designed to carry all the capacity demand through the steel section of the packing straps. The straps were tightened to a snug fit. While this tightening might have resulted in some small amount of post-tensioning due to the application process, the load induced was not significant compared to the demand capacity. Using the hand tensioning tools available at FSEL, the straps were given a close fit as shown in Figure 4.23, but a mechanized tensioner might result in more of a post-tensioning situation. To achieve the desired strength in the repair region, six 0.75 inch wide straps were distributed over the ten inch repair region. The straps were spaced at approximately 0.5 inches edge to edge as shown in Figure 4.24. For the purposes of this test, the author used Signode's Alex Plus 0.75-inch wide by 0.017-inch thick steel strapping, which had an ultimate load of 1.9 kips (ultimate strength of 149 ksi) per strap. As the literature on packing strap repair made no mention of special surface preparation, the straps were applied to the specimens as they were after mechanical splitting.

Figure 4.23: Tightening Packing Strap using Hand Tools

Figure 4.24: Packing Strap Repair before Testing

4.6.4 Fiber Reinforced Polymer Wrap

A carbon fiber wrap was selected due to its cost, potentially large improvements in column capacity based upon the literature review, and availability in the laboratory. Carbon fiber reinforced polymer repairs were, at the time of this study, being tested at FSEL by In Sung Kim, who generously contributed the materials and expertise to this repair application. The wrap was designed to carry the repair load by using one layer of material, running parallel to level. Prior to application of the carbon fiber wrap, the surface of the concrete was prepared by grinding the corners to a two inch radius and grinding off the cement paste layer on the face of the region to receive the wrap. The cement paste was ground off so that the repair could bond with the aggregate in the concrete to form a more substantial bond with the specimen[102,103]. Dust from the grinding was blown off the specimen using compressed air. Figure 4.25 shows the prepared surface on both a short side, shown to the left, and a long side of the specimen, shown on the right. The wrap was applied in two sections to better accommodate the taper. The wrap was centered on the long face and extra material was allowed to wrap up the short sides. The sections overlapped by at least five inches on each short face of the bearing blocks. A five inch overlap was required to provide full continuity across the splice. In order for the wrap to bond, the carbon fiber fabric was saturated with epoxy and additional epoxy was applied to the dust-free concrete surface by a paint roller. Excess epoxy was squeezed out of the saturated fabric by pulling the material through a hand held PVC roller, which is shown without the fabric in Figure 4.26. Prior to applying the FRP wrap to the specimens, a trial run was conducted using a one half scale Styrofoam mock-up in order to ascertain that the application plan would allow for sufficient overlap. The mock-up and a repaired specimen are shown in Figure 4.27.

Figure 4.25: Prepared Concrete Surfaces for FRP Application

Figure 4.26: PVC Rollers

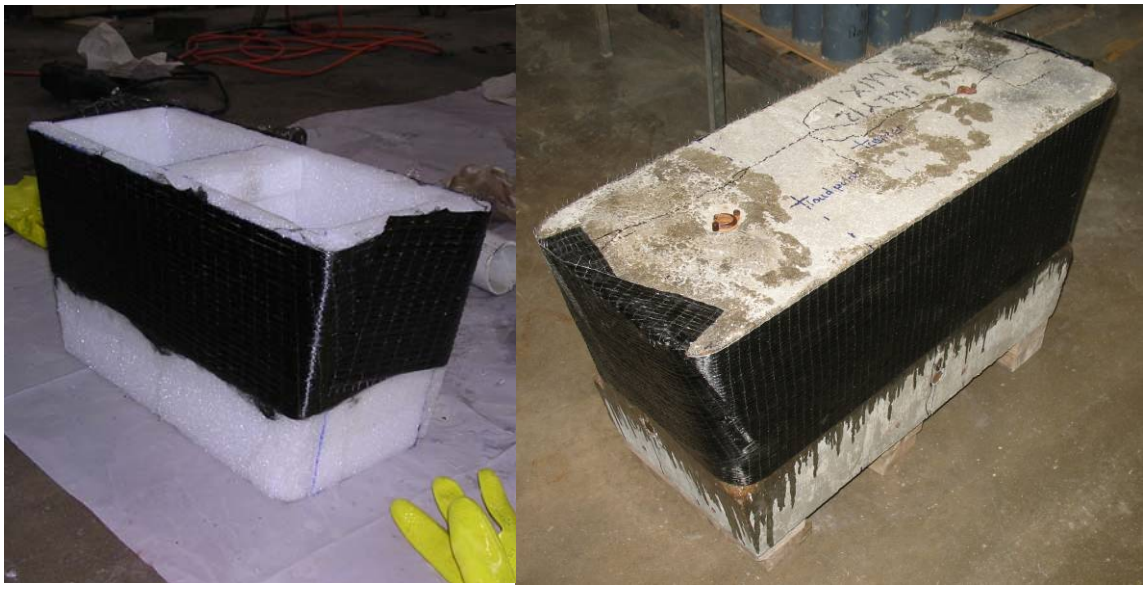

Figure 4.27: Mock-up of Specimen (Left), FRP Repaired Specimen (Right)

4.7 TEST SET-UP

The testing took place in the SATEC Systems, Inc. 600 kip capacity universal testing machine as shown in Figure 4.28. To accommodate the biaxial bending, the specimens were aligned under the spherical loading head so that the proper eccentricities were developed. As this alignment created a small overhang of the specimen beyond the bottom platen, a steel plate was added beneath the specimens to carry the load to the platen as shown in Figure 4.29. Calculations for the size of plate required are presented in Appendix B. Neoprene padding was used between each specimen base and the steel plate to accommodate any imperfections in the bottom face of the concrete, which could otherwise result in high local stress concentrations and thus a local failure at the base of the specimen. As the bearing blocks examine the effects of the same loading condition used in the scaled column specimens the same bearing pads and spreader beam as used by Kapitan were used for these tests. The strain gauges within each specimen were monitored by a data acquisition system, which is housed in the plywood cabinet seen in the left side of the picture in Figure 4.28. A specimen set-up for testing is shown in Figure 4.30.

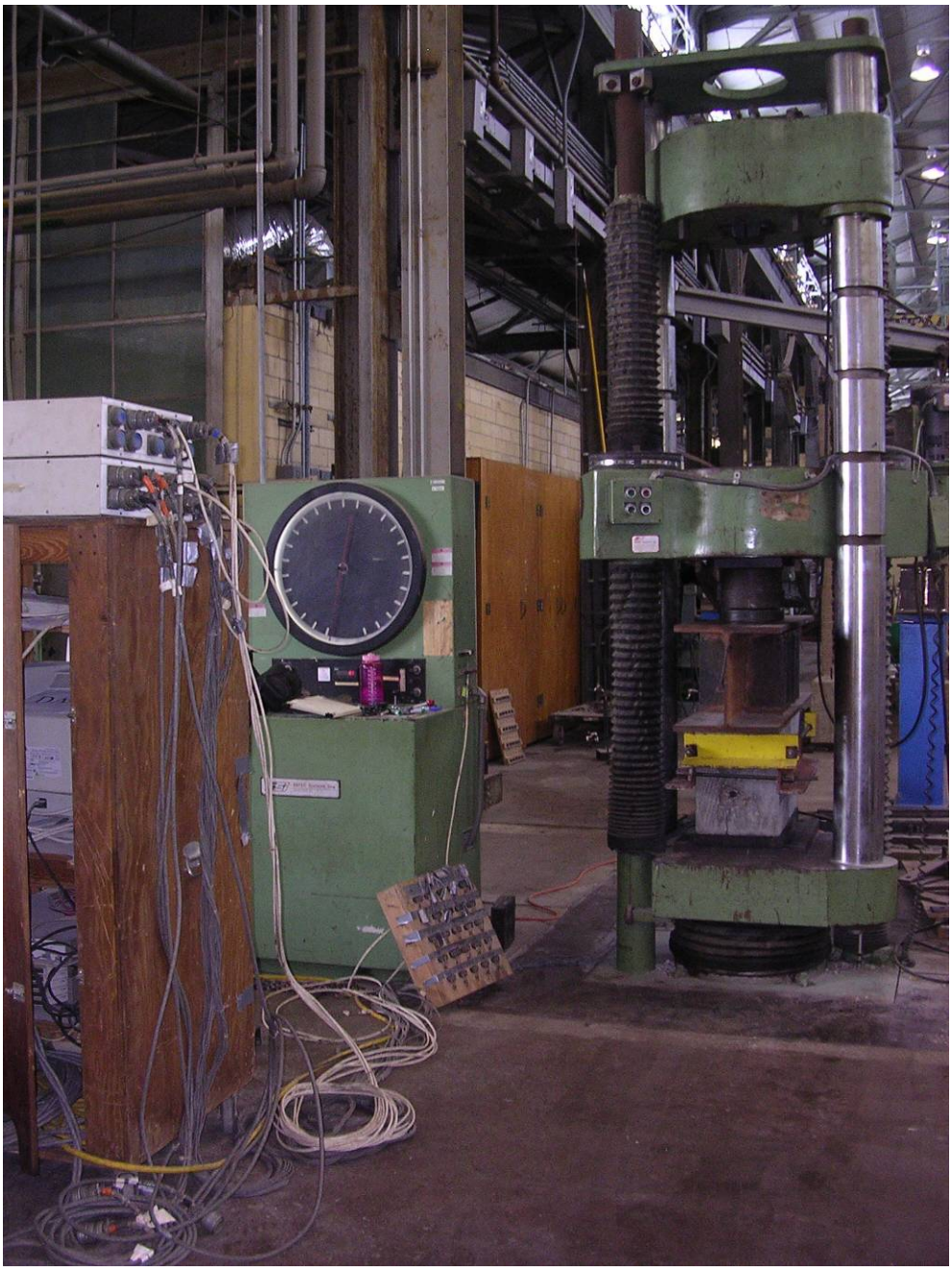

Figure 4.28: Testing Set-up

Figure 4.29: Steel Plate used in Testing

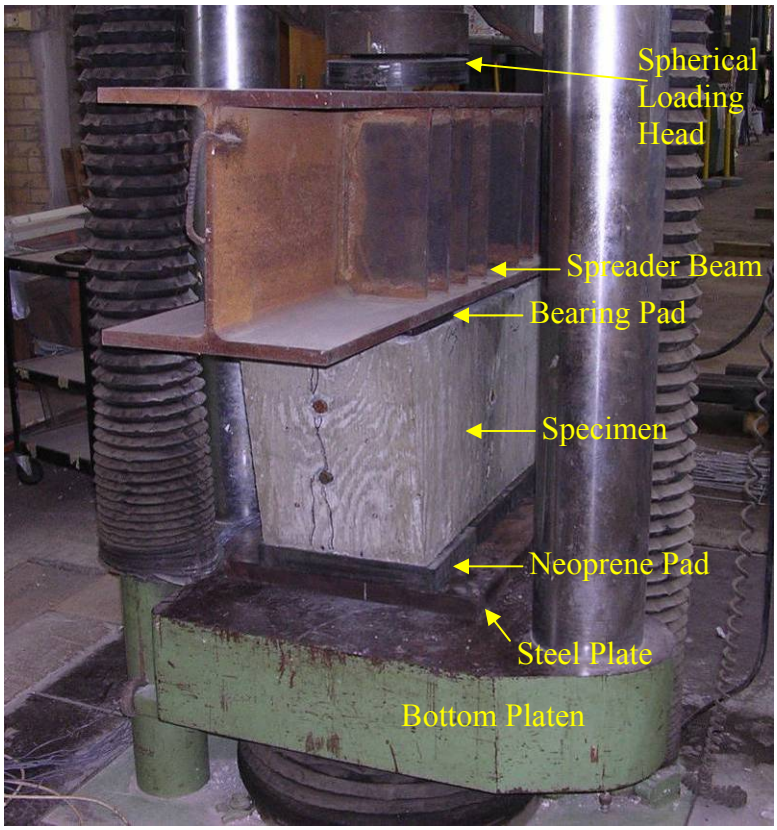

Figure 4.30: Specimen Ready for Testing

CHAPTER 5
Computer Model

5.1 INTRODUCTION

As stated in Chapter 1, one of the goals of this research project was to develop a computer model that could predict the capacity of columns with pre-existing cracks. To accomplish this goal, a computer model of the scaled column specimens was generated. Once calibrated to Kapitan's control specimen results, the model was used to model Kapitan's other results. The analytical study achieved another of the project's goals: using the calibrated model to calculate the capacity of the scaled column with increasingly large widths of pre-existing cracks. The development of the computer model and the results from the analytical are described in this chapter.

5.2 BACKGROUND ON ATENA

Cervenka Consulting Inc. developed the computer program ATENA (Advanced Tool for Engineering Nonlinear Analysis) to model the non-linear behavior of concrete and reinforced concrete structures[104-107]. The company, which is located in the Czech Republic, was founded in 1992. Ensoft, Inc. of Austin, TX (USA) is the ATENA distributor for the United States of America. The program ATENA uses finite element theory to model reinforced concrete structures. ATENA also models how cracks develop and propagate in structures, which is an important program feature for this research program. ATENA was the only program that the author found that explicitly models the cracking of concrete. Modeling the cracking in the computer program was essential as the size and pattern of the concrete cracking was what first alerted TxDOT to the ASR and DEF presence in San Antonio. As well, crack size gives an indication as to the amount of ASR/DEF expansion that has taken place in the columns. For instance, the variable in Kapitan's specimens was the level of cracking induced in the columns prior to loading[3]. Therefore, it would not be prudent to ignore the pre-existing cracks in the computer model. ATENA features a graphical user interface for defining the modeled

structure. This interface then automatically creates an input file for the analysis portion of the program. Other finite element programs require the user to write this input file. An input file is typically a text file where the user defines every node by coordinate as well as defining the load steps. The graphical interface is a great advantage as it streamlines the modeling process for the user[104-106].

5.3 BASE MODEL

A base model of the Kapitan columns, including the footings, was developed. The model included the entire reinforcing cage, PVC voids, and concrete material properties. Figure 5.1 shows the model with the surface removed so that the reinforcing is visible. Figure 5.2 shows the model with its exterior surface. The modeled column was loaded through the column's four bearing pads, as shown in Figure 5.3. These bearing pad surface loads, which are shown in Figure 5.4, proportioned the total load following Kapitan's bearing pad load calculations. Thus, the most heavily loaded bearing pad carried 56% of the total vertical load, just as it did during laboratory testing[3].

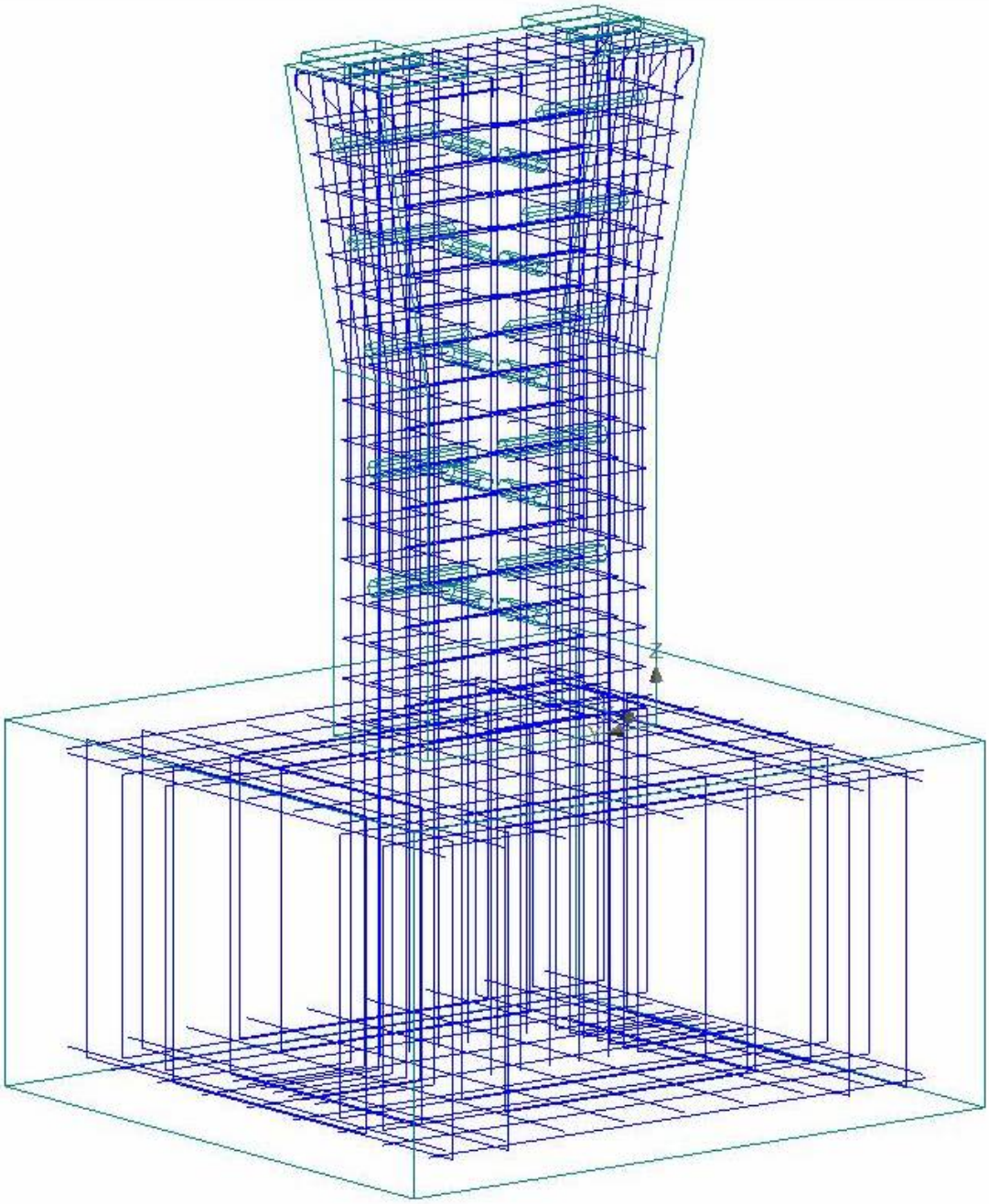

Figure 5.1: ATENA Model, Interior View

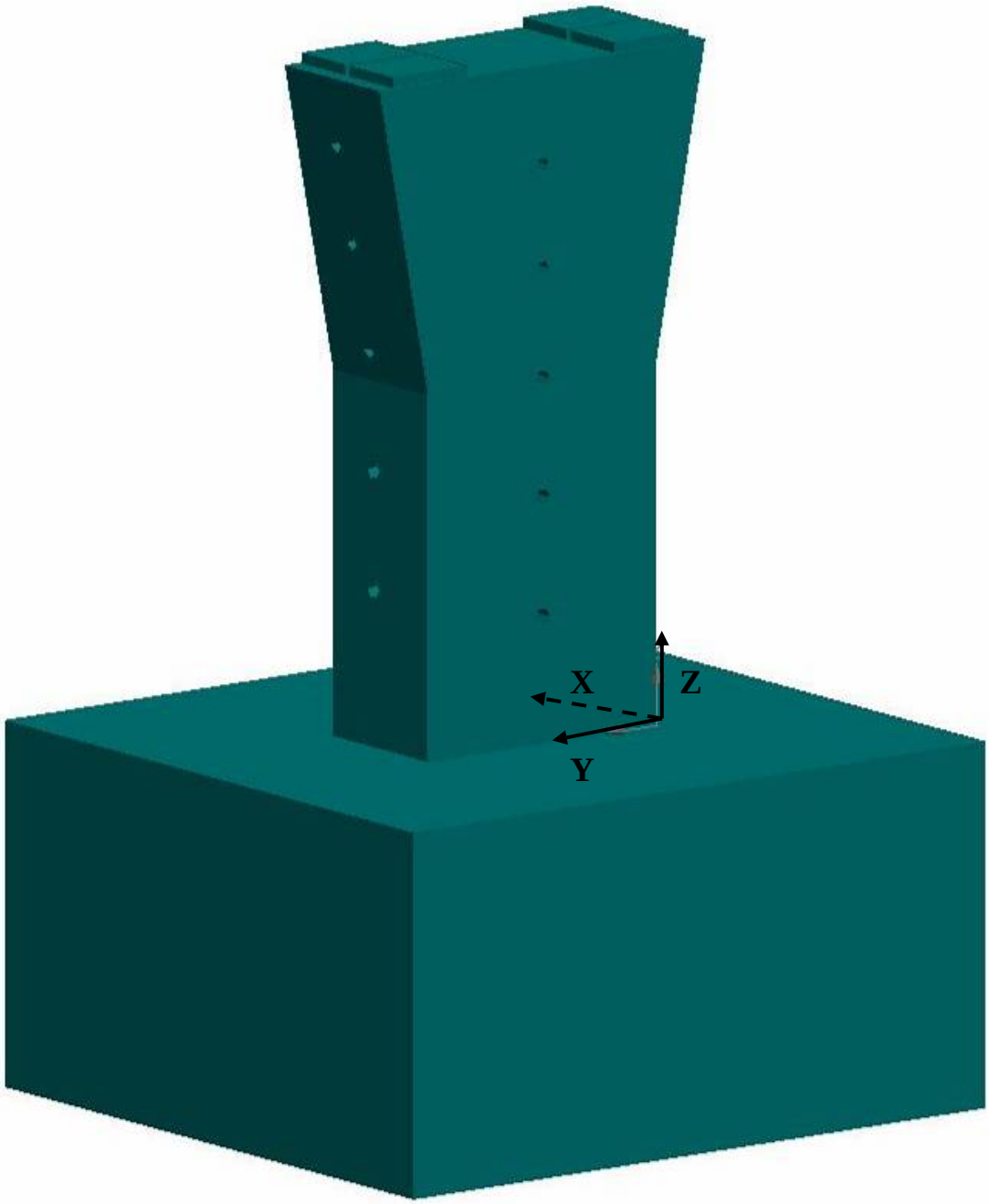

Figure 5.2: ATENA Model, Exterior View

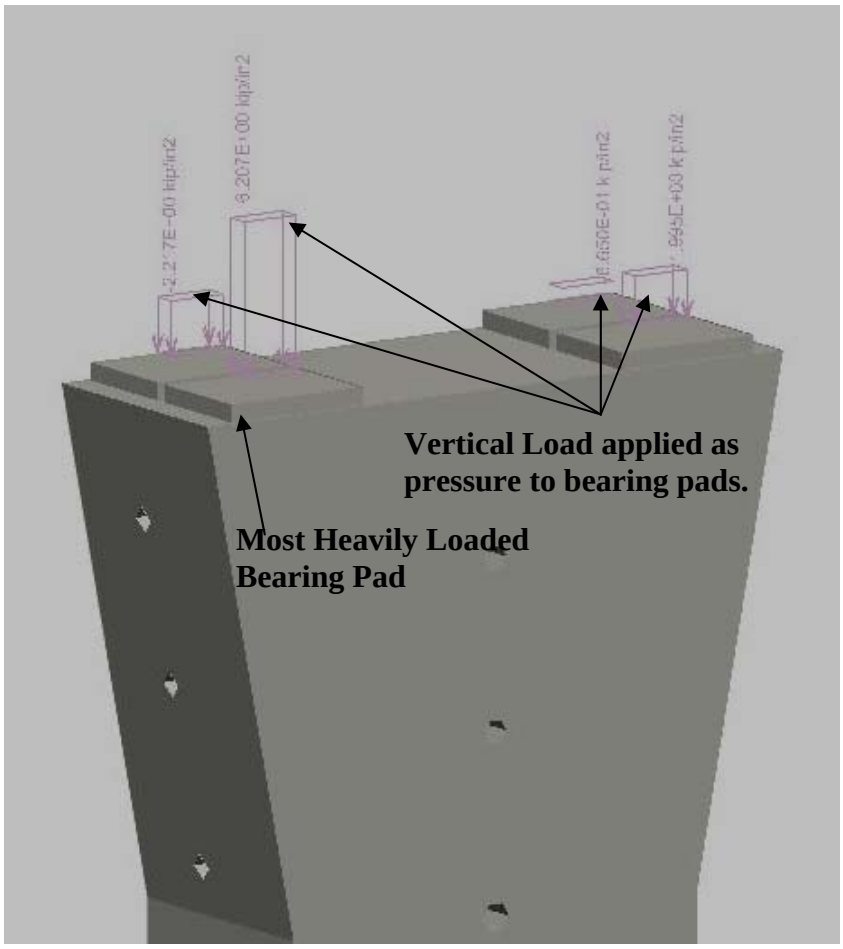

Figure 5.3: Top Loading as Applied in ATENA

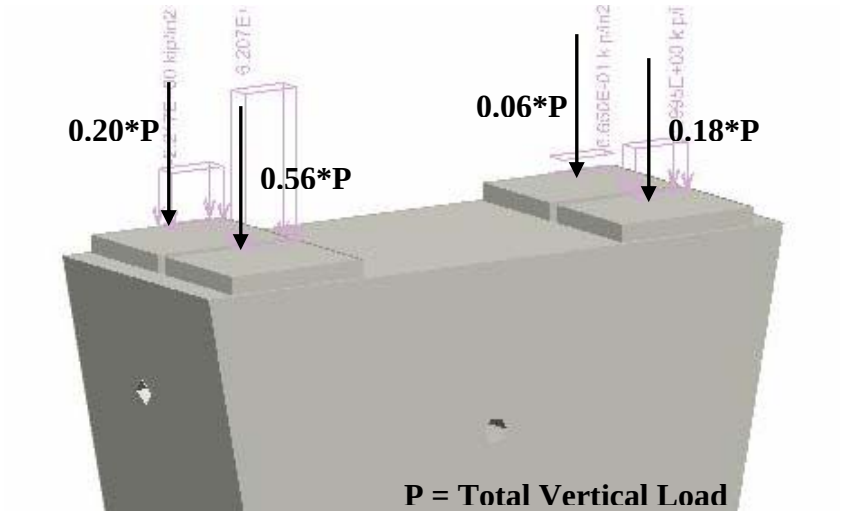

Figure 5.4: Load Distribution by Bearing Pad, based on Kapitan

Once the physical dimensions of the column were entered, ATENA generated a finite element mesh, as shown in Figure 5.5, for evaluation of the column. In the column proper there were 9938 elements, the column footing contained 726 elements, and each of the four bearing pads contained 30 elements. Thus, the model contained a total of 10784 finite elements. The footing and bearing pad meshes contained brick elements, whereas tetrahedral elements made up the column mesh. Figure 5.6 illustrates the appearance of a generic brick and a generic tetrahedral element. The size of these elements was flexible as the program developed a best fit considering the geometric constraints input by the user. For instance, each bearing pad mesh was comprised of thirty brick elements. This mesh was one element tall, five elements wide, and six elements long. The brick elements could not be perfect cubes as the bearing pad was 7.5 inches long, a value that is not a multiple of 0.88 inches, the bearing pad's height. Thus, to accommodate the bearing pad dimensions, each brick element was 1.15 inches wide by 1.25 inches long by 0.88 inches tall. The column, meshed with tetrahedral elements, had greater fluctuation in element size than the block shaped footing or bearing pads. The program was constrained by the flared column capital and the PVC voids. Figure 5.5 shows the mesh as it appeared on the column surface. The variation in size was especially prominent around the voids. Where the tetrahedral elements developed a more regular pattern, they averaged 3.25 inches in height. The footing, which was a plain rectangular block, had brick elements of a consistent size. These elements were 5.23 inches long, 4.91 inches wide, and 5 inches tall. ATENA did not report the total number of nodes generated during the creation of the finite element mesh. Each brick element had eight nodes and each tetrahedral element had four nodes as shown in Figure 5.6. Determining the number of nodes is not as simple as multiplying the number of elements by the number of nodes per element. When elements adjoin, they share nodes along their common side, as shown in Figure 5.7. With all brick elements it is fairly simple to determine the number of nodes through multiplication: (# elements long + 1)*(# elements wide + 1)*(# elements tall + 1). For meshes comprised of tetrahedral elements, especially when their spacing varies, determining the number of nodes requires

painstaking counting and some guesswork. It would be far simpler if the program that generated the mesh would report the number of nodes used. It would be impossible for a tetrahedral mesh to have more than four times the number of elements, although the number of nodes is probably much lower. It is more likely that the value is closer to one node per element, due to considerable sharing of nodes.

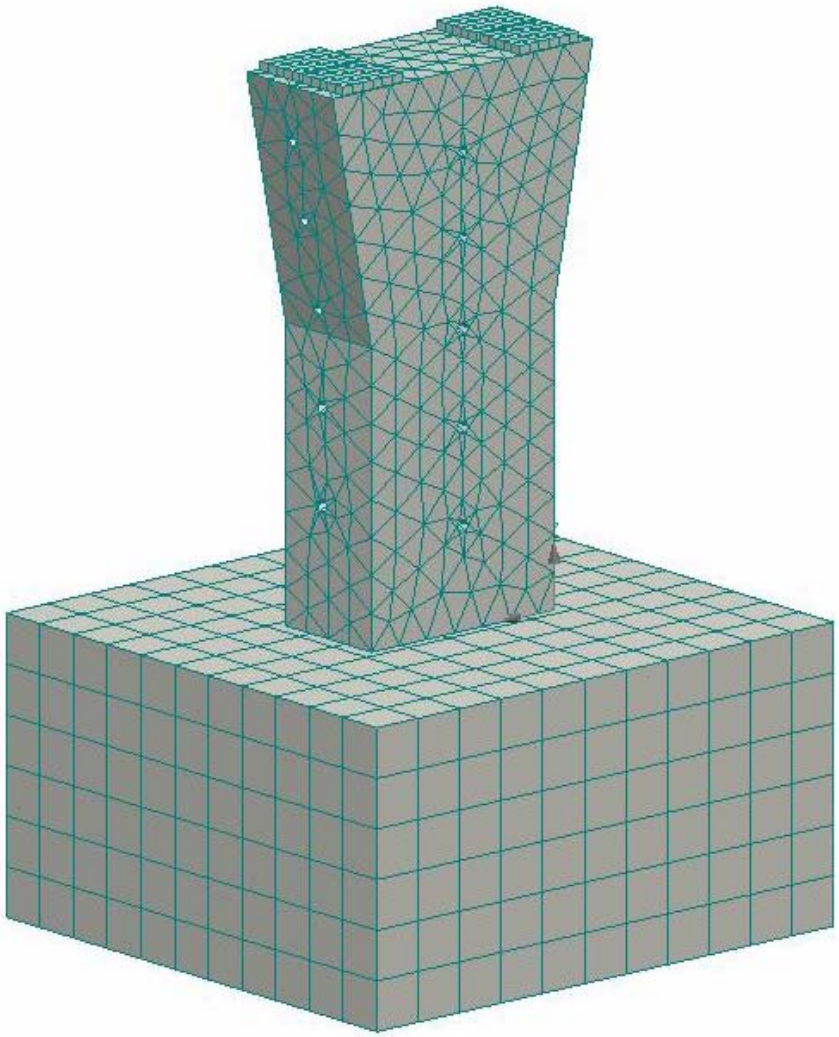

Figure 5.5: Finite Element Mesh Generated by ATENA

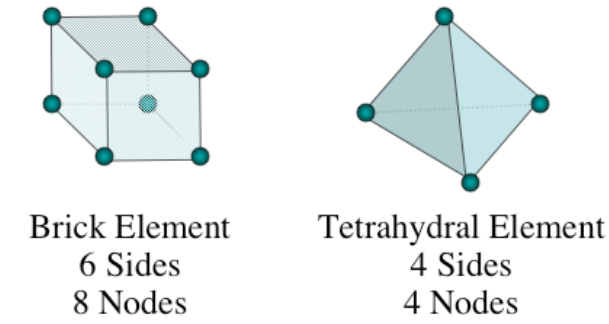

Figure 5.6: Brick and Tetrahedral Elements

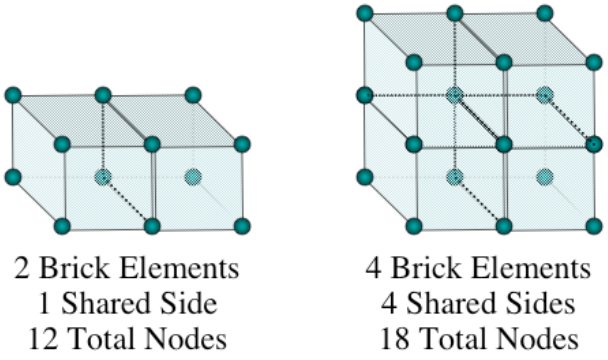

Figure 5.7: Multiple Elements Share Nodes

The details of the material model are presented in Table 5.1. Only the cylinder strength of concrete was known from testing. Thus, the elastic modulus and tensile strength of concrete values were based upon relationships, used in ACI 318-05, between these two values and the cylinder strength. Two additional concrete material properties, specifically the critical compressive displacement and plastic strain at the compressive strength used in the model, were calculated from the work of Ford, Chang, and Breen[108]. Except for the properties described above and the concrete's specific fracture energy, all other concrete material properties in the table were default values.

Table 5.1: Material Model Details

Property Name	Value Used

Elastic Modulus, E	4341 ksi
Poisson's ratio, μ	0.200
Tensile Strength, f_t	0.5712 ksi
Compressive Strength, f'_c	-5.800 ksi
Specific Fracture Energy, G_F	$3.308*10^{-4}$ kip/in
Critical Compressive Displacement, W_d	-0.0083 in
Plastic Strain at f'_c, ε_{cp}	-0.001364
Failure Surface Eccentricity	0.520
Multiplier for the Plastic Flow Dir., β	0.00
Specific Material Weight, ρ	$8.681*10^{-5}$ kip/in^3
Coefficient of Thermal Expansion	$6.667*10^{-6}$ 1/°F
Fixed Crack Model Coefficient	1.000

5.4 MATERIAL CALIBRATION

The base model was compared to the measured control specimen results reported by Kapitan[3] in order to calibrate the material model. ATENA has the capability to account for numerous details of concrete properties such as specific fracture energy. As described previously, a number of these details were assumed using relationships between these characteristics and cylinder strength. A general value provided as a default by the program was used for all other values. The specific fracture energy, critical compressive displacement (W_d), and plastic strain at compressive strength (ε_{cp}) were the parameters that were originally adjusted to calibrate the model. Once the W_d and ε_{cp} values were changed to their final values by using the Chang, Ford and Breen formulas, the specific fracture energy value was the only parameter modified for calibration. Interestingly, the specific fracture energy value that provided the best calibration for the model was the default value originally supplied by the program.

The application of top loading in the computer model was based on arc length theory, in which both the actual load applied and the resulting displacements were adjusted during iterations to solve for equilibrium. The arc length method was thus able to model the descending branch of loading. The force adjustment allowed the program to reduce the

load at each load step, including in the post-peak region[105]. Although the force adjustment of the arc length method was useful to model the plastic behavior and post-peak performance of the modeled structure, the program did not appear to provide a method to monitor the final applied load at each load step. Thus, the user knew the number of load steps that were solved successfully, but needed to exercise some creativity in determining the actual load applied by the program.

The author developed a method to determine the total vertical load applied to the column by monitoring the maximum vertical nodal force in the column. An example of the load calculated after a certain load step will be intermingled with the following description of the calculation process to illustrate the process. As there were thousands of nodes in the finite element mesh, the force at a single node was small compared to the total vertical load. The maximum vertical nodal force was plotted versus the expected total vertical load based upon the load steps completed as shown in Figure 5.8. There are two x-axes in this figure. The top axis, which has units of percentage, corresponds directly to the value of load applied in the model. The bottom axis is the value of the percentage converted into kips. In the computer model, the loading was assigned in each load step as a percentage of the load assigned to the column when the model was built. The load assigned to this model was Kapitan's total measured vertical load of 478 kips for the control specimen. Therefore, in the first step of vertical loading, the model applied ten percent of the experimental load. The expected total load in Figure 5.8 was based upon the completed load steps and thus was a summation of the load assigned at each step. Because the load steps were assigned percentages, the total load from this summation was also a percentage of the total measured load.

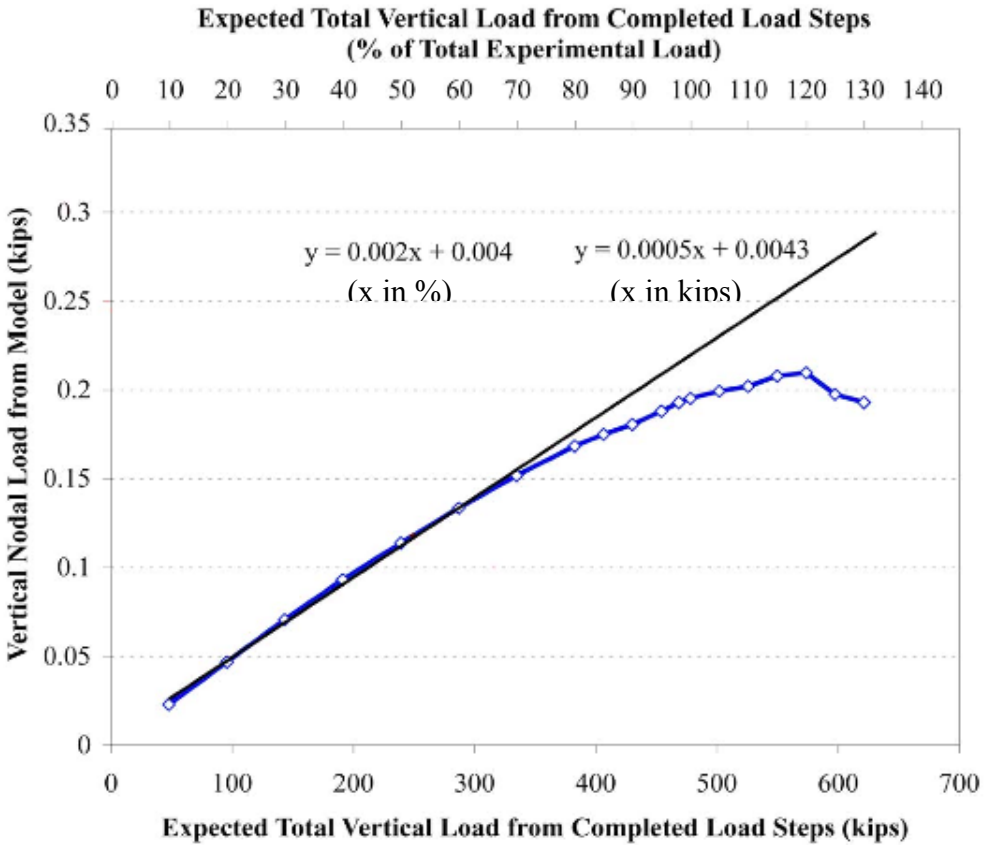

Figure 5.8: Calculated Nodal Load versus Expected Applied Load, Control Column

Under low levels of vertical load, at the start of top load application, the nodal load and expected load increased linearly as shown in Figure 5.8. As well, a black linear trendline was fitted through this linear portion of the plot in order to determine the slope of this proportional relationship. There were two trendline equations shown to correspond to the different x-axes. If the arc length method had not adjusted the applied load, then the entire curve in Figure 5.8 would be linear. The total vertical load was reduced during load steps, however, and thus the nodal load fell short of the behavior predicted by the trendline in the inelastic response and post-peak regions. This shortfall is shown in Figure 5.8 as the difference between the black trendline and the blue plotted line. Equation 5.1 presents the approach used for the total vertical load calculation. Calculations of the total vertical load are presented in Appendix C.

$$\frac{\text{nodal load from model}}{\text{expected nodal load (from trendline)}} * \text{expected applied load (based upon completed load step)} = \text{calculated applied load}$$

Equation 5.1: Calculating Applied Vertical Load

The maximum nodal load reported at each load step was assumed to be proportional to the total vertical load applied by the program. Recall that the black trendline in Figure 5.8 was the proportional relationship between nodal load and the total expected load. The reported nodal load as a percentage of expected nodal load from the trendline projection was used to calculate the total applied vertical load. This percentage was multiplied with the expected total load to determine the total load applied by the program after the arc length method reduction of load. For example, after fifteen load steps, the expected total vertical load was 115% of measured load (550 kips). Recall that each load step assigns a percentage of the load. Thus, percentages were used in the calculation of the adjusted total load, which were converted to kips at the end of the calculation. As well, the trendline equation in kips needed four significant digits to have a non-zero slope. As ATENA's load application provides at most three significant figures, the kip-based trendline equation indicates a greater level of precision than is justified, which is another reason why the percent-based trendline equation was used. After fifteen load steps were completed, the trendline equation indicated a maximum nodal load of 0.234 kips (=.002*115%+.004). The maximum nodal load reported by the model was only 0.208 kips. To find the "percentage of the nodal load expected by the trendline projection" (from Equation 5.1) simply divide the reported nodal load by the predicted nodal load and multiply by 100. To continue the example: 0.2078 kips / 0.234 kips * 100 = 88.8%. To calculate the total applied vertical load, multiply the expected load by this percentage. In this example the 88.8% of 115% of the measured load equals 0.888(115%) = 102% measured load = 1.02(478 kips) = 488 kips.

Figure 5.9 presents the assumed proportional relationship between vertical nodal load and the calculated total applied vertical load. Note that the arc length theory reduced the actual load applied to a value less than the load assigned by the load steps. For instance, in the preceding example, the expected load of 550 kips corresponded to a calculated load of 488 kips. Thus while Figure 5.8 shows the maximum expected load to be over 600 kips, in Figure 5.9 the total calculated load for the same model, which was corrected for the arc length reduction, is just shy of 500 kips.

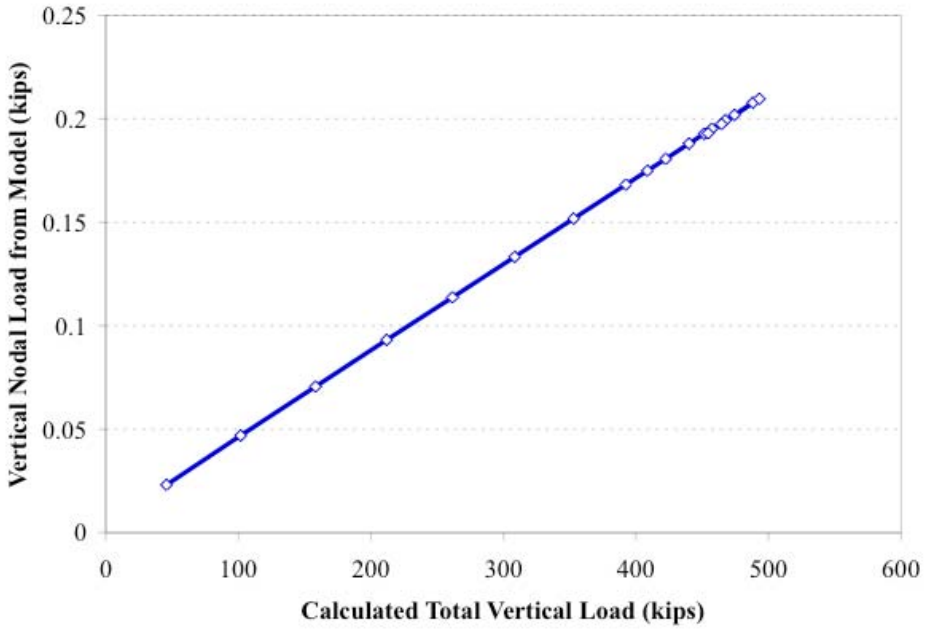

Figure 5.9: Assumed Relationship between Nodal Load and Calculated Load

Figure 5.10 is a load deflection curve for the movement of the tip of the most heavily loaded corner of the specimen in the control column model. The left side axis displays the total vertical load in kips and the right side axis relates the loads to the measured maximum loads for the control column. The displacements are negative or positive in relation to the model's axis orientation, which is illustrated in Figure 5.11. For instance, the z-axis was in the vertical direction and so the negative displacement indicates the corner was moving down. The y-axis paralleled the long sides of the specimen and the x-axis paralleled the short sides of the specimen. Figure 5.10 also shows the x- and y-axis displacements from the top of the control column as measured by Kapitan. These

displacements were measured at the top center of one long and one short column face, as indicated in Figure 5.11. As the load-deflection curves from the computer model and the experimental testing were from similar (but not identical) locations, the curves were expected to be comparable with some variations. For example, Figure 5.10 shows that the two load deflection curves have similar slopes until the load neared its peak value. The cause of variation could be that as the most heavily loaded corner crushed, it deflected outwards (positive along the y-axis and negative along the x-axis) to a greater extent than the sides of the column, which were monitored by Kapitan. When the concrete crushed near the peak value, the monitoring point on the tip of the most heavily loaded corner, which was going through a local bearing failure, deflected more than the monitoring point away from the localized failure. That the calculated curve was sloped similarly curve to the measured curve indicated the excellent fit of the material model. The offset between the measured and calculated curves was likely from experimental error, such as bumping the instrumentation while mapping cracks.

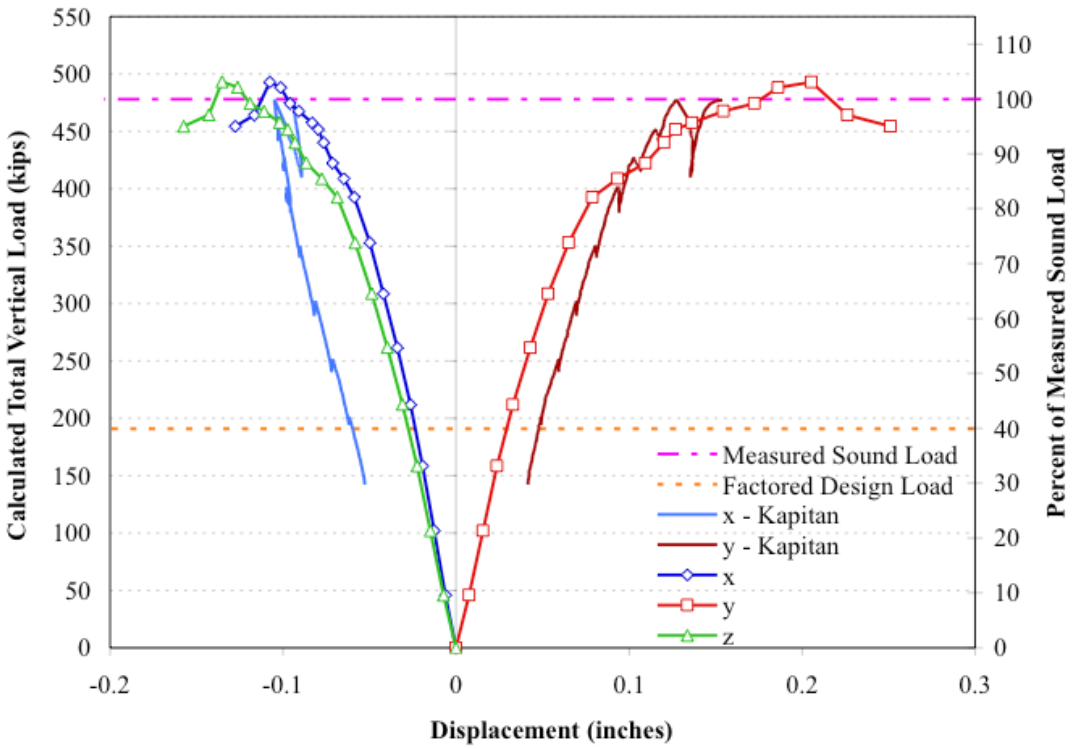

Figure 5.10: Load v. Displacement at Heavily Loaded Corner, Control Column

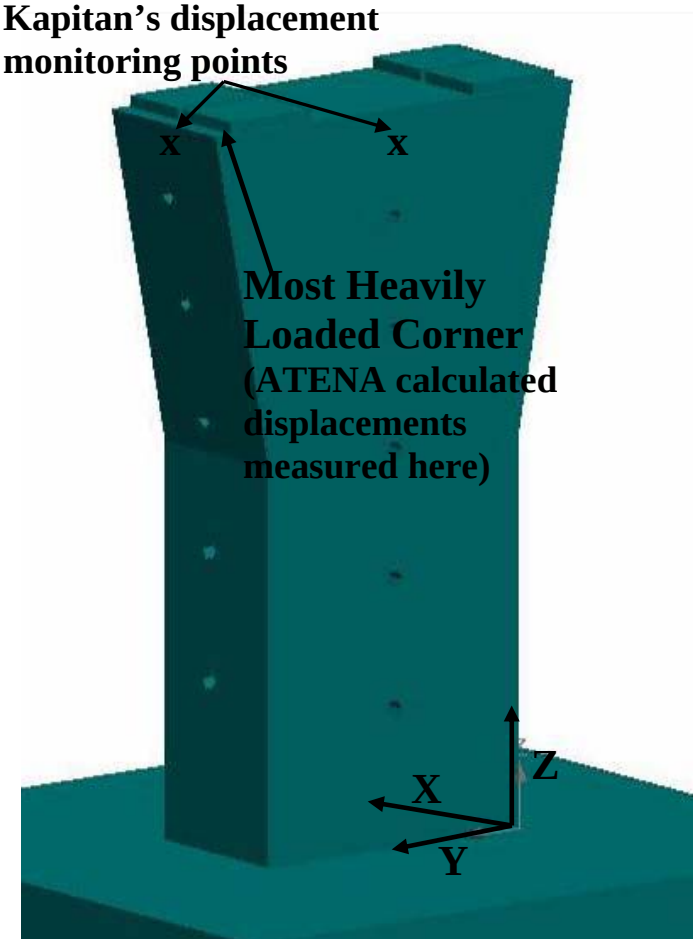

Figure 5.11: Reference Axis for Column Model

An analytical solution within ten percent of the observed behavior was considered good, and within five percent considered excellent. The model overestimated the control column capacity by only three percent, which was well within the tolerances allowed by the author. As well, the crack pattern calculated by ATENA for the control column model closely followed the pattern observed during testing, as shown in Figure 5.12 and Figure 5.13, respectively.

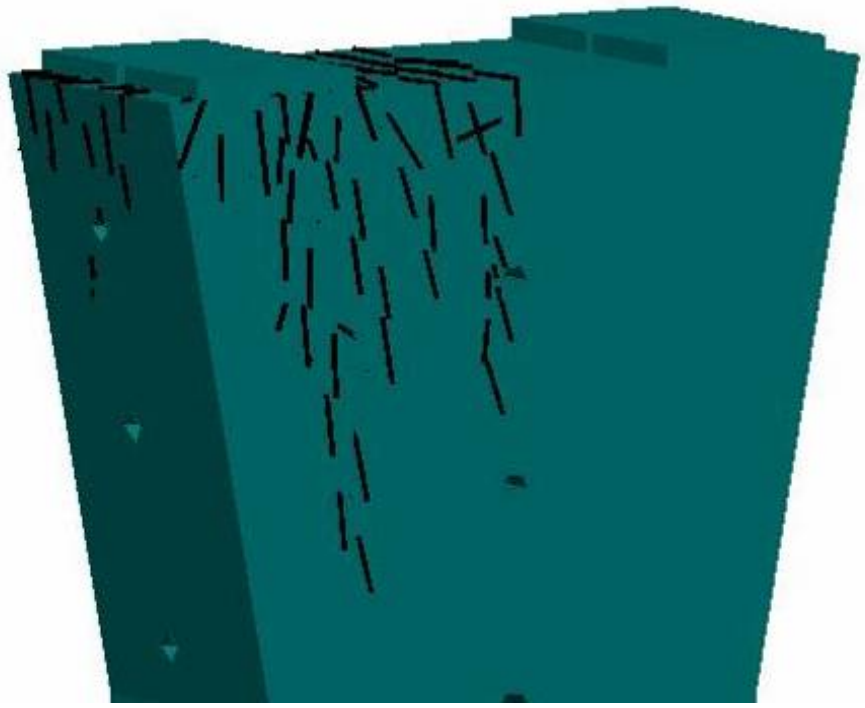

Figure 5.12: Cracking Pattern at Failure from ATENA for Control Column

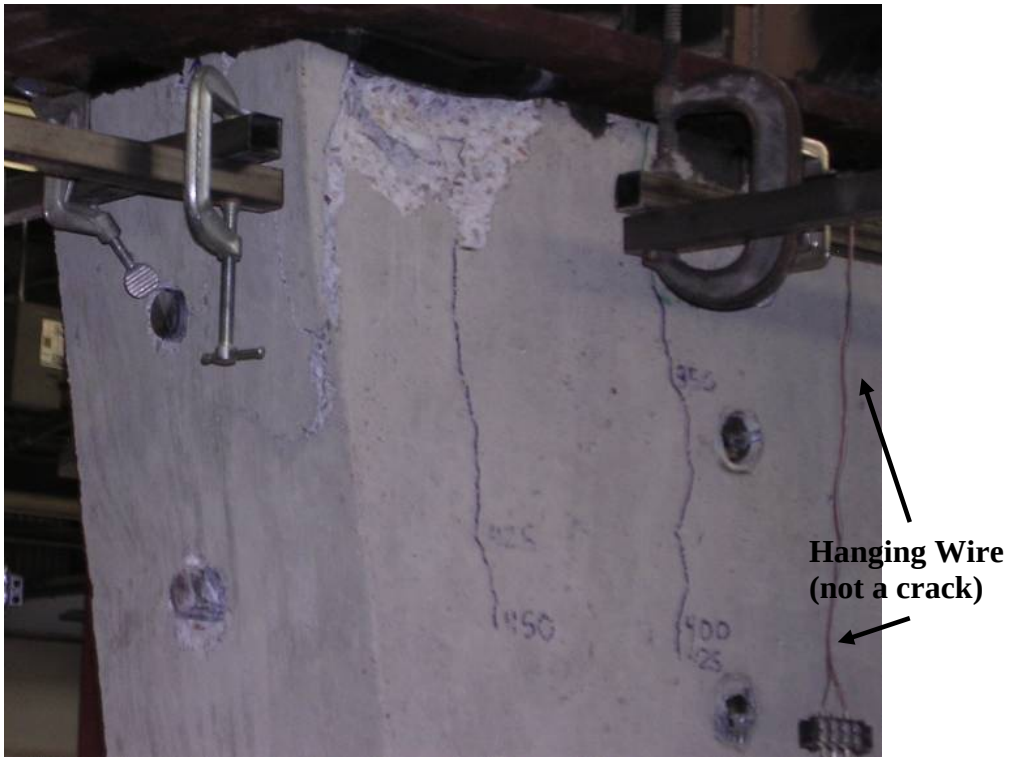

Figure 5.13: Cracking Pattern at Failure for Kapitan's Control Column

5.4.1 Calculated versus Measured Results

Once the material model was calibrated to the results from the control column testing, initial cracking steps were introduced to model Kapitan's other column tests. At this time, ATENA did not have the capability to input a crack map to be integrated with the model. To recreate the damaged (pre-cracked) column condition, a series of initial cracking load steps was used to simulate the splitting wedges that Kapitan used in the laboratory. The initial crack widths were created by applying prescribed displacements along the interior sides of the PVC voids to model the splitting wedge action, as shown in Figure 5.14. Figure 5.15 shows the PVC voids modeled in ATENA as well as the prescribed deformations in the y-axis direction, which opened cracks in the long face of the column. The highlighted bearing pad in this figure was the most heavily loaded bearing pad. During the initial cracking load steps, prescribed deformations in both the x- and y-axis directions were applied simultaneously. Figure 5.16 presents the model's representation of initial cracking locations prior to top loading. Figure 5.17 shows the model with a scalar representation of crack widths in the column after the initial cracking load steps but prior to top loading. The initial cracking load steps were modeled using Newton-Raphson finite element theory. This theory, in typical use, maintains the prescribed force of each load step and then adjusts the displacement until equilibrium (within tolerance) is satisfied[105]. For the case of prescribed deformations, the deformation was held constant and the force required to create this displacement was varied. The Newton-Raphson method was not used for finding ultimate loads because if the prescribed load step overshot the maximum load of an element, the program would return an error. As well, this method would be unable to determine the descending branch of post-peak behavior because it cannot reduce the prescribed loads to follow the descending branch. For the prescribed deformations applied, the "load steps" were instead increments of displacement. Thus, the typical step size was 0.001 inches. Some steps were varied in size if the program was unable to reach equilibrium using the typical width in one hundred iterations.

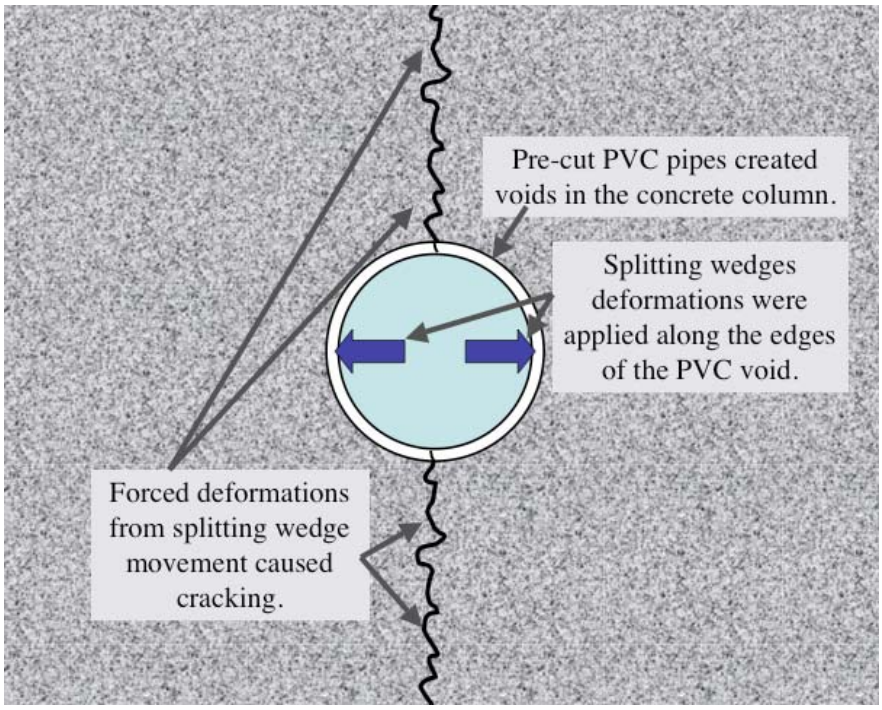

Figure 5.14: How Splitting Wedges Applied Initial Cracking Deformations

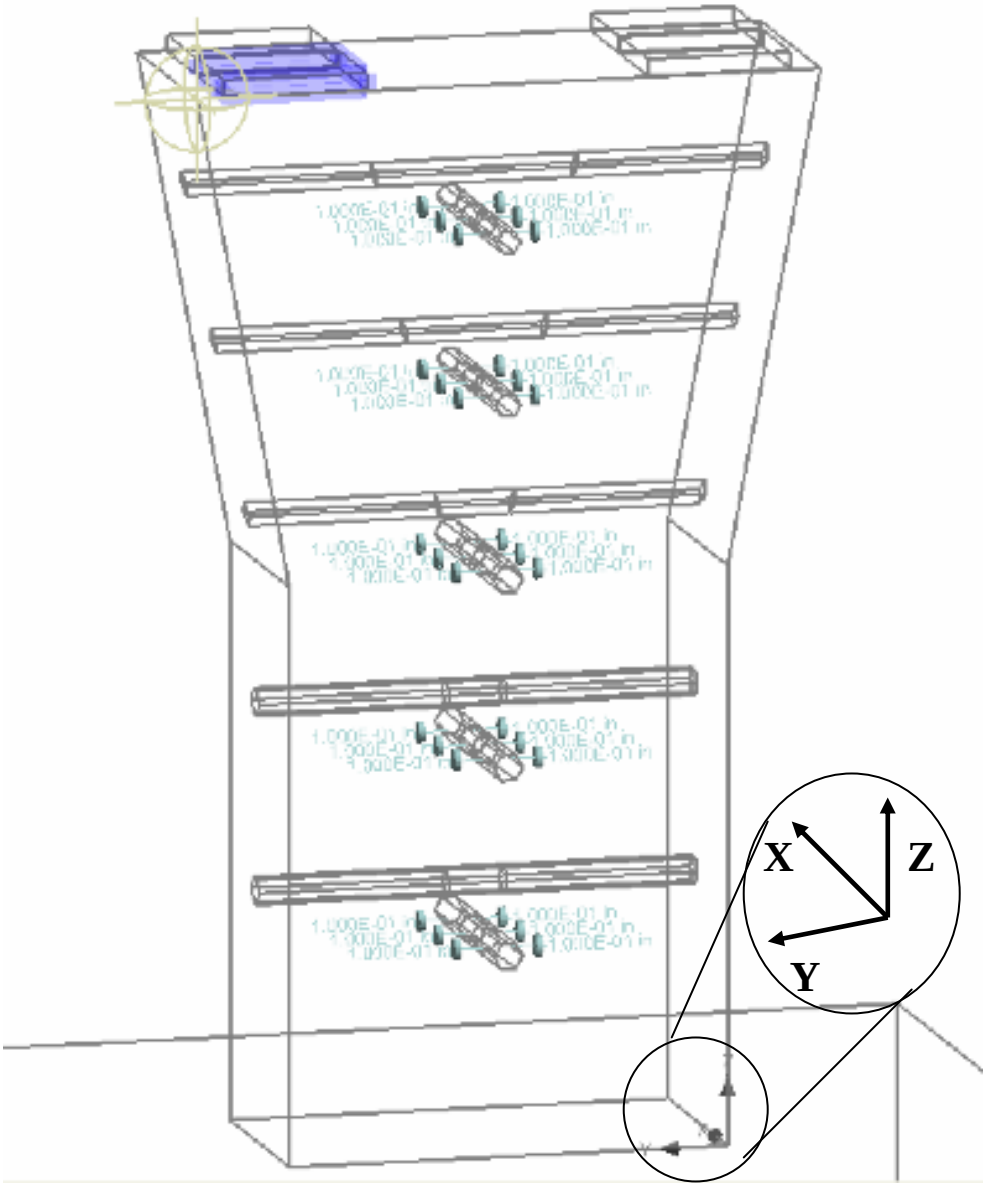

Figure 5.15: Prescribed Deformations along Y-axis Represent Splitting Wedges

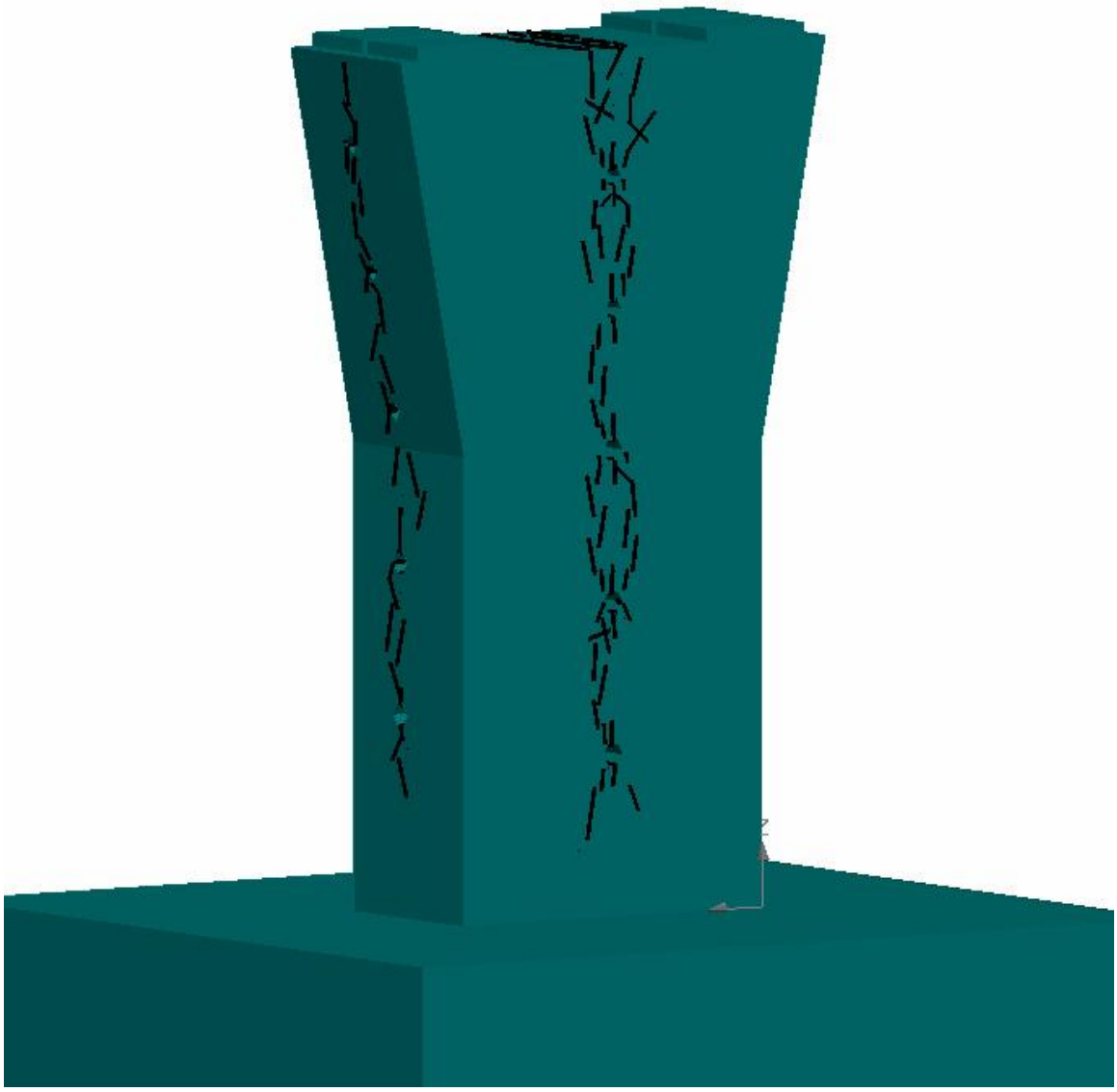

Figure 5.16: Initial Cracking Modeled by ATENA

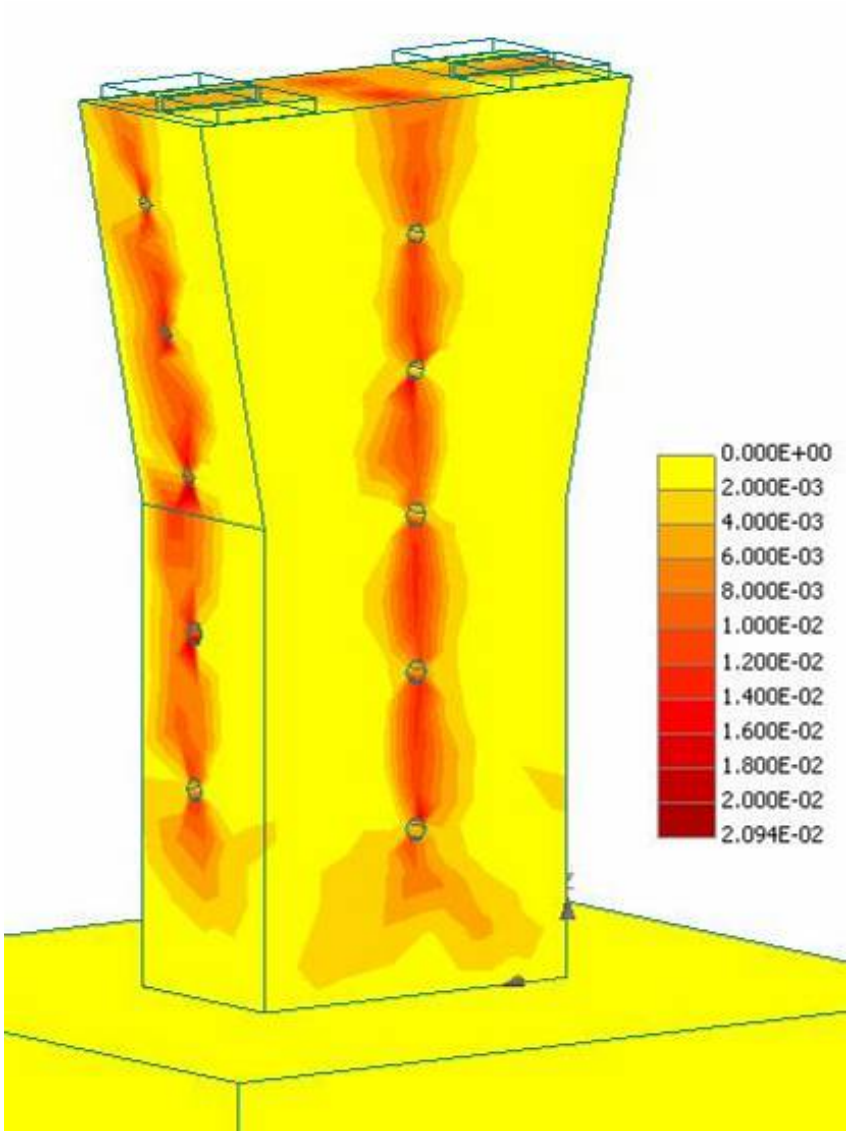

Figure 5.17: Scalar Representation of Crack Width after Initial Cracking (values are in inches)

Figure 5.18 through Figure 5.20 present the load versus displacement curves calculated by ATENA for Kapitan's pre-cracked columns. The figures are in order of increasing initial cracking width. Thus, Figure 5.18 is for 0.02 inches of initial crack width, 0.048-inches of initial cracking is shown in Figure 5.19, and Figure 5.20 presents the 0.084-inch initial crack width model. The displacement curves tracked the movement of the most heavily loaded corner with load. These load-displacement graphs also show the control column's measured capacity, the scaled factored design load, and the load-displacement

data recorded during Kapitan's testing. As described in section 5.4 and illustrated in Figure 5.11, the displacements were measured at the top center of the column along the x- and y-axes. The point monitored by ATENA was near these locations, but did not match them. ATENA, instead, calculated displacements at the corner. From comparison of the measured and calculated load-displacement behavior, the different locations could explain divergent behavior near peak load. This divergence was especially noticeable in the y-axis displacements of Figure 5.18 and Figure 5.19, which were for 0.02-inch and 0.048-inch initial crack widths respectively. Potentially, the divergence could be due to the localized crushing of the concrete at the most heavily loaded corner, which would result in a greater deflection than what would be experienced at the middle of the column.

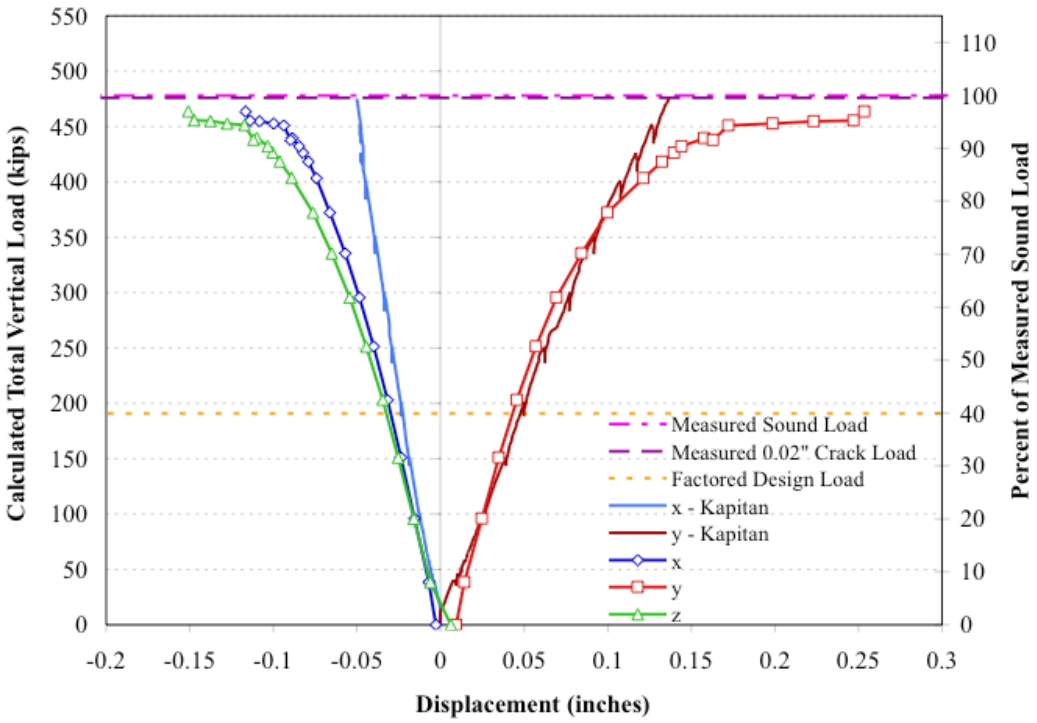

Figure 5.18: Load v. Displacement, 0.02-inch Initial Cracking Width

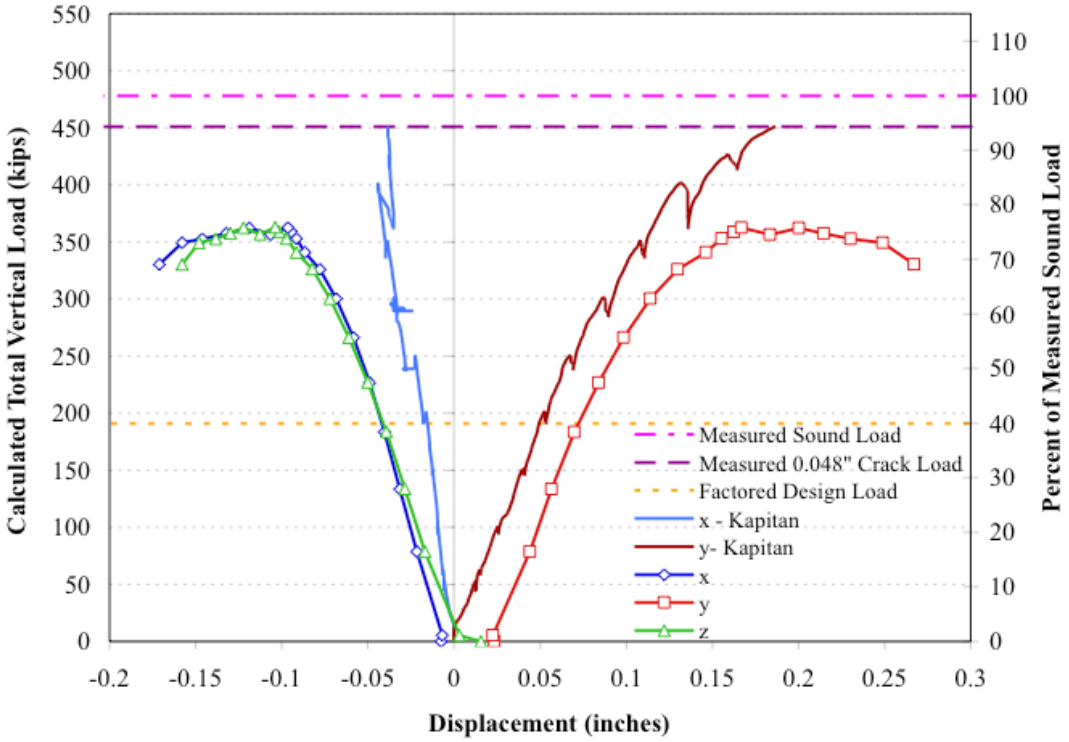

Figure 5.19: Load v. Displacement, 0.048-inch Initial Crack Width

In Figure 5.20, which presents the 0.084-inch initial crack width displacement, the measured data in the y-direction diverges from the calculated behavior throughout the load application. The y-axis measured curve here appears very linear compared to the load-displacement curve calculated by ATENA. The difference could be a result of the wide initial crack width in the program. More likely, the specimen behaved differently because it was previously used to test a smaller initial crack width. While there were no flexural cracks visible on the surface of the specimen after its first test, it is possible that there was some internal cracking that occurred which reduced the specimen's initial stiffness during the 0.084-inch pre-crack width test.

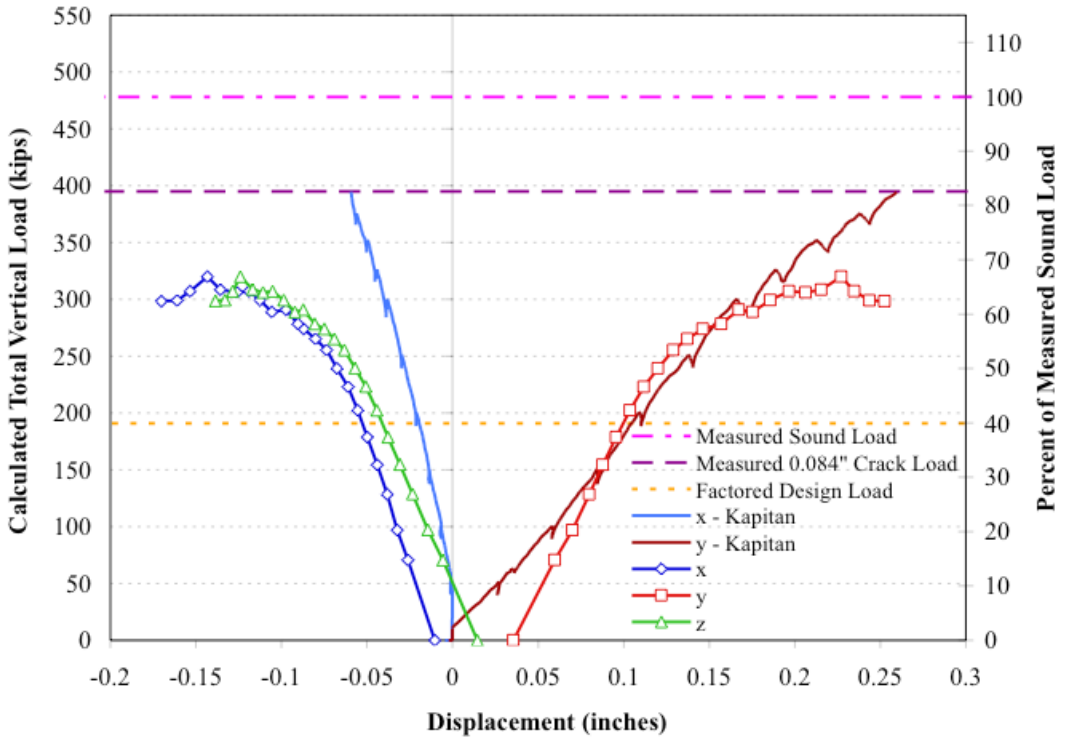

Figure 5.20: Load v. Displacement, 0.084-inch Initial Crack Width

Figure 5.21 shows the load versus displacement along the y-axis behavior, as calculated by ATENA, for all of Kapitan's columns. The measured capacity from Kapitan's pre-cracked columns was also shown on the individual column's load-displacement curves (Figure 5.18 through Figure 5.20) and the load-displacement summary plot. In the summary plot, Figure 5.21, the measured maximum loads and measured load-displacement curves were color coded to their corresponding calculated load-displacement curves. In this comparison, the initial stiffness, which was represented by the initial slope, of the measured 0.084-inch pre-crack specimen was obviously much lower than the initial stiffness of the other measured curves. As mentioned earlier, this difference in behavior could have been a result of the re-use of this specimen. The individual curves and this summary plot showed that for small levels of initial cracking the calculated capacity of the columns was very close to the values observed in the laboratory. For the larger crack sizes, the model became somewhat conservative. Recall that a model that predicted within ten percent of the target was considered a good match.

Thus, while the gap between the calculated and measured values was certainly much wider for these conservative predications than those that were nearly identical, the predictions are not far out of the acceptable matching (10%) range. For instance, the 0.048-inch and 0.084-inch initial crack width models both reached 82% of their measured loads, which was 8% outside of the acceptable range.

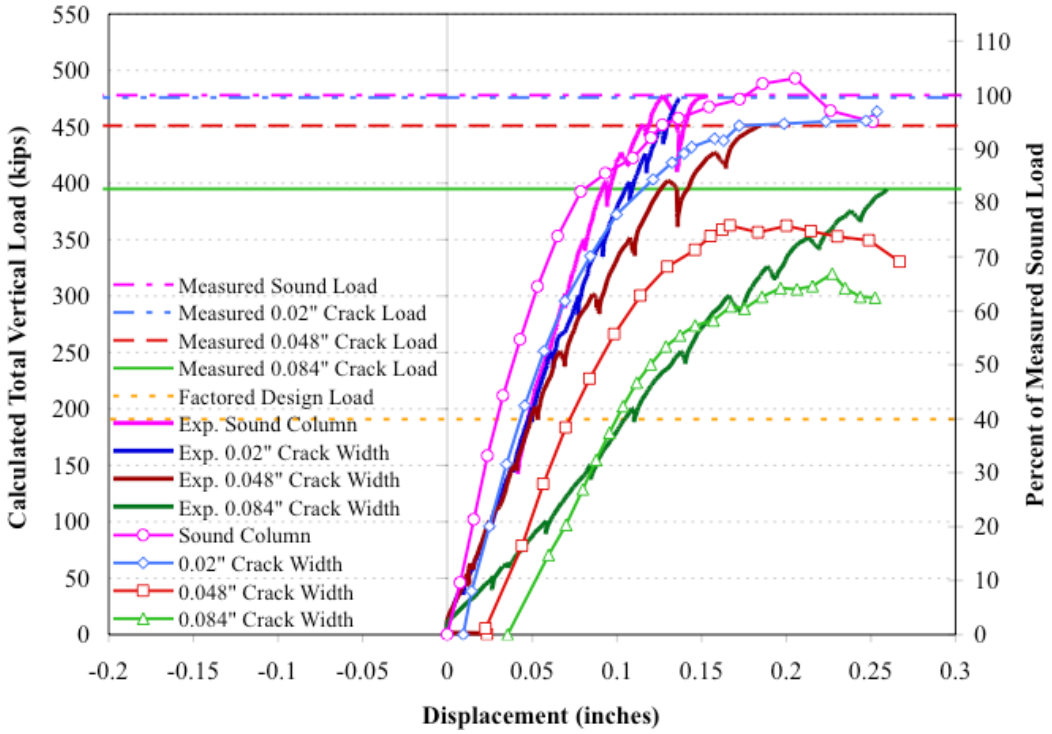

Figure 5.21: Y-axis Displacements from Modeling Kapitan's Columns

Comparisons between the calculated capacity of the columns and the measured normalized capacity are shown in Table 5.2. The table and load-displacement curves showed that the calculated and measured column capacities were very close for the undamaged and 0.02-inch crack width specimens. Recall that the 0.02-inch width was for the 1/3.67 scaled model and corresponded to a crack observed in the field of 0.078 (5/64) inches, which is about the thickness of a nickel. Thus, the model gave very accurate results up to moderately large crack widths. Once the crack widths became very large, such as for the model widths of 0.048 inches and 0.084 inches (which correspond

to cracks in the field of 0.177 inches and 0.30 inches respectively), the model became somewhat conservative. At these higher levels, the calculated capacities were just over eighty percent of the measured maximum loads. Figure 5.22 directly compares the capacities calculated by ATENA with the normalized measured results. This figure also shows that the bearing capacity predicted by Kapitan was met by the measured and calculated results of both the control column and pre-cracked column with 0.02-inch wide cracks.

Table 5.2: ATENA Calculated Results versus Measured Results

Scaled Crack Width (in)	Field Crack Width (in)	Description of Specimen	Normalized Measured Maximum Load[3] (kips)	Calculated Maximum Load (kips)	$\frac{\text{Calculated}}{\text{Normalized Measured}}$
0.00	0.00	Control Case: Control Column	478	492	1.03
0.02	0.078	Widest crack on typical column	476	464	0.97
0.048	0.177	Widest crack observed in the field	443	363	0.82
0.084	0.3	Hypothetical crack: 75% wider than largest crack observed	388	320	0.82
Scaled Design Load = 191 kips				Average =	0.91

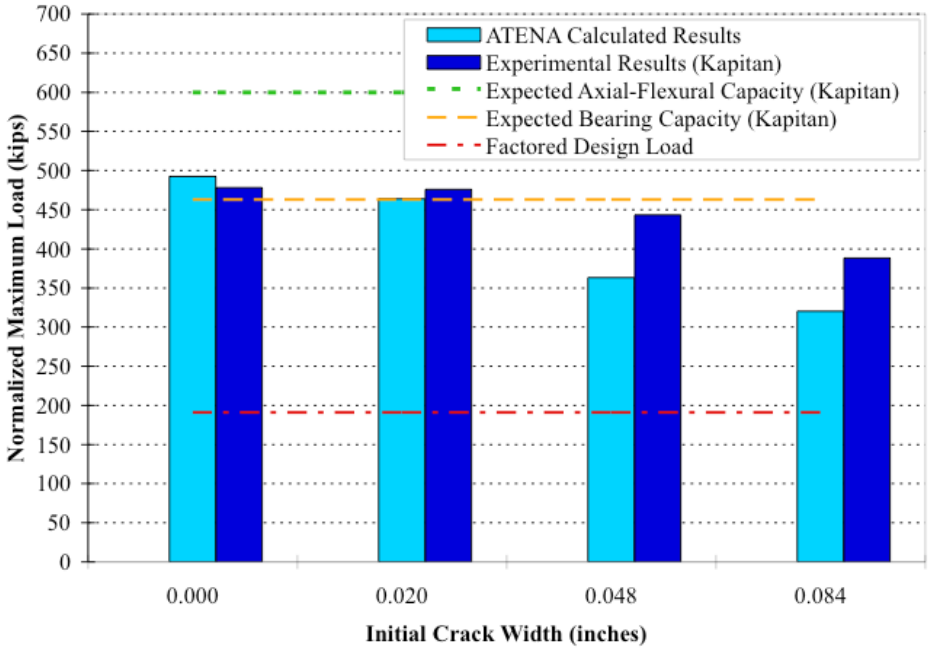

Figure 5.22: ATENA Calculations Compared with Normalized Measured Results

Figure 5.23 through Figure 5.26 present ATENA's calculated crack pattern at failure for Kapitan's column series. Figure 5.23 shows the calculated crack pattern at failure of the control column model. Figure 5.24, Figure 5.25, and Figure 5.26 present the calculated crack patterns at failure for the pre-cracked column models with 0.02-inch, 0.048-inch, and 0.084-inch wide cracks, respectively. These crack pattern predictions were the model's cracking pattern predictions from the load step applying peak load to each model. In the figures, a black crack line was plotted through the center of each finite element that cracked during loading. Thus, these crack representations were not expected to perfectly match the exact crack locations in the actual specimen. Instead, the model calculated the typical location of the cracks in the larger concrete element being modeled. For instance, the wavy crack down the center of the column face in Figure 5.24 was from 0.02 inches of initial cracking. This pattern was not merely a phenomenon of the computer simulation, but was observed during physical testing, as shown in Figure 5.27. The columns with larger initial crack widths, shown in Figure 5.25 and Figure 5.26, also exhibited this wavy central crack. It is somewhat obscured, however, in the ATENA prediction due to additional damage during initial cracking and loading. Following the

ATENA crack patterns are pictures of two specimens from Kapitan's column series after failure testing, which are shown in Figure 5.28 and Figure 5.29 for comparison. As mentioned in Chapter 4, all columns in Kapitan's series failed by concrete crushing beneath the most heavily loaded bearing pad. Figure 5.28 and Figure 5.29 show this typical failure as observed on the control column specimen and 0.048-inch pre-cracked column specimen, respectively. The models for the control column and columns with initial crack widths of 0.02 inches and 0.048 inches, presented in Figure 5.23 through Figure 5.25, all showed failure by cracking under the most heavily loaded bearing pad. This calculated failure mechanism matched the failure mode observed in the laboratory. The model for the column with 0.084 inches of initial cracking, shown in Figure 5.26, also calculated failure due to localized concrete crushing. The difference with this model was that it calculated the crushing to occur towards the base of the column at the most heavily loaded corner. The 0.048-inch wide initial crack model (Figure 5.25) also indicated some cracking in this region. It is possible that the conservatism found in these two models for the widest cracking levels of Kapitan's column series was due to the crushing calculated near the base of the column that was not observed during physical testing.

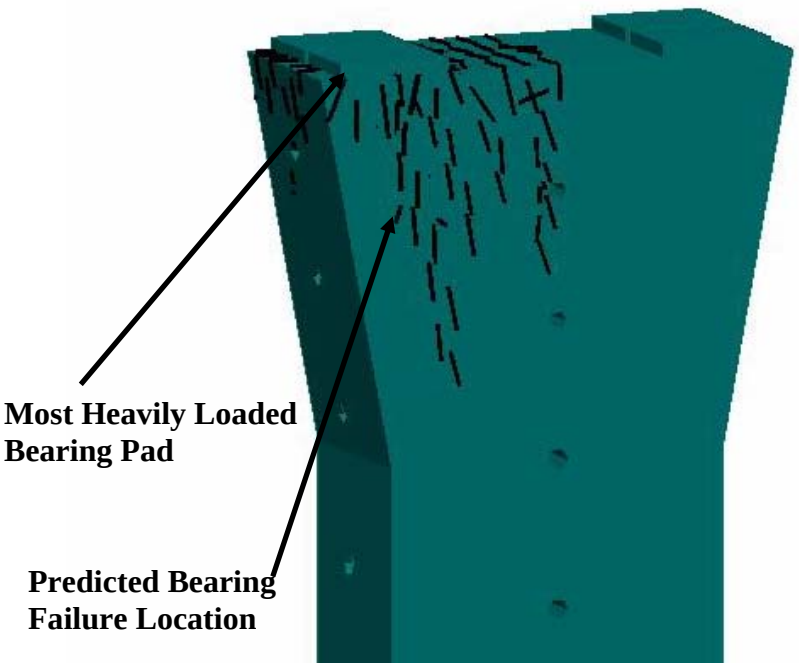

Figure 5.23: ATENA's Control Column Crack Pattern at Failure

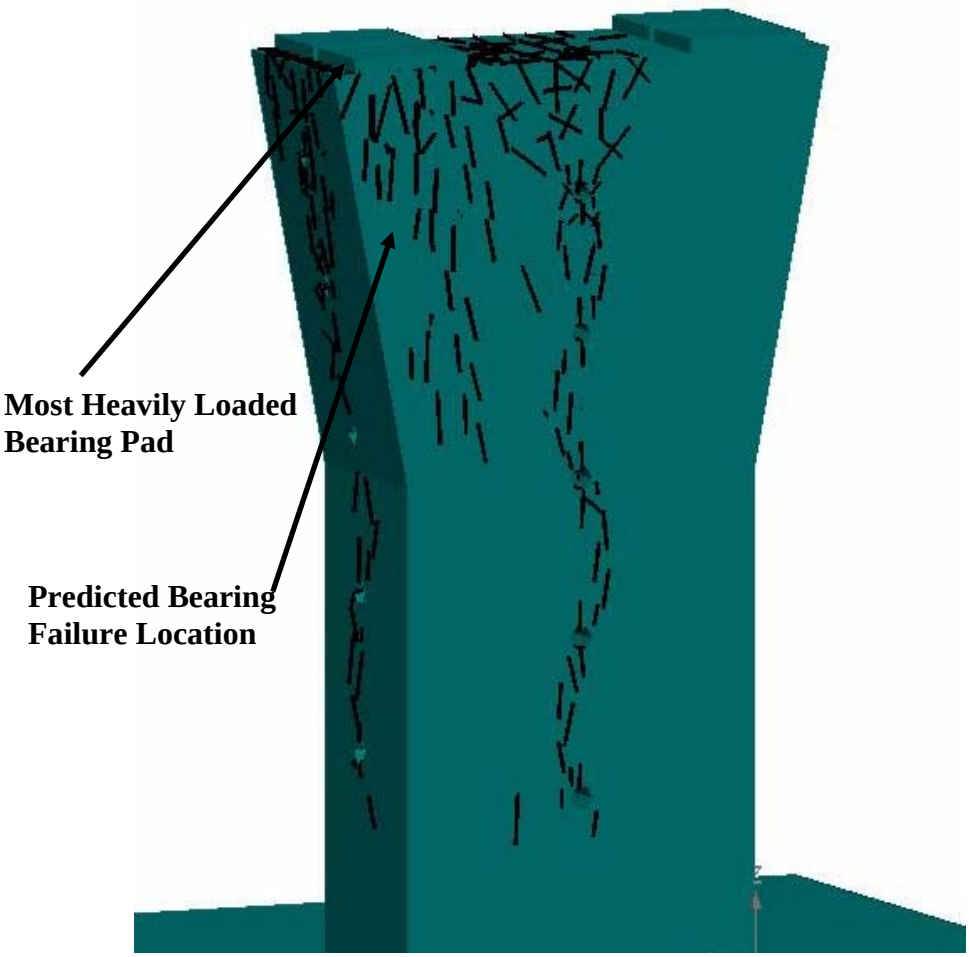

Figure 5.24: Crack Pattern at Failure for Model with 0.02-inch Wide Crack

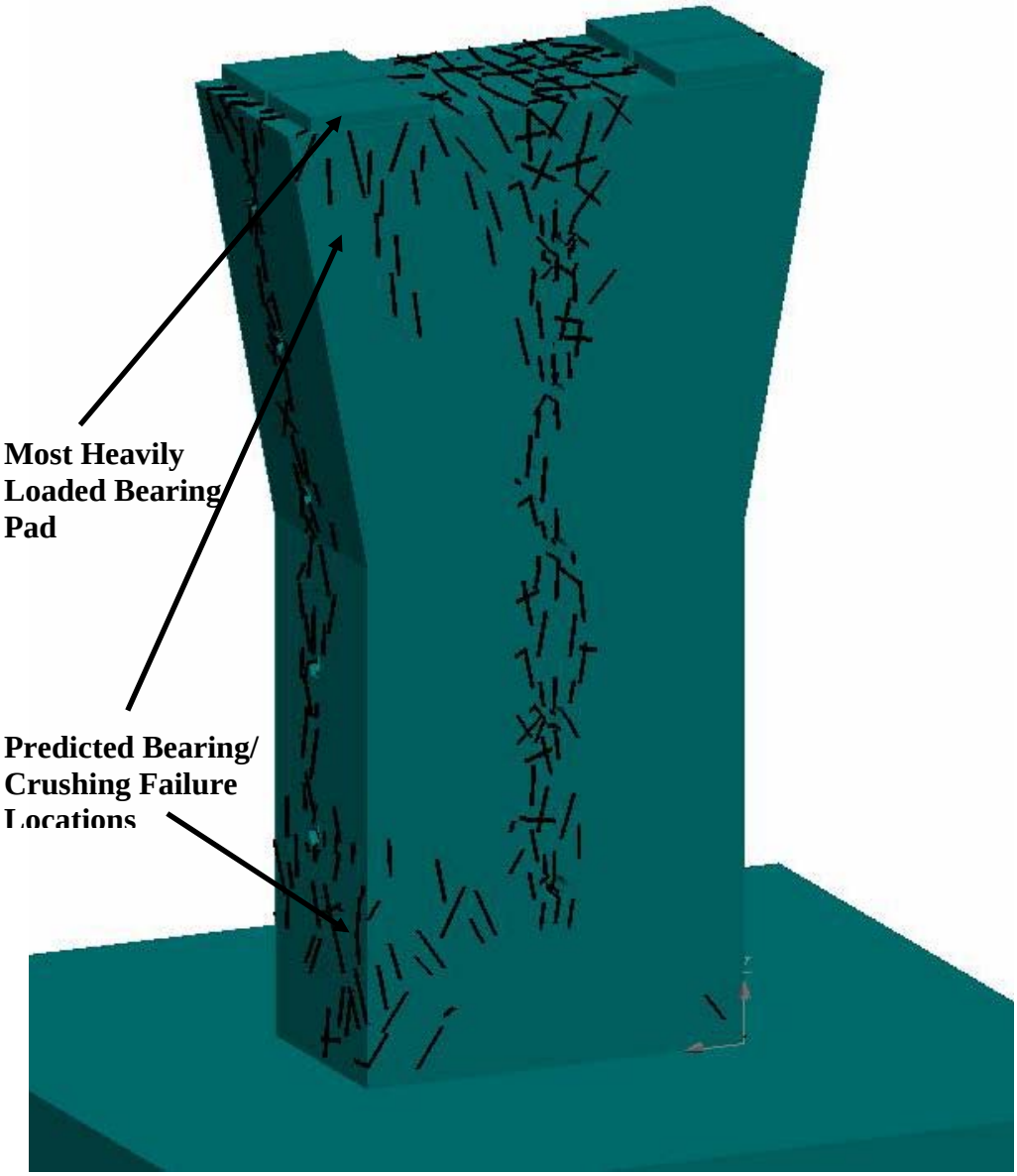

Figure 5.25: Crack Pattern at Failure for Model with 0.048-inch Wide Crack

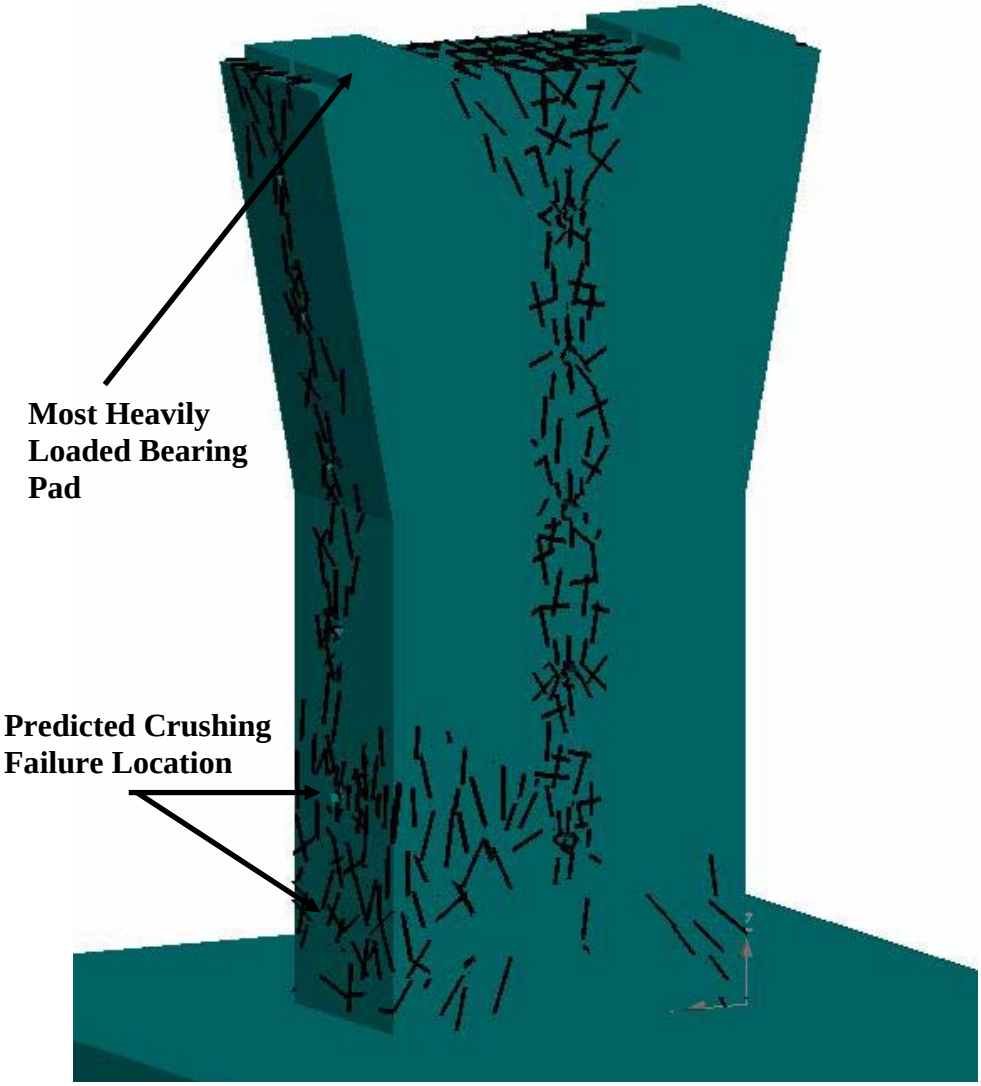

Figure 5.26: Crack Pattern at Failure for Model with 0.084-inch Wide Crack

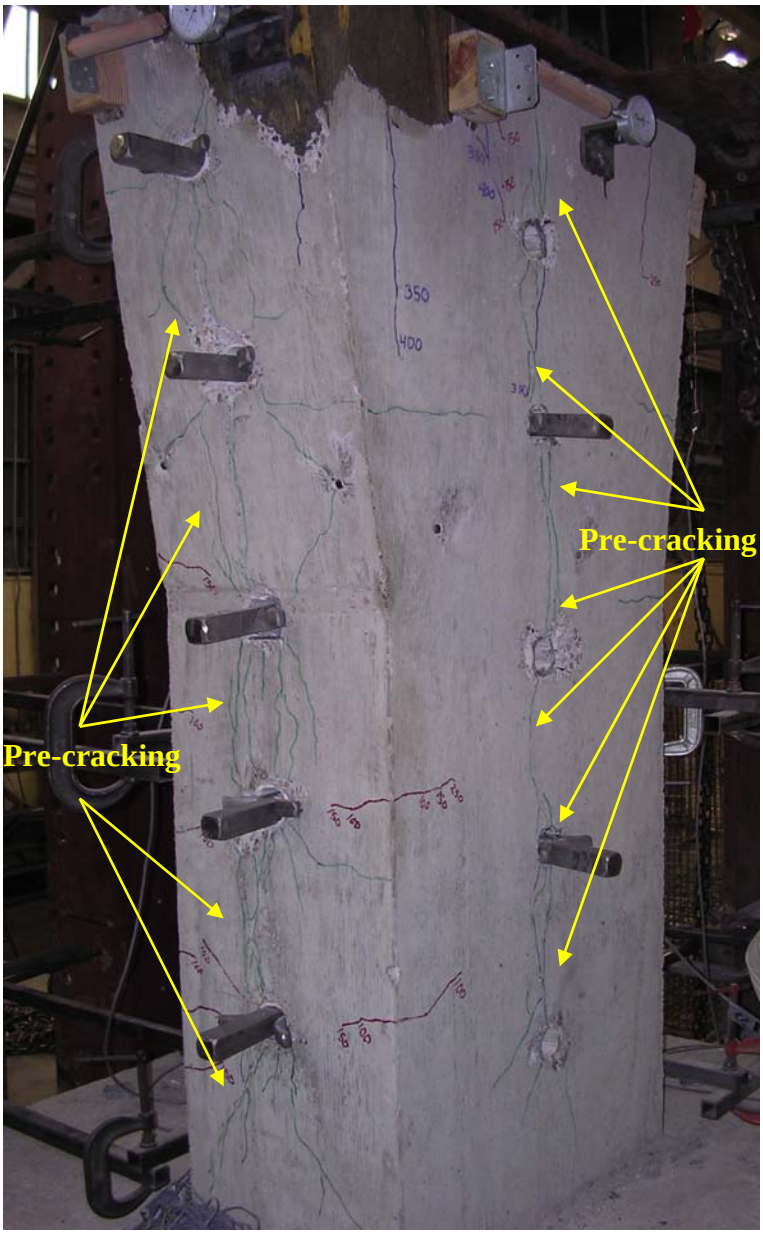

Figure 5.27: Wavy Initial Cracking (Marked in Green)

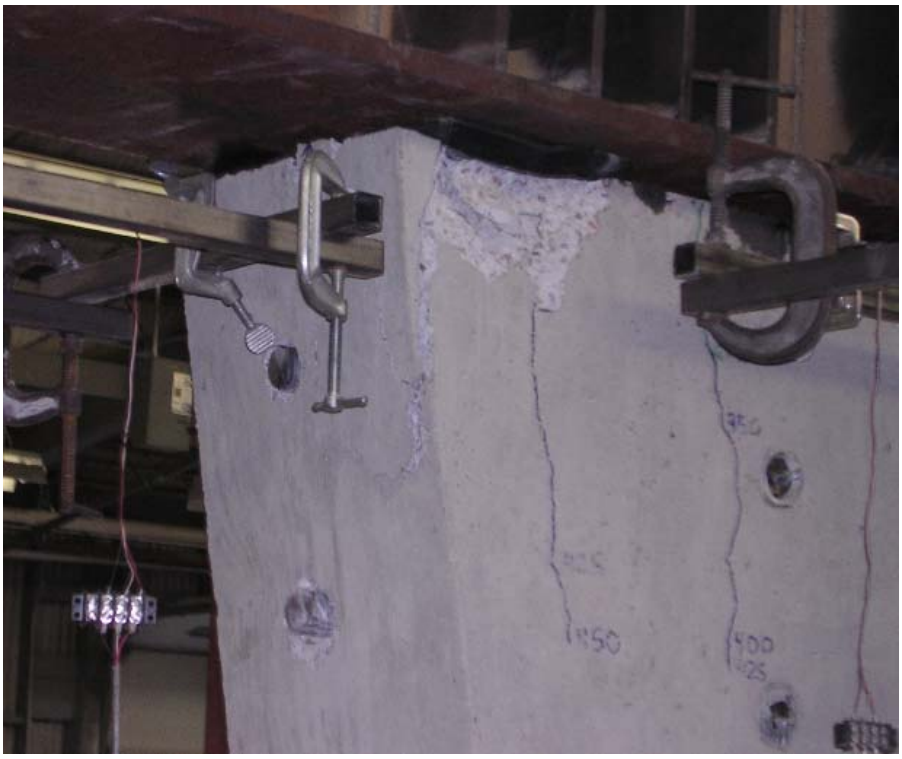

Figure 5.28: Laboratory Failure of Control Column

Figure 5.29: Laboratory Failure of Column with an Initial Crack 0.048-inch Width

5.5 PARAMETRIC STUDY: INTIAL CRACK WIDTH V. CAPACITY

Once equipped with a model that was calibrated to Kapitan's control scaled column specimen, the author was able to explore the effects of increasing the initial crack widths. The author was most interested in finding the initial crack width where the column could only support the factored design load. The scaled (factored) design load of 191 kips was only 40% of the scaled control measured column capacity of 478 kips. Defining this critical initial crack width would assist the bridge owner in crack monitoring. By knowing the point where capacity would be reduced to the design load, the bridge owner could decide on tolerable crack widths. Table 5.3 presents ATENA's calculated capacities for all of the crack widths considered in the parametric study, which sought this threshold value (40% of measured control column capacity). The table also lists the corresponding crack size in the field. Figure 5.30 shows, in bar chart form, the capacities calculated using ATENA for each initial crack width modeled. This figure includes Kapitan's measured data and a reference line for Kapitan's predictions and the factored design load. The 0.16-inch wide initial crack model (0.6 inch width crack in the field) was just slightly above the target capacity. Although this large scaled crack size reduces the column capacity to 45% of the control column capacity, as measured in the laboratory, it is just outside of the acceptable range to represent the design load. Recall that a model within 10% of the target would be considered an acceptable match. Thus, for the target of 191 kips (40% of control column capacity) the acceptable range would be 172-210 kips (36-44% of control column capacity.) The author's model for 0.17 inches (5/8 inch-wide crack in the field) of initial cracking could not reach equilibrium with the application of vertical loads.

Table 5.3: ATENA Calculated Results for All Models

Scaled Crack Width (in)	Field Crack Width (in)	Calculated Maximum Load (kips)	Factored Design Load / Calculated	Percentage of Control Column Measured Load
0.00	0.00	492	0.39	103
0.02	0.078	464	0.41	97
0.048	0.177	363	0.53	76
0.084	0.3	320	0.60	67
0.10	0.37	272	0.70	57
0.11	0.40	272	0.70	57
0.12	0.44	263	0.73	55
0.13	0.48	258	0.74	54
0.14	0.51	249	0.77	52
0.15	0.55	234	0.82	49
0.16	0.59	215	0.89	45

Scaled Factored Design Load = 191 kips or 40% of Control Column Measured Load

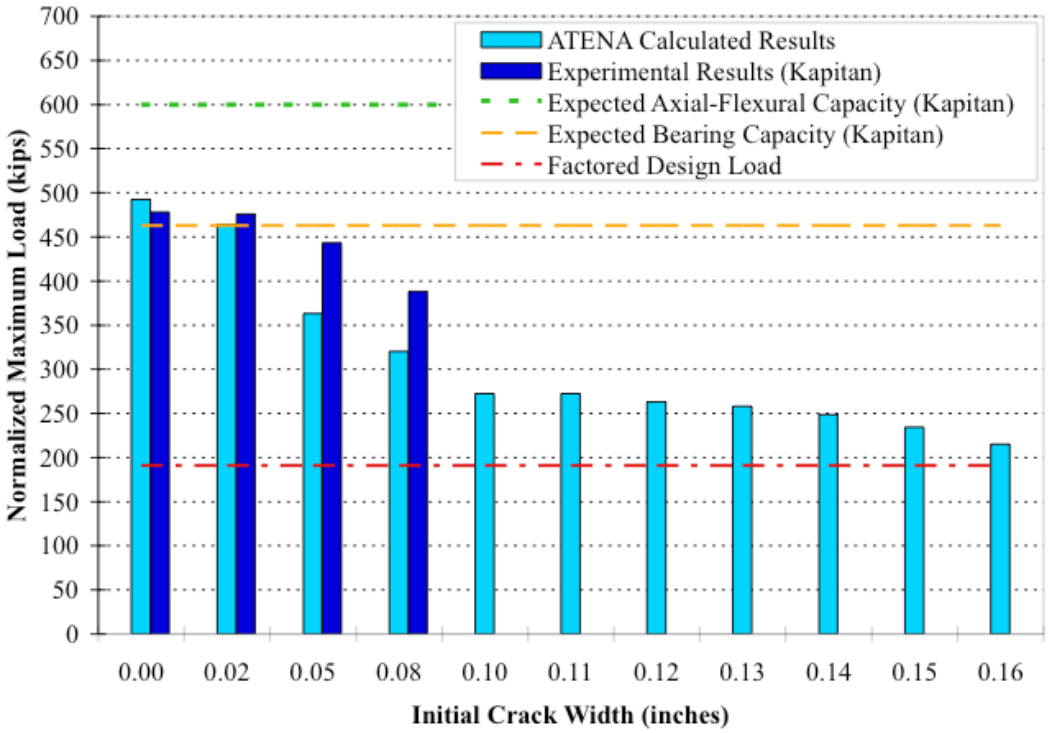

Figure 5.30: Capacity Predictions of All ATENA Models

During the modeling of the various initial crack widths, the load-displacement data of the most heavily loaded corner was collected for each model. The resulting load-displacement graphs for all of the ATENA models are presented in Appendix C. For comparison, the load-displacements along the y-axis for all models are compiled in Figure 5.31. This summary plot shows that as the initial crack widths grew increasingly large, the relative stiffness of the column decreased. The stiffness was represented by the initial slope of the load-displacement curve. The control column and those with smaller initial crack widths (such as 0.02 inches and 0.048 inches) had similar, steep linear portions of the curve. With the initial crack width growing quite large (over half an inch field cracking size for the scaled crack of 0.14 inches, for example), the load-displacement curve showed softening of column response. As all models were run for a similar amount of vertical loading, and thus a similar number of vertical loading load steps, the models share similar cut off points along their curves. This similarity should not imply that all of the modeled columns had similar ductilities. That case may be true. However, the model did not continue to add load until the entire descending branch of the curve was plotted for the majority of the models. The 0.02-inch wide initial crack model would take no further vertical loading than is reported here. Thus, for this model, the entire load-displacement curve was plotted. Instead of finding the full load-displacement curves for each level of initial cracking, the goal of the model was to determine the capacity of the column with increasing widths of initial cracking.

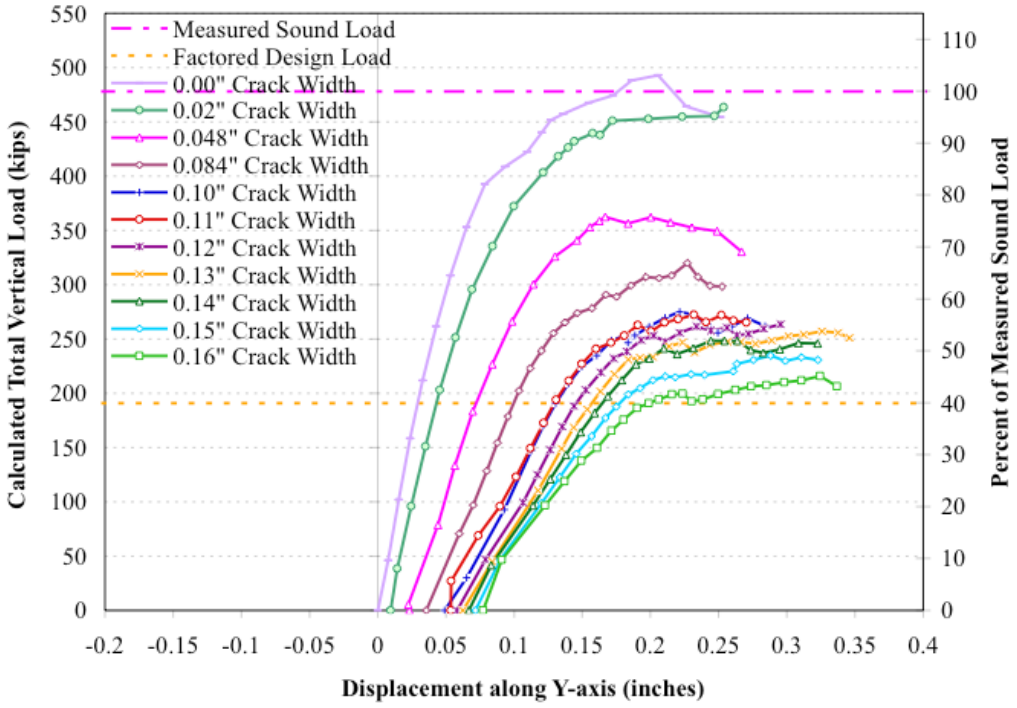

Figure 5.31: Load-Displacement along Y-axis for all ATENA Models

As well, to aid in the search for the threshold initial crack width, the author plotted crack width to capacity of each model in order to establish a relationship between these values. This plot, which is shown in Figure 5.32, was updated after each additional initial crack width was modeled in order to refine the target initial crack width. A linear relationship was found between these two values, which was represented by the trendline in the plot. The resulting threshold crack width was determined to be 0.17 inches, which corresponds to a crack width of 0.62 inches (5/8 inches) in the field. Recall that this crack width was not just of the cover concrete, but continues through the column's core. Thus, the bridge owner should watch for deep cracks (greater than the 2.25 inch concrete cover) of half an inch in size.

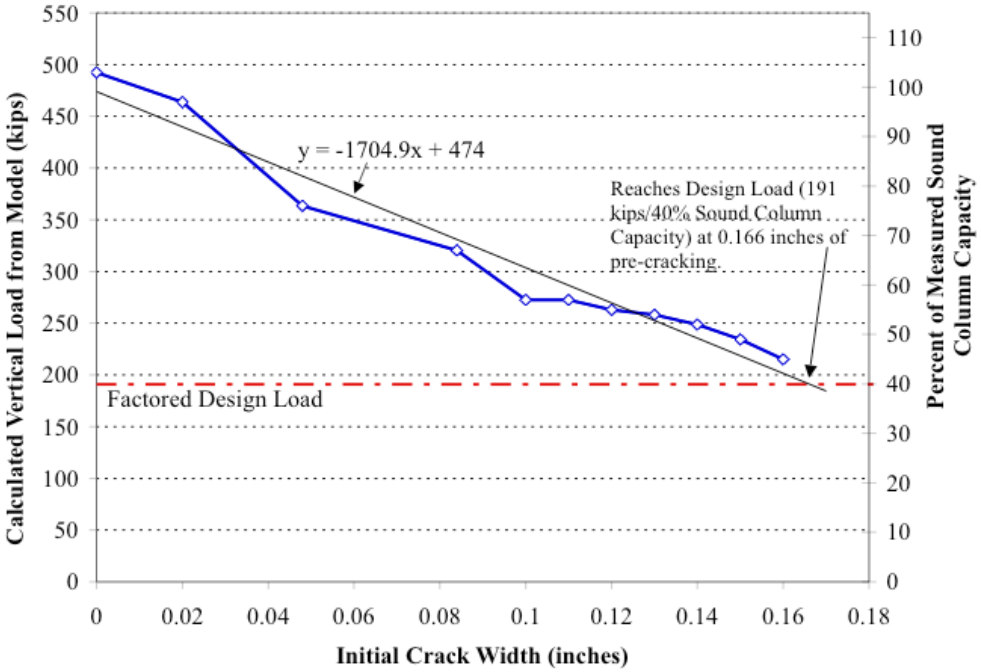

Figure 5.32: Calculated Vertical Load from Model versus Initial Crack Width

5.6 SUMMARY

ATENA was used to model the specimens tested by Kapitan and to extend the study to the effects of larger initial crack widths than he considered. The material model was calibrated to Kapitan's control scaled column specimen results. After calibration, the model was run for each of Kapitan's initial crack widths. After seeing the good correlation between predicted and measured results, the ATENA model was used to predict the capacities of columns with increasing large initial through-section cracks. From this analytical process the following summary points were made:

- Using ATENA to predict the column's capacity at larger levels of initial cracking, a critical initial cracking width of 0.17 inches for the scaled specimen was determined. At this threshold crack width the column could only just support its factored design load.

- The threshold width of 0.17 inches was for the scaled column and corresponds to a width in the field of 0.62 inches (5/8 inches). By knowing this value, the bridge owner is better equipped to interpret the reported crack widths in the field as observed during bridge inspections.
- With the computer material model calibrated to Kapitan's control column results, ATENA calculated a close approximation to the capacities of the control and 0.02-inch wide initial crack models. The location and mode of failure at these levels was the same as observed in the test specimens.
- As the initial cracking levels reached 0.084 inches, the ATENA prediction was somewhat conservative and calculated a local crushing failure in a different location in the column than was observed in the test specimens.

Future researchers interested in further exploring ATENA's ability to model ASR/DEF affected concrete may want to explore the following options.

- To model the deterioration of various engineering properties of concrete due to ASR/DEF, the user would need to adjust the material model. Table 5.1 listed all of the material properties that can be modified. As many properties as can be determined from ASR/DEF affected concrete should be entered in order to have the most accurate material model for predicting behavior.
- ATENA has the ability to assign expansive materials. It might be useful to combine the basic expansive material model with concrete properties in order to model the expansion of concrete due to ASR/DEF. Through the expansion of the concrete material, ATENA would model the effects on the reinforcing cage.
- The initial cracking from Kapitan's specimens was modeled here by applying forced deformations along voids in the column (which modeled actual PVC-created voids). To adapt this approach to model a specific initial cracking pattern, it may be necessary to create small voids along the desired crack locations. Then prescribed deformations in these voids could create the cracks similar to a child's connect-the-dots drawing.

CHAPTER 6
Scaled Column Specimens: Results

6.1 INTRODUCTION

The two scaled column specimens affected by ASR/DEF completed the scaled column series begun by Kapitan[3]. In this earlier work, Kapitan tested undamaged specimens to determine baseline capacities and then explored the effects of differing initial crack widths on the maximum capacity of the column. The two ASR/DEF columns were intended to determine the capacity of the same scaled column specimen after the onset of ASR and/or DEF. As discussed in Chapter 3, these columns duplicated the reinforcing pattern, loading, and concrete strength as used in Kapitan's series. The differences in these specimens and the earlier columns were the use of ASR/DEF susceptible concrete, initial heat curing, and moist exposure whilst applying a post-tensioned axial load to the column. The average capacity of the two ASR/DEF specimens was of interest as compared to Kapitan's baseline status, in order to quantify the ASR/DEF effect on capacity of these columns. Additionally, by comparing the results of these specimens to the results of Kapitan's tests a correlation could be drawn between the effects of the widespread cracking of ASR/DEF affected reinforced concrete and the concentrated center cracks of Kapitan's series.

This chapter presents the results of the ASR/DEF affected scaled column specimens. Results from the monitoring program are presented first. These results include monitored strain gauges, external demec gauge readings, and crack maps. Following the monitoring results are the results from testing these two specimens. Maximum load applied, load-displacement curves, and comparisons with Kapitan's results are presented.

6.2 MONITORING

The total monitoring system consisted of five elements: strain gauges, demec points, vibrating wire gauges, loading spring height, and crack mapping. Of these elements, the demec point measuring and monitoring of the vibrating wire gauges were overseen by Ford Burgher and the remainder of the elements were monitored by the author.

6.2.1 Strain Gauges

6.2.1.1 Introduction

All transverse strain gauges and two longitudinal strain gauges were monitored for each column during the exposure period. Figure 6.1 shows the locations of all strain gauges in the column with the monitored gauges highlighted. As shown in Figure 6.1, the two monitored longitudinal strain gauges (L1) were from the upper and lower instrumentation layers on the same longitudinal bar. This arrangement was selected because ASR and DEF are both three dimensionally expansive. Thus, with the presence of the post-tensioning system restraining the longitudinal expansion, the majority of the expansion was expected to occur circumferentially. Two points on the same longitudinal bar were to examine whether the ASR/DEF expansion would create a difference in strain of the reinforcing cage along the direction of restraint.

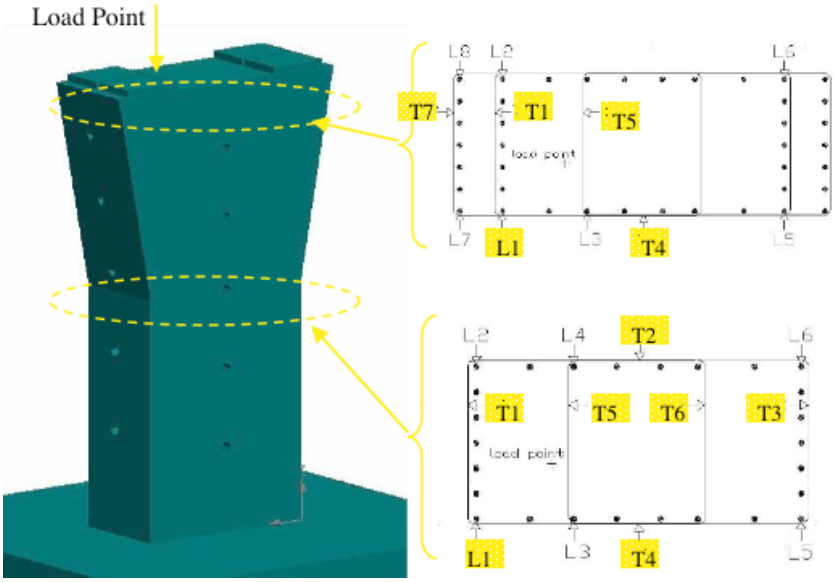

Figure 6.1: Location of Monitored Strain Gauges

6.2.1.2 Results and Discussion

Figure 6.2 to Figure 6.8 show the monitored strain values. These graphs have been simplified by eliminating readings that were erratic and further smoothing the lines with moving-average trendlines representing the data. The monitoring data from the upper layer of instrumentation in Column A is shown in Figure 6.2 and Figure 6.3. Figure 6.2 presents the data without smoothing and Figure 6.3 shows the trendline-smoothed data. All subsequent monitoring data shown in Chapter 6 use trendlines. A complete record of measured strains for all graphs (without trendlines) is located in Appendix A. Figure 6.3 shows that gauge T5, which was nearest the core, showed low expansion. Its fluctuation, which sometimes exceeds the concrete cracking strain, indicated that the surrounding concrete likely cracked. This deduction was consistent with other monitoring results from this layer. Gauges T1 and T7, which were progressively farther from the core than gauge T5, showed increasing amounts of expansion. Even at an age of five months gauge T7 showed that expansion near the surface of the concrete was approaching steel yield. Gauge T4, though monitored at this level, had erratic results that indicated a bad gauge and was therefore excluded from the results. Upper L1, on a longitudinal bar in

this upper lower of instrumentation, exhibited fairly consistent compression strains after post-tensioning at 63 days after casting.

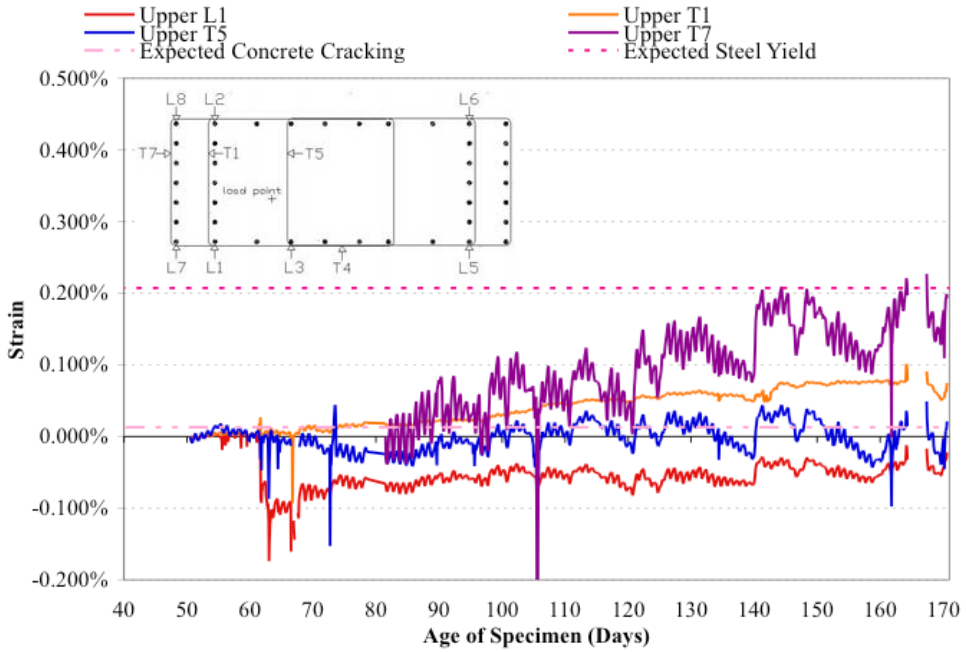

Figure 6.2: Column A Upper Layer Strain Monitoring

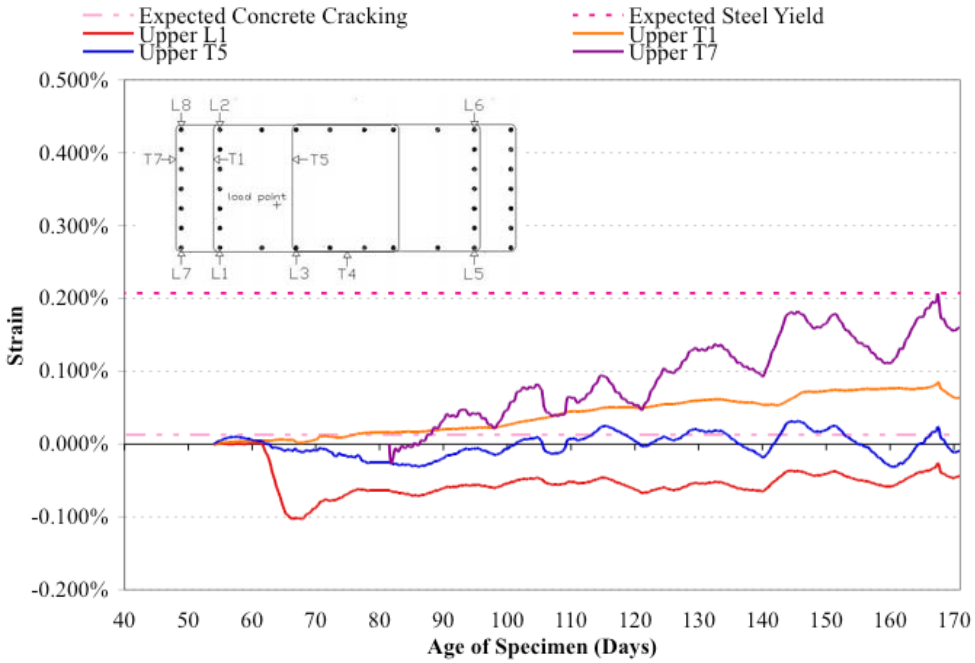

Figure 6.3: Column A Upper Layer Strain Monitoring, with Trendlines

In the lower layer of Column A, shown in Figure 6.4, the effect of confinement by surrounding concrete was especially evident in gauges T5 and T6. These gauges were the nearest to the center of the column and showed very little expansion, especially in comparison to the other monitored transverse gauges. That these core gauges exhibited expansion that met and exceeded the tensile strain of expected concrete cracking indicated that the column core was expanding, although at a much slower rate than the surface concrete. At approximately 155 days, gauge T6 suddenly began reporting compressive strains, which would be illogical for one part of the core to suddenly contract whilst the remainder of the column expanded, thus this data was truncated at 155 days. That gauge T1 jumped suddenly from zero to 0.06% expansion could indicate that the value used to zero the gauge was an anomaly, just as most of the gauges show occasional dips or peaks that are ignored as scatter. Gauge T1 showed continuous expansion after its sudden jump, indicating expansion of the concrete near the surface. Gauges T2, T3, and T4 were also on ties near the surface of the concrete (only 0.5 inches of clear cover to the ties) and all of these gauges indicated expansion at their locations, some with expansions near expected yielding of the ties. Lower L1, on the longitudinal bar, consistently read compressive strains, indicating that the axial compressive force was maintained throughout this period. As well, Figure 6.5 shows the upper and lower L1 gauges on the same graph. This comparison shows that the upper gauges showed a more dramatic change in compressive strain at the application of axial post-tensioning. After that point, however, the two longitudinal monitoring points had very similar readings. This similarity indicated that the axial post-tensioning led to fairly consistent axial compression of the columns and that ASR/DEF expansion was thus circumferential as intended.

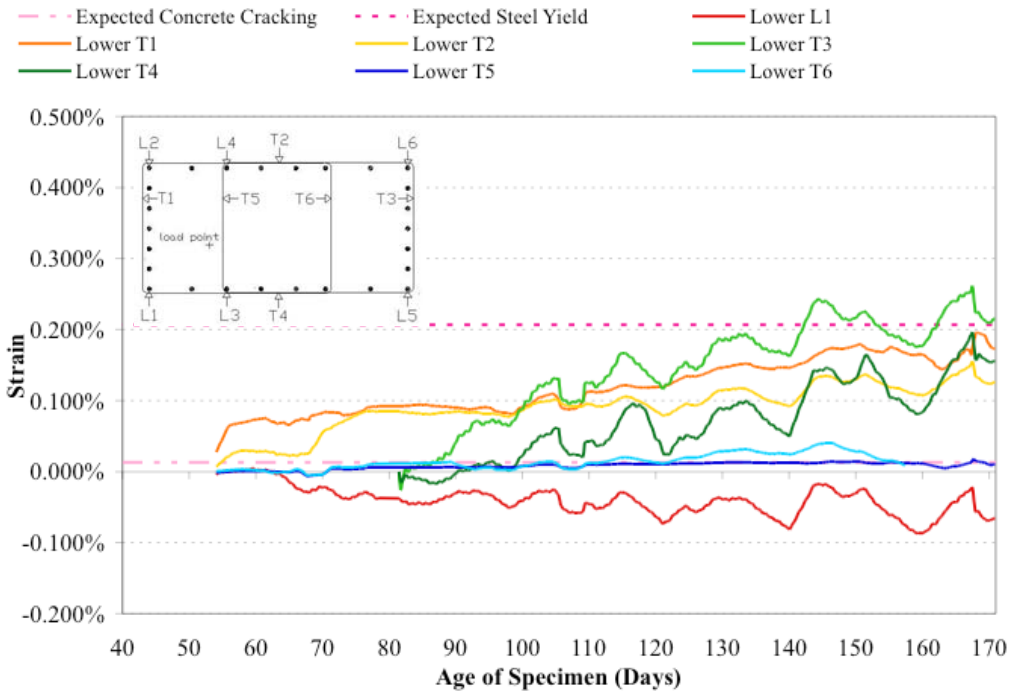

Figure 6.4: Column A Lower Layer Strain Monitoring

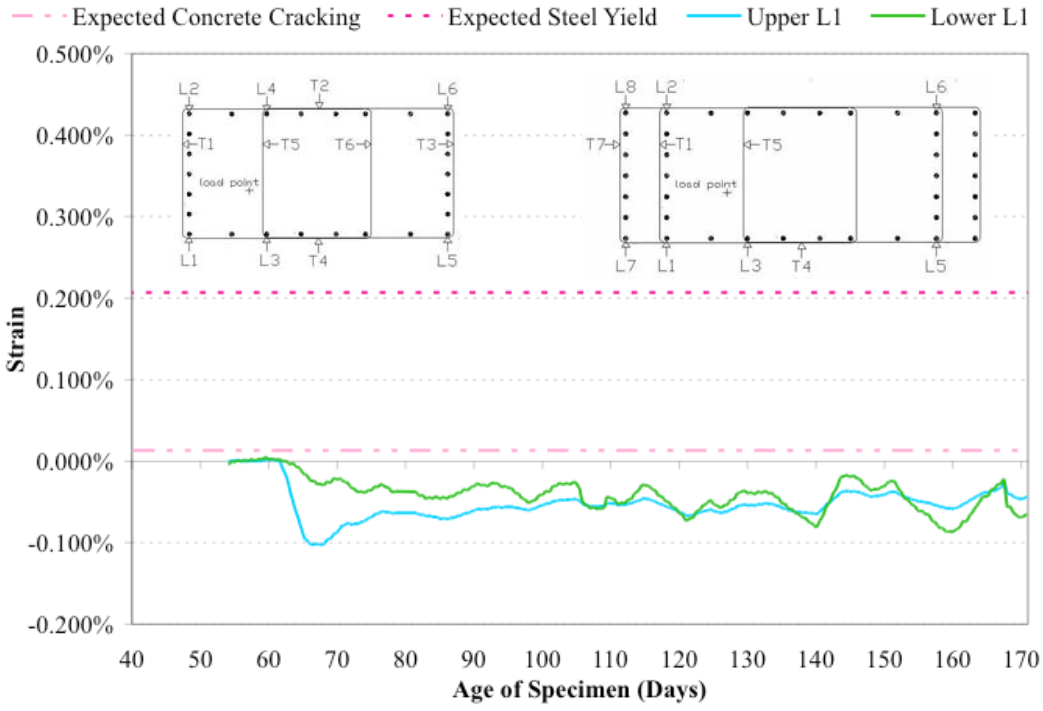

Figure 6.5: Column A Longitudinal Bar Monitoring

In the upper layer of instrumentation in Column B, shown in Figure 6.6, gauges T4 and T5 did not work. Additionally, gauge T1 reported highly erratic readings after 66 days. Thus, there was no data for gauges T4 and T5, and gauge T1 was limited to strains up to day 66. As the available trusted data for gauge T1 was so limited, it showed approximately no expansion during the first two months of the column's existence. Upper T7, showed very little expansion, which was surprising as this gauge is located near the concrete's surface. It was showing some expansion, however, and was approximately at the level of concrete cracking at six months. Gauge L1, which was monitoring the longitudinal bar at the upper level of column B, always showed compressive strains. As this bar was located under a bearing pad transferring the post-tensioned axial load into the column, the consistently compressive strain was expected. After about 120 days, however, this gauge reported that the compressive force was increasing, which is illogical as the axial load was constant throughout the monitoring period. Thus, the data for gauge L1 was truncated at 120 days.

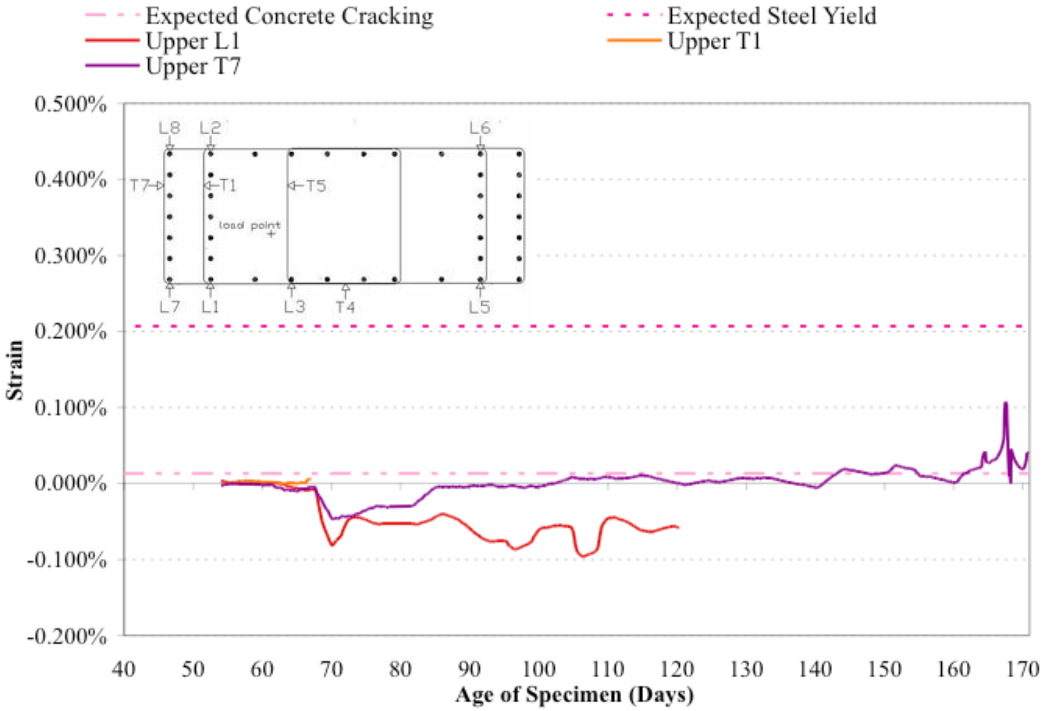

Figure 6.6: Column B Upper Layer Strain Monitoring

The lower layer of Column B, shown in Figure 6.7, also had some bad gauges, with gauge T1 and T3 both broken at the start of monitoring. Unlike the core behavior observed in Column A, Column B's core gauges, T5 and T6, exhibited definite expansion at the concrete core. Gauge T5 recorded some fluctuation, including strains above the cracking strain of concrete. Gauge T6 recorded more pronounced expansion and appeared to be heading towards steel yield at six months of age. Results from gauges near the surface, T2 and T4, were contradictory. Gauge T2 indicated expansion whilst gauge T4 recorded purely compressive strains. The concrete in these locations was definitely expanding, as evidenced in the crack patterns and external expansions measured. Longitudinal bar gauge L1 had a period between 65 and 85 days when it reported an error value for unknown reasons. The data recorded at this location, however was consistently compressive, albeit with fluctuation in the amount. Compressive strain was expected in the longitudinal bar as the column carried a post-tensioned axial load. Figure 6.8 compares the two gauges on this monitored longitudinal bar. Although Column B's gauges showed greater fluctuation than did Column A, this plot still shows the compressive effect of the axial load. Therefore, for both columns, the post-tensioned axial load during exposure created the desired effect of restraining the ASR/DEF expansion longitudinally and instead forcing circumferential expansion.

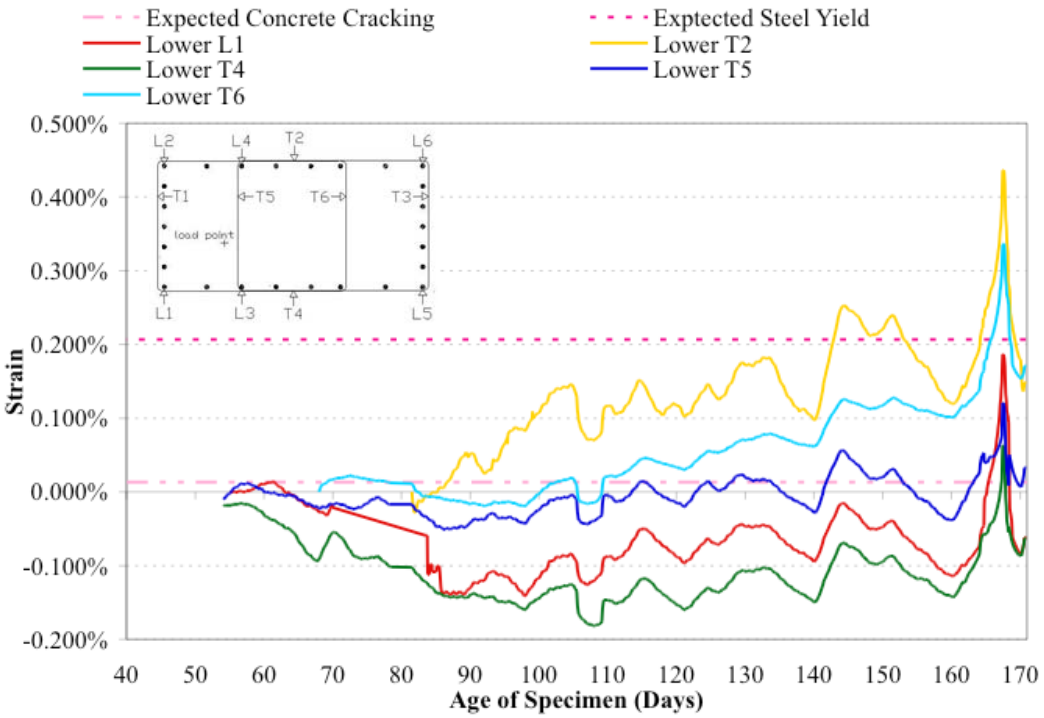

Figure 6.7: Column B Lower Layer Strain Monitoring

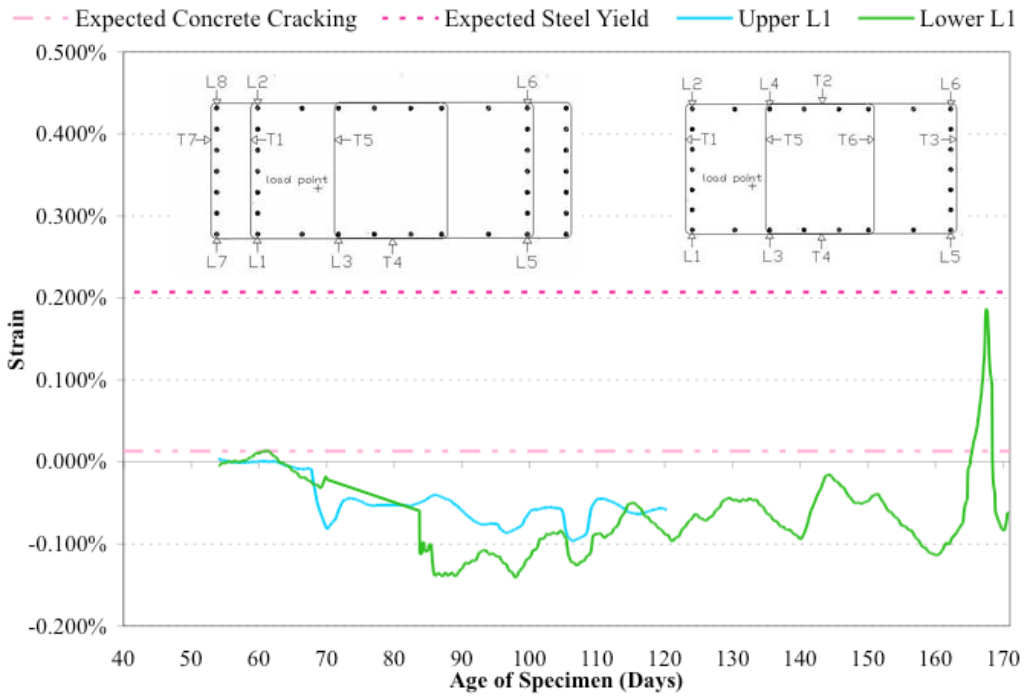

Figure 6.8: Column B Longitudinal Bar Monitoring

At 170 days after casting, the data logging system measured strains beyond the limits of the instrument (+/- 3% expansion) for ten days and thus the datalogger recorded a placeholder value indicating the error. This period correlated with a significant ice storm in Austin, TX, where the columns were located in outdoor exposure. Just prior to this anomaly, the gauges were reporting less than a 0.3% expansion and concrete cannot expand 2.5% in less than two hours (1.75 hours between readings). Thus, these readings were rejected as an error. After the gauges started returning in-range (+/- 3% expansion) values again, the majority of the gauges showed readings with wide variation. It is not known what mechanism took place within the column to cause damage to so many strain gauges at once, but it is evident that scatter in the data increased significantly after the event. The scatter was accompanied by many gauges reporting illogical readings. For instance, many gauges indicated the column was shrinking (in compression) when the column was expanding as measured externally. Figure 6.2 through Figure 6.8, therefore, stopped at 170 days after casting. Past this point only a few strain gauges were reporting logical results. Figure 6.9 and Figure 6.10 present the results from the four strain gauges that continued reporting logical results for a long period of time. In Figure 6.9, the behavior of Column A's Lower T1 is shown. This gauge showed there was sufficient expansion near the concrete surface to cause yielding of the transverse tie. While this was the only gauge that reported longer term data for Column A, it was evident that at least one transverse tie was likely to have yielded due to the ASR/DEF expansion. Column B had a few more gauges working for an extended period, as shown in Figure 6.10. This plot shows one longitudinal gauge, Lower L1, as well as two transverse tie gauges, Upper T7 and Lower T6. Gauge Lower L1 maintained a fairly consistent level of compressive strain during this period, which gave further evidence that the post-tensioned axial load successfully restrained vertical ASR/DEF expansion. Gauge Upper T7 stayed near zero strain, even reporting slightly compressive strains with time, which would imply little expansion near the concrete surface. From crack mapping and external expansion measurement, however, there was expansion at this location. At the same time, gauge Lower T6 exhibited the largest amount of expansion of all the strain gauges,

reaching a peak of 0.8% expansion. This level of expansion measured at a tie going through the center of the column would indicate that the core was certainly expanding and that the scaled reinforcing cage was not sufficient to prevent ASR/DEF expansion.

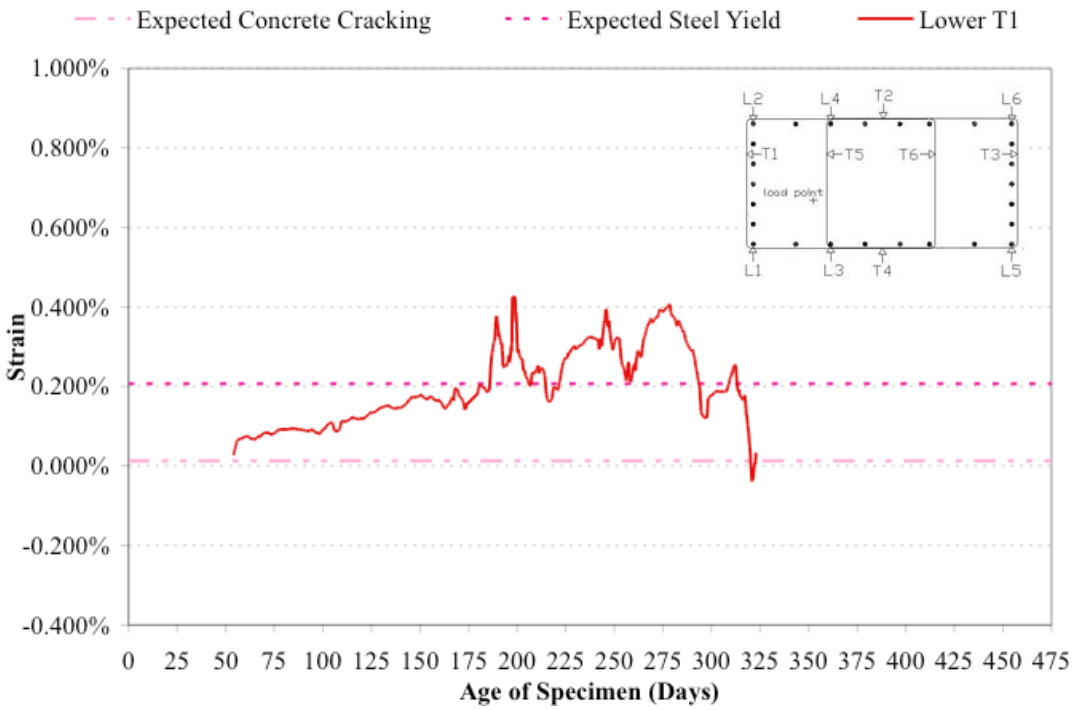

Figure 6.9: Column A Long-Lasting Gauge

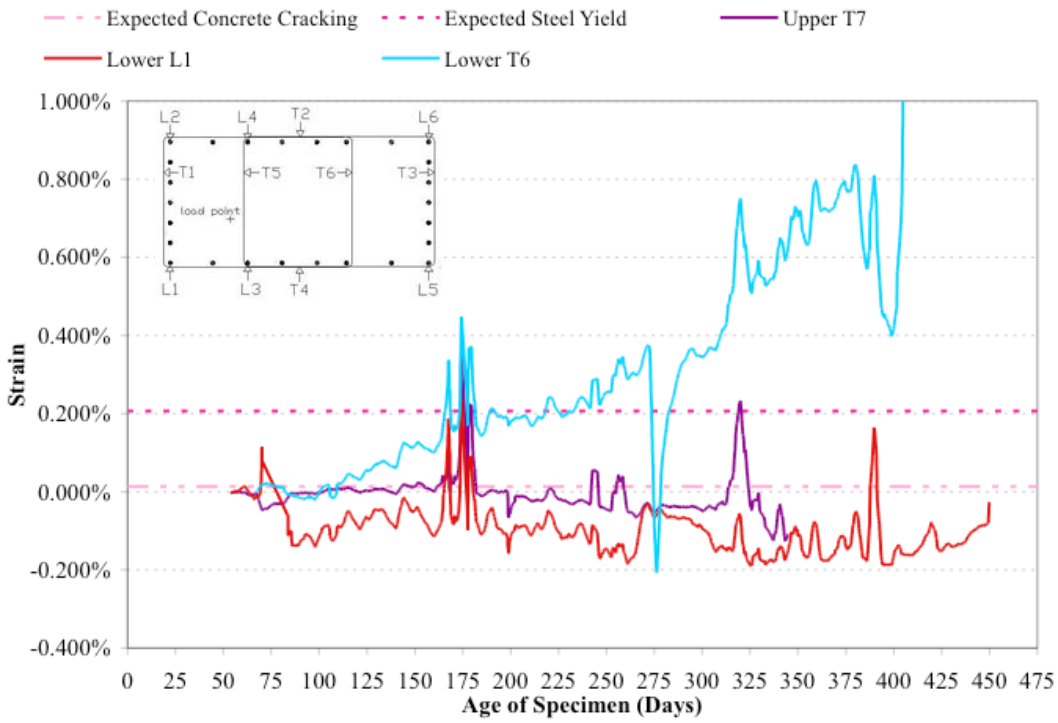

Figure 6.10: Column B Long-Lasting Gauges

6.2.1.3 Summary

While all of the monitored gauges stopped returning meaningful numbers before the end of the monitoring period, 642 days after casting, some trends were seen from the recorded values. From Figure 6.5 and Figure 6.8 the relative consistency of the longitudinal strain in the post-tensioned column was evident. The post-tensioned axial load in place during monitoring and exposure successfully restricted the ASR/DEF expansion longitudinally. Instead, the expansion in the column was forced to be circumferential as desired to imitate the observed behavior in the San Antonio Y columns. Figure 6.2 through Figure 6.7 show the wide variation in ASR induced expansion that was recorded in reinforcing steel strain. At the transverse strain gauges, an increase in strain at least equal to concrete cracking strain was recorded. Two strain gauges recorded strains beyond expected steel yield, followed by a subsequent loss of strain. Thus, it is probable that at least in two locations the transverse ties of the reinforcing steel were yielded by ASR expansion. These yielding strains were recorded at the lower layer of instrumentation, and thus the

affected ties were not critical to the bearing performance of the columns. It is evident from this strain behavior that the scaled reinforcing cage was not sufficient to prevent ASR/DEF expansion through confinement.

6.2.2 Demec Points

6.2.2.1 Introduction

Team members that were working on concrete materials research monitored the demec points of the ASR/DEF affected scaled column specimens. The following figures of external expansion measured by demec points are courtesy of those team members: Ford Burgher, Phillip Pesek, and Arnaud Thibonnier. Figure 6.11 illustrates the demec locations used in monitoring external expansion. The footings shown in this figure were not drawn to scale so that they would not overlap in the figure. Figure 6.12 through Figure 6.15 show the expansion of each column with time. Figure 6.16 through Figure 6.19 show the variation of the expansion along the profile of the columns, again showing the increase of expansion with time. Further, Figure 6.20 and Figure 6.21 show comparisons of expansion as measured by select strain gauges and the demec point measured expansion from the side of the column corresponding to those particular strain gauge locations.

6.2.2.2 Results and Discussion

In Figure 6.12 through Figure 6.15, a significant drop in expansion rate occurred at approximately 425 days after casting. This dramatic change in growth rate reinforces the need to maintain the moisture environment developed by Burgher for these columns. When the felt backed plastic was removed in order to map cracks in November 2007, it was assumed that the typically rainy winter would negate the effects of increased evaporation of water from the concrete surface. As the plastic held moisture in contact with the concrete, its removal allowed a significant increase in evaporation of moisture form the columns' surfaces. Additionally, the assumption made at the time of the plastic removal was that the upcoming winter would bring its typical rains, which would keep

the column moist and thus negate the effects of the missing plastic wrap. Unfortunately, Austin, Texas (where the columns were located) had an exceptional drought in 2008 and thus the small amount of rain that fell did not equal the previous system in maintaining moisture on the columns.

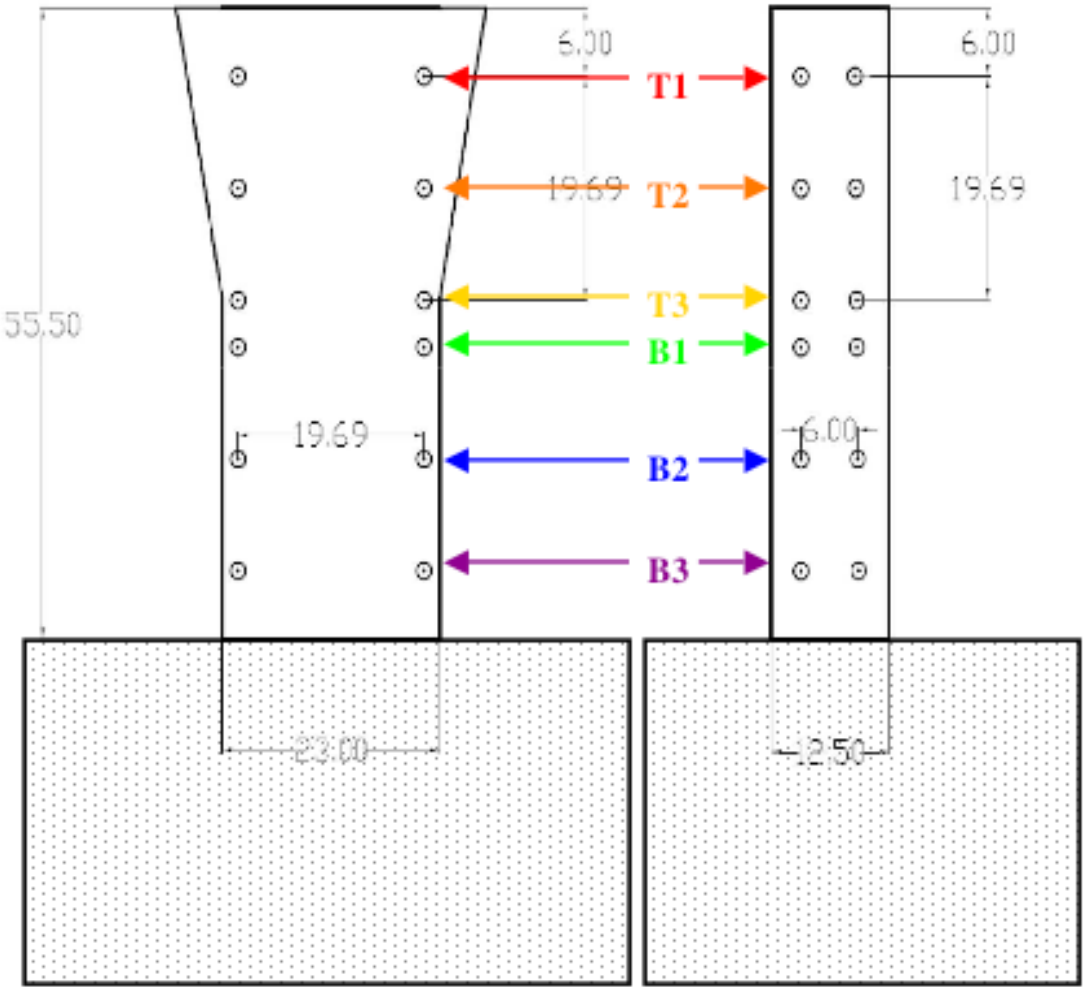

Figure 6.11: Demec Locations on Long Side (left) and Short Side (right) of Columns (Dimensions are in Inches)[109]

Consistent to all of these external expansion plots is that the lowest monitoring level, B3, exhibited the least expansion. As this point was the closest to the columns' large footings, the footings may have influenced expansion through two likely methods. The first method is from the initial heat curing. The column bases had been cast before the

columns and thus were at ambient temperature at the time of casting. These large bases (54 ft^3) would have acted as a thermal sink, absorbing heat from the adjacent column bottom and thus preventing it from reaching the 158 ºF threshold for causing DEF. Equally likely, the base acted as a significant restraining force for circumferential expansion at the column base. The footings were cast with non-reactive concrete and thus were not expanding with the column. Therefore, with the post-tensioned axial load restricting expansion vertically and the footing preventing circumferential expansion at the very bottom of the column, ASR/DEF expansion was largely suppressed at the base. Above location B3, however, both columns showed significant expansion, as seen in Figure 6.12 through Figure 6.15. Column A typically exhibited more expansion than Column B. This difference reflects the variable nature of ASR/DEF and the resulting difficulty in designing concrete mixtures to have a prescribed amount of expansion. These plots also show that the maximum expansion reached during the exposure period was in the range of 1.0 to 1.5%. As discussed in Chapter 2, the potential for future expansion from ASR or DEF in the San Antonio Y columns was up to 1.2% for ASR expansion and 1.3% for DEF expansion. Thus, this level of potential expansion was comparable to the expansion triggered in the ASR/DEF columns.

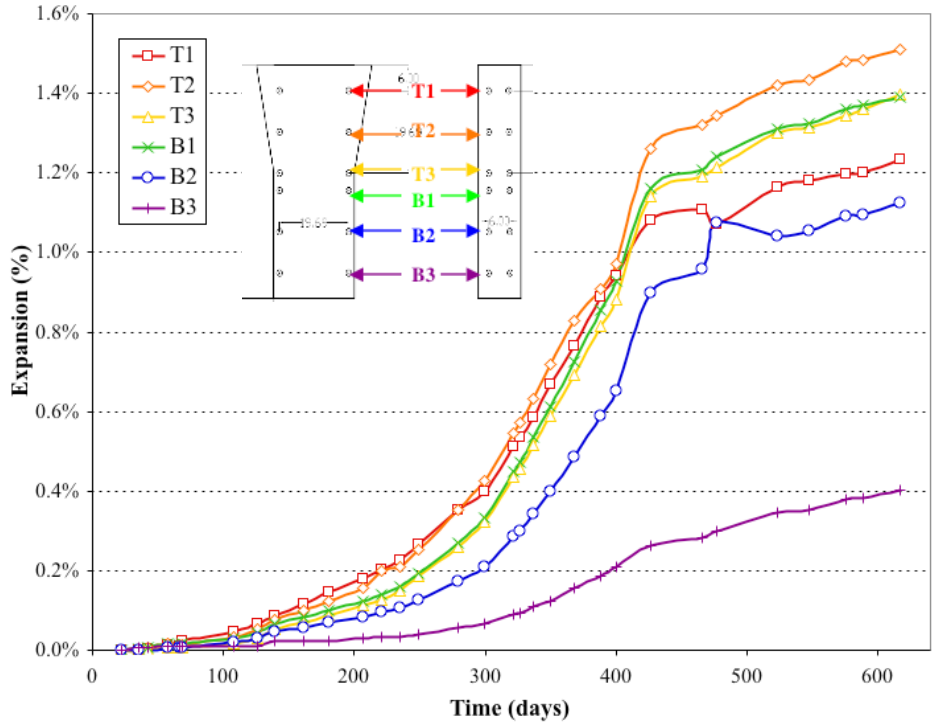

Figure 6.12: Column A Average Long Side Demec Expansion Monitoring[98]

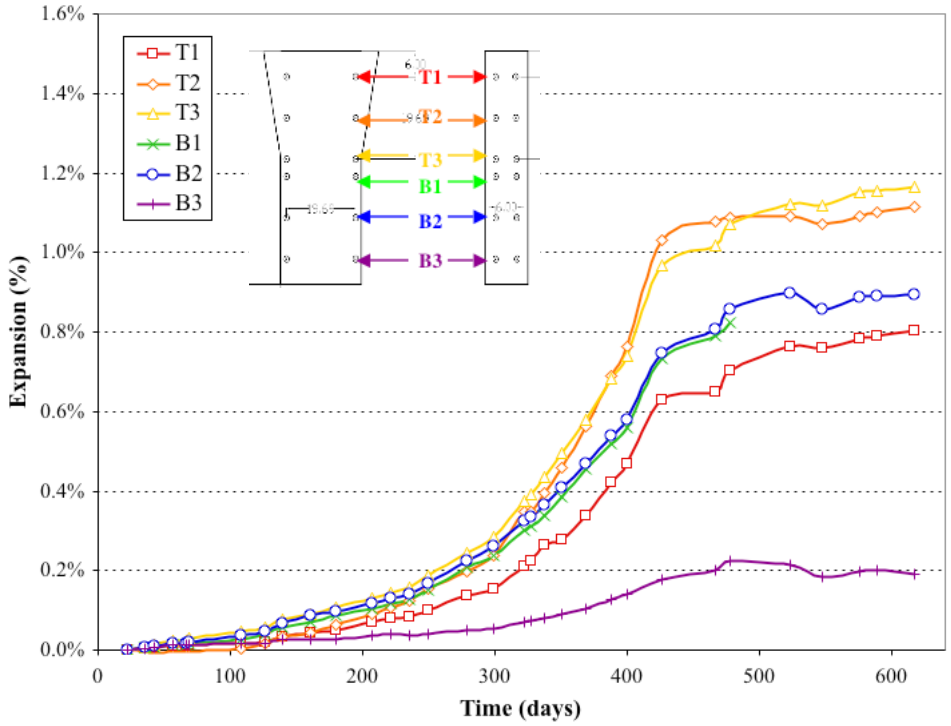

Figure 6.13: Column A Average Short Side Demec Expansion Monitoring[98]

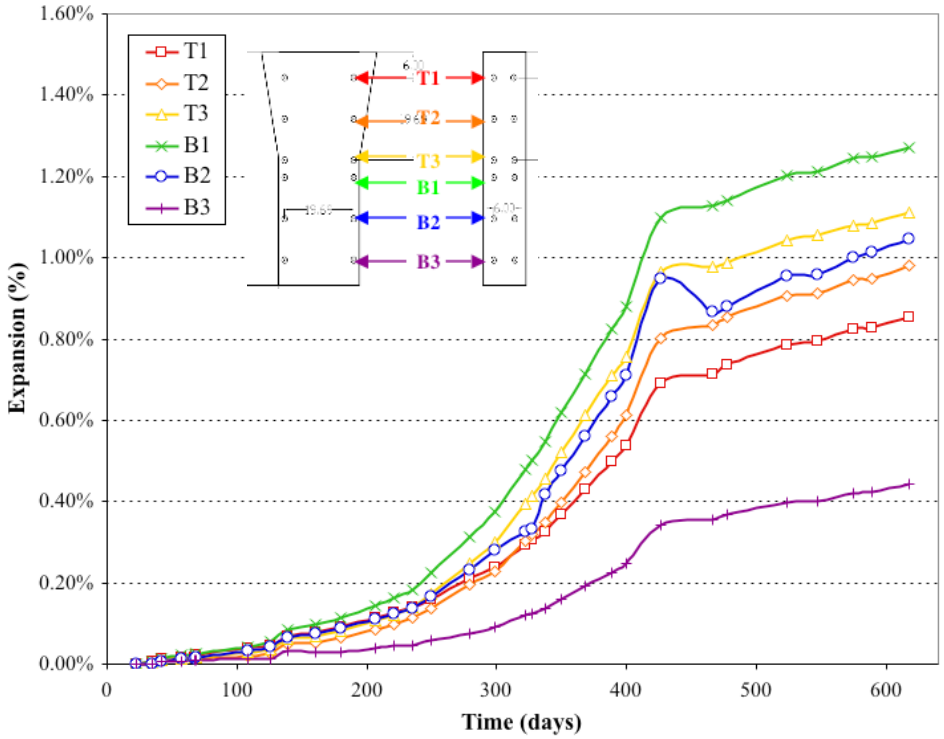

Figure 6.14: Column B Average Long Side Demec Expansion Monitoring[98]

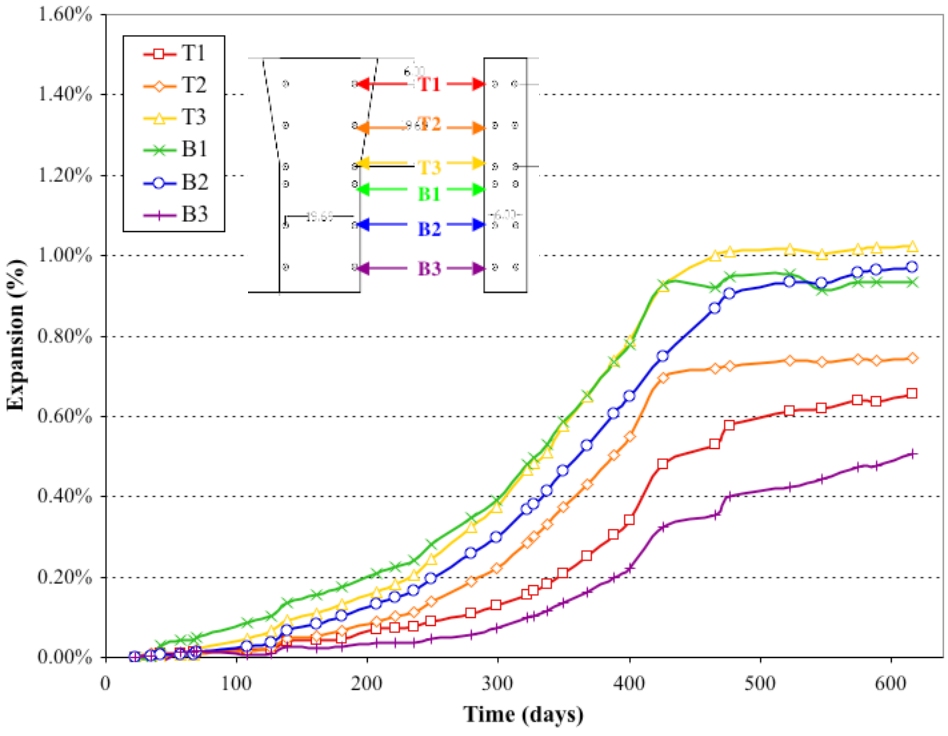

Figure 6.15: Column B Average Short Side Demec Expansion Monitoring[98]

Figure 6.16 through Figure 6.19 present the demec measured external expansion data in profile view. The long side profiles of Figure 6.16 and Figure 6.18 show the average expansion that was measured on the long faces of Column A and B, respectively. Likewise, Figure 6.17 and Figure 6.19 show average expansions measured on the short faces of columns A and B, respectively. These profiles show that the center (mid-height) of both columns exhibited the greatest amount of expansion. The core concrete at mid-height likely stayed at temperatures above 158 ºF during heat curing for the longest period of time simply from being in the center. Heat is most readily dissipated from the surface of the concrete. Thus, the core concrete was insulated by the surrounding concrete and took more time to cool, even after the external heaters were turned off. Extra heat curing could have caused more primary ettringite to decompose during early curing and thus became more susceptible to DEF expansion. It is also possible that the bearing pads and spreader beam at the column top prevented this region from expanding freely by restricting movement through friction between the bearing pads and concrete column as well as between the bearing pads and the spreader beam. As can be seen from these profiles, the restricting force of this load application assembly was not nearly as large as the restraining effect of the footing. Additional variation of expansion along the height of the columns is likely from the variable nature of ASR/DEF, as the length of the columns had no additional sources of lateral restraint beyond the footing and bearing pads discussed.

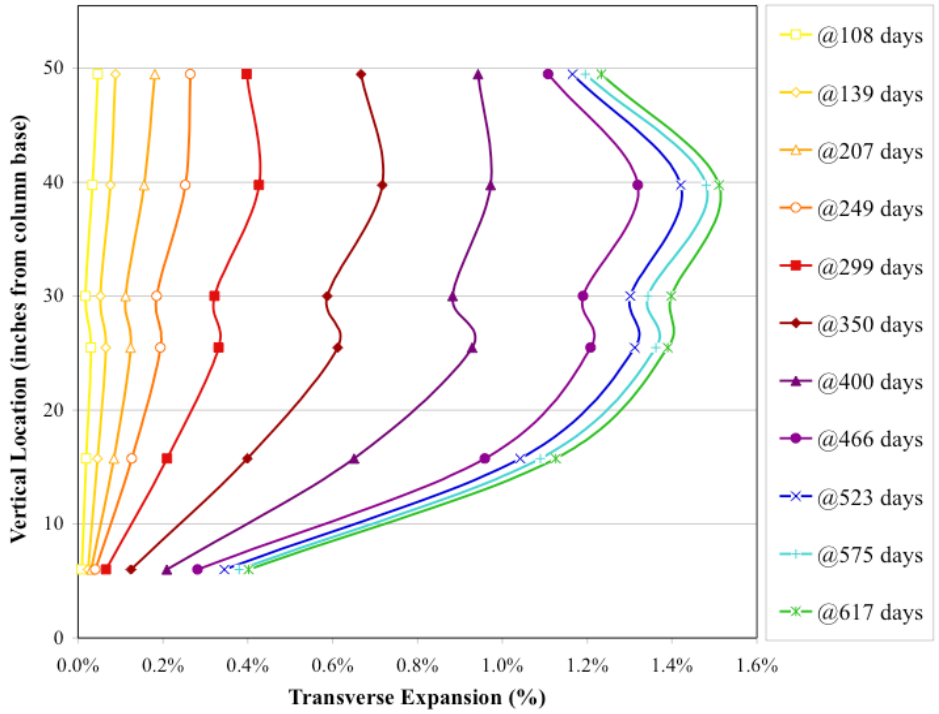

Figure 6.16: Column A Average Long Side Profile of Expansion with Time[98]

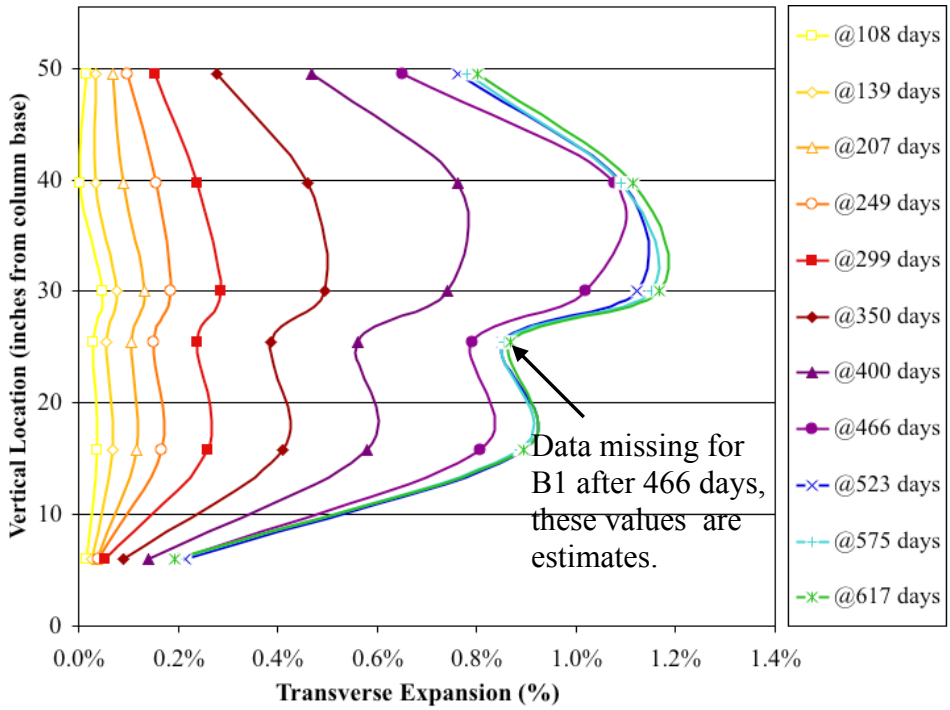

Figure 6.17: Column A Average Short Side Profile of Expansion with Time[98]

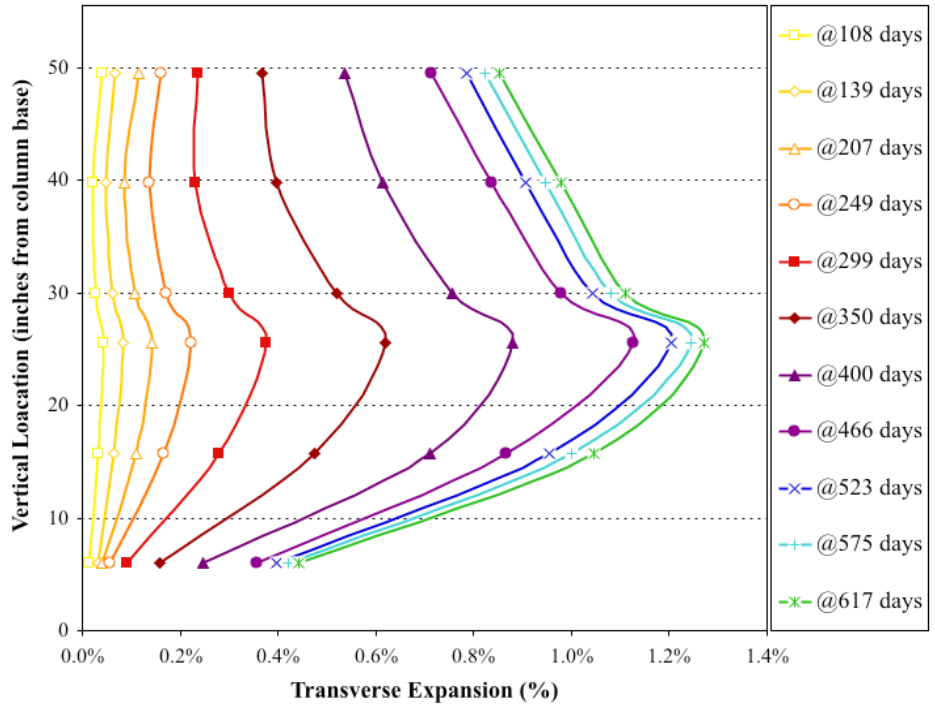

Figure 6.18: Column B Average Long Side Profile of Expansion with Time[98]

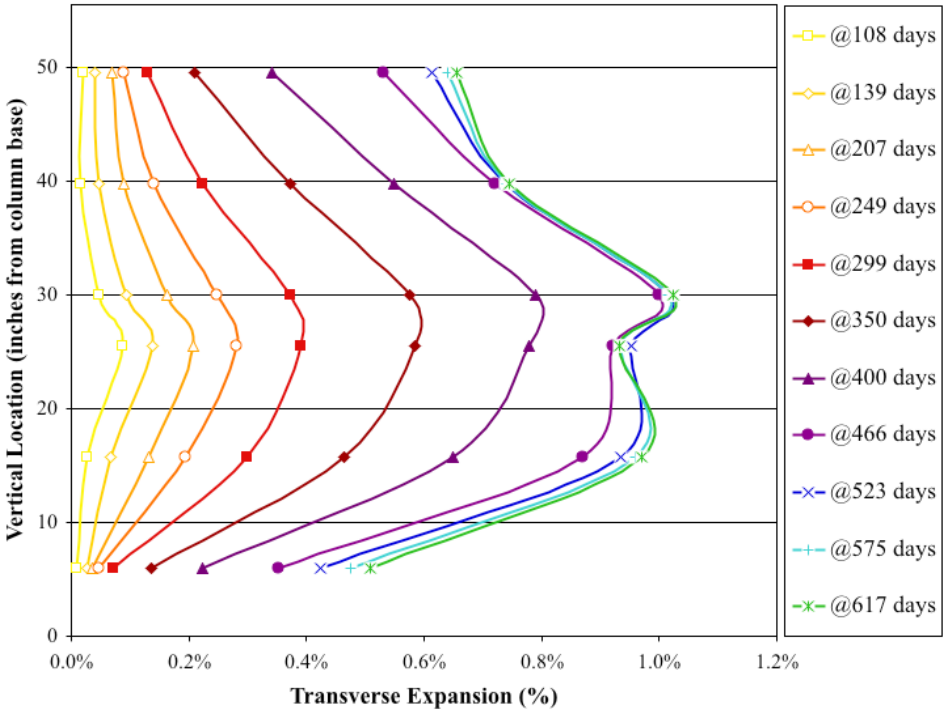

Figure 6.19: Column B Average Short Side Profile of Expansion with Time[98]

Figure 6.20 and Figure 6.21 present a comparison between select strain gauges and the demec readings from the corresponding column side. The selected gauges were the two (one in each column) that read strains beyond expected steel yield. Thus, these comparisons examine the greatest expansion levels measured by the monitored strain gauges versus the externally measured expansion. Both strain gauges were from the lower layer, and thus were closest in elevation to the demec points T3 and B1. Column A's gauge Lower T1 is shown in Figure 6.20 alongside the demec expansions from that column's short side. For this plot, the early jump in strain was subtracted from all of gauge Lower T1's readings for easier comparison of expansion rates. In this plot, the reinforcing strain and the external expansion started at similar rates. By about 125 days, however, the expansion measured by gauge Lower T1 was growing more quickly than the externally measured expansion at level T3. The difference in these expansion rates was similar in size to differences amongst the different demec measuring locations on the column (T1 versus B1 for example). Thus, the expansion rates at the reinforcing cage and the concrete surface were comparable. Figure 6.21 compares Column B's gauge Lower T6 with the short side demec measuring points of that column. This plot shows gauge Lower T6 to have nearly the same expansion rate as that measured at demec points T3 and B1 up to approximately day 350. After this time, the expansion rate at the reinforcing cage grew at a slightly faster rate than did the demec measured expansion. As with Figure 6.20, this difference in expansion rate was similar to the differences seen between demec measuring points. As the strain gauges measured change in length over a small gauge length (6mm, e.g.) and the demec readings recorded the average change in length over a longer gauge length (18 inches, e.g.), the similar rates suggest fairly uniform expansion at the column's mid-height (lower layer of strain gauges). Many of the strain gauges had lower rates of expansion than the two selected for comparison here. Thus, there were instances where the reinforcing cage was able to restrain the ASR/DEF expansion to some degree. What was clear from these plots and the varying expansion rates recorded by the strain gauges was that this scaled reinforcing cage was unable to uniformly suppress ASR/DEF expansion through confinement.

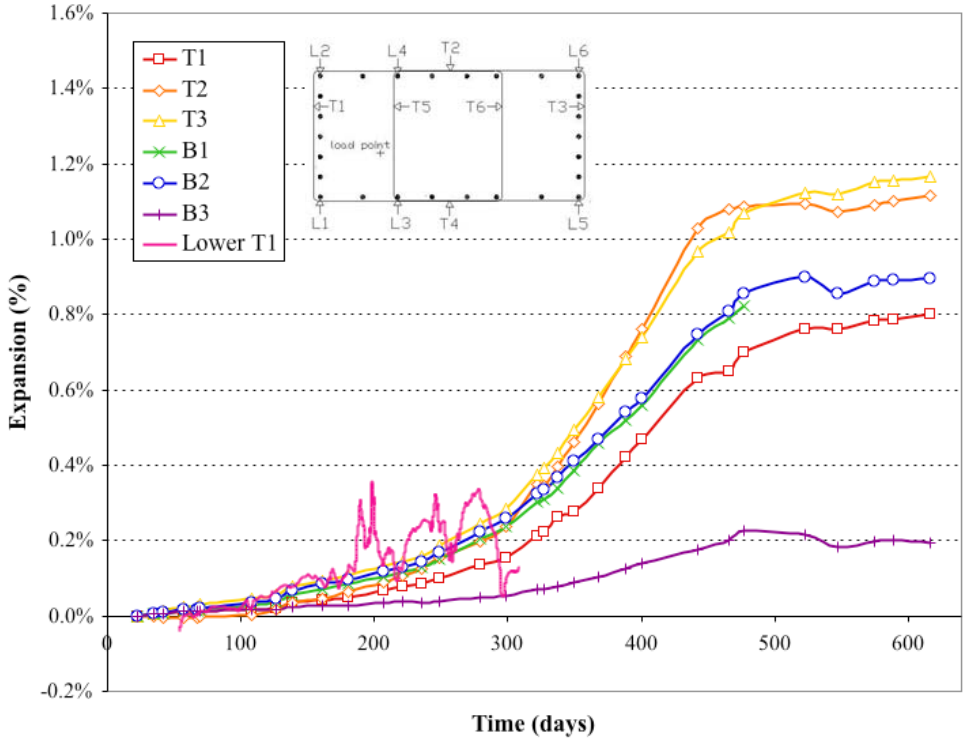

Figure 6.20: Column A, Lower T1 Comparison with Demec Expansion

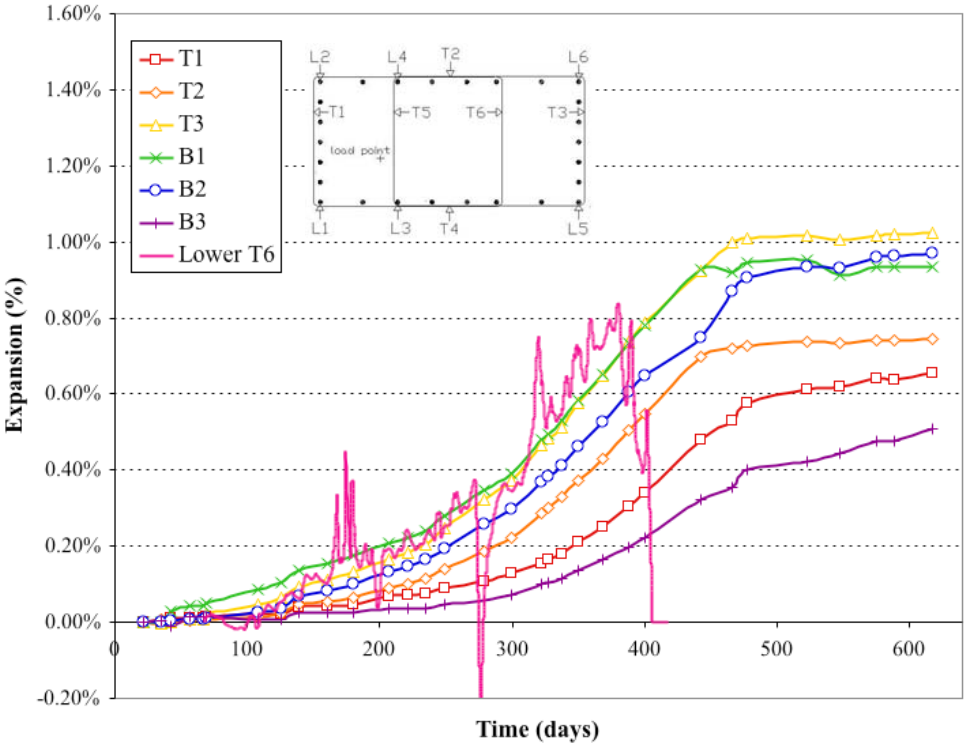

Figure 6.21: Column B, Lower T6 Comparison with Demec Expansion

6.2.2.3 Summary

From monitoring demec points on all sides of the columns, external expansion measurements were plotted for the full monitoring period. This monitoring showed circumferential expansion in the columns from 1.0 to 1.5%. This amount of expansion was similar to the potential for future expansion by ASR or DEF as measured on cores taken from the San Antonio Y[2]. Through comparison to the worst case strain gauge readings, it was seen that the external expansion rates were the same as the expansion rate of the reinforcing cage in places. Thus, the columns expanded circumferentially and the reinforcing cage was unable to prevent expansion from ASR/DEF in the core.

6.2.3 Vibrating Wire Gauges

Three vibrating wire gauges were inserted into each column at the top of the cage, approximately level with the top layer of transverse ties as shown in Figure 6.22. Each gauge was oriented to record expansion of the core concrete in a different direction: vertically and along both horizontal axes. The vibrating wire gauge system had valid data recorded during concrete casting and the following three days, which is presented in Appendix A, but no additional data points were recorded.

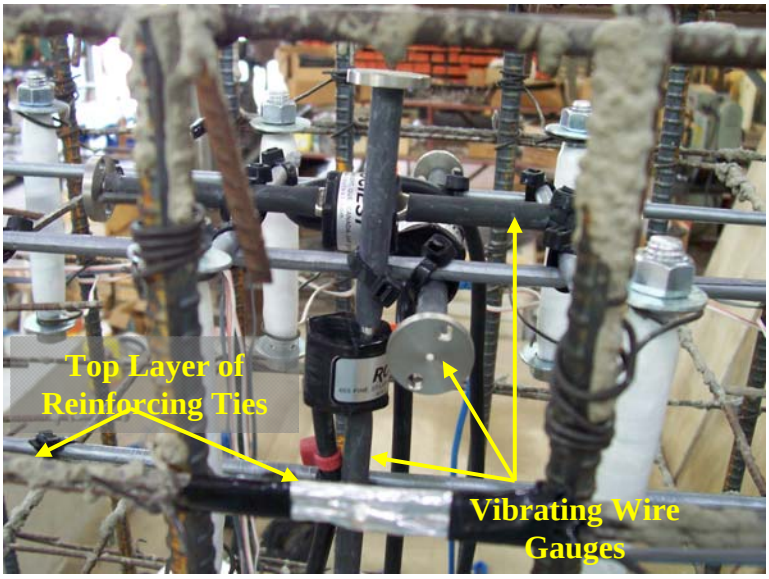

Figure 6.22: Vibrating Wire Gauges in Reinforcing Cage

6.2.4 Spring Height

6.2.4.1 Introduction

As mentioned in Chapter 3, the spring height was measured periodically to ascertain whether the post-tensioning system had lost load. As all of the post-tensioned axial load was transferred through the spring assembly, any loss of load (such as from concrete creep or steel relaxation) would result in an increase in overall spring height.

6.2.4.2 Results and Discussion

While the spring constant used was derived empirically, and thus must be taken as an approximate value, the measurements listed in Table 6.1 and Table 6.2 show that there was no significant change in post-tensioning load during the observed period. The spring heights are reported in inch fractions. Due to the approximate nature of the spring constant, only two significant figures were kept for the load calculation.

Table 6.1: Spring Height Monitoring for Column A

Date	North (inches)	South (inches)	Average (inches)	Approx. Load (kip)
4/14/07	-	-	7 1/4	200
5/15/07	7 1/8	7 5/8	7 1/4	200
7/20/07	7	7 17/32	7 17/64	200
8/31/07	7	7 1/2	7 1/4	200
11/14/07	7 1/16	7 3/8	7 7/32	200
4/2/08	6 31/32	7 7/16	7 13/64	200

Table 6.2: Spring Height Monitoring for Column B

Date	North (inches)	South (inches)	Average (inches)	Approx. Load (kip)
4/14/07	-	-	7 11/32	180
5/15/07	7 7/16	7 1/4	7 11/32	180
7/20/07	7 7/16	7 1/4	7 11/32	180
8/31/07	7 3/8	7 1/4	7 5/16	180
11/14/07	7 3/8	7 1/4	7 5/16	180
4/2/08	7 3/8	7 5/16	7 11/32	180

6.2.4.3 Summary

Measuring spring height on a post-tensioning system was a simple and efficient way to check for loss of load. In this instance, there was no significant change in load.

6.2.5 Crack Mapping

6.2.5.1 Introduction

Periodically the visible cracking on the specimen surface was mapped in order to compare the extension of cracking with time. Visual inspection of surface cracking is a simple assessment tool when evaluating structures with premature deterioration such as ASR[8]. As discussed previously, when ASR and DEF, which are three dimensionally expansive, are restrained during the concrete expansion the resulting cracking aligns in the direction of restraint.

6.2.5.2 Results and Discussion

Crack mapping occurred in April 2007, November 2007, and April 2008. Figure 6.23 through Figure 6.33 show the cracking documented in Column A on the listed dates. Figure 6.34 through Figure 6.44, likewise, show the cracking progression of Column B. Within each column series, the crack maps are presented in chronological order for each side of the column. The sides begin at the West face and proceed counter clockwise around the columns to finish at the North face (West, South, East, then North). In these mini-series the predominant observed trend was a dramatic increase in number and size of cracks between April 2007 and November 2007, times that correspond to approximately 270 and 490 days after casting. The final crack mapping in April 2008 (approximately 640 days after casting) shows an increase in the number of cracks as well as an increase in the size of the typical crack. This increase, however, is not nearly as dramatic as the previous change. The reduction in rate of crack propagation correlated with the reduction in expansion rate discussion in the demec point results section. The relationship between these monitoring methods was logical. With more expansion came more and/or larger cracks to accommodate the concrete's movement. In the crack maps

from April 2008 the regions of predominant crack size were shaded. During this crack mapping, all crack sizes had been recorded at the column top as well as representative crack sizes for these shaded regions down the column face. During the first round of crack mapping, in April 2007, no cracks were observed on the north face of either column. Thus, the following figures do not have April 2007 crack maps for the north face.

The typical orientation of all recorded cracks was vertical. Thus, the orientation followed the path of the greatest restraining force, the post-tensioned axial load. Between November 2007 and April 2008, the cracks in this main path of force transfer typically grew wider, even though there were not many new cracks that appeared. A second predominant crack orientation was evident on the long column sides (East and West faces) in November 2007 and April 2008. This pattern was a single or cluster of horizontal cracks forming along the top mat of reinforcing. This horizontal cracking occurred at the top center of the columns, in a region where the axial post-tensioning had negligible influence. Thus, the transverse reinforcing provided the primary source of restraint in this region, triggering the horizontal cracking.

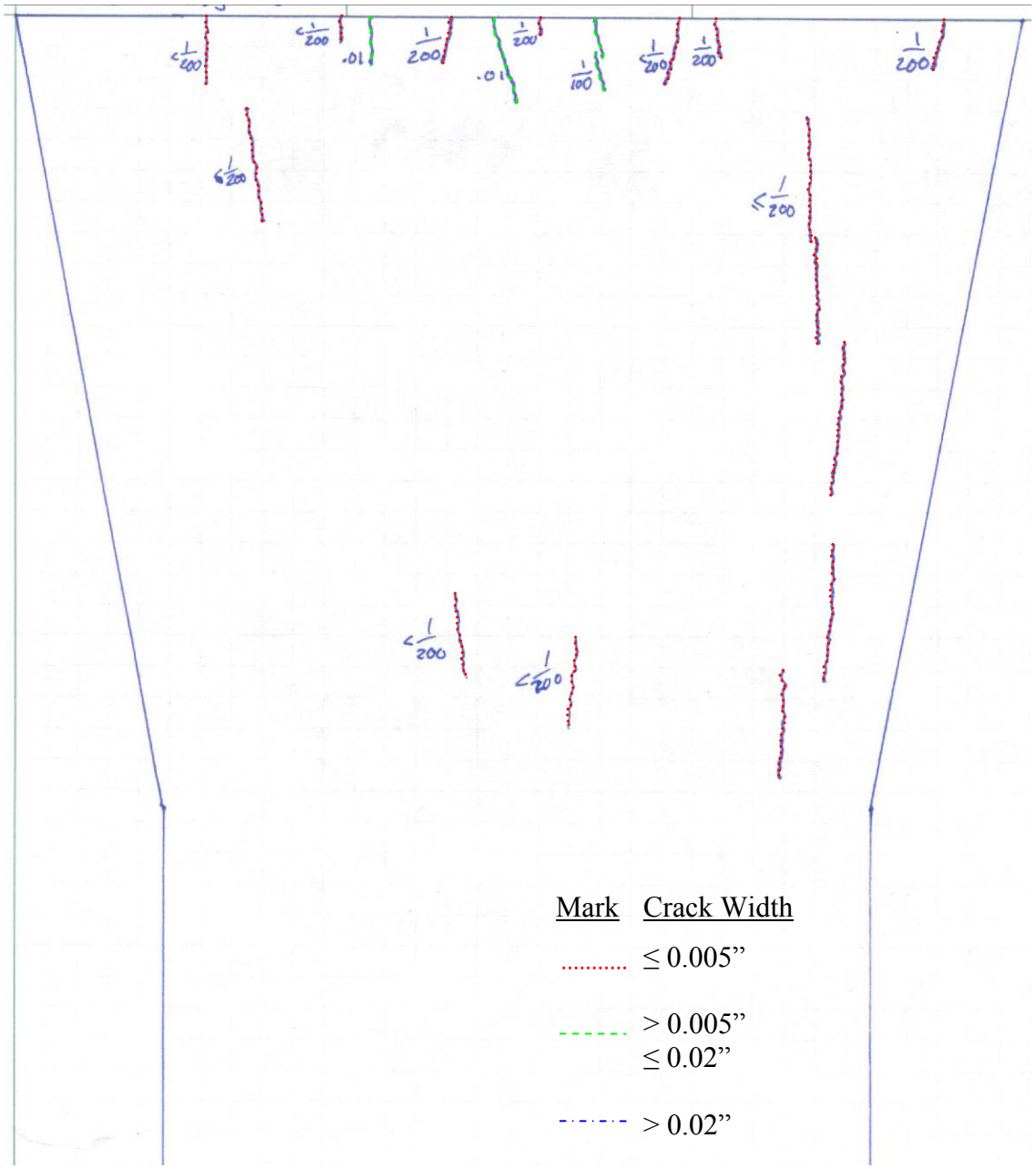

Figure 6.23: Column A West Side April 2007

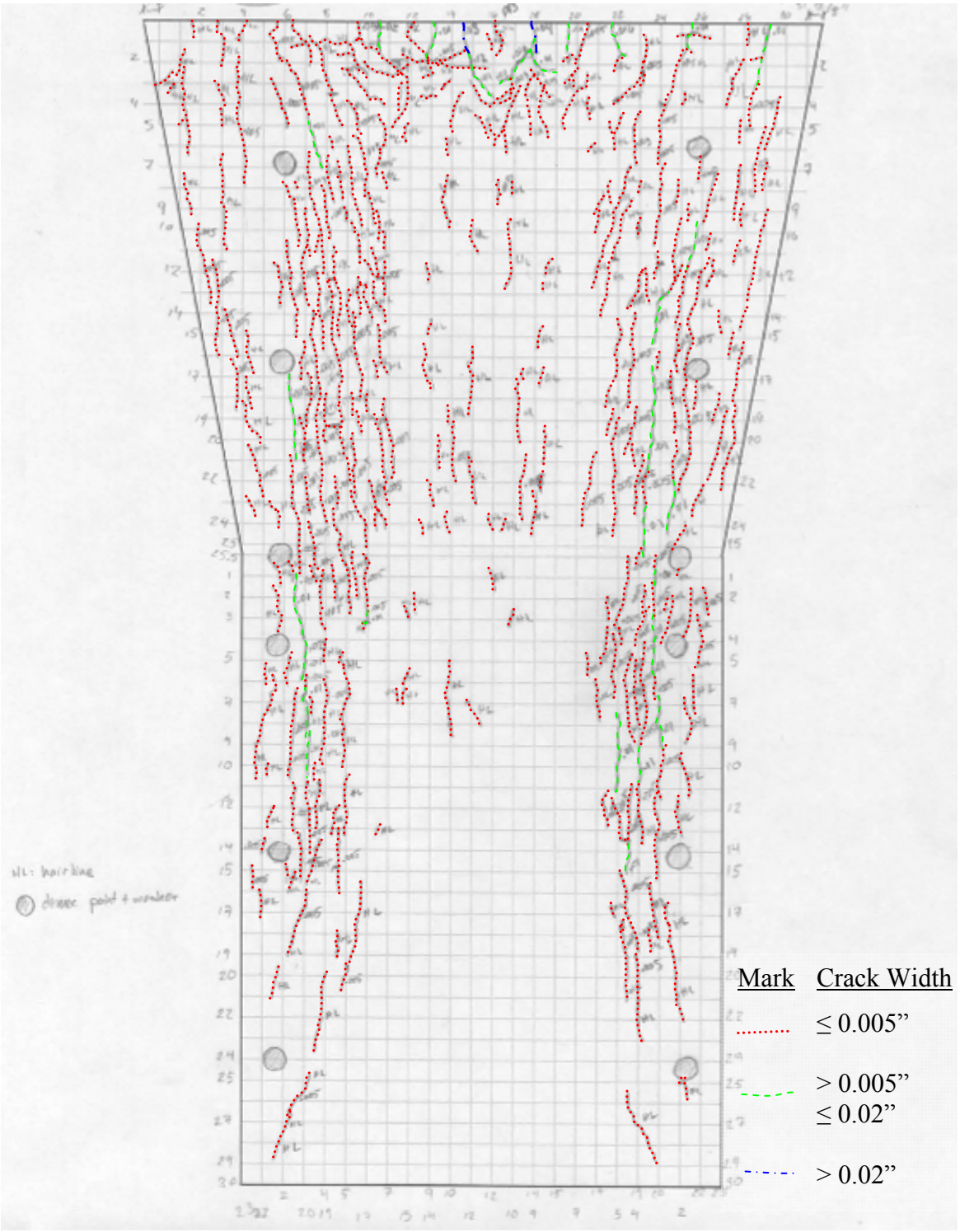

Figure 6.24: Column A West Side November 2007

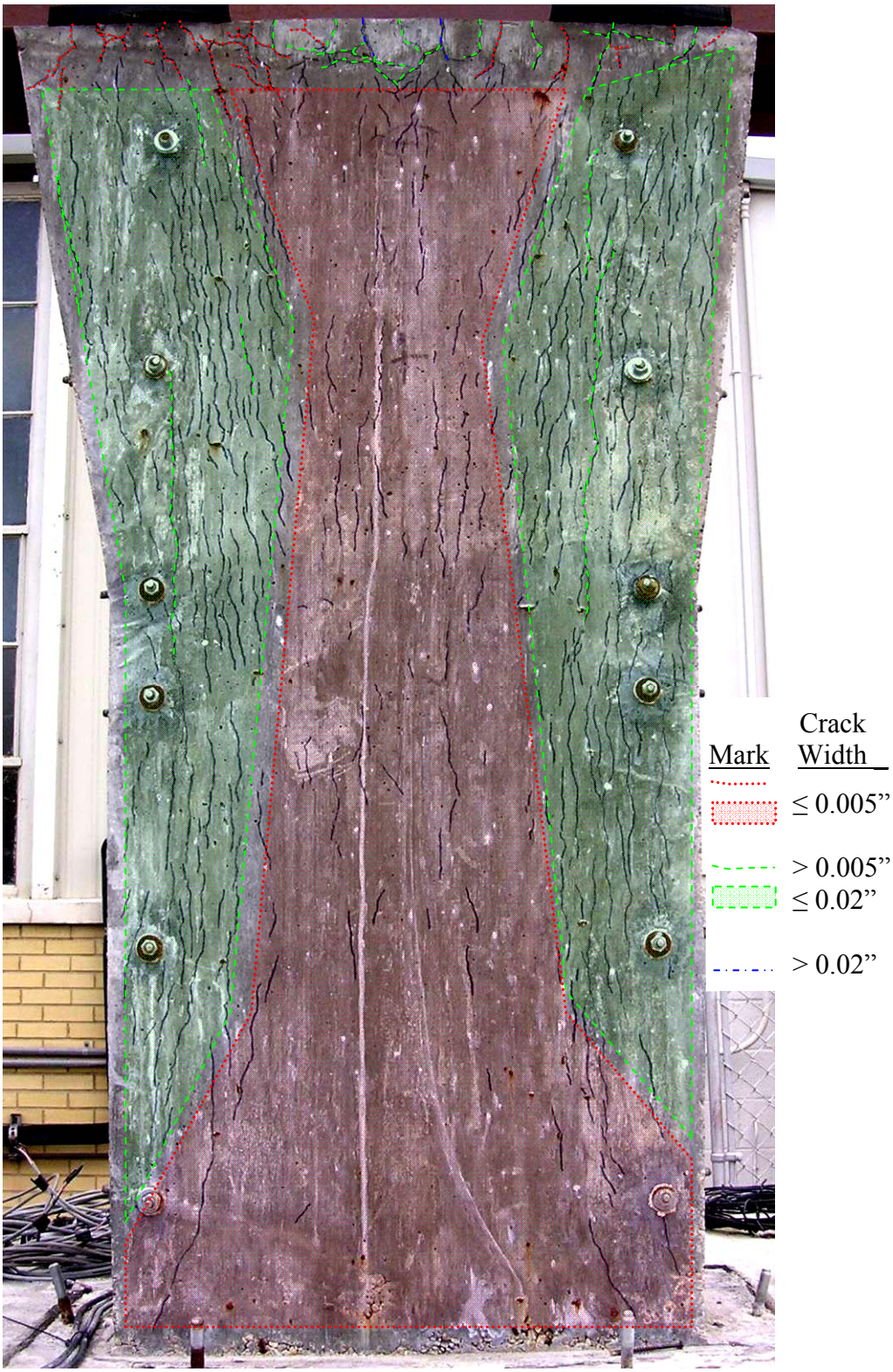

Figure 6.25: Column A West Face April 2008 (cracks marked in blue)

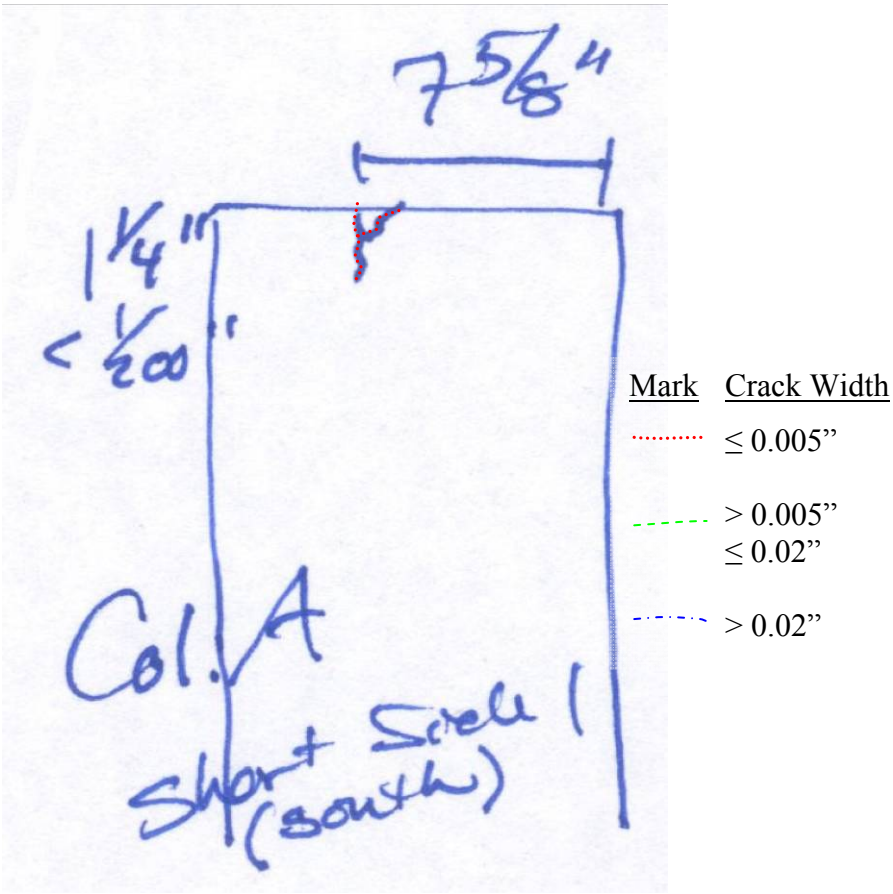

Figure 6.26: Column A South Side April 2007

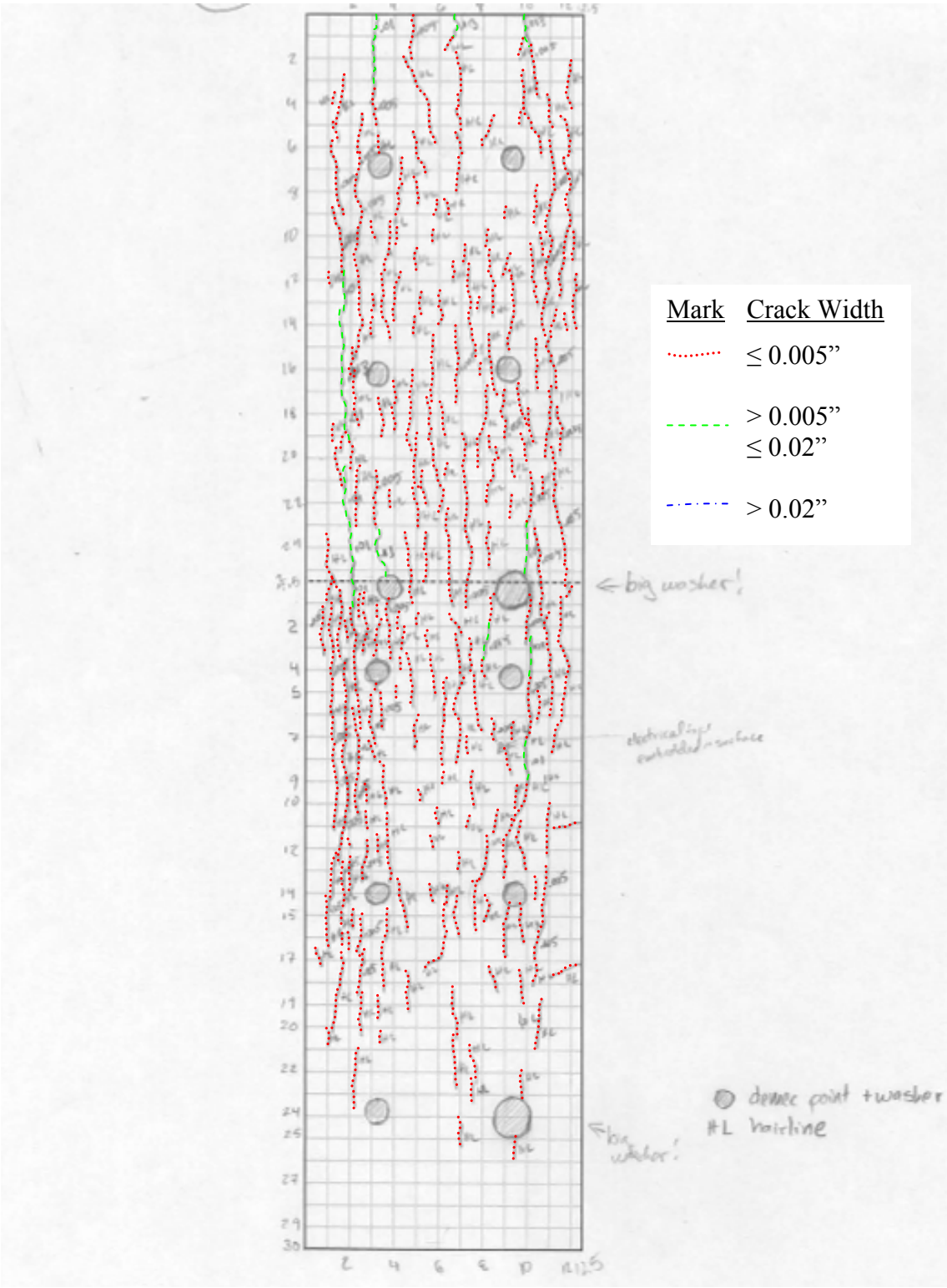

Figure 6.27: Column A South Side November 2007

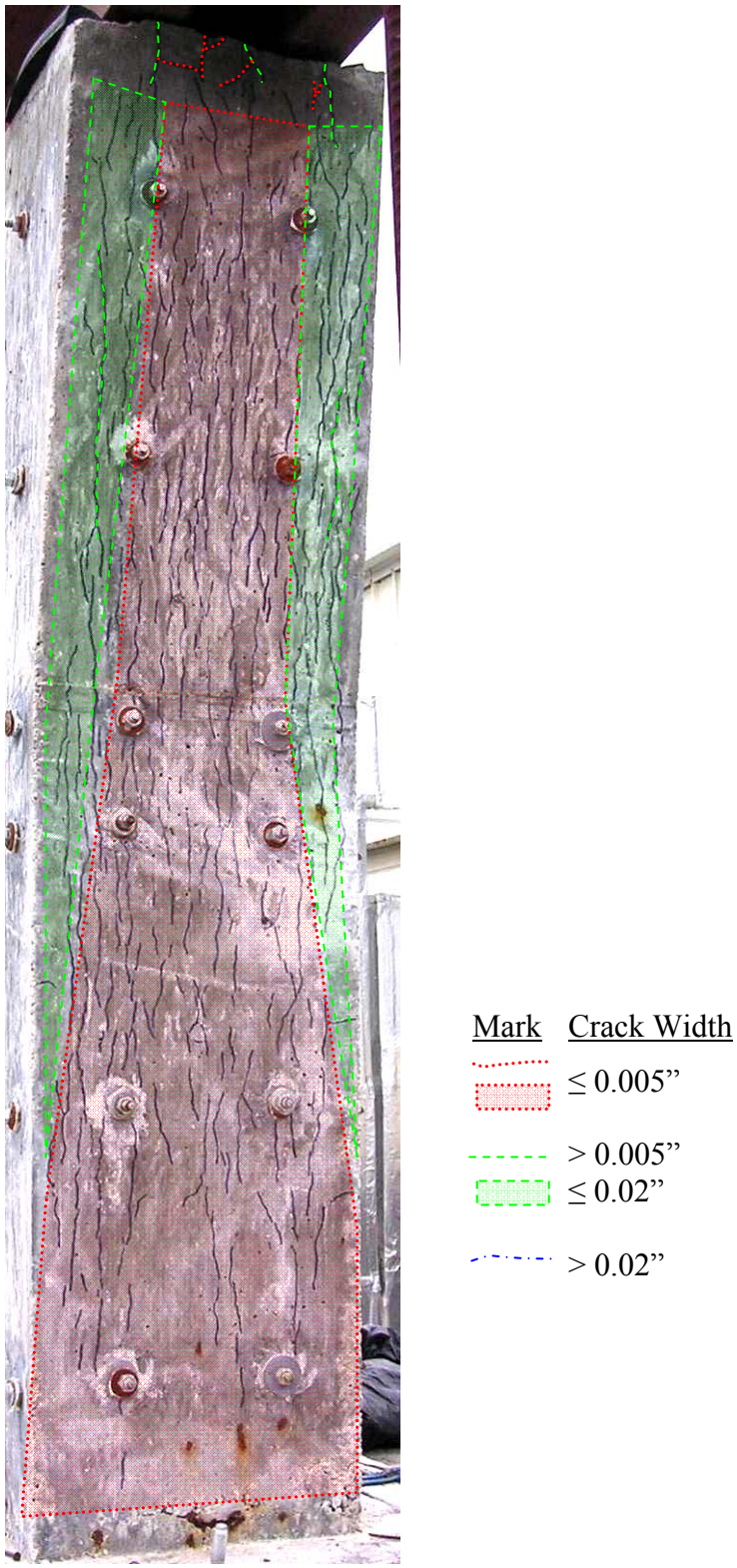

Figure 6.28: Column A South Face April 2008 (cracks marked in blue)

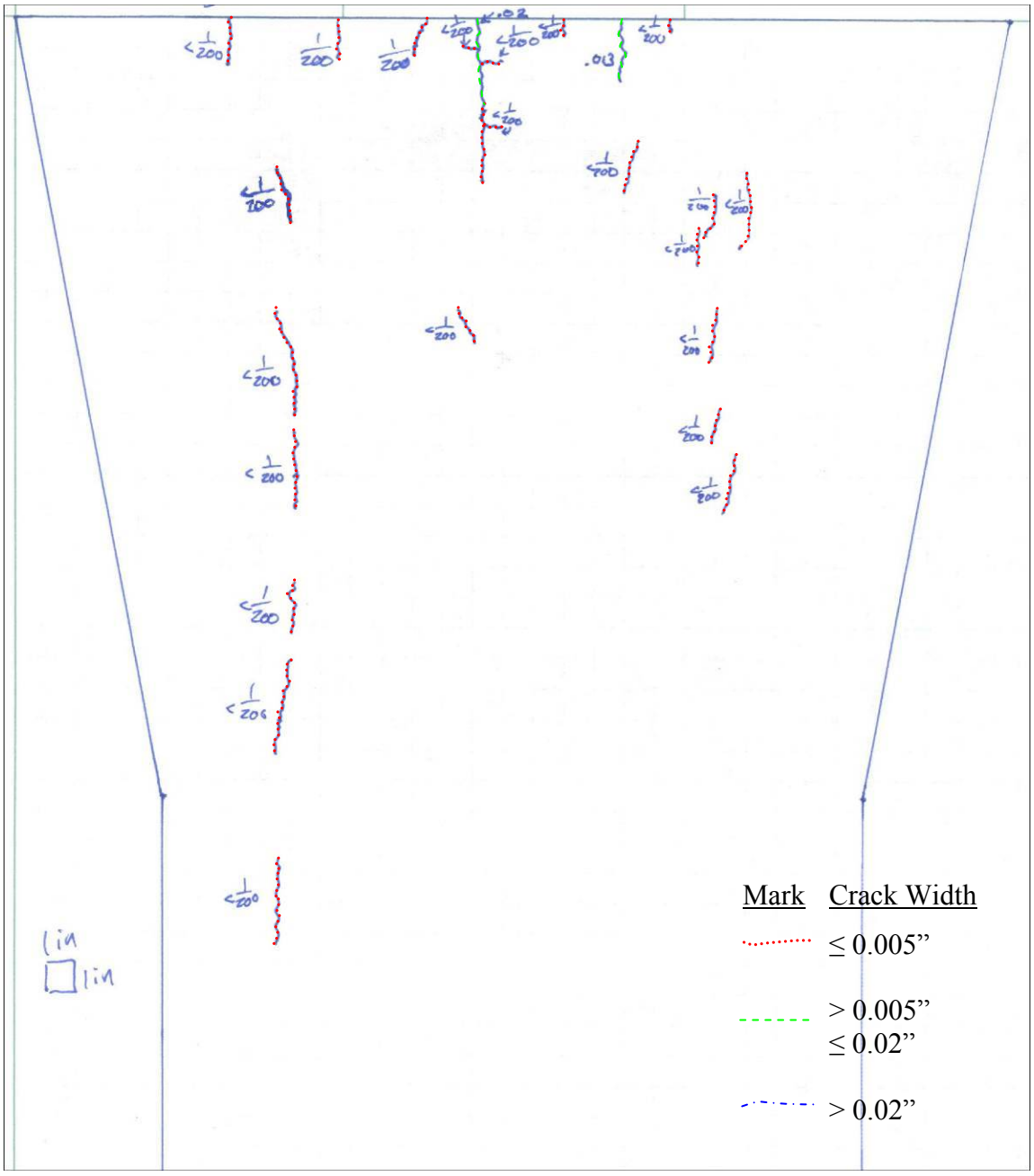

Figure 6.29: Column A East Side April 2007

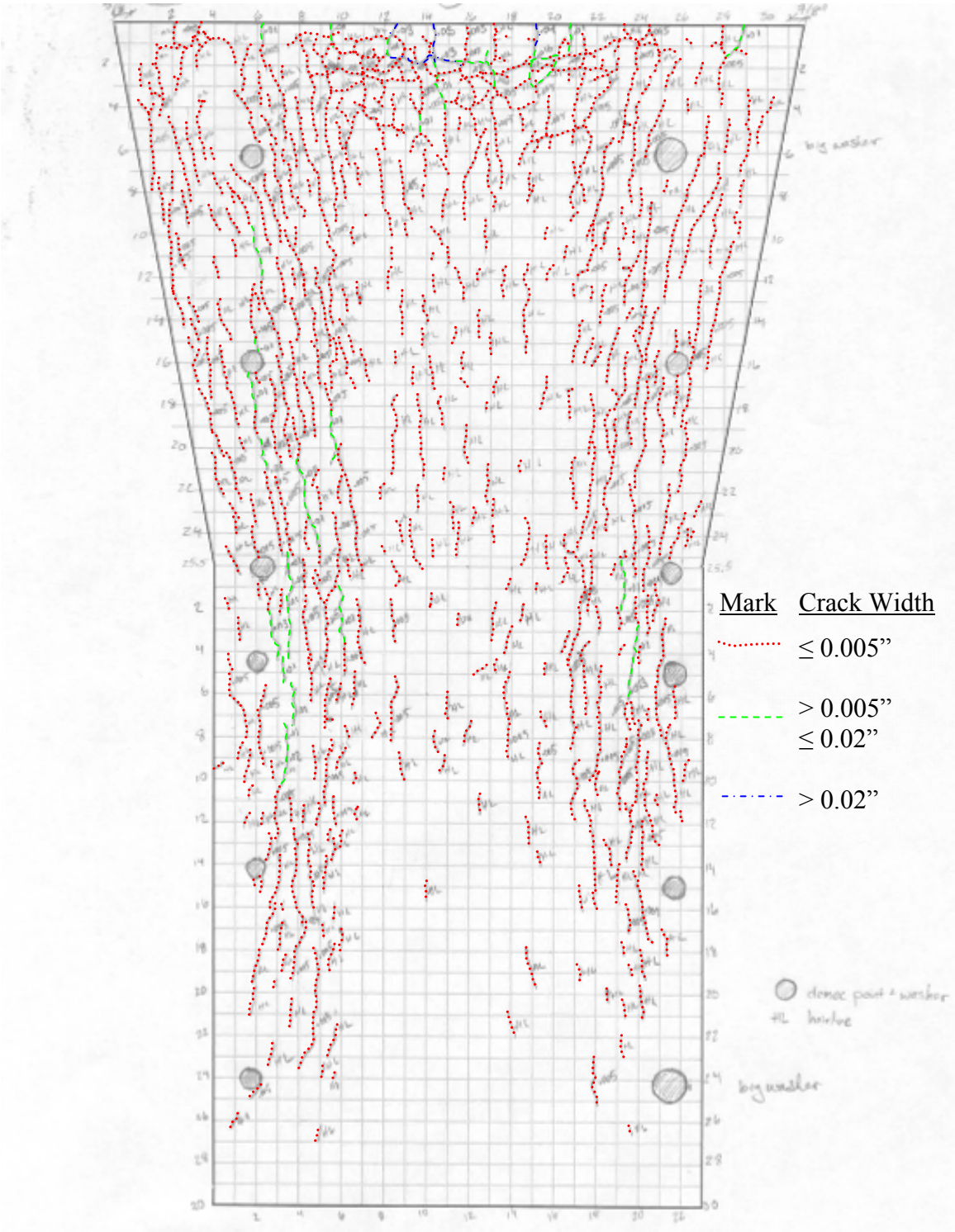

Figure 6.30: Column A East Side November 2007

Figure 6.31: Column A East Face April 2008 (cracks marked in blue)

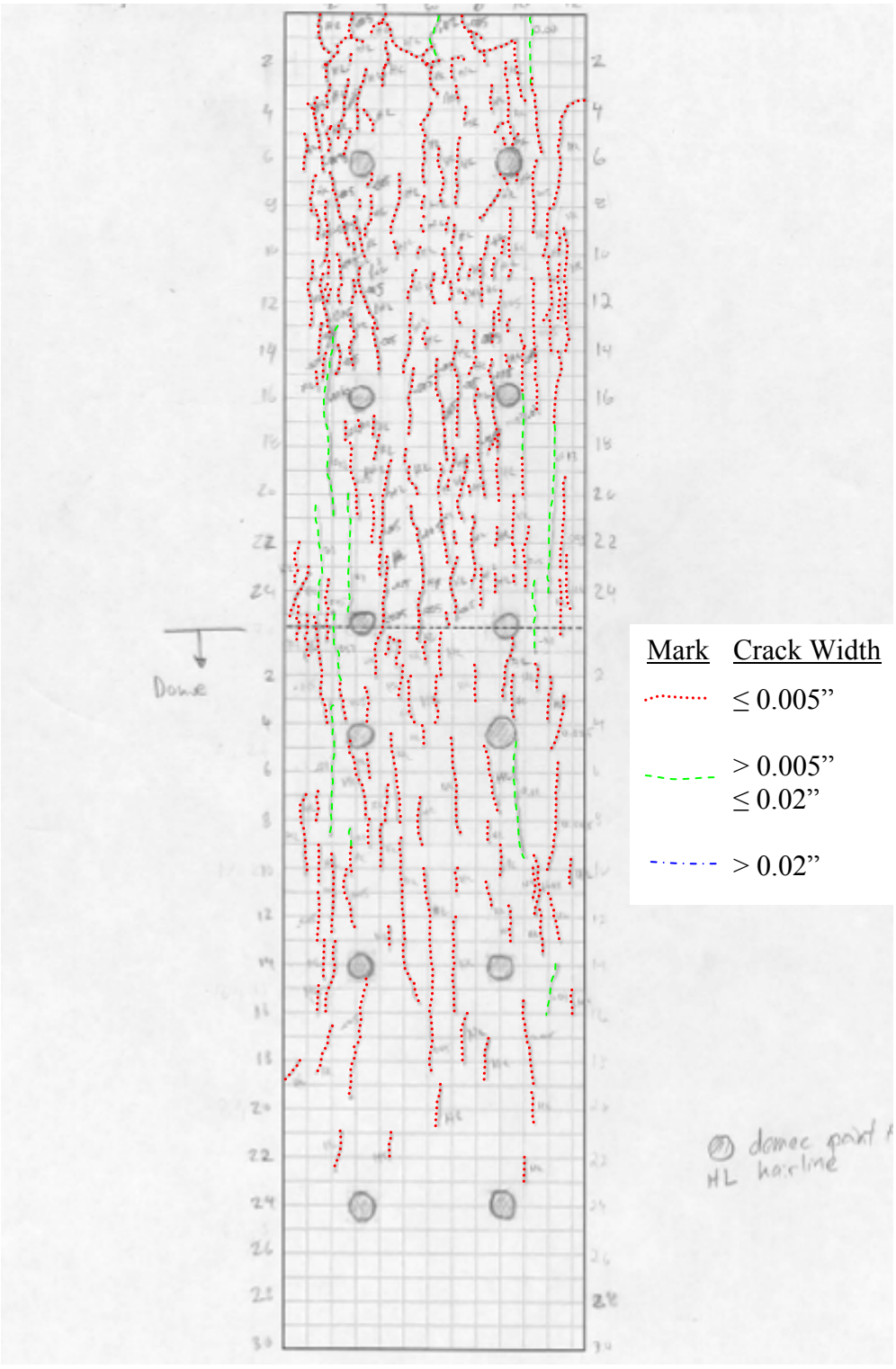

Figure 6.32: Column A North Side November 2007

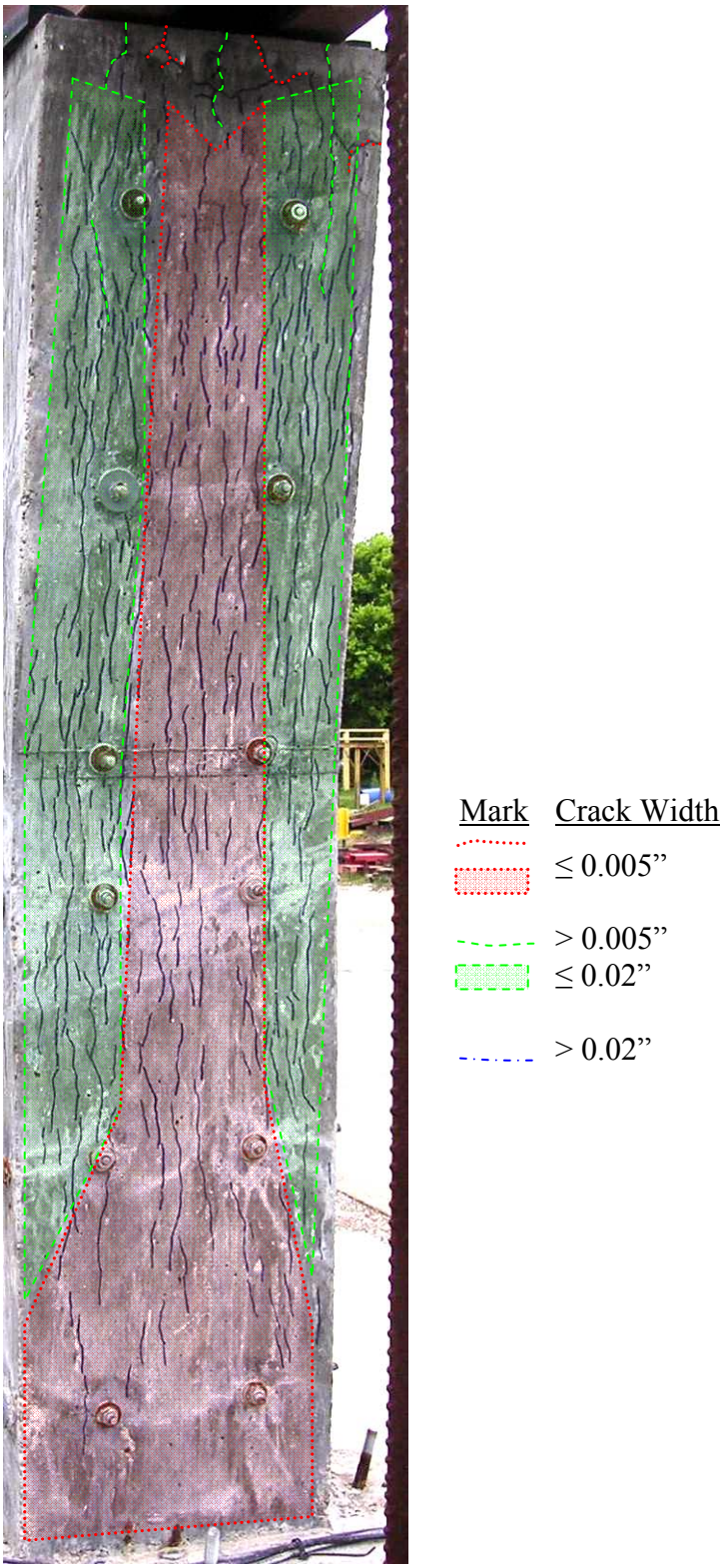

Figure 6.33: Column A North Face April 2008 (cracks marked in blue)

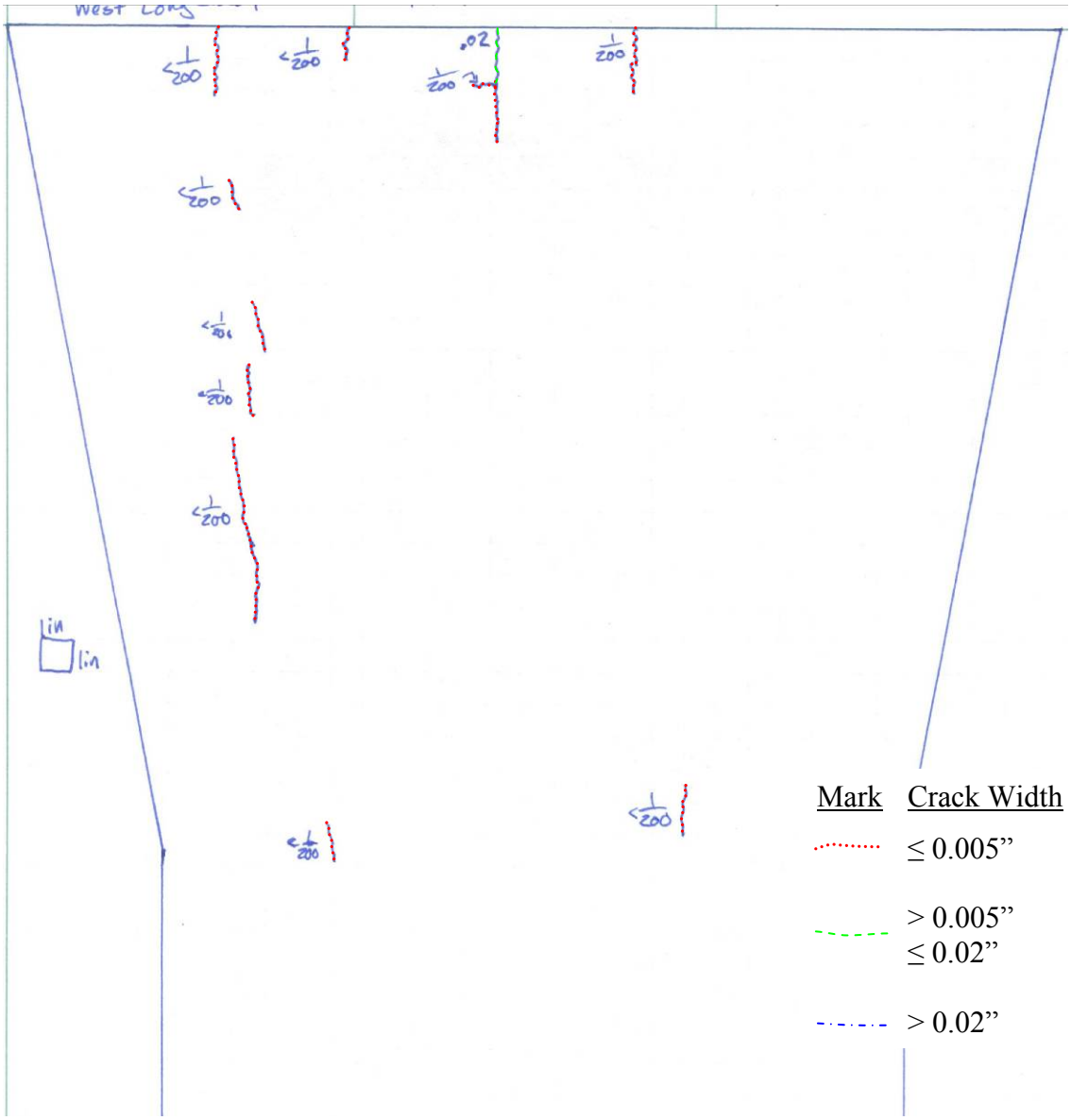

Figure 6.34: Column B West Face April 2007

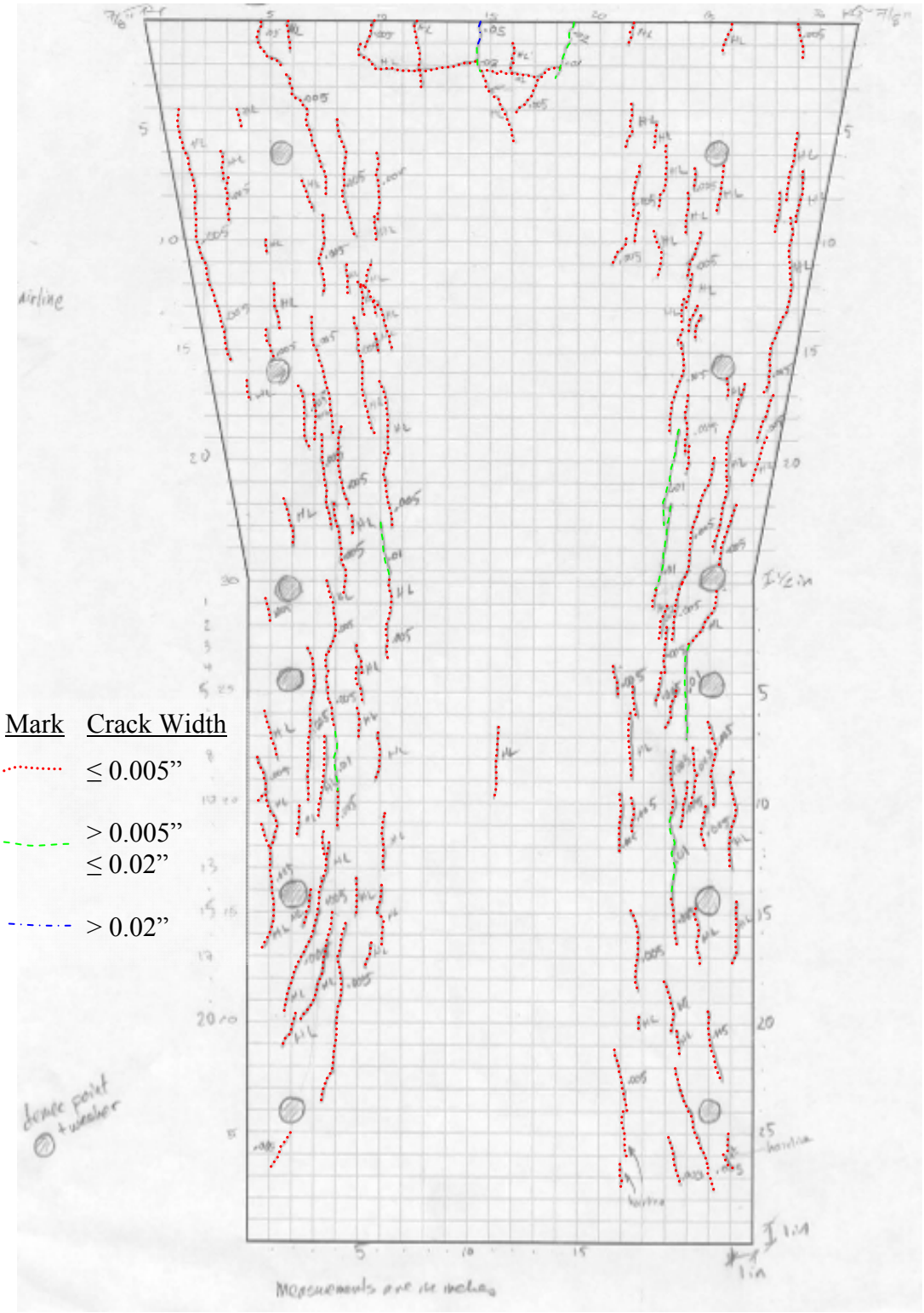

Figure 6.35: Column B West Side November 2007

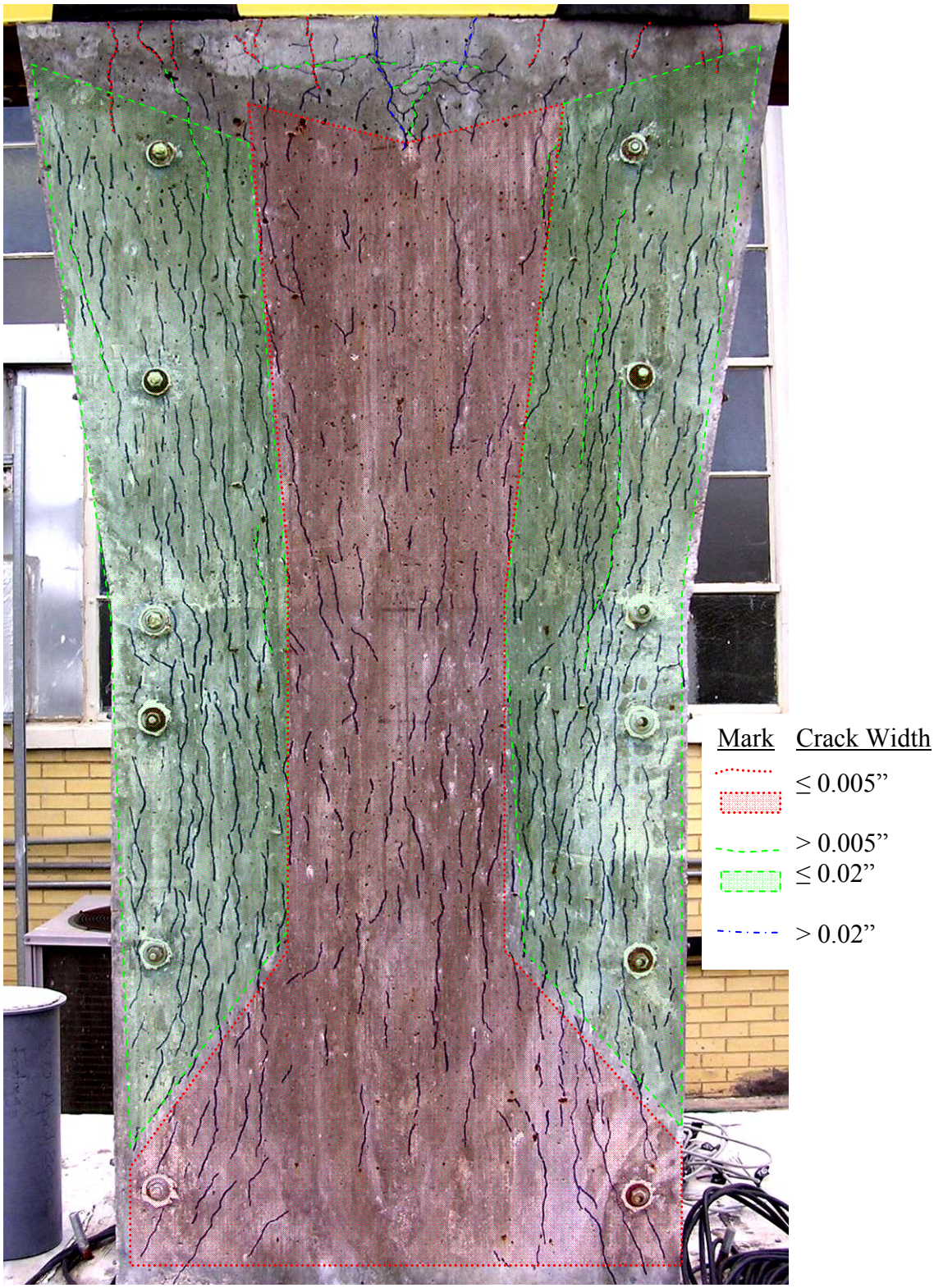

Figure 6.36: Column B West Face April 2008 (cracks marked in blue)

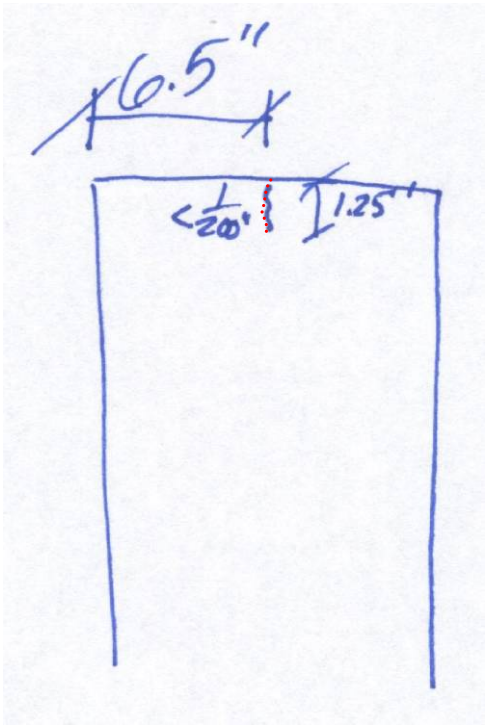

Figure 6.37: Column B South Side April 2007

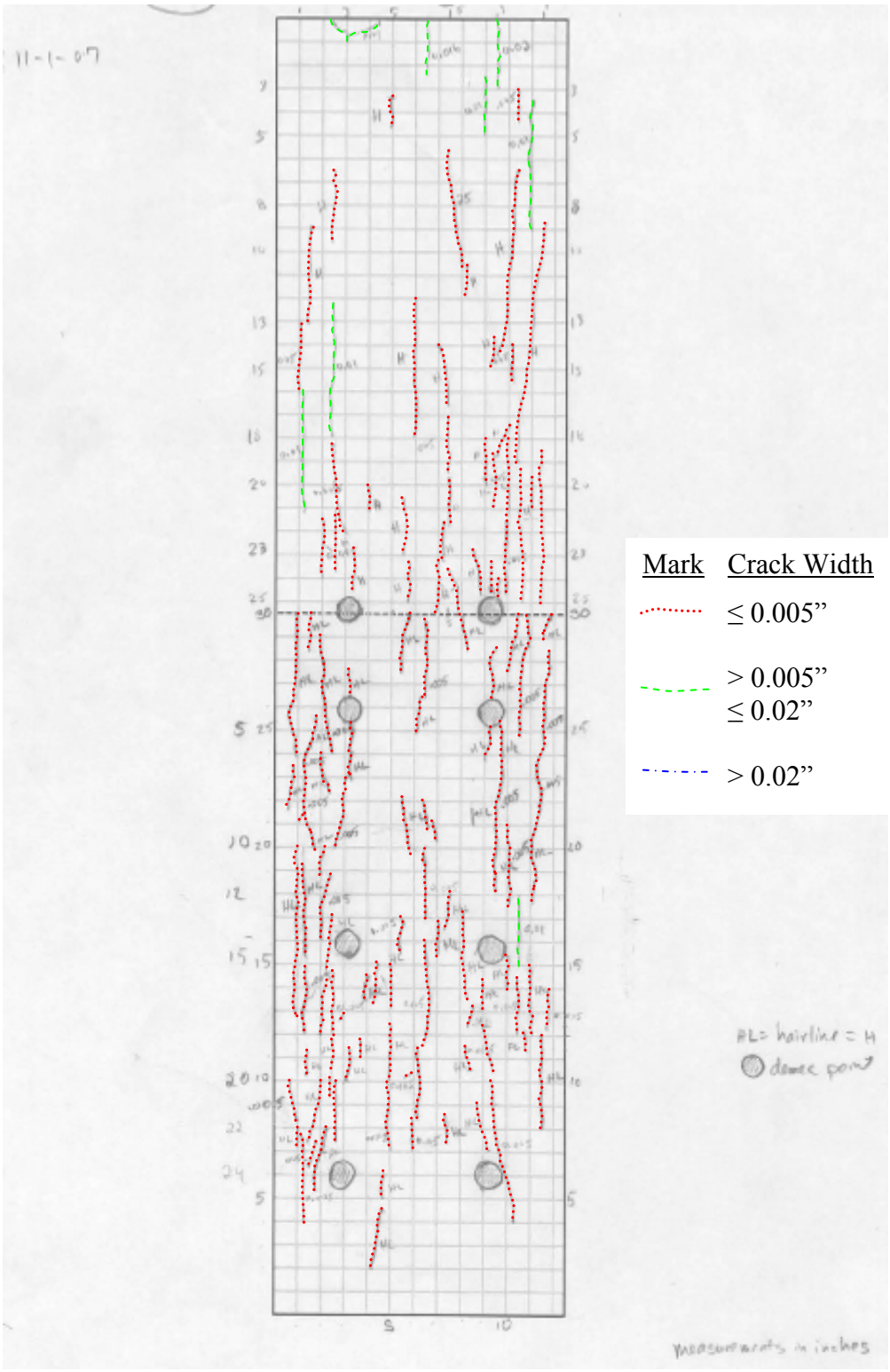

Figure 6.38: Column B South Side November 2007

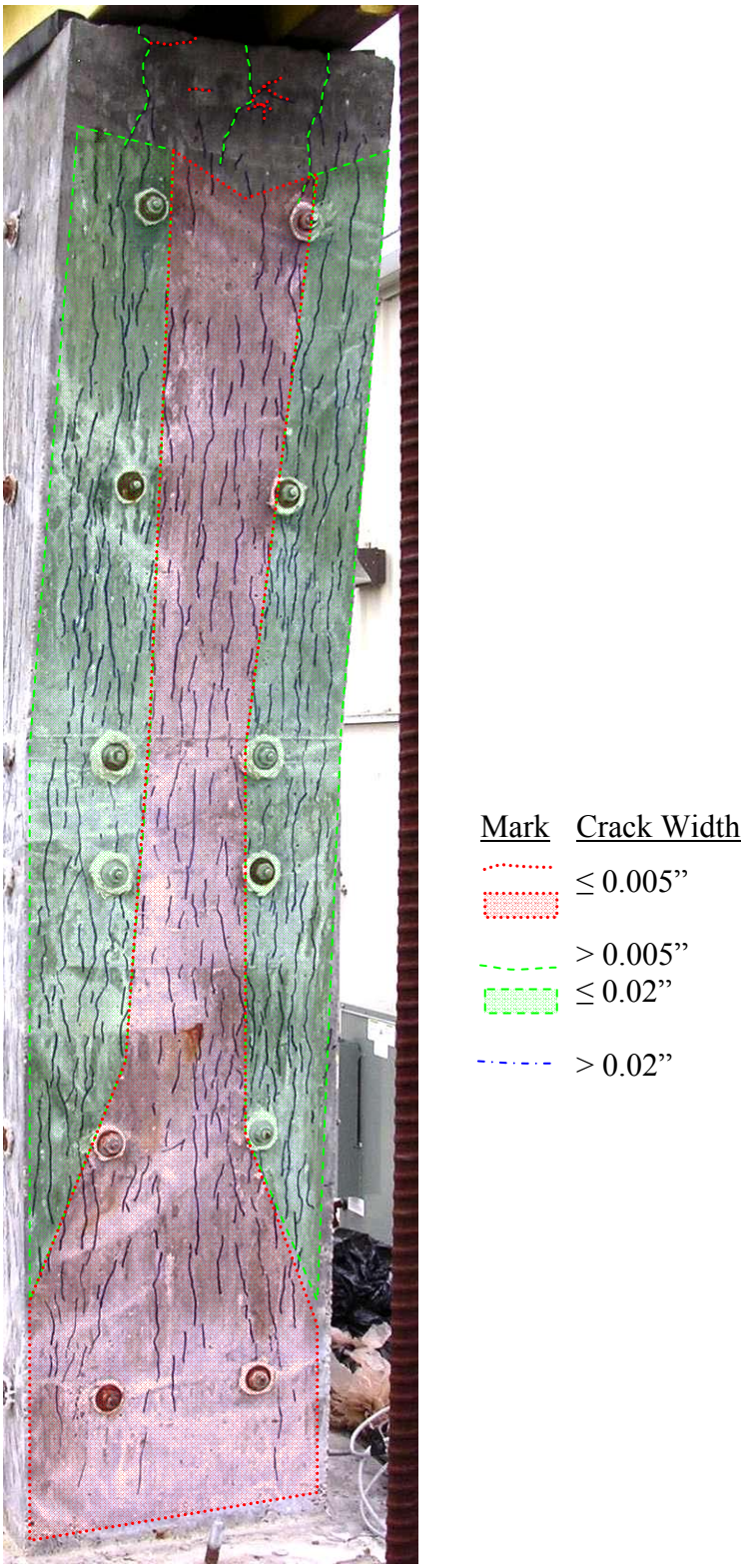

Figure 6.39: Column B South Face April 2008 (cracks marked in blue)

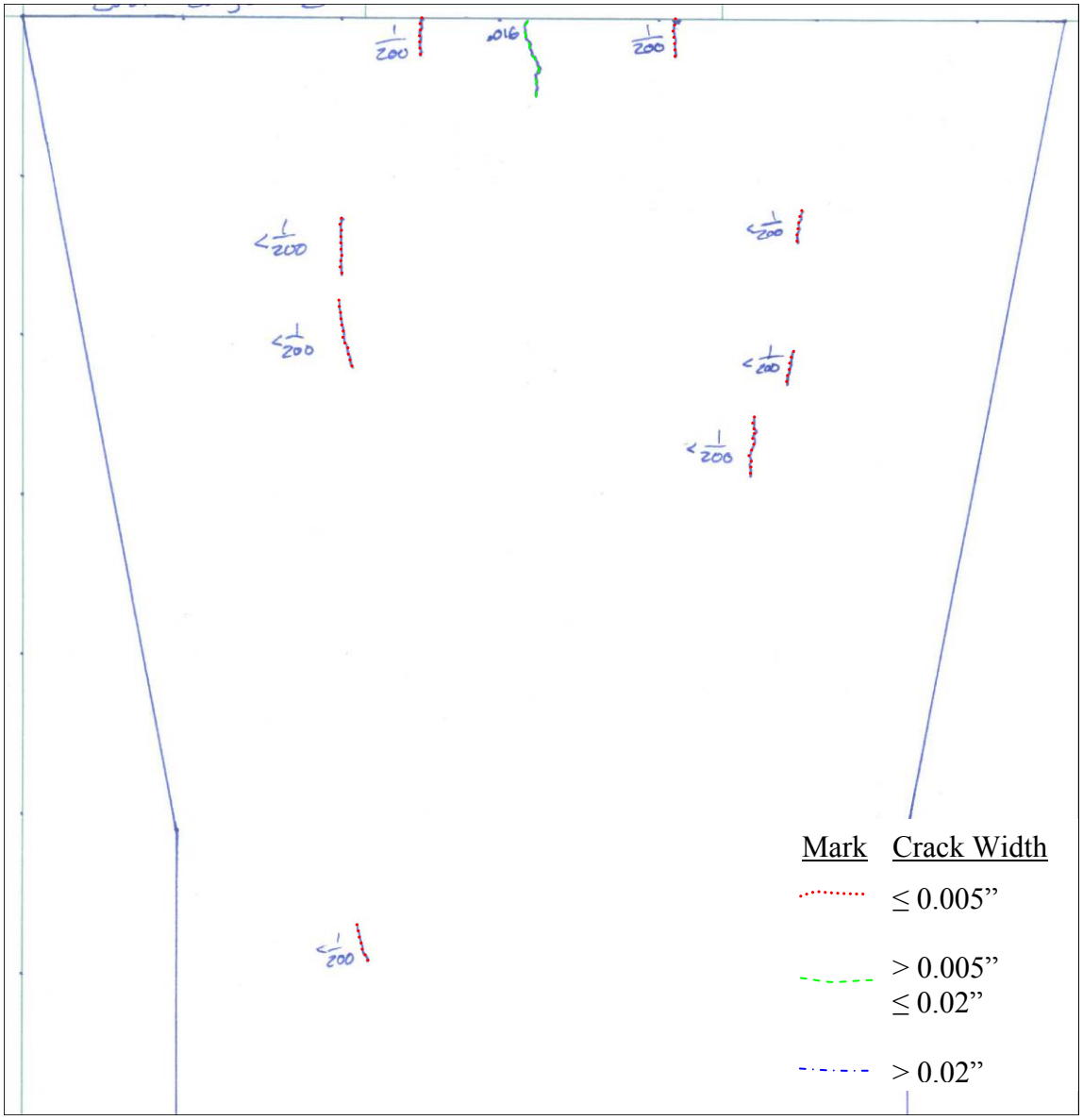

Figure 6.40: Column B East Side April 2007

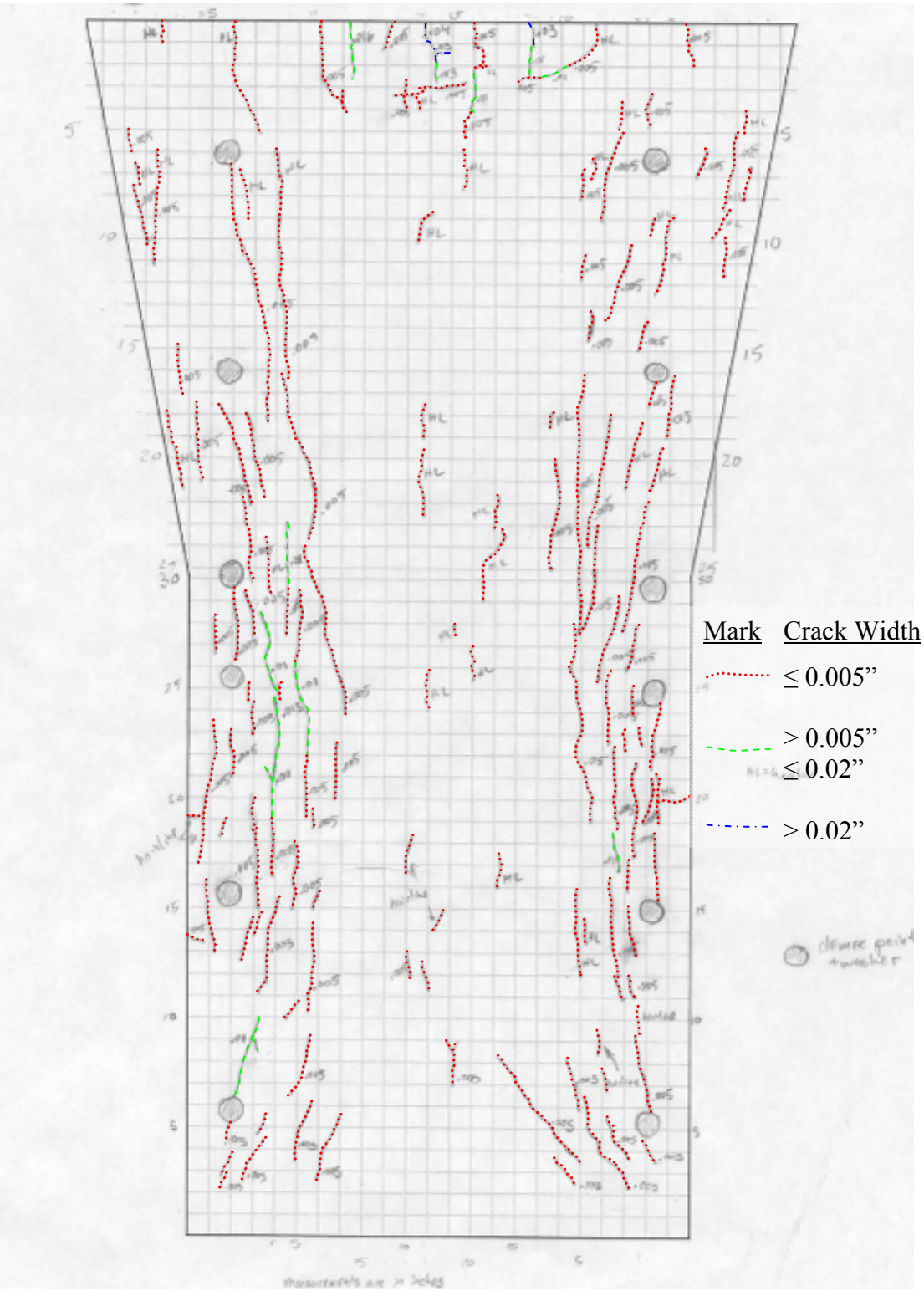

Figure 6.41: Column B East Side November 2007

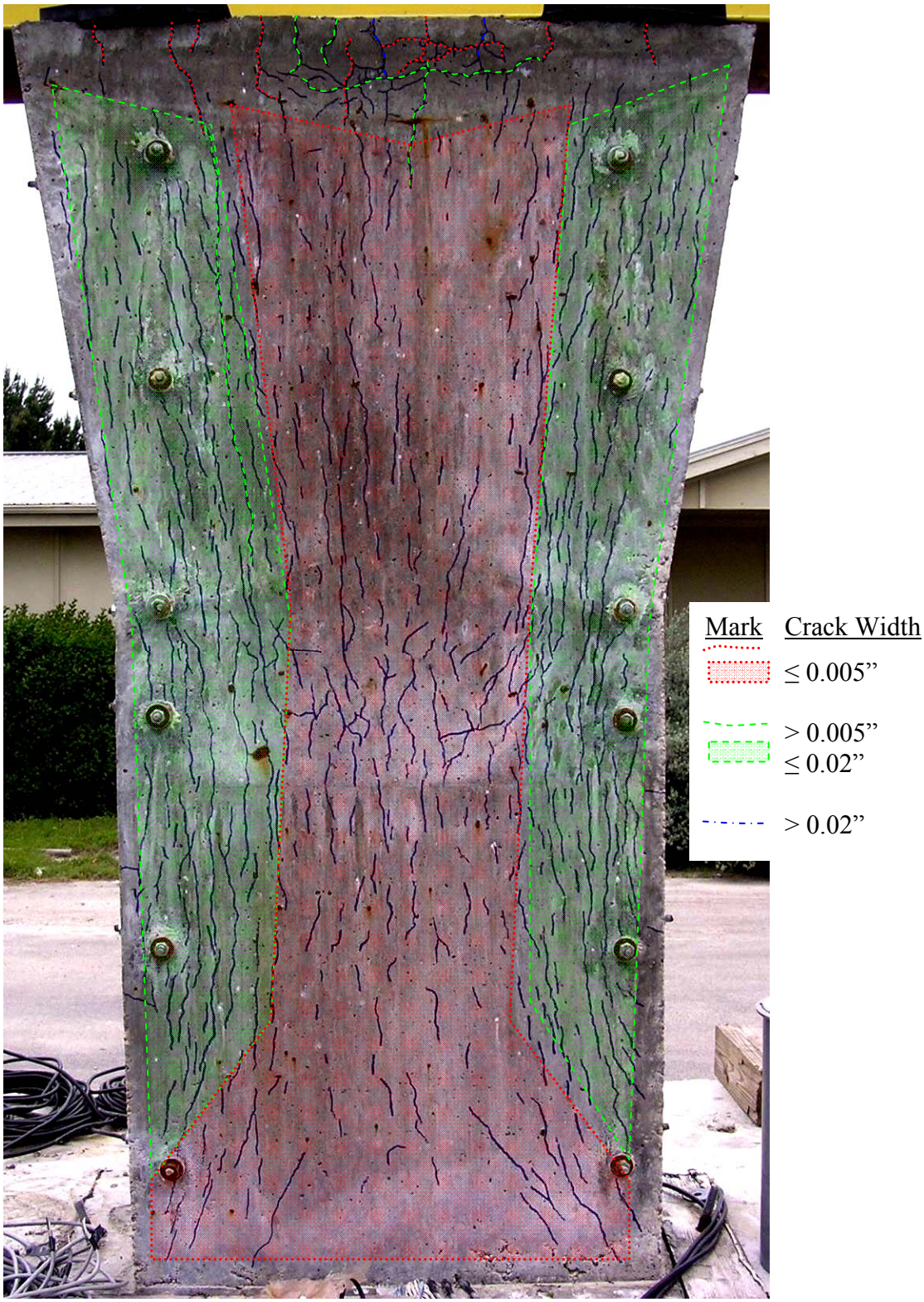

Figure 6.42: Column B East Face April 2008 (cracks marked in blue)

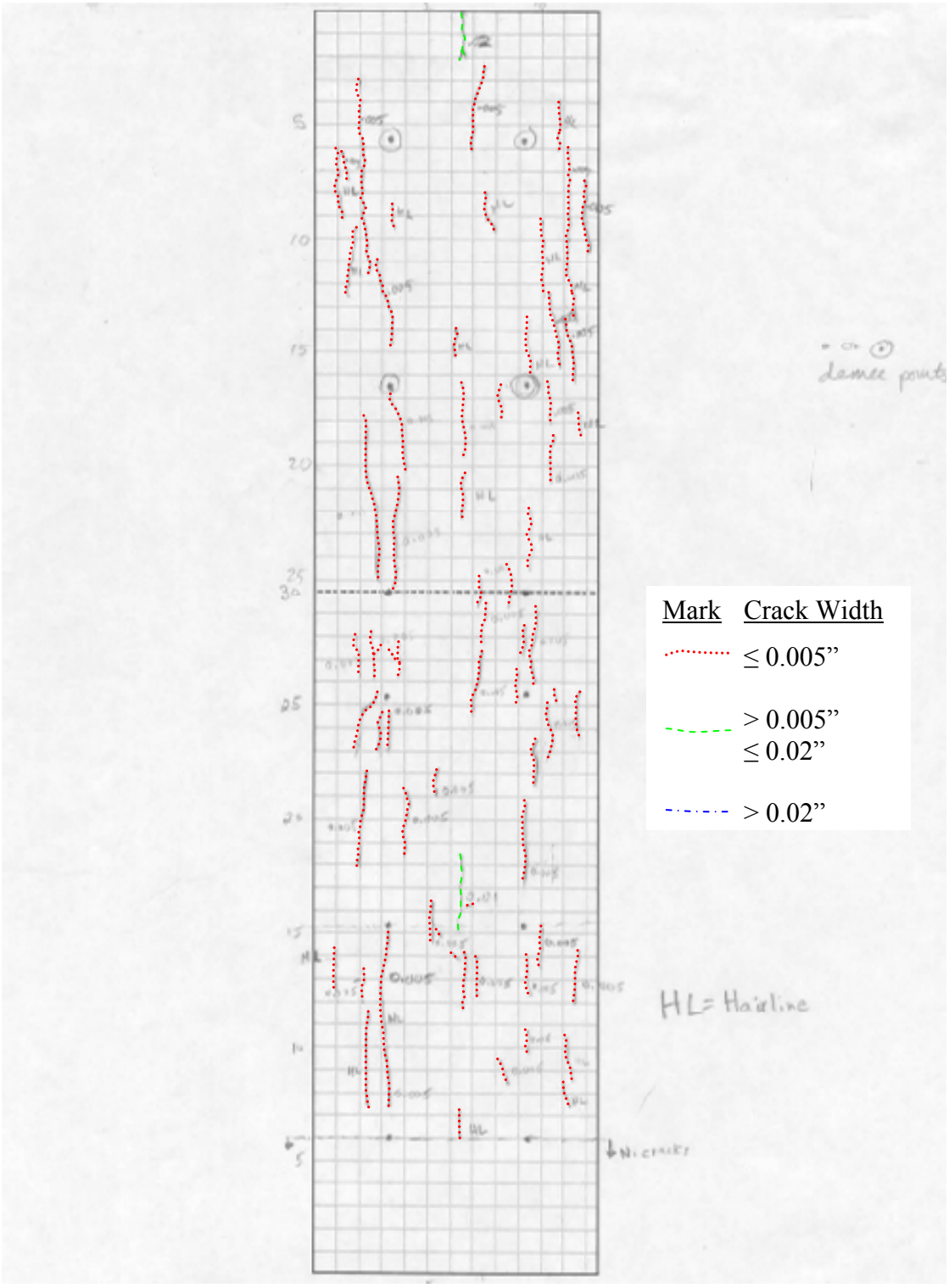

Figure 6.43: Column B North Side November 2007

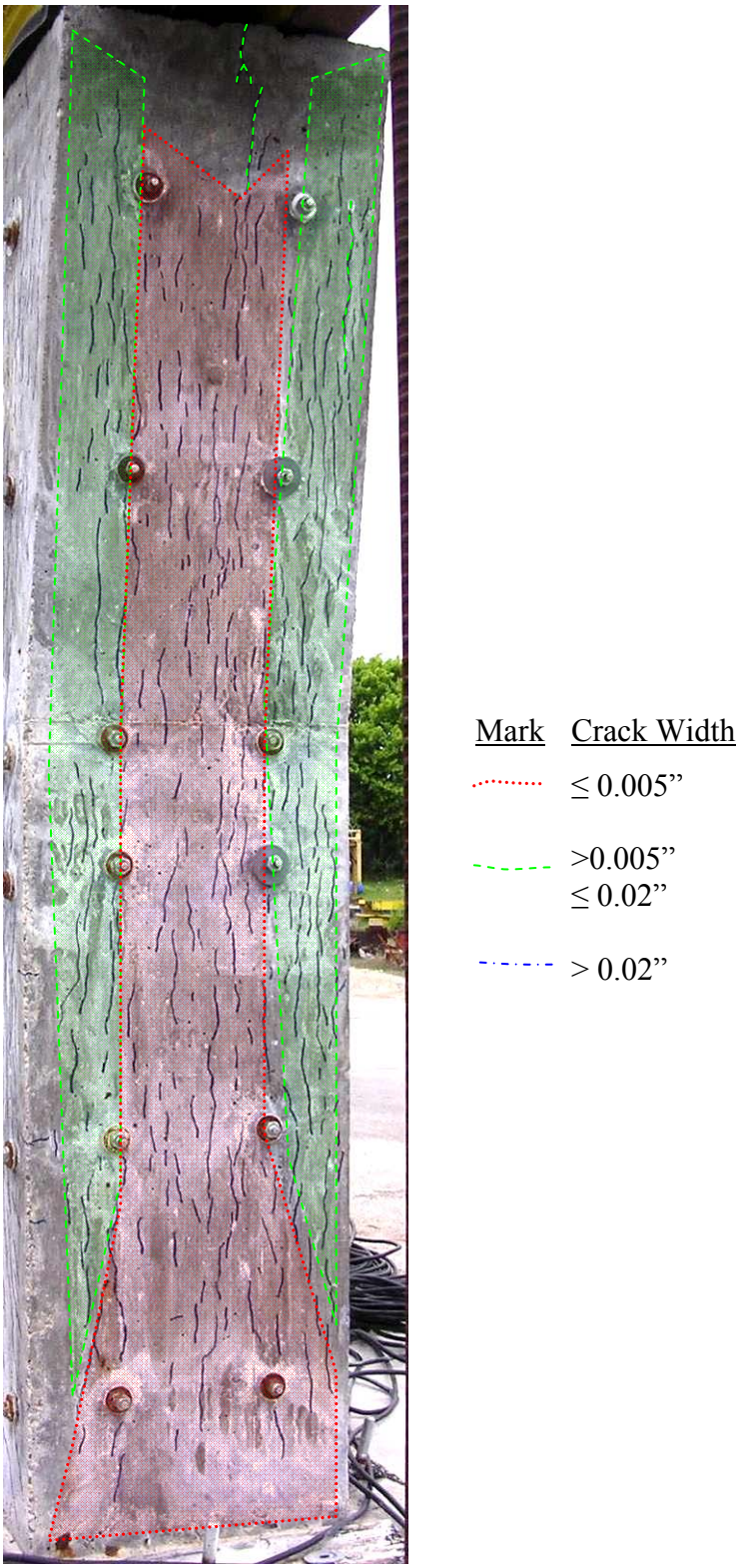

Figure 6.44: Column B North Face April 2008 (cracks marked in blue)

To illustrate the crack growth shown in the crack maps, Figure 6.45 and Figure 6.46 plot the average largest three crack widths at the time of each crack mapping. The three widest cracks on each of the columns' four sides were used to calculate the average. Thus, the average widest crack in the following plot is the average of the widest crack width from the four column sides, the second widest is the average of the second widest from each side and so on for the third widest. By averaging all sides of the column, this plot was intended to show the overall crack size and its trend with time. Figure 6.45 and Figure 6.46 follow the same growth trend with time as the external expansion measured from the demec points, which were shown earlier in Figure 6.12 through Figure 6.15. Figure 6.15, which shows Column B's average short side expansion as measured by the demec points, was included again here as Figure 6.47 for comparison to the average widest crack width plots. Both plot series showed early slow growth or expansion, then accelerating expansion, ending with a plateau of the growth or expansion.

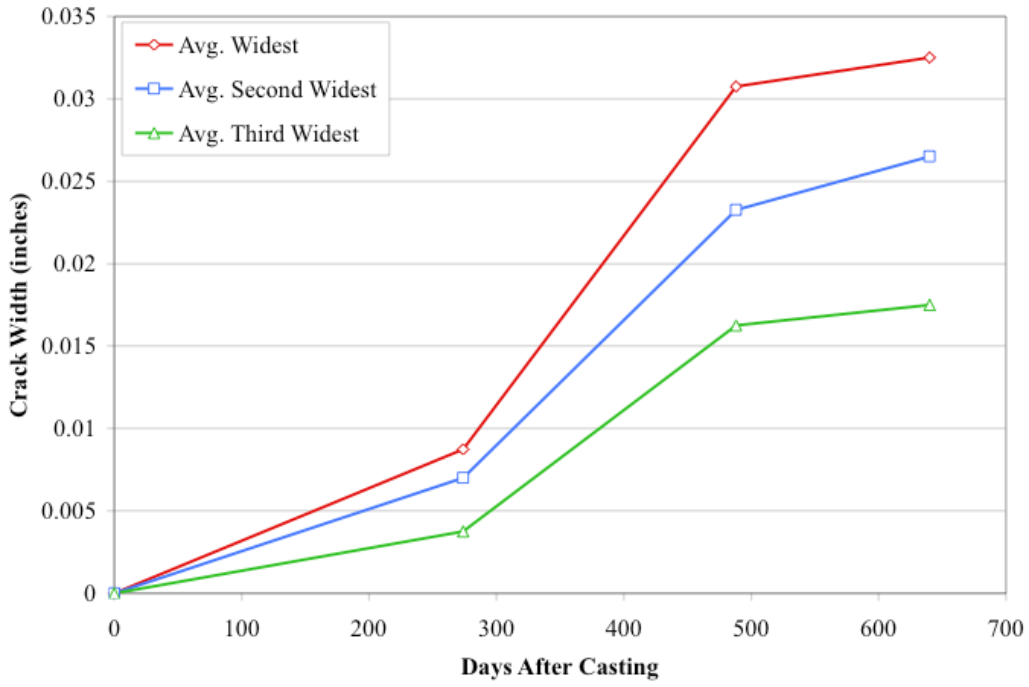

Figure 6.45: Column A Three Widest Average Crack Sizes

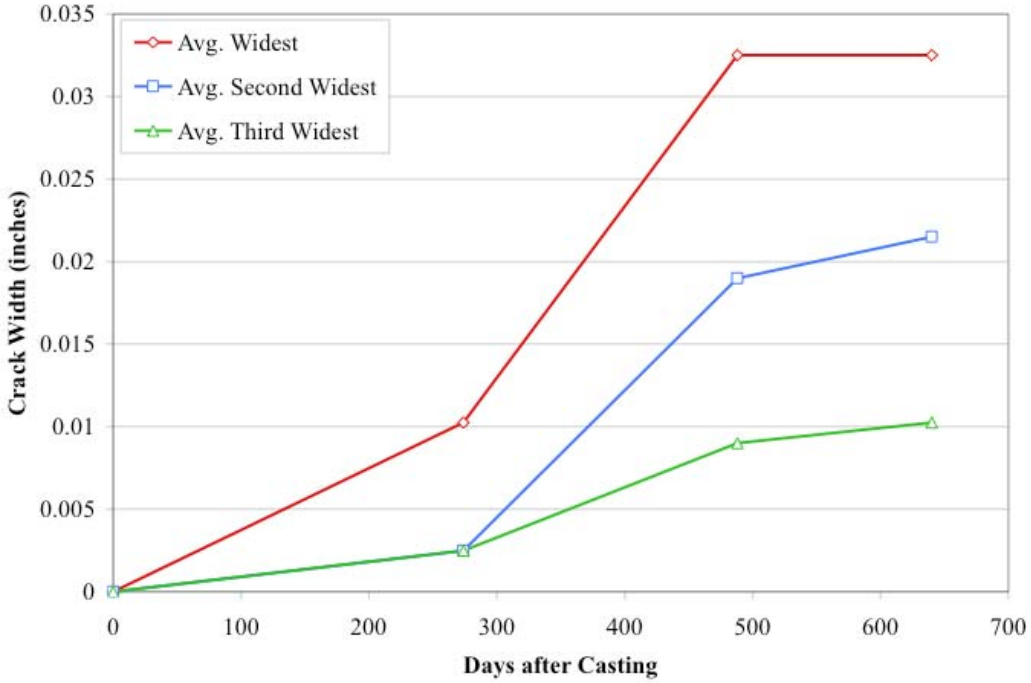

Figure 6.46: Column B Three Widest Average Crack Sizes

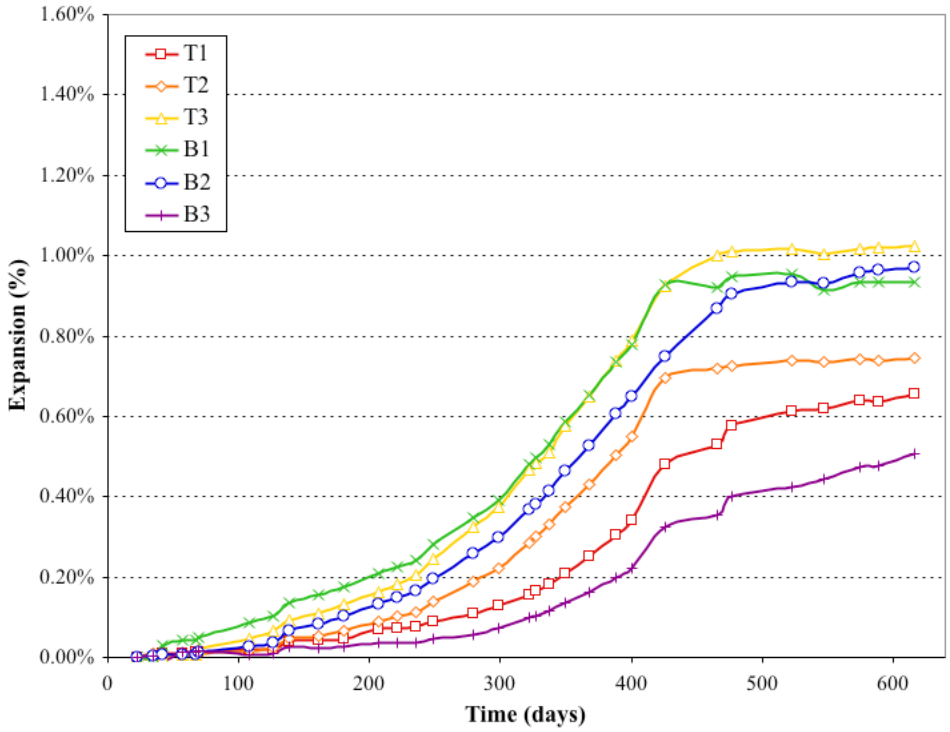

Figure 6.47: Average Short Side Expansion of Column B (Re-print of Figure 6.15)

Crack width and concrete expansion were logically tied together, as concrete fractures when the internal expansion pressure overcomes the concrete's tensile strength. The cracks, therefore, accommodate the expansion of the concrete. The leveling off of expansion rate, which was previously discussed in the demec expansion section, was here shown as a slowing of the crack width growth. Recall that the slowing expansion was believed to be tied to the removal of the felt backed plastic to map cracks. Thus, the crack rate further confirmed the importance of maintaining the moisture retention system developed by Ford Burgher for this project in order to maintain the rapid ASR/DEF expansion seen prior to the plastic removal. The reduction in rate of the crack width growth was logically tied to the reduction in the rate of expansion of the concrete.

6.2.5.3 Summary

The main goal from applying the post-tensioned axial load to the columns during exposure was to influence the orientation of the ASR/DEF column. In order to most effectively model the bridge columns in the San Antonio Y, with their predominantly vertical cracks, a vertical crack orientation was desired. As can be seen from the crack maps, that goal was achieved. From the average crack width graphs, it appeared that these columns best correlated with Kapitan's 0.02 inch level of initial cracking. By the end of exposure, widespread cracks of 0.01 inches wide were found along the main load paths from bearing pad to base. As well, the median value from the average largest crack widths was near 0.02 inches. Recall that Kapitan's initial crack widths were based on the largest observed crack width, not the most common crack width. Thus, the crack widths observed in the ASR/DEF columns indicate that Kapitan's initial crack width of 0.02 inches would be the best correlation for these columns.

6.2.6 Summary of Monitoring

Through the monitoring program during exposure several observations can be made. One item that was confirmed through the monitoring program was that the axial post-tensioning load was maintained throughout the exposure period. Additionally, it was shown that this post-tensioned load served as the main restraining force against

ASR/DEF expansion in the columns. As such, cracking from expansion in the columns was mostly vertical. This result was desired to create a similar cracking pattern to that observed on the San Antonio Y. Further, the columns experienced considerable expansion during the exposure period. As measured externally with demec points, this expansion reached up to 1.5%. From the plateau of the expansion rate, the importance of maintaining the integrity of the moisture retention system was shown. As well, the scaled reinforcing cage proved to be unable to uniformly prevent and restrain ASR/DEF expansion through confinement. By comparison of the crack sizes, it was determined that Kapitan's 0.02 inches of initial cracking best correlated with the ASR/DEF scaled column specimens.

6.3 LOADING TO FAILURE

6.3.1 Introduction

The purpose of testing columns affected by ASR/DEF was to determine the influence of premature deterioration on this typical column's capacity. The measured capacity was then compared to the results of Kapitan's column series. Further, the load-deflection and concrete strain behavior of the ASR/DEF columns were compared to Kapitan's results to determine a correlation between the average crack size observed on the ASR/DEF columns and Kapitan's initial crack widths.

6.3.2 ASR/DEF Column A

The post-tensioned exposure load for Column A was removed on April 17, 2008 and the specimen was tested to failure on April 30, 2008. Figure 6.48 shows the column prior to testing. The results of strain gauge, strain meter, and linear potentiometer readings are given in the subsequent sections.

Figure 6.48: Column A Prior to Testing

6.3.2.1 Load Capacity

Based upon the model used by Kapitan[3], the combined axial and flexural capacity and the bearing capacity of Column A (assuming an undamaged section) were calculated for the concrete strength measured on the day of testing. These values, along with the maximum load measured during testing, are listed in Table 6.3. The twenty percent reduction in bearing capacity versus predicted combined axial and flexural capacity shown here was the same difference observed by Kapitan in both his control column and the column with a initial crack width of 0.02 inches[3].

Table 6.3: Predicted and Measured Capacities for Column A[3,110]

	Predicted Combined Axial-Flexural Capacity (undamaged)	Predicted Bearing Capacity (undamaged)	Measured Maximum Load
Maximum Load (kips)	605	479	491
Compressive Strength (psi)	6000	6000	6000

6.3.2.2 Deflection Measurements

Deflections were measured by linear potentiometers at the top, middle, and bottom of two faces on the column, as illustrated in Figure 6.49. The monitored faces were chosen based on the load eccentricity so that the selected faces were closest to the loading point. Figure 6.50 presents the deflections measured perpendicular to the short face (along the x-axis). Figure 6.51 shows deflections measured perpendicular to the long face of the column (along the y-axis). Negative deflections indicated the column was moving towards the potentiometers.

As can be seen from comparing Figure 6.50 and Figure 6.51, there was significantly more deflection along the x-axis than along the y-axis. This difference in deflection was due to the eccentricities of the applied load. The load was applied with a 5.9 inch eccentricity in the x-direction but only a 1.5 inch eccentricity in the y-direction. These load deflection curves remained linear until the corner began crushing/spalling at approximately 400 kips. At that point, the top deflection measurement location along the x-axis (in Figure 6.50) showed a large gain in displacement as the concrete beneath the potentiometer was spalling off the column. As the most heavily loaded corner crushed, the column moved back from its maximum y-axis deflection, as can be seen especially well in the top deflection monitoring location in Figure 6.51. In both plots, the fixity of the column base was shown in the difference of displacement along the height of the column. The nearer the fixed base the less deflection measured. Likewise, the farther the monitoring point

was from the base the more that it moved. The potentiometer at mid-height always measured the median amount of displacement.

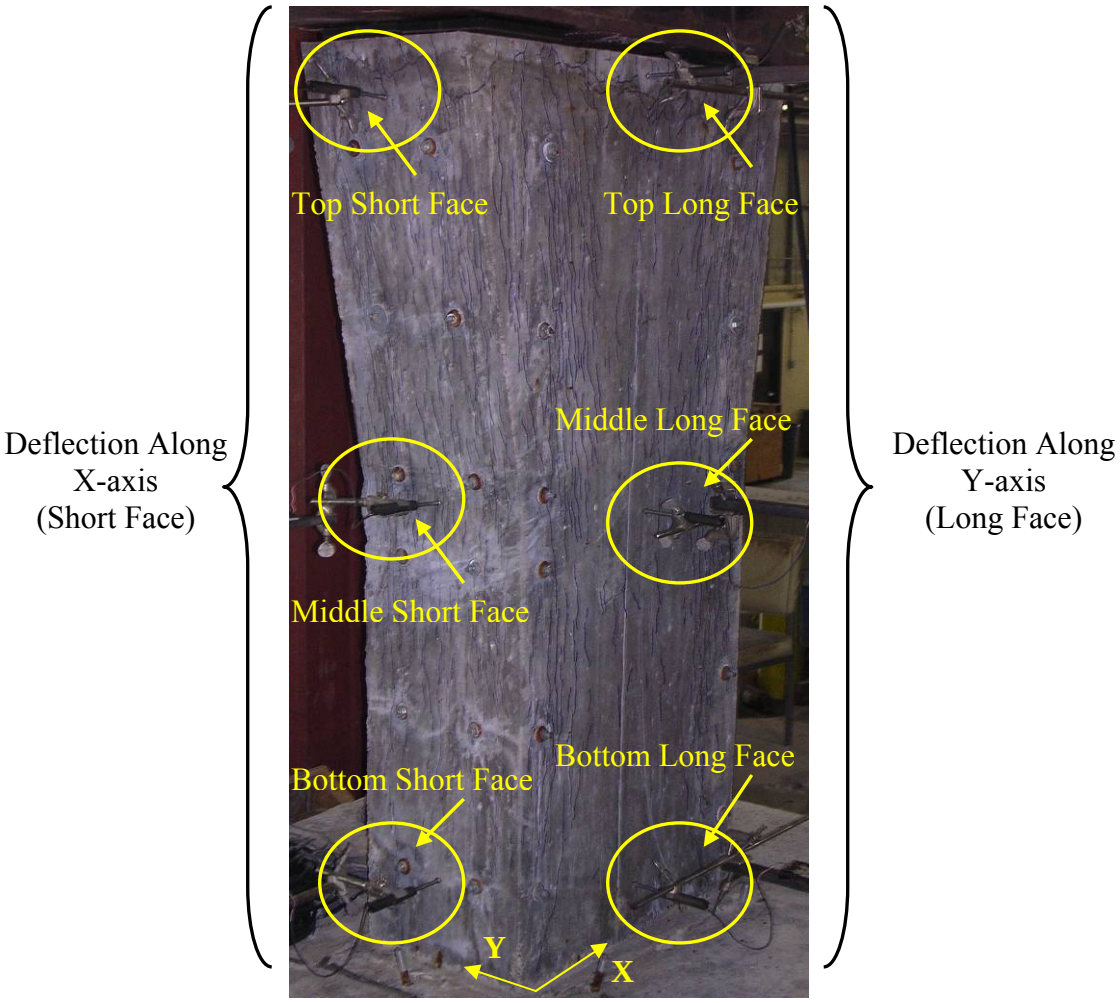

Figure 6.49: Linear Potentiometer Locations and Labeling

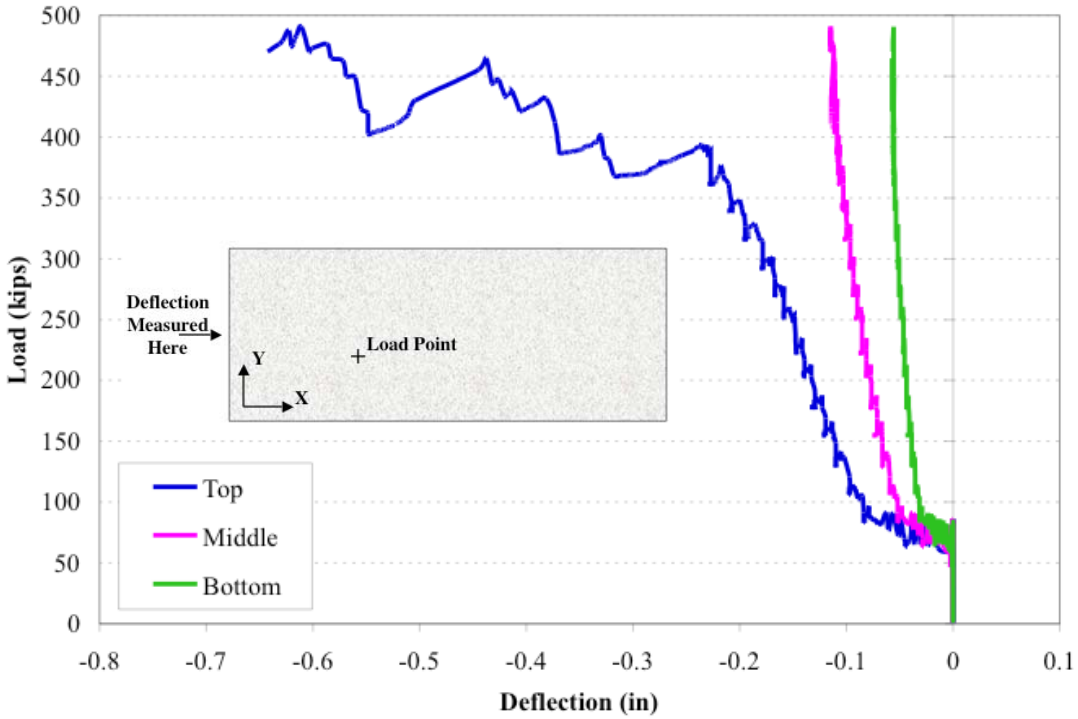

Figure 6.50: Column A Deflections along the X-axis (on Short Face)

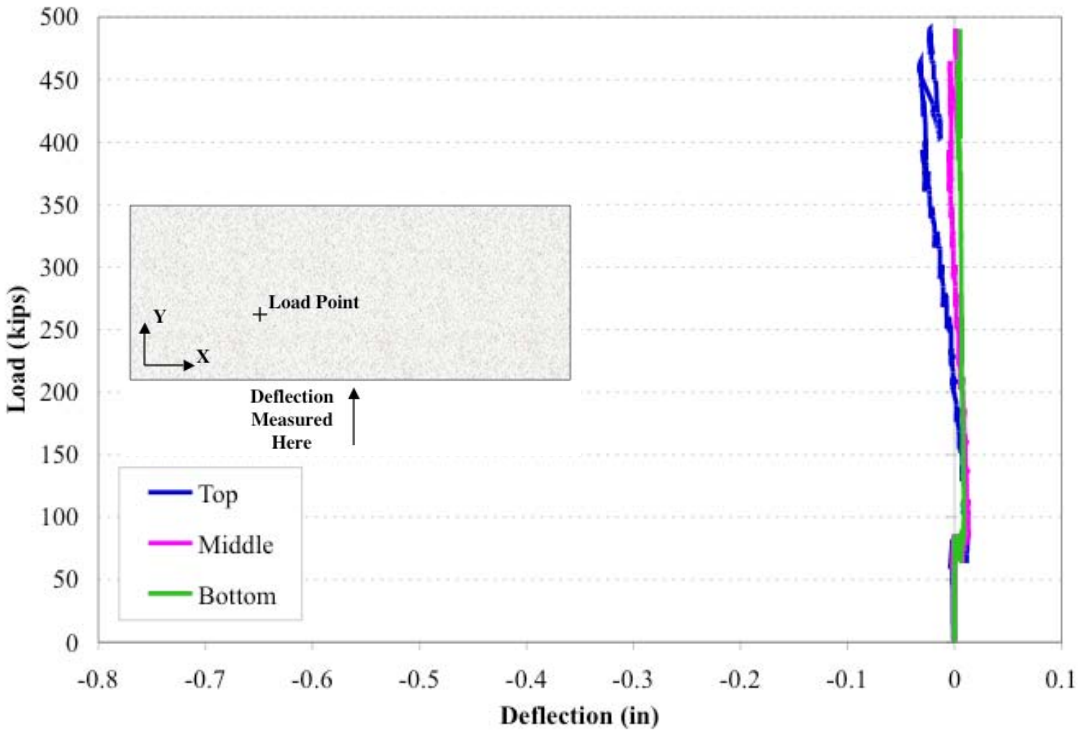

Figure 6.51: Column A Deflections along the Y-axis (on Long Face)

6.3.2.3 Strain Measurements

Strain in both the reinforcing steel and interior concrete were measured during loading. Figure 6.52 and Figure 6.53 present the upper and lower layers of strain meter readings, respectively. The strain meters recorded the core concrete strains. Figure 6.54 is the diagram of the upper layer strain meter locations from Chapter 3 with the bearing pad locations superimposed for reference. Figure 6.56 and Figure 6.57 present the upper and lower layers of reinforcing steel strain gauge readings, respectively. Figure 6.58 is the diagram of the upper layer strain gauge locations from Chapter 3 with the bearing pad locations superimposed for reference. Negative strain values indicated compression. Not all gauges that were applied to the reinforcing cage were still working on the day of testing. For this column, only one transverse gauge was still functioning, Lower T3, and three longitudinal gauges had failed: Upper L2, Lower L1, and Lower L6. Figure 6.55 presents the gauge locations within the column, with the gauges working on the testing day highlighted for reference.

The upper and bottom layer of strain meters (Figure 6.52 and Figure 6.53) both showed greatest compressive strain with increasing load in meter M1, which was closest to the load point. In the upper layer (Figure 6.52), which was about five inches below the top surface, the greatest compressive strain after meter M1 were recorded in meters M2 and M7. These meters were below bearing pads, as shown in Figure 6.54, and therefore saw much greater strains than the meters nearer the load point but not under a bearing pad. In the lower layer (Figure 6.53), this bearing pad effect had dissipated. Instead, the lower level meters with the greatest strain are M1, M2, and M3. These meters were nearest the load point, as illustrated in Figure 6.53. Meter M8, which was farthest from the load point, went into tension at the lower layers of instrumentation. As the column was in bending, leaning towards the heavily loaded corner, the compression at that corner was balanced with the tension at the far corner. The strain behavior recorded by the strain meters shows linear strain increasing with load until a new crack had significantly propagated at approximately 375 kips, whereupon the load paths redistributed in the

column to accommodate the cracking. After new cracks were observed, the column no longer had the same stiffness as when testing began. The strain curves shift to reflect the change in stiffness and load sharing that resulted from the cracking section.

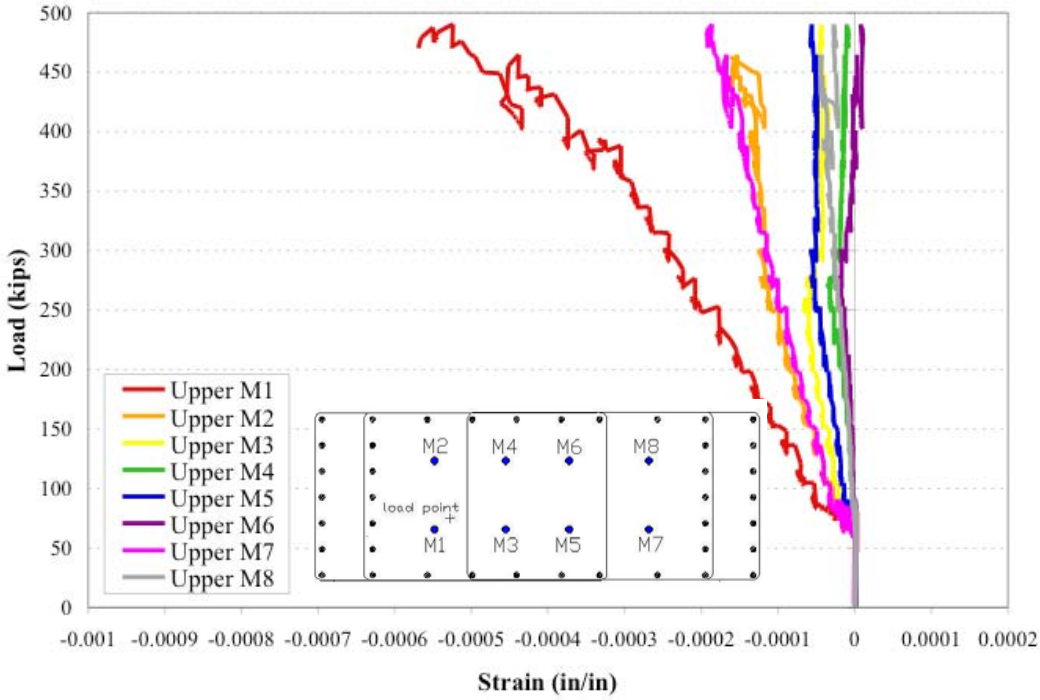

Figure 6.52: Column A Upper Layer Strain Meter Readings

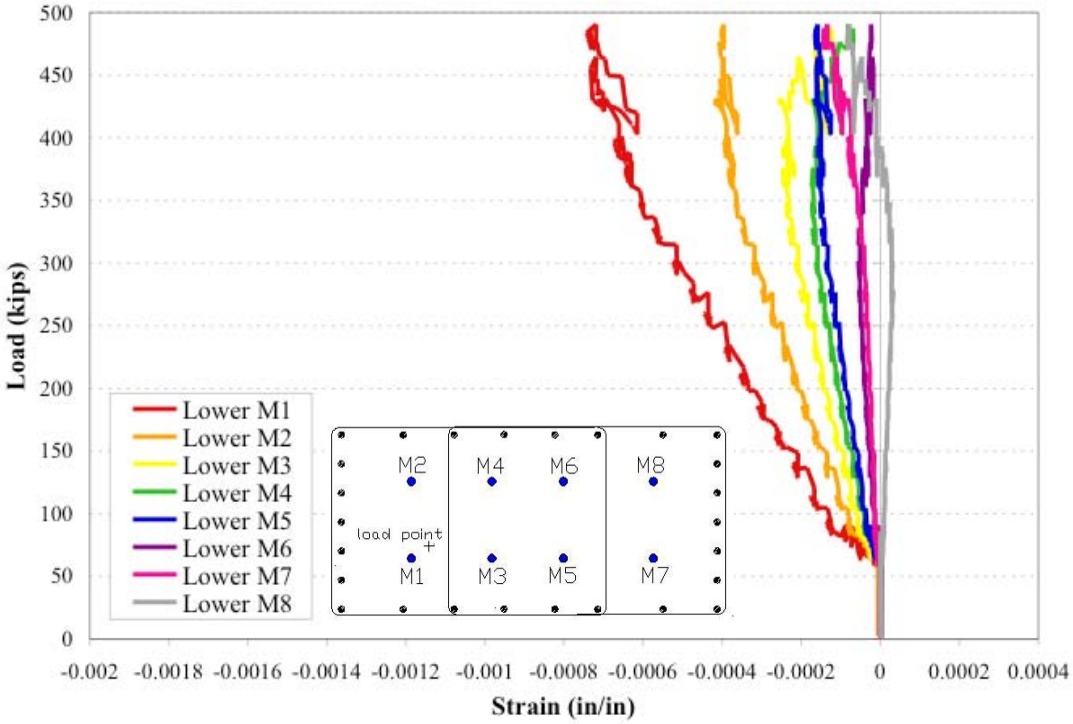

Figure 6.53: Column A Lower Layer Strain Meter Readings

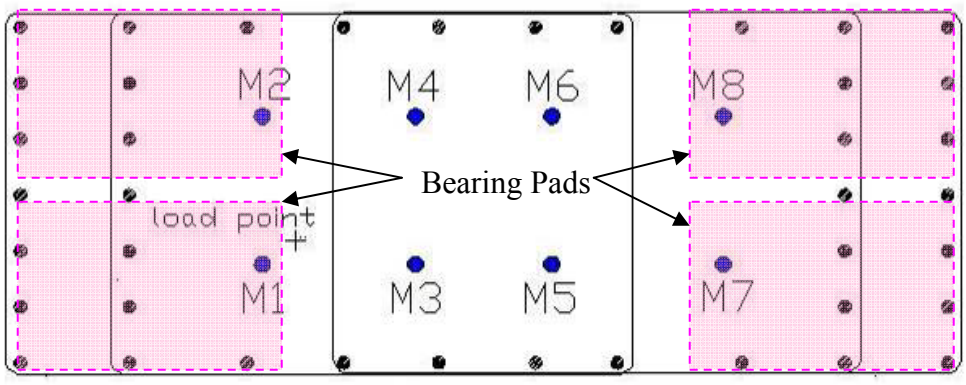

Figure 6.54: Upper Layer Strain Meter Locations

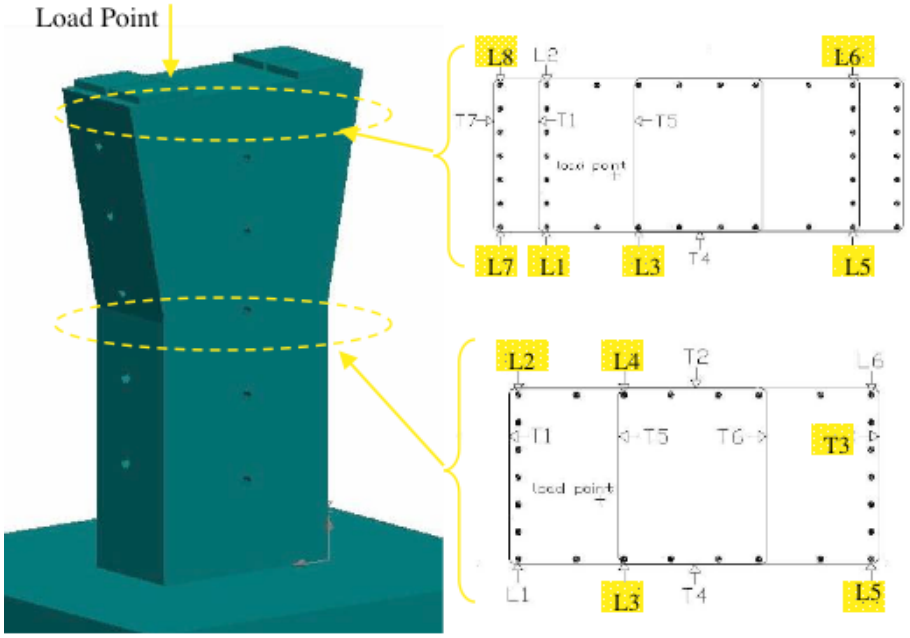

Figure 6.55: Column A Gauges Working on Testing Day

Figure 6.56 presents the strain readings during loading for the upper layer of instrumentation. From this figure, gauge L1 stood out has having received the most strain during loading. Gauge L7 had a very similar strain rate at the start of loading, but eventually fell behind gauge L1. As shown on the inset of the strain gauges these two gauges were close together and at the most heavily loaded corner of the column. As gauge L7 was at the corner, it was logical for the longitudinal bar with this gauge to receive the most compressive strain during loading. This bar, however, was inclined rather than the vertical orientation of the bar with gauge L1. Thus, gauge L7 recorded strains along the incline. The compression along the incline was similar to but less than the compressive strains recorded by gauge T1. The gauges registering the most compressive strain after gauges L1 and L7 were gauges L8 and L5. These gauges registered nearly identical amounts of strain even though they were not the same distance form the load point. The likely reason for this behavior was that the bars with these gauges were underneath bearing pads, as shown in Figure 6.58. At this upper layer of instrumentation, the load had not yet spread out over the full cross section of the column and thus there were locally higher strain levels due to load application locations (bearing

pad locations). In the lower layer of instrumentation, shown in Figure 6.57, this bearing pad effect had dissipated. In this layer, the gauges closest to the most heavily loaded corner showed the largest compressive strains. For instance, gauges L3 and L2 exhibited the most strain at this level. Unfortunately, on the day of testing neither lower level gauge L1 or L6 were working. Thus, there was no strain information recorded at these extreme corners. Gauge L1 should have seen the greatest compressive strain while gauge L6 should have seen the least compressive (and possible tensile) strain. From the information available, however, it is apparent that the column's bending behavior, as measured at the reinforcing cage and in the core via strain meters, was linear until the corner began spalling concrete. At this point significant cracks developed that forced the load path to reroute and the strain curves became non-linear.

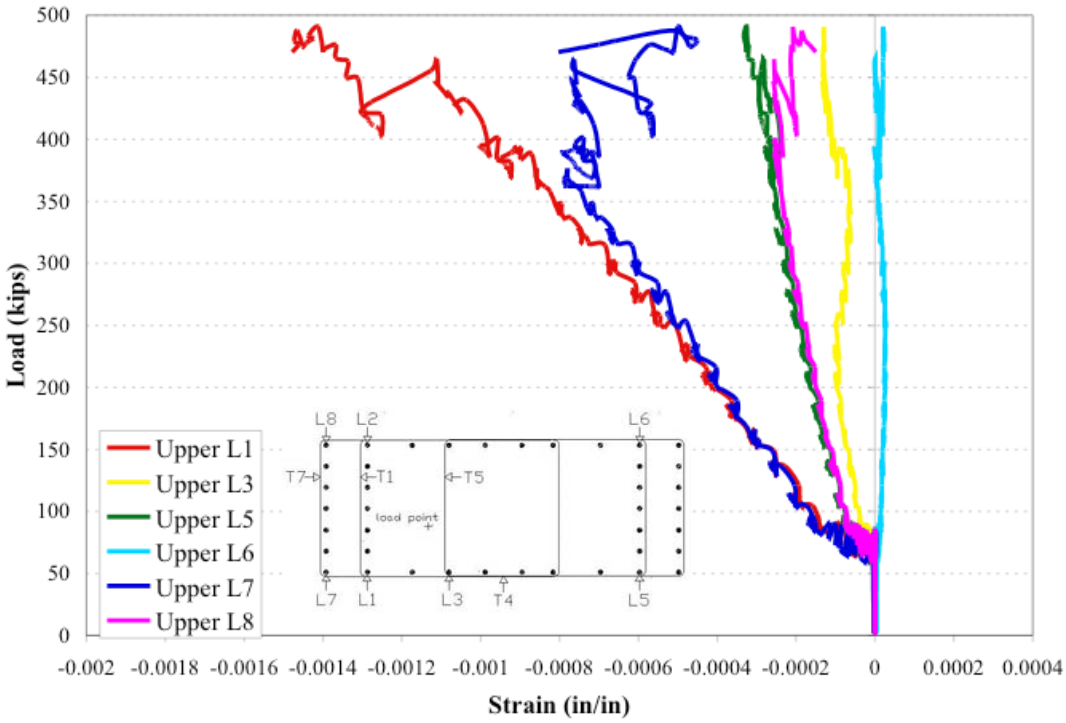

Figure 6.56: Column A Readings from Upper Layer of Strain Gauges

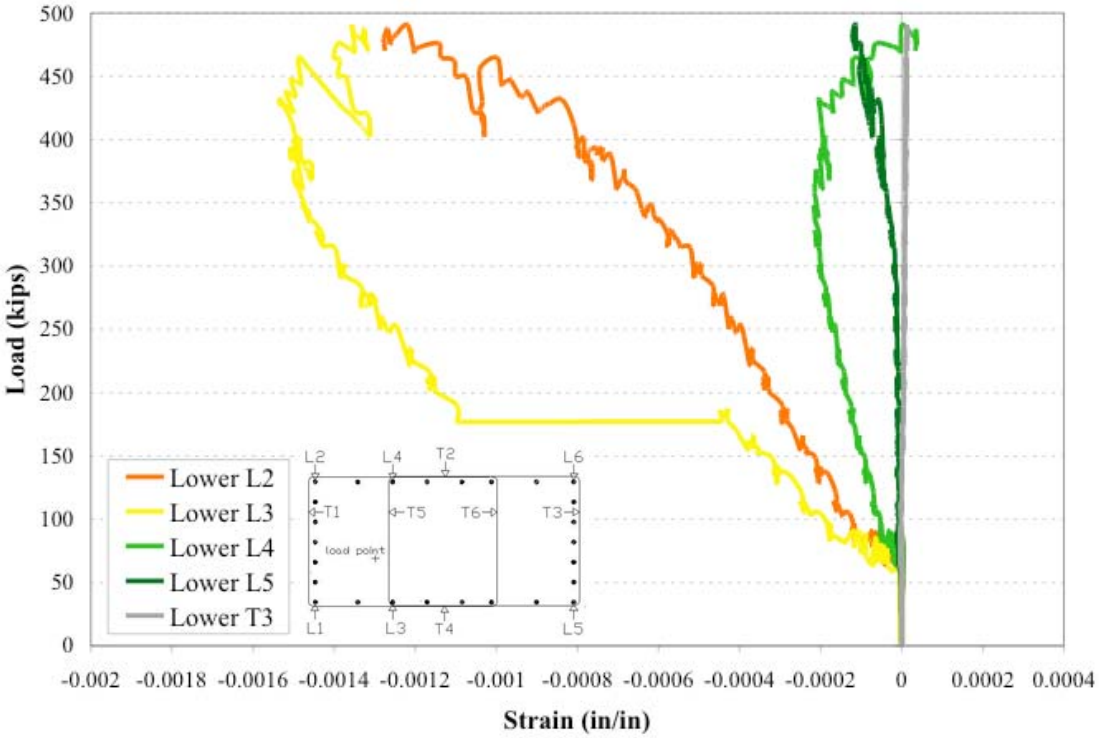

Figure 6.57: Column A Readings from Lower Layer of Strain Gauges

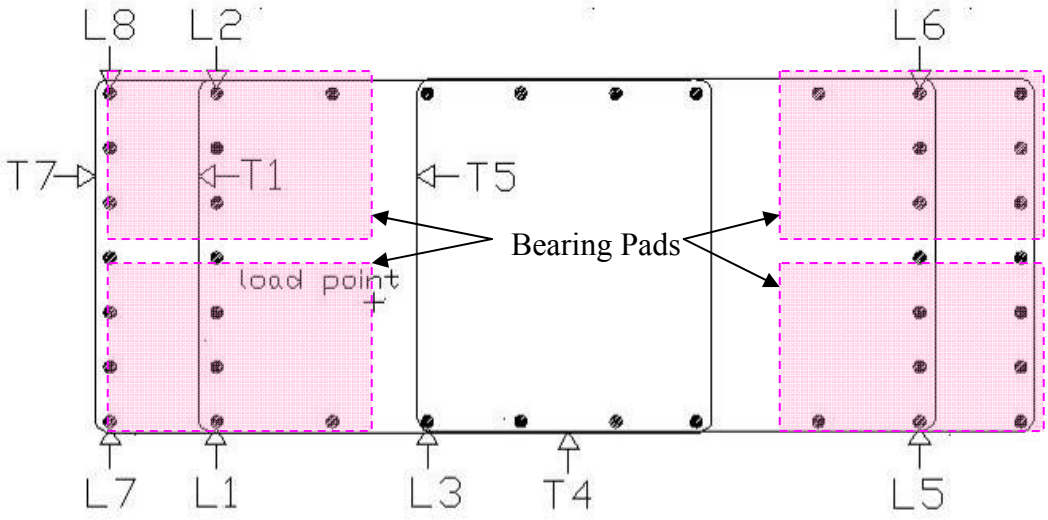

Figure 6.58: Upper Layer Strain Gauge Locations

6.3.2.4 Failure

The initial cracking caused by loading was observed at 150 kips. This cracking, which is shown in Figure 6.59, developed near the center of the column's long face that was nearest the load point. Cracks caused by ASR/DEF were marked in blue ink and cracks caused by load testing were marked in green ink. The center of the load point was marked with a black arrow. As shown in Figure 6.60, with the loading increasing through 375 kips a main crack developed underneath the load point. By 425 kips, the most heavily loaded corner spalled the concrete cover, as shown in Figure 6.61. Additional spalling under the most heavily loaded bearing pad, as shown in Figure 6.62, occurred at 455 kips. The column reached a maximum load of 491 kips when the most heavily loaded end began crushing beneath additional load, as shown in Figure 6.63.

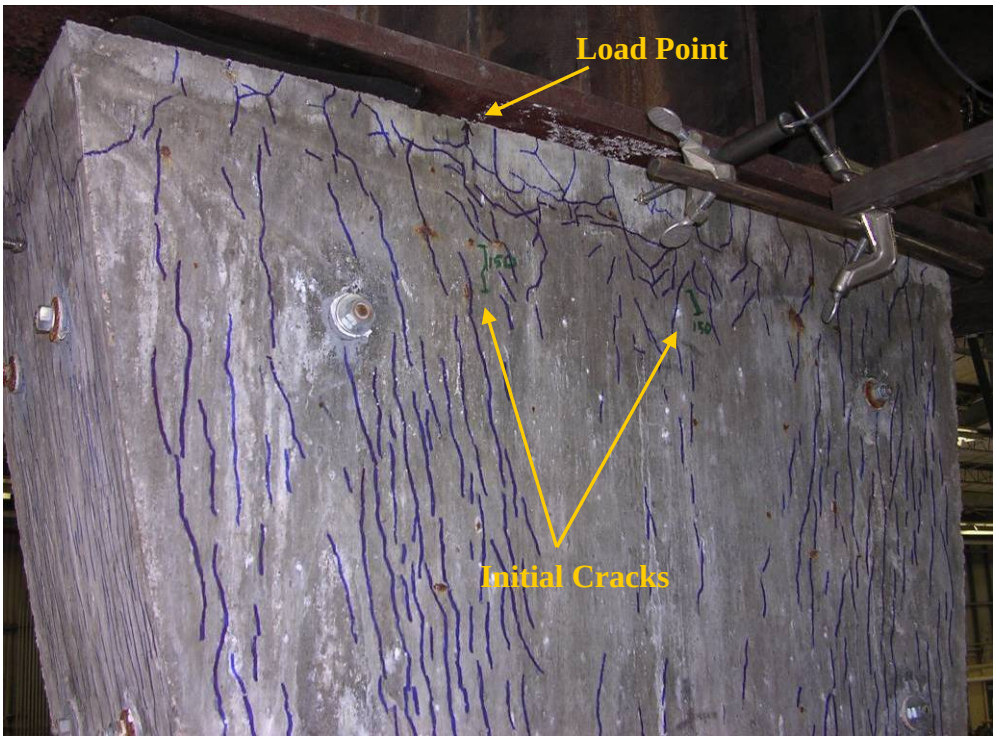

Figure 6.59: Inital Cracking of Column A[111]

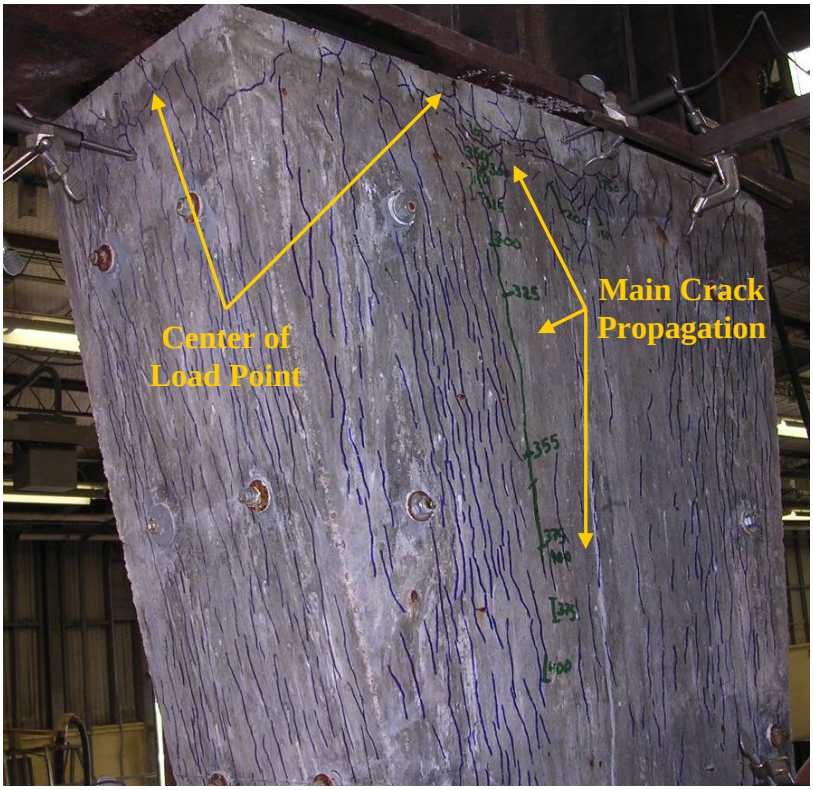

Figure 6.60: Main Crack Propagation in Column A[111]

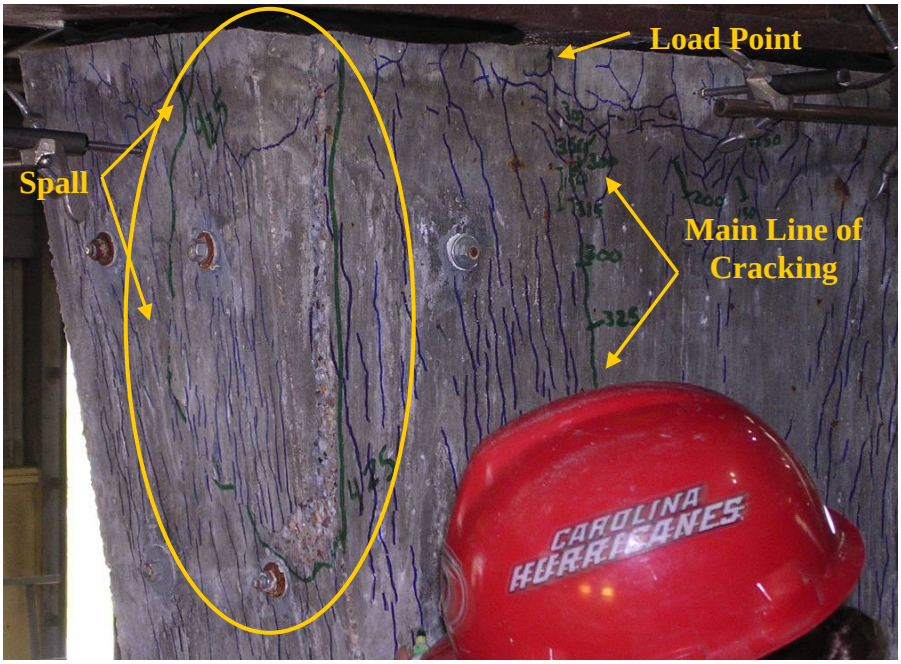

Figure 6.61: Corner Spall on Column A[111]

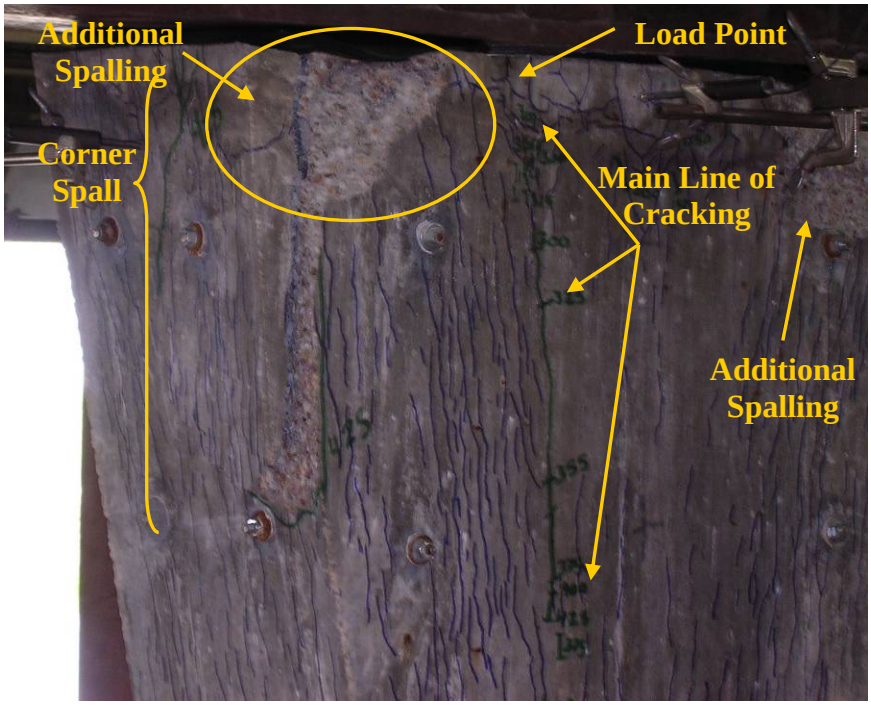

Figure 6.62: Additional Spalling on Column A[111]

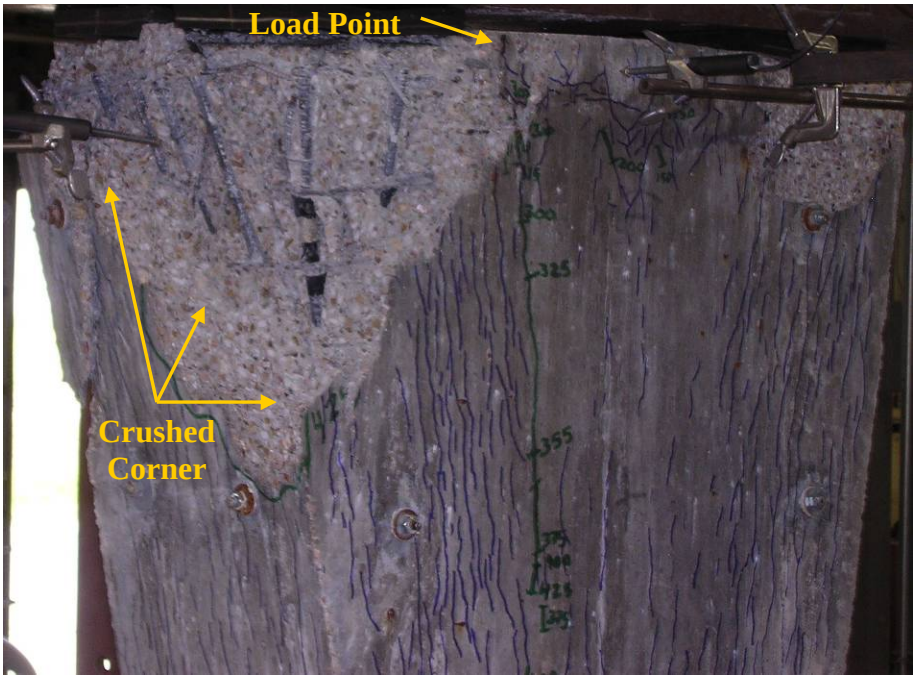

Figure 6.63: Failure of Column A[111]

6.3.3 ASR/DEF Column B

Column B served as a duplicate to Column A in order to increase confidence in the results. The post-tensioned exposure load was removed from Column B on April 18, 2008 and the specimen was tested on May 5, 2008. Figure 6.64 shows Column B prior to testing. The following sections present the strain gauge, strain meter, and linear potentiometer readings.

Figure 6.64: Column B Prior to Testing

6.3.3.1 Load Capacity

Like Column A, the flexural and bearing capacities of Column B were predicted based upon its concrete strength on the testing day and assuming an undamaged section. These capacities, along with the maximum measured load, are given in Table 6.4. Again, like Column A, the control column, and the column with a initial crack width of 0.02 inches[3],

Column B experienced a peak load that was twenty percent lower than its predicted flexural capacity and about five percent greater than the predicted bearing capacity.

Table 6.4: Predicted and Measured Capacities of Column B[3,110]

	Predicted Axial-Flexural Capacity (undamaged)	Predicted Bearing Capacity (undamaged)	Measured Maximum Load
Maximum Load (kips)	590	455	480
Compressive Strength (psi)	5700	5700	5700

6.3.3.2 Deflection Measurements

As was the case for Column A, deflections were measured by linear potentiometers at the top, middle, and bottom of two faces on the column. The monitored faces were chosen based on the load eccentricity so that the selected faces were closest to the loading point. Figure 6.65 presents the deflections measured perpendicular to the short face (along the x-axis). Figure 6.66 shows deflections measured perpendicular to the long face of the column (along the y-axis). In this second graph the deflection of the middle location had a large jump at 165 kips where it was bumped during testing. Negative deflections indicated the column was moving towards the potentiometers.

Similarly to Column A, and as seen from comparing Figure 6.65 and Figure 6.66, there was significantly more deflection along the x-axis than along the y-axis. As discussed for Column A, this difference in deflection was due to the eccentricities of the applied load. Also akin to Column A's behavior, the load deflection curves remained linear until additional cracking damage propagated, near 350 kips. The top deflection curve along the x-axis was especially upright (stiffer response to load) compared to Column A and appears to have two similar linear regions, which was likely from variation introduced by the non-uniform expansion of ASR/DEF. Beyond about 350 kips the top deflection measurement location along the x-axis (in Figure 6.65) showed a large gain in displacement as the concrete beneath the potentiometer was spalling off the column.

Figure 6.66 shows a sudden jump in displacement for the bottom location where the potentiometer was bumped during testing. In both plots, the column base's fixity was apparent in the difference of displacement along the height of the column. The nearer the fixed base, the less deflection measured. Likewise, the farther the monitoring point was from the base (closer to the top of the column), the more that it moved. The potentiometer at mid-height always measured the median amount of displacement.

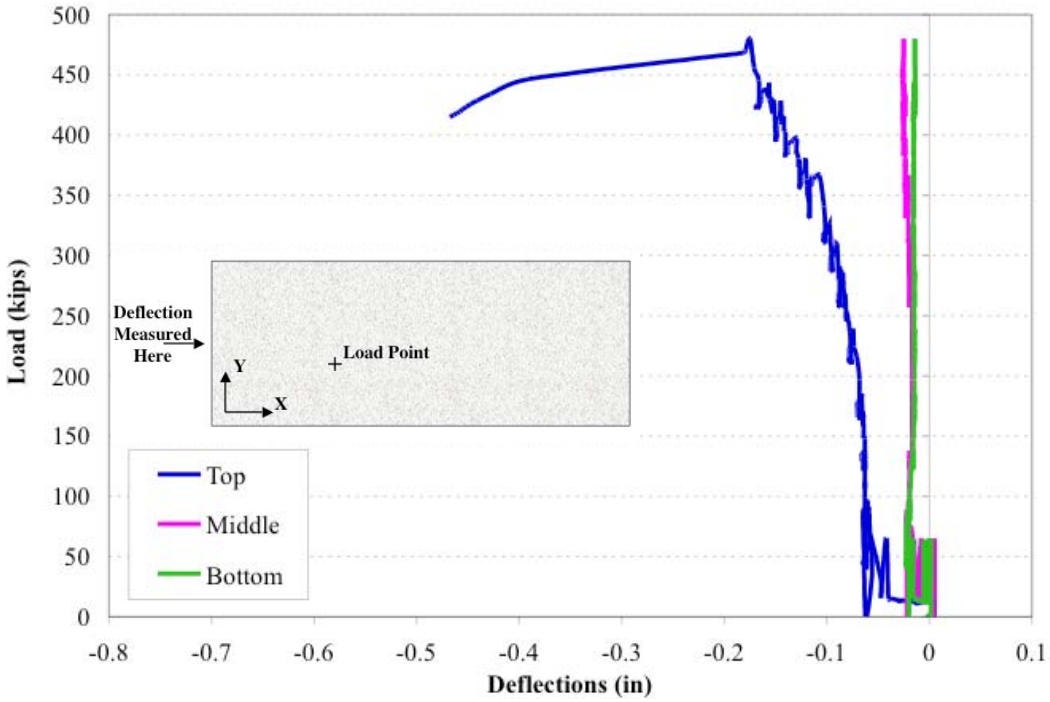

Figure 6.65: Column B Deflections along X-axis (on Short Face)

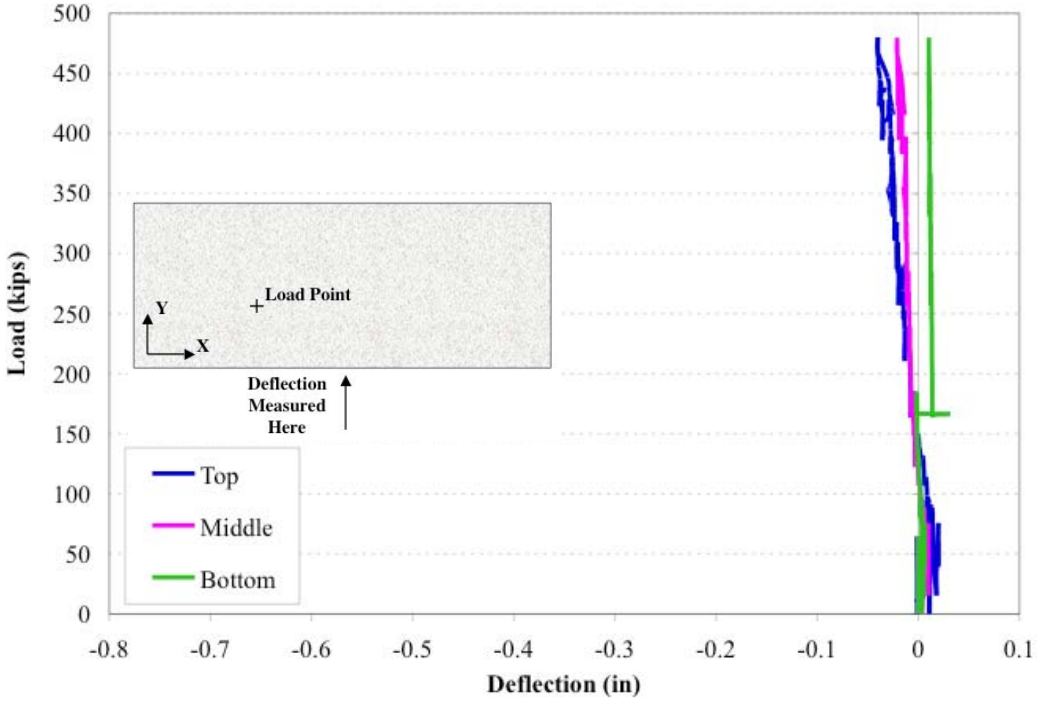

Figure 6.66: Column B Deflections along Y-axis (on Long Face)

6.3.3.3 Strain Measurements

Strains in both the reinforcing steel and core concrete were measured during loading. Figure 6.67 and Figure 6.68 present the upper and lower layers of strain meter readings, respectively. The strain meters recorded the core concrete strains. Figure 6.69 is the diagram of the upper layer strain meter locations from Chapter 3, included here for reference with bearing pad locations indicated. Figure 6.71 and Figure 6.72 present the upper and lower layers of reinforcing steel strain gauge readings, respectively. The diagram of the upper layer strain gauge locations from Chapter 3, with bearing pad locations highlighted, was included here for reference as Figure 6.73. Negative strain values indicated compression. Not all gauges that were applied to the reinforcing cage were still working on the day of testing. Figure 6.70 presents the upper and lower layer strain gauge locations, with gauges highlighted that were working on testing day. In the upper layer of this column, only two transverse gauges had failed, Upper T4 and Upper T5. In the lower layer, all the transverse gauges had failed.

Figure 6.67 presents the strain meter measurements at the upper layer of instrumentation. As was the case for Column A, in Column B meter M1 saw the greatest compressive strain. Since this strain meter was below the most heavily loaded bearing pad, that response was expected. Meters M2 and M7 were under the next most heavily loaded bearing pads (with 20% and 18% of the total load, respectively[3]). While these meters began testing with similar responses, they diverged at about 250 kips of load. It was approximately at this point that new cracks were forming and thus could be responsible for the redistribution of strain in the column's cross section. Strain meters not under a bearing pad at this top layer (meters M3, M4, M5 and M6) saw very little strain as the load was concentrated under the bearing pads and had not distributed to the entire column cross section at this level.

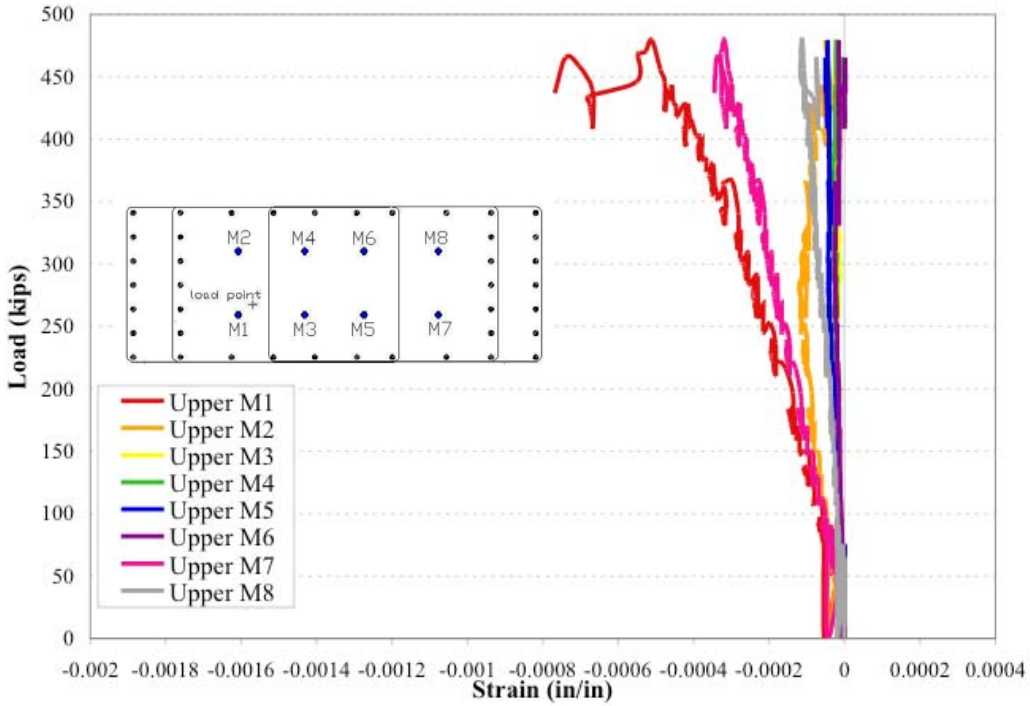

Figure 6.67: Column B Upper Layer Strain Meter Readings

In the lower layer of strain meters, presented in Figure 6.68, the localized load effects of the bearing pads had disappeared. In this plot, meter M1 recorded the most compressive strain, which was expected as this meter was the closest to the most heavily loaded corner. Meters M2, M3, and M4 had very similar strain curves, and as a group had the

next greatest compressive strain after meter M1. These three meters were roughly the same distance from the most heavily loaded corner, with meter M4 a little farther away than the other two and thus slightly lower strains. Meter M8, which was at the most lightly loaded corner recorded the lowest compressive strains as expected. From the strain meter behavior it appeared that the concrete core of Column B behaved linear elastically until the concrete exhibited additional cracking and redistributed load.

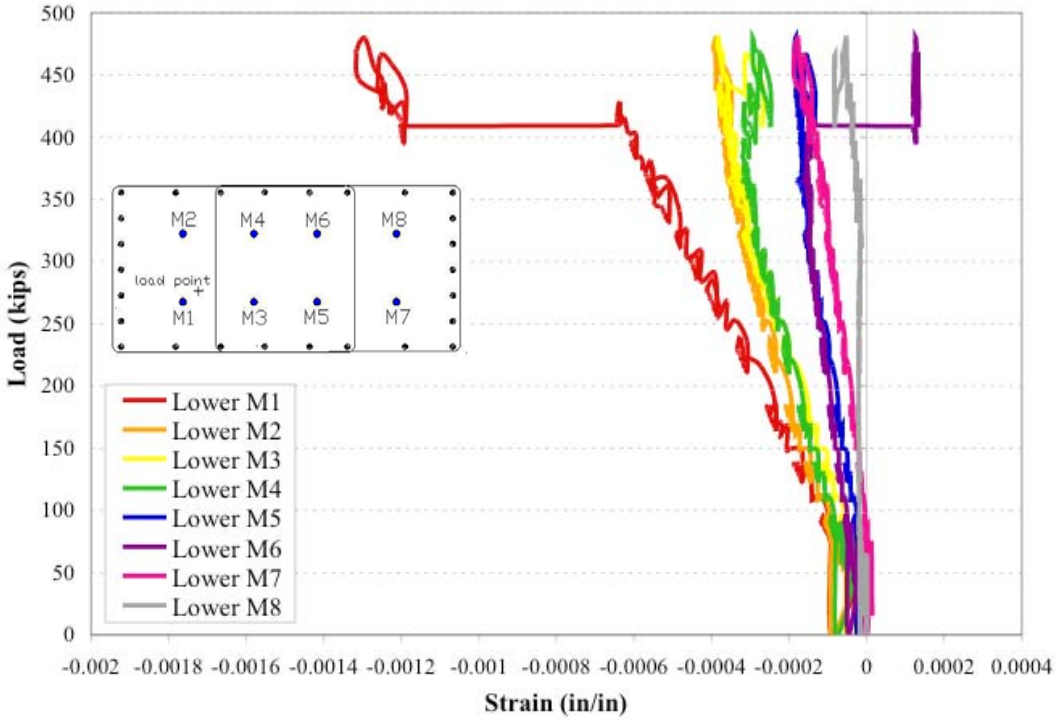

Figure 6.68: Column B Lower Layer Strain Meter Readings

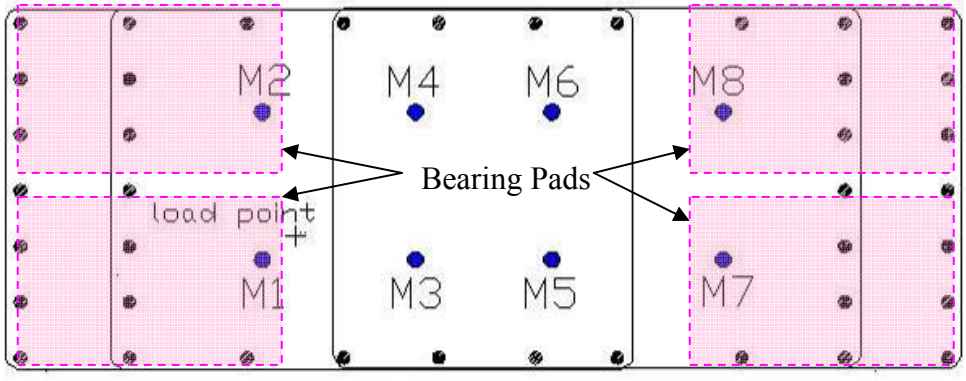

Figure 6.69: Upper Layer Strain Meter Locations with Bearing Pads

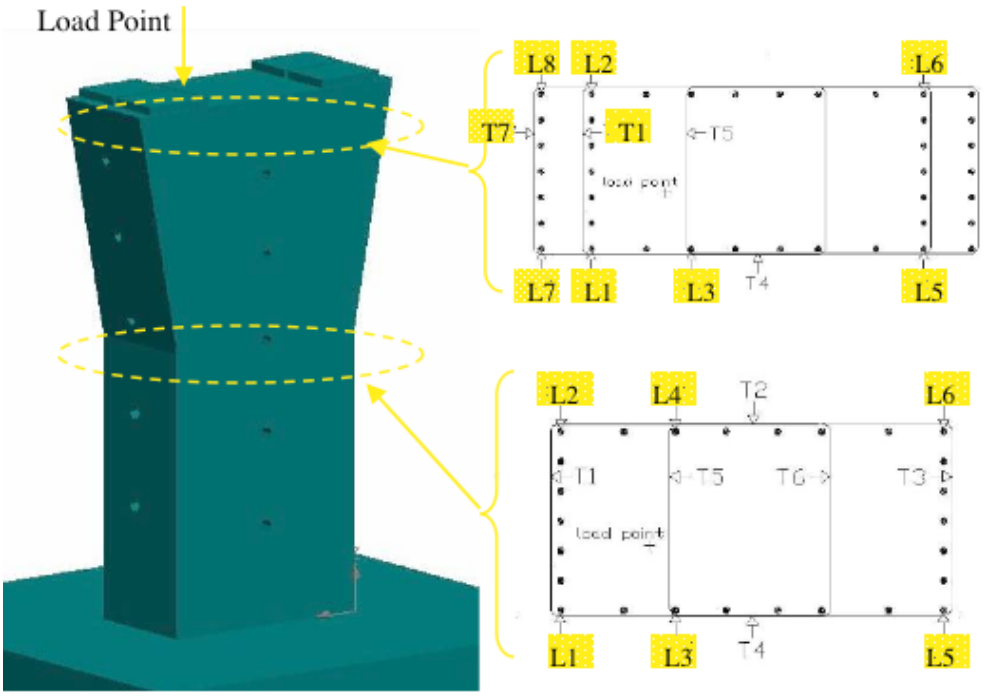

Figure 6.70: Column B Strain Gauges Working on Testing Day

Figure 6.71 presents the upper layer of strain gauges on Column B's reinforcing cage. In this layer the two working gauges on transverse ties, gauge T1 and T7, registered tensile strains. This behavior was expected as when the column was loaded axially, it was expected to expand circumferentially, which put the ties in tension as they confined the concrete core. In the longitudinal bars, gauges L1 and L7, which were at the most heavily loaded corner, measured the largest compressive strains at this layer of instrumentation. As discussed for Column A, although gauge L7 was closer to the heavily loaded corner, it was on an inclined bar. Thus this gauge, which read the strain along the bar's longitudinal axis, typically recoded similar to slightly lower strains than those recorded by gauge L1. Gauge L6, which was near the least loaded corner, recorded the least amount of compressive strain, as expected. There was some effect of locally high loads due to a bar's proximity to bearing pads. For instance gauge L5, which was considerably farther away from the most heavily loaded corner than gauge L3, recorded a larger strain than gauge L3. Gauge L5 was under a bearing pad and gauge L3 was not. The bearing pad effect was not as prominent in the reinforcing cage strain gauges as in

the strain meters simply because most of the longitudinal bars with strain gauges were beneath bearing pads.

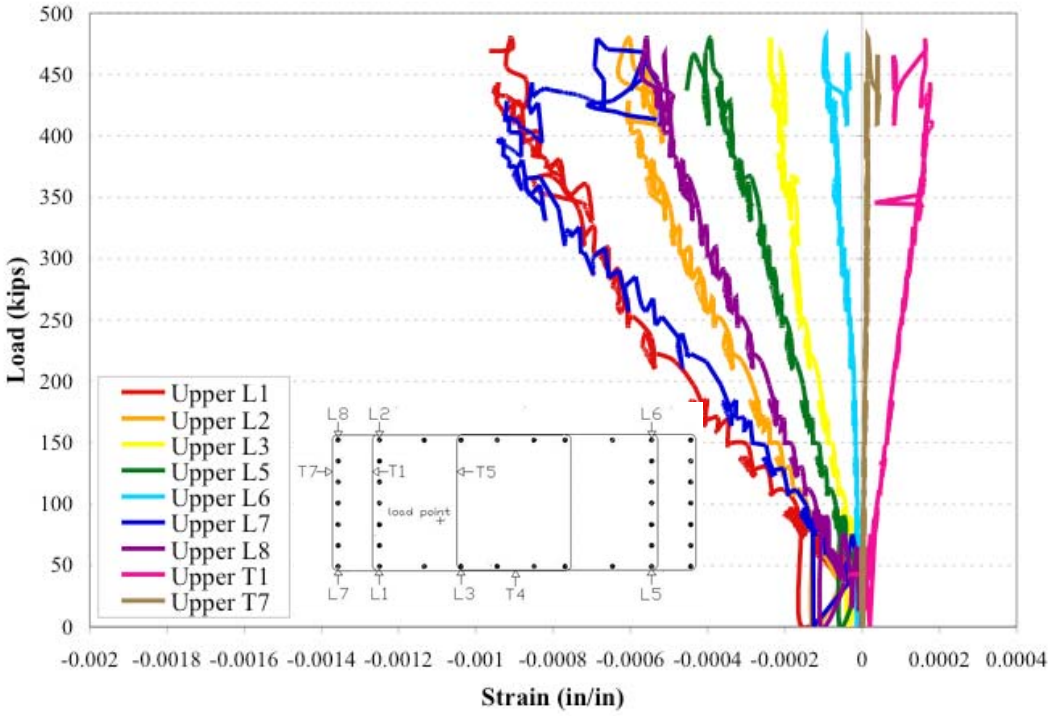

Figure 6.71: Column B Upper Layer Strain Gauge Readings

Figure 6.72 presents the lower layer of strain gauges for Column B. In this plot, gauges L1, L2, and L3 had nearly identical strain curves that also recorded the greatest amount of compressive strain at this level of instrumentation. It would have been expected that the three longitudinal bars with these gauges would carry the greatest compressive strains due to their location relative to the load point. It was expected, however, that gauge L1 would record the greatest compressive strains when the column was in biaxial bending. It was possible that this unexpected behavior resulted from the ASR/DEF damage redirecting the load path from the very beginning of loading. It could have been that the most heavily loaded half of the column (containing gauges L1, L2, L3 and even L4) carried the majority of the axial load as if it were a nearly concentric axial load on a smaller column made up of this column half. That gauge L6 was registering tensile strains meant that there was some bending in the column cross section. Thus, the half-column load carrying theory was not the only load path acting in the column. What was

evident was that the eccentric load was not shared amongst the longitudinal bars as expected for the ideal biaxial bending scenario.

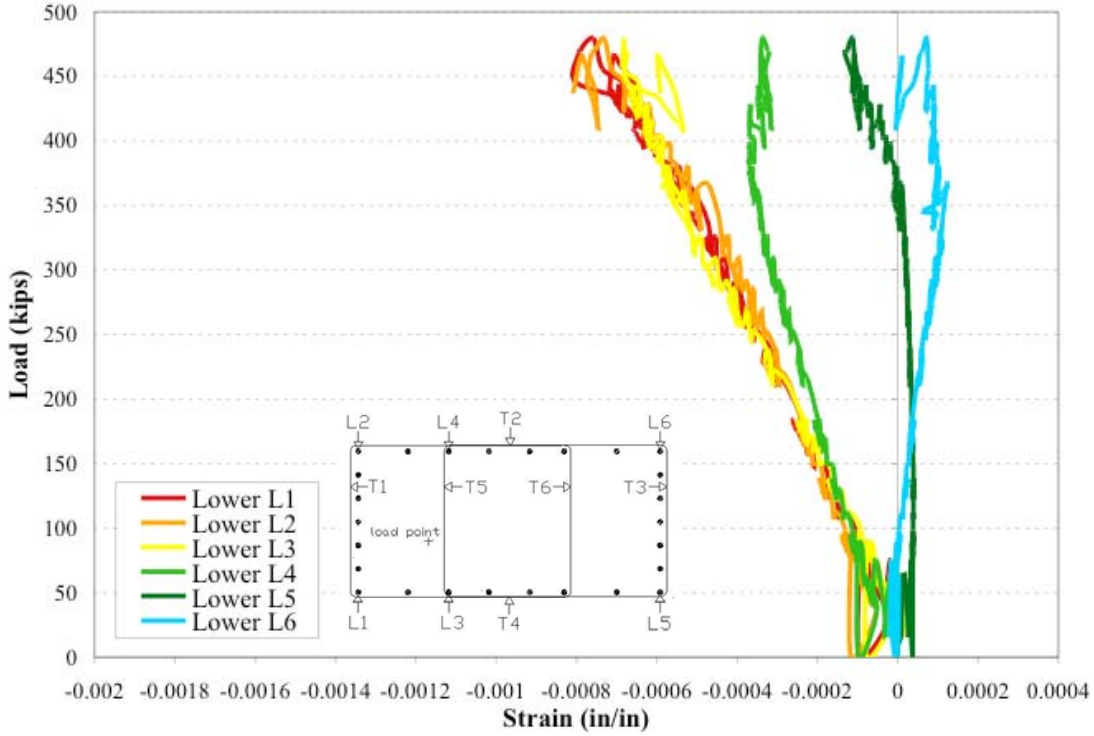

Figure 6.72: Column B Lower Layer Strain Gauge Readings

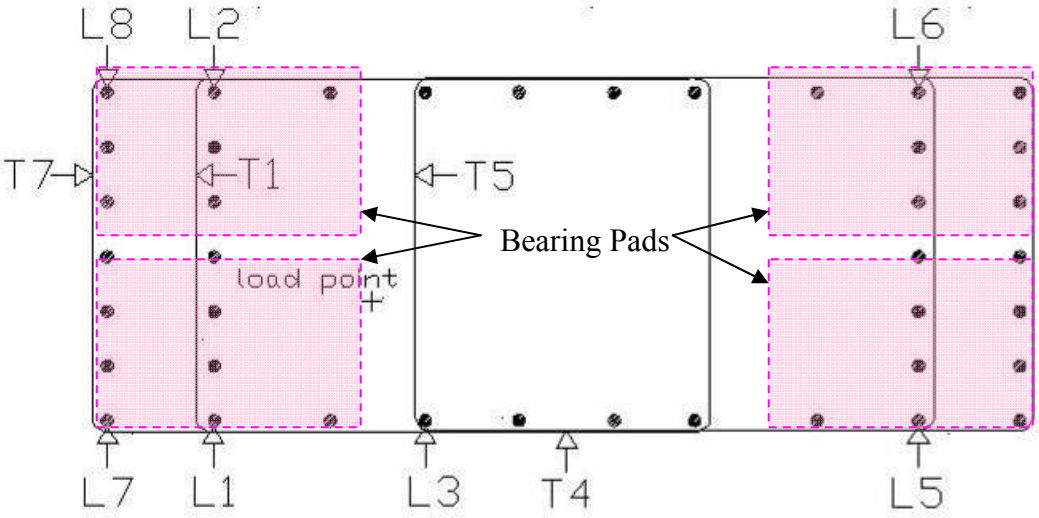

Figure 6.73: Upper Strain Gauge Locations

6.3.3.4 Failure

Initial cracking developed at 300 kips, as shown in Figure 6.74. Cracking caused by ASR/DEF was marked in blue ink and new cracks caused by load testing were marked in green ink. The center of the load point was marked with a black arrow. The initial cracking was an extension of existing cracks occurring near the center of the column's long side nearest the load point. Figure 6.75 showed the crack propagation with increasing load and spalling beneath the most heavily loaded bearing pad at 390 kips. Additional spalling at this location, which is shown in Figure 6.76, followed shortly at 400 kips. Figure 6.76 also shows crack propagation in Column B with increasing load. The column failed at 480 kips by concrete crushing beneath the most heavily loaded bearing pad, as shown in Figure 6.77

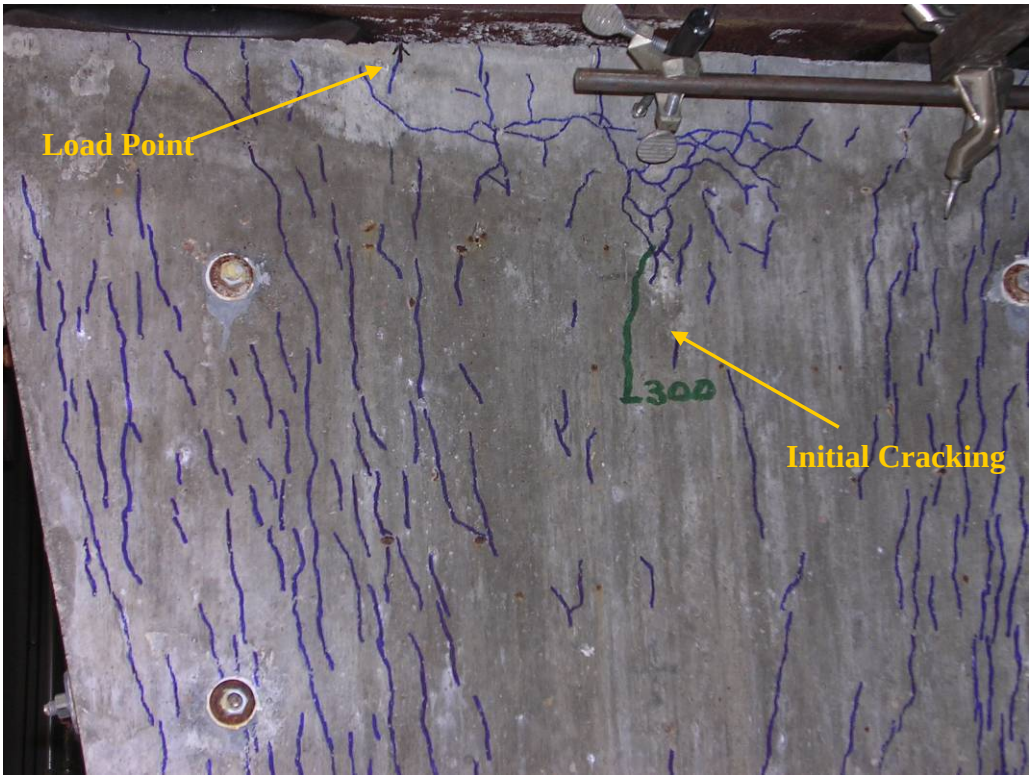

Figure 6.74: Initial Cracking of Column B

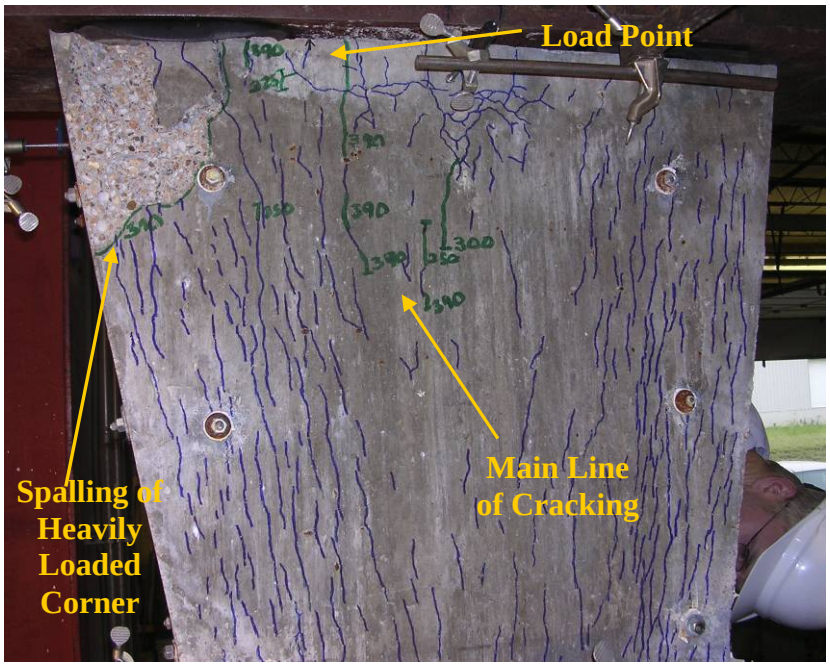

Figure 6.75: Spalling on Column B

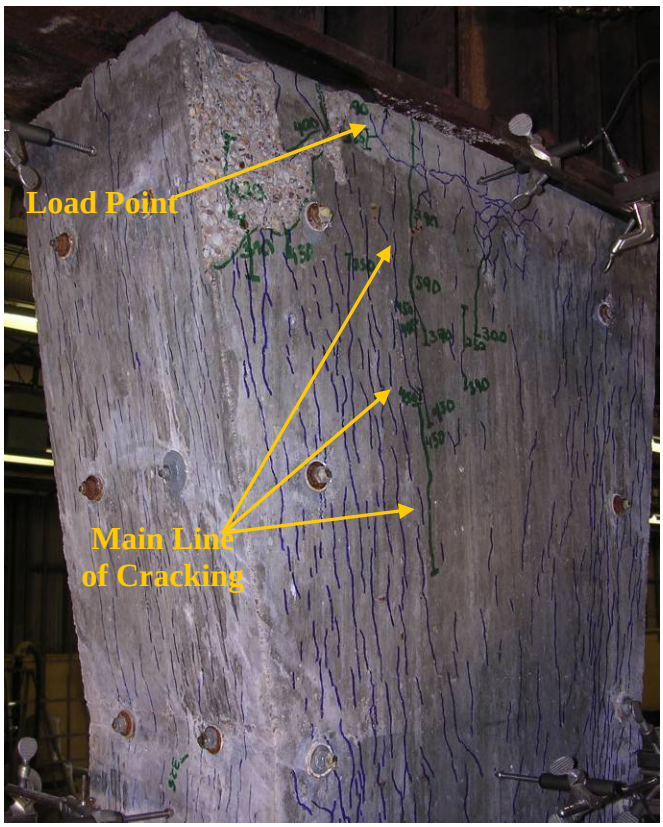

Figure 6.76: Crack Propagation in Column B

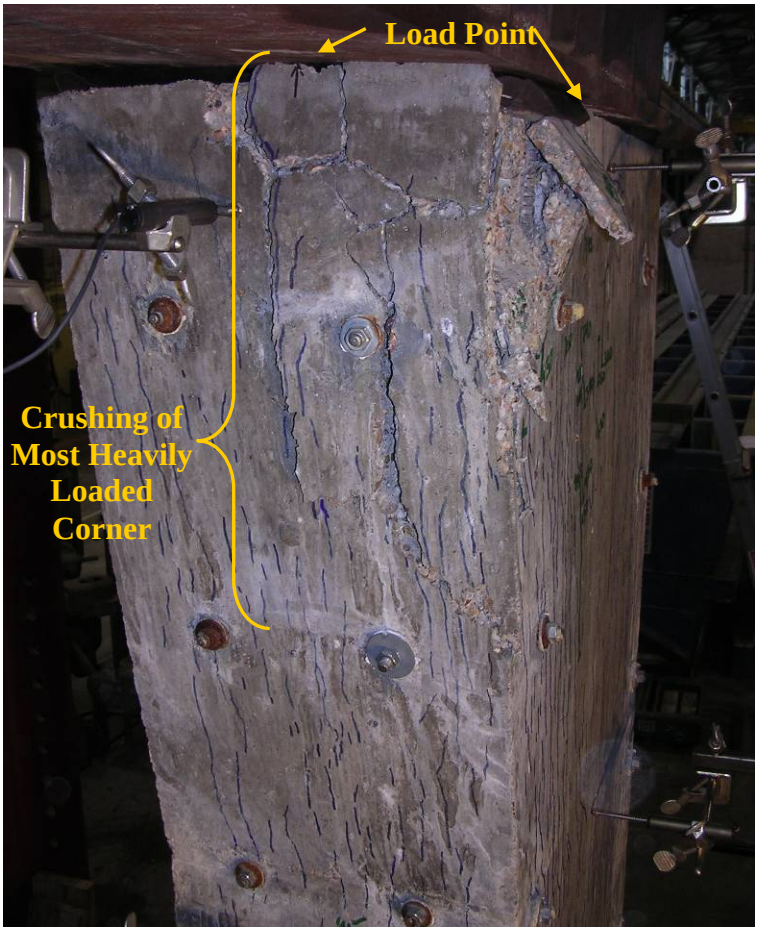

Figure 6.77: Failure of Column B

6.3.4 Comparison with Kapitan's Column Series

Both of the ASR/DEF columns had maximum loads similar to Kapitan's control and 0.02 inch pre-cracked columns, as shown in Table 6.5. Kapitan's control and 0.02 inch pre-cracked columns had nearly the same performance of approximately eighty percent of the predicted axial-flexural load per each specimen's concrete strength due to the limited bearing strength. The axial-flexural and bearing capacity predictions assumed an undamaged column, and were based on Kapitan's calculations[3]. The ASR/DEF columns' normalized maximum load was within 2% of the control, undamaged specimen. As well, all of these columns experienced the same failure mechanism, with concrete crushing beneath the most heavily loaded bearing pad. The bearing capacities, as compared in

Table 6.5, show that the ASR/DEF columns had the same performance versus predicted bearing capacity as both Kapitan's control (undamaged) and 0.02-inch wide pre-cracked specimens. Thus, the ASR/DEF affected columns had no significant reduction in capacity resulting from their 1 to 1.5% lateral expansion and resulting cracking deterioration.

Table 6.5: ASR/DEF Columns Compared with Kapitan Columns[3,110]

Specimen	f'_c (psi)	Predicted Axial-Flexural Capacity (undamaged) (kip)	Predicted Bearing Capacity (undamaged) (kip)	Measured Maximum Load (kip)	Measured Max. / Predicted (axial-flexural)	Measured Max. / Predicted (bearing)	Normalized Maximum Load (kips)	Normalized Max. / Control (Control)
Control (Undamaged)	5800	595	463	478	0.80	1.03	478	1.00
0.02 in	5800	595	463	476	0.80	1.03	476	0.996
0.048 in	5900	600	471	451	0.75	0.96	443	0.927
0.084 in	5900	600	471	395	0.66	0.84	388	0.812
ASR/DEF Col. A	6000	605	479	491	0.81	1.03	475	0.994
ASR/DEF Col. B	5700	590	455	480	0.81	1.05	488	1.02

Figure 6.78 presents the load-displacement behavior form testing ASR/DEF Columns A and B as well as Kapitan's results as measured at the top of the column along the y-axis (on the long face). This figure showed that none of the various levels of initial cracking nor ASR/DEF expansion created a significant difference in behavior as measured at this location. Instead, the figure showed the similarity of bending response of all of the specimens.

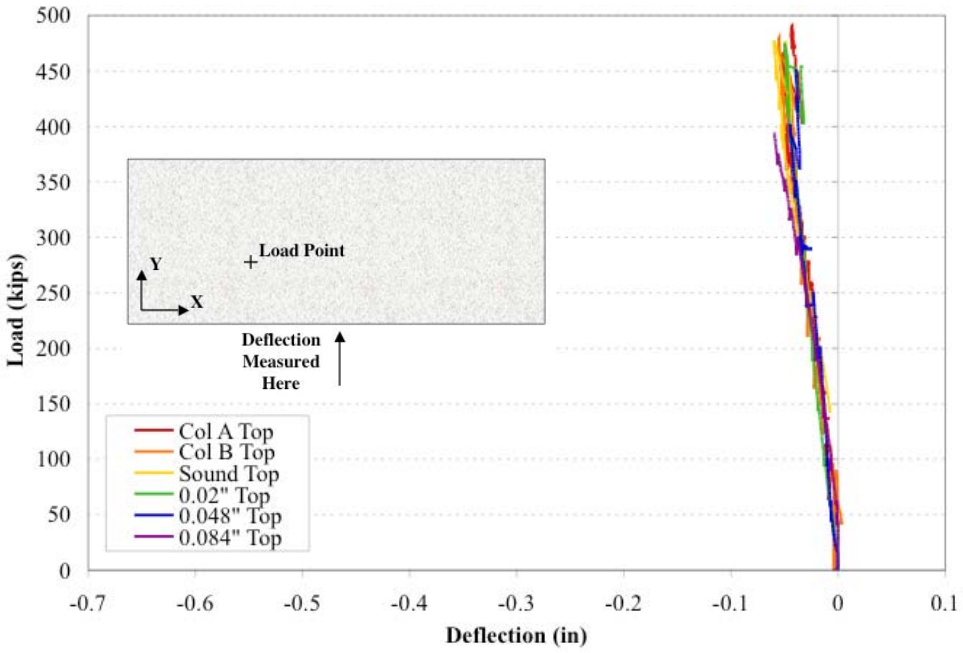

Figure 6.78: Load v. Deflection on the Long Face (along Y-axis)

The load-displacement behavior of all scaled column series specimens is presented in Figure 6.79. This plot presents the measurements of displacement from the top of the column along the x-axis (on the short face). Here, the two ASR/DEF affected columns had different total displacements and stiffness. Column B behaved similarly to Kapitan's column with 0.02 inches of initial cracking, although Column B did have a higher initial stiffness than any other column. By a load of about 150 kips, Column B's behavior had begun closely following the deflection curves of the control (undamaged) and 0.02-inch wide pre-cracked columns. Above approximately 325 kips, column B's displacement curve diverged from the 0.02 inch specimen, although they remained close until peak loads. Column A had a much softer response from the start of loading. For each increment of load, Column A had a greater displacement than all other column specimens except for the 0.084 inches of initial cracking specimens. The column with 0.084-inch wide pre-cracks, had been reused from the control (undamaged) column test. As the control specimen suffered only localized damage and the columns are symmetric, this specimen was repaired, rotated about its longitudinal axis, cracked, and tested again. It

was believed that its divergent load-displacement behavior (versus Kapitan's other columns) was a result of micro-cracks induced during the first test. Thus, Column A's reduced stiffness versus Column B could have been from additional micro-cracks, which would correspond to the higher expansion levels.

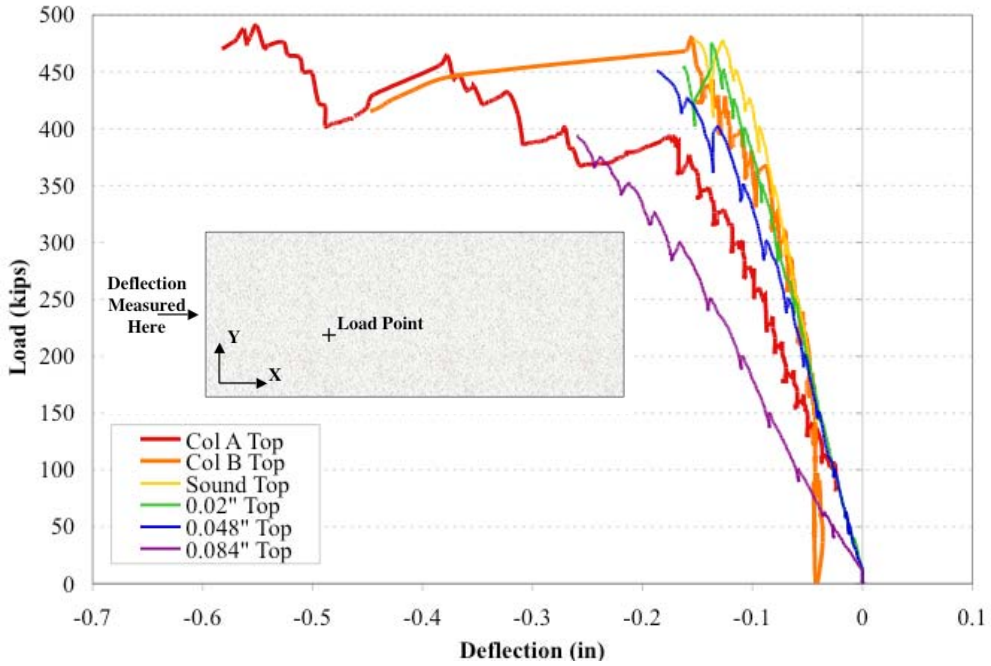

Figure 6.79: Load-Displacement Comparison On Short Face (Along X-Axis)

Figure 6.80 presents the concrete strains during testing at meter M1 for all specimens expect Kapitan's column with 0.084 inches of initial cracking. When Kapitan tested this column, he was reusing a previously tested specimen, as discussed previously. As such, he did not monitor any of the internal gauges during testing and therefore this column was absent from the strain comparisons. In this plot, ASR/DEF Columns A and B had different responses to applied loading, although not as great a difference as was seen in the load-displacement curves along the x-axis. Figure 6.80 shows Column B aligning with the undamaged, control specimen. Column A, meanwhile, behaved somewhat similarly to the control specimen, but edged towards the 0.02 inches of initial cracking specimen. The difference in performance between the two ASR/DEF columns was likely from their different maximum expansion levels (1.5% for Column A and 1.3% for

Column B). With more expansion, Column A likely had more micro-cracking and thus had a response indicating more damage.

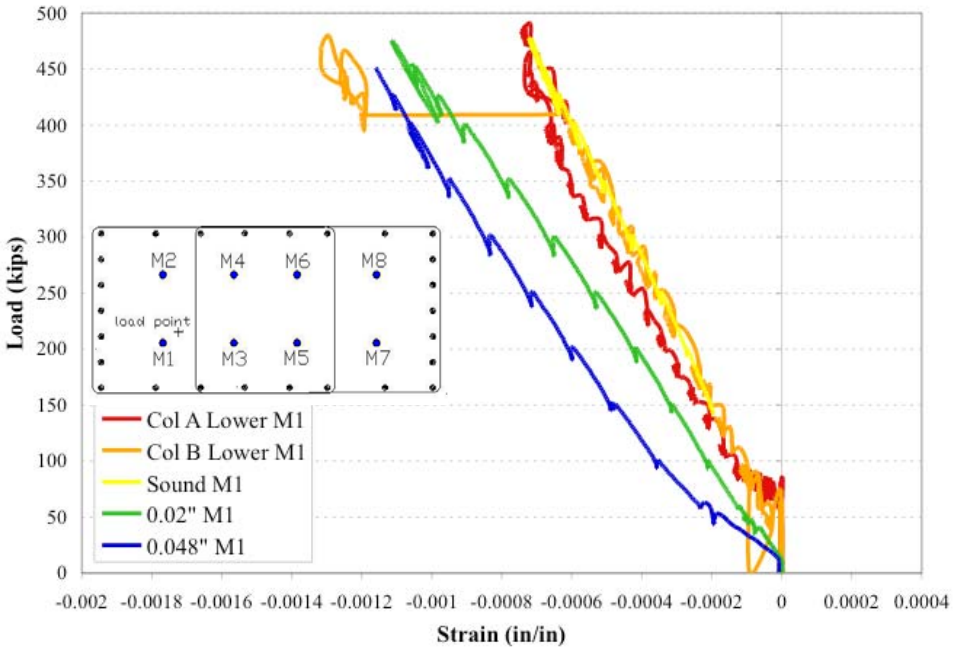

Figure 6.80: Comparison of Strain Meter M1 Readings

In the comparison of strain meter M4 readings (lower level), shown in Figure 6.81, there was overt trend amongst Kapitan's specimens to establish the effect of increasing initial damage. The specimen with 0.02 inches of initial cracking had nearly identical response as the control specimen, although the 0.02-inch specimen received slightly more strain for the applied load than did the control. Kapitan's column with 0.048 inches of initial cracking clearly experienced less compressive strain for the applied load than either of these two less damaged specimens. If it was assumed that the responses of the control and the 0.02-inch specimen were the same because 0.02 inches of initial cracking was not enough damaged to alter the load transfer through the column's cross section, then a damage trend could be established. This trend proposed that with increasing levels of cracking damage, the concrete was less able to transfer load from the heavily loaded corner to the remainder of the cross section. Thus, Kapitan's column with 0.084 inches of initial cracking had little compressive strain for the applied load because this strain meter was on the far side of a initial cracking location from the most heavily loaded

corner. The ASR/DEF affected columns had a non-linear response at high loads that differ from Kapitan's columns' linear behavior. Thus, at high loads while cracking damage increased in the column, the ASR/DEF affected columns were less able to transfer load from the lost heavily loaded corner out to the remainder of the column cross section. Kapitan's columns, by contrast, maintained their load distribution relationships and thus were not as influenced by additional cracking damage during loading. From Column B's initial response, it appeared better able to share load than even the undamaged specimen. This behavior may be due to ASR/s ability to pre-stress the concrete, which can increase member capacity[37,38,49]. Column A, which its larger expansion levels, did not show the same pre-stress improvement as Column B. Instead, Column A's response mimicked the control column until its response became non-linear at approximately 325 kips of load. At peak load, Column A's meter M4 was approaching zero strain, indicating that with increasing damage this ASR/DEF affected column was least able to transfer load to its full cross-section.

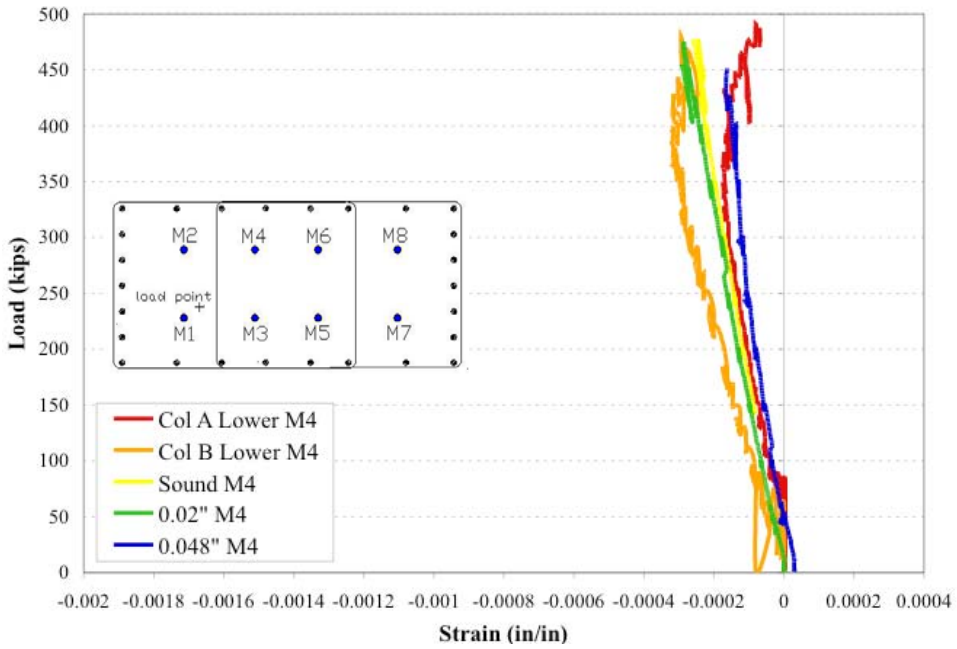

Figure 6.81: Comparison of Strain Meter M4 Readings

While the two ASR/DEF affected columns did not have behavior matching Kapitan's columns in either load-displacement or concrete strain, a correlation was still proposed. The difference in behavior of the two ASR/DEF columns reinforced the variability in engineering properties that results from ASR/DEF deterioration, and thus any mechanically cracked specimen was only an approximation of this variable behavior. From the insignificant difference in capacity versus the control specimen, load-displacement curves, and strain behavior, Kapitan's specimen with 0.02 inches of initial cracking appeared to give the best overall approximation of response. This correlation was previously suggested in the monitoring section based upon observed cracking widths.

6.3.5 Summary of Failure Testing

For the ASR/DEF damage (1-1.5% lateral expansion) observed in Columns A and B, the widely distributed cracking had no significant effect on failure mechanism or load carrying capacity. The ASR/DEF affected columns showed variability in their responses to load in both strain and displacement behavior, emphasizing the variability in engineering properties caused by ASR/DEF deterioration. Kapitan's specimen with 0.02 inches of initial cracking appeared to give the best overall approximation of the ASR/DEF affected columns. This mechanically cracked specimen had nearly the same normalized load, similar stiffness in load-displacement behavior (at least for one of the two specimens), and similar to conservative concrete strain behavior as the ASR/DEF affected specimens.

6.4 SUMMARY OF ASR/DEF COLUMNS

Through the monitoring and testing of the ASR/DEF affected scaled column specimens, several summary points can be made:

- The post-tensioned axial load served as the main restraining force against ASR/DEF restraint in the columns, creating a similar cracking pattern to the pattern observed on the San Antonio Y.
- An effective moisture retention system should be maintained throughout exposure to generate maximum expansion.

- The columns experienced considerable expansion, 1-1.5%, during the exposure period, as measured externally with demec points.
- For the 1-1.5% lateral expansion from ASR/DEF as seen in Columns A and B, the widespread vertical cracking had no significant effect on failure mechanism or load carrying capacity versus the control specimen.
- Failure of all columns was governed by bearing capacity at the top bearing surface (under the most heavily loaded bearing pad).
- The ASR/DEF affected columns showed variability in their responses to load in strain and displacement behavior, emphasizing the variability in engineering properties caused by ASR/DEF deterioration.
- Kapitan's specimen with 0.02 inches of initial cracking appeared to give the best overall approximation of the ASR/DEF affected columns' performance.
- By considering the median of the columns' average largest three crack widths, the same correlation to Kapitan's specimen with 0.02 inches of initial cracking exists.

CHAPTER 7
Bearing Specimens: Results

7.1 INTRODUCTION

During Kapitan's scaled column specimen testing[3], each specimen failed in bearing by crushing beneath the most heavily loaded bearing pad. As discussed in the preceding chapter, this failure mode also governed the scaled column specimens affected by ASR/DEF. The crushing failure resulted from a deficiency in the bearing design of the columns. The columns were designed to only carry bending in one direction, rather than the biaxial bending scenario identified as the critical load case by Kapitan[3]. As a result of this deficiency, it was desired to investigate repair scenarios to increase confinement of the column capital.

As described in Chapter 4, the concrete mixture in the bearing specimens used the same design as the ASR/DEF scaled column models, which was highly susceptible to ASR. The specimens were also heat treated during initial curing in order to initiate DEF. The bearing specimens were post-tensioned with the scaled dead load of the modeled bridge columns so that, during exposure, the cracks that formed aligned in the direction of restraint. For the exposure period, the specimens were subjected to a high humidity environment to facilitate expansion from ASR and DEF.

For the testing program, the bearing specimens were subjected to the same loading arrangement as used by both Kapitan and the scaled column specimens. This arrangement included the same loading point, spreader beam, and bearing pad layout as the scaled column specimens and Kapitan's columns. This chapter presents the results of the bearing specimen series, which modeled the column capital and four different repair options.

7.2 MONITORING

Expansion of the bearing specimens was monitored using demec points. Figure 7.1 through Figure 7.5 show the average expansions on the long sides, short sides, and vertical measuring points of the monitored blocks. As the internal temperature of the bearing specimens was not monitored during exposure, the expansion measurements were corrected for changes in the ambient temperature. For comparison, Figure 7.6 through Figure 7.8 show the average expansions in the ASR/DEF columns along with the bearing specimen expansions. Note that these comparison graphs used a larger scale for the expansion axis. For reference, 0.01% expansion equals 0.0001 in/in strain or $0.1*10^{-3}$ in/in strain. Figure 7.6 and Figure 7.7, which compare long side and short side expansions respectively, clearly illustrate the difference in concrete expansion levels for the different style specimens during the same ages of concrete. Both series of specimens used the same concrete mixture and heated initial curing. A main difference between the series was the moisture exposure after the heat treatment. The ASR/DEF columns were wrapped in felt-backed plastic and wetted by soaker hose four times a day, as explained in Chapter 3. The bearing block specimens, however, were suspended over a pool of water in order to expose them to a high humidity environment, as explained in Chapter 4. As a result of these different exposures, the ASR/DEF columns exhibited significantly greater expansion than the bearing blocks for the same time period. In fact, there was no significant expansion of the blocks at the time they were removed from exposure in November 2008 at the ages of 125 to 130 days. In Figure 7.8, the vertical expansion comparison, post-tensioning was applied to the ASR/DEF column specimens when they were 61 and 62 days old, which reduced their vertical expansion rate. Thus, for the specimen ages presented, the two specimen types had similar average vertical expansion levels. The bearing specimens were post-tensioned throughout the demec monitoring period. The lack of or very low expansion in the bearing specimens indicated that the high humidity environment, which was proven successful in triggering expansion in small samples[100], did not work as effectively in larger specimens. Wrapping the large

specimens in felt-backed plastic and wetting by a soaker hose four times a day proved the more effective method of inducing expansion.

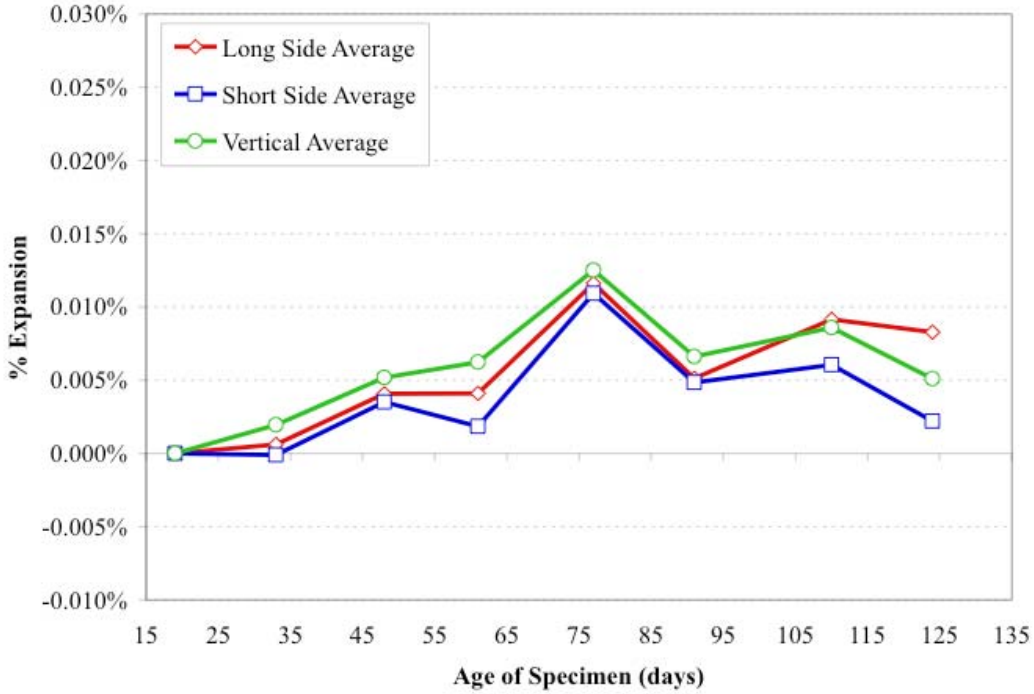

Figure 7.1: Average Expansion in Block Cast 18 July 2007, Mix 1

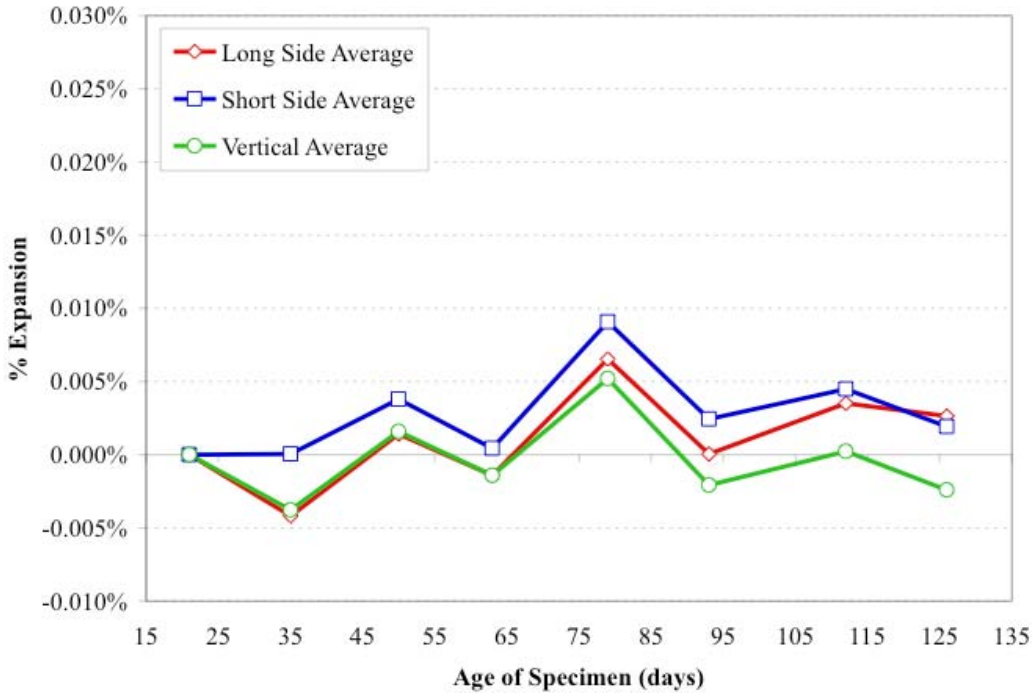

Figure 7.2: Average Expansion in Block Cast 16 July 2007, Mix 2

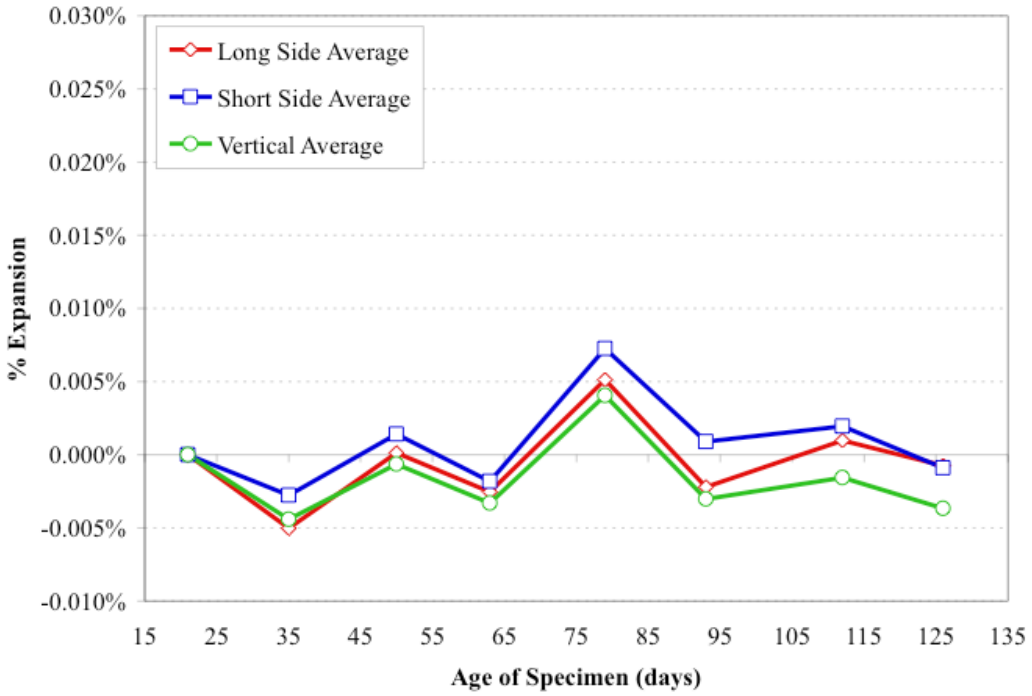

Figure 7.3: Average Expansion in Block Cast 16 July 2007, Mix 1

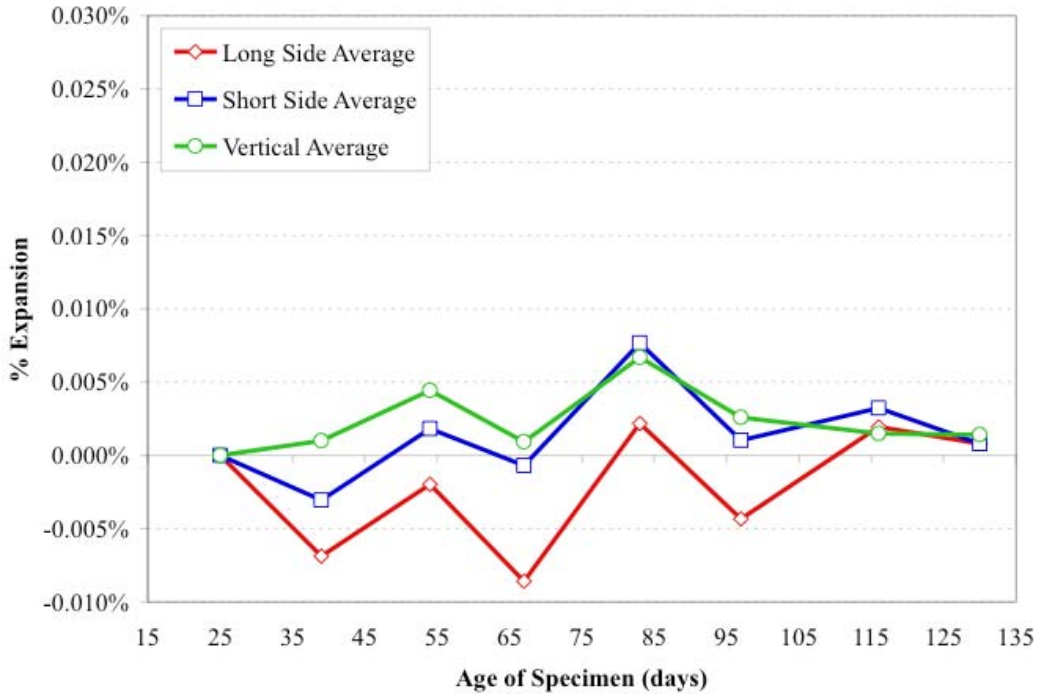

Figure 7.4: Average Expansion in Block Cast 12 July 2007, Mix 3

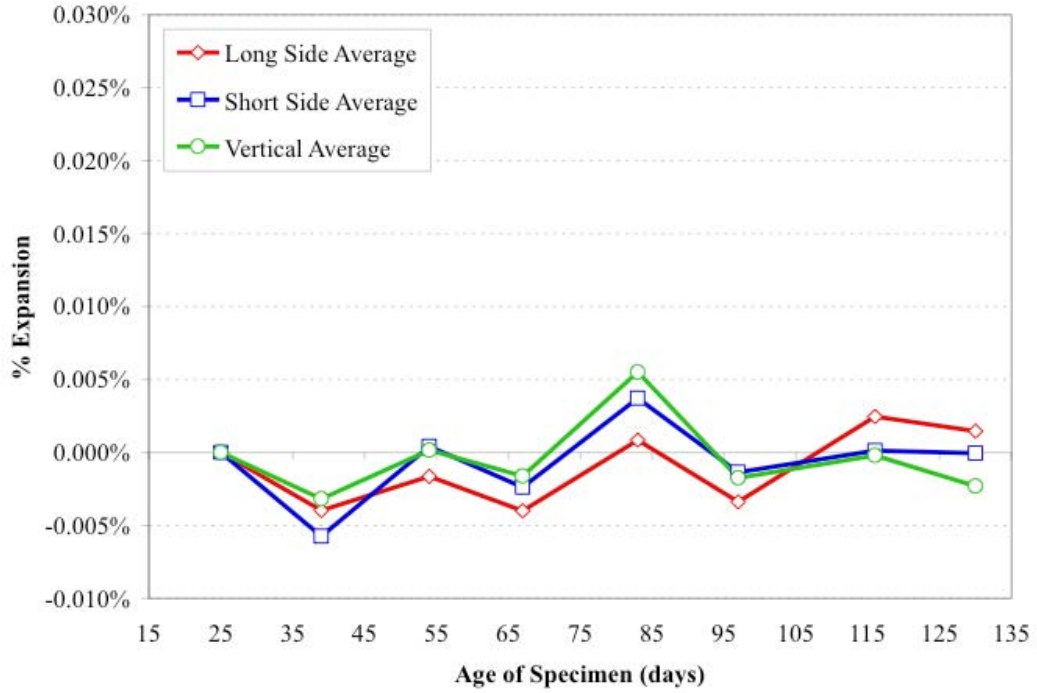

Figure 7.5: Average Expansion in Block Cast 12 July 2007, Mix 2

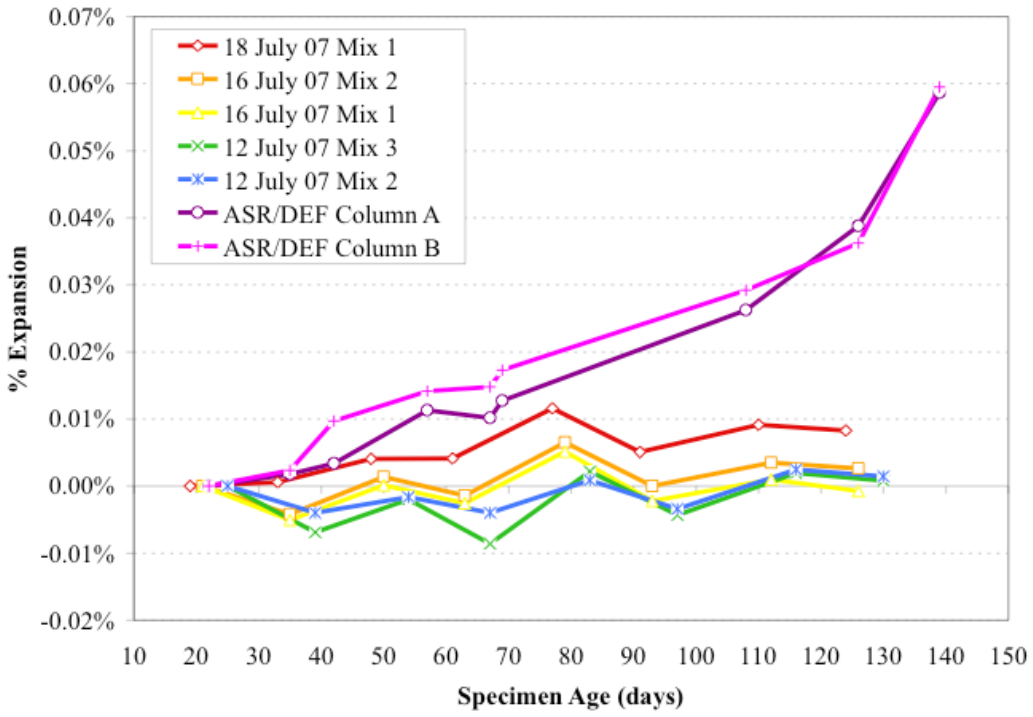

Figure 7.6: Comparison of Average Long Side Expansion

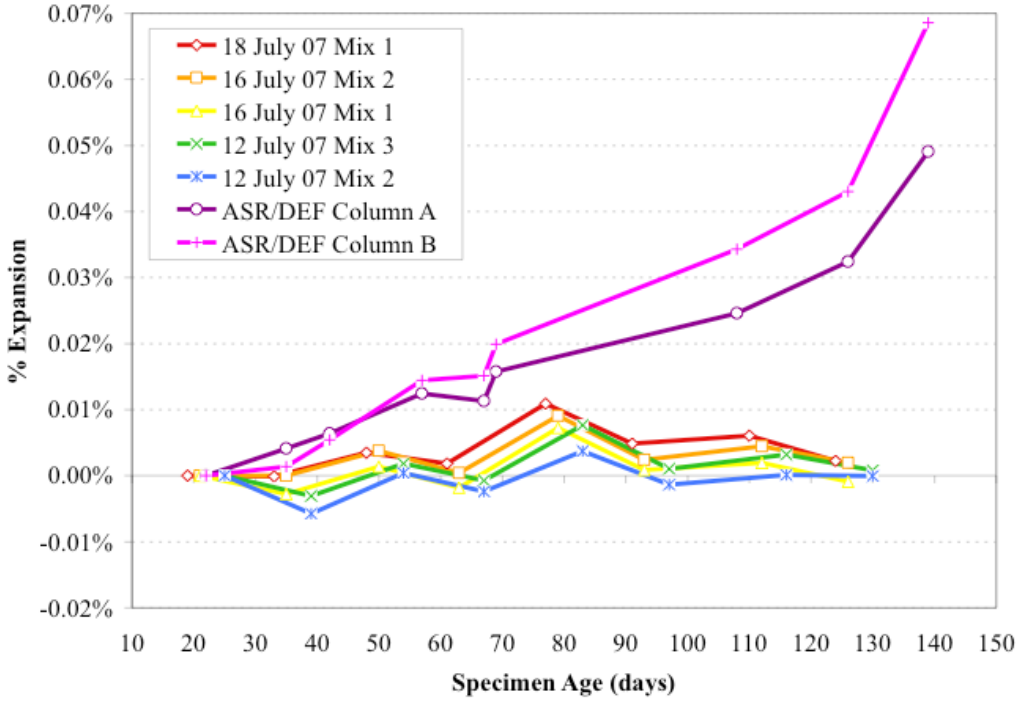

Figure 7.7: Comparison of Average Short Side Expansion

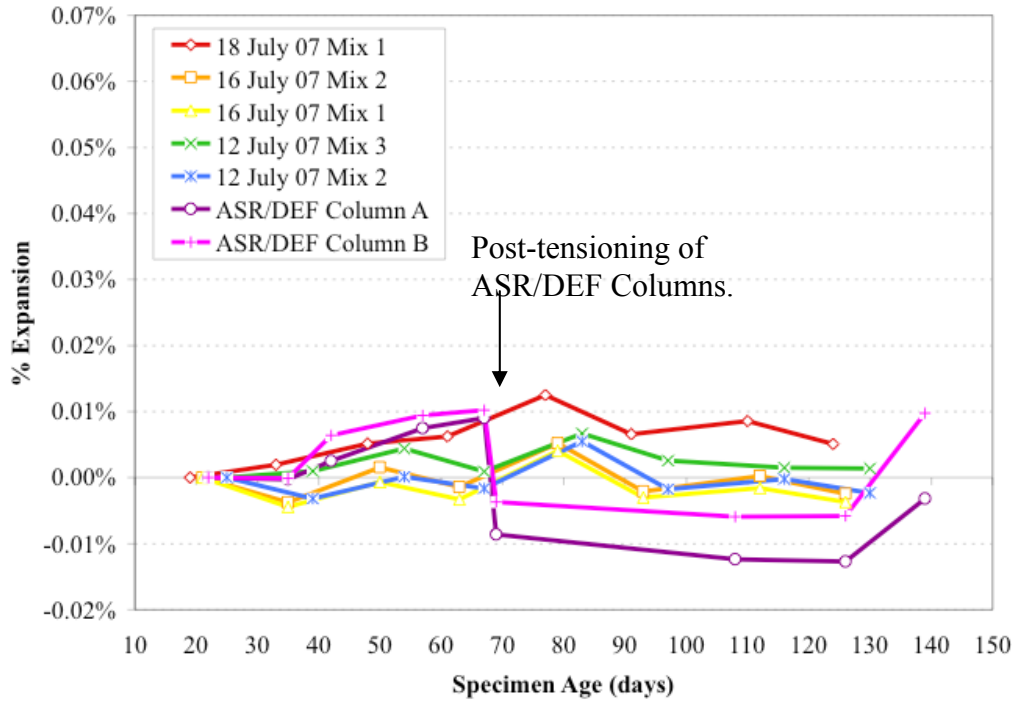

Figure 7.8: Comparison of Average Vertical Expansion

7.3 LOADING TO FAILURE

7.3.1 Undamaged Control Specimen

The undamaged control specimen was tested on December 4, 2007. Figure 7.9 shows this control specimen prior to testing. In order to find a baseline capacity this block was not pre-cracked like the rest of the series. The goal of the repairs was to bring the capacities of the damaged specimens up to or exceeding the capacity of an undamaged specimen. Thus, having an undamaged control specimen test was necessary. The PVC voids in the specimen were filled with reinforcing bar cut to the length of the voids, just as the pre-cracked specimens were treated. Three concrete cylinders, which were cast from the same concrete batch as this specimen, were tested on the same day as this specimen. These cylinders had an average strength of 7100 psi. The results from the undamaged control specimen are presented in the following subsections and a summary of both control specimens is included after the cracked control specimen results.

Figure 7.9: Undamaged Control Specimen Prior to Testing

7.3.1.1 Strain Measurements

Figure 7.10 and Figure 7.11 present the transverse and longitudinal strain measurements, respectively. Figure 7.12 shows the strain gauge locations within the bearing specimens, reproduced from Chapter 4. Figure 7.10 shows that by an applied load of 140 kips, both long side transverse strain gauges, T2 and T4, showed the ties yielding. This yielding correlated with the first cracks, which were observed at 100 kips of top loading, on the long side monitored by these strain gauges. Gauge T5's yielding pattern showed a dip in load when the testing was halted for marking cracks at 175 kips. Upon reloading after this stop, the top steel fractured and the load dropped while T5 continued to yield. With the fracture of the undamaged control specimen it appeared that some of the strain gauge leads failed as well. For instance, further data recorded for T1 and T7 past this point was nonsensical scatter. This scatter was removed from the plot. Although the yielding of T5 indicated a tendency of the most heavily loaded half of the block to break in half again, through the short face, no cracking developed on the short faces for the undamaged control specimen. Thus, there was a possibility that such a fracture through the long length of the block was developing from the center out towards the most heavily loaded short face (end closest to the load point as shown in Figure 7.12). As gauges T3, T6, and T8 recorded only small strains during testing there was no evidence of the ties or concrete in more lightly loaded half (end farthest from the load point) fracturing down the center.

Figure 7.11 presents the strain gauge measurements of the longitudinal bars. The bars with gauges L7 and L9 were inclined and the bars with gauges L1 and L5 were straight vertical. As a result, it was expected that the inclined bars would experience lower strains from the top loading for the same load as the straight bars, which was observed in Figure 7.11. What was not expected was for the bar with gauge L5 to experience greater strains than gauge L1. The bar with gauge L1 was located beneath the most heavily loaded bearing pad and thus was expected to experience the greatest stresses and strains. It was unlikely that the labels of the strain gauge leads were mistakenly reversed during construction. Instead, it was more likely that since the monitored bars were on the edge

of the specimen, it was possible that they were not fully beneath the bearing pads. It was also possible that an uneven top surface created a local high spot under the most heavily loaded bearing pad that attracted additional load to an adjacent longitudinal bar and away from the bar monitored by gauge L1. Thus, it was possible that gauge L1 reported an abnormally low strain for the load in this quadrant of the specimen. Considering the eventual bearing failure by concrete crushing beneath this bearing pad, the empirical evidence indicated that this quadrant was indeed the most heavily loaded, and not the quadrant containing gauge L5 as indicated by the strains in Figure 7.11.

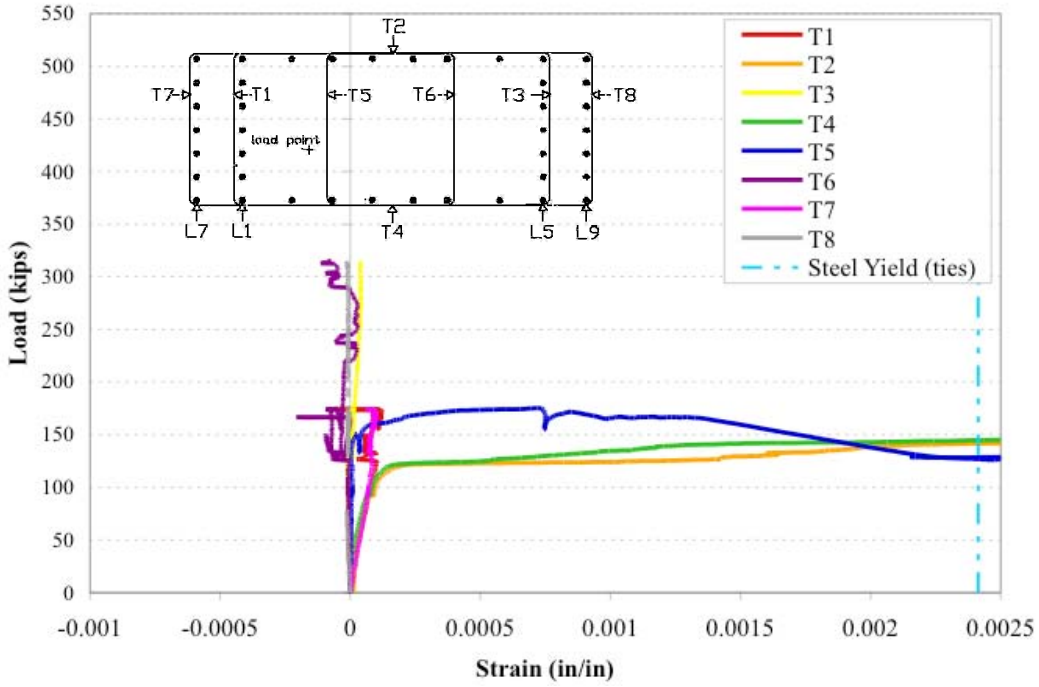

Figure 7.10: Undamaged Control Transverse Strain Measurements

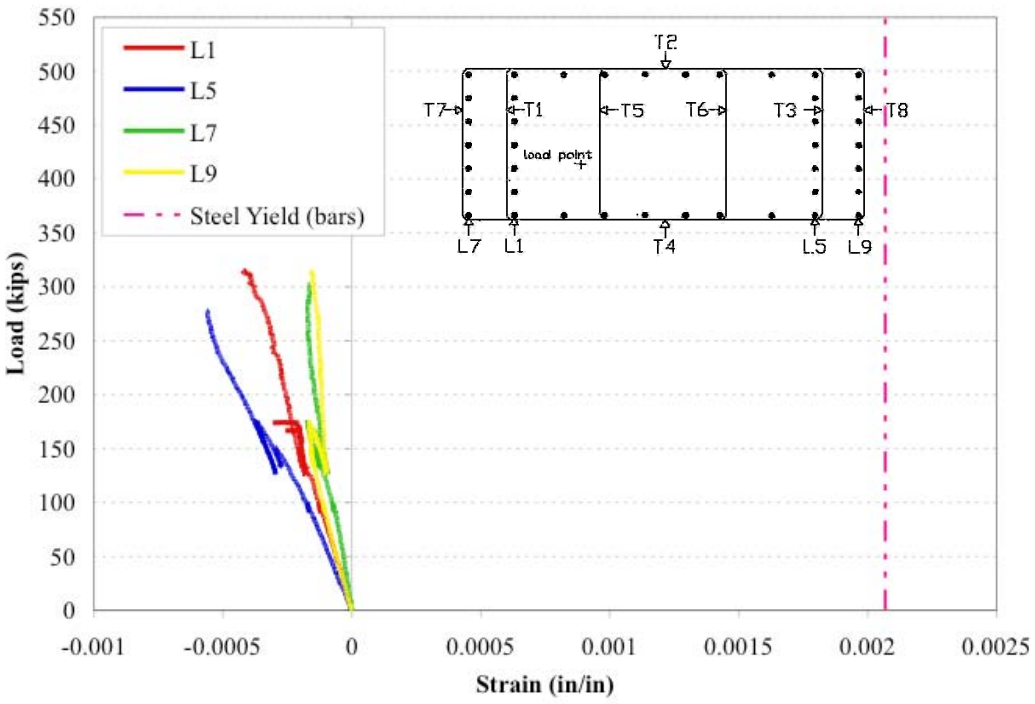

Figure 7.11: Undamaged Control Specimen Longitudinal Strain Measurements

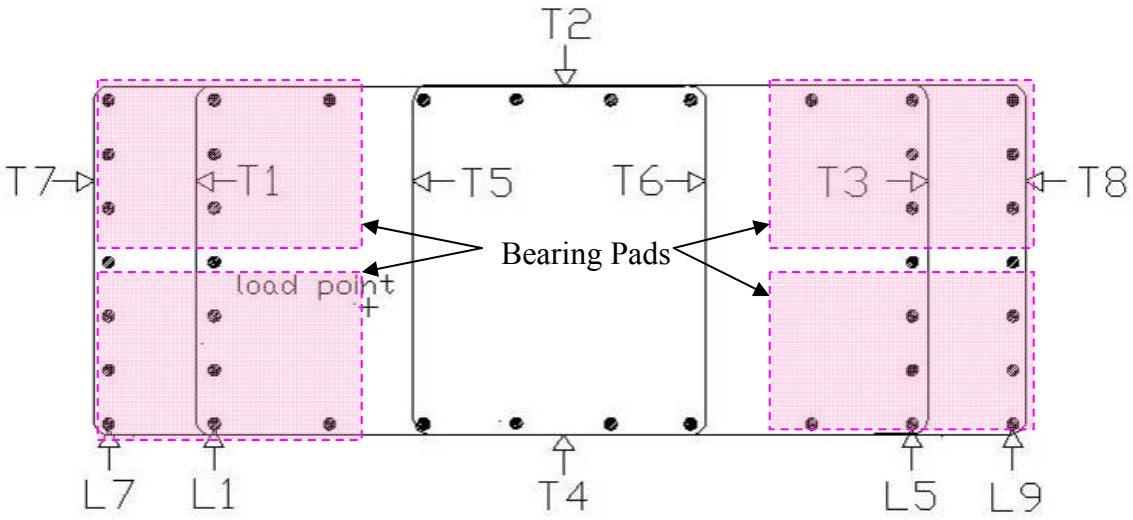

Figure 7.12: Strain Gauge Locations in Bearing Specimens

7.3.1.2 Failure

When loading was stopped to check for cracks at 150 kips, the first new cracks were noted. As shown in Figure 7.13, the first cracks formed on the long sides of the specimen, just off center towards the load point. These first cracks formed parallel each other on both long sides. As discussed previously, this long side cracking correlated to the yielding of the transverse ties. The presence of the top steel kept the crack widths small at the start of cracking. The primary cracking in the specimens propagated through the full height of the blocks at the location of the first cracks. After the initial crack propagation, the top steel fractured and allowed this center crack to open very wide (about one inch), as shown in Figure 7.14, at an applied load of 175 kips. In effect, the block broke in half down the middle. As noted in the previous section, this fracture occurred during reloading after marking cracks at 175 kips. Figure 7.15 shows the concrete crushing under the heavily loaded bearing pad that resulted in failure of the specimen at 315 kips.

The bearing failure load was lower than the values observed for the ASR/DEF columns and Kapitan's series as shown in Table 7.1, which is a summary of the undamaged control specimen's performance. The difference in capacities resulted from the difference in specimen geometry. As the bearing specimens were simply the top sixteen inches of the column, once the cracking propagated through that depth there was no adjoining column to hold the crack together. The bearing specimens were not restrained by additional ties and concrete as they rested on neoprene bearing pads. These bearing pads did not offer lateral restraint to the base of the specimens and so the cracking became a wide fracture during loading. In the scaled column specimens the main crack propagated farther down the column, while the additional ties and concrete of the column held the crack together. The continuous concrete of the scaled column specimens further prevented lateral movement of the column capital. This sort of lateral restraint was not provided by the bearing pads.

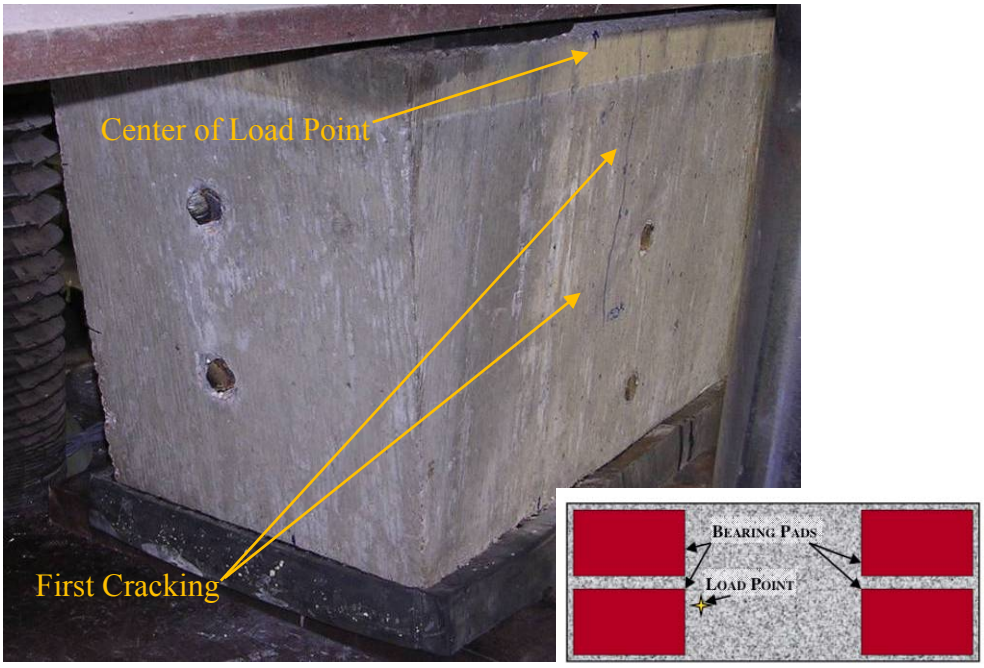

Figure 7.13: Undamaged Control Specimen's First Cracking

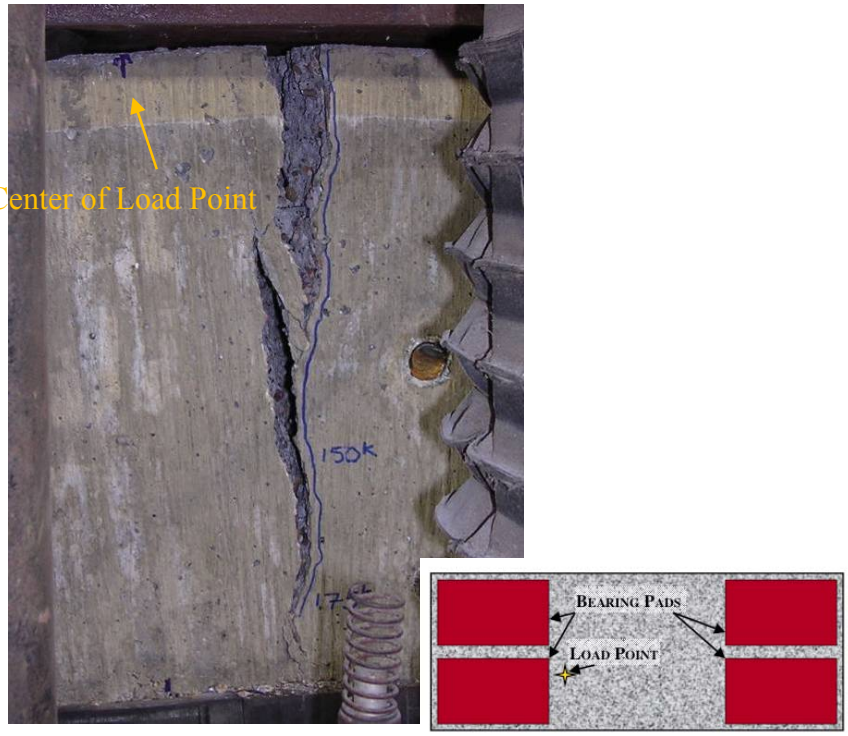

Figure 7.14: Undamaged Control Specimen Fracture at Initial Crack Location

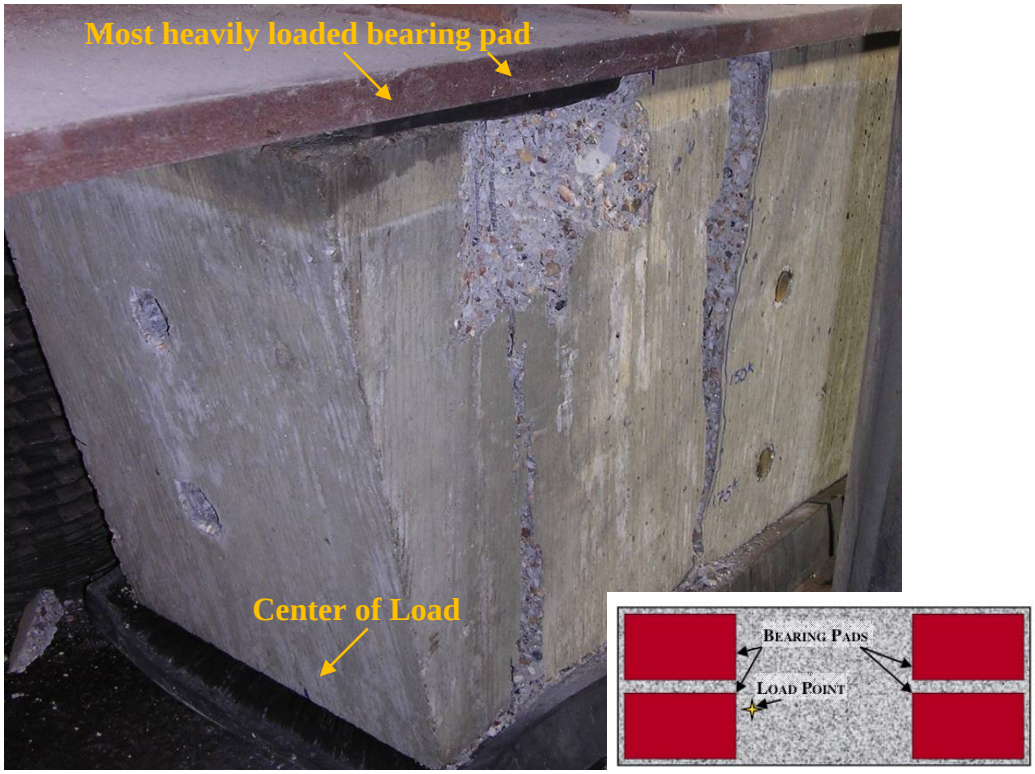

Figure 7.15: Undamaged Control Specimen Failure

Table 7.1: Summary of Undamaged Control Specimen Performance

Specimen	f'c (psi)	Measured Peak Load (kips)	Predicted Bearing Load (kips)	Measured / Predicted	Normalized Peak Load (kips)	Normalized Undamaged Control
Undamaged Control	7100	315	567	0.56	315	1.00
ASR/DEF Column A	6000	491	479	1.03	581	1.84
ASR/DEF Column B	5800	480	455	1.05	588	1.87

7.3.2 Cracked Control Specimen

The damaged control specimen was tested on December 7, 2007. This block, which is shown in Figure 7.16, was pre-cracked to an average width of 0.09 inches like the rest of the series, but not repaired in order to determine if the level of damage resulted in a decrease of capacity greater than anticipated. The cracked control specimen also created a baseline for the repairs. If a repaired specimen failed below the capacity for the

damaged and un-repaired specimen, then that repair had no positive effect on the capacity. The PVC voids in the specimen were filled with reinforcing bar prior to testing. Three concrete cylinders made from the same batch of concrete as the specimen were tested for strength on the day of testing. An average strength of 6700 psi was found from the cylinders. The results of the testing are in the subsequent sections, followed by a comparison to the undamaged control specimen.

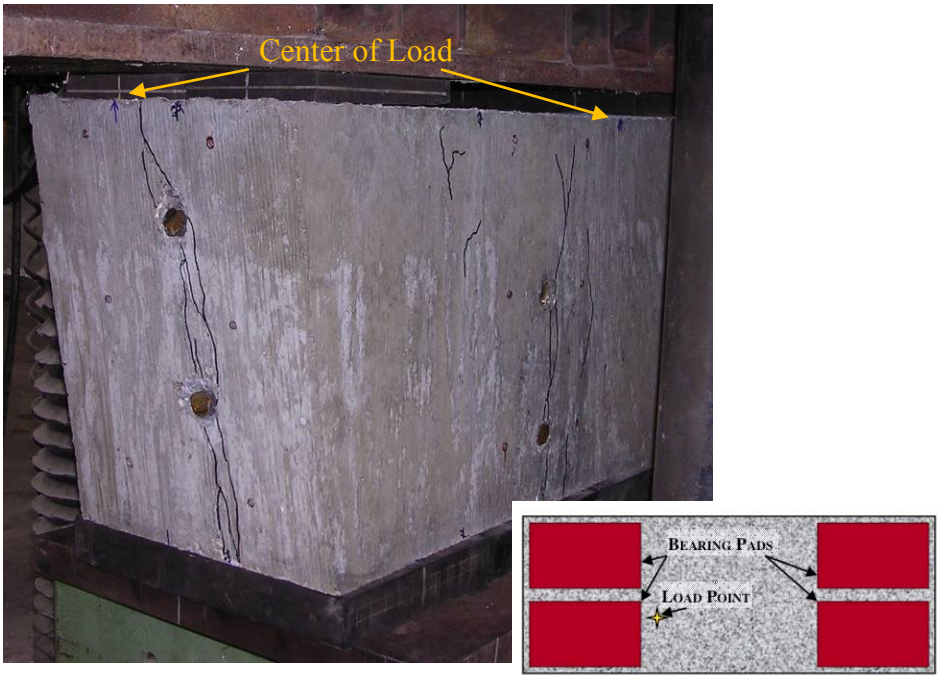

Figure 7.16 : Cracked Control Specimen Prior to Testing

7.3.2.1 Strain Measurements

Figure 7.17 and Figure 7.18 present the transverse and longitudinal strain measurements, respectively. Smaller versions of Figure 7.12 are inset in the graphs and show the strain gauge locations within the bearing specimens. For this specimen, transverse gauge T4 was not working at the time of testing. The initial cracking of the cracked control specimen had a significant effect on the strains observed during testing compared to the undamaged control specimen. For instance, gauge T1 indicated a yielding failure at 40 kips of load for this specimen compared to the undamaged control specimen, which recorded only a small amount of strain in T1 before the lead broke at 175 kips. The

earlier yielding of T1 in the cracked control specimen did not correlate to a surface crack, however, as gauge T1 monitors an interior tie and the external tie was still taking load at that point. The external tie on the most heavily loaded short side was monitored by gauge T7. At a load of 90 kips this external tie yielded. At the same load, gauge T5 indicated yielding. From the exterior tie to the center tie, gauges T7, T1, and T5 monitor the ties holding the specimen from splitting apart on the short face. With the yielding of all of these ties, the pre-existing crack began to open wider. At this time, a wedge of concrete at the base of this short face began to push out as shown in Figure 7.22. The wedge's edges followed pre-existing cracks, but with the widening of the cracks, it was no longer held in place. The other half of the block was monitored by gauges T8, T3, and T6, exterior to interior. These gauges noted no significant opening forces and the crack did not open. Also at 90 kips, the first new cracks in the form of crack extensions were noted on the long faces as shown in Figure 7.21.

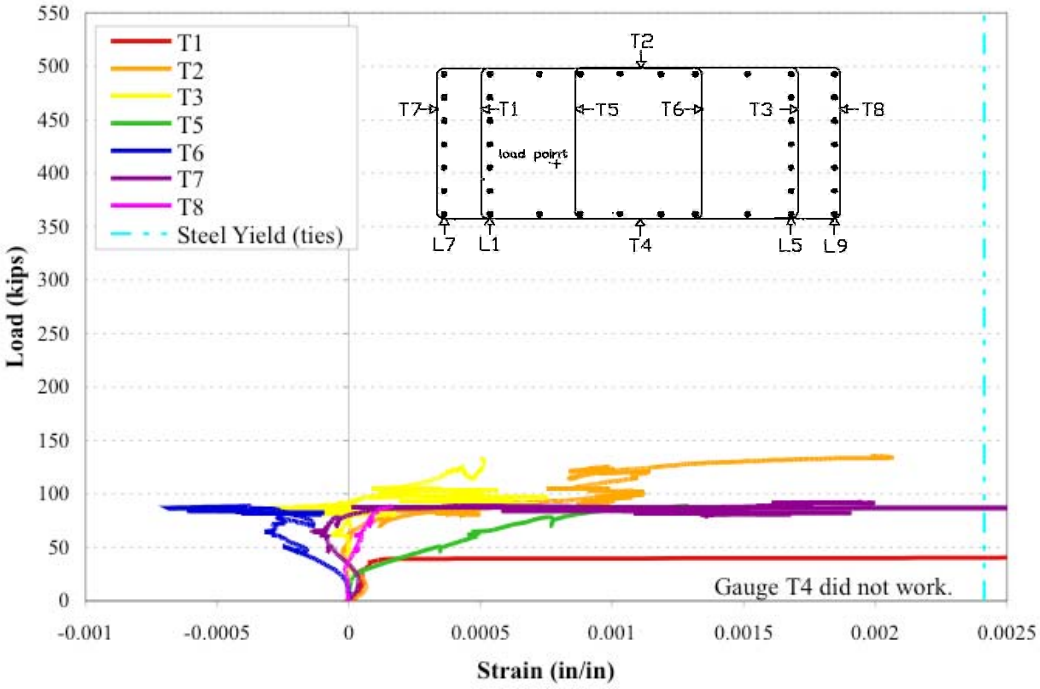

Figure 7.17: Cracked Control Transverse Strain Measurements

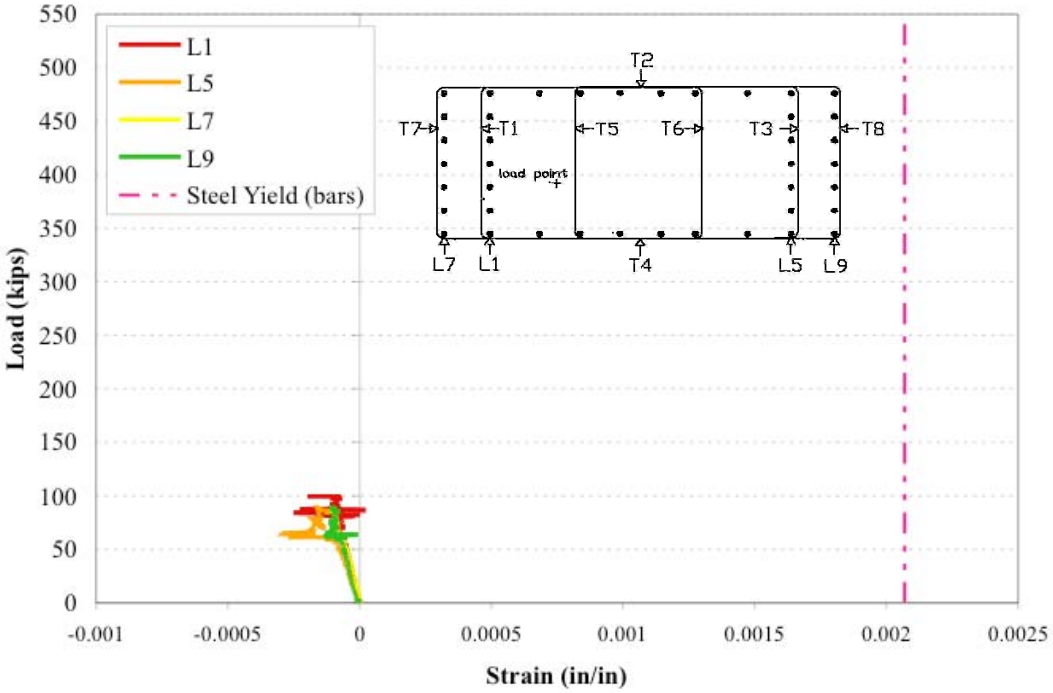

Figure 7.18: Cracked Control Longitudinal Strain Measurements

Comparisons with the undamaged control specimen of long side strain gauge measurements are shown in Figure 7.19. Figure 7.20 presents a comparison between the two control specimens with respect to two short side gauges, T1 and T7. For these two figures, the load was normalized for the concrete strength of the undamaged control specimen. As shown in Figure 7.19, the cracked control specimen experienced yielding in the long side ties about 30 kips before the undamaged control specimen, considering normalized loads. Although the gauge did not indicate failure until the long sides fracture in the damaged specimen, the effect of the initial cracking was seen in the earlier crack extensions. The major influence of the initial cracking was the short side cracking. Without the weak plane introduced by the splitting wedges, the loading scenario was not able to generate enough force to fracture this short face on the undamaged control specimen. With the initial cracking present, however, the ties spanning the short face of the more heavily loaded short side experienced yielding at much lower levels than the undamaged specimen, where if any yielding occurred it did so above 175 kips.

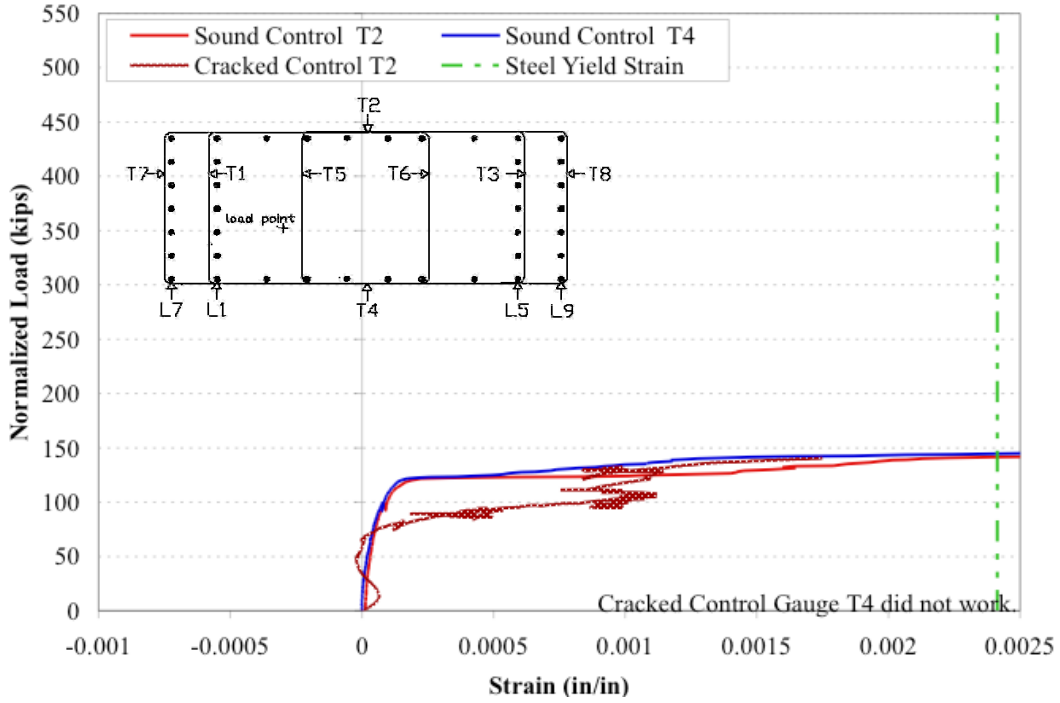

Figure 7.19: Control Specimen Comparison, Long Side Gauges

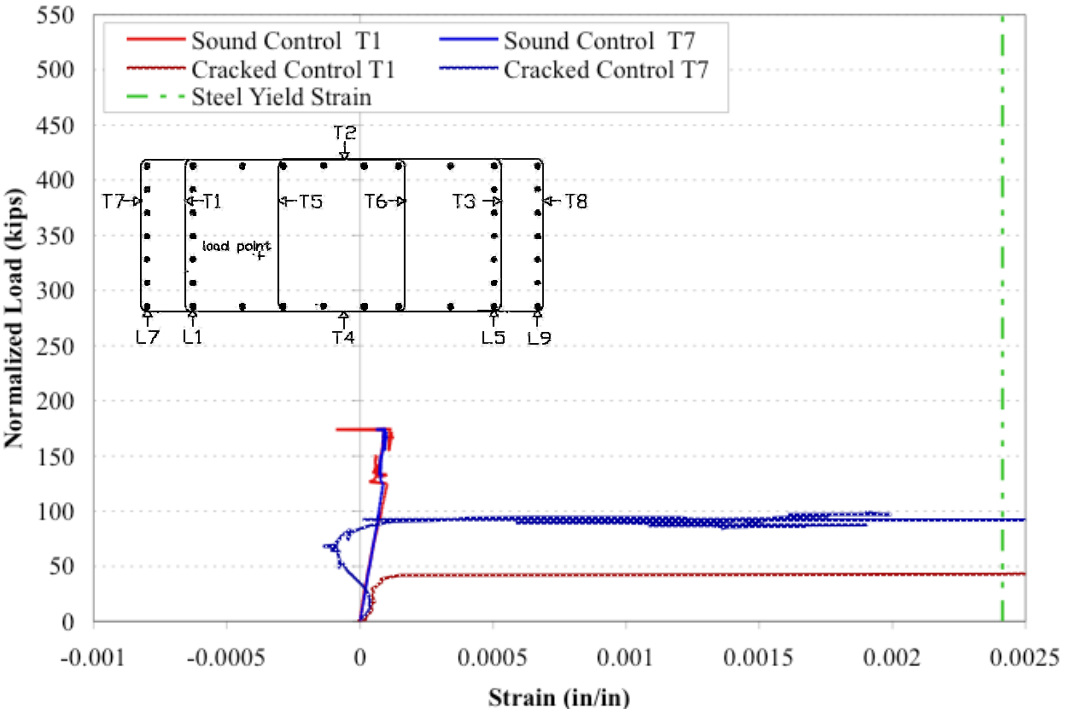

Figure 7.20: Control Specimen Comparison, Select Short Side Gauges

7.3.2.2 Failure

As noted previously, the first new cracks occurred at 90 kips as shown in Figure 7.21. At the same time, the most heavily loaded short side had the pre-existing center crack open slightly wider and a wedge of concrete began pushing out, as shown in Figure 7.22. Pre-existing cracks from the splitting wedges were marked in black ink and new cracks from testing were marked in blue ink. Crack extensions developed on both long sides of the specimen and extended the pre-existing cracks to the very top of the specimens. During initial cracking the top mat of reinforcing held cracks closed and prevented significant propagation of cracks to the specimen top on the long faces. Although the monitored ties holding the most heavily loaded short face together yielded at 90 kips, it was at a load of 120 kips that the remaining ties yielded and the crack suddenly opened very wide (about one inch), as shown in Figure 7.23. At 125 kips, new cracks formed on the long side between the load point and the center of the specimen. As the specimen reached a load of 150 kips, the cracking on the long sides opened wide, as shown in Figure 7.24, and the load dropped. The specimen continued to gain load as the corner under the load point slowly rotated out away from the rest of the specimen, which is shown in Figure 7.25. Also in this figure, bulging of the bearing pad is visible. It was typical during all of the load tests that as the load increased, the bearing pad compressed beneath the specimen. Where the specimen did not fully cover the bearing pad at the edges, the uncompressed portion of the bearing pad appeared to bulge at the specimen edges. This behavior likely added some additional upward pressure to the bearing specimens at their bottom edges. When a wedge of concrete would spall at the base, the compressed bearing pad would tend to push it out. This action appeared to be the natural behavior of a compressed elastic material reacting to a removal of load; returning to its original position. While there was likely some edge pressure, it was not expected that this pressure had significant influence over the behavior of the bearing specimens. The bearing pad's significant impact was from the difference in the lateral restraint boundary condition compared to bearing on additional concrete, as discussed in undamaged control specimen's section. Concrete crushing, as shown in Figure 7.26, under the bearing pad of this most heavily

loaded corner caused failure at 284 kips. Table 7.2 summarizes the performance of the cracked control specimen with the undamaged control specimen's performance listed for comparison. Even with an average initial cracking width of 0.09 inches, the normalized capacity was only reduced by 4% compared to the undamaged control. Overall, the control specimens did not come close to their predicted bearing behavior because the prediction was based upon the scaled column dimensions. The base of all the bearing specimens lacked a source of lateral restraint, such as the remainder of the column, that was needed to achieve the higher predicted loads.

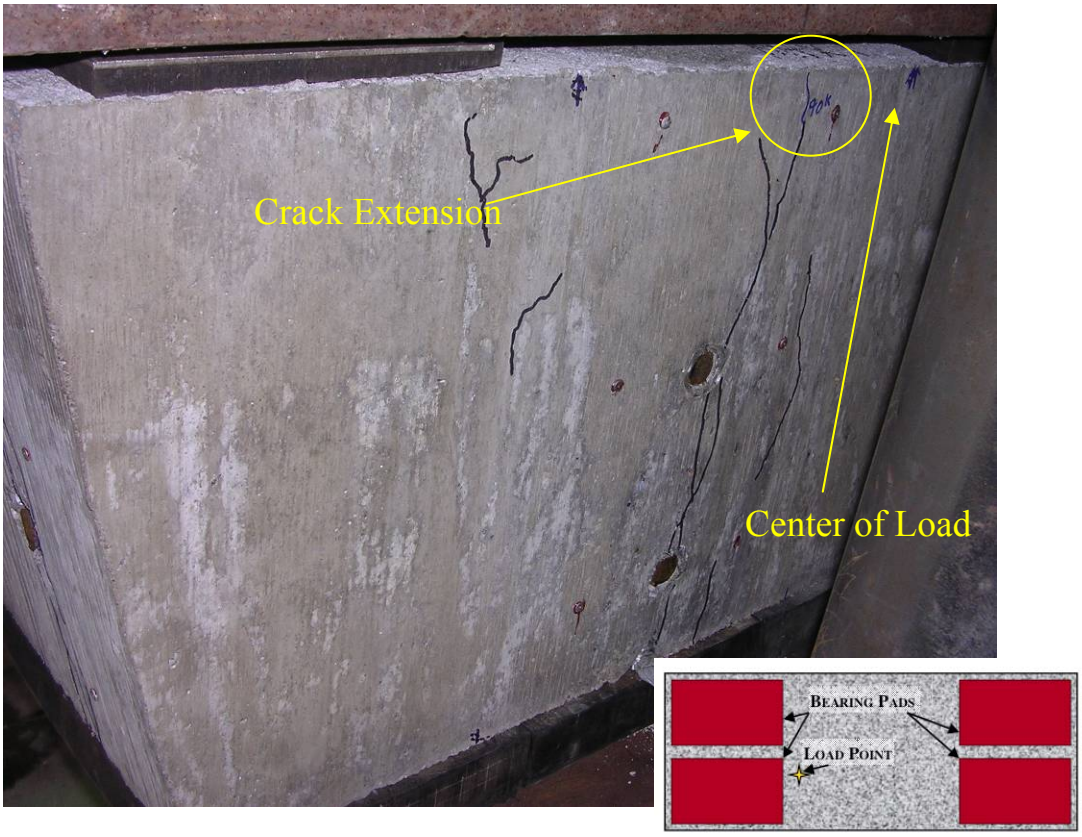

Figure 7.21: New Cracking of Cracked Control Specimen

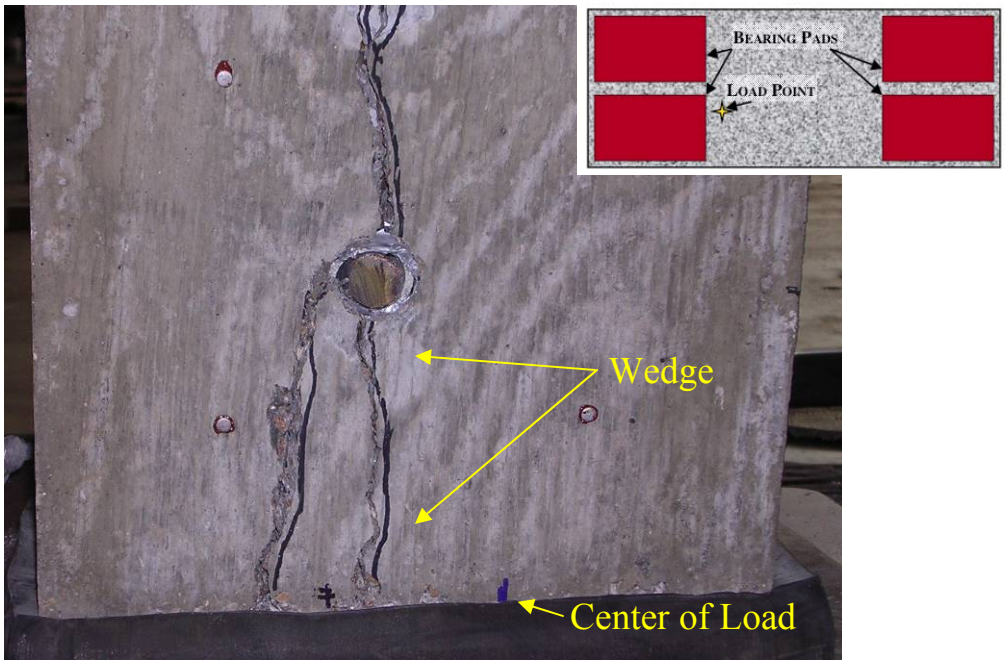

Figure 7.22: Wedge Pushing Out at Base of Cracked Control Specimen

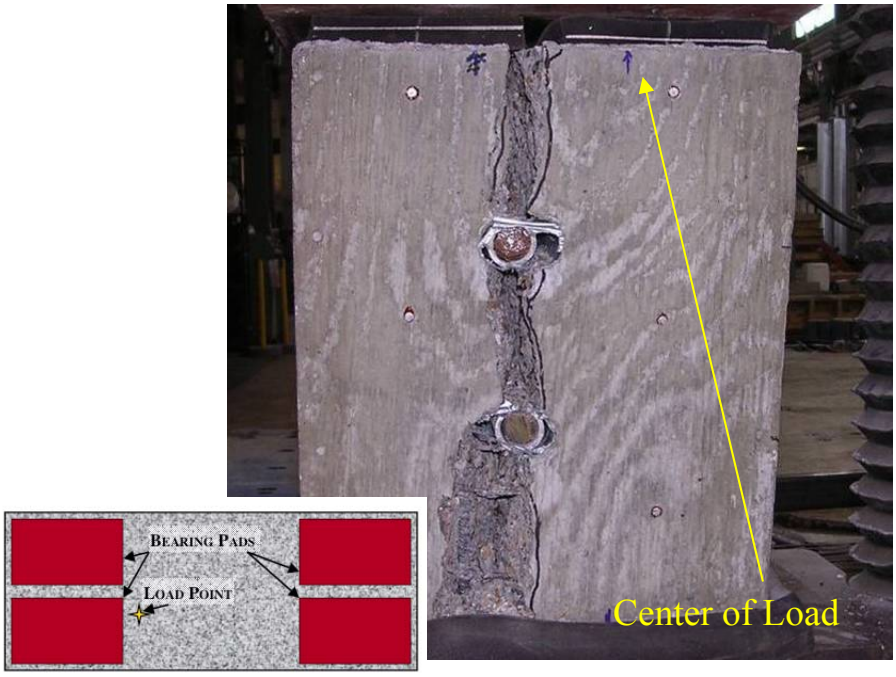

Figure 7.23: Cracked Control's Heavily Loaded Short Side Crack Opens Wide

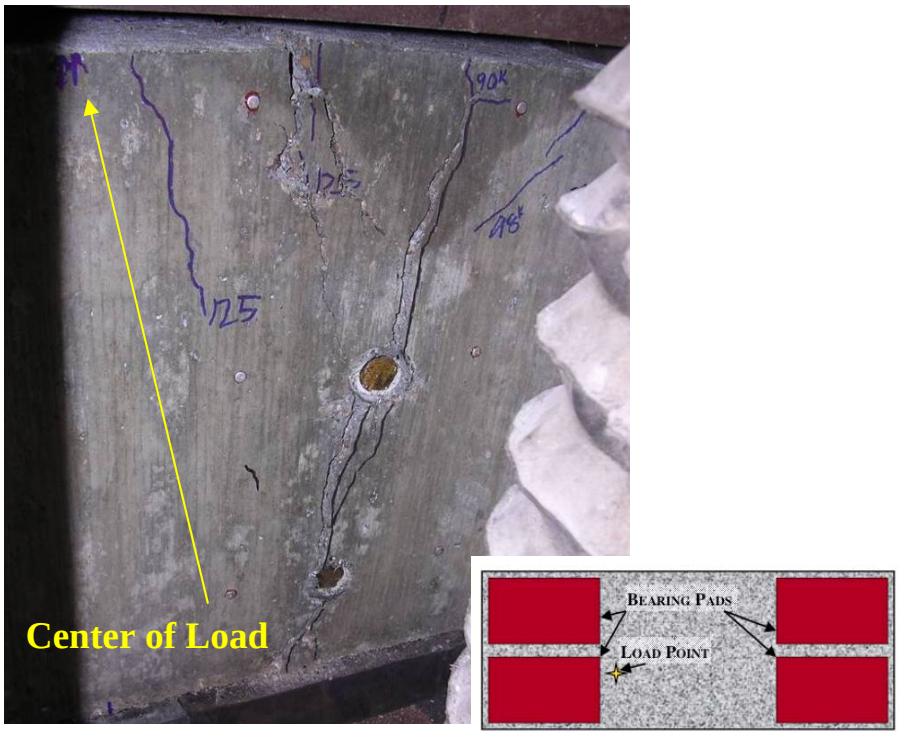

Figure 7.24: Long Side Crack Opens Wide in Cracked Control Specimen

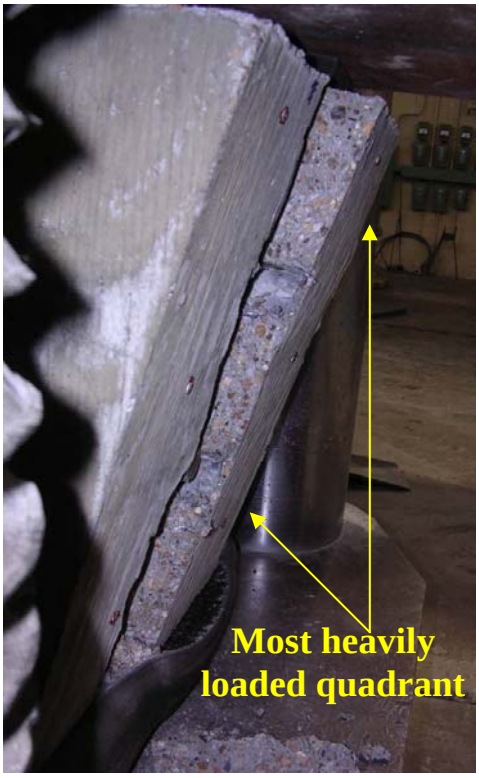

Figure 7.25: Corner (Far Side) Rotating Out from the Cracked Control Specimen

Figure 7.26: Crushing under Heavily Loaded Bearing Pad of Cracked Control

Table 7.2: Summary of Cracked Control Specimen Performance

Specimen	f'c (psi)	Measured Peak Load (kips)	Predicted Bearing Load (kips)	Measured / Predicted	Normalized Peak Load (kips)	Normalized / Undamaged Control
Undamaged Control	7100	315	567	0.56	315	1.00
Cracked Control	6700	284	535	0.53	301	0.96

7.3.3 Packing Strap #1 Specimen

The first specimen repaired with steel pallet strapping was tested on December 17, 2008. Figure 7.27 shows the specimen prior to testing. Prior to repair, the block was pre-

cracked to an average width of 0.09 inches. As with the other specimens, the PVC voids were filled with reinforcing bars. The three concrete cylinders cast from the same batch of concrete as this specimen averaged 5800 psi of strength on the day of testing. Results from the test are given in subsequent sections. After the results from Packing Strap #2 Specimen there is a summary of the overall packing strap repair performance.

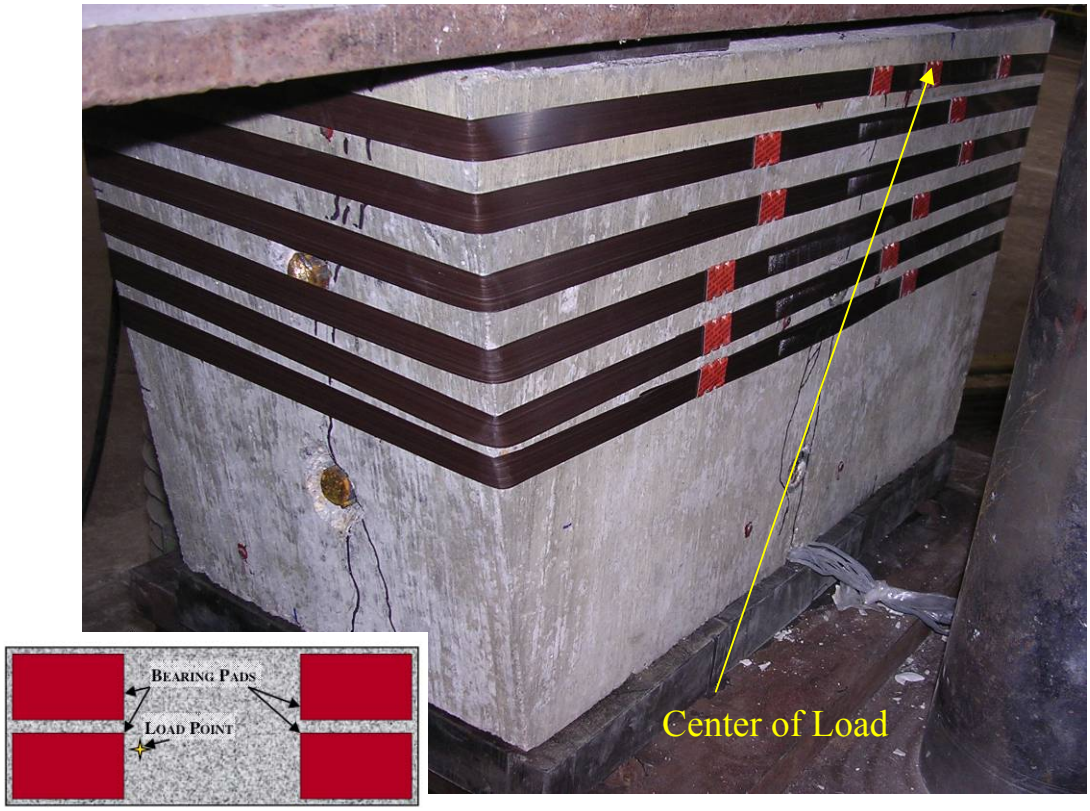

Figure 7.27: Packing Strap #1 Specimen Prior to Testing

7.3.3.1 Strain Measurements

Figure 7.28 and Figure 7.29 present the transverse and longitudinal strain measurements, respectively. Smaller versions of Figure 7.12 are inset in the graphs and show the strain gauge locations within the bearing specimens. Although the packing strap repair failed below the cracked control capacity, the strapping did have a positive effect while in place. Gauges T2 and T4, which monitor the transverse ties on the long sides, started

yielding early, but were then restrained as shown in Figure 7.28. The crack extensions were noted on these long sides at 75 kips and 100 kips for the lighter loaded (T2 side) and heavily load (T4 side), respectively. Thus, it appeared that once the concrete cracked it then was supported by the packing straps, which then carried the lateral load more efficiently. This load carrying improvement was likely due to the better fit between the pallet strap and the concrete, a phenomenon noted by Ramirez[76]. The longitudinal strain measurements, shown in Figure 7.29, again exhibited the unexpected phenomenon of gauge L5 recording more strain than gauge L1 was observed. As L1 also showed less strain than the inclined bars, it lent credence to the theory that the top of this longitudinal bar was not fully underneath the bearing pad. Thus, with the gauge so close to the top of the bar, the stress may not have had the distance from the loading point to evenly distribute to all the longitudinal bars. Also, a local high spot in the top surface could attract more load to an adjacent longitudinal bar and thus L1 was reading an abnormally low value for a bar beneath the most heavily loaded bearing pad. The physical behavior of the specimen, with the most heavily loaded quadrant partially rotating away from the rest of the specimen at failure, showed empirically that the most load was going to the heavily loaded corner as expected. Thus, it appeared that the gauge L1 read an abnormally low value. The longitudinal strain gauges ceased to record reliable strains between 130 kips and 159 kips. These loads correlated with the failure of the long side ties and the packing straps. Likely, the strain gauge leads were damaged in the fracture of the specimen along the long side cracks.

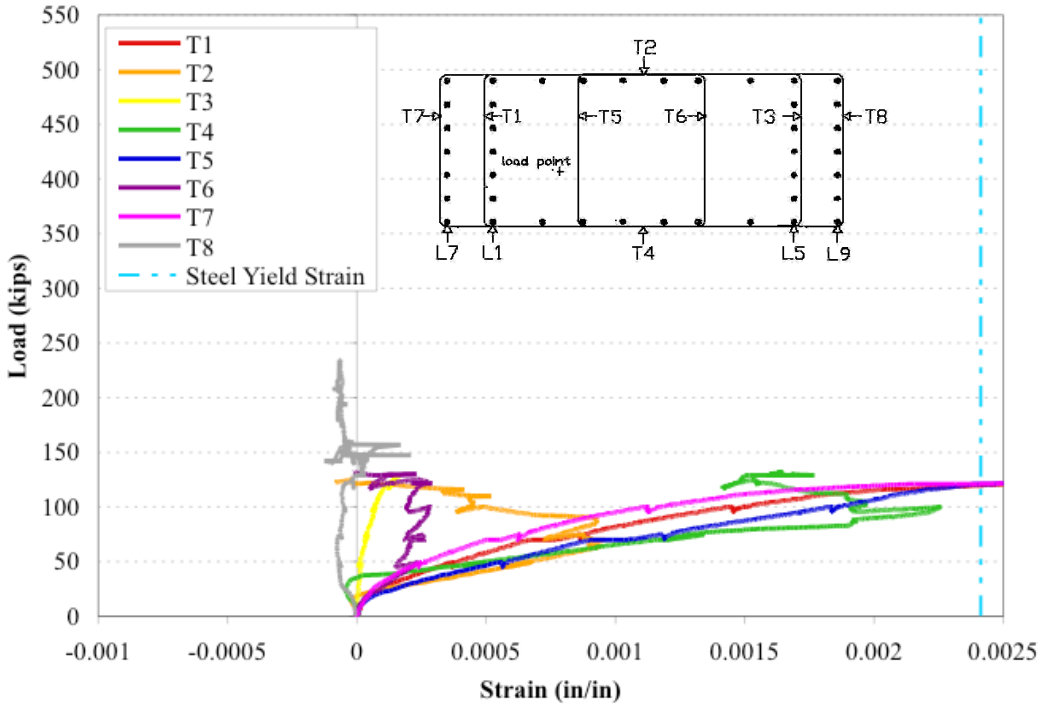

Figure 7.28: Packing Strap #1 Specimen Transverse Strain Measurements

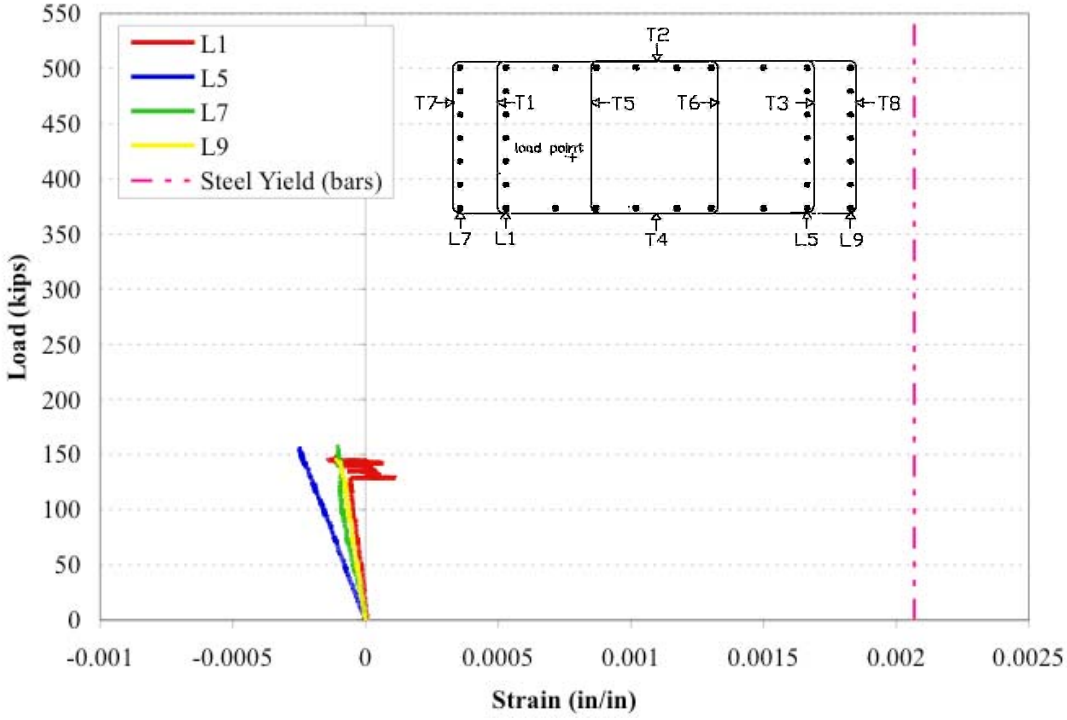

Figure 7.29: Packing Strap #1 Specimen Longitudinal Strain Measurements

For comparison, Figure 7.30 presents the gauges on the long sides, T2 and T4, with the measurements from the same gauges in the control specimens. Figure 7.31 shows the results of two short side gauges, T1 and T7, for comparison between Packing Strap #1 Specimen and the control specimens. These graphs used loads that were normalized to the concrete strength of the undamaged control specimen. Strain gauges T1 and T7, which monitored ties holding the most heavily loaded short side together were compared to the control specimens in Figure 7.31. This figure shows the improvement in performance versus the cracked control specimen. With the external restraint of the packing straps these ties carried load until a normalized top load of 148 kips. Compared to the cracked control specimens, where these ties yielded at 43 kips and 90 kips, the restraint created a 240% and 60% improvement in performance, respectively. The packing strap repair was not able to increase the performance of these short side gauges to the levels observed in the undamaged control, but they did offer a definite improvement over the cracked control behavior.

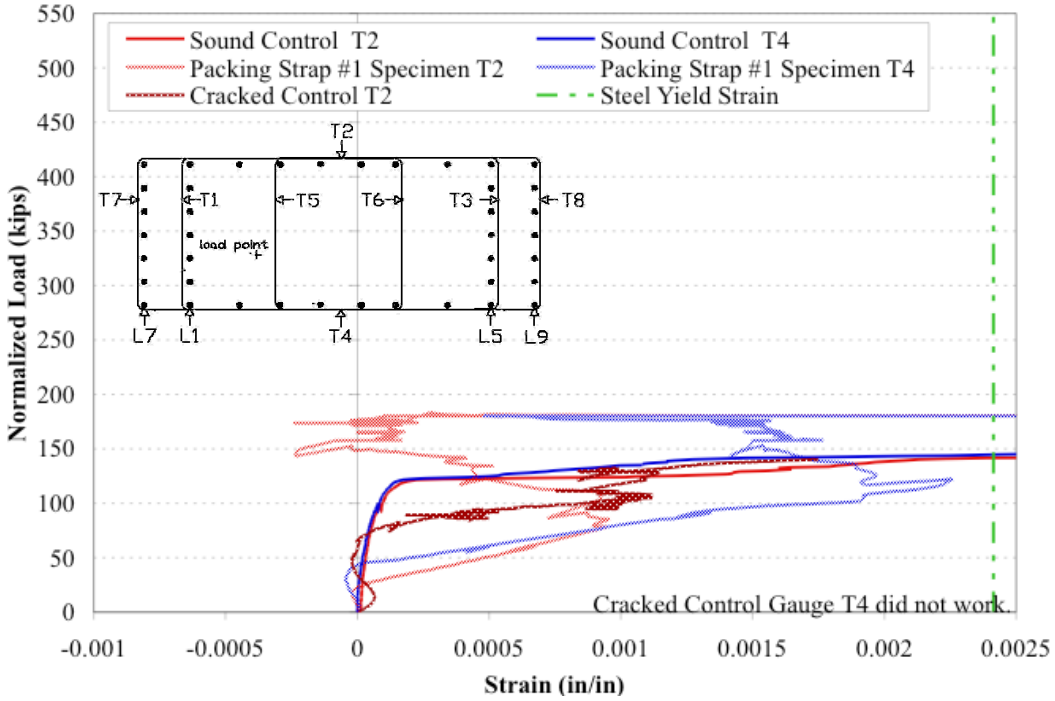

Figure 7.30: Packing Strap #1 Specimen Long Side Gauge Comparison

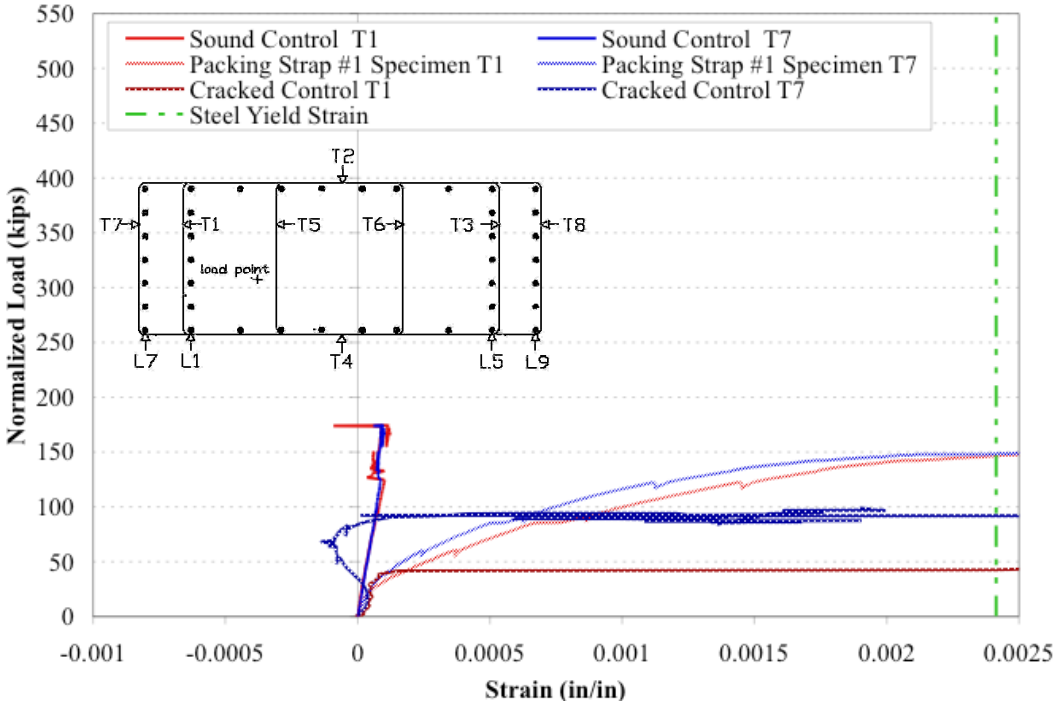

Figure 7.31: Packing Strap #1 Specimen Select Short Side Gauge Comparison

7.3.3.2 Failure

At a load of 75 kips, existing cracks from the splitting wedges extended to the top of the specimen on the less heavily loaded long side. The other long side developed a crack extension that was parallel to the first by a top load of 100 kips. These crack extensions on the specimen's long sides, which were shown being marked in Figure 7.32, were the first new cracks observed due to loading. Pre-existing cracks were marked in black ink and new cracks were marked in blue ink. As the specimen reached 147 kips of applied load, one of the packing straps broke off as shown in Figure 7.33. At 157 kips four additional packing straps broke in rapid succession and the load dropped to 140 kips, whereupon the remaining packing strap broke. Figure 7.34 shows the specimen just after the straps have broken off. The repair had failed at a maximum load of 157 kips. After the packing straps broke, the specimen split open along the long side cracks. Load continued to be added to the specimen until the concrete failed at a load of 239 kips by crushing under the most heavily loaded bearing pad, as shown in Figure 7.35. Table 7.3

shows the performance of Packing Strap #1 Specimen compared to the control specimens. In this table the failure load of the repair was noted since the testing was intended to evaluate the repair's effectiveness. While the packing strap repair helped keep concrete cracks small compared to the cracked control specimen, its early failure did not increase the capacity of the specimen.

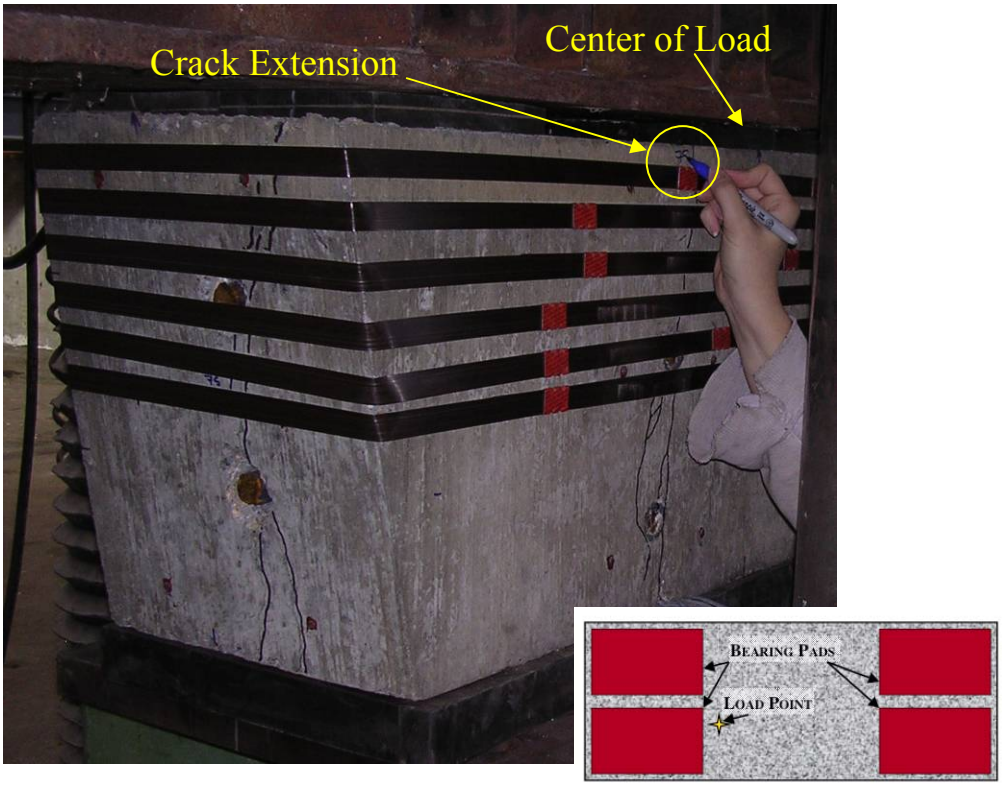

Figure 7.32: Initial Cracking Damage of Packing Strap #1 Specimen

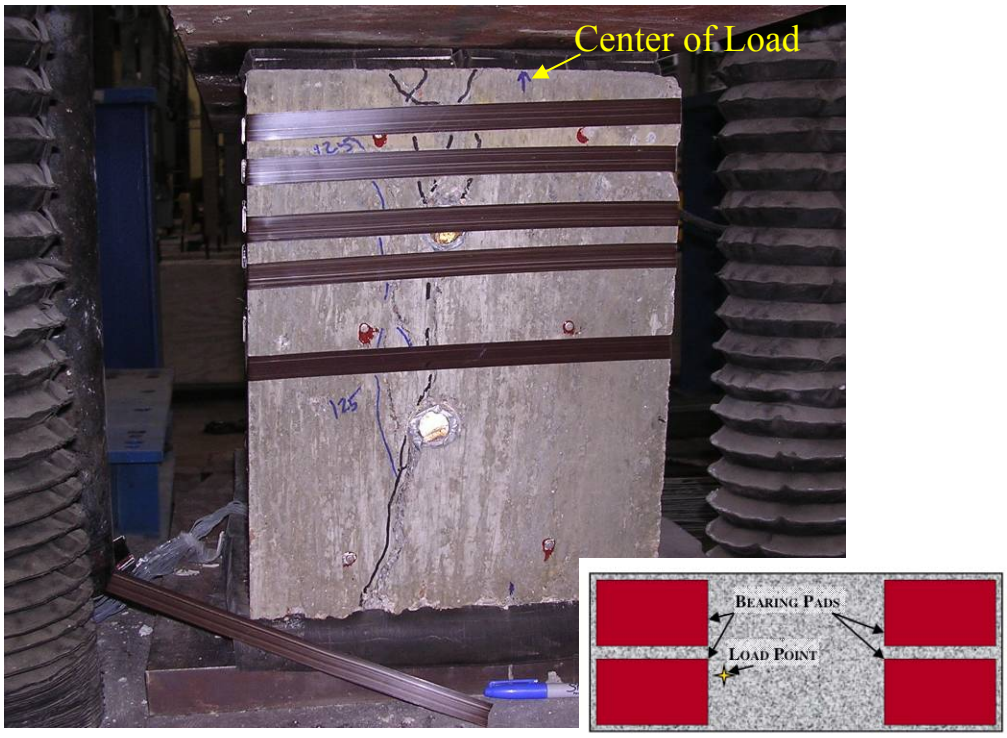

Figure 7.33: One Strap Broken on Packing Strap #1 Specimen

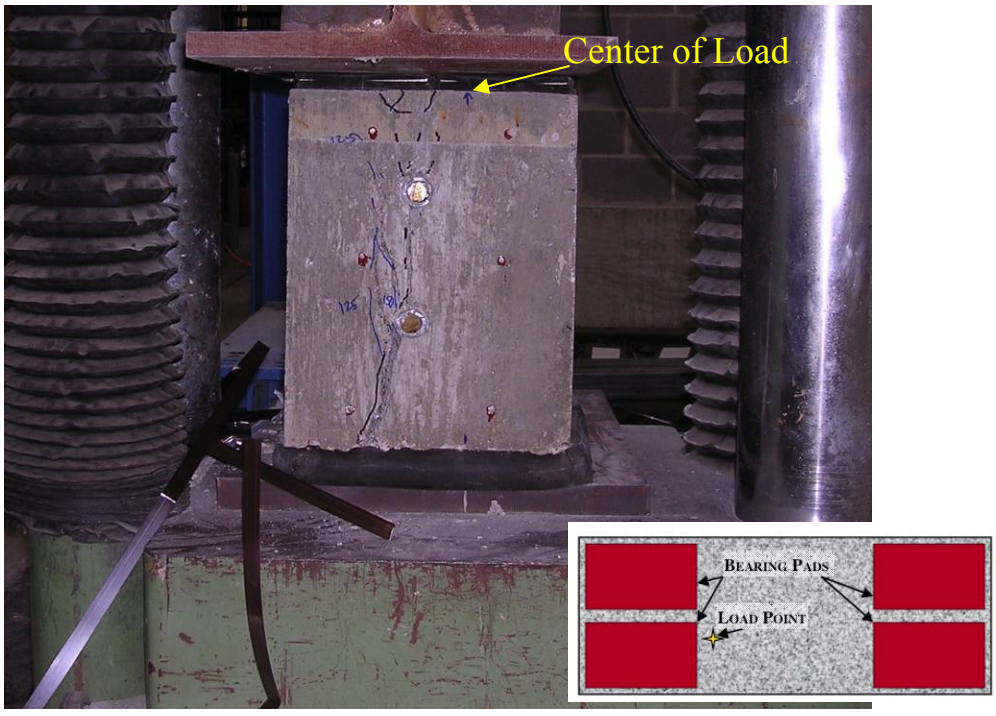

Figure 7.34: All Straps Have Broken on Packing Strap #1 Specimen

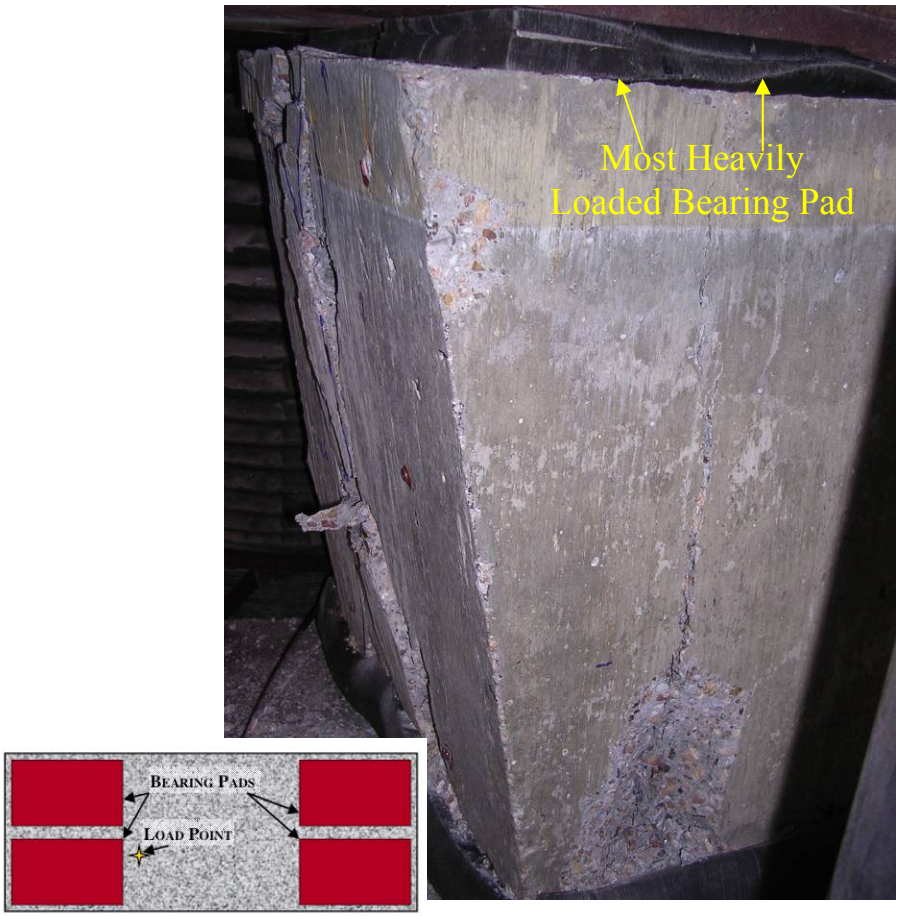

Figure 7.35: Concrete Failure by Crushing Under Heavily Loaded Bearing Pad

Table 7.3: Summary of Packing Strap #1 Specimen Performance

Specimen	f'c (psi)	Measured Peak Load (kips)	Predicted Bearing Load (kips)	Measured / Predicted	Normalized Peak Load (kips)	Normalized / Undamaged Control
Undamaged Control	7100	315	567	0.56	315	1.00
Cracked Control	6700	284	535	0.53	301	0.96
Packing Strap #1 Specimen	5800	157*	455	0.35*	192*	0.61*

* Failure Load of the Repair

7.3.4 Packing Strap #2 Specimen

The second packing strap repair was tested on January 8, 2008. This specimen, shown in Figure 7.36, was a duplicate of the first packing strap specimen. The repetition was intended to increase confidence in the results by allowing the tests to be averaged or trends to be noted. Prior to repair, this block was cracked to an average width of 0.09 inches. As were the other specimens, the PVC voids were filled with reinforcing bars. Three concrete cylinders cast from the same concrete batch averaged 6300 psi on the day of testing. Results from this test can be found in the following sections. Immediately following the failure description of Packing Strap #2 Specimen is a summary of the overall packing strap repair performance.

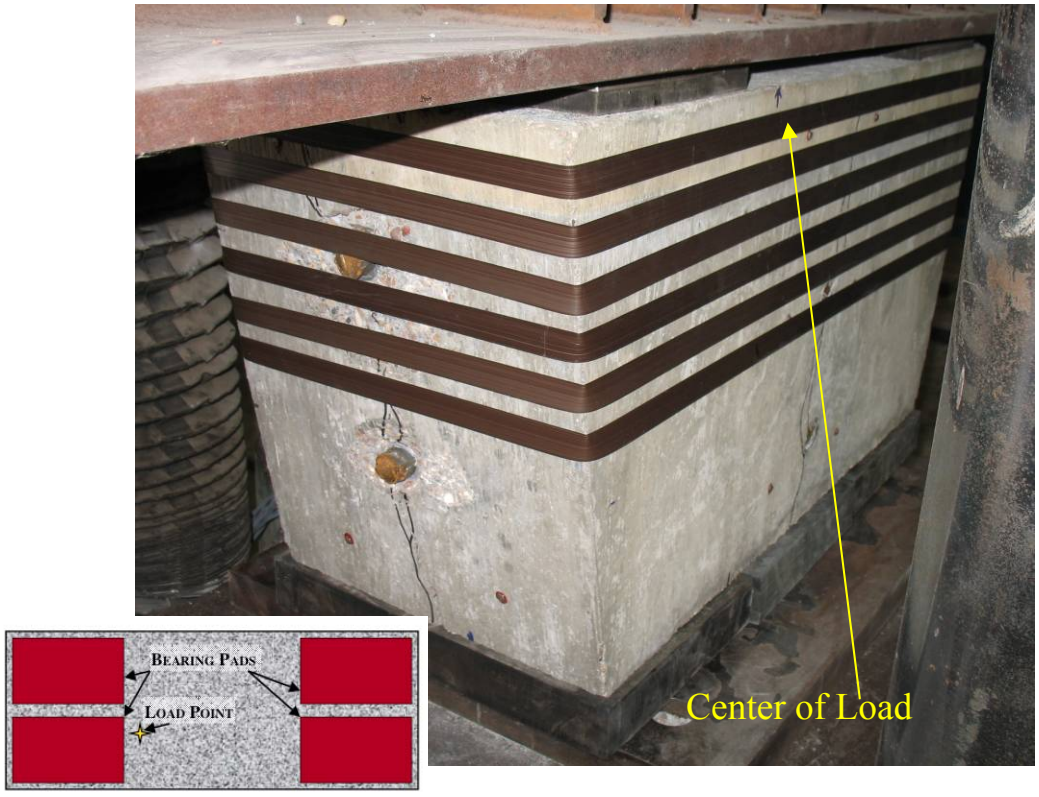

Figure 7.36: Packing Strap #2 Specimen Prior to Testing

7.3.4.1 Strain Measurements

Figure 7.37 and Figure 7.38 present the transverse and longitudinal strain measurements, respectively. Smaller versions of Figure 7.12 were inset in the graphs and show the strain gauge locations within the bearing specimens. Transverse gauge T1 and longitudinal gauge L1 did not work on the day of testing. Unlike Packing Strap #1 Specimen, this duplicate specimen did not show the same restraining effect on the long side gauges T2 and T4. As the earlier restraint came after these ties had begun to yield, it is possible that some of the straps in this specimen were not quite as tight or were not able to engage actively with the concrete to carry lateral loads until the block had gone through a greater deformation than the previous specimen. While the external restraint did not have a significant influence on the long side gauges, it did make an impact on the most heavily loaded short side gauges, as seen in Figure 7.37. At 104 kips of load, gauge T7 showed the effect of restraint. As well, gauge T5 read compressive strain for this tie. By 125 kips, however, the packing straps had begun to break and they did not last past 130 kips of load. With the loss of external restraint, the specimen fractured and many of the strain gauges began reporting random data, which were removed from the graphs.

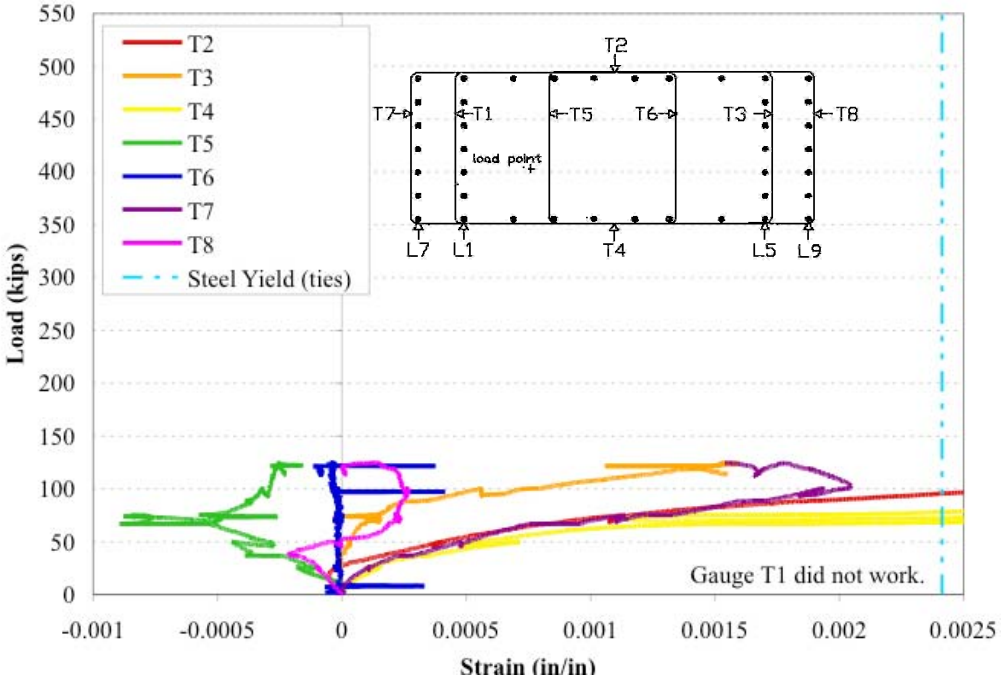

Figure 7.37: Packing Strap #2 Specimen Transverse Strain Measurements

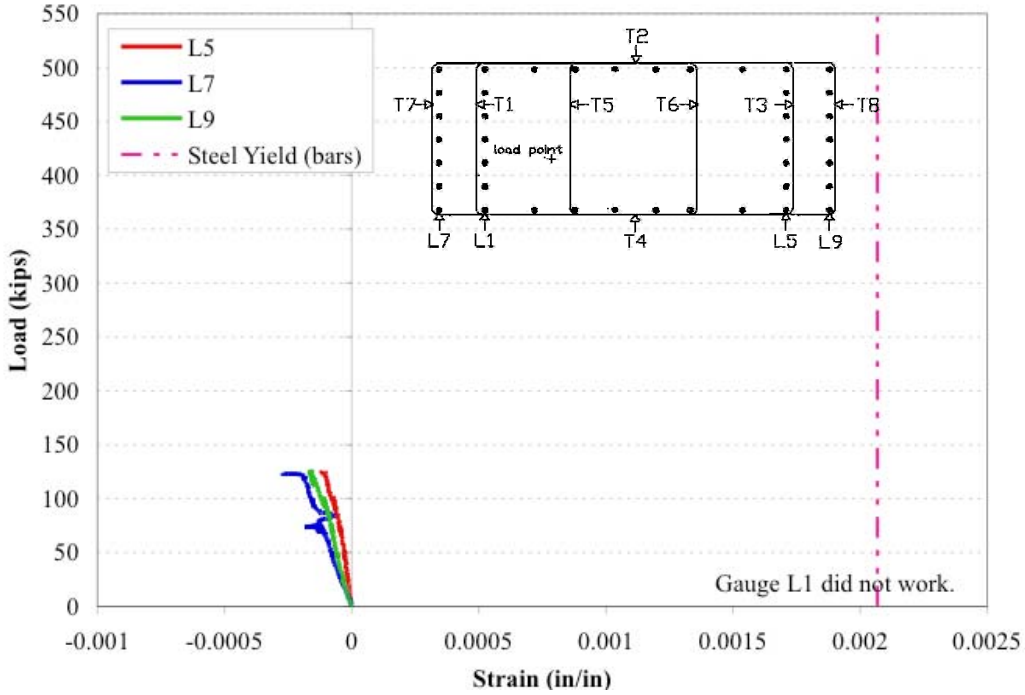

Figure 7.38: Packing Strap #2 Specimen Longitudinal Strain Measurements

For comparison with the control specimens, Figure 7.39 and Figure 7.40 show the behavior of long side and select short side strain gauges, respectively. The loads used in this comparison were normalized to the concrete strength of the undamaged control specimen. Figure 7.39 shows that the external restraint did not have a significant effect on the strain carried by the transverse ties on the long sides compared to the performance of the control specimens. Figure 7.40 compares the selected short side gauges with the control specimens. In this figure the effect of restraint is clearly shown in the behavior of gauge T7. With the restraint, the yielding behavior was more gradual and required a higher normalized load to failure versus the cracked control specimen (140 kips to 43 kips or 90 kips).

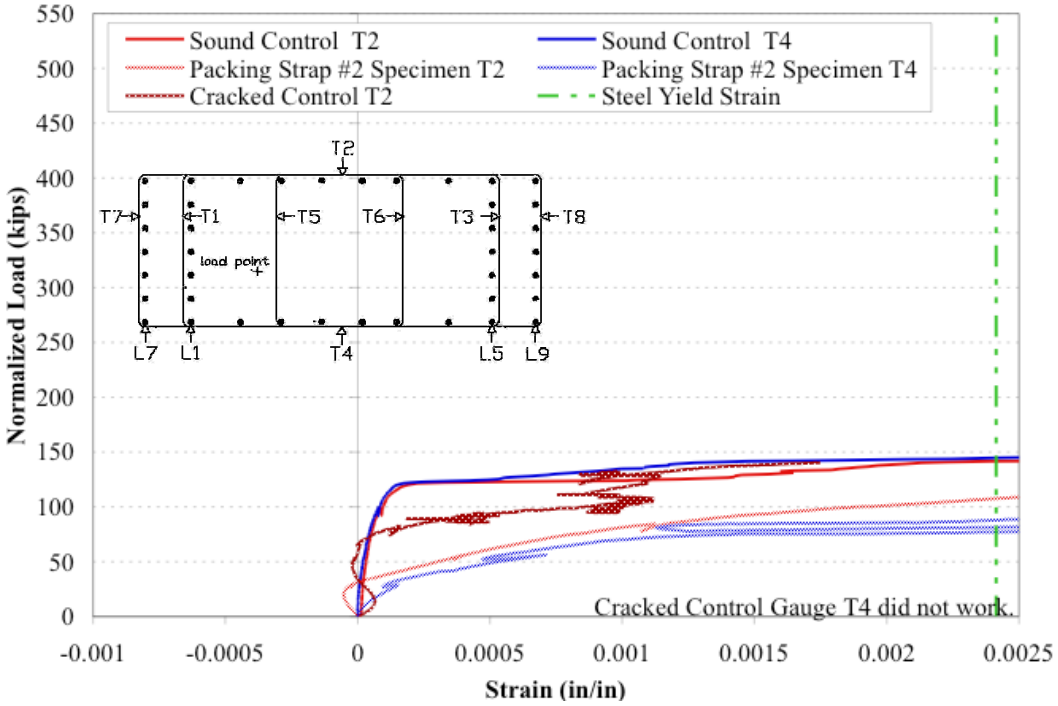

Figure 7.39: Packing Strap #2 Specimen Long Side Gauge Comparison

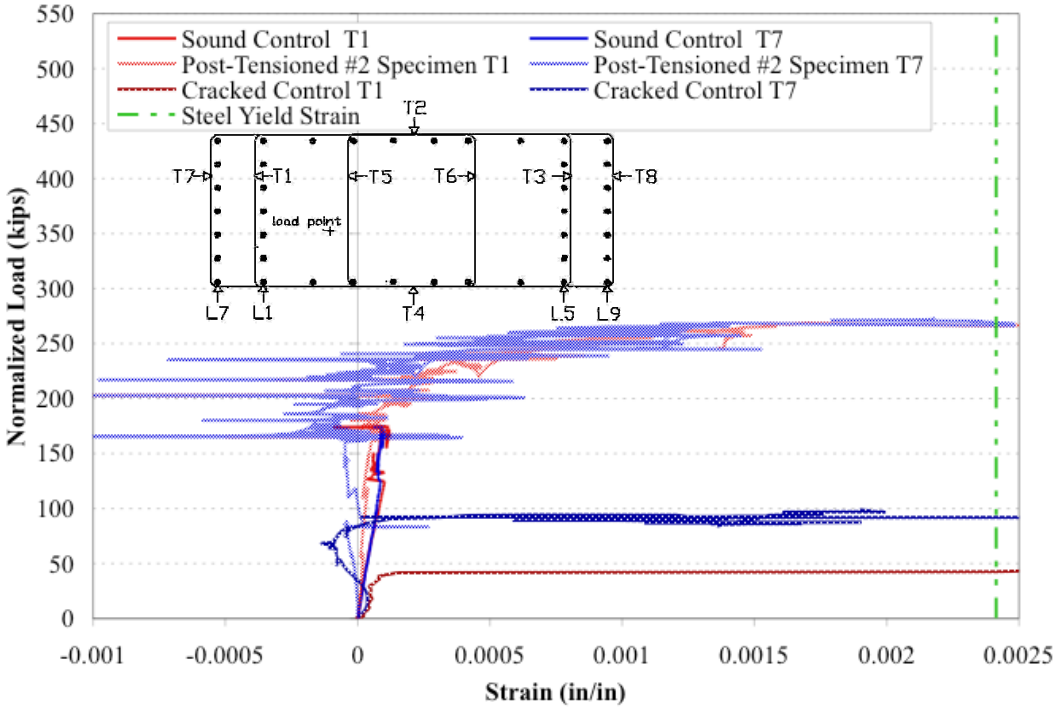

Figure 7.40: Packing Strap #2 Specimen Select Short Side Gauge Comparison

7.3.4.2 Failure

Crack extensions on both long faces were again the new cracking damage observed during loading. For this specimen the cracks, which are shown in Figure 7.41, were noted at 50 kips. At 125 kips three packing straps broke as shown in Figure 7.42, causing a loss in load. As the specimen regained the 125 kip load, a fourth packing strap broke off as shown in Figure 7.43. The last two straps broke off and a spall formed at the base of the most heavily loaded short side at 130 kips, as shown in Figure 7.44. Thus, for the second packing strap specimen, the repair reached an ultimate load of 130 kips. After the straps broke, the specimen fractured along the existing long side cracks. Even after fracture, the specimen continued taking load until the concrete failed by crushing under the most heavily loaded bearing pad at 305 kips, as shown in Figure 7.45. Table 7.4 presents a summary of Packing Strap #2 Specimen's performance. The failure load reported for this specimen is that of the repair since the test was conducted to evaluate the repair's effectiveness.

Figure 7.41: First New Cracks on Packing Strap #2 Specimen

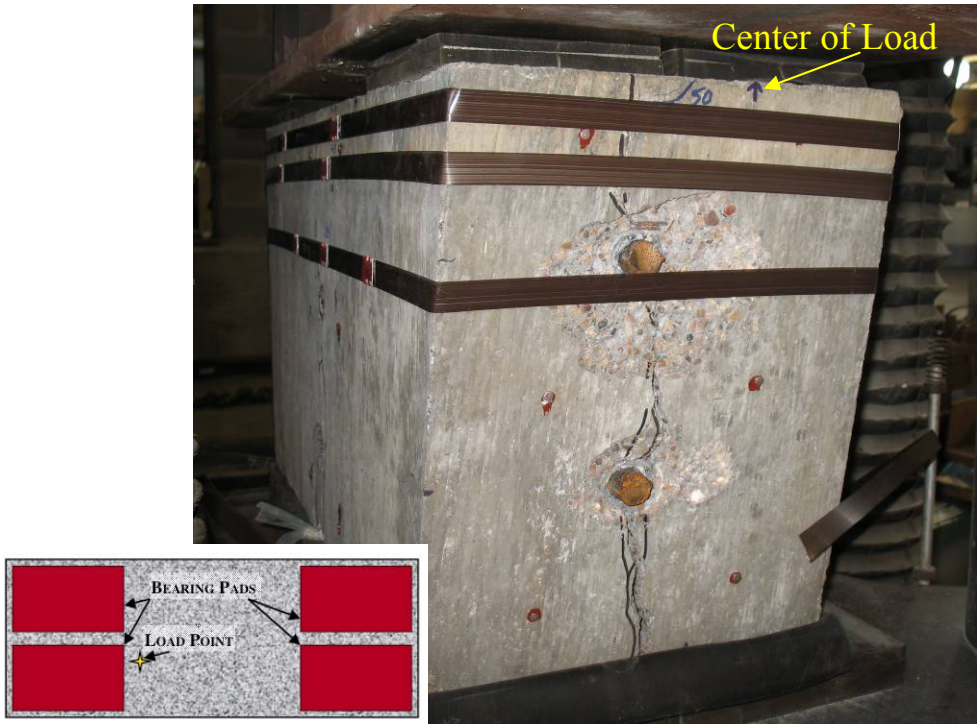

Figure 7.42: Packing Strap #2 Specimen after Initial Strap Breakage

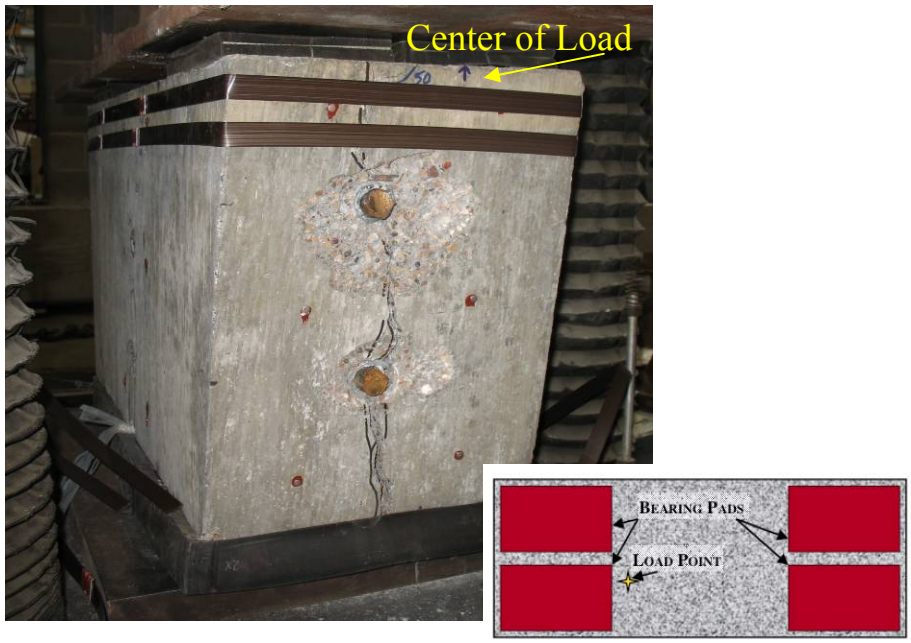

Figure 7.43: Last Two Packing Straps of Packing Strap #2 Specimen

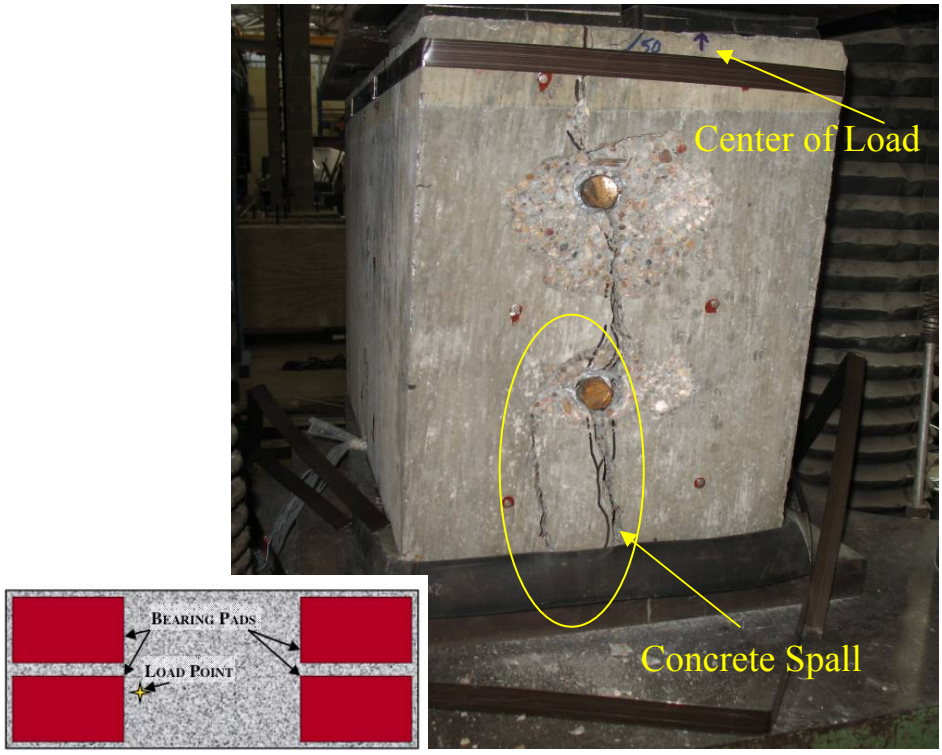

Figure 7.44: Spalling at the Base of Heavily Loaded End as the Last Straps Broke

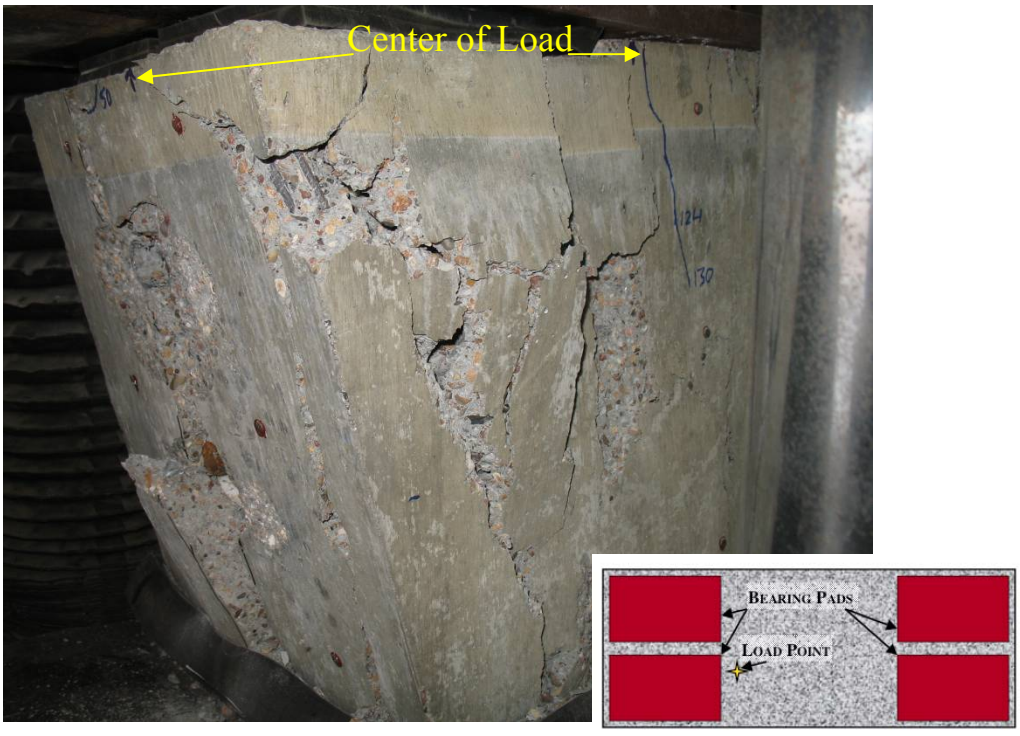

Figure 7.45: Packing Strap #2 Specimen Concrete Failure

Table 7.4: Summary of Packing Strap #2 Specimen Performance

Specimen	f'c (psi)	Measured Peak Load (kips)	Predicted Bearing Load (kips)	Measured / Predicted	Normalized Peak Load (kips)	Normalized Undamaged Control
Undamaged Control	7100	315	567	0.56	315	1.00
Cracked Control	6700	284	535	0.53	301	0.96
Packing Strap #2 Specimen	6300	130*	503	0.26*	147*	0.47*

* Failure Load of the Repair

7.3.5 Packing Strap Repair Summary

Figure 7.46 and Figure 7.47 show the comparison of long side and short side gauges, respectively. These comparisons used normalized loads and showed the performance of both packing strap specimens along with the control specimens. Figure 7.46 clearly shows the variability in results from using the hand strap tightening tools. Having treated the two specimens identically, one was able to restrain the yielding at gauges T2 and T4 until the specimen was at a higher load than the yielding of the undamaged control specimen whilst the other packing strap specimen exhibited yielding below the yielding load of the cracked control specimen. For the short side gauges, however, both packing strap specimens had short side yielding at approximately the same load, as shown in Figure 7.47. This uniformity suggests that over the shorter length of the short side, the packing straps were more likely to get a consistent tension. The least loaded long side of the specimen was the location of the strap tensioning and clamps, which could also have caused the difference of behavior. Thus, the long side farthest from the load point (the more lightly loaded side), which is where all the clamps were located, always had a little more slack than the other sides. This additional slack might be the source of variability in the results.

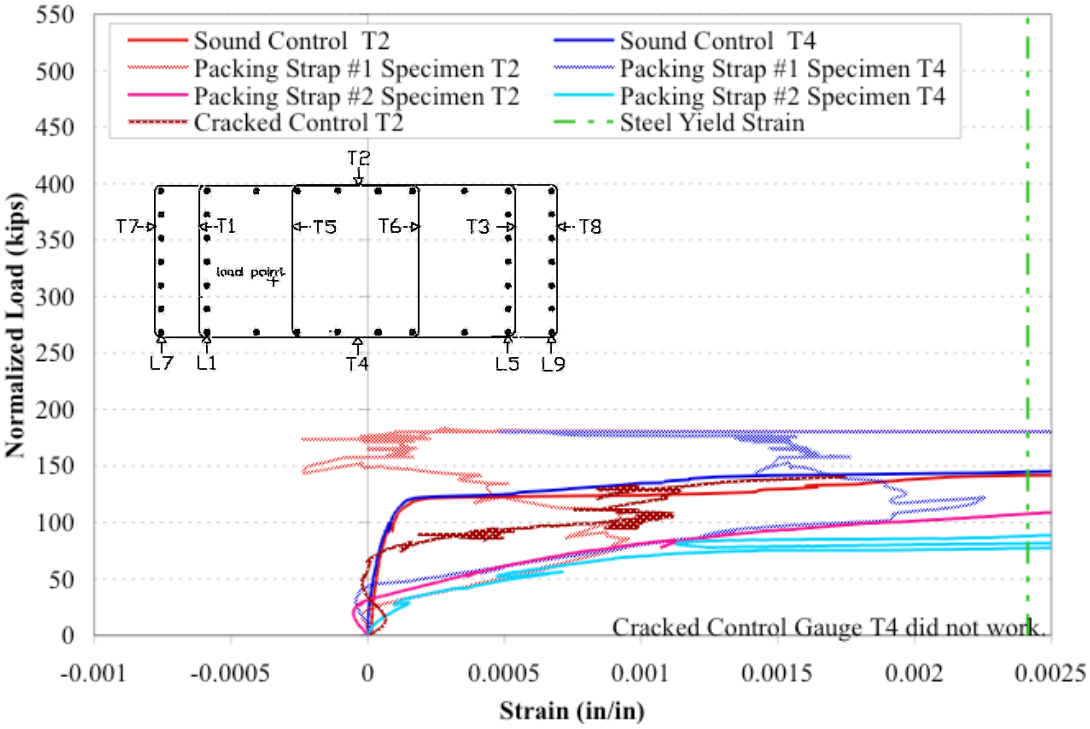

Figure 7.46: Packing Strap Repairs Long Side Strain Gauge Comparison

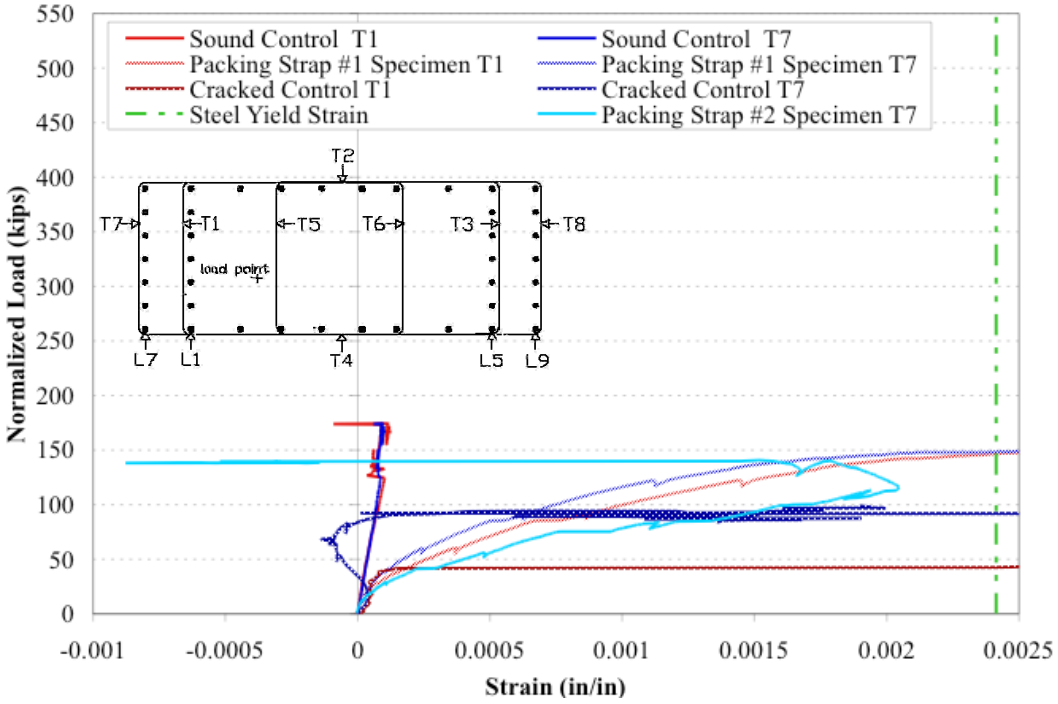

Figure 7.47: Packing Strap Repairs Select Short Side Strain Gauge Comparison

The packing straps, when present, did prevent the cracks from opening wide and retarded yielding of some ties as discussed in the individual specimen results. Once the straps broke off, however, the cracks caught up with the wide widths of the cracked control specimen. Inspection of the broken straps showed that all breaks occurred in the corners where the metal straps were bent, as shown in Figure 7.48 and Figure 7.49. The bend might have decreased the ductile capacity of the straps by further working the metal. The straps also wrapped around tapered specimens. Thus, there was a stress concentration at the upper edge of the straps, causing them to fracture below the manufacturer's design load, which assumes uniform stress distribution. This repair would likely be more effective if not applied to a tapered column so that there is not a stress concentration at one edge of the strap. As well, if a mechanized tightener were used, the repair would not have needed to have the internal ties begin to yield before it could efficiently transfer force. With hand tools used for tightening there was always some extra room needed between the strap and the concrete for attaching the metal clips and for the base plate of the tightening tool. A mechanized system could likely post-tension the strap so that the extra room needed for attaching the clip would immediately be taken out of the system.

Figure 7.48: Packing Strap Corner Damage from Packing Strap #1

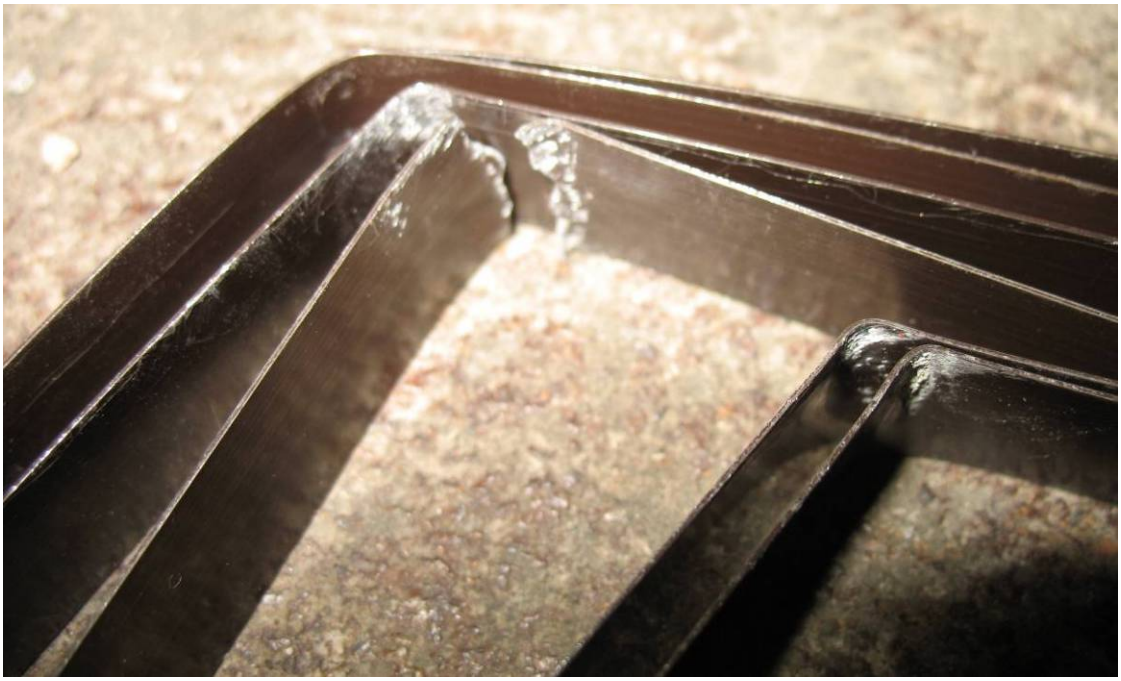

Figure 7.49: Packing Strap Corner Damage from Packing Strap #2

Both packing strap repairs failed at lower loads than the cracked control failure load. The average packing strap repair failure load was 144 kips and the cracked control failure load was 284 kips. Even when the different concrete strengths of the specimens were taken into account, as shown in Table 7.5, the packing strap repairs failed at a low load. By normalizing the failure loads of the repairs to the concrete strength of the undamaged control specimen, Table 7.5 was developed. The normalized average load of the repair failure was 170 kips, which was only 54% of the undamaged control load of 315 kips.

Table 7.5: Summary of Packing Strap Specimen Performance

Specimen	f'c (psi)	Measured Peak Load (kips)	Predicted Bearing Load (kips)	Measured / Predicted	Normalized Peak Load (kips)	Normalized Undamaged Control
Undamaged Control	7100	315	567	0.56	315	1.00
Cracked Control	6700	284	535	0.53	301	0.96
Packing Strap #1 Specimen	5800	157*	455	0.35*	192*	0.61*
Packing Strap #2 Specimen	6300	130*	503	0.26*	147*	0.47*
ASR/DEF Column A	6000	491	479	1.03	581	1.84
ASR/DEF Column B	5800	480	455	1.05	588	1.87

* Failure Load of the Repair

7.3.6 FRP #1 Specimen

The first test of a specimen repaired with FRP occurred on January 10, 2008. Figure 7.50 shows the specimen prior to testing. Before the specimen was repaired, it was pre-cracked to an average width of 0.08 inches. The PVC voids were filled with reinforcing bar prior to the FRP application. Tests of three concrete cylinders cast from the same batch as the specimen averaged 6600 psi on the day of testing. The results from the tests are found in the following sections. Immediately following the results from FRP #2 Specimen is a summary of the overall FRP repair performance.

Figure 7.50: FRP #1 Specimen Prior to Testing

7.3.6.1 Strain Measurements

Figure 7.51 and Figure 7.52 present the transverse and longitudinal strain measurements, respectively. Smaller versions of Figure 7.12 were inset in the graphs and show the strain gauge locations within the bearing specimens. The significant impact that the FRP wrap made on the specimen performance can be seen in Figure 7.51. Strains were retrained from yielding until over 200 kips of load was applied. The restraining effect of the repair was able to quickly become effective as the repair was applied using a wet lay-up technique, which allows the fabric to follow the contours of the specimen with nearly zero slack. In the longitudinal bar strains, shown in Figure 7.52, gauge L1 behaved as expected by carrying the greatest strains. That the gauges on the inclined bars, L7 and L9

recorded greater strains than L5 indicated that the external restraint from the FRP wrap was contributing to the lateral compression of the specimen corners. As the gauges on the inclined bars were oriented along the bars' length, the gauges recorded a combination of strain from the top loading and resulting lateral forces in the specimens.

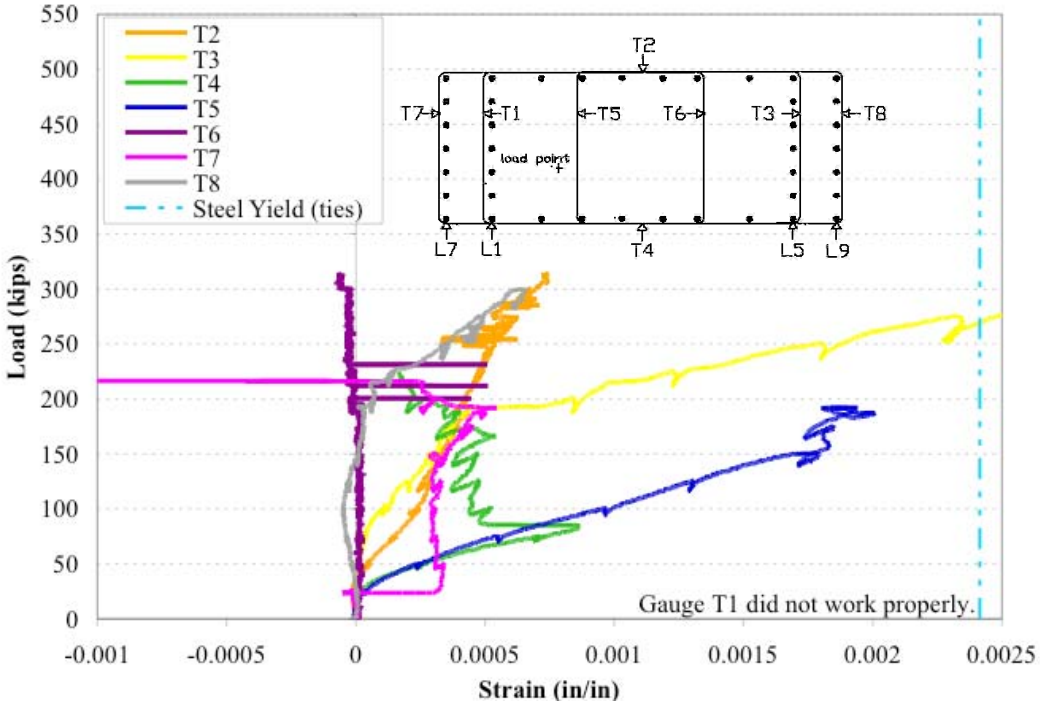

Figure 7.51: FRP #1 Specimen Transverse Strain Measurements

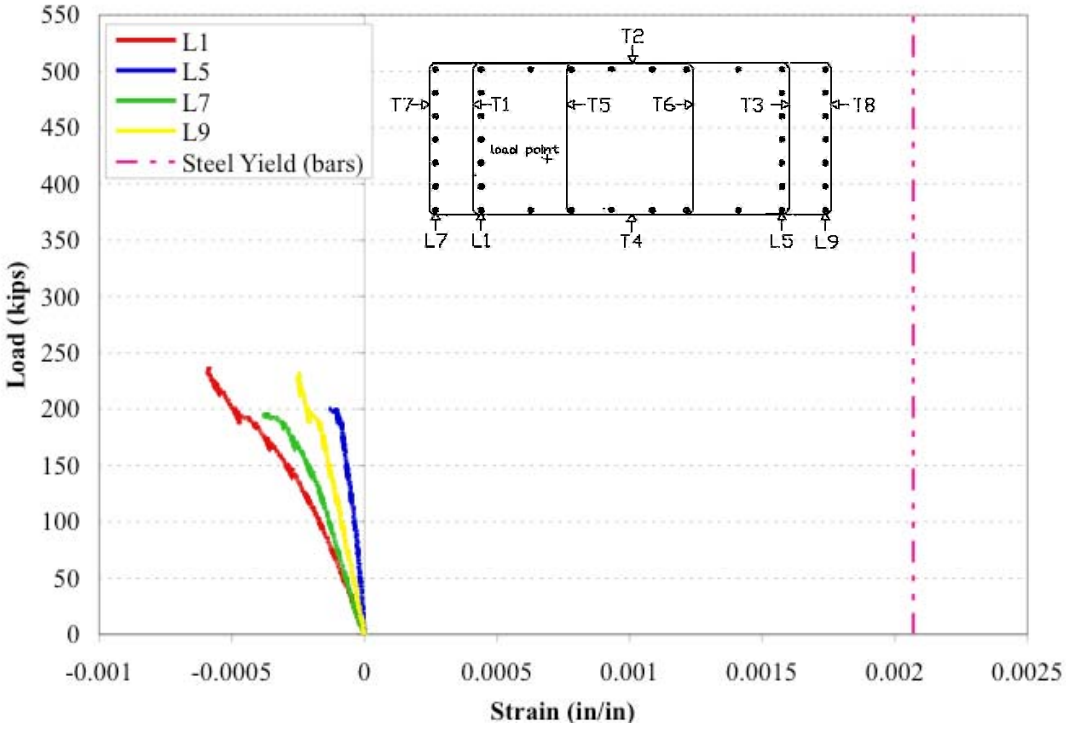

Figure 7.52: FRP #1 Specimen Longitudinal Strain Measurements

Figure 7.53 and Figure 7.54 present comparisons of strain gauge measurements for long and select short side gauges, respectively. These comparisons with the performance of the control specimens used loads that were normalized to the concrete strength of the undamaged control specimen. Figure 7.53 shows the remarkable influence of the FRP repair in the long side strain gauges. FRP #1 Specimen gauge T2 did not yield throughout the test. This strain behavior represented the physical behavior of the specimen. Unlike the previous tests, FRP #1 Specimen did not fracture into two blocks during testing. Instead the specimen failed by fracturing the repair on the most heavily loaded short side and crushing the confined concrete in this location. Figure 7.54 shows the restraining effect on the short side from when it first engaged at the normalized load of 25 kips until the gauge stopped reporting at the normalized load of 232 kips. The FRP wrap kept the strain increase at this location very small, in a manner close to the undamaged specimen strain behavior.

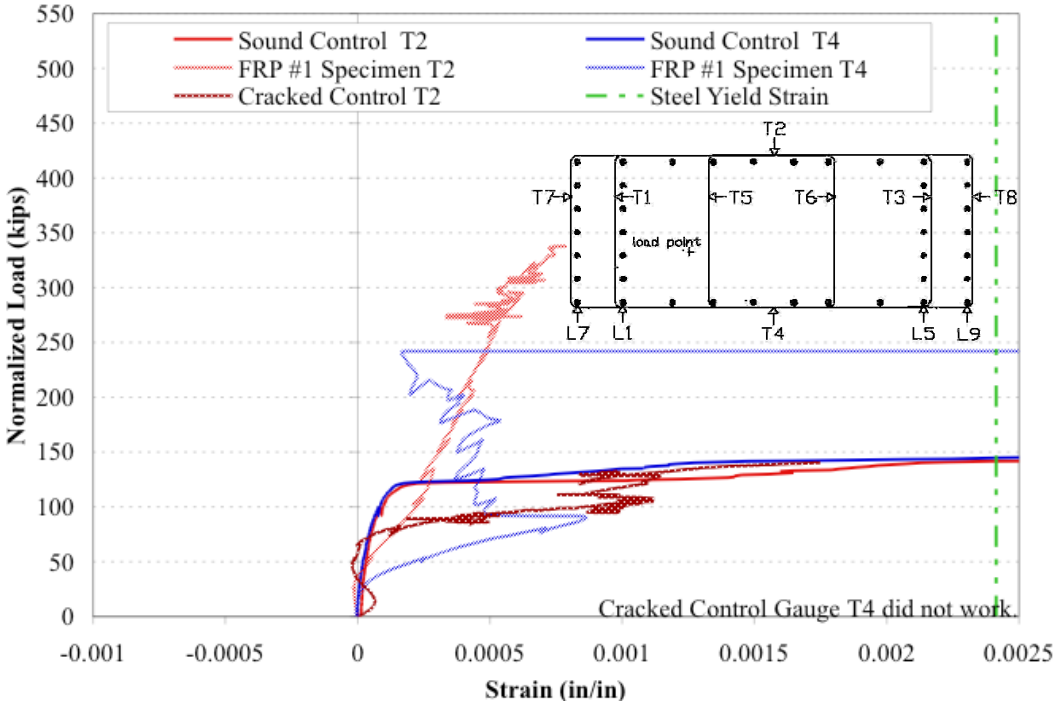

Figure 7.53: FRP #1 Specimen Long Side Gauge Comparison

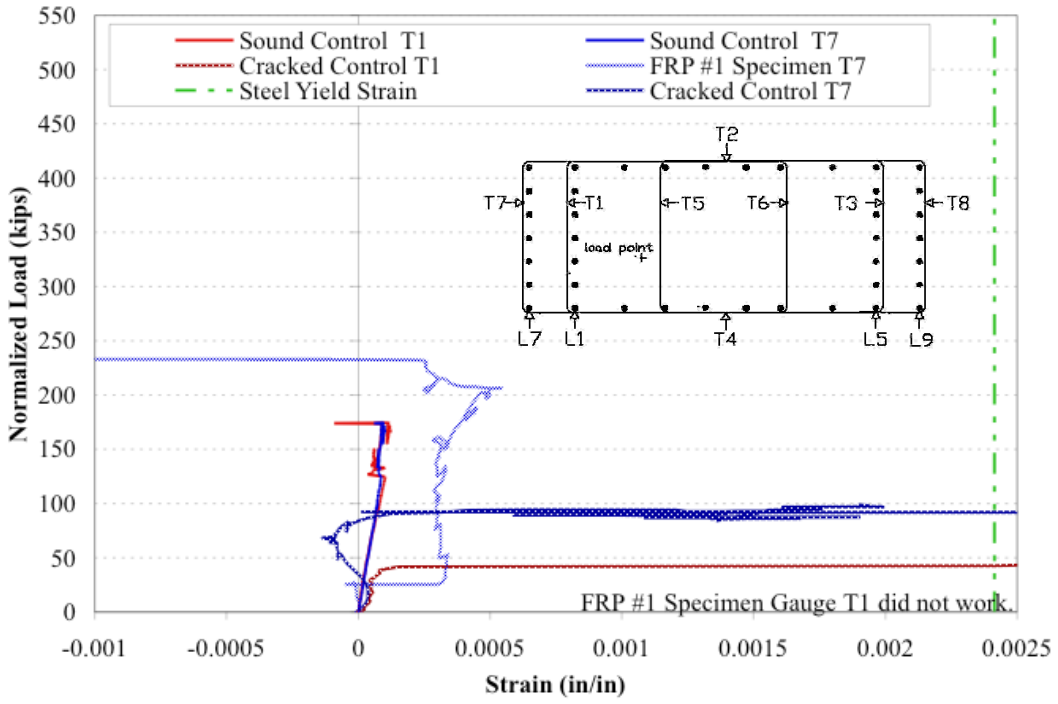

Figure 7.54: FRP #1 Specimen Select Short Side Gauge Comparison

7.3.6.2 Failure

At 125 kips of load, a small curved crack was noted at the bottom edge of the FRP repair on the heavy long side of FRP #1 Specimen (the load point was nearest this long side), as shown in Figure 7.55. This cracking, which appeared to be the edge of a small spall under the FRP repair, was the first damage to FRP #1 Specimen. The pre-existing cracking, from the splitting wedge damage, was marked in black ink and the new cracking, from the testing, was marked in blue ink in the pictures. At 275 kips, new cracks developed in the exposed concrete on the most heavily loaded short side of the specimen, as shown in Figure 7.56. This picture also shows the pre-existing cracks, which were marked in black ink, opening wide. As shown in Figure 7.57, at 311 kips the FRP fibers had begun to fracture on the most heavily loaded short side of the specimen. The fractured fibers appeared grey-white among the black carbon fiber strands. By 317 kips the repair had completely torn at this location, as shown in Figure 7.58, and the specimen failed. Table 7.6 presents a summary of FRP #1 Specimen performance along with the performance of the control specimens for comparison. The repair caused the specimen to exceed the capacity of the undamaged control specimen and thus achieved the goal of the repair testing.

Figure 7.55: Initial Damage of FRP #1 Specimen

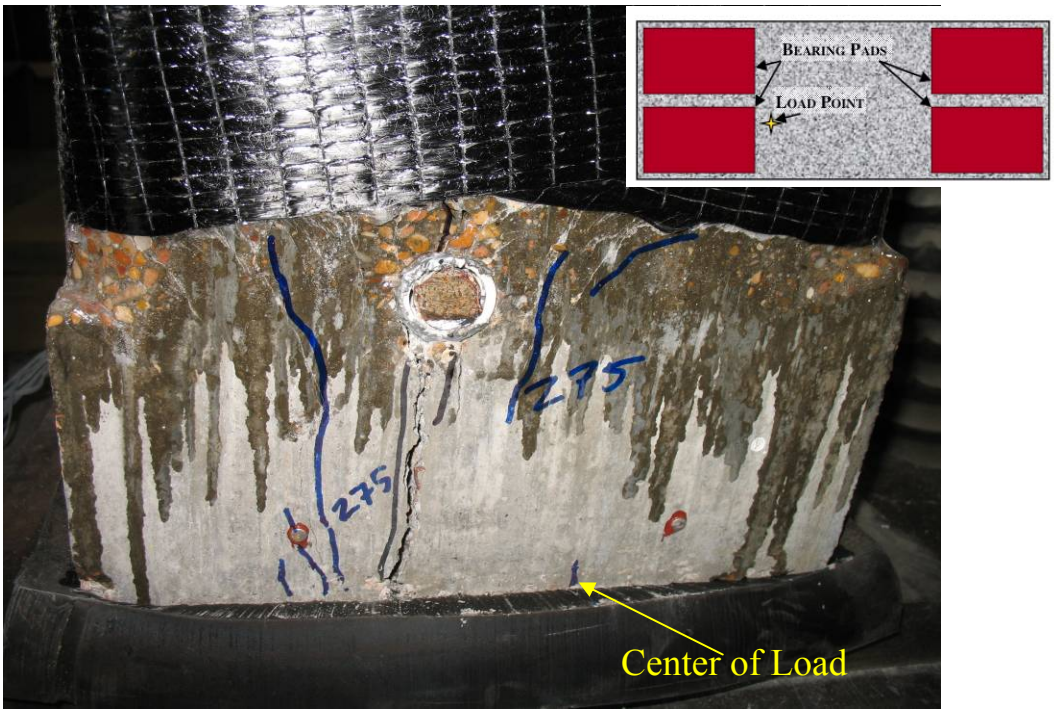

Figure 7.56: Additional Cracking in FRP #1 Specimen

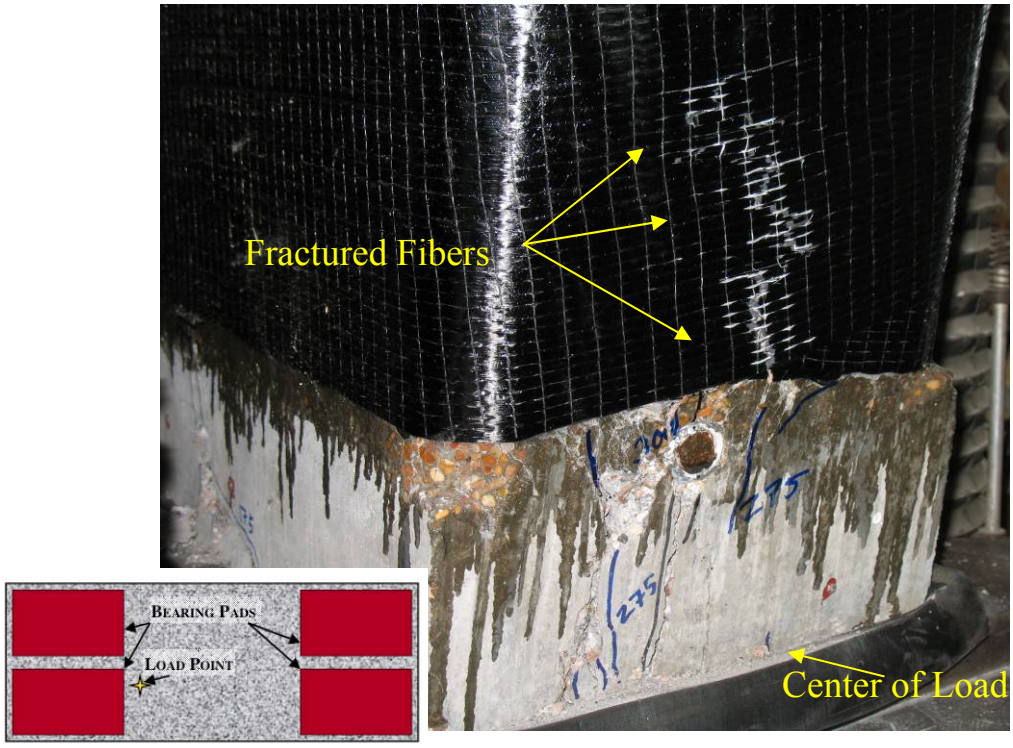

Figure 7.57: Fractured Fibers in FRP #1 Specimen

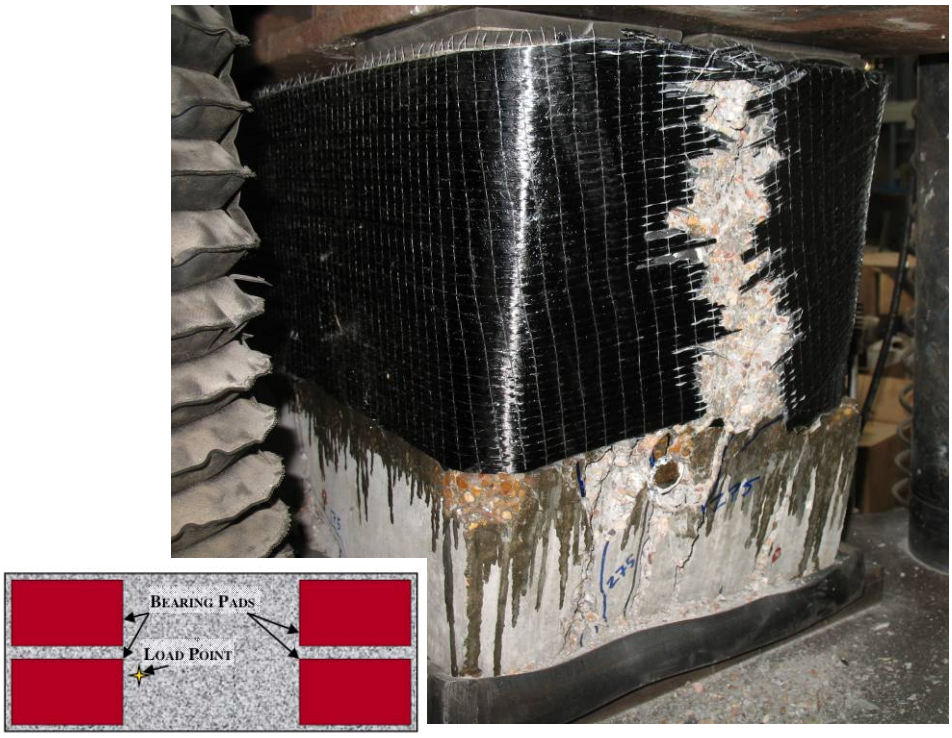

Figure 7.58: Failure of FRP #1 Specimen

Table 7.6: Summary of FRP #1 Specimen Performance

Specimen	f'c (psi)	Measured Peak Load (kips)	Predicted Bearing Load (kips)	Measured / Predicted	Normalized Peak Load (kips)	Normalized / Undamaged Control
Undamaged Control	7100	315	567	0.56	315	1.00
Cracked Control	6700	284	535	0.53	301	0.96
FRP #1 Specimen	6600	317	527	0.60	341	1.08

7.3.7 FRP #2 Specimen

The second specimen repaired with FRP was tested on January 14, 2008. Figure 7.59 shows FRP #2 Specimen prior to testing. This specimen was intended as a duplicate to the first FRP specimen in order to increase confidence in the results. Prior to the repair, the block was pre-cracked to an average width of 0.11 inches. As was the case with the other FRP specimen, the PVC voids were filled with reinforcing bar prior to application of the repair. Tests of three concrete cylinders cast from the same batch of concrete as

this specimen had an average strength of 6200 psi on the day of testing. The results from the test are shown in the subsequent sections. Following the results of this specimen is a summary of overall FRP repair performance.

Figure 7.59: FRP #2 Specimen Prior to Testing

7.3.7.1 Strain Measurements

Figure 7.60 and Figure 7.61 present the transverse and longitudinal strain measurements, respectively. Smaller versions of Figure 7.12 were inset in the graphs and show the strain gauge locations within the bearing specimens. As was the case for the previous FRP repaired specimen, the FRP wrap on this specimen also helped restrain the strains in the ties by confining the specimen. Although Figure 7.60 shows gauge T2 indicating yielding of the long side tie, a fracture through the long side of the specimen never occurred. The other long side gauge, T4, exhibited significant restraint, hovering near zero new strain while the gauge was still recording meaningful values. On the short side, the monitored ties all exhibited increasing strains towards yield, although they did not pass the steel yield strain. Gauge T7, which monitored the exterior tie of the most

heavily loaded short side, continued to record strains below yielding through the maximum load, indicating that although the specimen failed due to FRP fracture on this side, the underlying tie was not fractured.

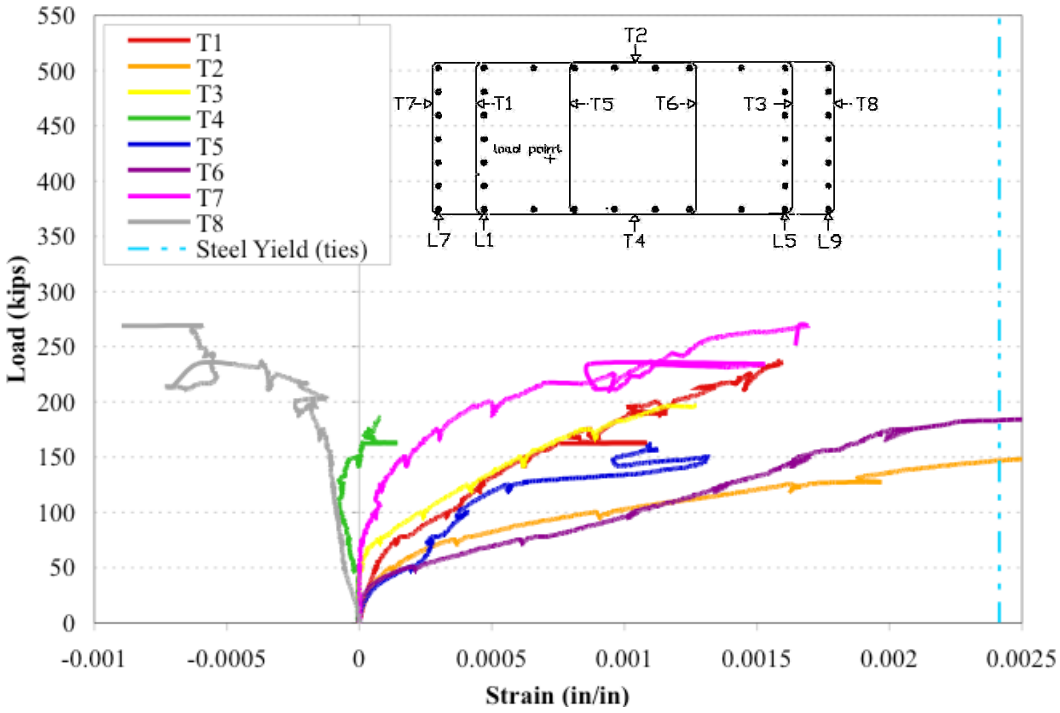

Figure 7.60: FRP #2 Specimen Transverse Strain Measurements

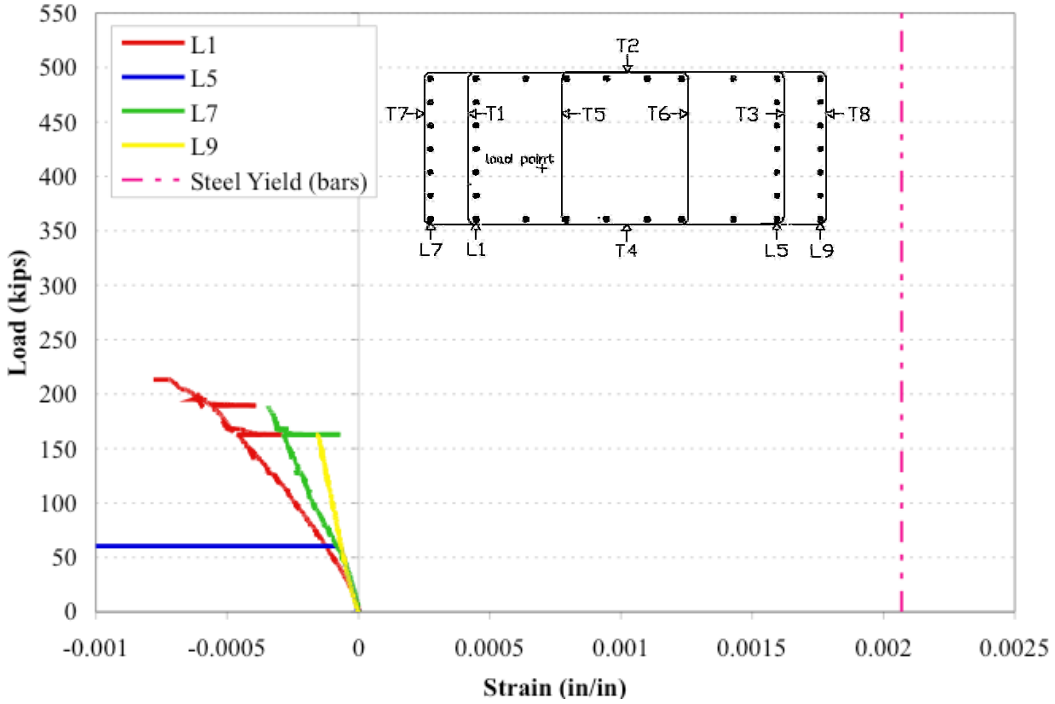

Figure 7.61: FRP #2 Specimen Longitudinal Strain Measurements

Figure 7.62 and Figure 7.63 present the long side and select short side strain gauge measurements, respectively, of FRP #2 Specimen along with results from the same gauges in the control specimens. For these comparison graphs, the loads were normalized to the concrete strength of the undamaged control specimen. Figure 7.62 shows the long side gauge comparison with the control specimens. As mentioned before, gauge T2 indicated yielding of the long side tie, although at a normalized top load 25 kips higher than the undamaged control yielding. Gauge T4 well surpassed the undamaged control specimen behavior with the last recorded strain at a normalized load of 213 kips, about 70 kips greater than the undamaged control behavior. Figure 7.63 shows the more striking improvement from the repair with the two short side gauges surpassing the recorded undamaged control data. Compared to the cracked control data, the FRP #2 Specimen at least tripled the loads for these short side gauges.

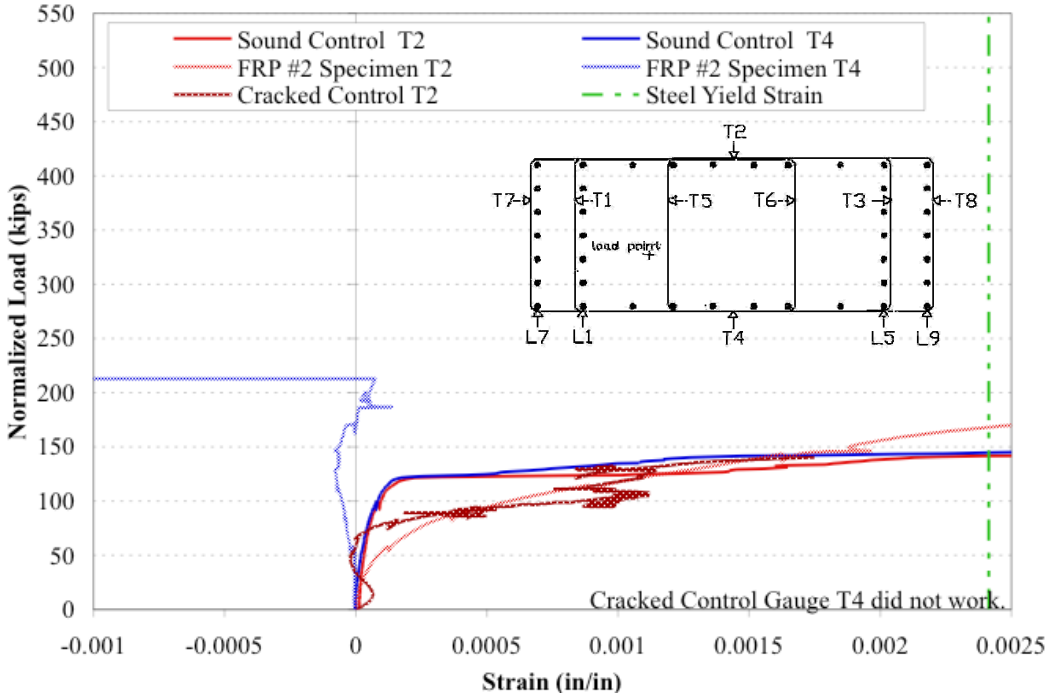

Figure 7.62: FRP #2 Specimen Long Side Gauge Comparison

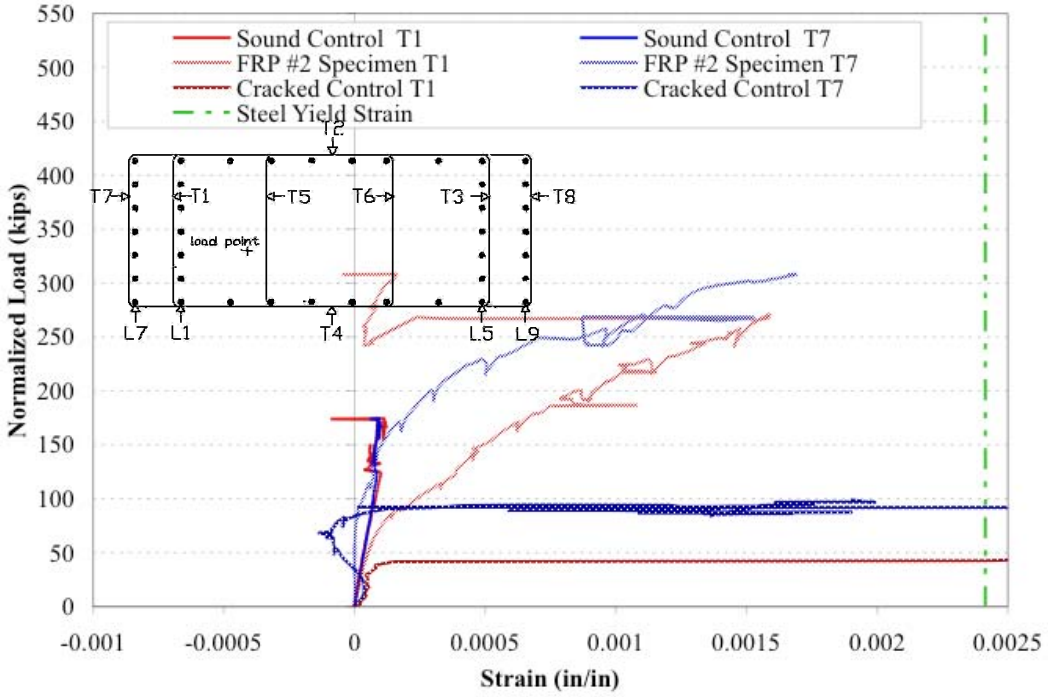

Figure 7.63: FRP #2 Specimen Select Short Side Gauge Comparison

7.3.7.2 Failure

At 125 kips, the initial damage to FRP #2 Specimen was noted to be cracking at the base of the light long side (the load point is farthest from this long side), as shown in Figure 7.64. The pre-existing cracks, from splitting wedge induced damage, were marked in black ink and new cracks, from load application, were marked in blue ink. As shown in Figure 7.65, some fibers at the bottom of the repair on the most heavily loaded short face fractured at a load of 217 kips. The fractured fibers appeared grey-white against the black carbon fiber fabric. At 225 kips additional cracks appeared on the exposed concrete of the most heavily loaded short face of the specimen, as shown in Figure 7.66. Additional fibers had fractured by this load, which are shown in the figure as well. Fibers continued to fracture, as shown in Figure 7.67, as load was added from 230 kips through the ultimate load of 269 kips. At 269 kips, the last fibers in the repair fractured, as shown in Figure 7.68, and the specimen reached failure. Table 7.7 presents a summary of FRP #2 Specimen performance compared to the control specimens. This table shows that even with normalized loads, this FRP repair did not quite reach the level of the undamaged specimen capacity. It did, however, exceed the cracked control specimen's capacity. As well, the strain gauge data showed that the confinement provided by the FRP wrap did restrain the strains in the ties. The average width of the initial cracking of this specimen was slightly higher than the rest of the specimens (0.11 inches instead of 0.09 inches) and so the greater damage level that was repaired may account for the slightly lower load.

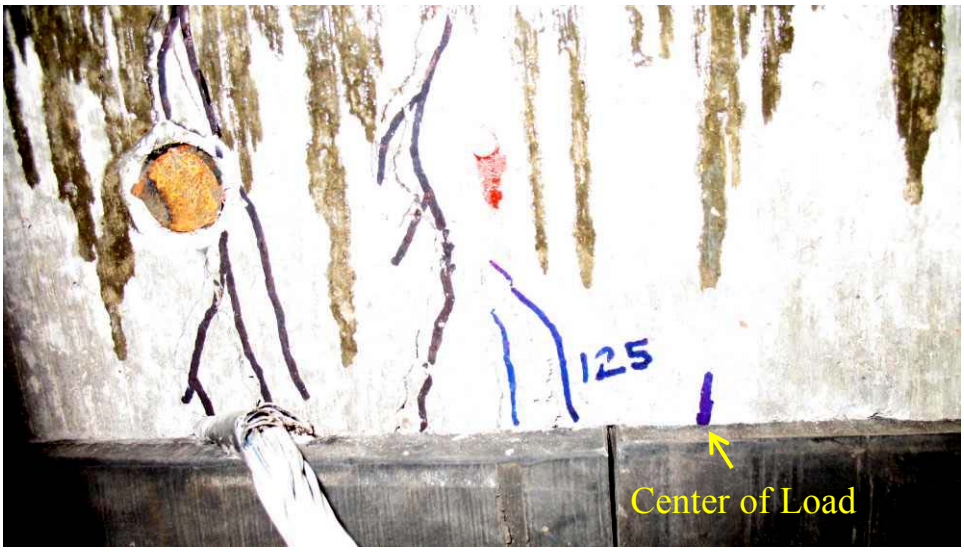

Figure 7.64: Initial Cracking in FRP #2 Specimen

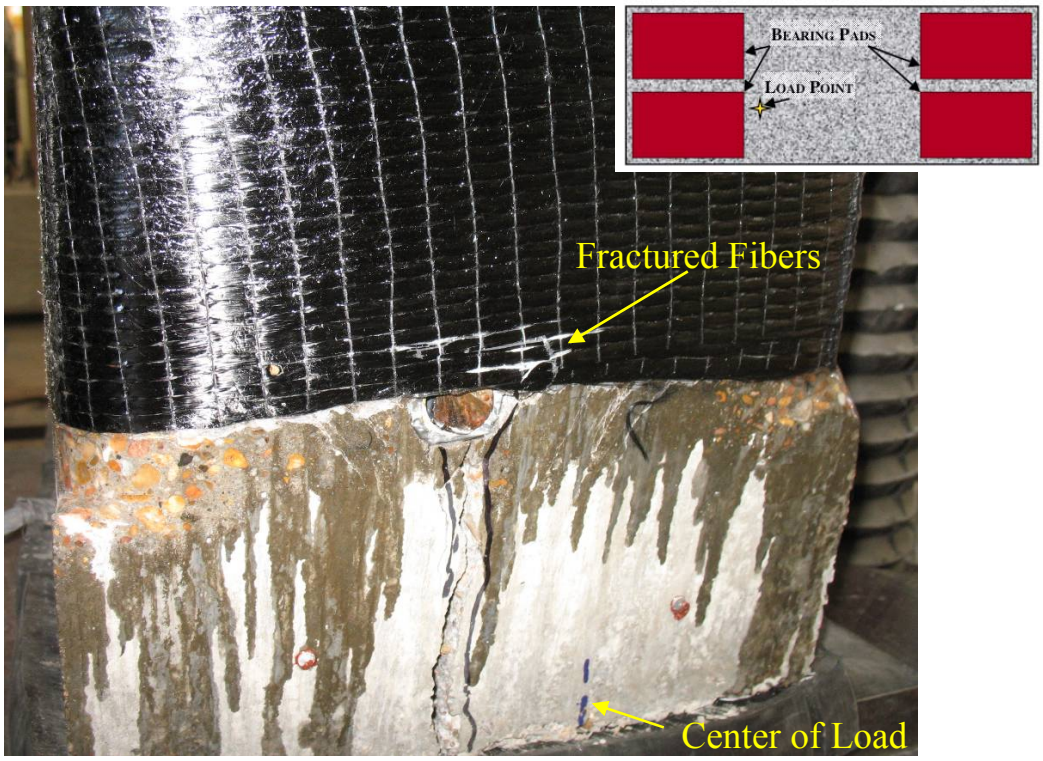

Figure 7.65: Fibers Starting to Fracture on FRP #2 Specimen

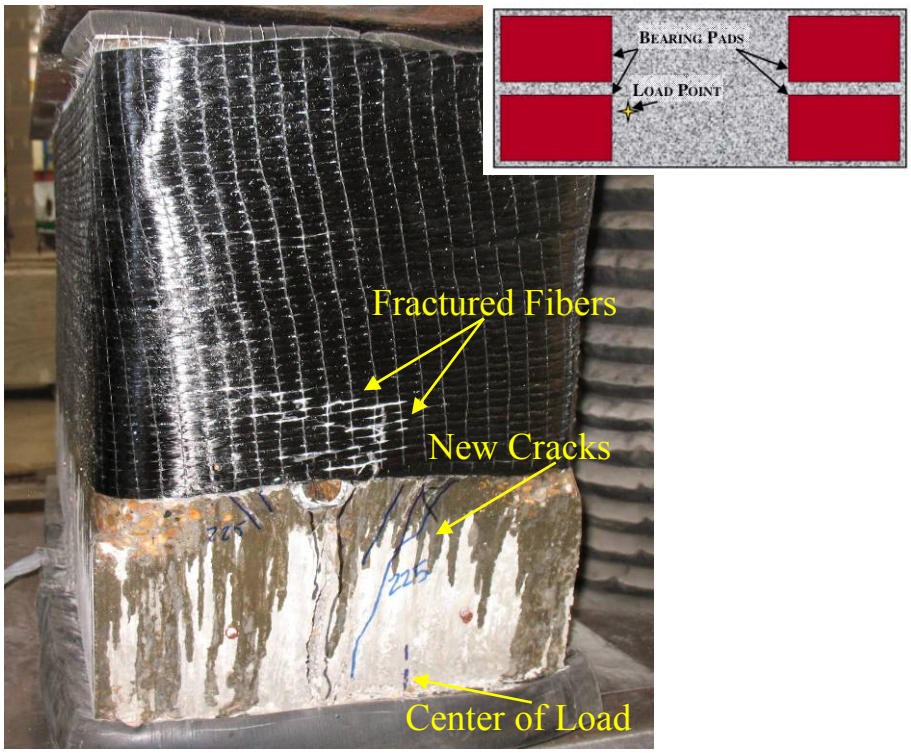

Figure 7.66: Additional Fibers Fractured in FRP #2 Specimen

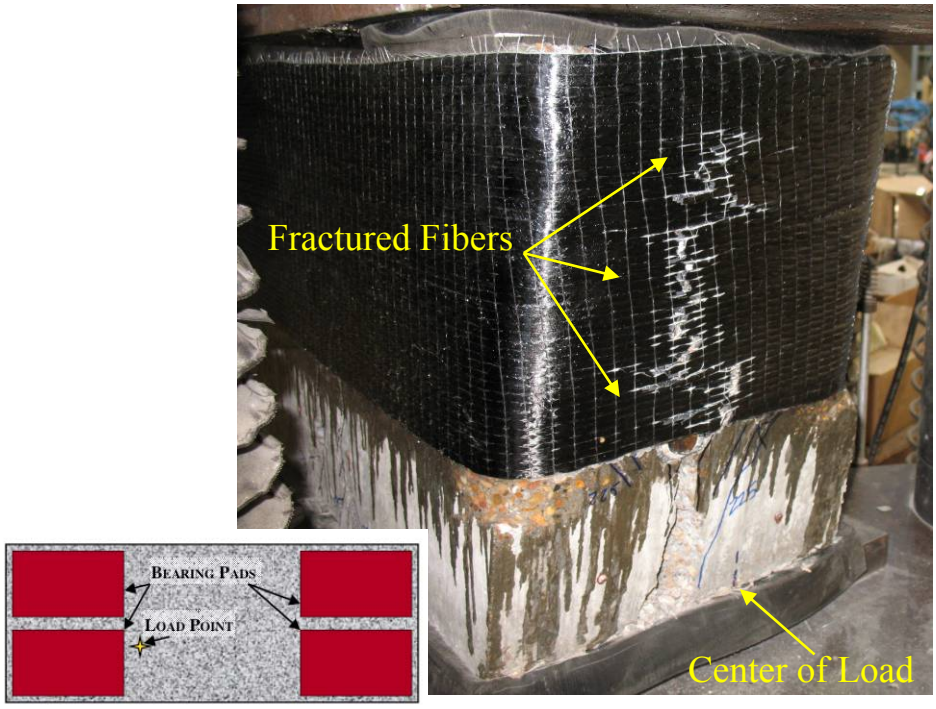

Figure 7.67: Fibers Continued to Fracture in FRP #2 Specimen

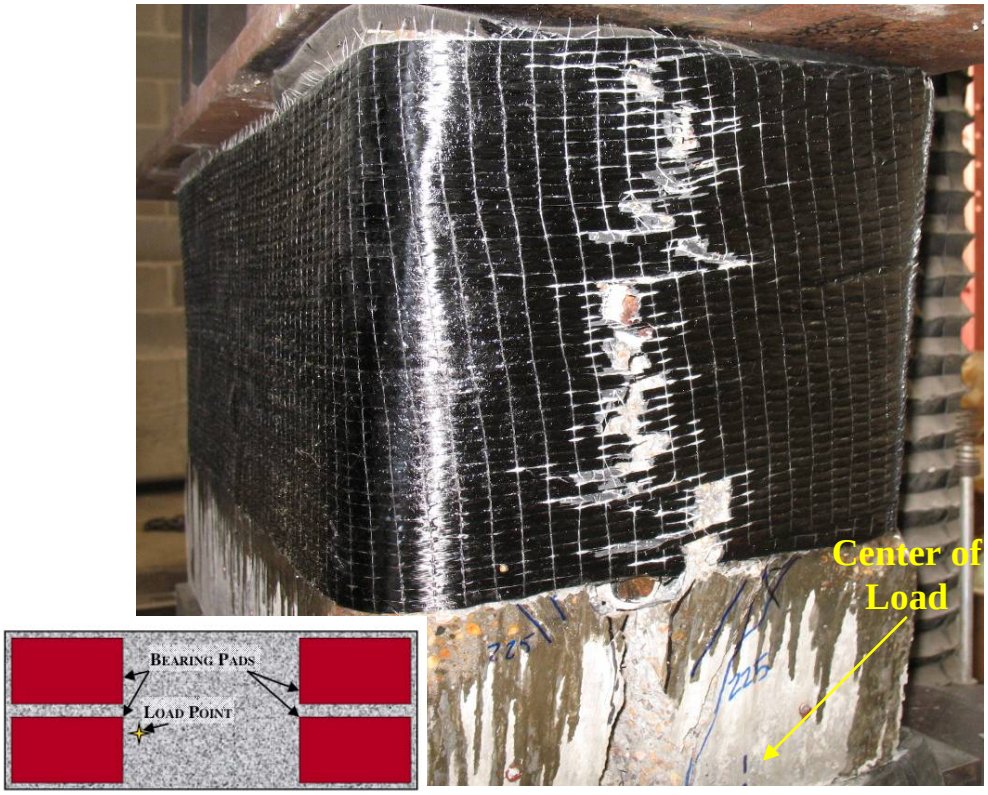

Figure 7.68: Failure of FRP #2 Specimen

Table 7.7: Summary of FRP #2 Specimen Performance

Specimen	f'c (psi)	Measured Peak Load (kips)	Predicted Bearing Load (kips)	Measured / Predicted	Normalized Peak Load (kips)	Normalized / Undamaged Control
Undamaged Control	7100	315	567	0.56	315	1.00
Cracked Control	6700	284	535	0.53	301	0.96
FRP #2 Specimen	6200	269	495	0.54	308	0.98

7.3.8 FRP Repair Summary

Figure 7.69 and Figure 7.70 show the long side and select short side gauge comparison, respectively, of the FRP repaired specimens and the control specimens. The loads for these two graphs were normalized to the undamaged control specimen's concrete strength. The graphs both show the significant increase of load to strain behavior that was achieved through good external restraint. By confining the concrete specimens, the

FRP repairs restored the specimen capacity beyond the cracked control specimen's capacity. On average, the FRP repairs exceeded the undamaged control's capacity.

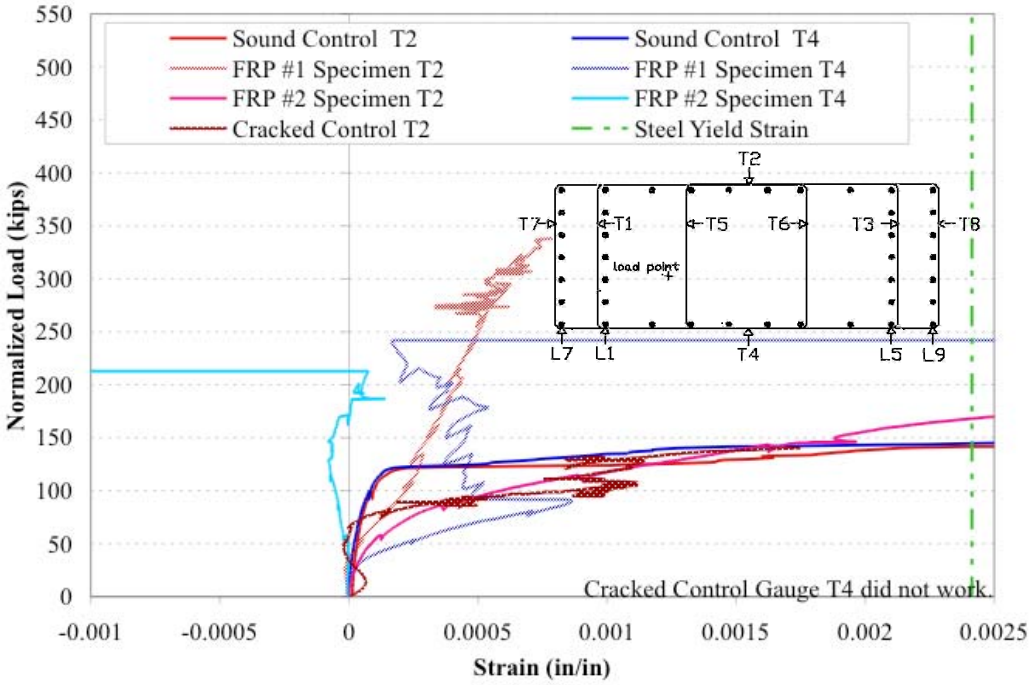

Figure 7.69: FRP Repaired Specimens Long Side Strain Gauge Comparison

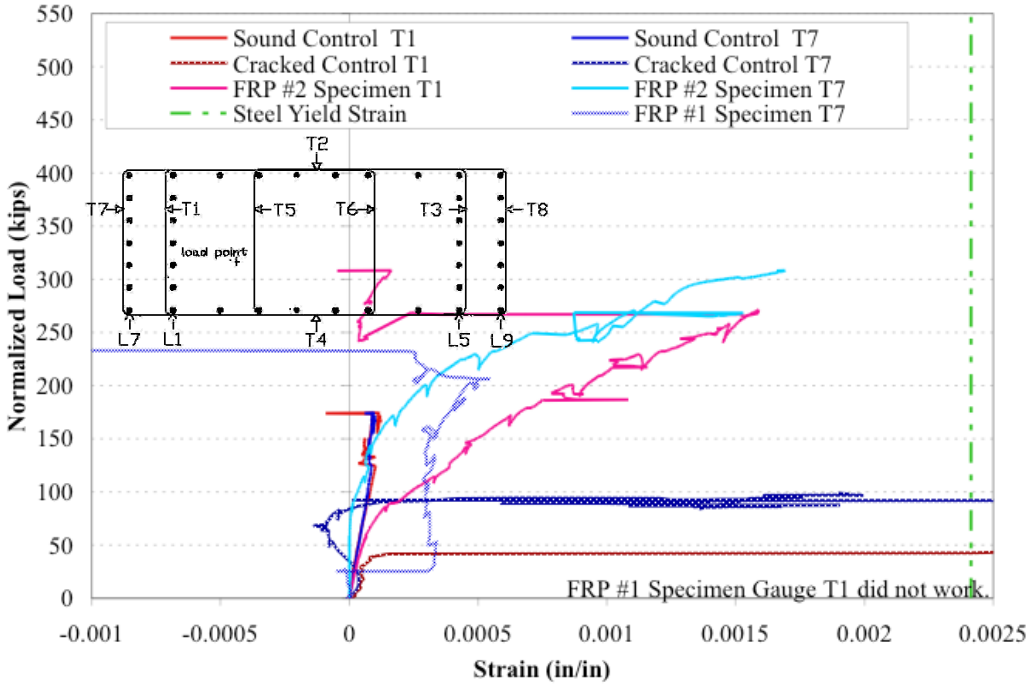

Figure 7.70: FRP Repaired Specimens Select Short Side Gauge Comparison

The FRP repairs behaved as designed, increasing the capacity of the specimens to approach the undamaged capacity. The average failure load of the specimens was 293 kips, which exceeded the cracked control specimen's failure load of 284 kips. FRP #1 Specimen's failure load exceeded the maximum load of the undamaged control specimen as well (317 kips versus 315 kips). When these values are adjusted for differences in concrete strength the capacity increase becomes more apparent. By normalizing values to the undamaged control specimen's concrete strength of 7100 psi, Table 7.8 was developed. In normalized values, the FRP specimens averaged a failure load of 325 kips, which is 103% of the undamaged control value of 315 kips. Thus, the FRP specimens behaved as designed by returning the repaired specimens to the capacity of the undamaged control specimen.

Table 7.8: Summary of FRP Specimen Performance

Specimen	f'c (psi)	Measured Peak Load (kips)	Predicted Bearing Load (kips)	Measured / Predicted	Normalized Peak Load (kips)	Normalized / Undamaged Control
Undamaged Control	7100	315	567	0.56	315	1.00
Cracked Control	6700	284	535	0.53	301	0.96
FRP #1 Specimen	6600	317	527	0.60	341	1.08
FRP #2 Specimen	6200	269	495	0.54	308	0.98
ASR/DEF Column A	6000	491	479	1.03	581	1.84
ASR/DEF Column B	5800	480	455	1.05	588	1.87

7.3.9 Post-tensioned #1 Specimen

The first specimen with a post-tensioned repair was tested on May 27, 2008. Figure 7.71 shows this specimen prior to testing. Before the post-tensioning repair was added, the block was pre-cracked to an average width of 0.09 inches and the PVC voids were filled with reinforcing bars after initial cracking. On the day of testing, three concrete cylinders cast from the same concrete batch as the specimen had an average strength of 5900 psi.

The results from this test are found in the following sections. A summary of post-tensioned repair performance is presented immediately after the failure description of Post-tensioned #2 Specimen.

Figure 7.71 : Post-tensioned #1 Specimen Prior to Testing

7.3.9.1 Strain Measurements

Figure 7.72 and Figure 7.73 present the transverse and longitudinal strain measurements, respectively. Smaller versions of Figure 7.12 were inset in the graphs and show the strain gauge locations within the bearing specimens. The post-tensioned repair did have a significant restraining effect on the short side strains, as shown in Figure 7.72. Gauges T1, T3, T7, and T8, which monitored ties near the faces of the short side of the specimen, all exhibited low to nearly zero strain during loading. However gauges T2 and T4, which monitor long side ties, showed yielding of their ties. Gauge T4 recorded yielding strains at 100 kips of load, which corresponds with the initial cracking damage on the long side

of the specimen that was monitored by this gauge. This specimen did fracture down the center of the long face, along existing cracks. This fracture took place by 225 kips of load. Gauge T2 had been recording some slightly erratic strains from 175 kips to 300 kips of top loading. It was possible that due to the initial cracking these tie monitored by this gauge had been partially yielded prior to testing and so the lower yield level represented steel yield. Regardless, the ties were certainly broken by the load of 225 kips when the crack opened to half an inch of width. All of the longitudinal gauges had fairly small strains, likely due to the confinement provided by the post-tensioning. As the post-tensioning was applied before the gauges were monitored, the stress induced in the inclined bars by this external restraint was not evidenced by these strain readings, as shown in Figure 7.73.

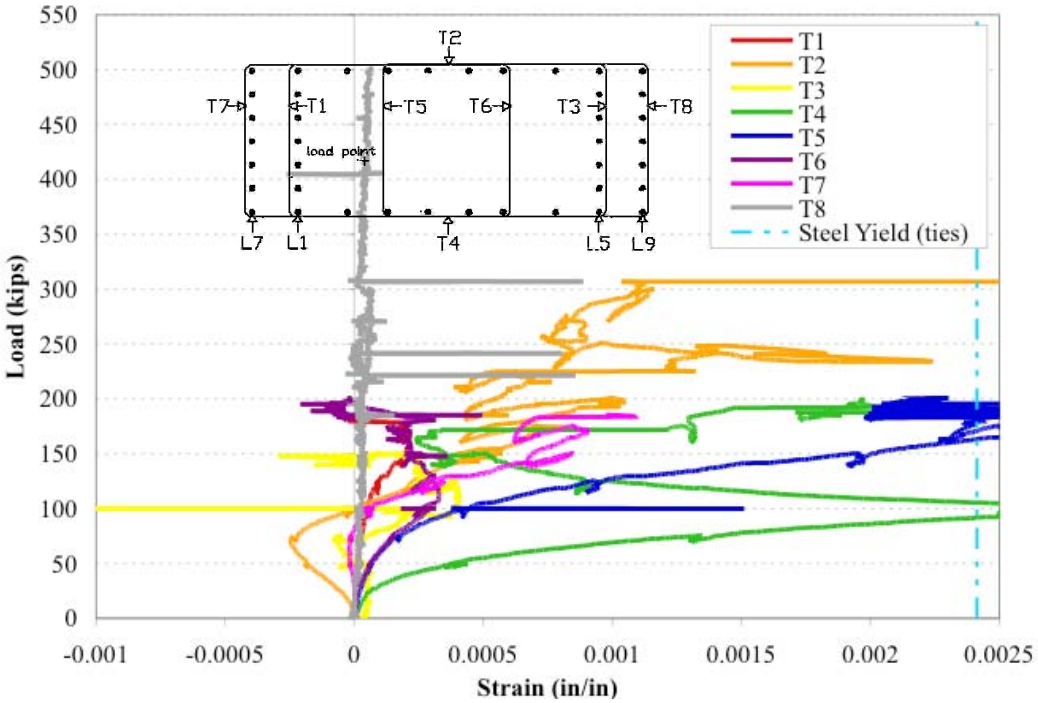

Figure 7.72: Post-tensioned #1 Specimen Transverse Strain Measurements

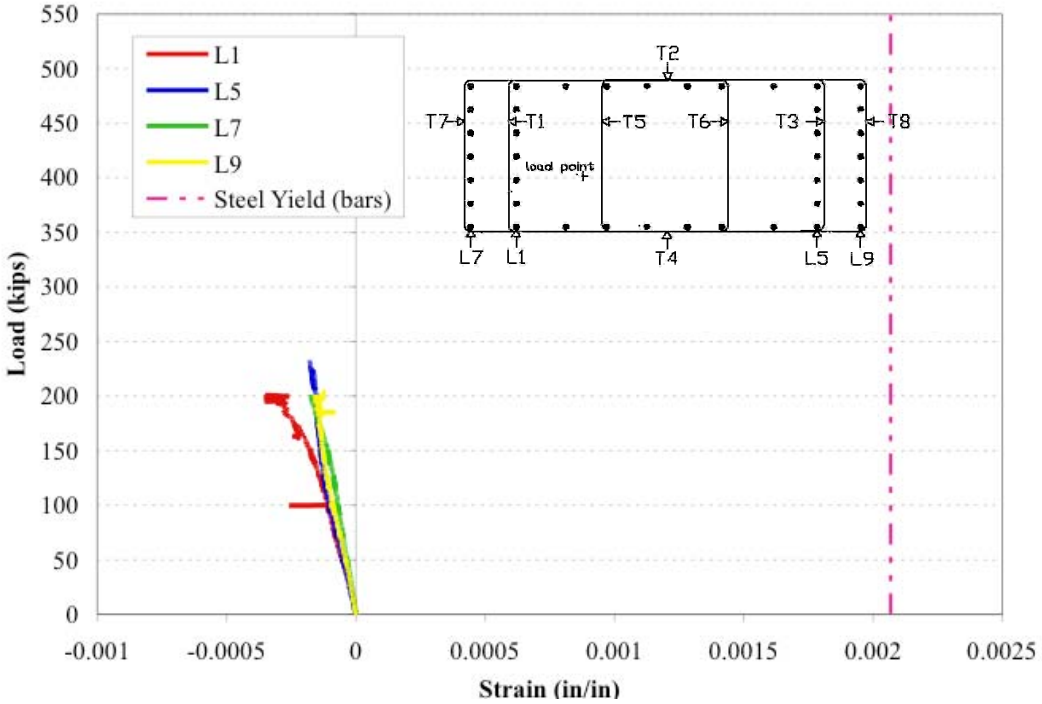

Figure 7.73: Post-tensioned #1 Specimen Longitudinal Strain Measurements

Figure 7.74 and Figure 7.75 present comparison of the long side and select short side strain gauge measurements, respectively, between Post-tensioned #1 specimen and the control specimens. The loads in these graphs are normalized to the undamaged control specimen's concrete strength. Compared to the control specimens in Figure 7.74, the long side gauges were split in performance improvement. Gauge T2 recorded strains at higher loads than either control specimen. Gauge T4, however, recorded a yield strain below the ones observed for the control specimens. The weakness of the post-tensioned repair turned out to be the steel angles spanning the short side of the specimen. These angles acted as the clamp holding the long face in compression. The angles were sized to carry the repair load of 9.25 kips, not the gross section capacity of the post-tensioning bars. Thus, at high loads these angles deformed as the fracturing block pushed against the angles. Figure 7.75 shows the efficiency of the repair at restraining the short side gauges. Gauge T2 recorded very small strains similar to those of the undamaged control specimen. Gauge T7 recorded restrained strains and higher loads than were observed for the control specimens.

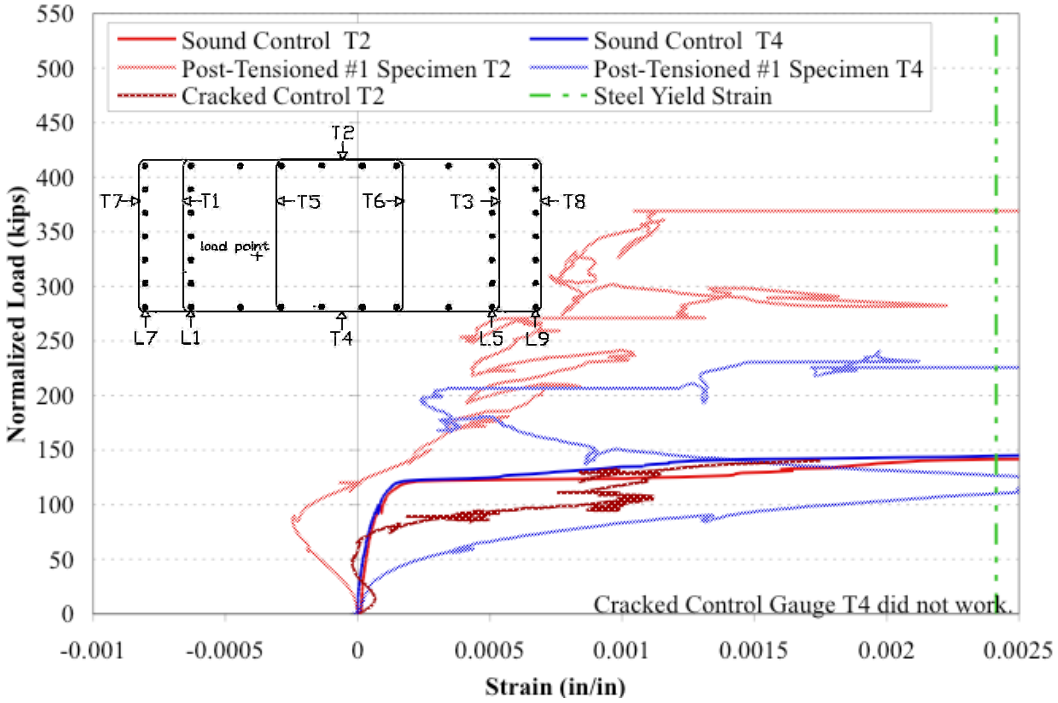

Figure 7.74: Post-tensioned #1 Specimen Long Side Gauge Comparison

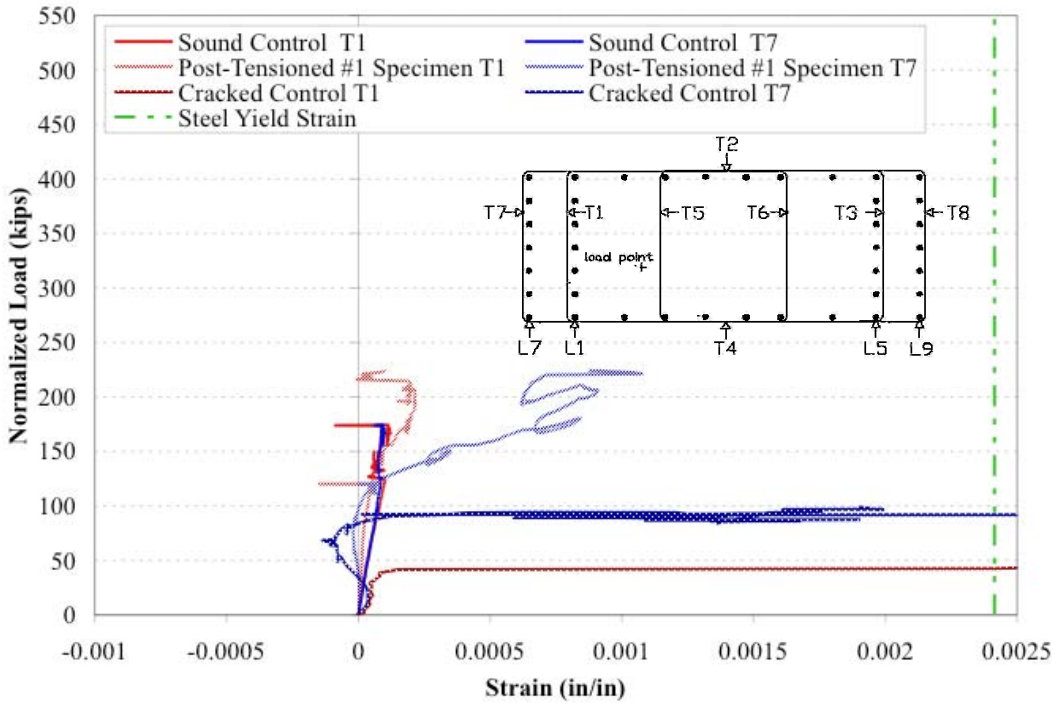

Figure 7.75: Post-tensioned #1 Specimen Select Short Side Gauge Comparison

7.3.9.2 Failure

At a load of 100 kips, cracking was noted on the most heavily loaded long face of Post-tension #1 Specimen. This cracking, shown in Figure 7.76, was the initial damage caused by load testing. In the pictures, existing cracks were marked in blue ink and new cracks were marked in green ink. The initial cracking included some extension of existing cracks in the middle of the specimen and a new crack forming adjacent to the center of the load point, which was marked with a black arrow on the specimen in the picture. By 225 kips, as shown in Figure 7.77, the new crack at the load point had extended down to the repair and the center crack had opened wide. The specimen continued to take load while the center crack widened as shown in Figure 7.78. The test was stopped for safety concerns at 502 kips as the yellow angle in the repair had deformed considerably, as shown in Figure 7.79. Table 7.9 summarizes the performance of Post-tensioned #1 Specimen compared to the control specimens. With this repair, the specimen was able to exceed the predicted bearing load for its concrete strength. Considering normalized loads, this repair nearly doubled the undamaged control specimen's capacity.

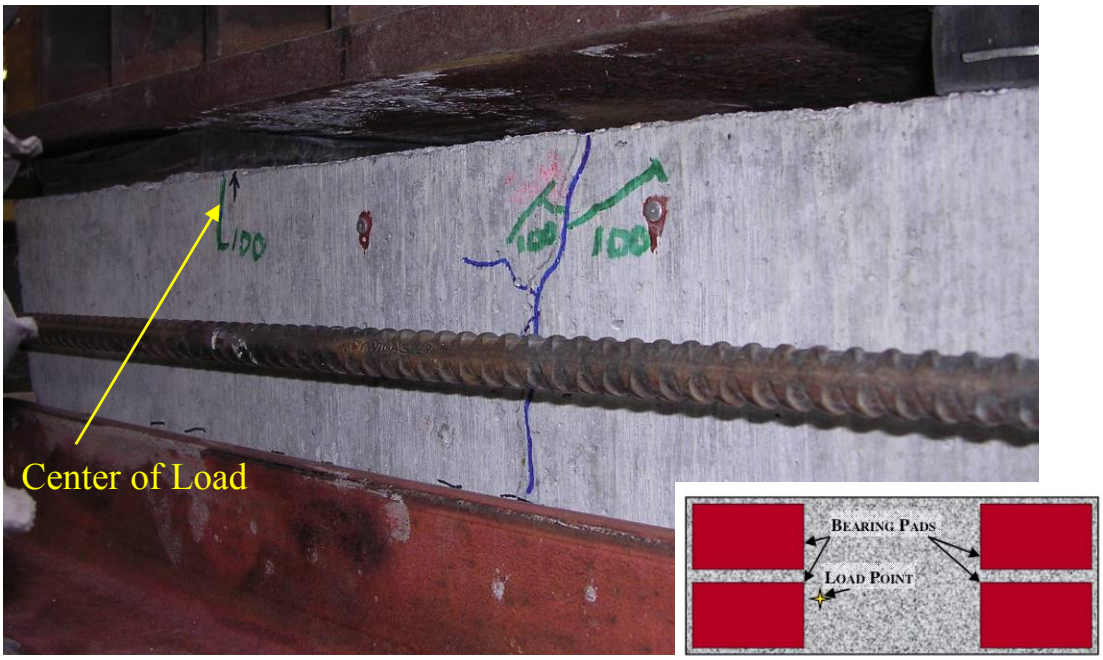

Figure 7.76: Initial Cracking in Post-tensioned #1 Specimen

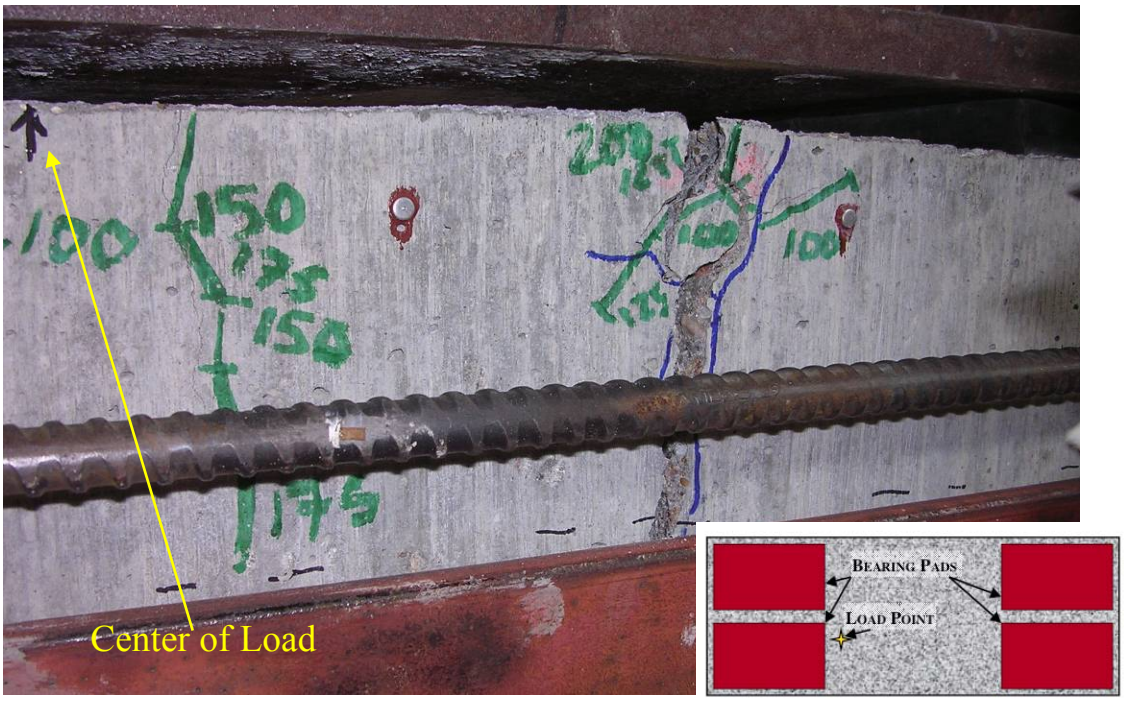

Figure 7.77: Widening of Center Crack in Post-tensioned #1 Specimen

Figure 7.78: Center Crack Widens in Post-tensioned #1 Specimen

Figure 7.79: Failure of Angle on Post-tensioned #1 Specimen

Table 7.9: Summary of Post-tensioned #1 Specimen Performance

Specimen	f'c (psi)	Measured Peak Load (kips)	Predicted Bearing Load (kips)	Measured / Predicted	Normalized Peak Load (kips)	Normalized / Undamaged Control
Undamaged Control	7100	315	567	0.56	315	1.00
Cracked Control	6700	284	535	0.53	301	0.96
Post-tensioned #1 Specimen	5900	502	471	1.07	604	1.92

7.3.10 Post-tensioned #2 Specimen

The second post-tensioned repair specimen was tested on May 28, 2008. Figure 7.80 shows the specimen prior to testing. This specimen was a duplicate of the first post-tensioned repair specimen. Prior to repair, the block was pre-cracked to an average width of 0.09 inches. Reinforcing bar was also inserted into the PVC voids after initial cracking, but before the repair was applied. On the day of testing, three concrete

cylinders from the specimen's concrete batch had an average strength of 6000 psi. Testing results are presented in the following sections. A summary of post-tensioned repair performance is presented following the results of this specimen's test.

Figure 7.80: Post-tensioned #2 Specimen Prior to Testing

7.3.10.1 Strain Measurements

Figure 7.81 and Figure 7.82 present the transverse and longitudinal strain measurements, respectively. Smaller versions of Figure 7.12 were inset in the graphs and show the strain gauge locations within the bearing specimens. Again, the effect of restraint was evident in the strains measured in the transverse ties. Figure 7.81 presents these measurements of Post-tensioned #2 Specimen. Although gauge T4 stopped providing reliable data at 74 kips of load, the other long side gauge T2 showed yielding at a load of 185 kips. Crack extensions in the center of the specimen's long side nearest gauge T4 appeared at 75 kips. The center crack started opening up at 200 kips of top load, which coordinated with the next pause in loading to mark cracks following the yielding at gauge T2. The short side gauges of the more heavily loaded half, gauges T7, T1, and T5, all exhibited yielding at 225 kips of top load. At this load, a wedge of concrete at the base of this short side began to come out of the specimen. However, there was no apparent damage higher on the

specimen, near the monitored ties, until a load of 250 kips, when the center crack widened and additional cracks were found on this short side face.

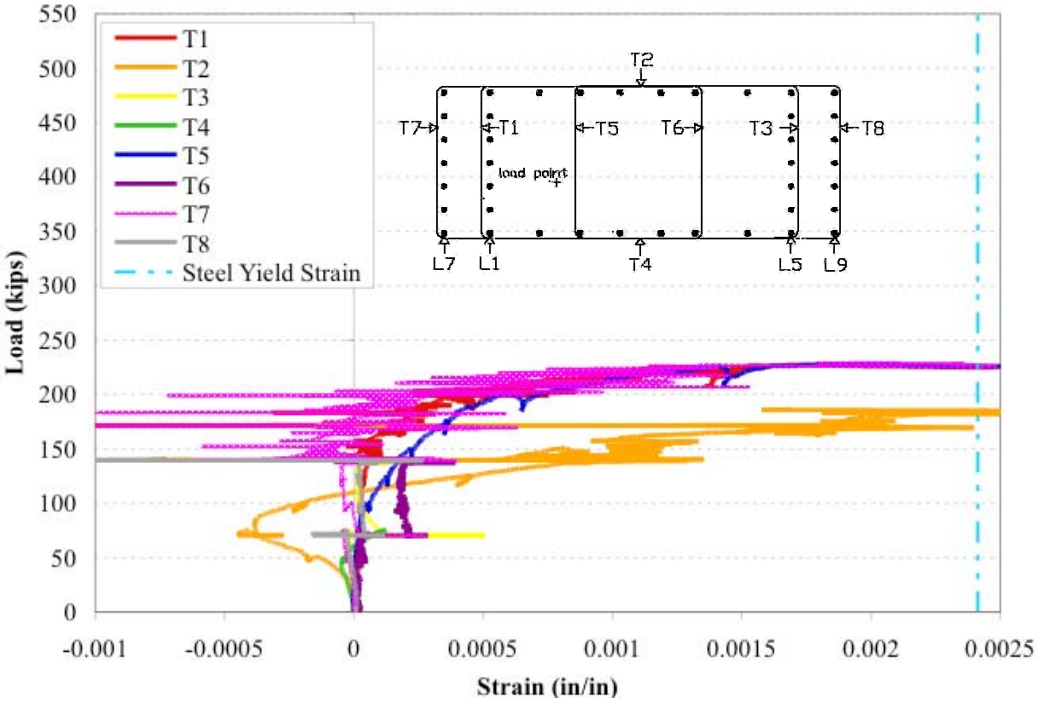

Figure 7.81: Post-tensioned #2 Specimen Transverse Strain Measurements

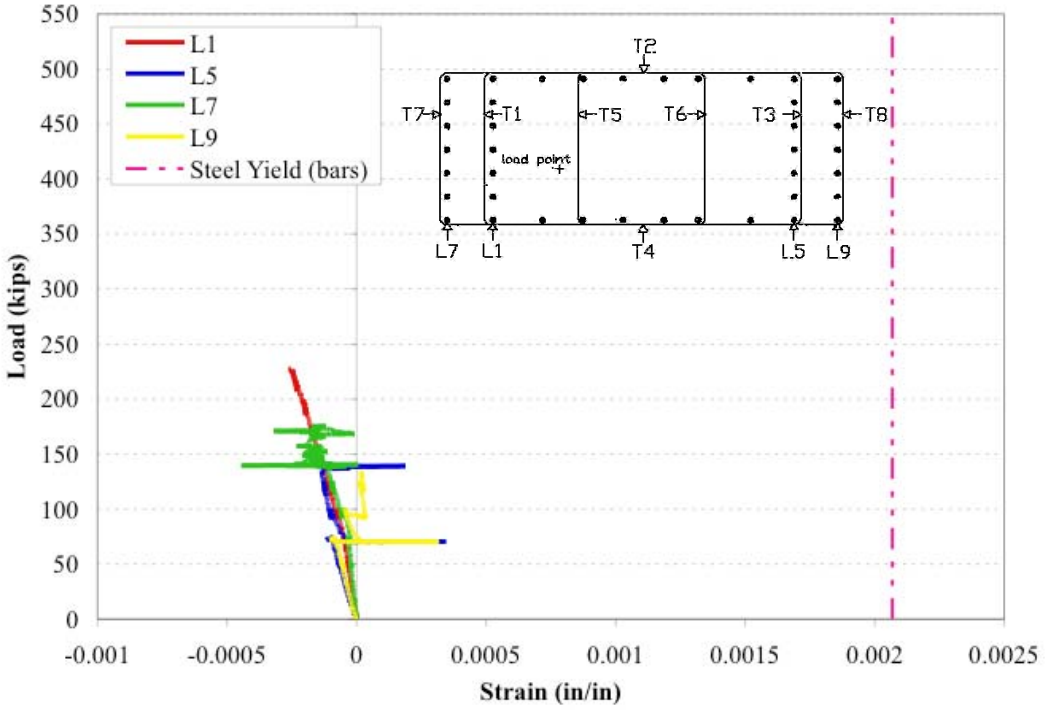

Figure 7.82: Post-tensioned #2 Specimen Longitudinal Strain Measurements

Figure 7.83 and Figure 7.84 show comparisons of the long side and select short side strain gauge measurement, respectively, between Post-tensioned #2 Specimen results and the control specimens' results. For these graphs, the loads were normalized to the concrete strength of the undamaged control specimen. Comparing the long side gauge of Post-tensioned #2 Specimen with the control specimens in Figure 7.83, the improvement in performance was apparent. Gauge T2 exceeded the performance of both controls by over 50 kips of normalized load. The performance improvement of the short side ties, presented in Figure 7.84 was more noticeable. Here the repaired specimen had yield strains at a load nearly threefold the yielding load for the cracked control gauge T7 and over six-fold the normalized load of cracked control gauge T1. Up until a normalized load of 160 kips, the repaired specimen exhibited short side strains that were comparably small to the values recorded in the undamaged control specimen. Above that load, these gauges recorded the yielding curves of their ties. Thus, the repair did have a significant restraining effect on the yielding of transverse ties.

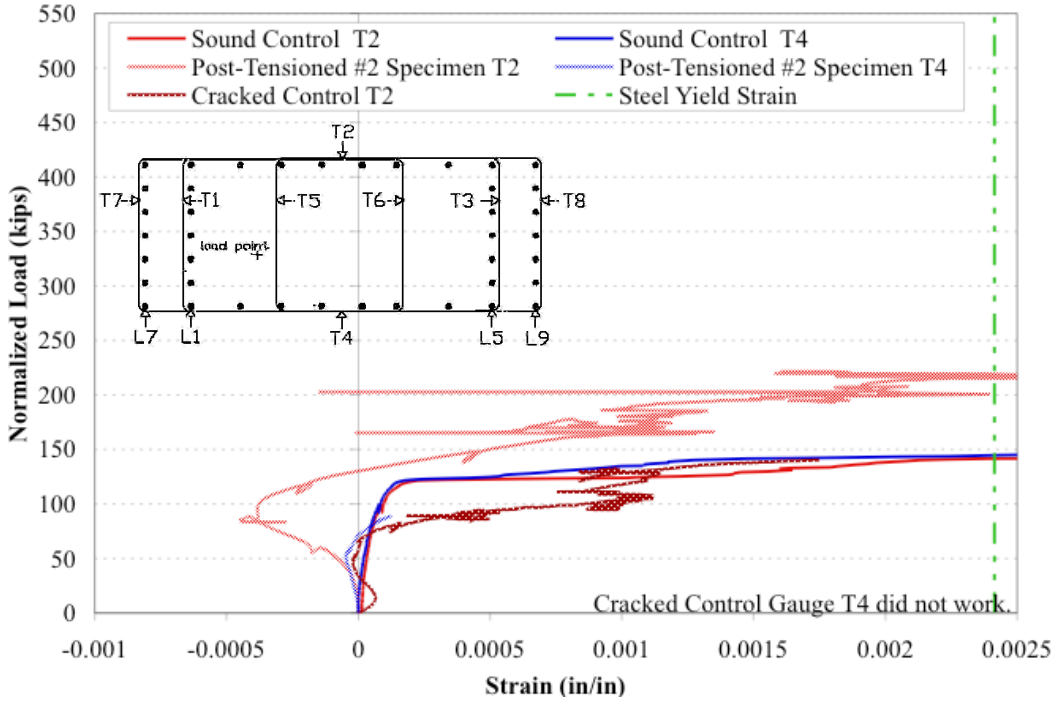

Figure 7.83: Post-tensioned #2 Specimen Long Side Gauge Comparison

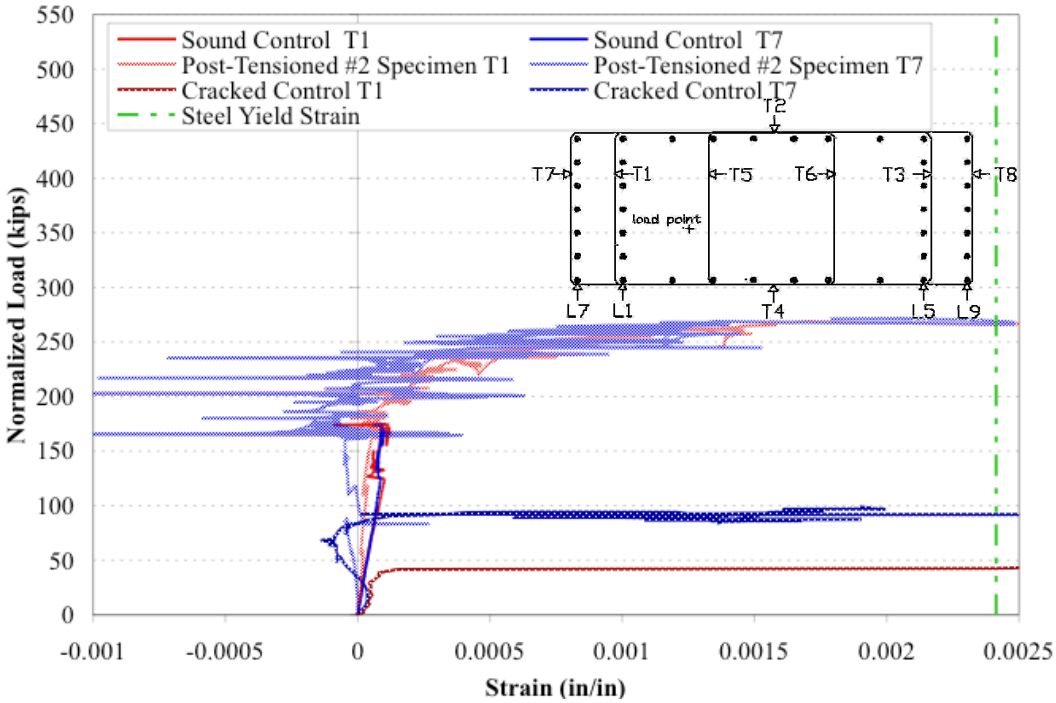

Figure 7.84: Post-tensioned #2 Specimen Select Short Side Gauge Comparison

7.3.10.2 Failure

At 50 kips, a crack extension on the long face of the specimen furthest from the load point was noted as the initial damage of Post-tensioned #2 Specimen, as shown in Figure 7.85. Existing cracks from the splitting wedge damage were marked in blue ink and new cracks, from load application, were marked in green ink. By 200 kips, as shown in Figure 7.88, the center crack had begun to open as the specimen continued taking load. A load of 225 kips caused a block of concrete to push out of the most heavily loaded short side, as shown in Figure 7.86. A the next load stoppage for crack marking, 250 kips, the center existing crack on this side began to open wide, as shown in Figure 7.87, which corresponded to the yielding of short side ties on this side, as discussed previously. At 350 kips the concrete under the most heavily loaded bearing pad began spalling, as seen on the left in Figure 7.89. As well, this picture shows the continued widening of the center crack. At 416 kips a washer in the post-tensioning system cracked, as shown in Figure 7.90, and the specimen testing was halted for safety. Table 7.10 summarizes the performance of Post-tensioned #2 Specimen along with the control specimens. Although the test was halted for safety prior to reaching the predicted bearing load, the test still showed that the repaired specimen met its goal of matching or exceeding the undamaged control capacity.

Figure 7.85: Initial Cracking of Post-tensioned #2 Specimen

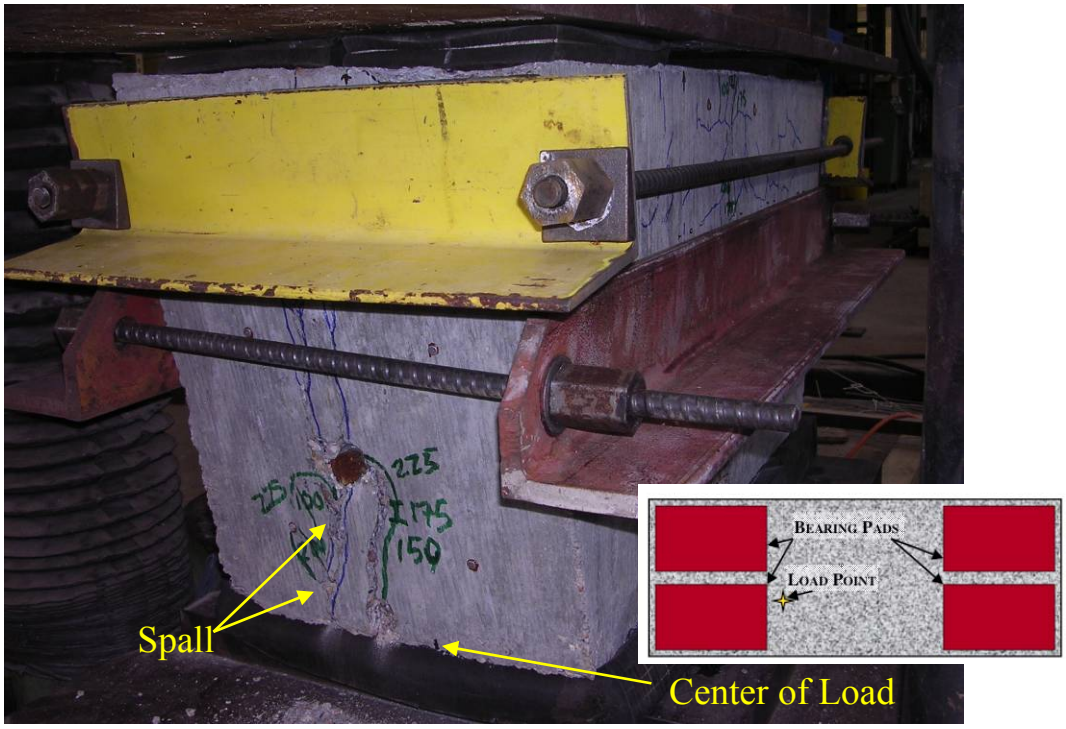

Figure 7.86: Base Spall on Post-Tensioned #2 Specimen

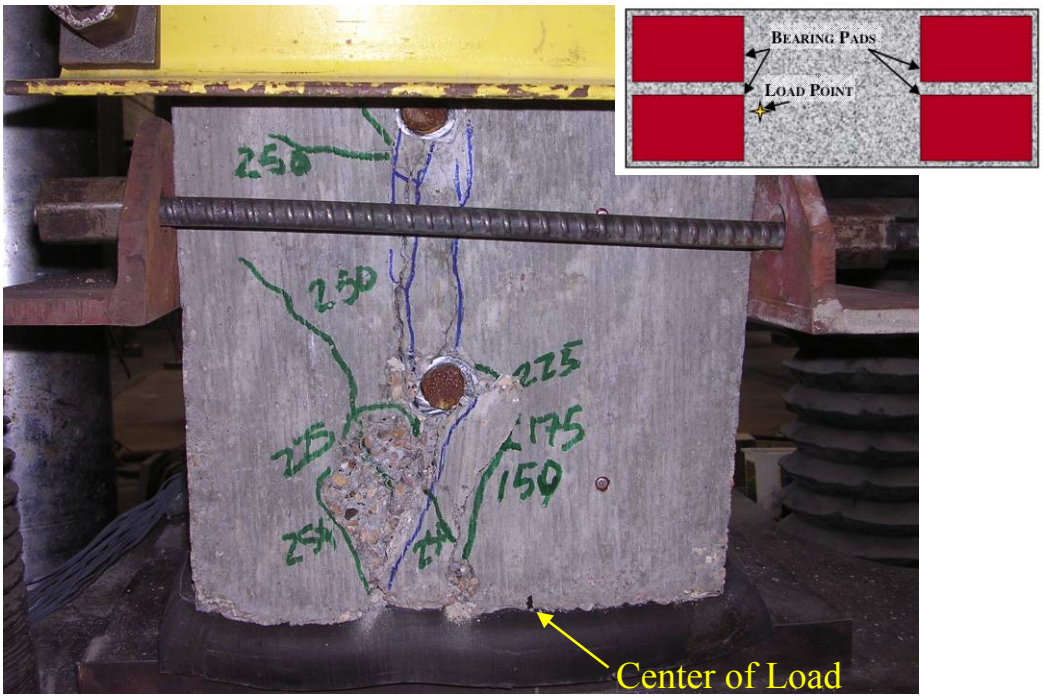

Figure 7.87: Post-tensioned #2 Specimen Short Side Crack Opening

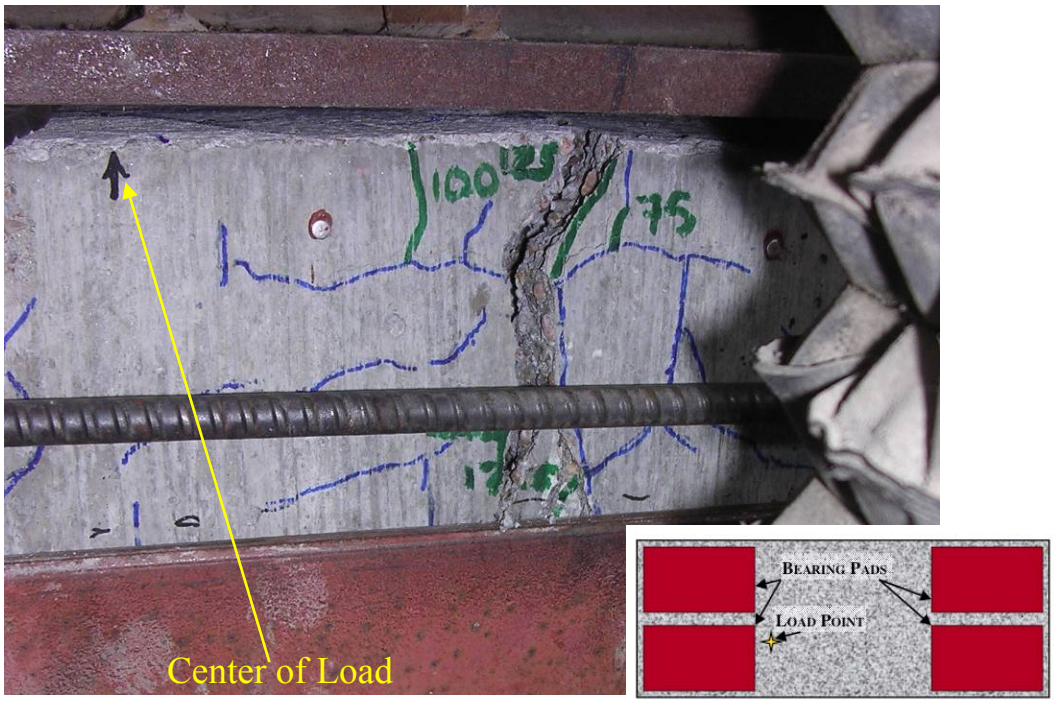

Figure 7.88: Center Crack Opened in Post-tensioned #2 Specimen

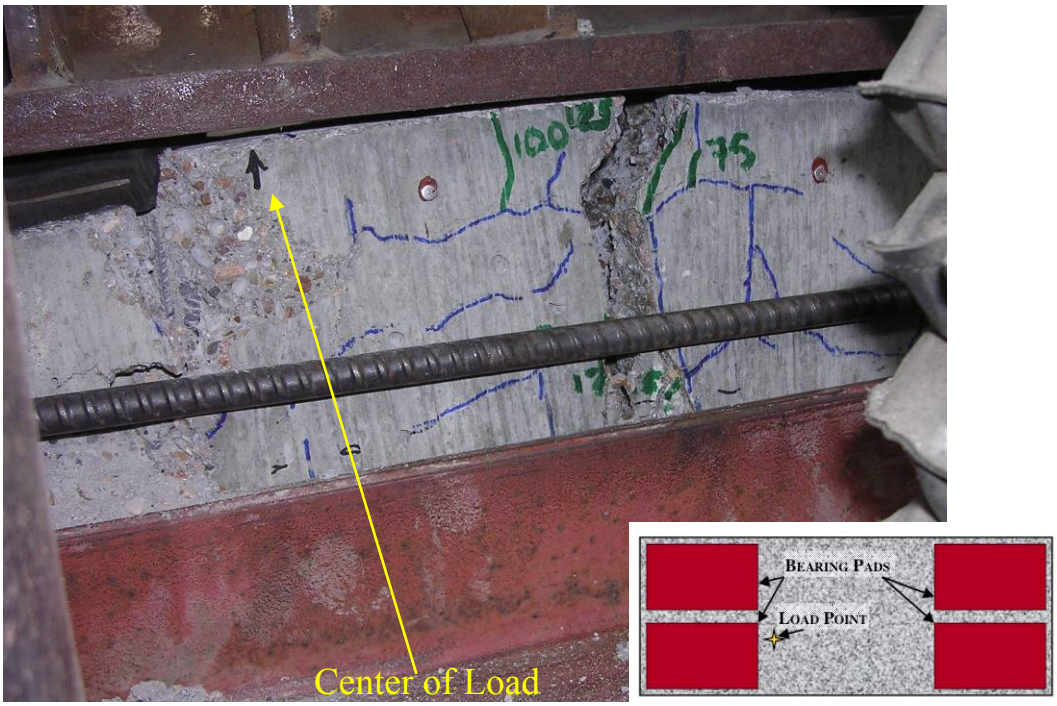

Figure 7.89: Wide Center Crack and Crushing under Heavy Bearing Pad

Figure 7.90: Washer Failure of Post-tensioned #2 Specimen

Table 7.10: Summary of Post-tensioned #2 Specimen Performance

Specimen	f'c (psi)	Measured Peak Load (kips)	Predicted Bearing Load (kips)	Measured / Predicted	Normalized Peak Load (kips)	Normalized / Undamaged Control
Undamaged Control	7100	315	567	0.56	315	1.00
Cracked Control	6700	284	535	0.53	301	0.96
Post-tensioned #2 Specimen	6000	416	479	0.87	492	1.56

7.3.11 Post-tensioned Repair Summary

Figure 7.91 and Figure 7.92 present a comparison of the long side and select short side gauge readings, respectively, of the post-tensioned repairs along with the control specimens. For these graphs, the loads were normalized to the concrete strength of the undamaged control specimen. Figure 7.91 shows the mixed results of the long side gauges. This figure shows the possibility for the confinement to greatly increase yield loads, as evidence in the gauge T2 measurements. The figure also shows the weakness of this particular application of the repair, in that the deformation of the angles allowed for the long side to open and for these long side ties to yield. Figure 7.92 shows more of this repair's success at restraining the concrete. The short side gauge readings were typically of small strain sizes similar to the undamaged control specimen, up to a normalized load of 160 kips. At this point, three of the four repair gauges recorded the beginning of yield curves. The fourth gauge, Post-tensioned #1 Specimen Gauge T7, showed that its tie had begun yielding at a normalized load of 117 kips. All the short side ties showed significant improvement in performance compared to the cracked control specimen.

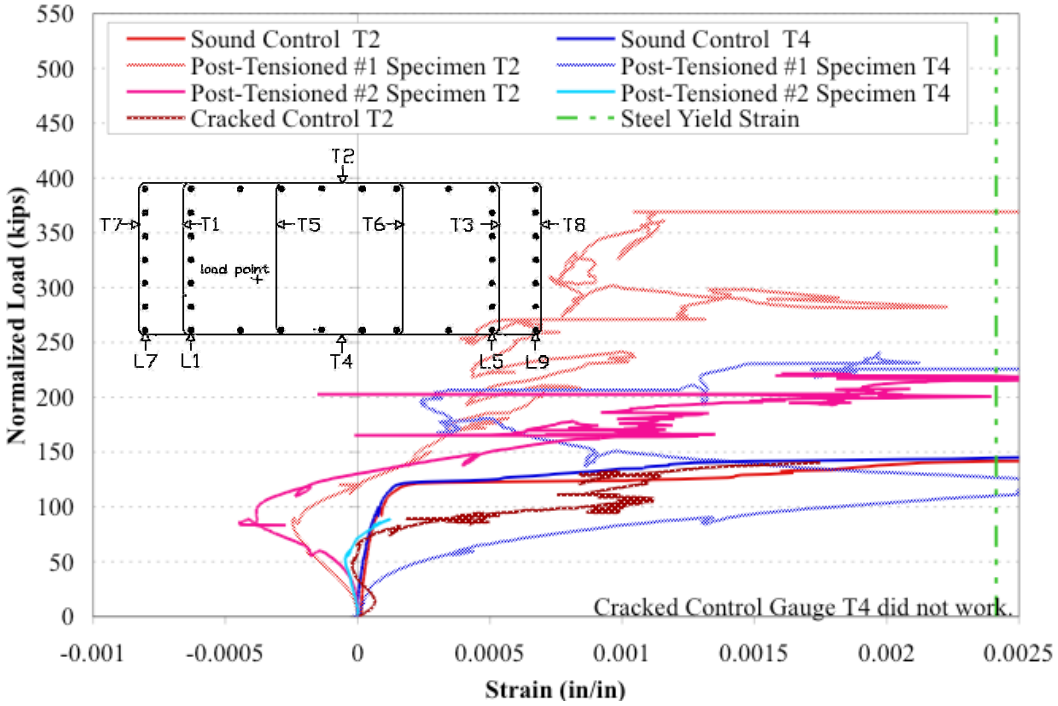

Figure 7.91: Post-tensioned Specimens Long Side Gauge Comparison

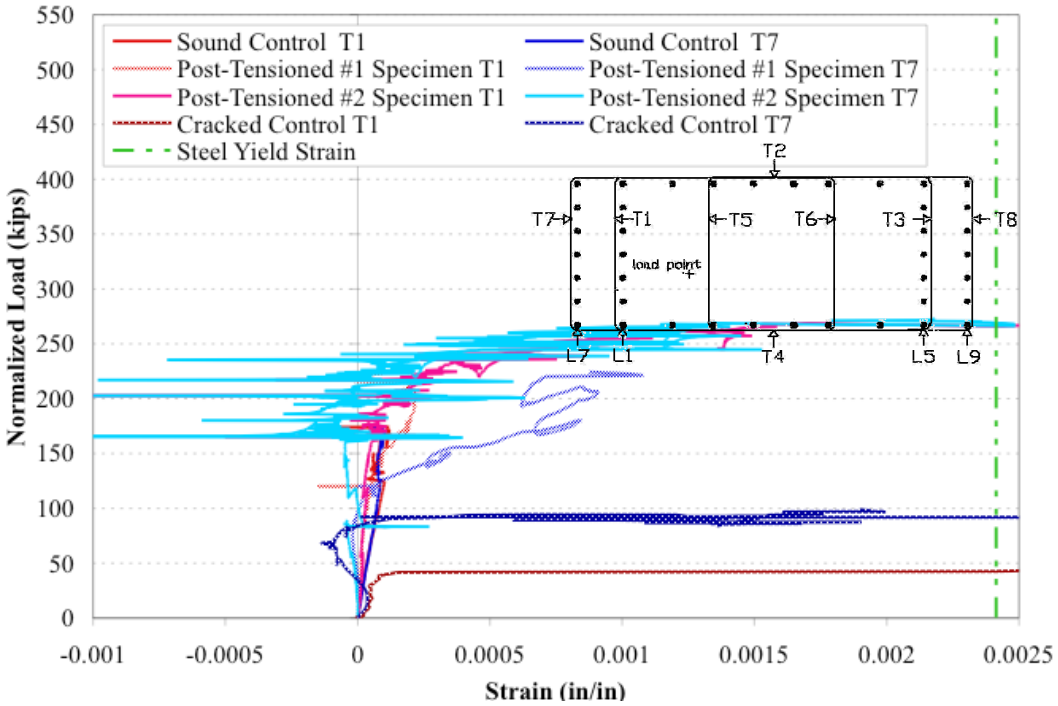

Figure 7.92: Post-tensioned Specimens Select Short Side Gauge Comparison

Even before considering the effects of differing concrete strengths, the post-tensioned repair averaged a high failure load. The measured maximum load average of 459 kips was greater than the undamaged control specimen load of 315 kips. The failure loads were normalized to the undamaged control specimen's concrete strength and the summary for the post-tensioned repair is given in Table 7.11. Using normalized values, the post-tensioned repairs averaged 548 kips, which is 174% of the undamaged control specimen's failure load. Post-tensioned #1 Specimen showed the potential of this repair method to confine the concrete to a point that it can carry its predicted load. Thus, the post-tensioning overcame both the damage to the specimens and the specimens' lack of lateral restraint boundary condition. The post-tensioned specimens did fracture down the center of the long face, however the repair continued to confine the concrete enough for it to keep taking additional load. If the angles spanning the short face had been sized to carry the gross capacity of the post-tensioning bars rather than the repair design load, it was possible that even higher loads for the post-tensioning repaired specimens could have been recorded. The post-tensioned repair met and surpassed the goal of returning the repaired specimen to the undamaged control specimen's capacity.

Table 7.11: Summary of Post-tensioned Specimen Performance

Specimen	f'c (psi)	Measured Peak Load (kips)	Predicted Bearing Load (kips)	Measured / Predicted	Normalized Peak Load (kips)	Normalized / Undamaged Control
Undamaged Control	7100	315	567	0.56	315	1.00
Cracked Control	6700	284	535	0.53	301	0.96
Post-tensioned #1 Specimen	5900	502	471	1.07	604	1.92
Post-tensioned #2 Specimen	6000	416	479	0.87	492	1.56
ASR/DEF Column A	6000	491	479	1.03	581	1.84
ASR/DEF Column B	5800	480	455	1.05	588	1.87

7.3.12 Concrete Jacket #1 Specimen

The first specimen repaired with a concrete jacket was tested on May 29, 2008. Concrete Jacket #1 Specimen is shown in Figure 7.93 prior to testing. Before beginning the repair, the specimen was pre-cracked to an average width of 0.09 inches. The PVC voids in the section were filled with reinforcing bars after initial cracking but prior to the jacket casting. On the day of testing, three concrete cylinders cast from the same concrete batch as the specimen had an average strength of 5300 psi. Three additional concrete cylinders cast from the same batch as the concrete jacket repair were tested at the same time and had an average strength of 7200 psi. Results from the test are given in the following sections. A summary of concrete jacket repair performance is presented immediately following the results of Concrete Jacket #2 Specimen.

Figure 7.93: Concrete Jacket #1 Specimen Prior to Testing

7.3.12.1 Strain Measurements

Figure 7.94 and Figure 7.95 present the transverse and longitudinal strain measurements, respectively. Smaller versions of Figure 7.12 were inset in the graphs and show the strain gauge locations within the bearing specimens. Figure 7.96 and Figure 7.97 present comparisons with the control specimens of long side and select short side strain gauge measurements, respectively. For these comparison graphs, the loads were normalized to the concrete strength of the undamaged control specimen. The effect of external restraint provided by the concrete jacket repair was shown in the short side ties of Figure 7.94. For instance, although the tie monitored by gauge T1 did reach yielding, it did so at an applied to load of 250 kips. When this load was normalized and compared to the control specimens in Figure 7.97, the yield load was 330 kips, which is over seven times the yield load of the same tie in the cracked control specimen. As well, gauge T7, which monitors the exterior tie on this most heavily loaded short face, recorded only very small strains throughout the test. The concrete jacket repair thus effectively confined the short side faces of the specimen. Figure 7.94 also shows the yielding of the long side tie monitored by gauge T2 at an applied load of 87 kips. This performance did not measure up to the behavior observed in the control specimens when compared in Figure 7.97. The long side tie yielding at 87 kips did not, however, translate into specimen fracture at this load. Instead, the jacket repair transferred the lateral forces around the specimen which were no longer being carried by the monitored tie It was not until an applied load of 200 kips that the concrete jacket began to open along the path of the underlying center crack damage.

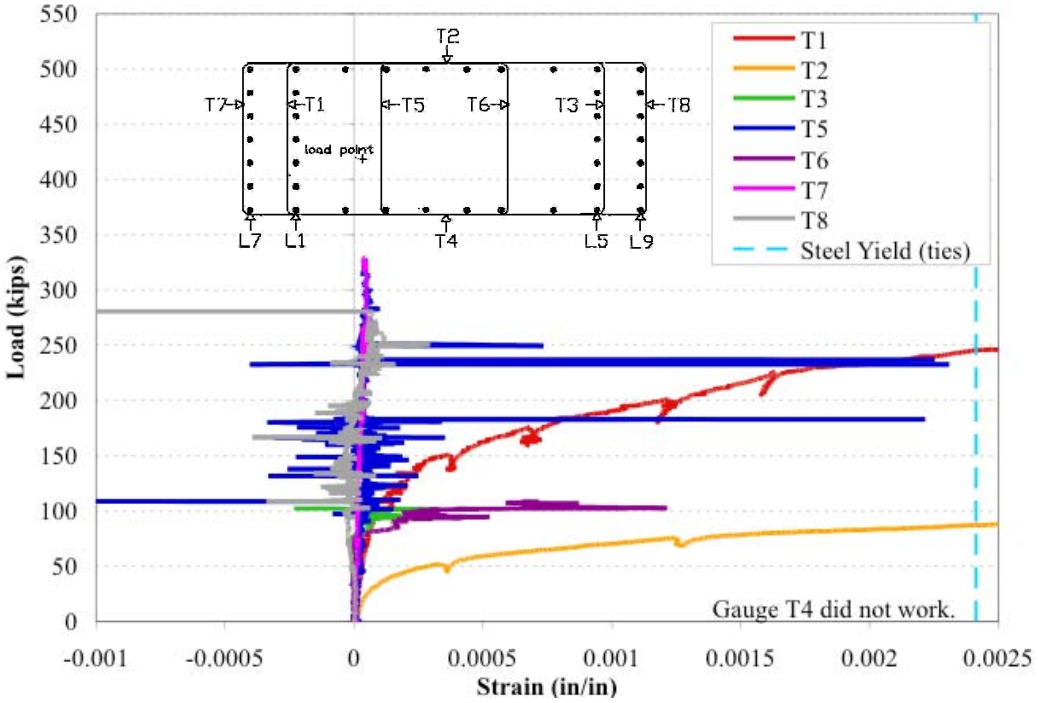

Figure 7.94: Concrete Jacket #1 Specimen Transverse Strain Measurements

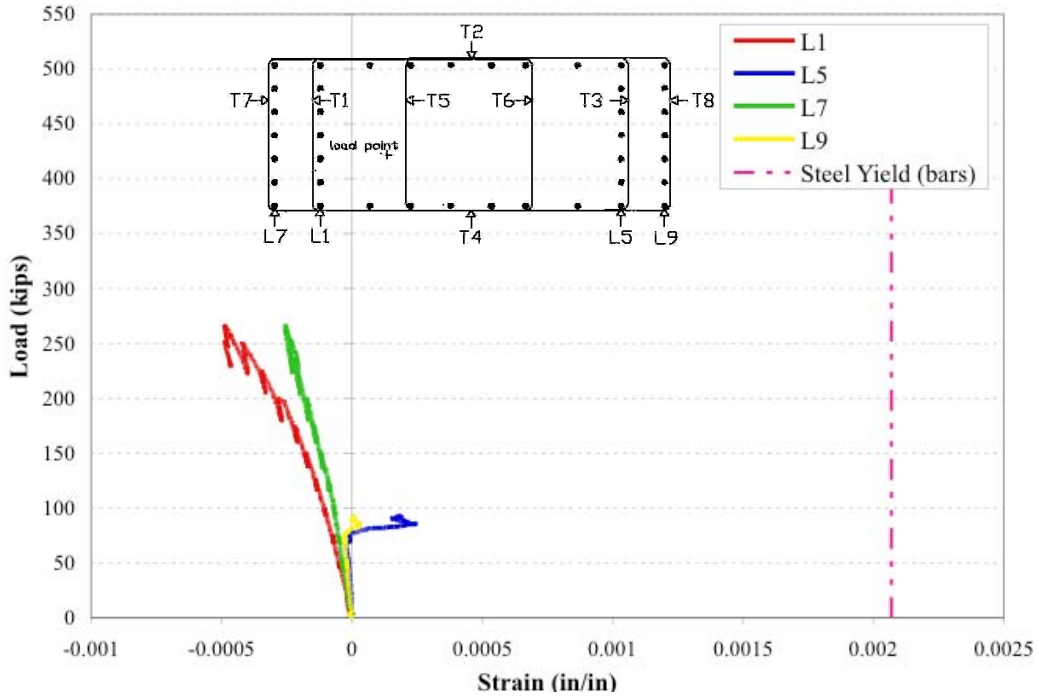

Figure 7.95: Concrete Jacket #1 Specimen Longitudinal Strain Measurements

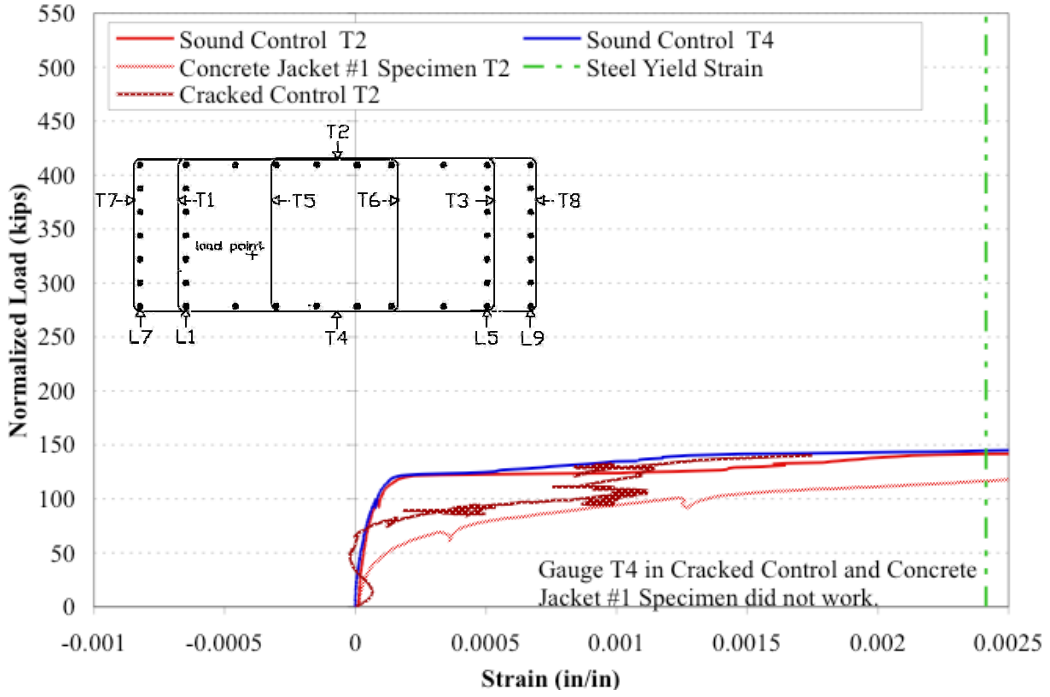

Figure 7.96: Concrete Jacket #1 Specimen Long Side Strain Gauge Comparison

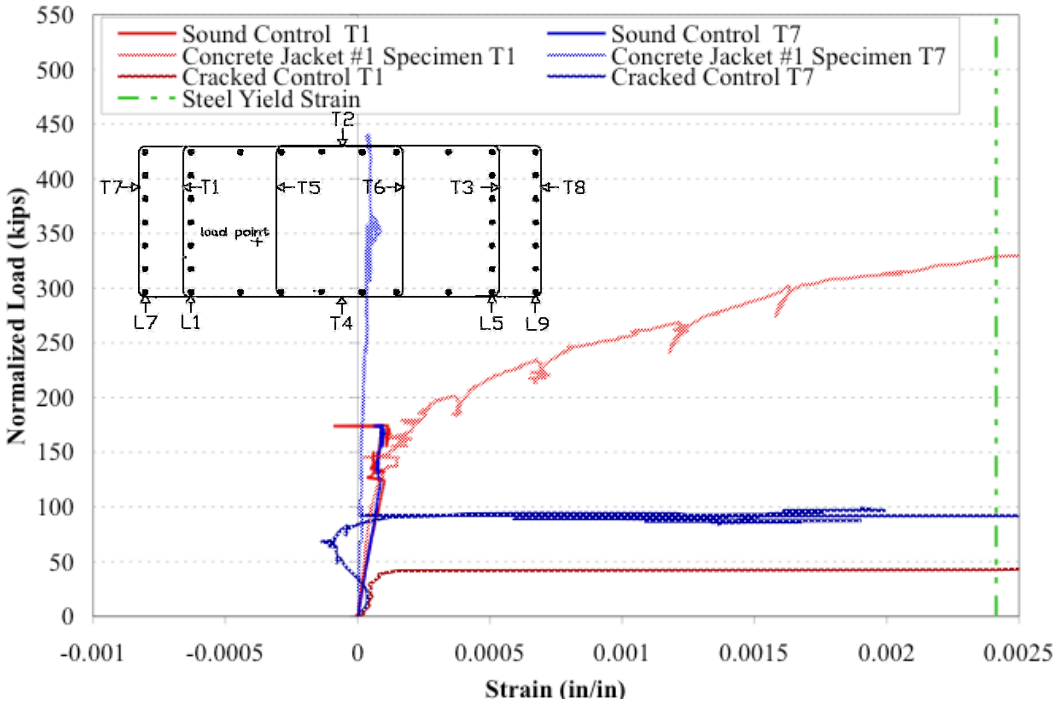

Figure 7.97: Concrete Jacket #1 Specimen Select Short Side Gauge Comparison

7.3.12.2 Failure

At 50 kips of top load, a small crack was found in center of the concrete jacket on the most heavily loaded long side of the specimen (the long side nearest to the load point). This crack, which is shown in Figure 7.98, was the initial cracking damage caused by load testing. Existing cracks were marked in blue ink and new cracks were marked in green ink in the pictures. The black arrow in this picture indicated the center of the load point. As the load increased through 200 kips, the initial crack lengthened and widened, as shown in Figure 7.99. As well, a new crack developed near the load point (on the left in the picture). At 325 kips, the concrete jacket repair fractured throughout its height and the center crack opened wide, as shown in Figure 7.100. The maximum load reached was 330 kips. At this load the concrete cover of the original specimen spalled from below the most heavily loaded bearing pad. As the original specimen's cover concrete was bonded to the concrete of the jacket repair, the resulting movement from the spall was that the repair peeled away from the specimen, as shown in Figure 7.101. Table 7.12 summarizes the performance of Concrete Jacket #1 Specimen along with the control specimens. Even without considering the normalized load, this specimen was able to exceed the maximum load capacity of the undamaged control specimen. Thus, the repair successfully met its goal of meeting or exceeding this load.

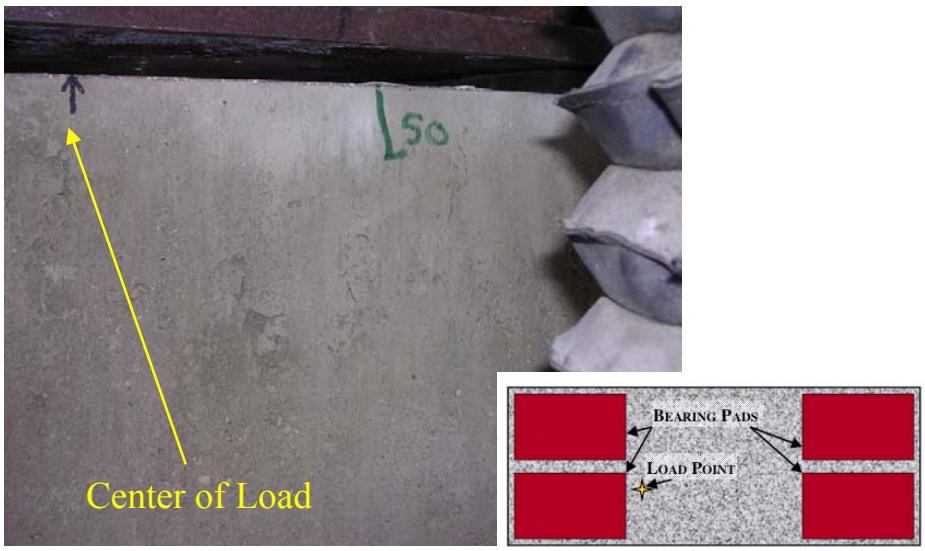

Figure 7.98: Initial Cracking in Concrete Jacket #1 Specimen

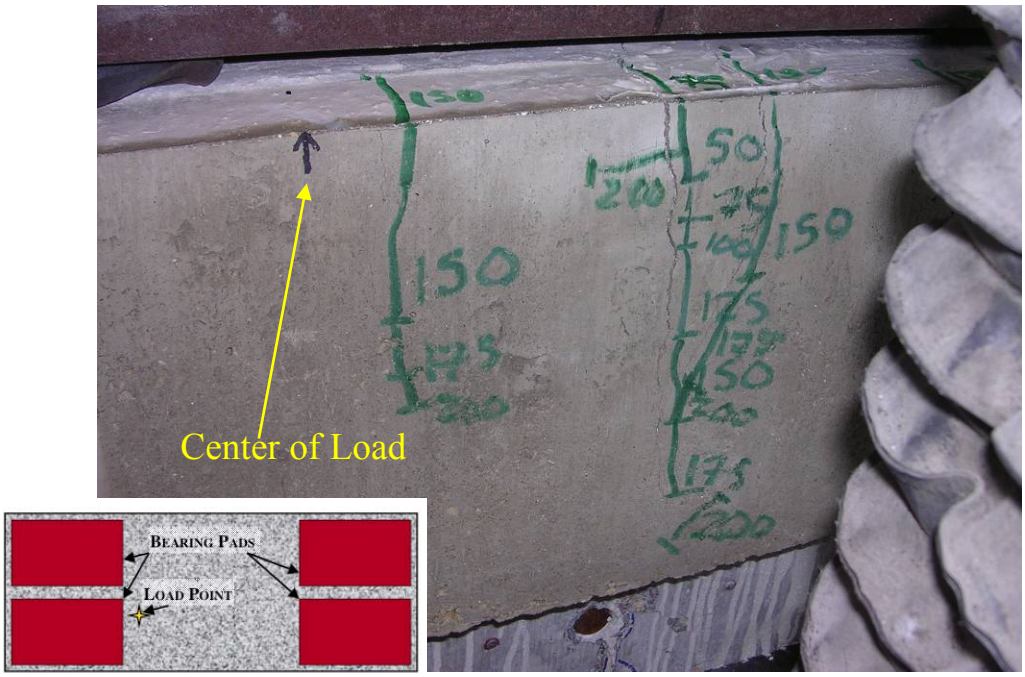

Figure 7.99: Center Crack Beginning to Open in Concrete Jacket #1 Specimen

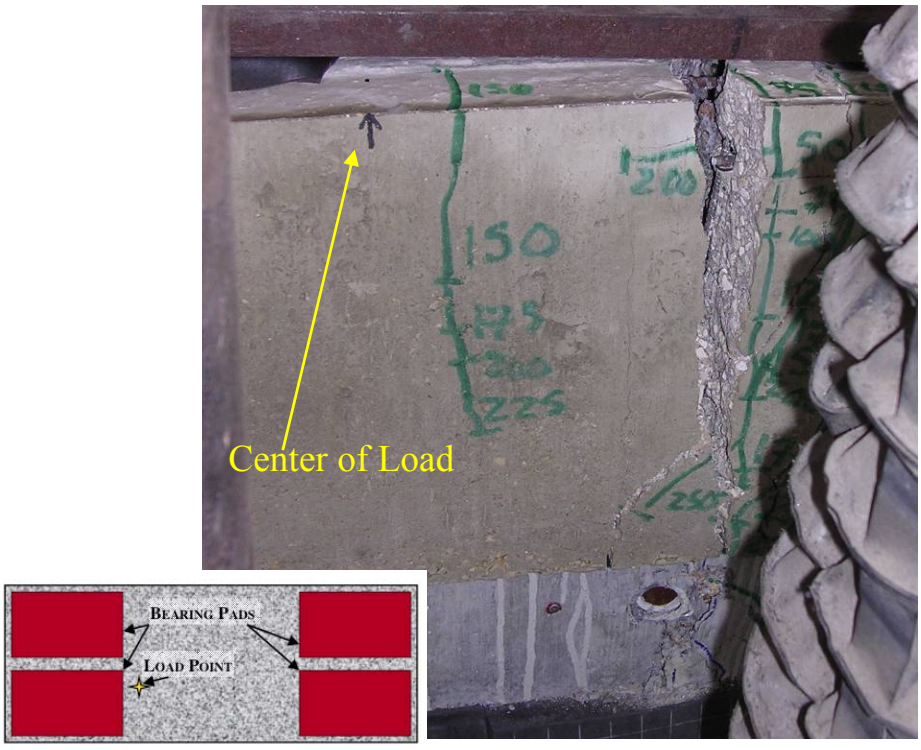

Figure 7.100: Fractured Concrete Jacket

Figure 7.101: Concrete Jacket #1 Specimen Failure

Table 7.12: Summary of Concrete Jacket #1 Specimen Performance

Specimen	f'c (psi)	Measured Peak Load (kips)	Predicted Bearing Load (kips)	Measured / Predicted	Normalized Peak Load (kips)	Normalized Undamaged Control
Undamaged Control	7100	315	567	0.56	315	1.00
Cracked Control	6700	284	535	0.53	301	0.96
Concrete Jacket #1 Specimen	5300	330	423	0.78	442	1.40

7.3.13 Concrete Jacket #2 Specimen

The second concrete jacket repaired specimen was tested on May 30, 2008. The specimen prior to testing is shown in Figure 7.102. This specimen duplicated the first concrete jacket repair in order to increase confidence in the results and look for trends. Prior to beginning the repair process, the specimen was pre-cracked to an average width of 0.09 inches. Before the concrete jacket repair was cast, but after the block was pre-cracked, the PVC voids were filled with reinforcing bars. On the day of testing three concrete cylinders each from the same batch of concrete as the specimen and the same batch of concrete as the concrete jacket were tested for strength. The specimen concrete average strength was 5600 psi and the concrete jacket average strength was 6100 psi. The results of load testing are given in the subsequent sections. A summary of the concrete jacket repair performance follows the results of this specimen.

Figure 7.102: Concrete Jacket #2 Specimen Prior to Testing

7.3.13.1 Strain Measurements

Figure 7.103 and Figure 7.104 present this specimen's transverse and longitudinal strain measurements, respectively. Smaller versions of Figure 7.12 were inset in the graphs and show the strain gauge locations within the bearing specimens. The restraining effect of the concrete jacket repair was especially evident on the short side strain gauges, as shown in Figure 7.103. Gauges T3, T6, T7, and T8 all monitor ties spanning the short width of the specimen and these gauges all reported relatively small strains during testing. Gauge T1 also monitored a short side tie and was the exception to the behavior of the short side ties in that it recorded some yielding behavior before it was restrained and took more load. This gauge's readings went erratic after a load of 110 kips. Figure 7.103 also shows the yielding behavior of the long side ties through the monitoring of gauges T2 and T4. At a top load of 155 kips, these gauges indicated the yielding behavior of their ties. Again, the concrete jacket then carried the transverse load around the specimen after the original specimen's ties yield. The jacket developed some cracks by a load of 100 kips. It did not, however, fracture along the line of initial cracking of the underlying specimen until a load of 250 kips was applied. This load was well above the yielding load for the monitored long side ties.

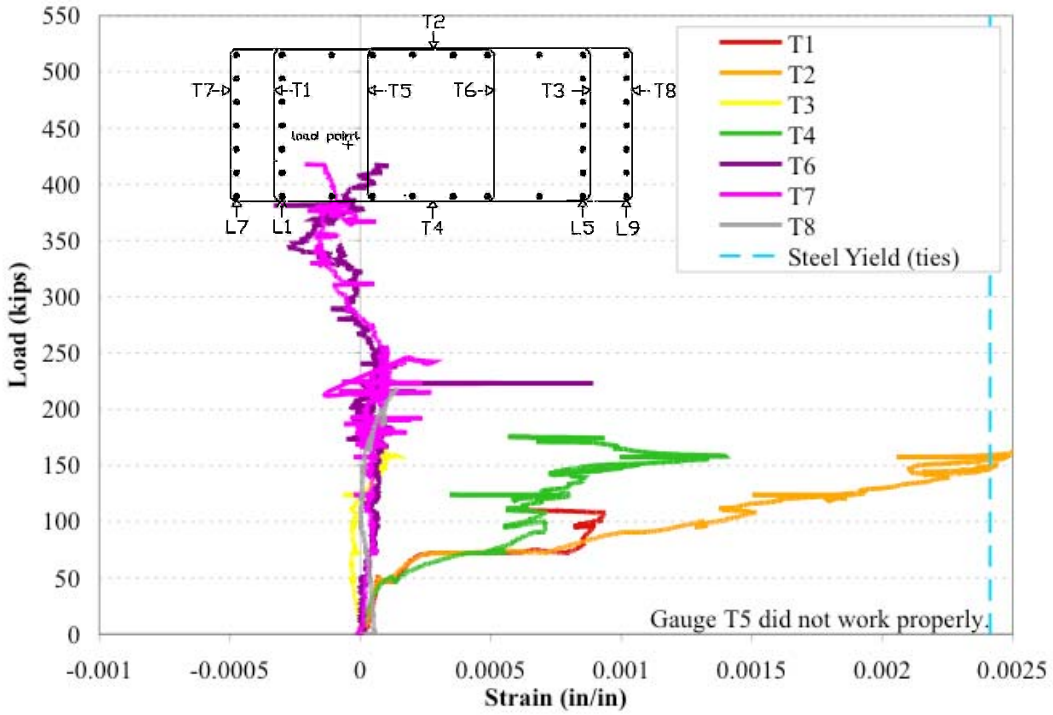

Figure 7.103: Concrete Jacket #2 Specimen Transverse Strain Measurements

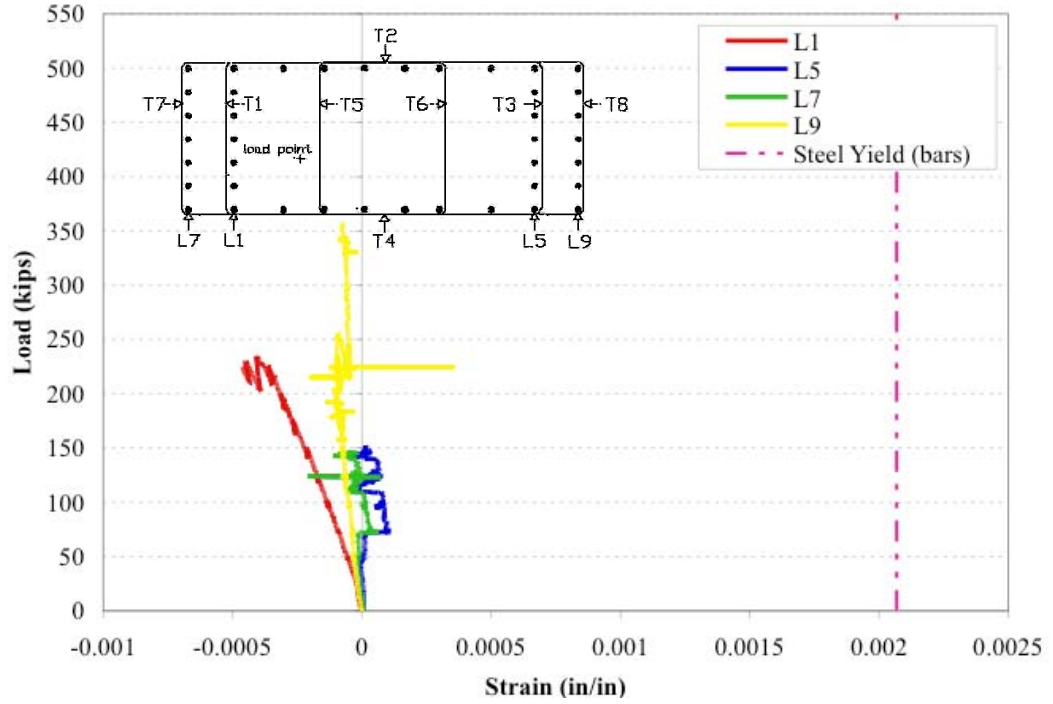

Figure 7.104: Concrete Jacket #2 Specimen Longitudinal Strain Measurements

The improvement in performance is shown more clearly in the comparison graphs of Figure 7.105 and Figure 7.106. These graphs present comparisons with the control specimens of the long side and select short side strain gauge measurements, respectively. The loads in the comparison graphs were normalized to the concrete strength of the undamaged control specimen. Figure 7.105 shows the improvement in long side tie performance due to the restraining effects of the concrete jacket repair. This graph shows the long side gauges reached yielding at a normalized load of 200 kips, which was over 50 kips greater than the yield load of the control specimens. Figure 7.106 more dramatically shows the potential improvement in strain behavior that was possible with this repair. Concrete Jacket #2 Specimen gauge T7 showed very little tensile strain during loading. As well, this gauge went into compression after the specimen fractured through the long side. After the fracture, the original concrete cover spalled beneath the most heavily loaded bearing pad, which caused the attached concrete jacket to peel away from the specimen. The compressive strain in T7, which was the exterior tie on the most heavily loaded short face, appeared related to the rotating concrete jacket. It seemed that as the jacket peeled away from the specimen, starting at the center, the short face was put into compression.

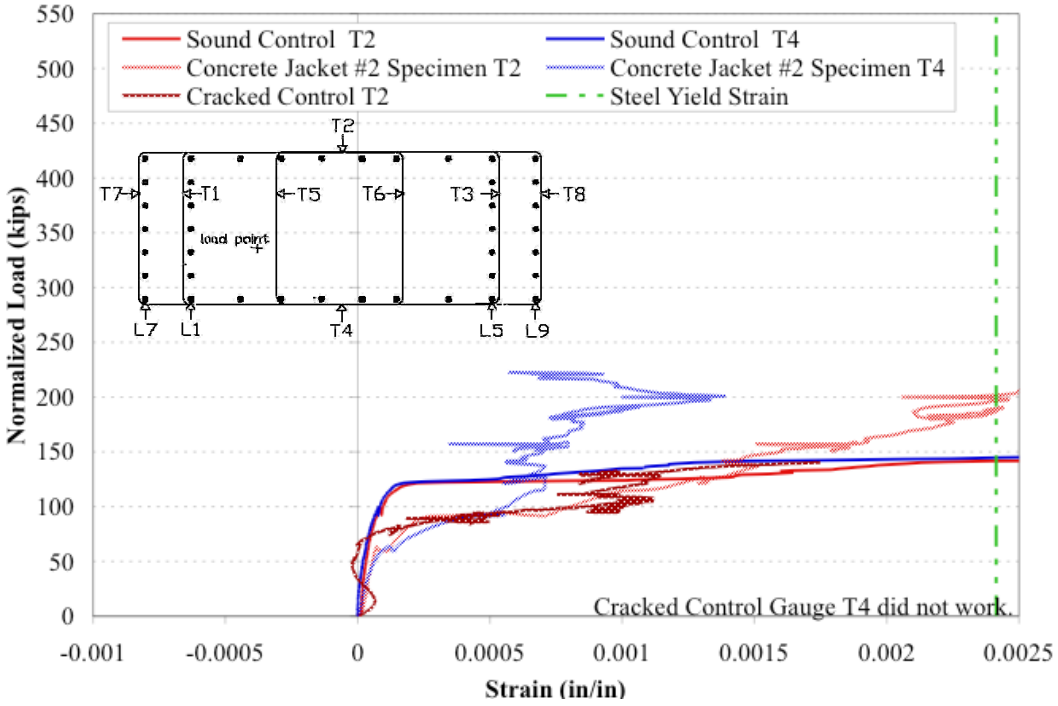

Figure 7.105: Concrete Jacket #2 Specimen Long Side Gauge Comparison

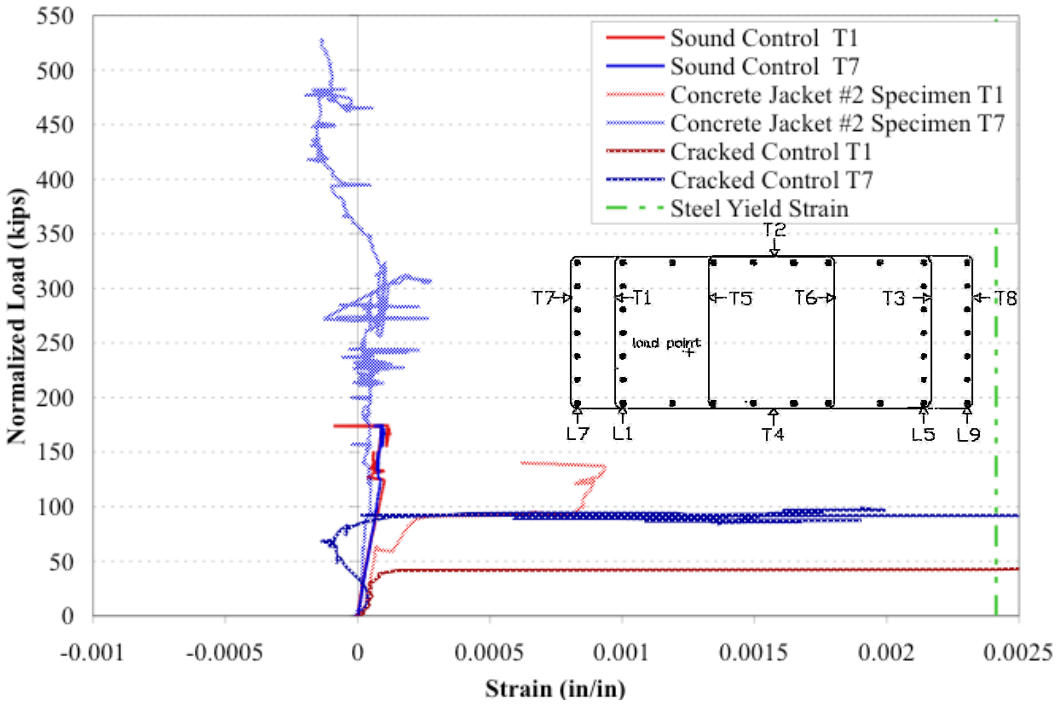

Figure 7.106: Concrete Jacket #2 Specimen Select Short Side Gauge Comparison

7.3.13.2 Failure

New crack formation at the top edge of the long jacket repair faces was noted at 100 kips. As shown in Figure 7.107, these new cracks at mid-length were the initial cracking damage to Concrete Jacket #2 Specimen. These initial cracks lengthened with increasing load. As well, additional distributed cracks developed in the jacket repair, as shown in Figure 7.108. At 230 kips the center cracks began to open wide as shown in Figure 7.109. By 250 kips the concrete jacket repair had fractured at the center crack location, as shown in Figure 7.110. At the maximum load of 418 kips, the concrete jacket repair peeled away from the long side of the specimen, as shown in Figure 7.111. Similar to Concrete Jacket #1 Specimen, the concrete cover of the original specimen spalled beneath the most heavily loaded bearing pad, which was bonded to the concrete jacket, and thus triggered the jacket peeling away from the specimen. Table 7.13 summarizes the performance of Concrete Jacket #2 Specimen along with the control specimens. This specimen easily exceeded the capacity of the undamaged control specimen with both gross load and the normalized load. The concrete jacket repair thus met its goal of meeting or exceeding the capacity of the undamaged control specimen.

Figure 7.107: Initial Cracking on Concrete Jacket #2 Specimen

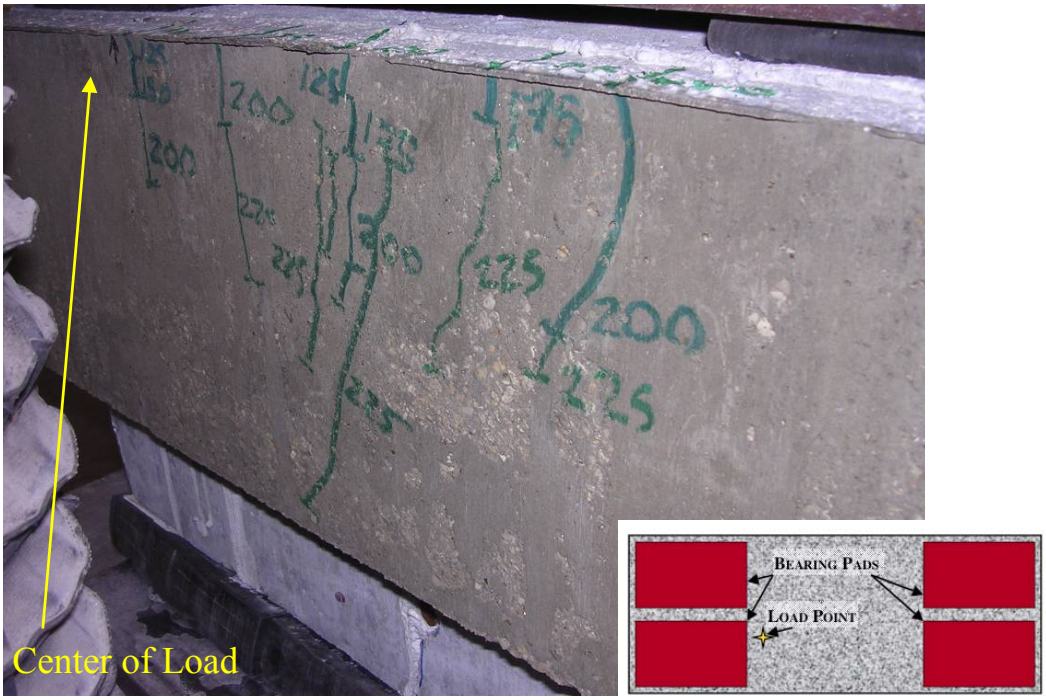

Figure 7.108: Distributed Cracking on Concrete Jacket #2 Specimen

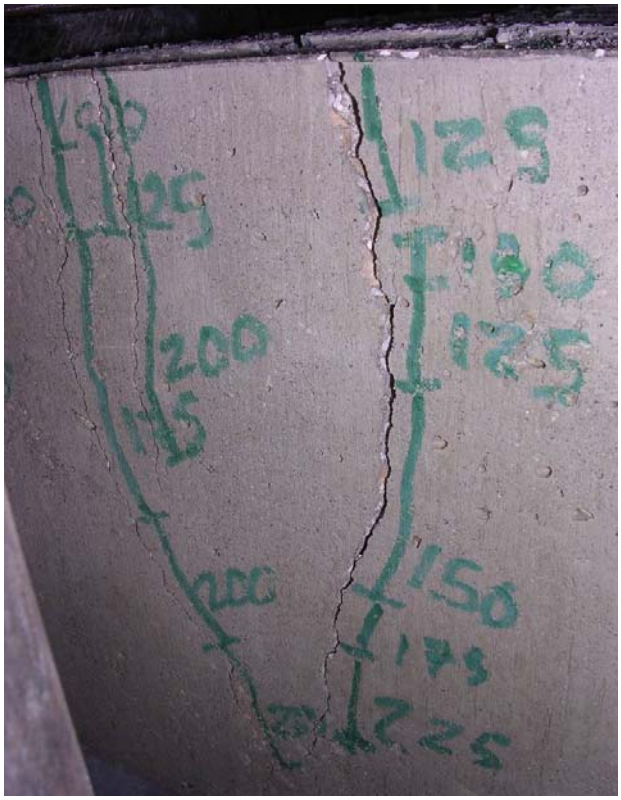

Figure 7.109: Center Crack Widens

Figure 7.110: Fractured Repair of Concrete Jacket #2 Specimen

Figure 7.111: Failure of Concrete Jacket #2 Specimen

Table 7.13: Summary of Concrete Jacket #2 Specimen Performance

Specimen	f'c (psi)	Measured Peak Load (kips)	Predicted Bearing Load (kips)	Measured / Predicted	Normalized Peak Load (kips)	Normalized Undamaged Control
Undamaged Control	7100	315	567	0.56	315	1.00
Cracked Control	6700	284	535	0.53	301	0.96
Concrete Jacket #2 Specimen	5600	418	447	0.94	530	1.68

7.3.14 Concrete Jacket Repair Summary

Figure 7.112 and Figure 7.113 present the long side and select short side strain gauge measurements, respectively, of the concrete jacket repaired specimens and the control specimens for comparison. These graphs use loads that were normalized to the concrete strength of the undamaged control specimen. Figure 7.112 shows a mixed result with one specimen exhibiting loads above the control specimens and the other indicating yielding at a lower load than the controls. As Concrete Jacket #1 Specimen's gauge T4 did not work, the long side of this specimen was judged by looking at only one gauge and its tie. It was possible that during initial cracking this tie experienced more yielding deformation than those in the other specimens. The mat of top steel featuring number two bars that ran along the long side of the specimen halted the initial cracking at the top of the long sides. The specimens had a varied crack width at the top of the long sides, which was accommodated by adjusting the width of the crack at the middle and lower demec points to achieve a consistent average crack width. It was possible that the bottom layers of lateral ties in Concrete Jacket #1 Specimen were yielded during initial cracking and so the top lateral tie, which had been sheltered by the top steel during initial cracking, then had to carry more stress during testing. As well, the low yielding load of Concrete Jacket #1 Specimen could have been from the long side ties having to yield before the jacket repair fully engaged in transferring force around the specimen. Thus, this difference in performance appeared to be variability of experimentation that was exacerbated by a small sample size. Figure 7.113, however, shows the fairly consistent improvement of short side tie behavior resulting from concrete jacket repairs. For instance, in this figure the T7 gauge of both repaired specimens, which monitored the exterior tie on the most heavily loaded short side, recorded very little strain throughout testing, indicating that the short side was consistently well restrained by the repair.

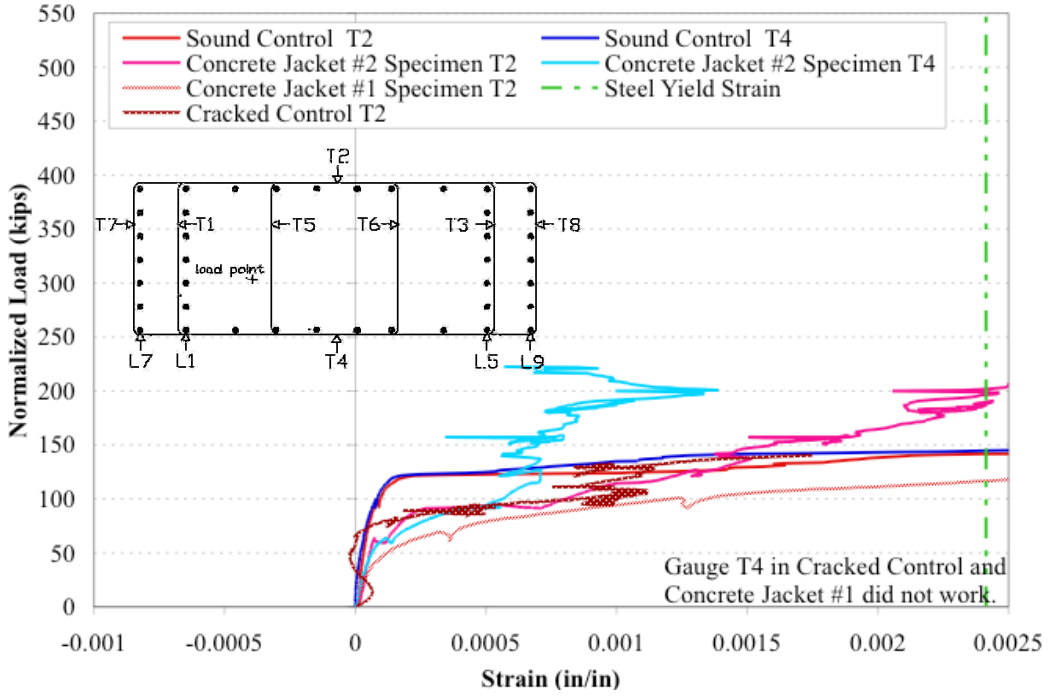

Figure 7.112: Concrete Jacket Specimens Long Side Strain Gauge Comparison

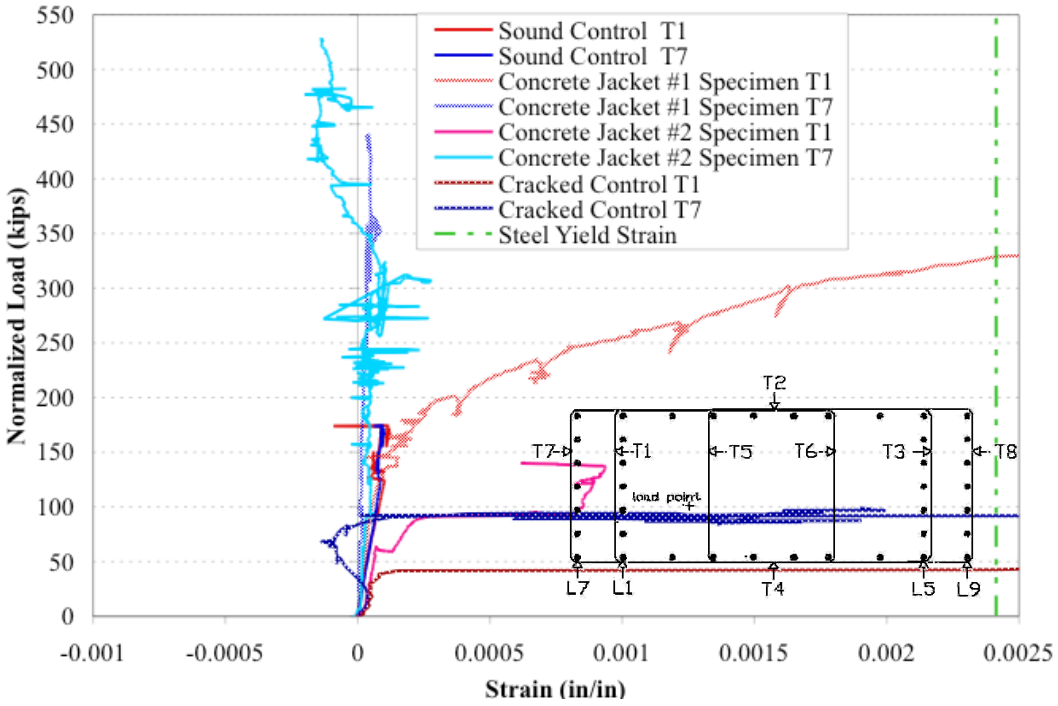

Figure 7.113: Concrete Jacket Specimens Select Short Side Gauge Comparison

As can be seen from Figure 7.114 and Figure 7.115, the concrete jacket specimens failed in identical fashions. Both failed by crushing the concrete underneath the most heavily loaded bearing pad (the bottom right hand corner of the specimens in these pictures), which caused the concrete cover of the original specimen to spall in this region. As well, the most heavily loaded quadrant tried to rotate away from the rest of the specimen, as was observed in the cracked control specimen. This rotation in combination with the cover spalling appeared to have triggered the jacket repair to peel away from the specimen.

Figure 7.114: Concrete Jacket #1 Specimen Damage

Figure 7.115: Concrete Jacket #2 Specimen Damage

Without accounting for the influence of concrete strength, the concrete jacket repairs' average failure load of 374 kips exceeded the undamaged control specimen's failure load of 315 kips. Table 7.14 summarizes the results of the concrete jacket repairs and the control specimens with the loads normalized to the undamaged control specimen's concrete strength. Considering the normalized results, the concrete jacket repair specimens' average failure load was 486 kips, which is 154% of the undamaged control specimen's failure load. The concrete jacket repairs also brought the load capacity of the specimens near the predicted values, which indicated they confined the initial cracking damage and overcame the specimens' lack of lateral restraint in their boundary conditions. Thus, the concrete jacket repair succeeded in meeting and exceeded the goal of bring the capacity of the repaired specimen up to the undamaged control specimen capacity.

Table 7.14: Summary of Concrete Jacket Specimen Performance

Specimen	f'c (psi)	Measured Peak Load (kips)	Predicted Bearing Load (kips)	Measured / Predicted	Normalized Peak Load (kips)	Normalized / Undamaged Control
Undamaged Control	7100	315	567	0.56	315	1.00
Cracked Control	6700	284	535	0.53	301	0.96
Concrete Jacket #1 Specimen	5300	330	423	0.78	442	1.40
Concrete Jacket #2 Specimen	5600	418	447	0.94	530	1.68
ASR/DEF Column A	6000	491	479	1.03	581	1.84
ASR/DEF Column B	5800	480	455	1.05	588	1.87

7.3.15 Loading Summary

This section will summarize the findings from testing the bearing specimens. It contains several figures and a table compiling the results of all specimens for direct comparison. As well, the summary table includes the capacities of Kapitan's undamaged specimen and design load to give perspective to the repair capacities.

Figure 7.116 through Figure 7.119 show strain comparisons of all the tested specimens. Each graph compares the behavior of the specimens at a single strain gauge location. The loads for these comparisons were all normalized to the concrete strength of the undamaged control specimen. As several ties (where the transverse strain gauges were located) yielded prior to a specimen's peak load, these plots frequently show yield plateaus at loads lower than the specimen's maximum normalized load. Some of the yield curves abruptly end when the lead wire, which connected the strain gauge to the data acquisition system, broke during testing. Figure 7.116 presents the readings from gauge T1 in all specimens. The graph shows that all of the repairs substantially improved behavior relative to the cracked control specimen. Several specimens, including both of

the post-tensioned repairs, had initial strains similar to the undamaged control specimen. The similar strain rate indicated that the post-tensioning repair returned the repaired specimen to the undamaged stiffness of the undamaged control specimen. Concrete Jacket #1 Specimen had the greatest yield load recorded for the tie monitored by gauge T1, which was at a normalized load of 330 kips. This load was higher than both the yield load for the same tie and the peak load of the undamaged control specimen. Figure 7.117, which presents the behaviors recorded at gauge T2 (located mid-length on the long side tie away from the load point, as indicated in the inset of Figure 7.117), did not show uniform improvement compared to the cracked control. Concrete Jacket #1 Specimen and Packing Strap #2 Specimen both yielded at normalized loads lower than the control specimens. The remaining specimens exhibited yield strains that were greater than both control specimens, although to varying degrees of improvement. For instance, Concrete Jacket #2 Specimen yielded on a gradual sloping curve that eventually surpassed the undamaged control performance whereas FRP #1 Specimen did not exhibit significant yielding behavior as its load-strain curve maintained a nearly linear course at a much steeper slope than the concrete jacket's slope. The other long side gauge monitored, T4, did not allow for comparisons with the cracked control specimen as this gauge did not work on the day of testing, as shown in Figure 7.118. Instead, the comparison here showed that most of the repaired specimens were unable to re-establish the initial stiffness of the undamaged control specimen, as evidenced by their initial slopes. Two notable exceptions were FRP #2 Specimen and Post-tensioned #2 Specimen, which started off registering compression before they begin sloping towards the tensile side of the graph. The FRP #2 Specimen maintained its small strains thanks to the repair preventing long side fracture, which occurred in all other specimens except for the FRP repaired specimens. Figure 7.119 presents the measured behavior at gauge T7. This figure, as did Figure 7.116, showed the universal improvement provided by the repairs as compared to the yielding load of the cracked control specimen. The packing strap repairs showed the least improvement, which corresponded to the straps breaking off the specimens at a load lower than the capacity of the cracked control specimen. The straps

did, however, improve the gauge T7 behavior. The concrete jacket repairs exhibited the most striking improvement with nearly zero strain in gauge T7 measured throughout these tests.

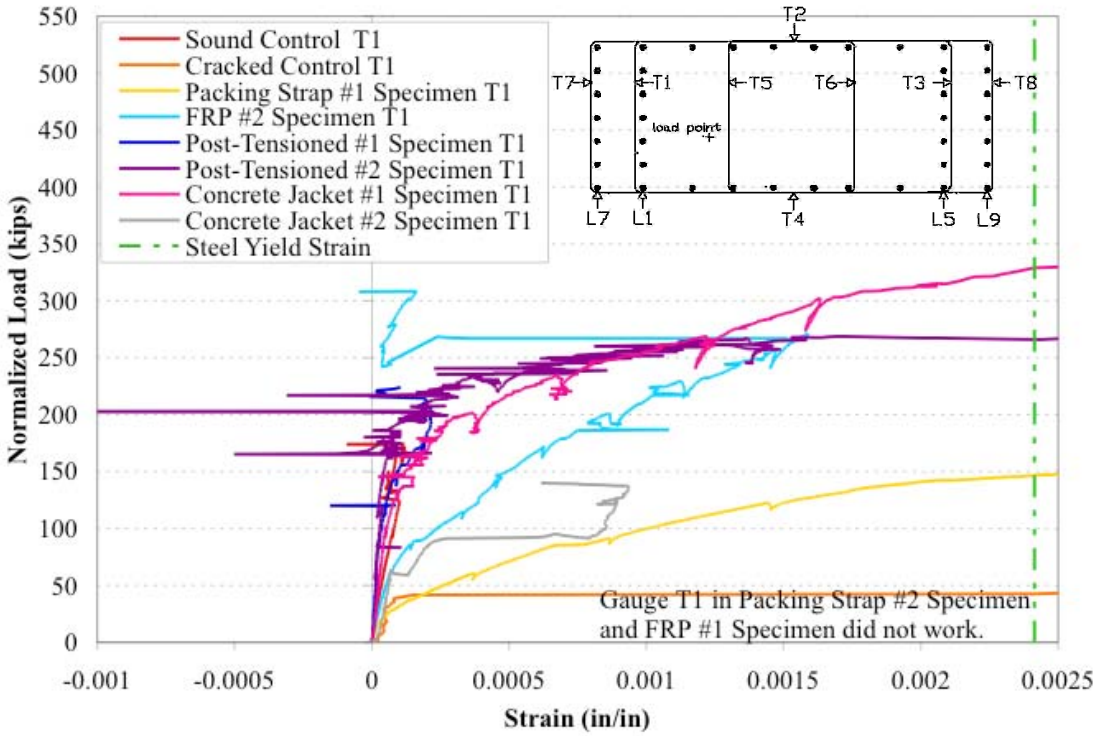

Figure 7.116: Strain Gauge T1 from all Bearing Specimen Tests

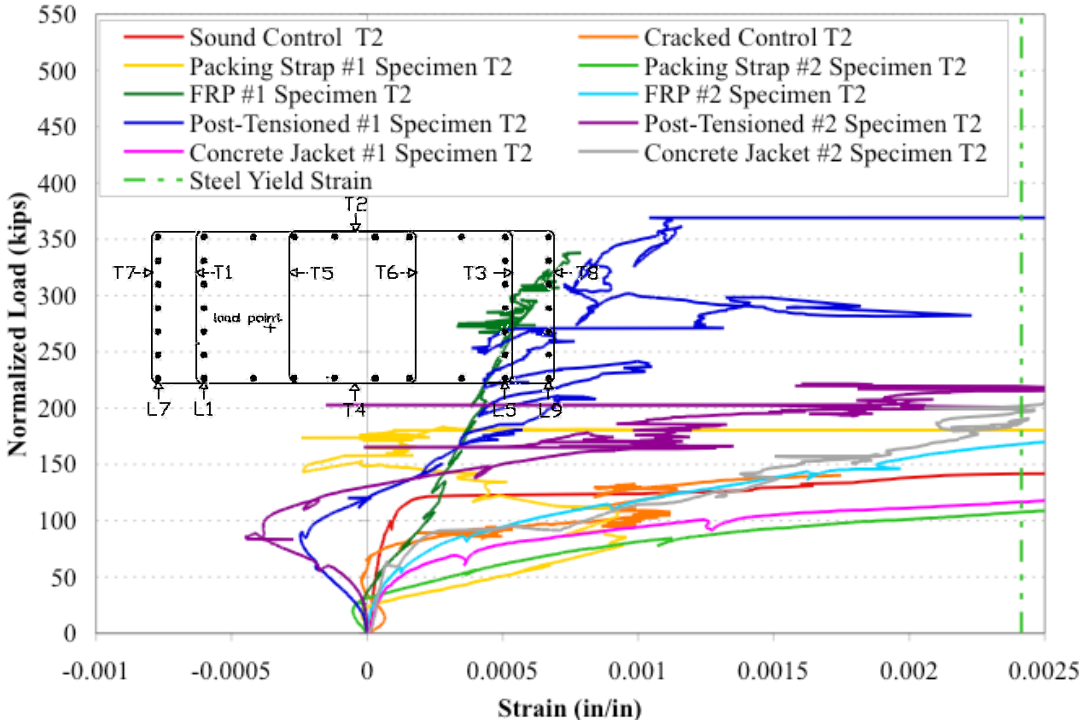

Figure 7.117: Strain Gauge T2 from all Bearing Specimen Tests

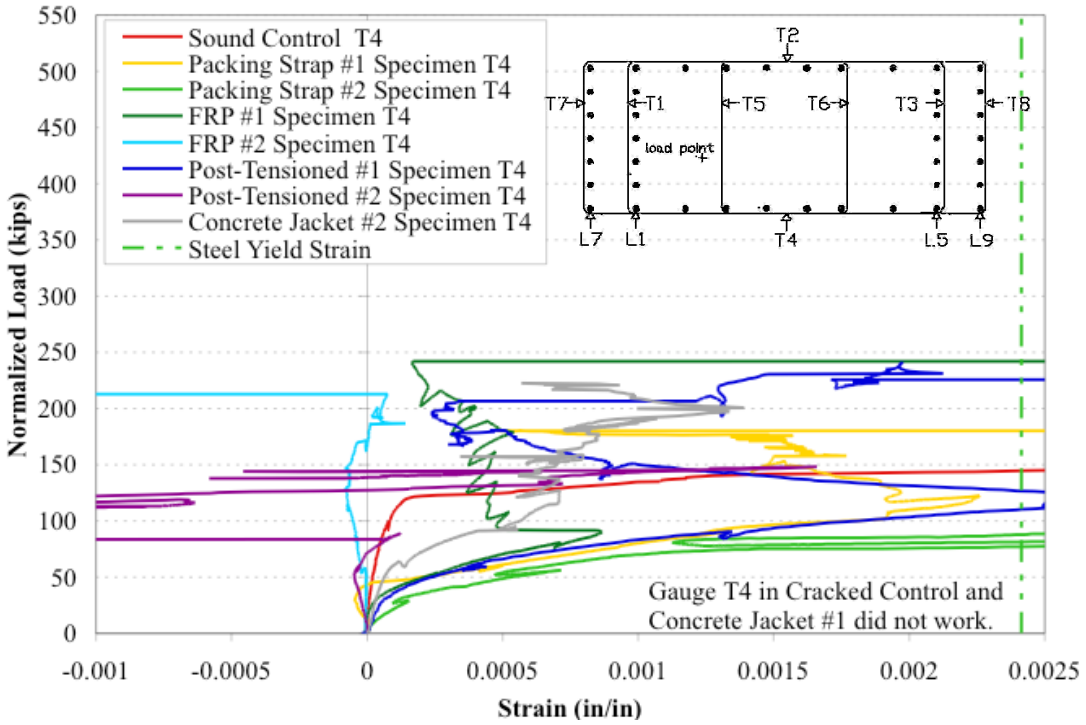

Figure 7.118: Strain Gauge T4 from all Bearing Specimen Tests

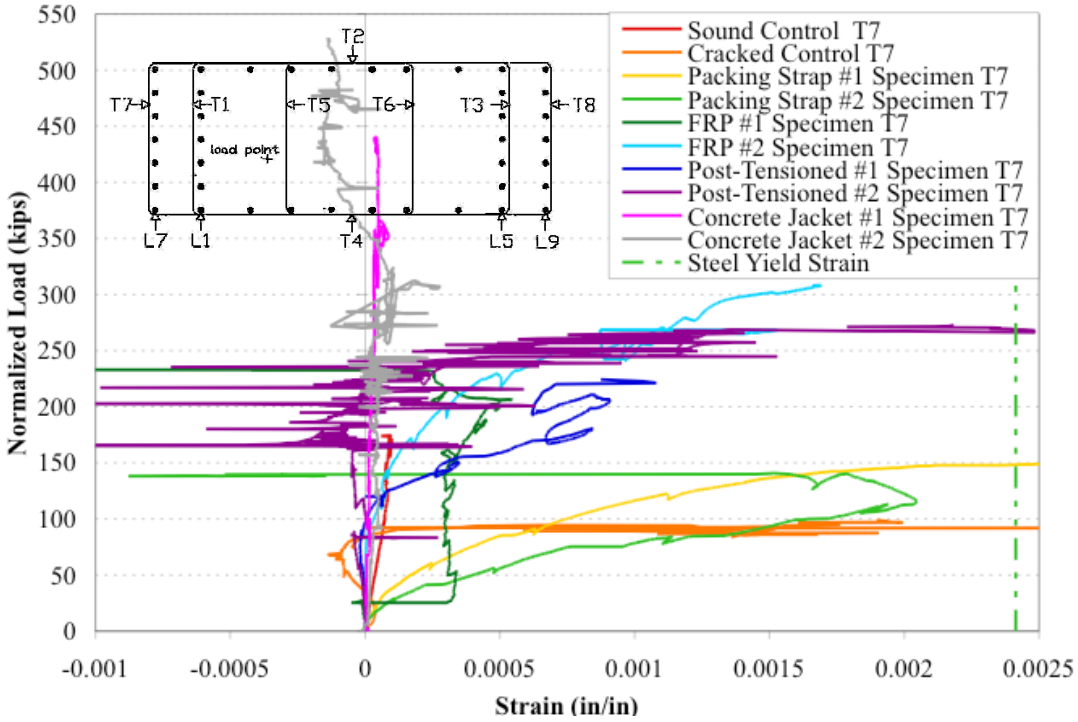

Figure 7.119: Strain Gauge T7 from all Bearing Specimen Tests

Table 7.15 summarizes the performance of all the repaired and control bearing specimens along with the control and ASR/DEF affected scaled column specimens and the factored design load, which were provided for comparison. As discussed with the results of the tests, there was a wide range of failure values. For instance, the packing strap specimens failed at a load less than the control specimens while the post-tensioned and concrete jacketed specimens nearly doubled the capacity of the control specimens. While there was some variation in the capacity of each repair, they were all designed to carry the same lateral (confining) load of 9.25 kips. As discussed in Chapter 4, this design capacity was developed from Kapitan's strut and tie model of his control scaled column specimen test. The one quarter of the load demand in the scaled column specimen's top reinforcing tie during peak applied load was used for repair design. Resulting from the nature of the repair, the post-tensioned specimens had more concentrated confining pressures than the other repairs. As the other repairs were fully distributed along the top ten inches of the bearing specimens, the concentrated post-tensioned repair likely had a different centroid (center of resistance/confinement) than the other repairs. Figure 7.120

through Figure 7.123 present select comparisons of data from Table 7.15 as bar graphs. Figure 7.120 shows the comparisons of each specimen's measured maximum load to predicted load. The predictions of bearing load capacity assumed the whole scaled column dimensions and were based on the concrete cylinder strength of each specimen. The solid blue line represented measured peak loads meeting the predicted load for that specimen's concrete strength. The ASR/DEF specimens, which were scaled column specimens, both exceeded this line. As discussed in Chapter 6, their performance demonstrates the full capacity retention of these specimens despite the ASR/DEF deterioration. The bearing specimens, however, did not share the same boundary conditions as the scaled column specimens. This effect was described earlier in this chapter. The effect of boundary condition resulted in the control specimens' peak load capacities fell well below the predicted bearing load. This figure also shows that the packing strap and FRP repairs were unable to overcome the boundary condition deficiency. Therefore, the measured-to-predicted ratio for these repairs were also well below the ideal ratio of one. The post-tensioned and concrete jacket repairs showed significant improvement of performance with ratios near one. This plot, therefore, showed the outstanding performance of the post-tensioned and concrete jacket repairs. In Figure 7.121 through Figure 7.123, three lines were plotted for the reader's reference. The dark blue line represented the performance of the undamaged control specimen. The goal of the repairs was to return the damaged specimens to meet or exceed the undamaged control specimen's peak capacity. This value was highlighted for easy assessment of the various repairs ability to reach that goal. The factored design load, scaled for the specimen size, was shown as a light blue line. This load was used to initially design the bridge columns in the field, which were modeled by these specimens. Therefore, this line represented the minimum capacity required for public safety. Repairs falling below this line were unacceptable. The green line, near the top of these plots, represented the capacity of Kapitan's undamaged scaled column specimen. Similar to the measured versus predicted ratio discussed earlier, this value highlighted the capacity reduction triggered by differing boundary conditions between the specimen types. As

well, the repaired specimens with capacities near or exceeding this line showed exceptional strengthening. Comparisons of each specimen's normalized peak load to the undamaged control's load are presented in Figure 7.121. This plot was a classic comparison of the results to the control in order to quantify the performance of the different repair techniques examined. As discussed when describing the dark blue line in these plots, the goal of the repairs was for the repaired specimens to meet or exceed the peak load capacity of the undamaged control specimen. In this plot, the successful meeting of this goal is represented by ratios greater than or equal to one. Thus, the plot shows that the FRP, post-tensioning and concrete jacket repairs all meet the experimental goal. Figure 7.122 compares the normalized peak loads to Kapitan's undamaged column specimen. In these three plots, this comparison was represented by the green line. While the scaled column and bearing specimen styles had different boundary conditions influencing their final capacities, this plot demonstratesd which repair techniques were able to overcome the bearing specimens' lack of lateral restraint in the boundary condition. Specifically, the post-tensioned and concrete jacket repairs showed outstanding improvements in capacity. This superior strengthening performance was evidenced by these repaired specimens nearing or exceeding the undamaged scaled column specimen's performance. In Figure 7.123, the normalized peak loads of the bearing specimens were compared to the original design load, scaled to the specimens size. In Figure 7.121 through Figure 7.123, this value was represented by the light blue line. This plot emphasized the reserve capacity in the existing columns and showed the ability of the post-tensioned and concrete jacket repairs to more than double the design load with their peak load capacities. The packing strap repair's average performance failed to meet this minimum required capacity. As such, this repair, as used in this experimental program, failed to give satisfactory performance. The normalized loads were based upon the concrete strength of the undamaged control specimen. Each load was normalized by dividing the measured maximum load by that specimen's concrete strength and then multiplying the resulting quotient by the undamaged control specimen's concrete strength. The resulting product was the normalized load. Figure 7.120 through

Figure 7.123 also show the average behavior of each repair technique. The averages and control specimen values were shaded for accent.

Table 7.15: Summary of Bearing Specimen Performance

Specimen	f'c (psi)	Measured Maximum Load (kips)	Predicted Bearing Load (kips)	Measured / Predicted	Normalized Maximum Load (kips)	Normalized / Undamaged Control	Normalized / Undamaged Column	Normalized / Factored Design Load
Undamaged Control	7100	315	567	0.56	315	1.00	0.54	1.65
Cracked Control	6700	284	535	0.53	301	0.96	0.51	1.58
Packing Strap #1	5800	157*	455	0.35*	192*	0.61*	0.33*	1.01*
Packing Strap #2	6300	130*	503	0.26*	147*	0.47*	0.25*	0.77*
FRP #1	6600	317	527	0.60	341	1.08	0.58	1.79
FRP #2	6200	269	495	0.54	308	0.98	0.53	1.61
Post-tensioned #1	5900	502	471	1.07	604	1.92	1.03	3.16
Post-tensioned #2	6000	416	479	0.87	492	1.56	0.84	2.58
Concrete Jacket #1	5300	330	423	0.78	442	1.40	0.76	2.31
Concrete Jacket #2	5600	418	447	0.94	530	1.68	0.91	2.77
ASR/DEF Column A	6000	491	479	1.03	581	1.84	0.99	3.04
ASR/DEF Column B	5700	480	455	1.05	588	1.87	1.01	3.08
Undamaged Column (Kapitan)	5800	478	463	1.03	585	1.86	1.00	3.06
Factored Design Load		191^{+}			191^{+}	0.61	0.33	1.00

* Failure Load of the Repair $^{+}$ Calculated

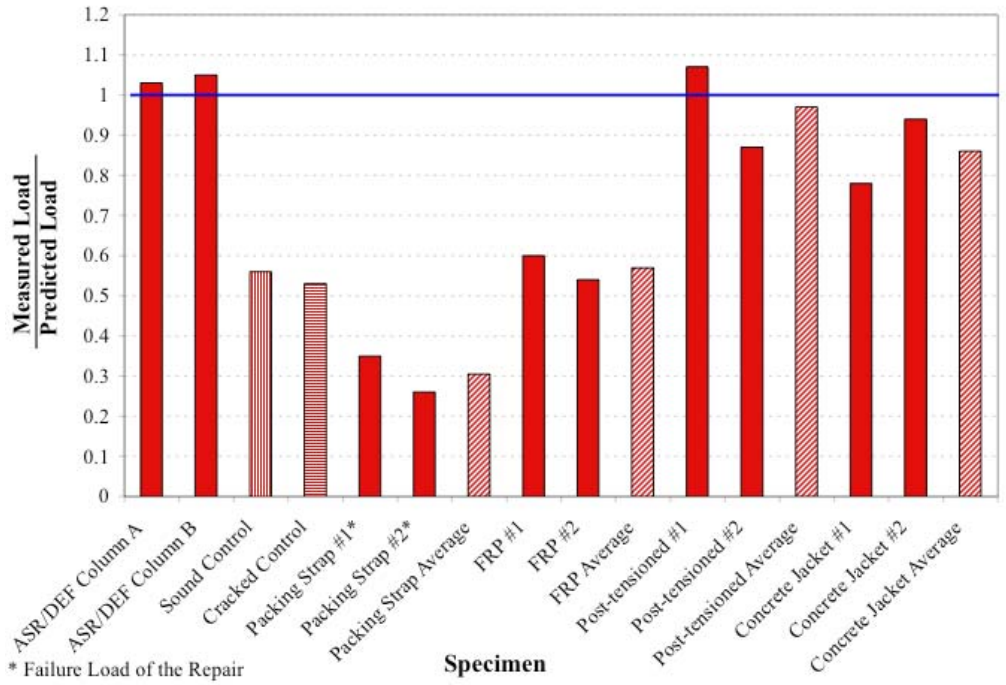

Figure 7.120: Specimens' Measured Load Compared to Specimens' Predicted Load

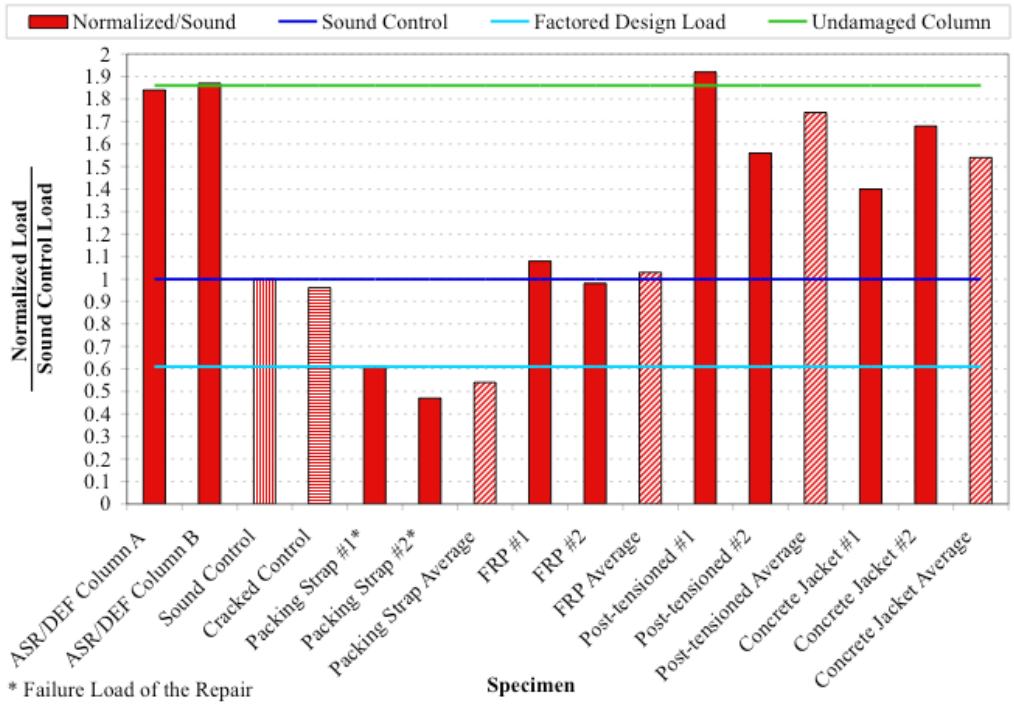

Figure 7.121: Specimens' Normalized Load Compared to Undamaged Control Load

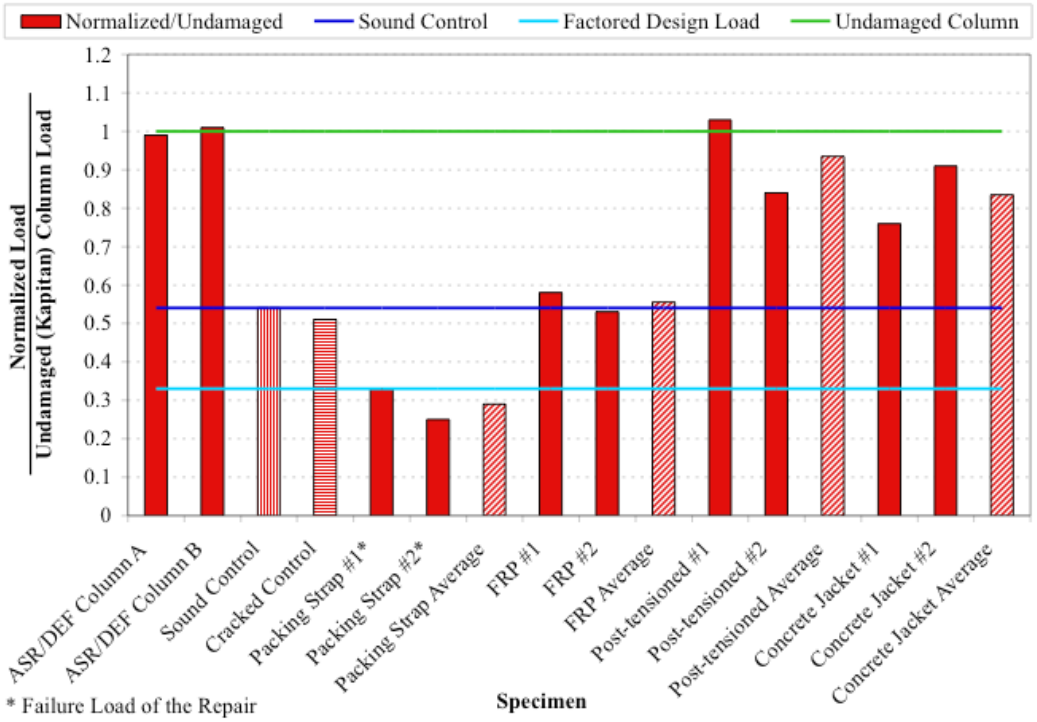

Figure 7.122: Specimens' Normalized Load Compared to Undamaged Column Load

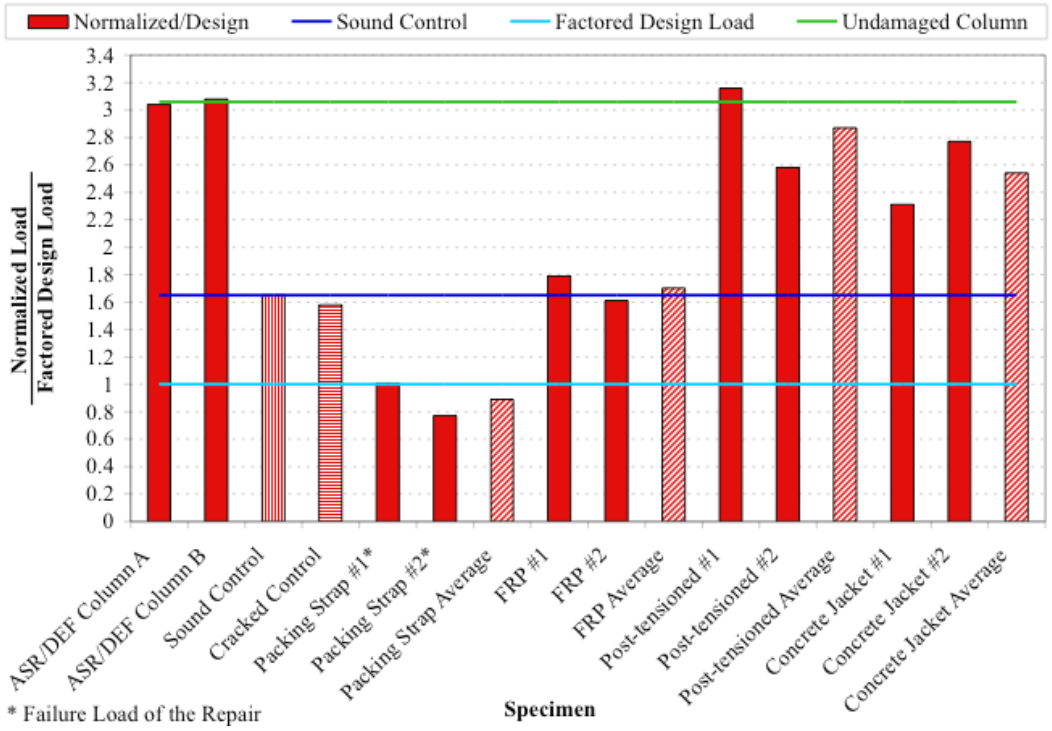

Figure 7.123: Specimens' Normalized Load Compared to Factored Design Load

Figure 7.120 shows that the undamaged control specimen had a measured maximum load well below the value predicted for a column with the same concrete strength. As described in the results section for the undamaged control specimen, the neoprene pad beneath the bearing specimens did not provide the lateral or rotational restraint equivalent to a continuous concrete column. Thus, when the cracking on the long side of the specimens propagated throughout the sixteen-inch height, the bearing specimens fractured. The scaled column specimens experienced cracks in the long face as well. These cracks propagated farther down the column than the sixteen-inch height of the bearing specimens. The scaled column specimens, however, were restrained from fracturing by the adjacent concrete and reinforcing steel of the remaining column. Thus, the significant difference in performance between the scaled column and bearing specimens was the different boundary condition at sixteen inches from the column top. The boundary conditions were differentiated by the restraint provided by the adjacent column in the scaled column series. Without the continuation of the column, the bearing blocks were able to rotate after fracture, which caused the center crack to open very wide. The continuous concrete of the scaled column specimens prevented the column capital from rotating after cracking and thus achieved the predicted bearing loads. The cracked control specimen, like the undamaged control specimen, lacked sufficient lateral restraint to achieve the predicted bearing load for its concrete strength. Additionally, the existing cracks of this control resulted in a fracture of the block at a lower load than the undamaged control, further reducing its capacity. The repairs, therefore, worked to overcome the capacity deficiency caused by the initial cracking and to provide additional lateral restraint to the specimen. Figure 7.120 also shows that the post-tensioned and concrete jacket repairs were able to provide enough lateral restraint that these specimens neared or exceeded their predicted loads during testing. As well, Table 7.15 shows these two repair types, post-tensioning and concrete jacketing, to near or exceed the ultimate capacity of Kapitan's control in the scaled column series. Thus, these repair types well exceeded the experimental goal of matching the undamaged control bearing specimen's capacity. Additionally, these techniques were able to overcome the difference in

boundary condition to reach loads comparable to the scaled column series. The packing strap repairs failed at a load less than the cracked control's capacity, and thus did not bring the specimen capacities near their predicted bearing loads. While the FRP repaired specimens also did not reach the predicted bearing loads, these specimens did average normalized peak loads greater than the undamaged control specimen's capacity, thus achieving the experimental goal for the repairs.

With the exception of the packing strap specimens, all of the repairs averaged normalized peak loads higher than the undamaged control specimen's capacity, as shown in Figure 7.121. FRP #2 Specimen's normalized peak load almost matched the undamaged control's load. Its small deficiency, which might be due to the slightly larger average cracking width of that block, emphasized the variability of FRP performance noted in the literature. The post-tensioned and concrete jacket repairs showed significant restraint and exceeded the undamaged control's capacity by 40-84% using normalized loads.

Figure 7.122 presents the normalized peak loads as a function of Kapitan's undamaged column specimen. This comparison highlighted the improvement possible with repair, especially in the performance of the post-tensioned specimens. Post-tensioned #1 Specimen exceeded the undamaged scaled column specimen's capacity. Recall from the description of the post-tensioned specimens' testing, that loading was stopped for safety when it appeared that the post-tensioning system was nearing failure before the concrete failed. Thus, it was probable that with increased robustness of the post-tensioning system the specimens could have reached values higher than Kapitan's undamaged scaled column specimen.

The normalized peak loads of the bearing specimens are compared to the original design load scaled to the specimens' size in Figure 7.123. As found by Kapitan and shown here in the ASR/DEF columns, the actual columns had significant reserve capacity compared to the design load. This plot and Table 7.15 show the scaled column specimens to have

three times the required capacity of the design load. With the difference in boundary condition, the control specimens of the bearing specimens had a greatly reduced capacity compared to the scaled columns, but these bearing specimens were still in excess of the design load. The packing strap repair is the only method to have failed at a load lower than the design value. Recall that the packing strap values were for the failure of the repair. The concrete specimen had not crushed at this value, although the packing straps had all fractured and thus could no longer improve performance. The FRP repaired specimens averaged performance in line with the undamaged control bearing specimen. This plot emphasized the improvement due to the post-tensioned and concrete jacket repairs. These repairs averaged well over twice the capacity required by the design load. With these two techniques, the impact of the differing boundary conditions between specimen types was largely negated.

7.4 SUMMARY OF BEARING SPECIMEN RESULTS

This summary of the bearing specimen results includes the author's ranking of the various repairs, presented in Table 7.16, and summary bullet points. In Table 7.16 the ease of repair application, strengthening performance, estimated cost, and aesthetic impact were ranked from first to fourth. For the ease of application, the ranking proceeded from easiest (first place) to the most complicated method (fourth place). Strengthening performance was based upon the average repairs' performance versus the undamaged control specimen's capacity. The first place went to the repair with the greatest improvement (post-tensioned). The estimate of cost category will vary significantly by region and the availability of the materials used. The ranking for this category was the author's opinion based upon conventional wisdom of relative costs. First place in this category went to the repair with the lowest possible cost estimate, the packing strap repair. The aesthetic impact category ranked the potential visual impact on the repaired structure. In this category the rankings proceeded from least noticeable (first place) to most obvious (last place).

Table 7.16: Repair Ranking by Author

Repair Method	Ease of Application	Strengthening Performance	Possible Cost Estimate*	Aesthetic Impact
Packing Strap	1st	4th	1st	2nd
FRP Wrap	3rd	3rd	3rd	1st
Post-tensioned	2nd	1st	2nd	4th
Concrete Jacket	4th	2nd	4th	3rd

*Cost will vary considerably based upon local labor costs and availability of materials.

- A humid environment was not as effective as direct wetting in triggering ASR/DEF development in large scale concrete specimens over short periods of time.
- Based upon the variability of FRP performance noted in the literature and the variation noted during testing, it would seem wise to always over-design FRP repairs to ensure adequate strength.
- The packing strap repair method failed to meet experimental strength goals. But, the method showed promise from its improved (versus the control specimens) of strain behavior observed during testing.
- The concrete jacket and post-tensioned repairs performed extremely well with capacities nearing that of the undamaged scaled column specimen.
- Overall, the post-tensioning repair appears to be the best repair method for confining the column capital, with the concrete jacket repair running a close second.

CHAPTER 8
Summary and Conclusions

8.1 SUMMARY

Deterioration in the form of extensive vertical cracking of some bridge columns of the San Antonio Y was noted during routine inspections by the bridge owner, TxDOT. From petrographic analysis of the most heavily cracked columns, the primary causes of deterioration were found to be ASR and DEF[1-3]. As well, TxDOT was primarily concerned with the public safety and wanted a method of evaluating the affected columns and recommendations for future action. Therefore, TxDOT sponsored research studies to determine the effect of ASR and DEF on the capacity of the columns, likelihood of future deterioration, and remediation recommendations[1].

Previous research by Kapitan found that several of the most affected columns of the San Antonio Y had a bearing design deficiency, which resulted in the bearing capacity of the columns being substantially lower than the axial-flexural capacity[3]. For instance, the undamaged control specimen failed in bearing at an axial load that was 20% lower than its axial-flexural capacity prediction. Fortunately, core tests indicated that the actual concrete compressive strength of the columns in the San Antonio Y was substantially greater (approximately 60% greater) than the required design concrete compressive strength. Therefore, the bearing design deficiency did not reduce the current load rating of the columns[3]. In Kapitan's column specimen series, which studied the effects of column capacity versus induced crack width, cracks of 0.084 inches in the model columns (that would scale to 0.3 inches in the field) reduced the column capacity to about 81% of the control maximum capacity (a 19% loss)[3]. The excess concrete compressive strength in the field increased the overall column bearing and axial-flexural capacity enough to negate the reduction in capacity from a single centered crack. The maximum observed load on this most heavily damaged test specimen was still over twice the

factored design load. However, not all of the columns in the San Antonio Y may have as much excess capacity. Thus, it was highly desirable to have available a proven repair technique to improve bearing capacity in case a column with less excess concrete compressive strength shows signs of distress.

This research study had three main components: scaled column specimens, bearing specimens, and computer modeling.

The scaled column specimens were identical to the specimens used in Kapitan's column series except these columns were cast with ASR susceptible concrete and heat treated to trigger DEF. The heat treating involved preheating the concrete materials and tenting the concrete during initial curing. To add to the heat of a July day in Central Texas, two propane heaters increased the temperature under the tent in order to raise the internal concrete temperature. As both ASR and DEF required moisture to cause concrete expansion, a moisture retention system was developed for the column specimens' exposure period. This system involved soaker hoses wrapped around the columns' tops and felt-backed plastic wrapped around the columns (including the hoses). Water was applied four times a day, regulated by an automatic timer, and the plastic wrapping prevented evaporation. Further, the columns were axially post-tensioned (with scaled dead and live load) during exposure in order to obtain distributed vertical cracking similar to that observed in the San Antonio Y columns. The specimen scale was set by Kapitan's earlier work to a ratio of 1/3.67, which corresponded to a number three reinforcing bar in the laboratory representing a number eleven reinforcing bar in the field. These two columns complemented the series by Kapitan. They were used to correlate ASR/DEF cracking and behavior to the behavior measured in Kapitan's mechanically cracked specimens.

Based on the bearing failure observed in the scaled column specimens, concrete repairs were designed to increase confinement of the column capital to address the bearing

capacity deficiency. The bearing specimens examined the ability of four different repair techniques to confine the column capital and thus improve the bearing strength of the columns. Packing straps, a fiber reinforced polymer wrap, external post-tensioning, and concrete jacketing were the repairs studied. These repairs were applied to bearing specimens that replicated the column capital (top sixteen inches) of the scaled column series. The original intent of the specimens was to repair ASR/DEF caused cracking damage. For that goal, the specimens were cast with ASR susceptible concrete and heat treated to trigger DEF. Due to the size of these specimens the heat treating included the materials and formwork heating overnight in an oven prior to placing the concrete. The specimens were then cast in and remained, for at least eighteen hours, in the oven. A different moisture system was used for these specimens than the one used for the scaled column specimens. This alternate system proved to be less effective than the scaled column specimen's system. The bearing specimens were axially post-tensioned with the same load as the scaled column specimens, but then placed above a pool of water and tented. The intent of this system was to create a warm, high-humidity environment. The axial post-tensioning was in place to cause any cracking to occur with a vertical orientation. As there was no significant expansion of these specimens during their exposure period, the bearing specimens were mechanically cracked with splitting wedges (0.1-inch wide cracks) prior to repair. The repairs were designed to provide lateral confinement sufficient to add a vertical load capacity corresponding to 25% of the maximum axial load carried by Kapitan's control scaled column specimen.

ATENA, a commercially available finite element program designed specifically to model reinforced concrete behavior, was used to model Kapitan's results. The model used the same scale as Kapitan (1/3.67) in order to directly compare results. Once calibrated to Kapitan's control specimen, the model was used in a parametric study to determine the maximum vertical through-section crack width that the column could have and still carry the factored design load.

8.2 CONCLUSIONS

8.2.1 Computer Model

- Using ATENA to predict the column's capacity at larger levels of initial cracking, a critical initial cracking width of 0.17 inches for the scaled specimen was determined. At this threshold crack width the column could only just support its factored design load.
- The threshold width of 0.17 inches was for the scaled column and corresponds to a width in the field of 0.62 inches (5/8 inches). By knowing this value, the bridge owner is better equipped to interpret the reported crack widths in the field as observed during bridge inspections.
- With the computer material model calibrated to Kapitan's control column results, ATENA calculated a close approximation to the capacities of the undamaged model and the 0.02-inch wide initial crack model. The location and mode of failure at these levels was the same as observed in the test specimens.
- As the initial cracking levels reached 0.084 inches, the ATENA prediction was somewhat conservative and calculated a local crushing failure in a different location in the column than was observed in the test specimens.

8.2.2 Scaled Column Specimens

- For the 1-1.5% lateral expansion from ASR/DEF as seen in Columns A and B, the widespread vertical cracking had no significant effect on failure mechanism or load carrying capacity when compared to those determined from testing the control specimen.
- Failure of all columns (ASR/DEF and Kapitan's series) was governed by bearing capacity at the top bearing surface under the most heavily loaded bearing pad.
- The columns experienced considerable lateral expansion, 1-1.5%, during the exposure period, as measured externally with demec points.

- The ASR/DEF affected columns showed substantial (20 to 60%) variability in their responses to load in strain and displacement behavior, emphasizing the variability in engineering properties caused by ASR/DEF deterioration.
- Kapitan's specimen with 0.02 inches of initial cracking gave the best overall approximation of the ASR/DEF affected columns' performance.
- The post-tensioned axial load, which was applied to simulate the effects of the superstructure dead load, served as the main restraining force against ASR/DEF vertical expansion in the columns, creating a cracking pattern similar to that observed on the San Antonio Y.
- An effective moisture retention system should be maintained throughout exposure to generate maximum expansion.
- Each ASR/DEF affected column's average second widest crack (averaged from each column face) was 0.02 inches, which gives a correlation to Kapitan's specimen series based on observed crack width.

8.2.3 Bearing Specimens

- The concrete jacket and post-tensioned repairs performed extremely well with capacities nearing that of the undamaged full length column specimen.
- The FRP, post-tensioned, and concrete jacket repairs all reached the goal of meeting or exceeding the undamaged control (reduced length) bearing specimen's capacity.
- Considering ease of application, estimated cost, and capacity improvements, the author recommends post-tensioning (but with concrete jacketing as a close second) for the remediation of ASR/DEF induced cracking deterioration.
- Based upon the variability of FRP performance noted in the literature and the variation noted during testing, it would seem wise to always over-design FRP repairs by at least 30% to ensure adequate strength.

- Exposure of the specimens in a humid environment is not as effective as direct wetting in triggering ASR/DEF development in large scale concrete specimens over short periods of time.
- The packing strap repair method showed promise from the literature and from its improvement of strain behavior during testing. This method would require additional study to develop application guidelines before being recommended for use. For instance, the author would not suggest applying the packing straps to a tapered specimen without first squaring the sloping corners. The localized stress concentration in the straps where they came in contact with the taper, did not agree with the design assumption of uniform stress in the strap.
- It is important to address the root cause of cracking in the concrete prior to application of a repair. If the cause is not addressed, then the existing cracking or spalling damage of the underlying concrete structure is likely to continue to deteriorate and to further damage the repaired structure.

8.3 RECOMMENDATIONS FOR FUTURE WORK

- Examine if the correlation between ASR/DEF expansion and mechanical cracking found in this study is also true for different column configurations (circular, square, non-flared, etc.).
- Examine the effects of ASR/DEF on large scale specimens to determine the scale effect of expansion.
- Use initial cracking line forces to create multiple crack patterns in ATENA and thus model the effect of distributed initial cracking.
- Develop a cracking module to work with finite element models such as ATENA to allow the user to input crack locations, orientations, and widths and then have the module create the necessary nodes and forced displacement load steps to recreate the crack patterns in the computer model.

- For long term exposure studies, use waterproof strain gauges that may be better able to survive in the concrete for years and correctly connect the generally stable vibrating wire gauges to the datalogging system.
- Study the concrete confining ability of commercial packing straps. The author would recommend avoiding tapered edges, but it is necessary to explore such effects as the rounding corners and using a circular versus a rectangular reinforced concrete specimen. Usefulness in emergency stabilization or for historic preservation would be especially interesting.

APPENDIX A

Scaled Column Specimens

A.1 DIMENSIONS & REINFORCING

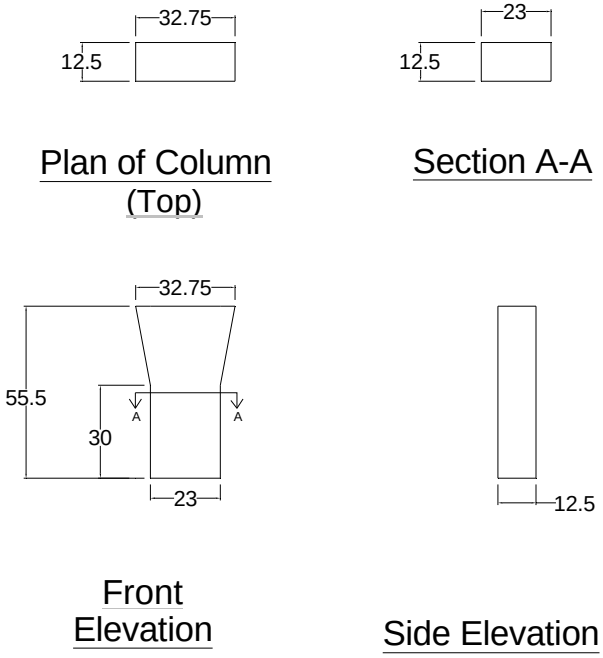

Figure A.1: External Dimensions of Scaled Column, from Ref. 3

(dimensions in inches)

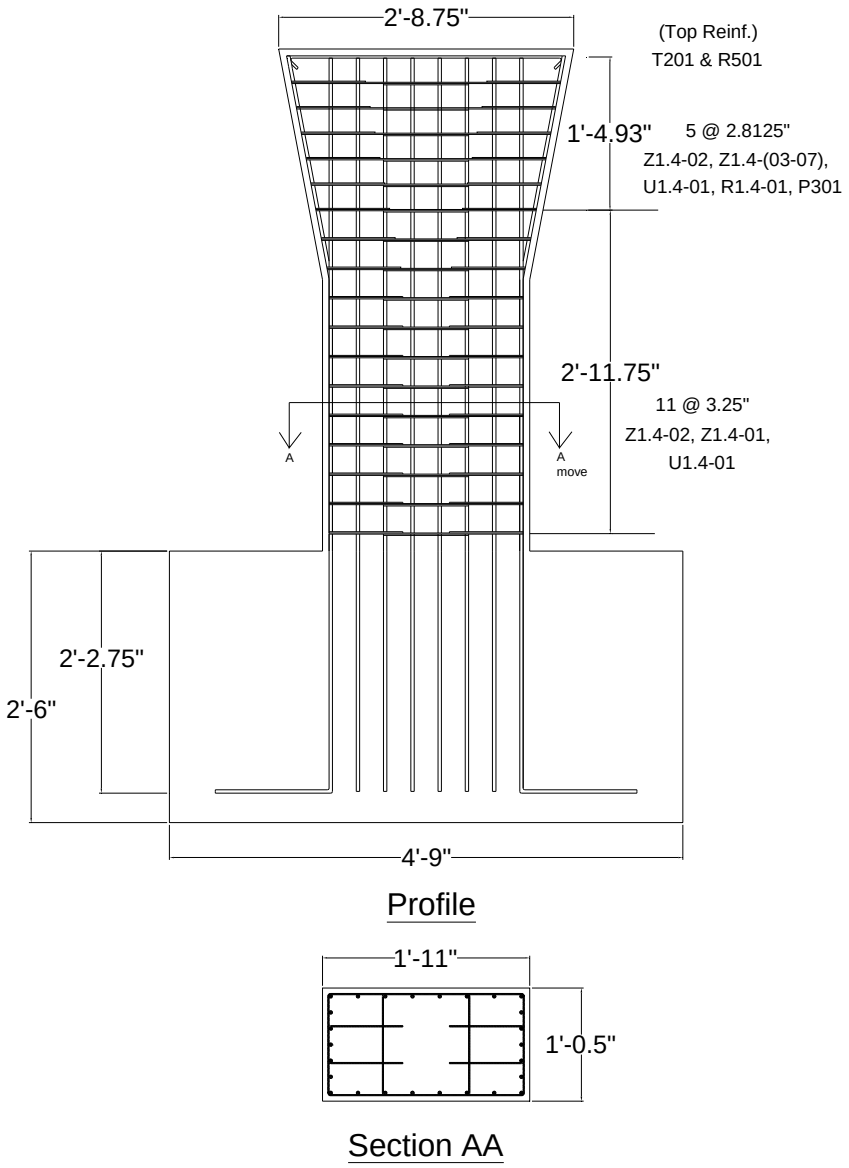

Figure A.2: Scaled Column Specimen Reinforcing Layout (1 of 4), from Ref. 3

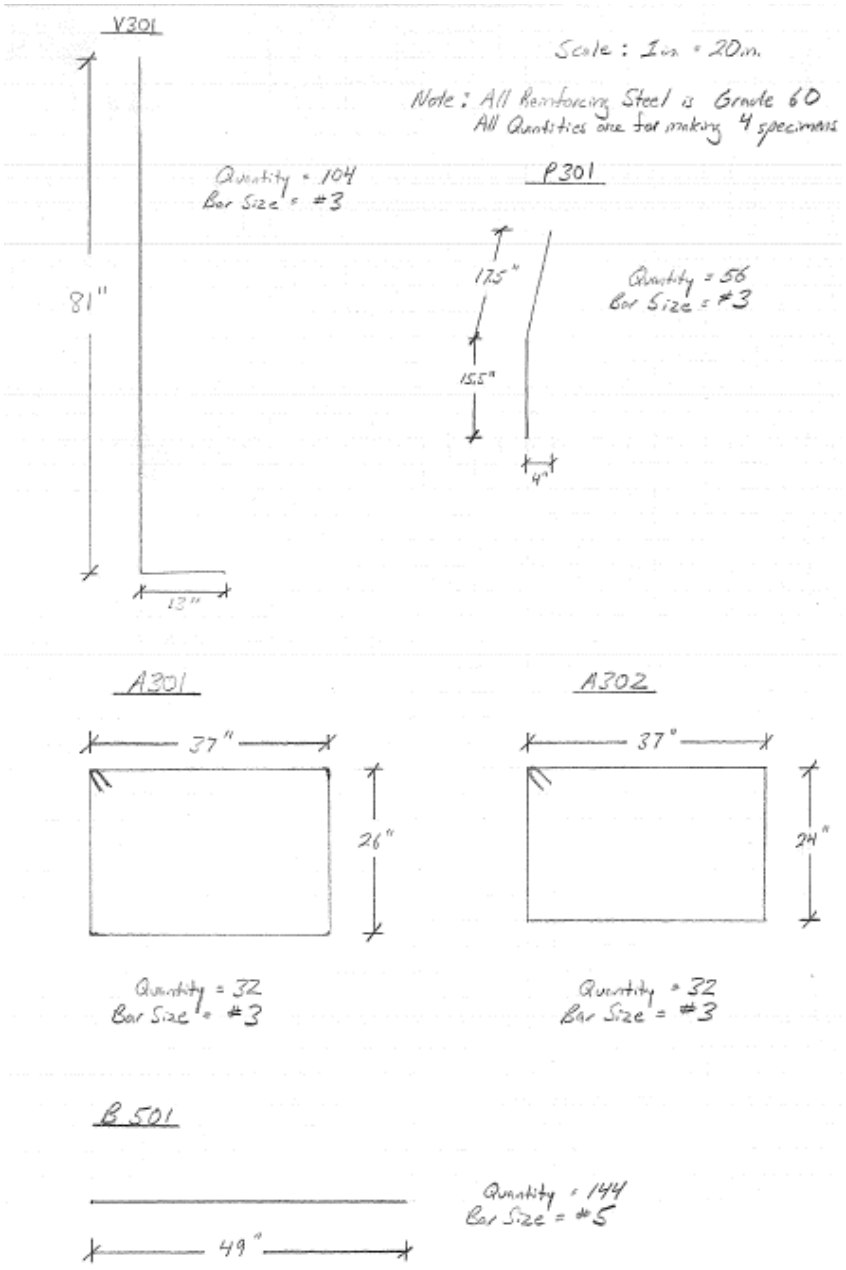

Figure A.3: Scaled Column Specimen Reinforcing Layout (2 of 4), from Ref. 3

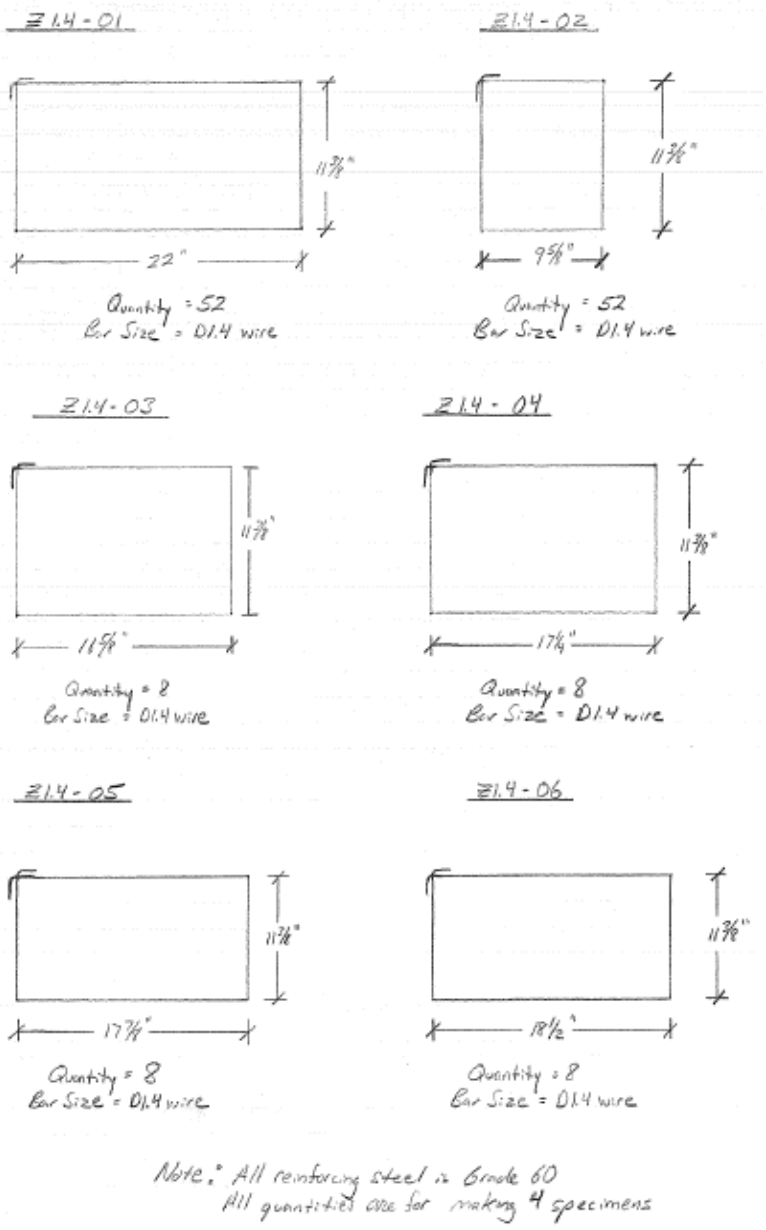

Figure A.4: Scaled Column Specimen Reinforcing Layout (3 of 4), from Ref. 3

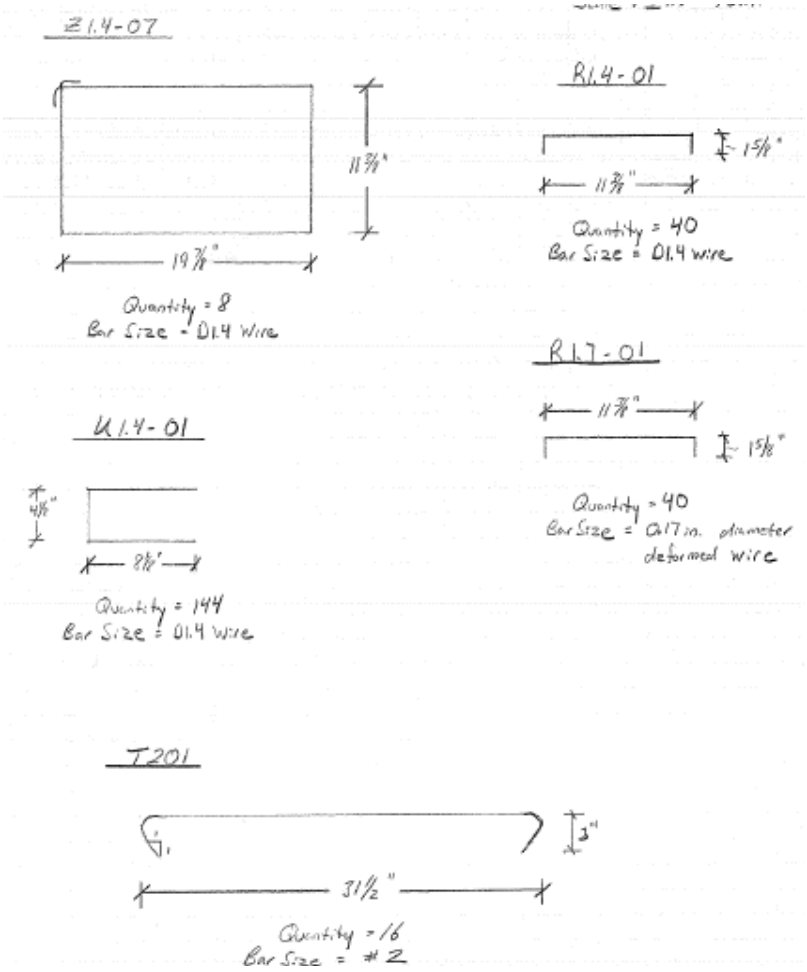

Figure A.5: Scaled Column Specimen Reinforcing Layout (4 of 4), from Ref. 3

A.2 STRAIN METERS

The strain meters used in this research project used William Stone's design as detailed in the following diagram from his dissertation.

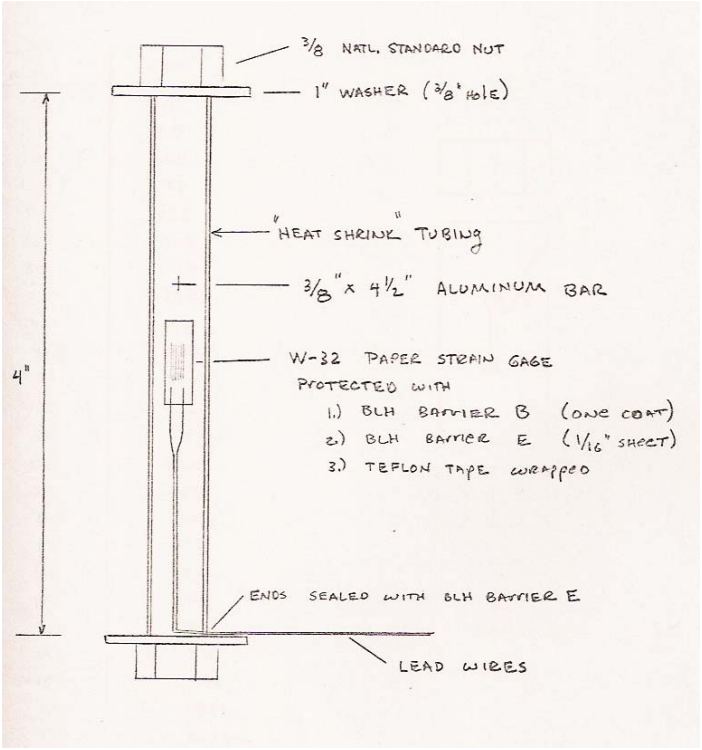

Figure A.6: Strain Meter Design, from Ref. 97

How to make a strain meter, a pictorial guide:

Figure A.7: First, Cut Five Inches of Aluminum Bar Stock

Figure A.8: Second, Thread the Ends to Take a Standard Nut

Figure A.9: Third, Apply Strain Gauge to Center

Figure A.10: Fourth, Paint with Gagekote (Barrier B)

Figure A.11: Fifth, Wrap in Four-Inch Wide Mastic Tape (Barrier E)

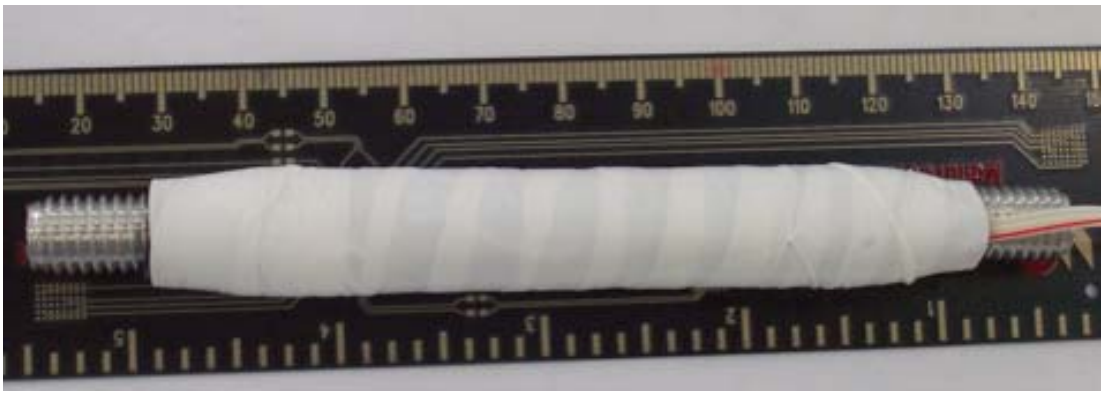

Figure A.12: Sixth, Wrap Gauge Length in Teflon Tape

Figure A.13: Seventh, Apply Heat Shrink Tubing (4”) as a Bond Breaker

Figure A.14: Finally, Attach Washers and Set Gauge Length by Adjusting Nuts

A.3 STRAIN GAUGES USED IN SCALED COLUMN SPECIMENS

All of the strain gauges were from TML Tokyo Sokki Kenkyujo Co., Ltd. All of the transverse gauges had a 1 mm gauge length and were type FLA-1-11-3LT gauges with a 2.15 gauge factor (GF). Gauges on longitudinal bars and strain meters all had 6 mm gauge lengths with details given in Tables A.1 and A.2. The "W" stands for waterproof.

Table A.1: Column A 6mm Gauges

Gauge Name/Location	Gauge Type	
	FLA-6-11-3LT (GF = 2.11)	WFLA-6-11-3LT (GF = 2.12)
Upper M1	✓	
Upper M2		✓
Upper M3		✓
Upper M4		✓
Upper M5		✓
Upper M6		✓
Upper M7	✓	
Upper M8		✓
Lower M1	✓	
Lower M2	✓	
Lower M3	✓	
Lower M4	✓	
Lower M5	✓	
Lower M6	✓	
Lower M7	✓	
Lower M8	✓	
Upper L1	✓	
Upper L2	✓	
Upper L3	✓	
Upper L5	✓	
Upper L6	✓	
Upper L7	✓	
Upper L8	✓	
Lower L1	✓	
Lower L2	✓	
Lower L3	✓	
Lower L4	✓	
Lower L5	✓	
Lower L6	✓	

Table A.2: Column B 6mm Gauges

Gauge Name/Location	Gauge Type	
	FLA-6-11-3LT (GF = 2.11)	WFLA-6-11-3LT (GF = 2.12)
Upper M1		✓
Upper M2		✓
Upper M3		✓
Upper M4		✓
Upper M5		✓
Upper M6		✓
Upper M7		✓
Upper M8		✓
Lower M1		✓
Lower M2		✓
Lower M3		✓
Lower M4		✓
Lower M5		✓
Lower M6		✓
Lower M7		✓
Lower M8		✓
Upper L1		✓
Upper L2	✓	
Upper L3		✓
Upper L5		✓
Upper L6	✓	
Upper L7		✓
Upper L8		✓
Lower L1	✓	
Lower L2	✓	
Lower L3	✓	
Lower L4	✓	
Lower L5	✓	
Lower L6	✓	

A.4 POST-TENSIONING DETAILS

The pressure in the stressing rams when the nuts were tightened and the pressure released, known as the release pressure, is given in Table A.3 along with the

corresponding loads to those pressures. The numbering scheme used in the table is illustrated in Figure A.15.

Table A.3: Final Release Pressures

Column A Release Pressures				
Bar	1	2	3	4
Pressure (psi)	3050	3000	3000	3050
Load (kips)	37.5	36.9	36.9	37.5
Column B Final release pressures				
Bar	1	2	3	4
Pressure (psi)	3050	2900	2800	3050
Load (kips)	37.5	35.7	34.5	37.5

(Column A) After release bar 2 was reloaded to check the actual stress level, which was found to be 2700 psi, the target pressure.

(Column B) After release, bar 2 was reloaded to check the actual stress level, which as found to be 2850 psi. As well, bar 3 was reloaded and its actual stress level was found to be 2750 psi.

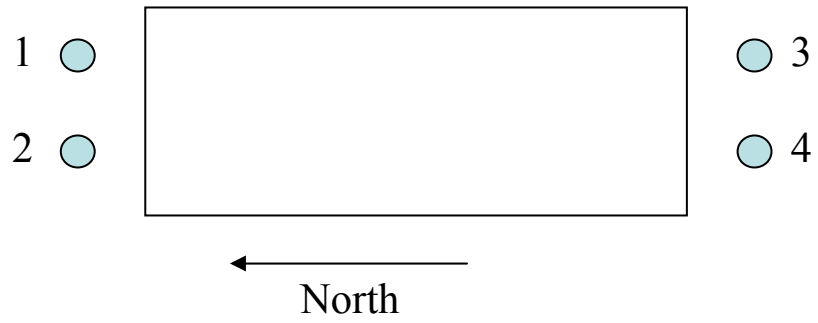

Figure A.15: Stressing Layout

The blue circles in Figure A.15 represent the Dywidag high strength threadbar used to post-tension the columns. In order to maintain symmetry of load while stressing, bars on opposing corners were stressed simultaneously. Thus, bars 1 and 4 were loaded together

and bars 2 and 3 were loaded together. The bars were stressed using hydraulic rams on seating chairs that were lowered over the top of the Dywidag bars. An electric powered hydraulic pump operated the rams and hydraulic pressures were read off a pressure dial gauge on the hydraulic oil line. As the bars were stressed, the top nut of the final assembly was tightened to lock in the stress. Due to the closeness of the Dywidag bars on either end, narrow seating chairs were required. While the hardware fit well within the chairs, the chair legs were too close to allow a wrench access to tighten the locking nut. As a result, the nuts were all hand tightened and there was a loss of stress in the bars at release of the rams. During stressing operations, the pressure at which the nut was loose enough to be turned by hand was noted and compared to the previous release load. This empirical method was used to check actual stress in the bars to ensure it met the target values.

The scaled dead load for these column specimens is 134 kips. Thus, each of the four Dywidag bars needed 33.5 kips of load. The rams used have an area of 12.31 square inches and thus the corresponding hydraulic pressure for 33.5 kips of force is approximately 2700 psi.

A.5 FULL STRAIN MONITORING DATA

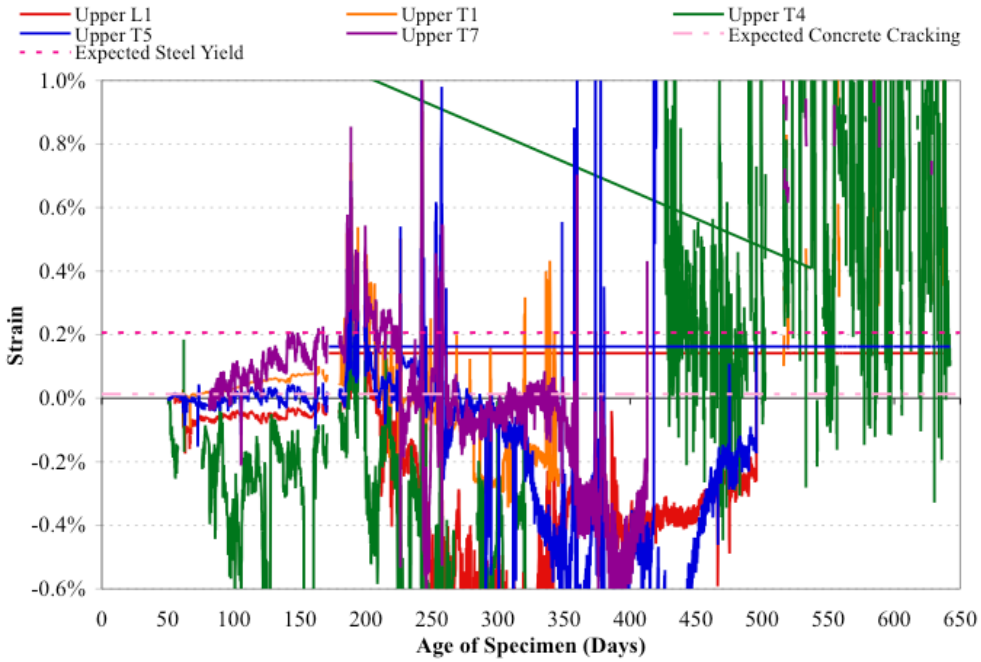

Figure A.16: Column A Upper Layer Strain Monitoring

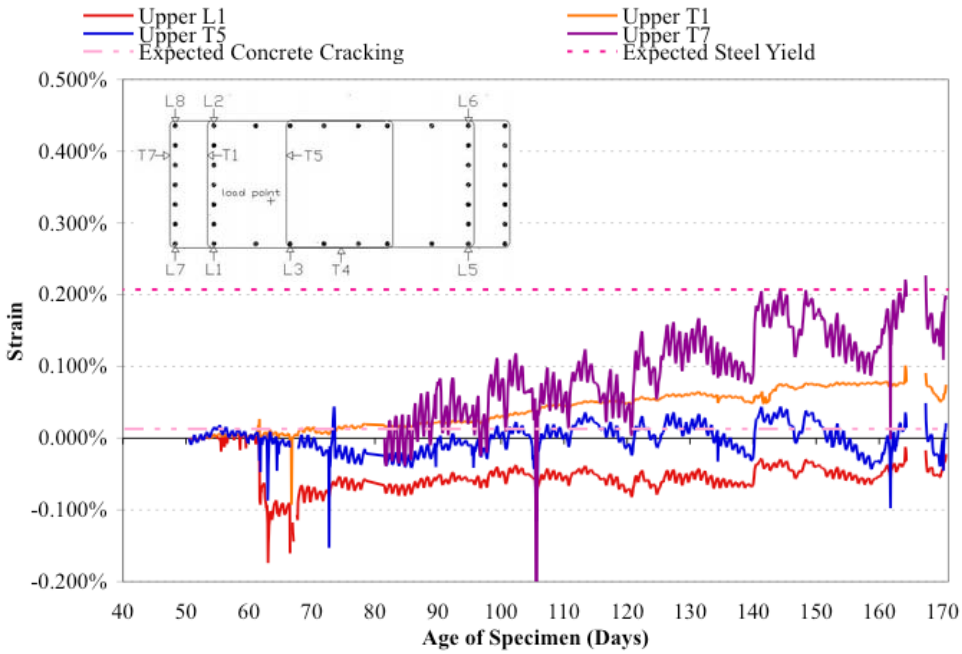

Figure A.17: Column A Upper Layer Strain Monitoring

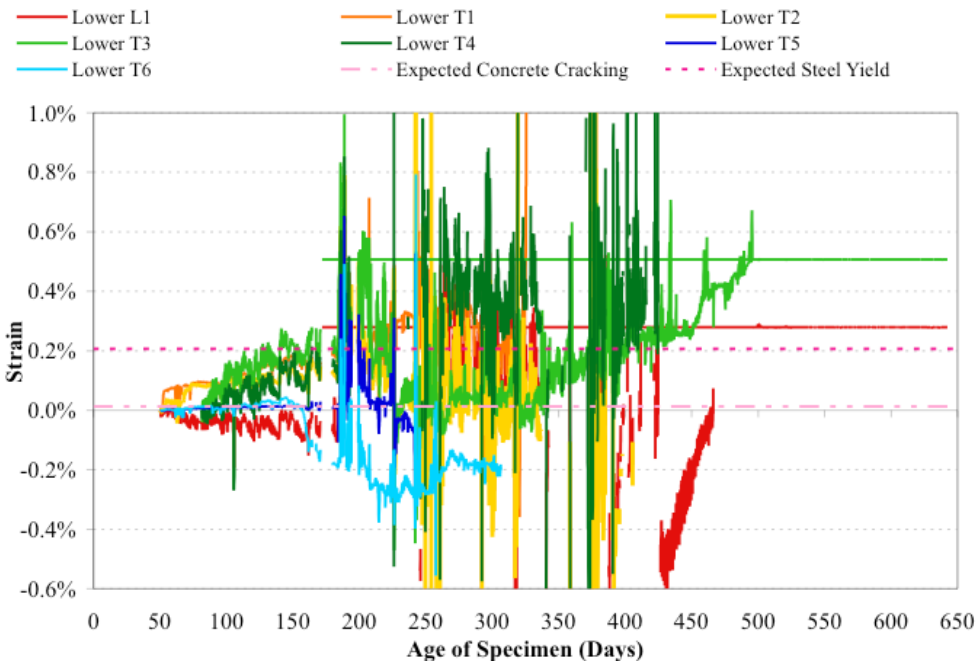

Figure A.18: Column A Lower Layer Strain Monitoring

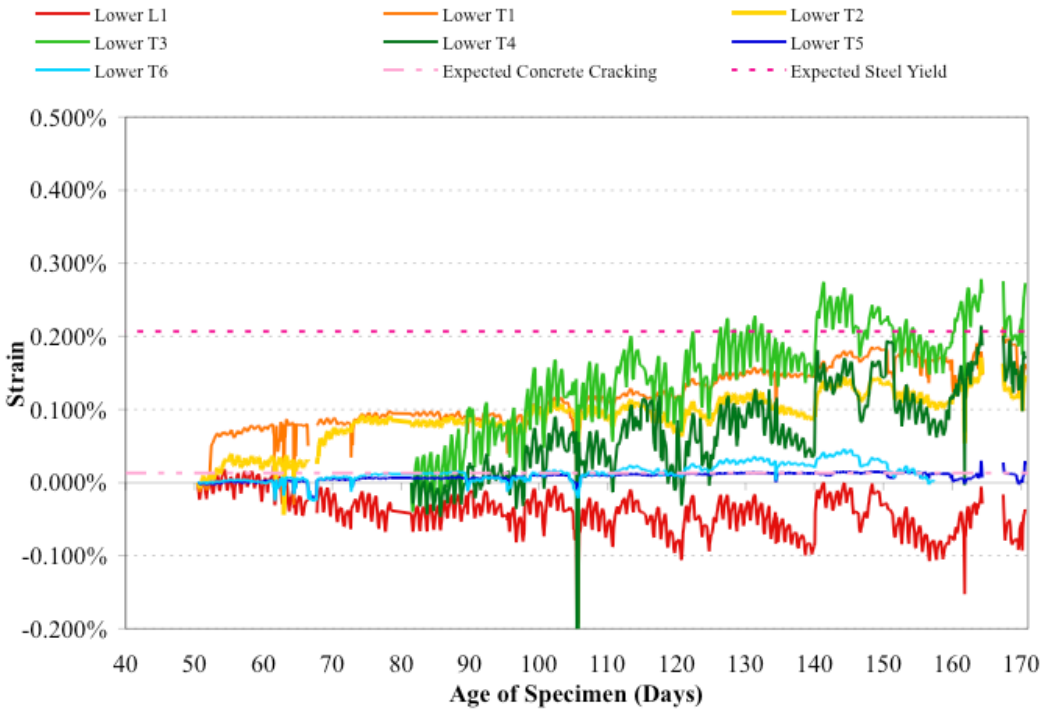

Figure A.19: Column A Lower Layer Strain Monitoring

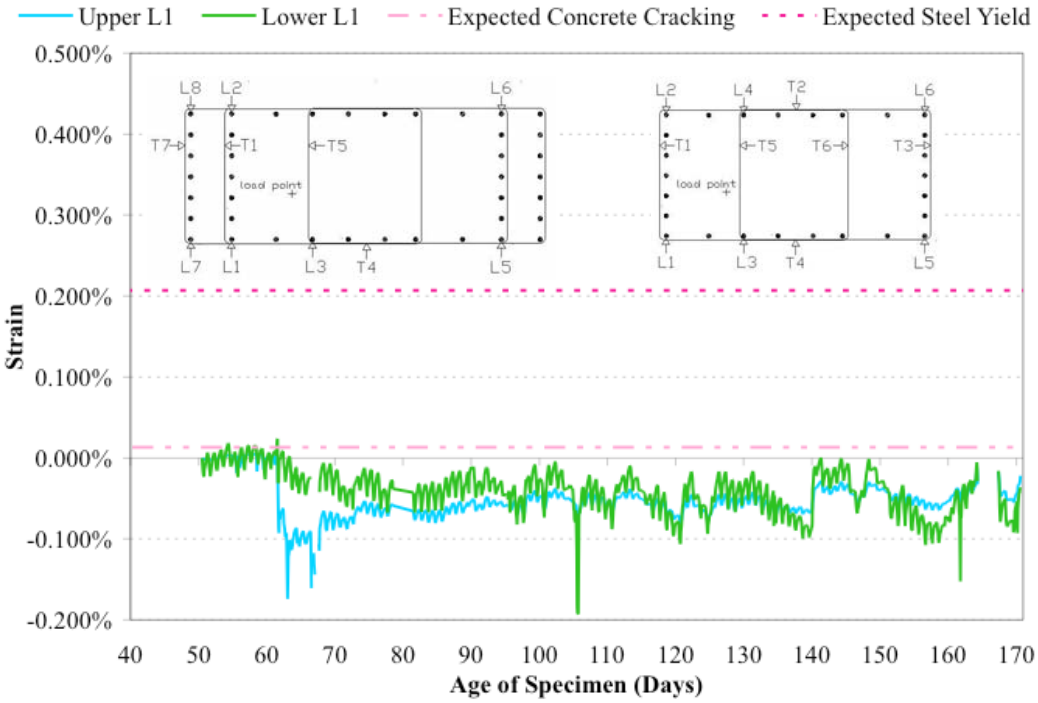

Figure A.20: Column A Longitudinal Bar Monitoring

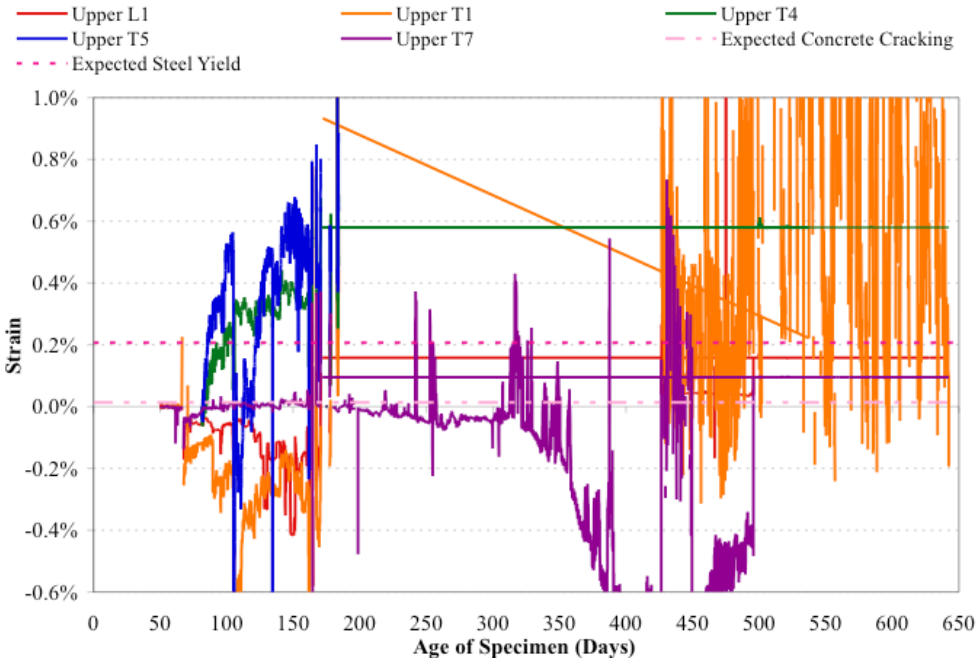

Figure A.21: Column B Upper Layer Strain Monitoring

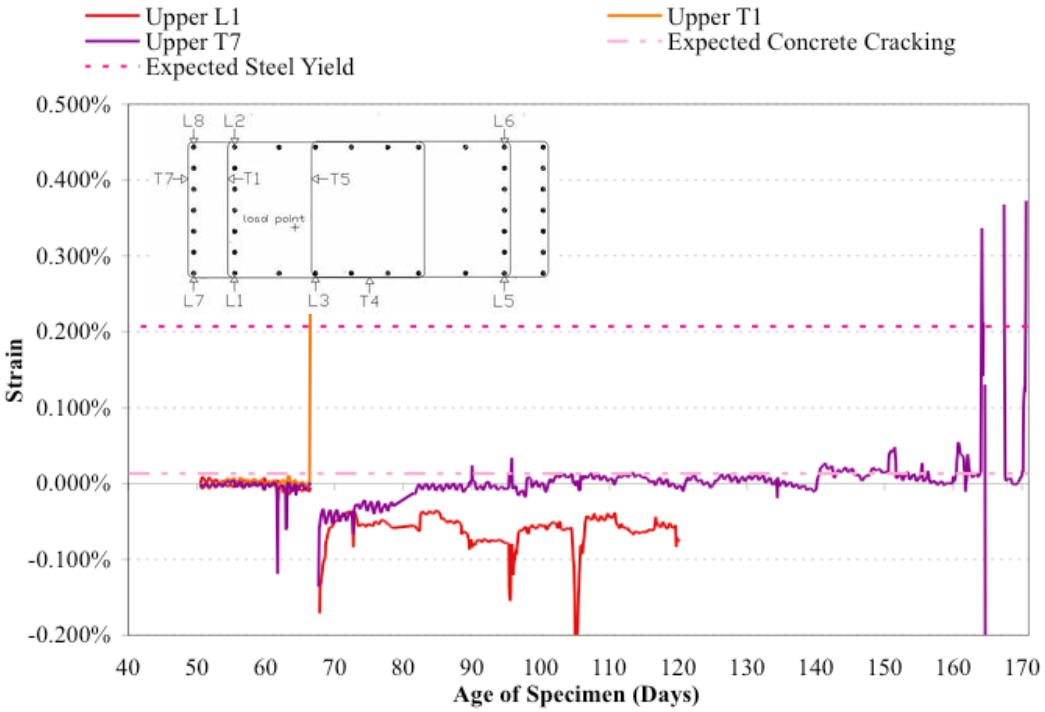

Figure A.22: Column B Upper Layer Strain Monitoring

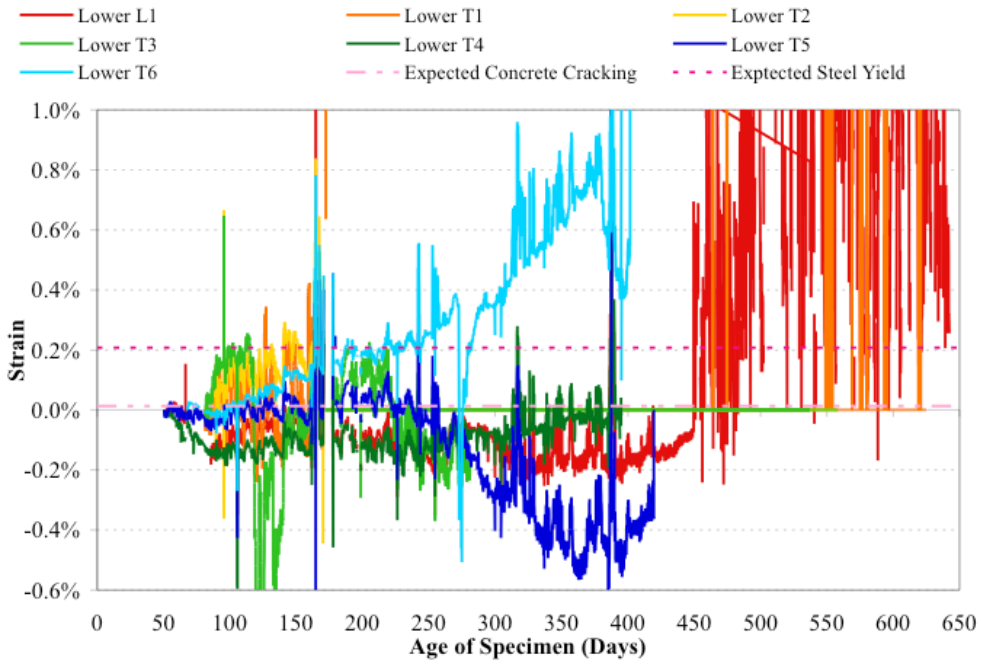

Figure A.23: Column B Lower Layer Strain Monitoring

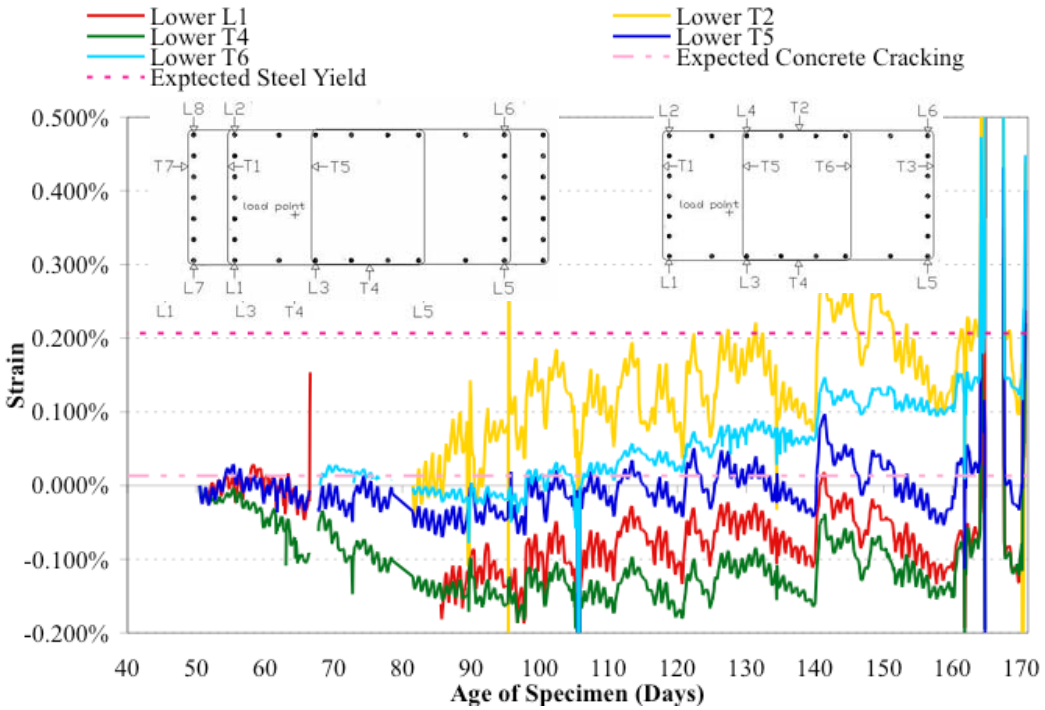

Figure A.24: Column B Lower Layer Strain Monitoring

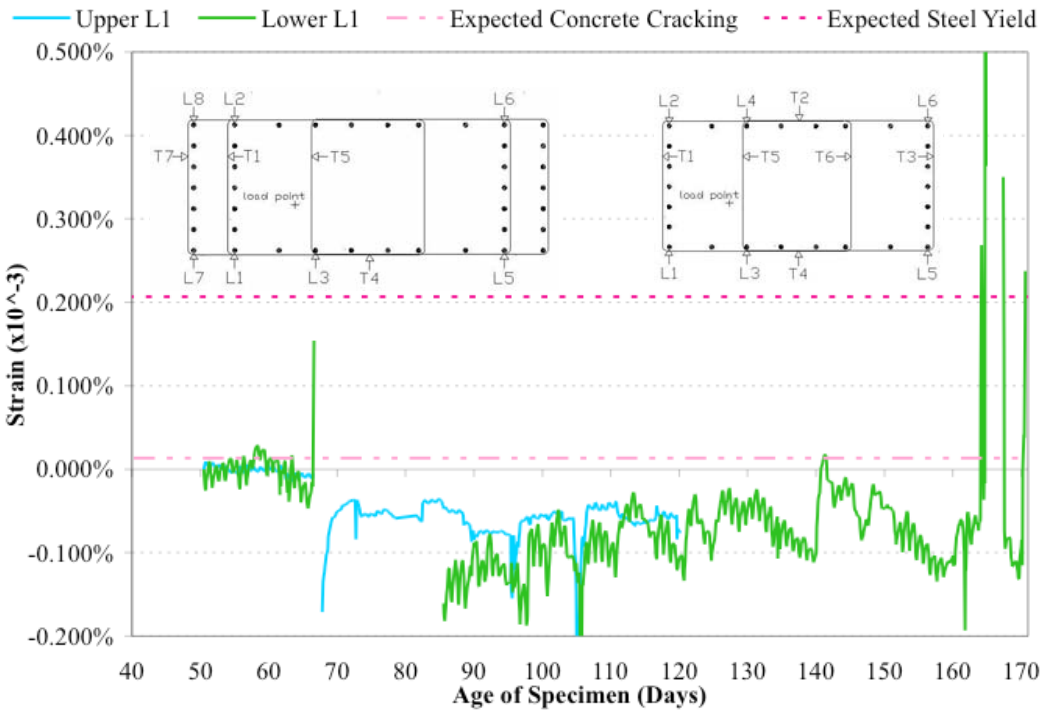

Figure A.25: Column B Longitudinal Bar Monitoring

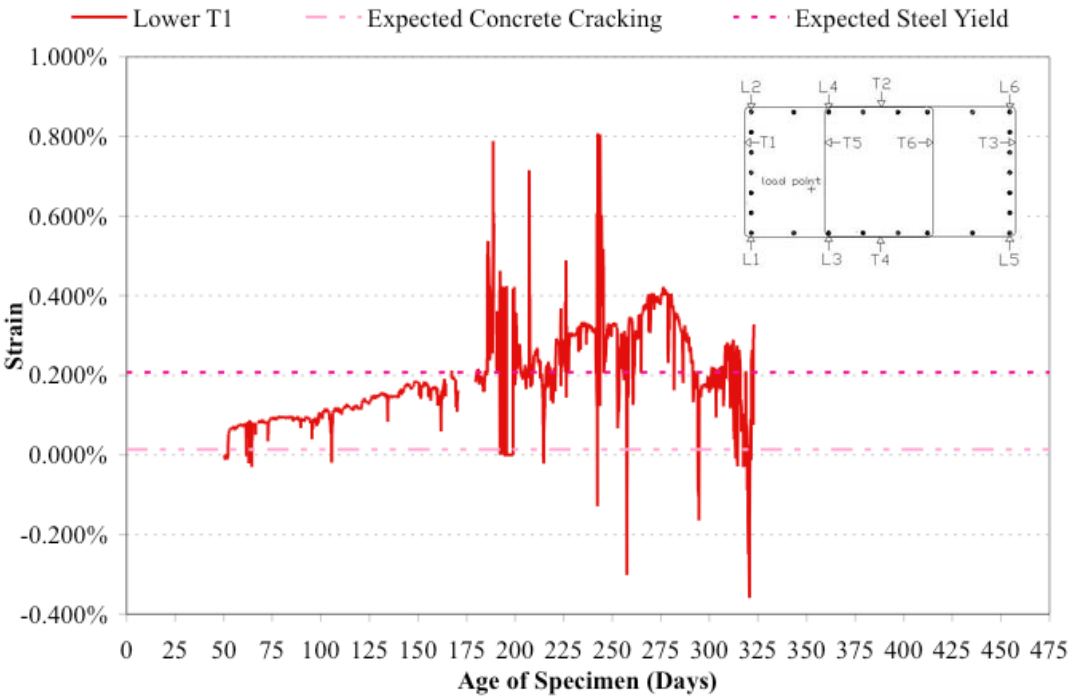

Figure A.26: Column A Long-Lasting Gauge

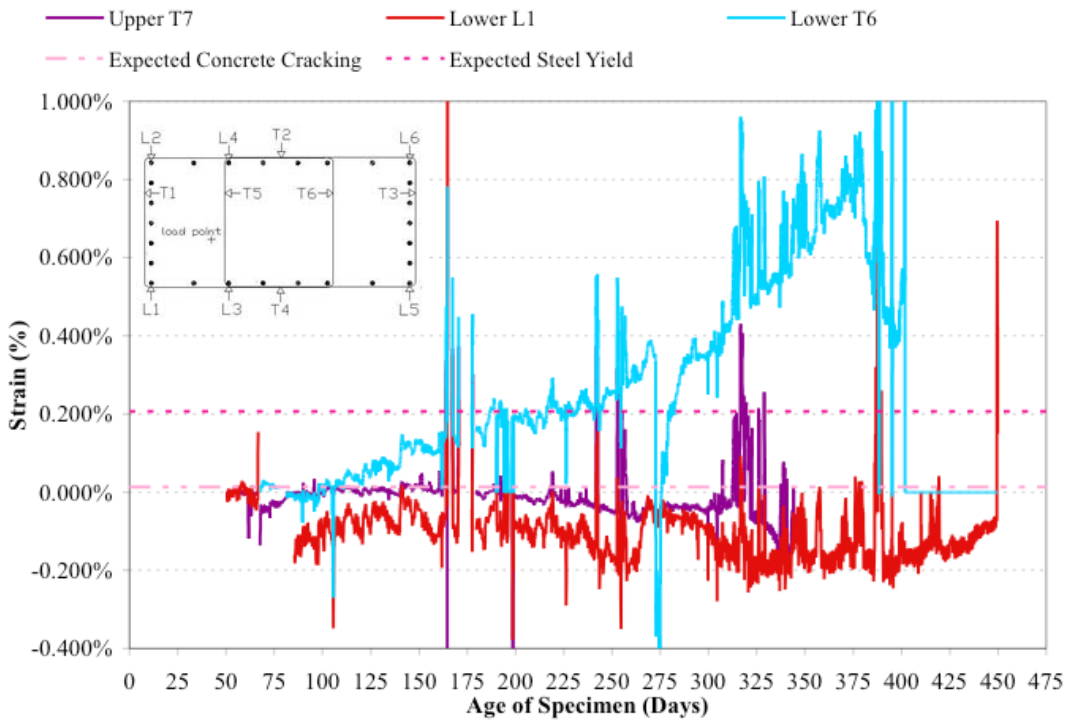

Figure A.27: Column B Long-Lasting Gauges

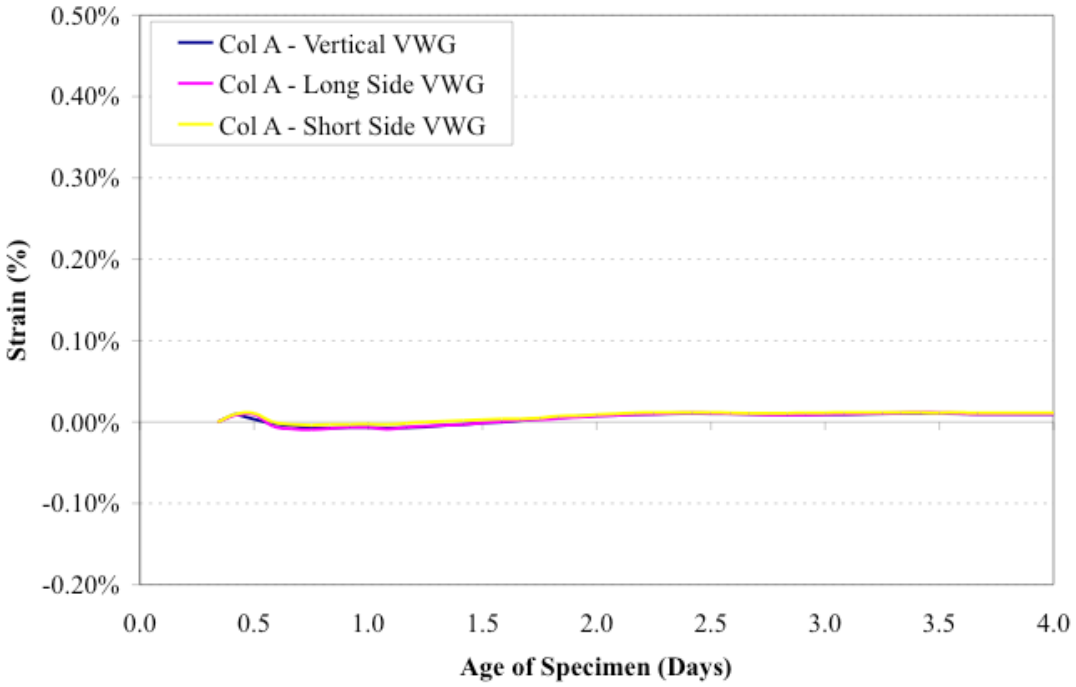

Figure A.28: Valid Vibrating Wire Gauge Data, Column A[98]

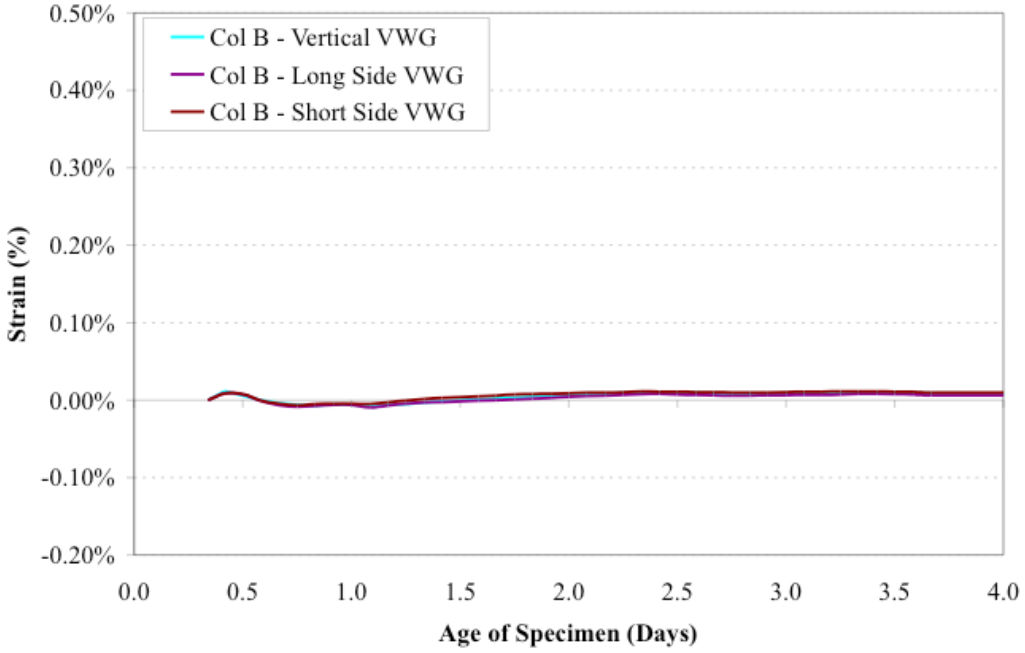

Figure A.29: Valid Vibrating Wire Gauge Data, Column B[98]

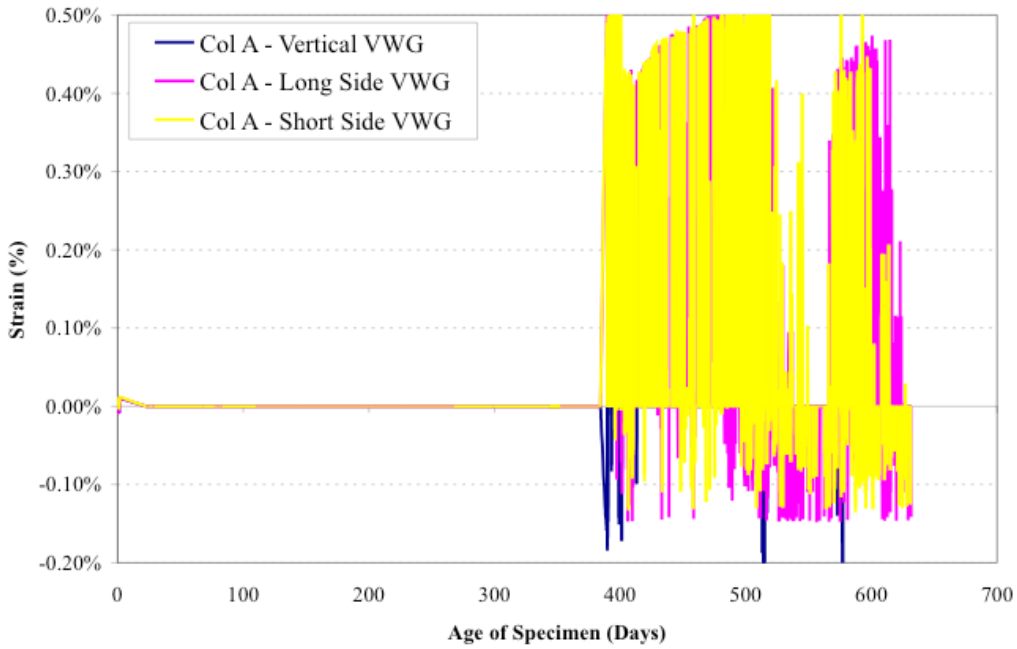

Figure A.30: Vibrating Wire Gauge Monitoring Data. Column A[98]

Figure A.31: Map Cracking at Top of Column A

Figure A.32: Map Cracking at Top of Column B

A.6 POTENTIOMETER LOCATIONS DURING TESTING

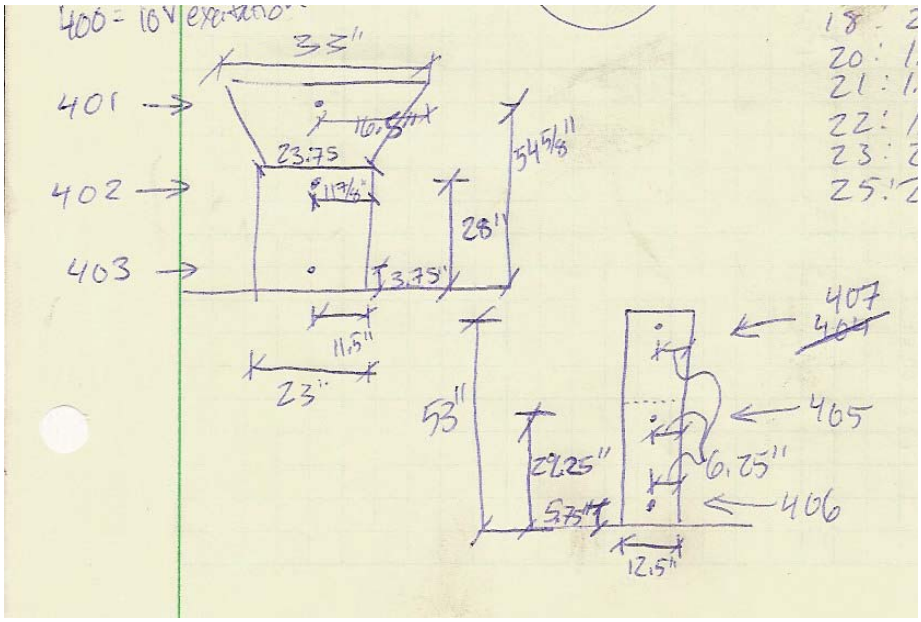

Figure A.33: Linear Potentiometer Locations on Column A

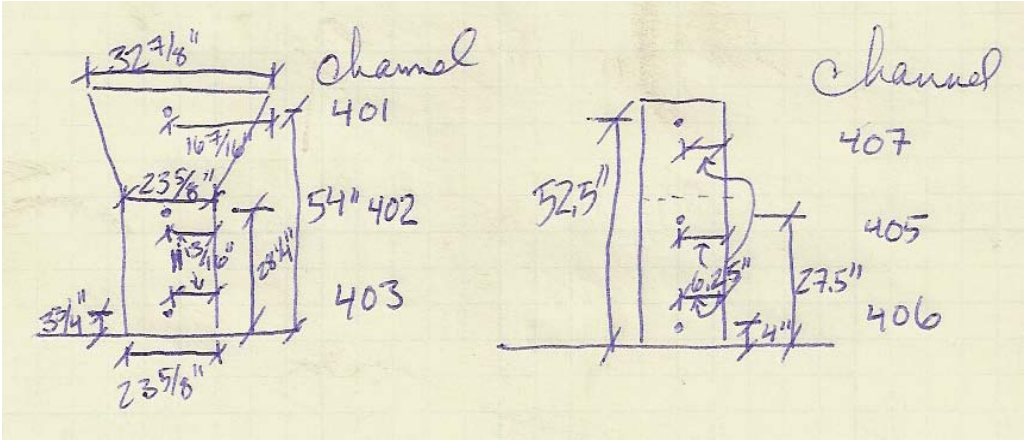

Figure A.34: Linear Potentiometer Locations on Column B

APPENDIX B

Bearing Specimens

B.1 REINFORCING LAYOUT OF BEARING SPECIMENS

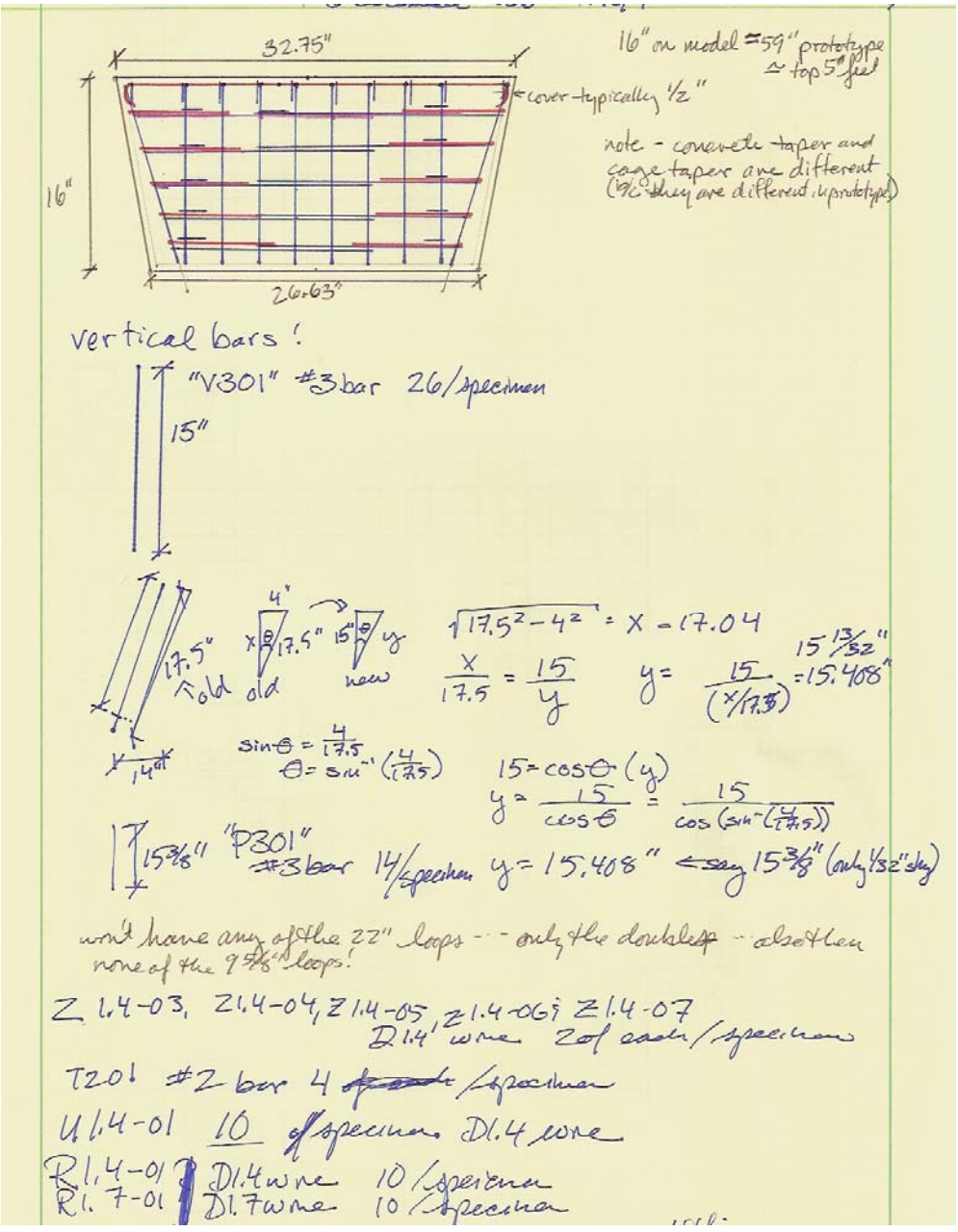

Figure B. 1: Bearing Specimen Reinforcing (1 of 3)

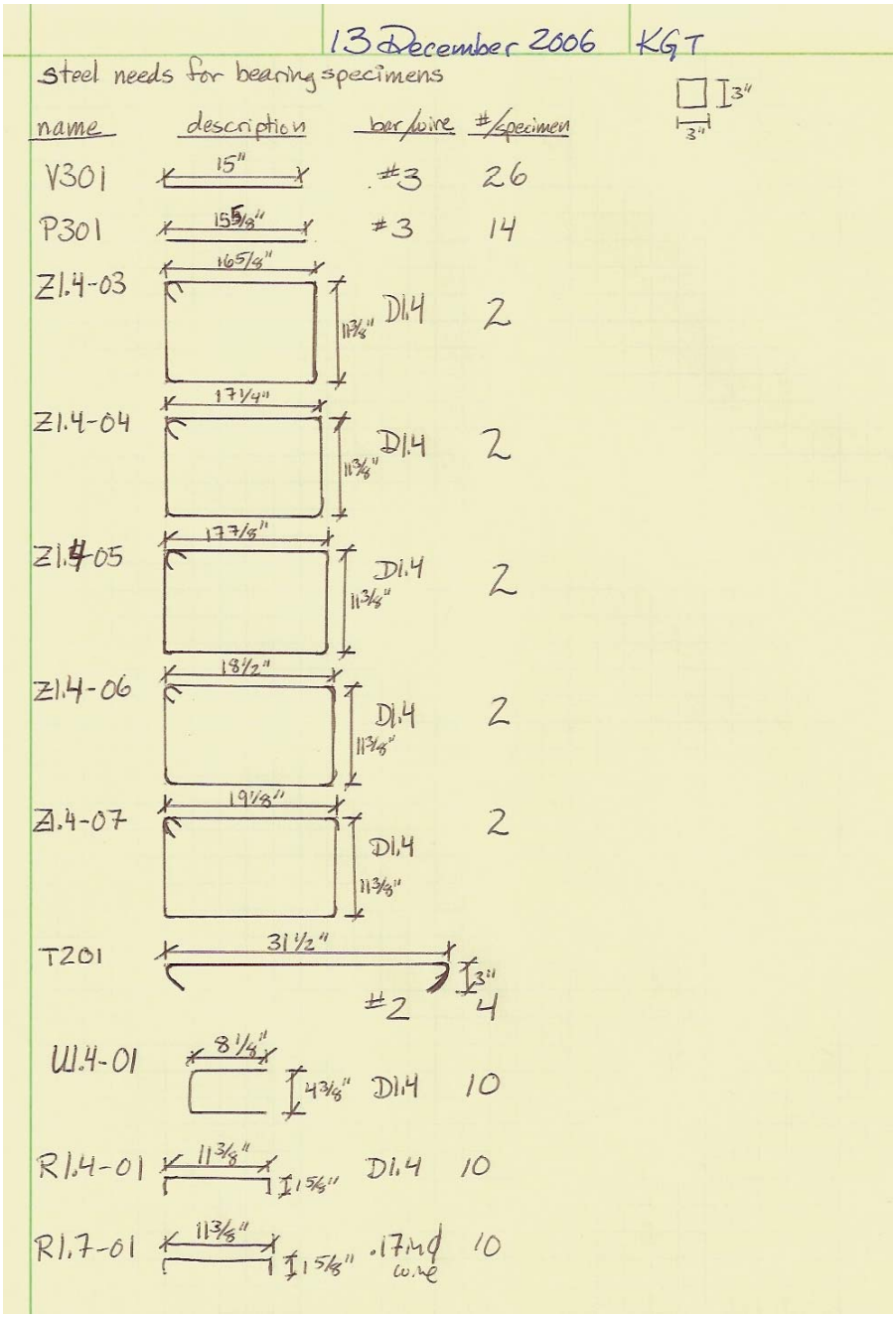

Figure B. 2: Bearing Specimen Reinforcing (2 of 3)

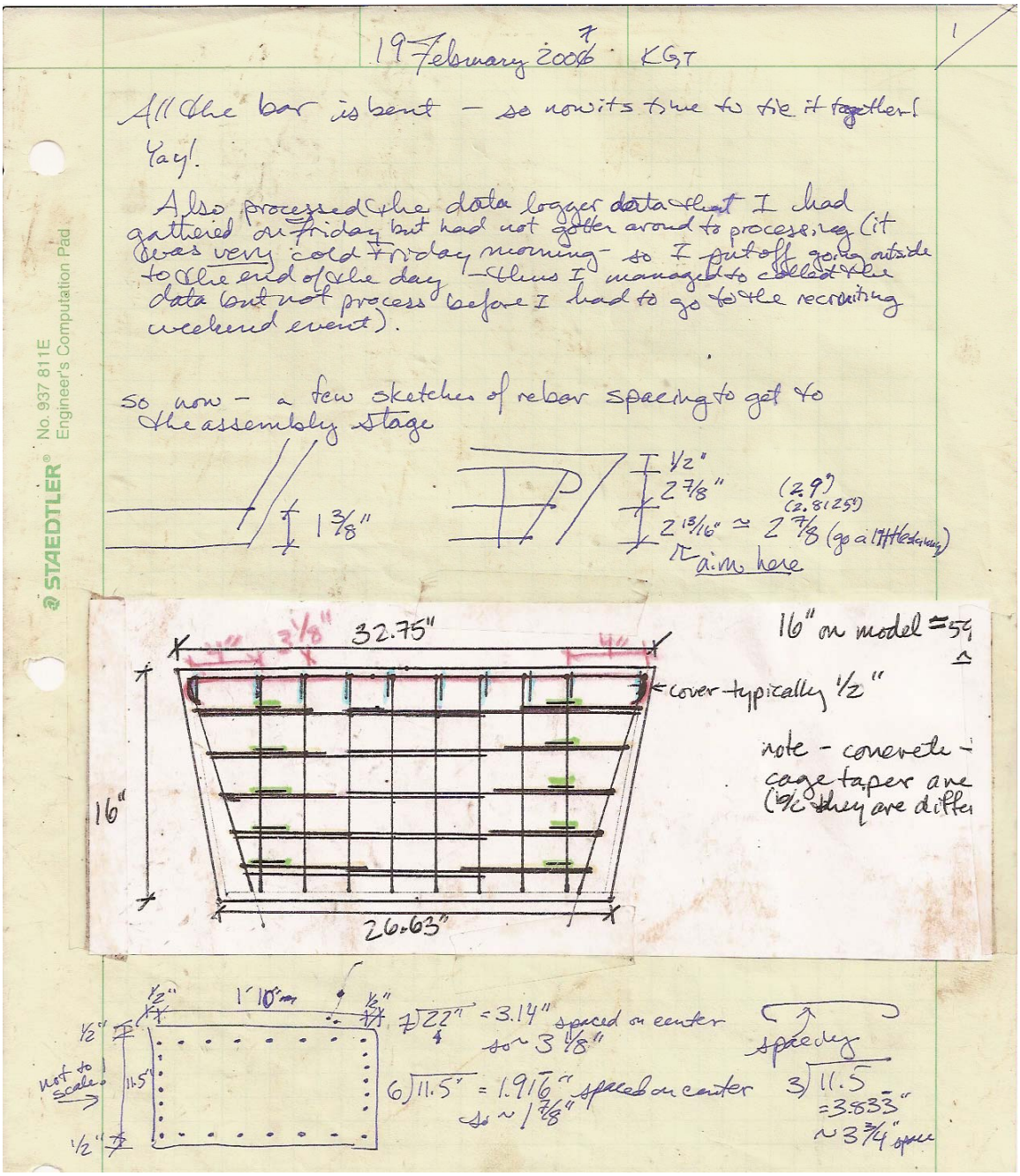

Figure B. 3: Bearing Specimen Reinforcing (3 of 3)

B.2 FORMWORK FOR BEARING SPECIMENS

The bearing specimen formwork was cut down from Kapitan's formwork from the scaled column series. The top eighteen inches of Kapitan's formwork was used with a false

floor to create the sixteen-inch deep bearing specimens. Figure B. 4 and Figure B. 5 show Kapitan's formwork plan with a dashed line indicating the cut point. As well, Figure B. 6 and Figure B. 7 present the planning for casting and the adaptations needed for the angled short formwork sides, respectively.

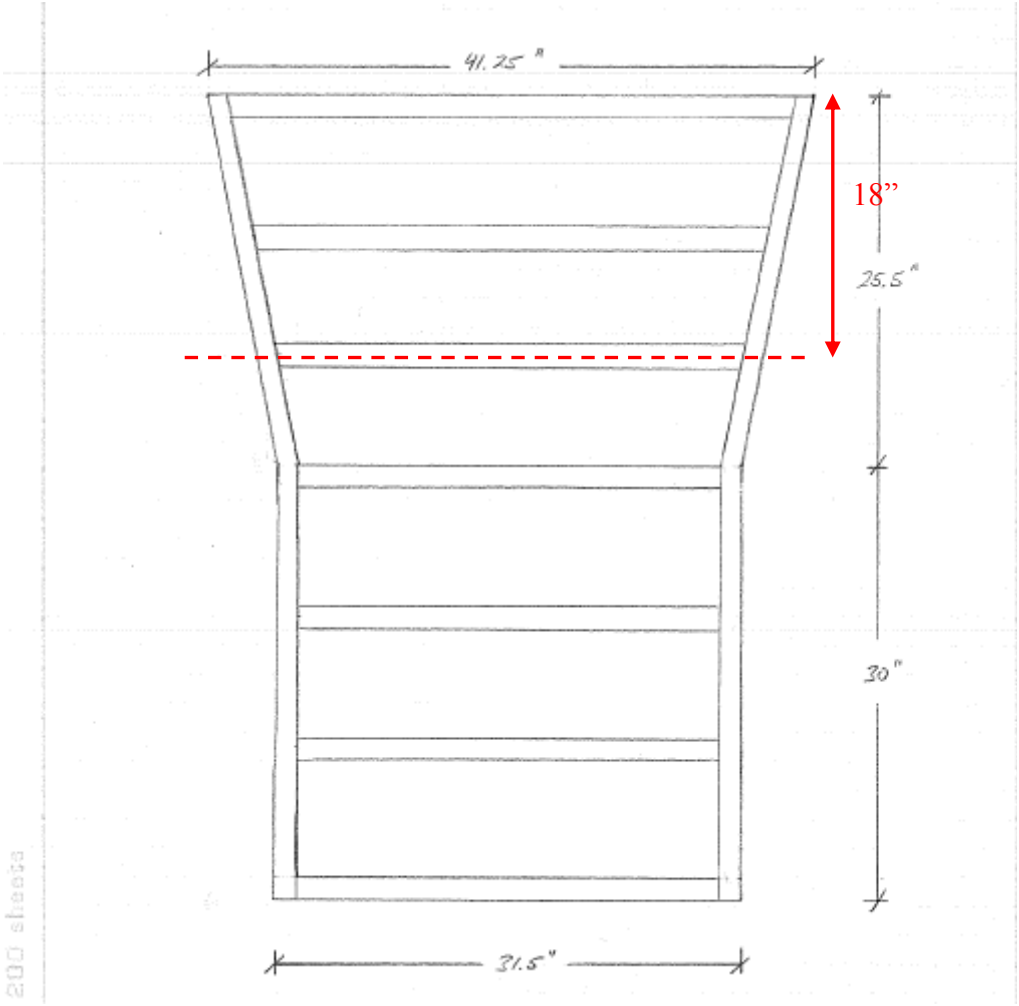

Figure B. 4: Scaled Column Formwork (from Ref. 3), with Cut Line (1 of 2)

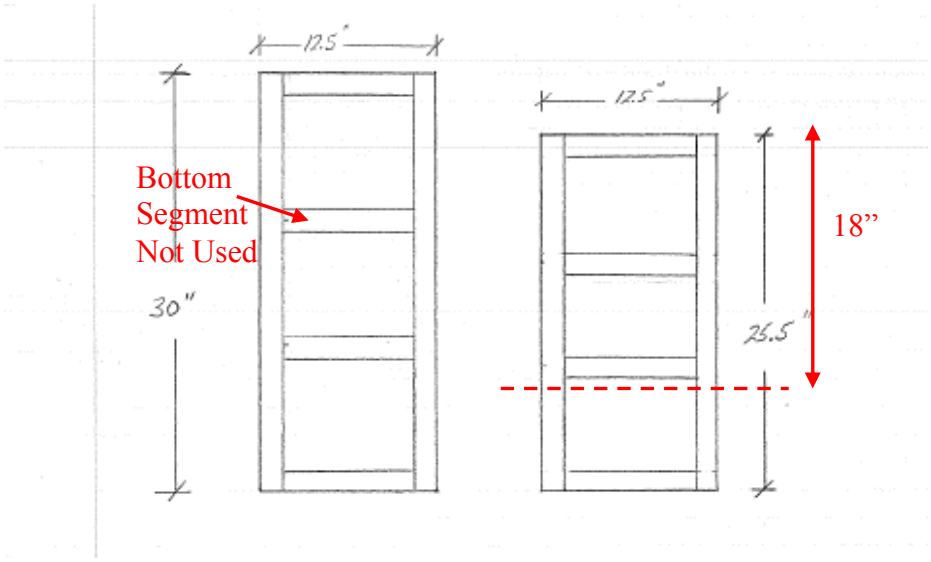

Figure B. 5: Scaled Column Formwork (from Ref. 3), with Cut Line (2 of 2)

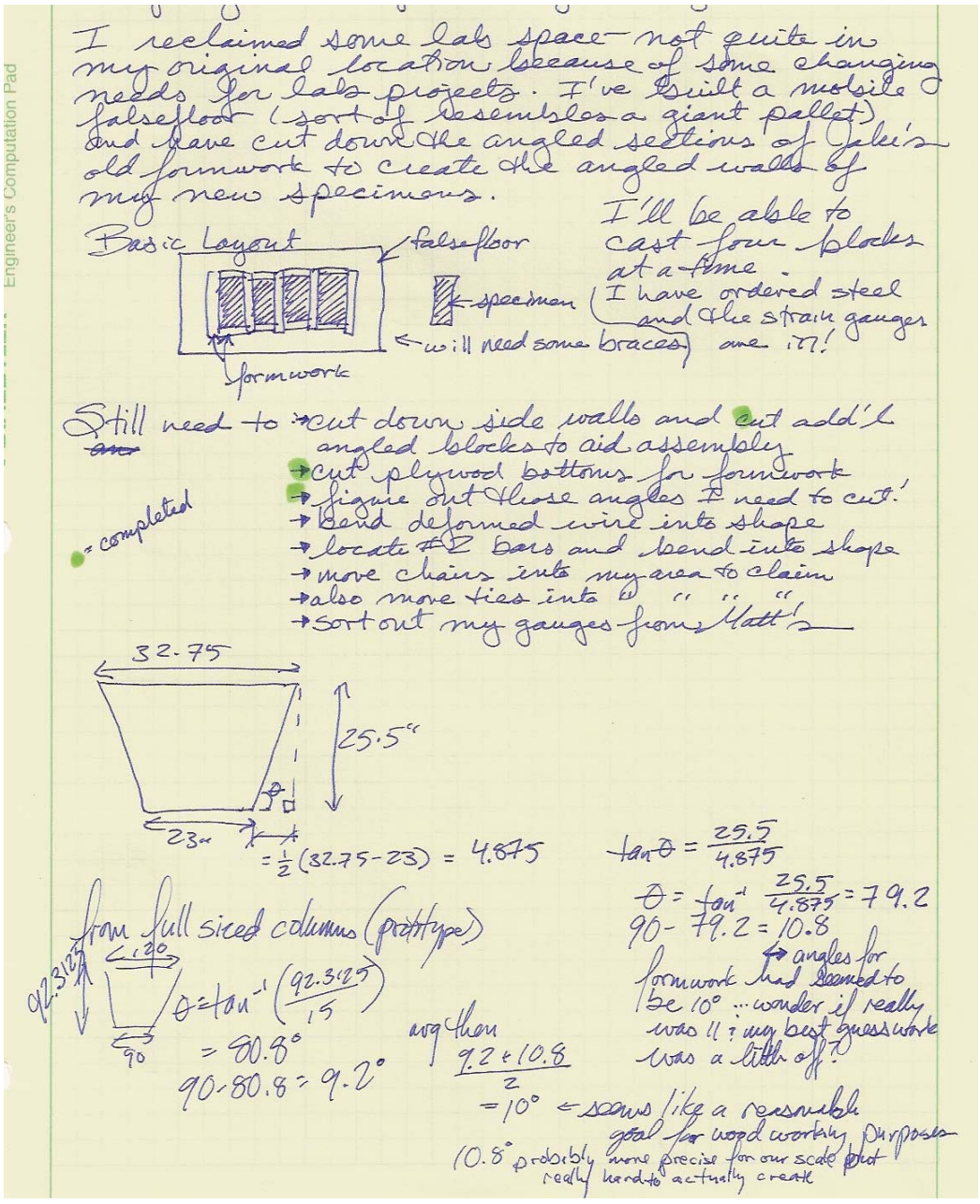

Figure B. 6: Bearing Specimen Formwork (1 of 2)

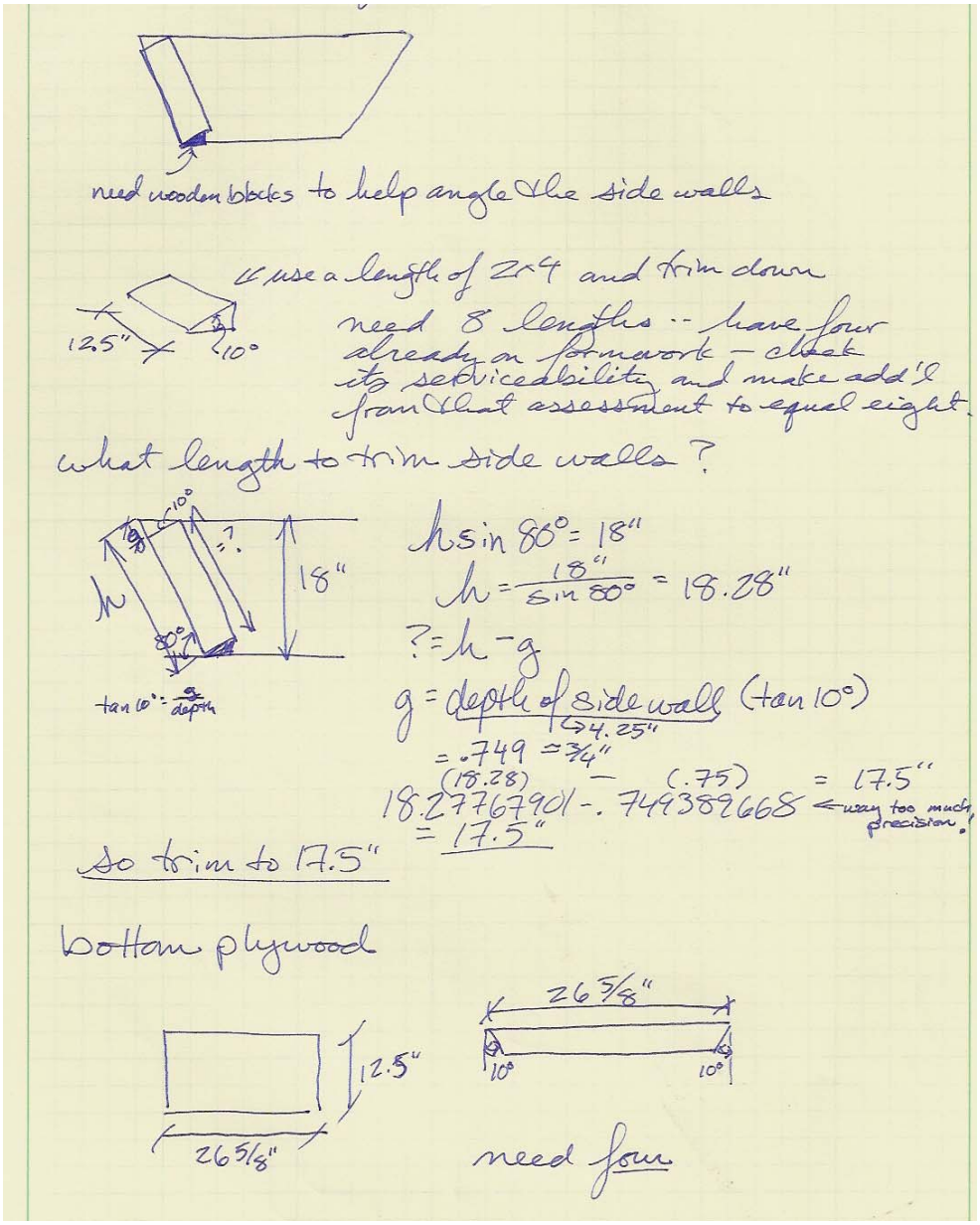

Figure B. 7: Bearing Specimen Formwork (2 of 2)

B.3 DESIGN LOCATION OF PVC IN BEARING SPECIMENS

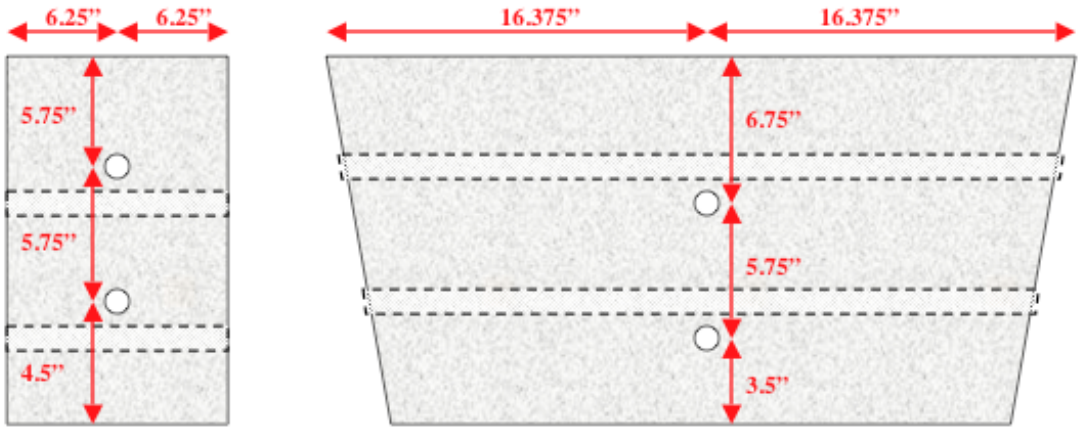

Figure B. 8: PVC Design Location in Bearing Specimens

B.4 HEAT TREATMENT TEMPERATURE PROFILES

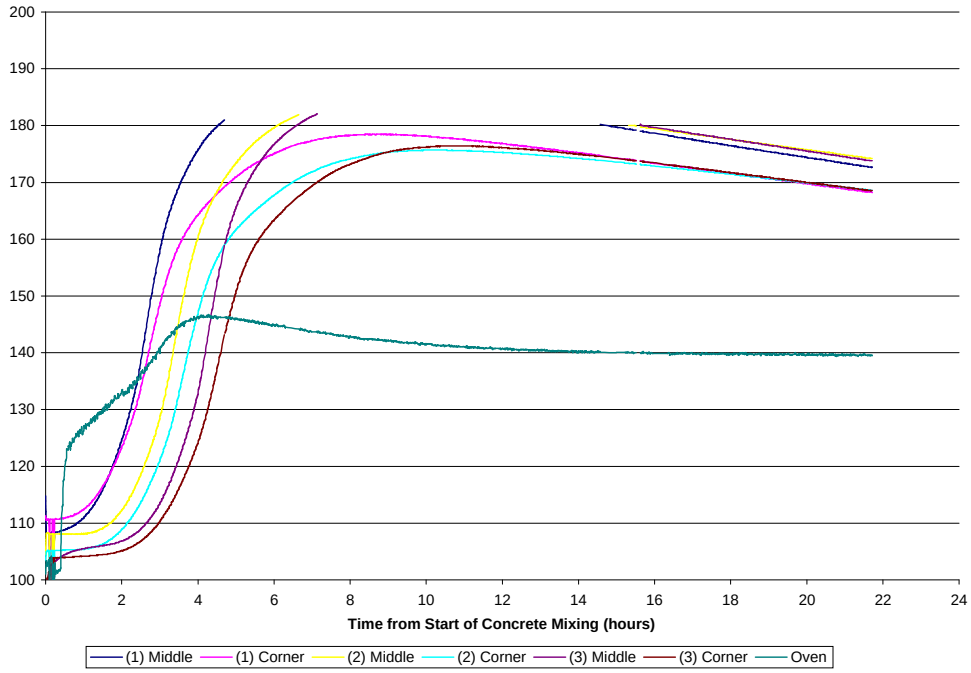

Figure B. 9: Heat Profile of Bearing Specimens Cast 10 July 2007[98]

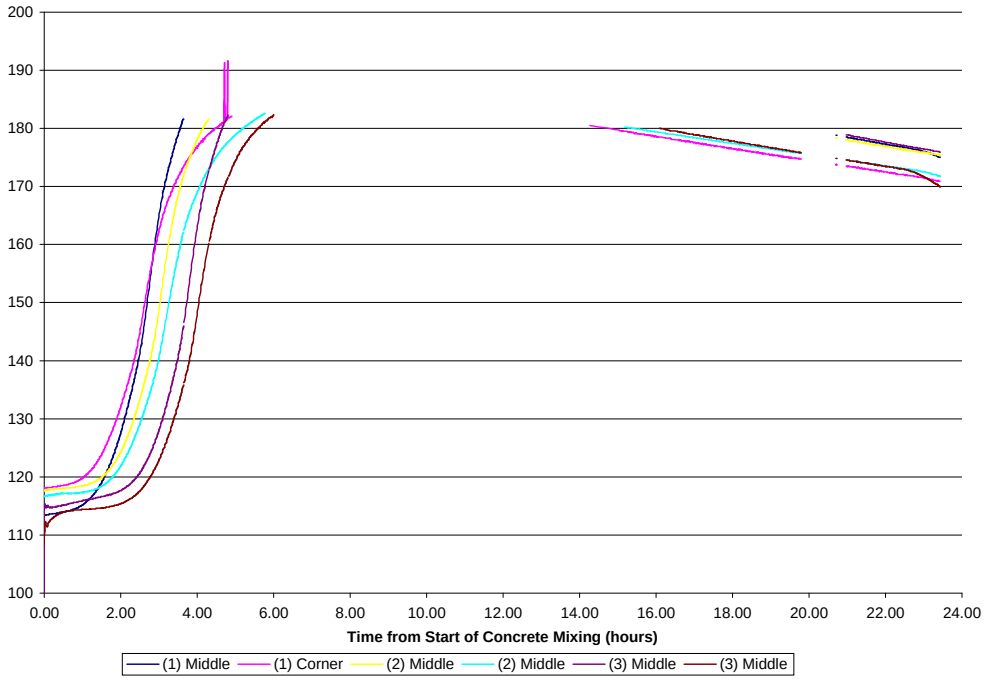

Figure B. 10: Temperature Profile of Bearing Specimens Cast 12 July 2007[98]

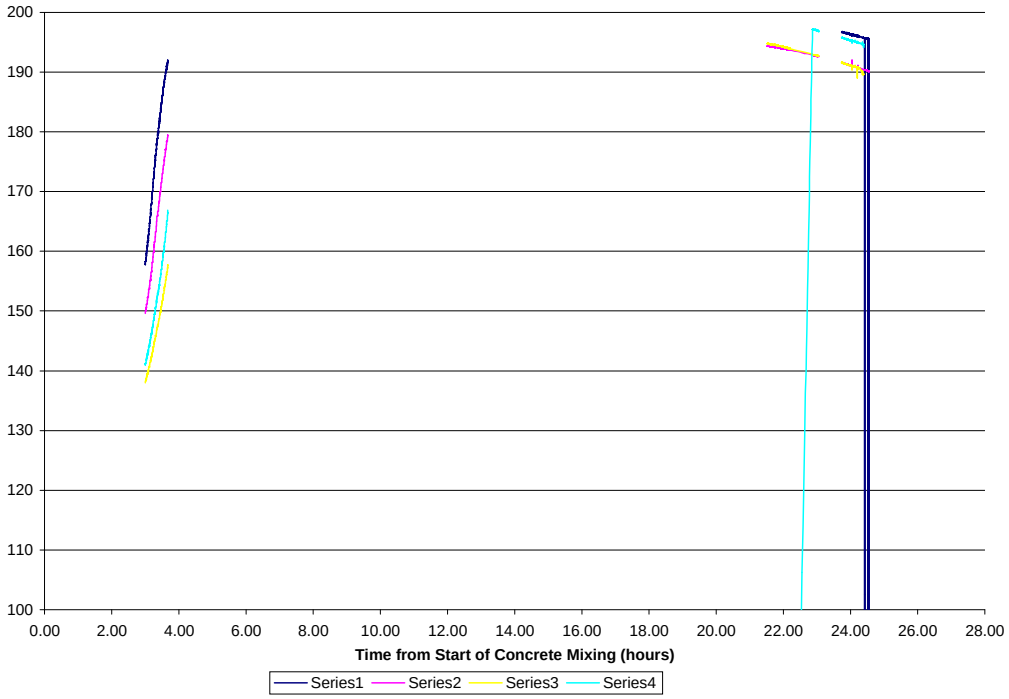

Figure B. 11: Temperature Profile of Bearing Specimens Cast on 16 July 2007[98]

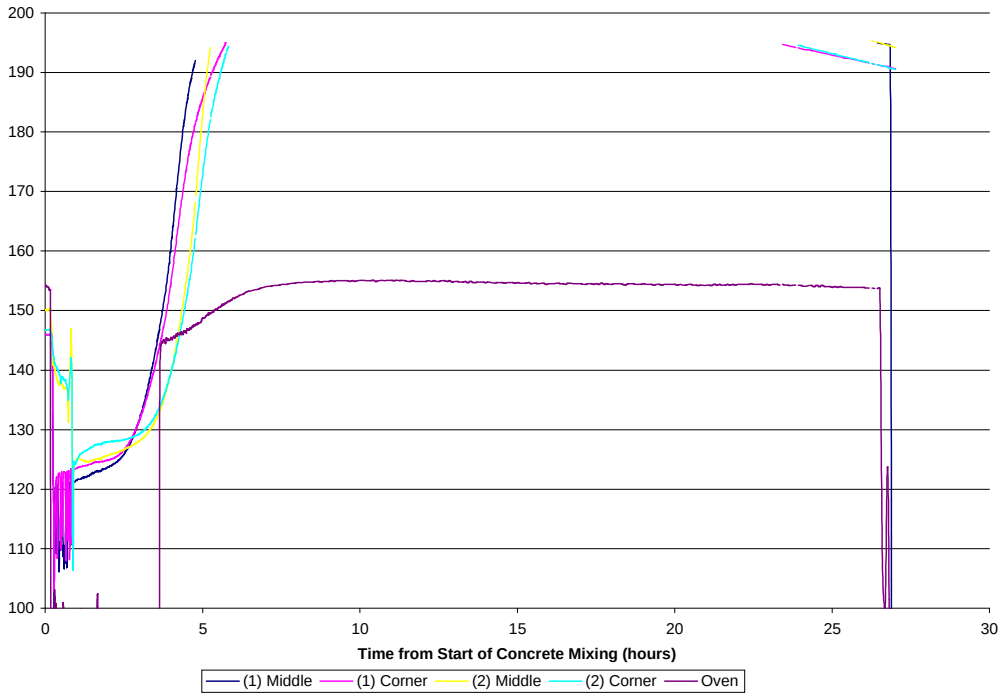

Figure B. 12: Temperature Profile from Bearing Specimens Cast 18 July 2[98]

B.5 TYPE OF STRAIN GAUGES USED IN BEARING SPECIMENS

All strain gauges used were from TML Tokyo Sokki Kenkyujo Co., Ltd. The transverse ties all had FLA-1-11-3LT type strain gauges, which had a 1 mm gauge length and a gauge factor of 2.15. The longitudinal bars all had FLA-6-11-3LT type gauges. This gauge type had a gauge length of 6 mm and a gauge factor of 2.11.

B.6 SPECIMEN ORGANIZATION WITHIN EXPOSURE TANK

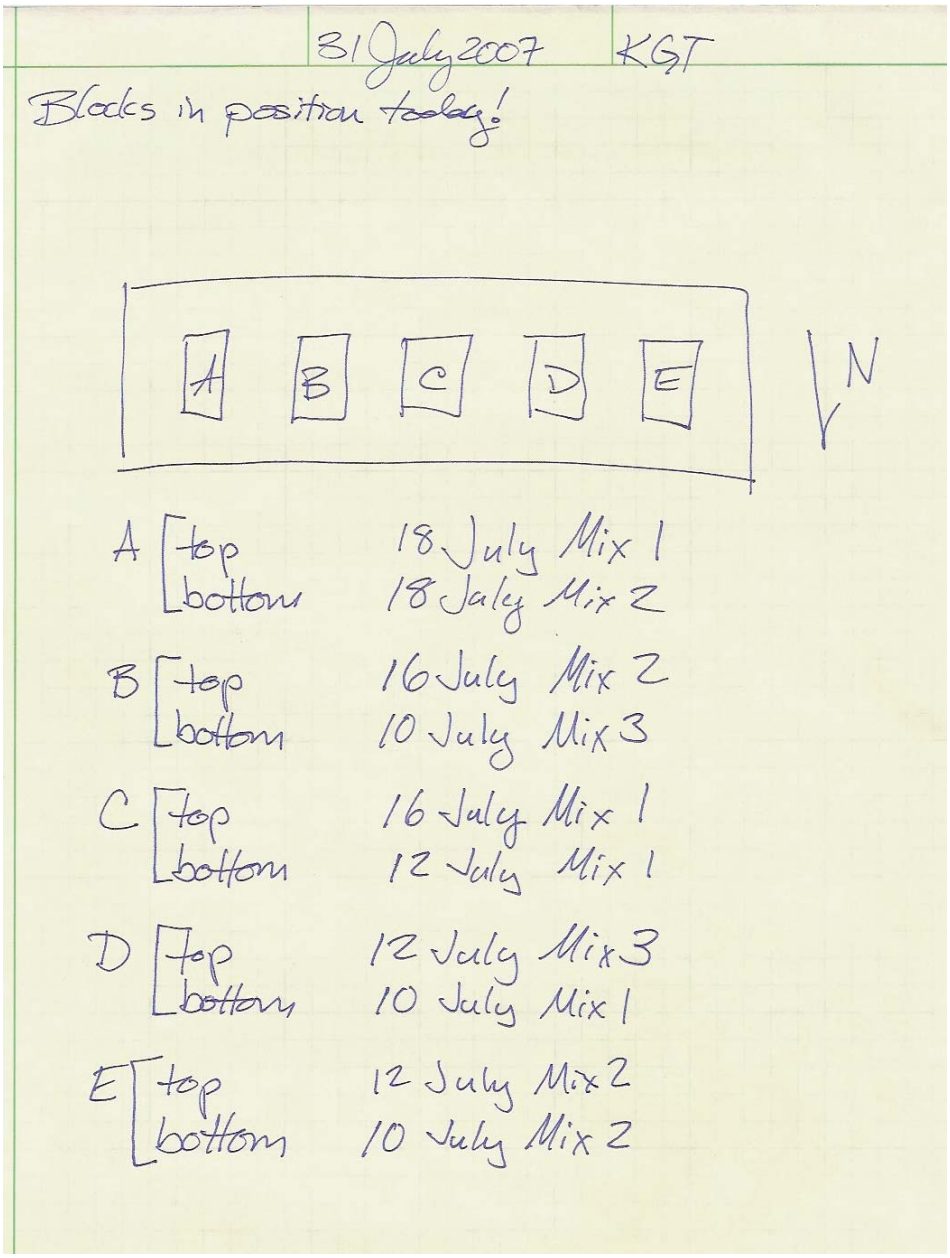

Figure B. 13: Bearing Specimen Arrangement in Exposure Tank

B.7 DEMEC READINGS FROM MECHANICAL CRACKING

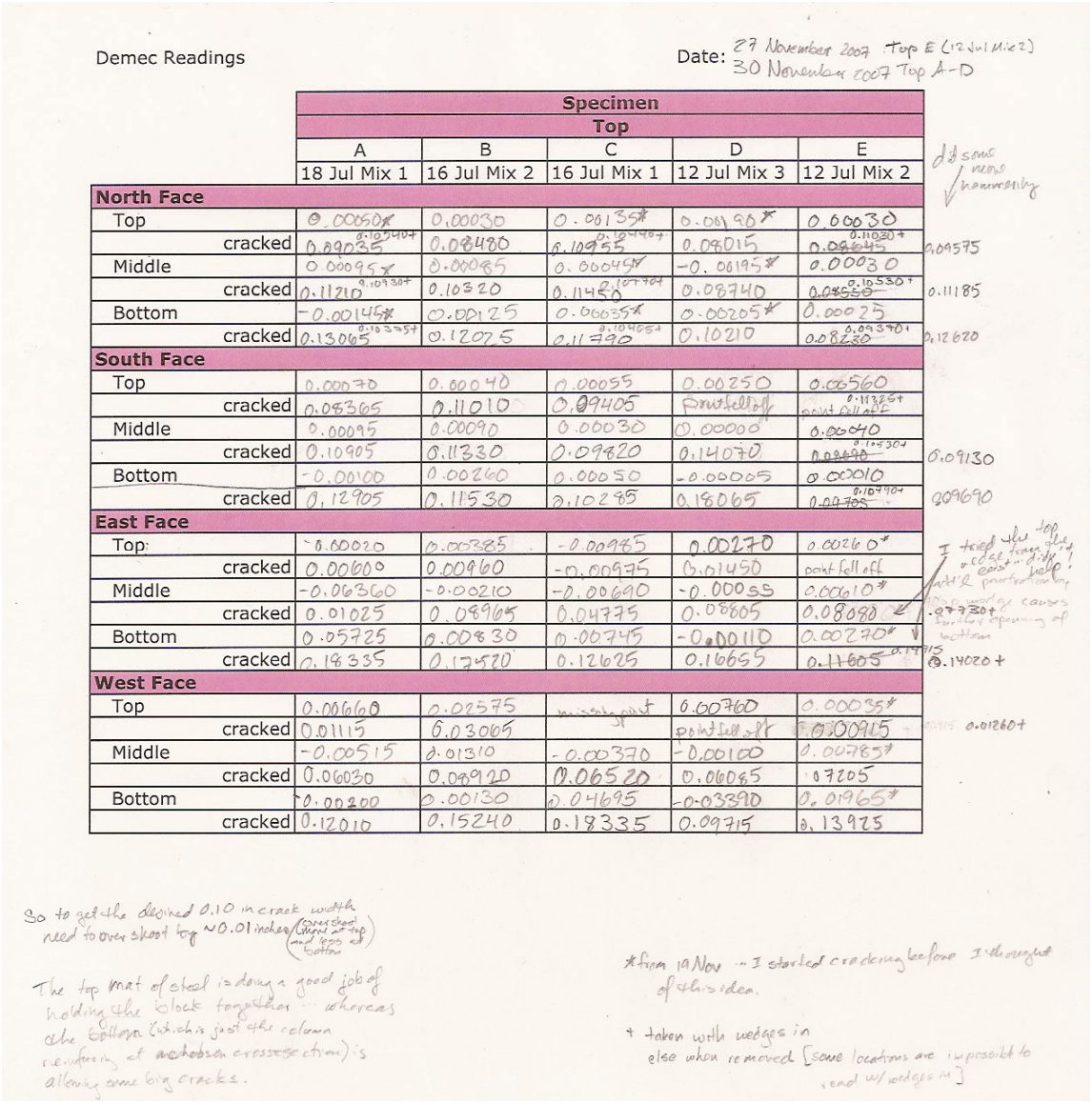

Demec Readings

Date: 27 November 2007 Top E (12 Jul Mix 2)
30 November 2007 Top A-D

	Specimen Top				
	A	B	C	D	E
	18 Jul Mix 1	16 Jul Mix 2	16 Jul Mix 1	12 Jul Mix 3	12 Jul Mix 2
North Face					
Top	0.00050*	0.00030	0.00135*	0.00190*	0.00030
cracked	0.09035 0.10540+	0.08480	0.10955 0.10440+	0.08015	0.08645 0.11020+
Middle	0.00095*	0.00085	0.00045*	-0.00195*	0.00030
cracked	0.11210 0.10930+	0.10320	0.11450 0.10770+	0.08740	0.07550 0.10550+
Bottom	-0.00145*	0.00125	0.00035*	0.00205*	0.00025
cracked	0.13005 0.10355+	0.12075	0.11790 0.10405+	0.10210	0.08230 0.09390+
South Face					
Top	0.00070	0.00040	0.00055	0.00250	0.00560
cracked	0.08365	0.11010	0.09405	fell off	0.11325+ point fell off
Middle	0.00095	0.00090	0.00030	0.00000*	0.00040
cracked	0.10905	0.11330	0.09820	0.14070	0.08690 0.10530+
Bottom	-0.00100	0.00260	0.00050	-0.00005	0.00010
cracked	0.12905	0.11530	0.10285	0.18065	0.09705 0.10490+
East Face					
Top	-0.00020	0.00385	-0.00985	0.00270	0.00260*
cracked	0.00600	0.00960	-0.00975	0.01450	point fell off
Middle	-0.06360	-0.00210	-0.00690	-0.00055	0.00610*
cracked	0.01025	0.08965	0.04775	0.08605	0.08080 0.07730+
Bottom	0.05725	0.00830	0.00745	-0.00110	0.00270*
cracked	0.18335	0.17520	0.12625	0.16655	0.11605 0.14715 0.14020+
West Face					
Top	0.00660	0.02575	inaccurate point	0.00760	0.00035*
cracked	0.01115	0.03065		point fell off	0.00915 0.01260+
Middle	-0.00515	0.01310	-0.00370	-0.00100	0.00785*
cracked	0.06030	0.08920	0.06520	0.06065	07205
Bottom	-0.00200	0.00130	0.04695	-0.03390	0.01965*
cracked	0.12010	0.15240	0.18335	0.09715	0.13925

0.09575
0.11185
0.12620
0.09130
0.09690

So to get the desired 0.10 in crack width need to overshoot top ~0.01 inches (Correspond w/ top and top of bottom)

The top mat of steel is doing a good job of holding the block together whereas the bottom (which is just the column reinforcing at anchobsen crosssection) is allowing some big cracks.

*from 19 Nov - I started cracking before I thought of this idea.

+ taken with wedges in else when removed [some locations are impossible to read w/ wedges in]

Figure B. 14: Demec Pre- and Post-Mechanical Cracking Readings (1 of 2)

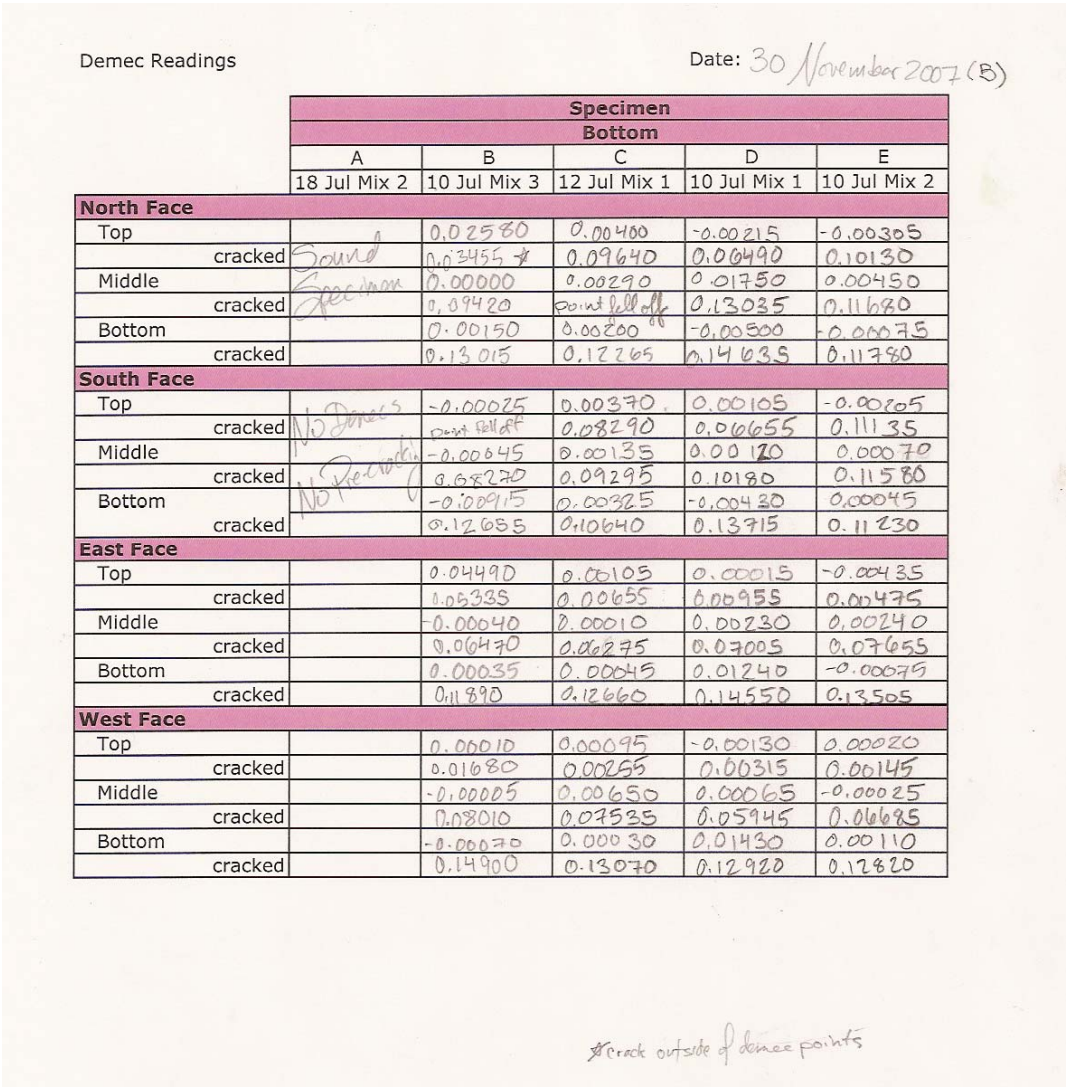

Demec Readings

Date: 30 November 2007 (B)

	Specimen Bottom				
	A	B	C	D	E
	18 Jul Mix 2	10 Jul Mix 3	12 Jul Mix 1	10 Jul Mix 2	10 Jul Mix 1
North Face					
Top		0.02580	0.00400	-0.00215	-0.00305
cracked	Sound	0.03455 *	0.09640	0.06490	0.10130
Middle	Specimen	0.00000	0.00290	0.01750	0.00450
cracked		0.09420	point fell off	0.13035	0.11680
Bottom		0.00150	0.00200	-0.00500	-0.00075
cracked		0.13015	0.12265	0.14635	0.11780
South Face					
Top	No Demecs	-0.00025	0.00370	0.00105	-0.00205
cracked		point fell off	0.08290	0.06655	0.11135
Middle	No Reading	-0.00645	0.00135	0.00120	0.00070
cracked		0.08270	0.09295	0.10180	0.11580
Bottom		-0.00915	0.00325	-0.00430	0.00045
cracked		0.12655	0.10640	0.13715	0.11230
East Face					
Top		0.04490	0.00105	0.00015	-0.00435
cracked		0.05335	0.00655	0.00955	0.00475
Middle		-0.00040	0.00010	0.00230	0.00240
cracked		0.06470	0.06275	0.07005	0.07655
Bottom		0.00035	0.00045	0.01240	-0.00075
cracked		0.11890	0.12660	0.14550	0.13505
West Face					
Top		0.00010	0.00095	-0.00130	0.00020
cracked		0.01680	0.00255	0.00315	0.00145
Middle		-0.00005	0.00650	0.00065	-0.00025
cracked		0.08010	0.07535	0.05945	0.06685
Bottom		-0.00070	0.00030	0.01430	0.00110
cracked		0.14900	0.13070	0.12920	0.12820

* crack outside of demec points

Figure B. 15: Demec Pre- and Post-Mechanical Cracking Readings (2 of 2)

B.8 REPAIR LOAD CALCULATION

The repair load demand was scaled from Kapitan's strut and tie model. The scaling assumed that the repair would need to carry a tensile demand at the column capital corresponding to 25% of the axial load modeled by Kapitan. Figure B. 16 presents Kapitan's model.

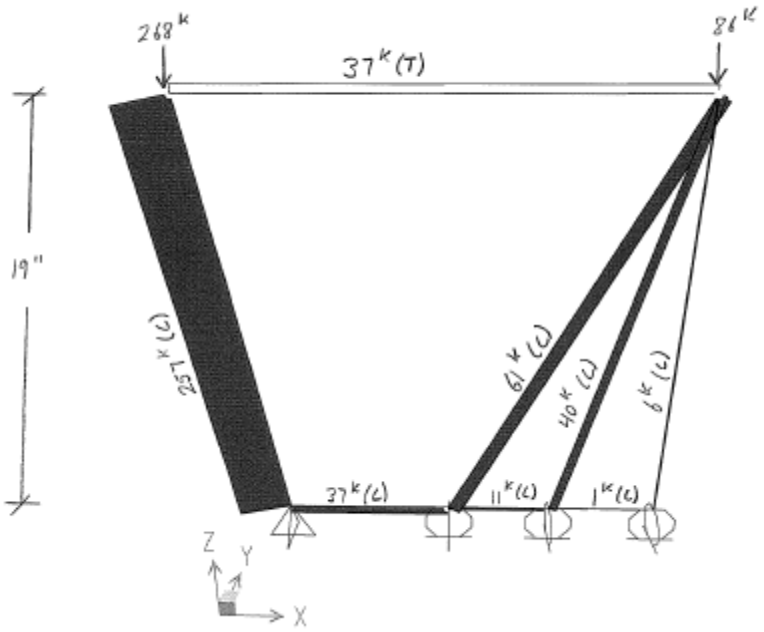

Figure B. 16: Kapitan's Strut and Tie Model

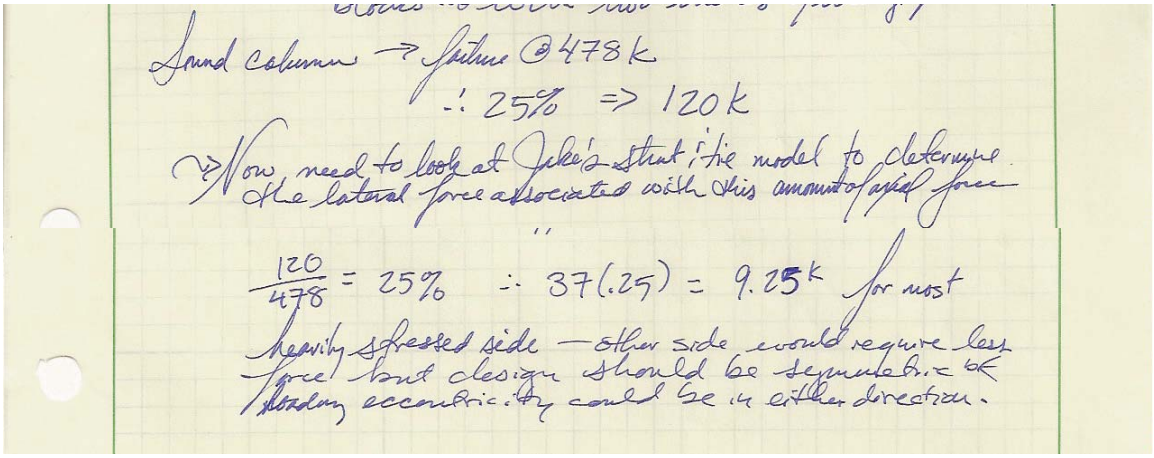
Sound column → failure @ 478 k

∴ 25% ⇒ 120 k

⇒ Now need to look at Jake's strut & tie model to determine the lateral force associated with this amount of axial force

$\frac{120}{478} = 25\%$ ∴ 37(.25) = 9.25 k for most heavily stressed side — other side would require less force but design should be symmetric bc loading eccentricity could be in either direction.

Figure B. 17: Scaling Tie's Tensile Force

B.9 INDIVIDUAL REPAIR CALCULATIONS (BY TYPE)

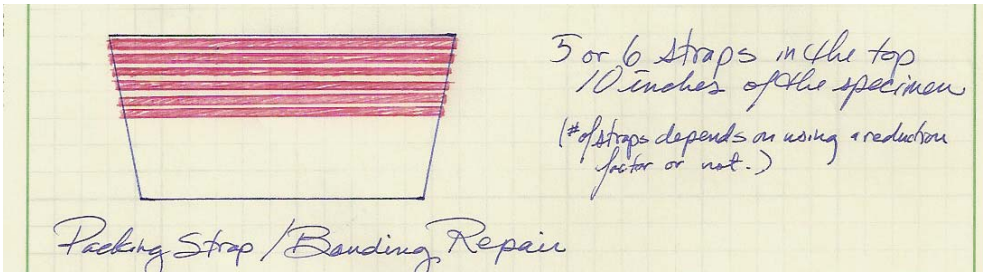

Figure B. 18: Packing Strap Repair Schematic

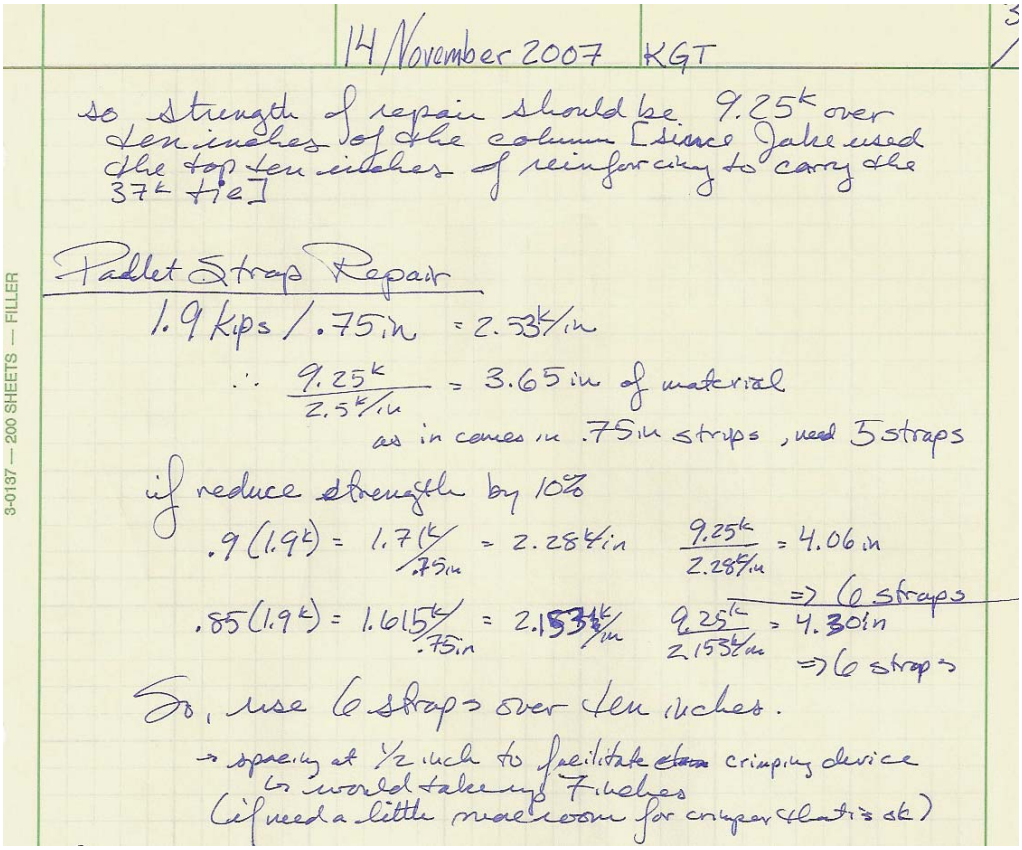

Figure B. 19: Packing Strap Repair Calculation

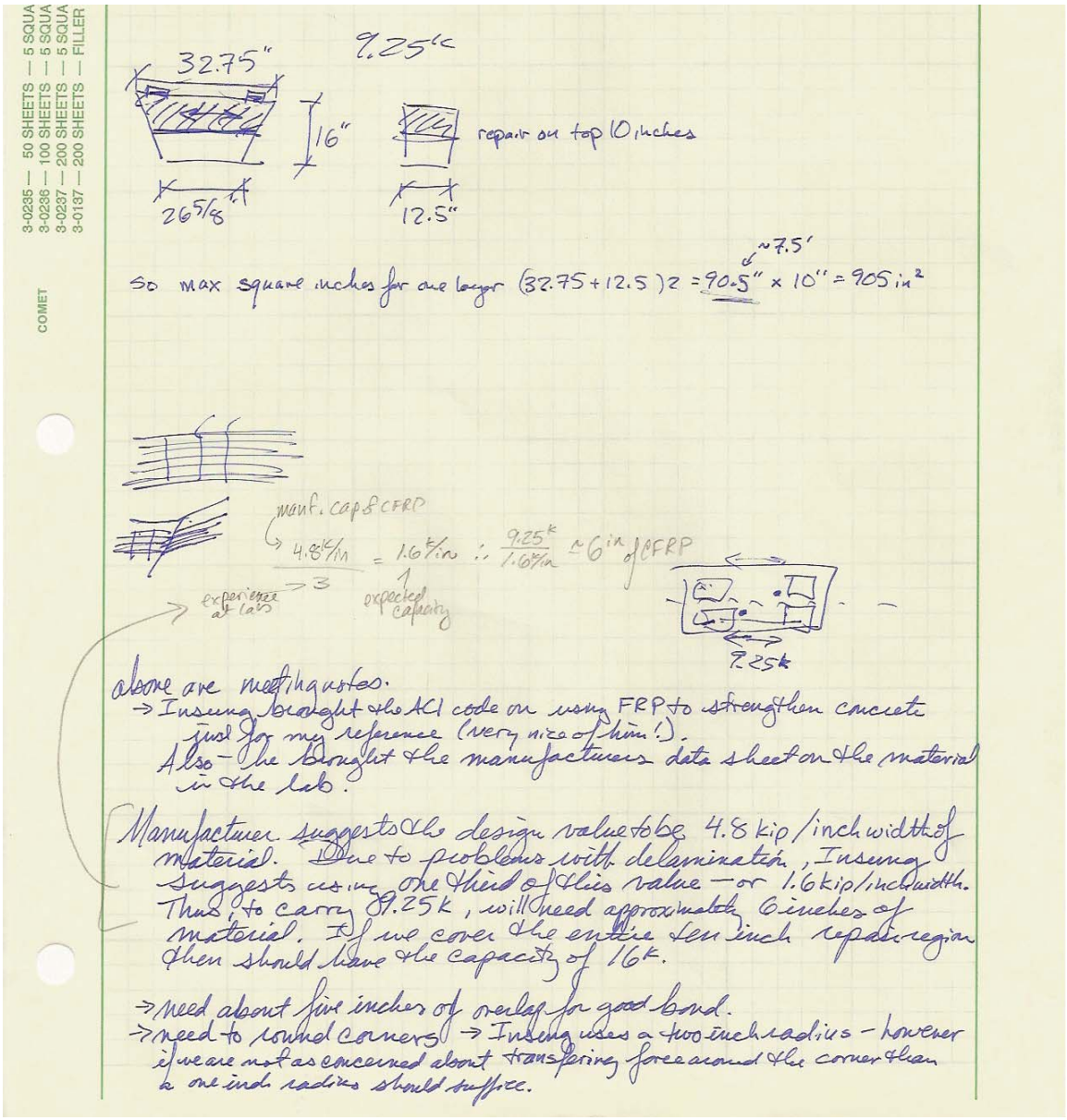

Figure B. 20: FRP Repair Schematic and Calculation

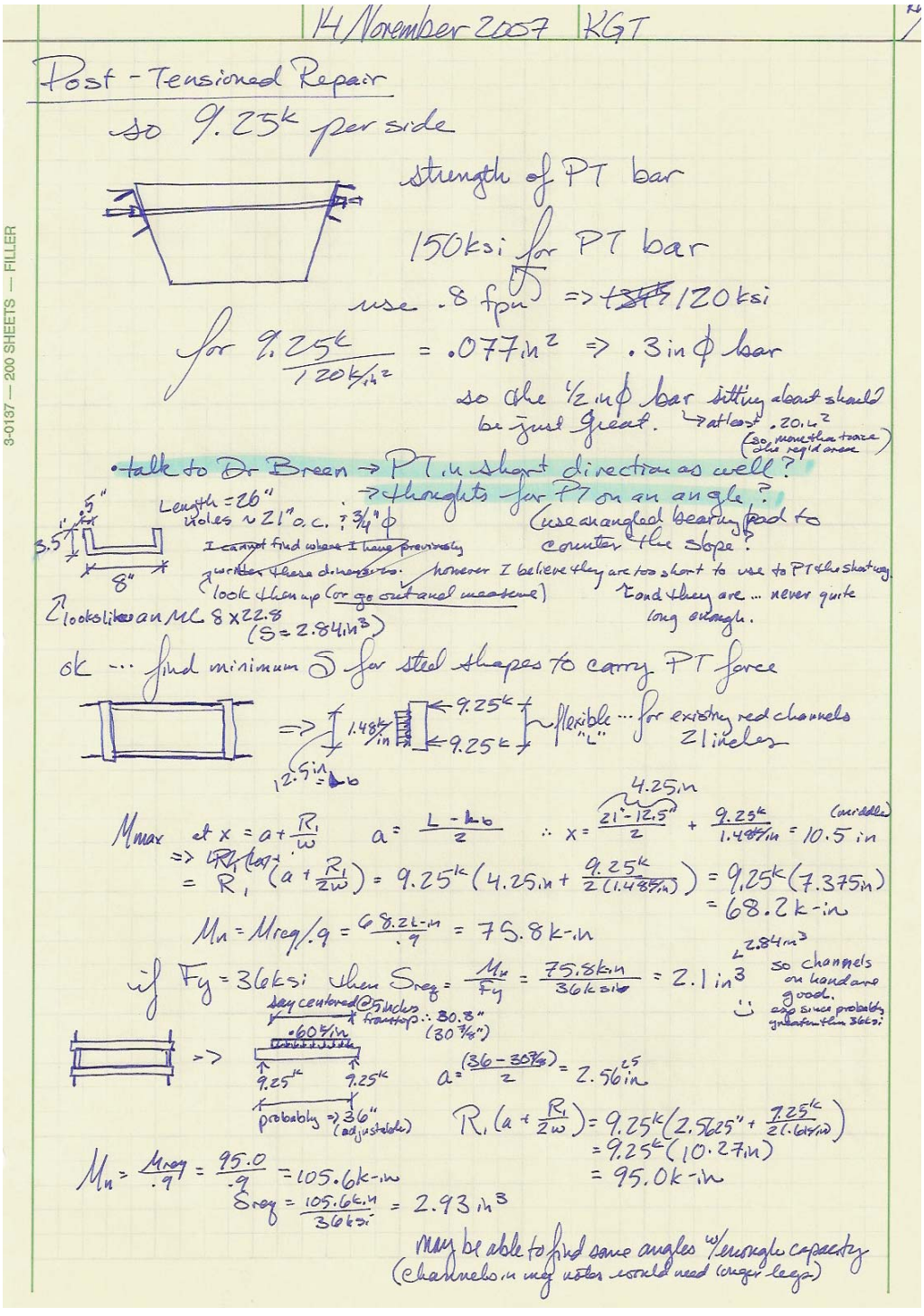

Figure B. 21: Post-tensioning Repair Schematic and Calculation

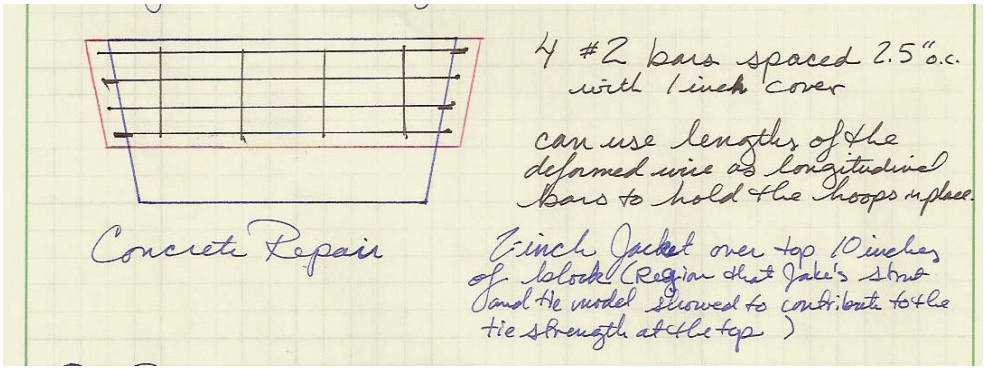

Figure B. 22: Concrete Jacket Repair Schematic

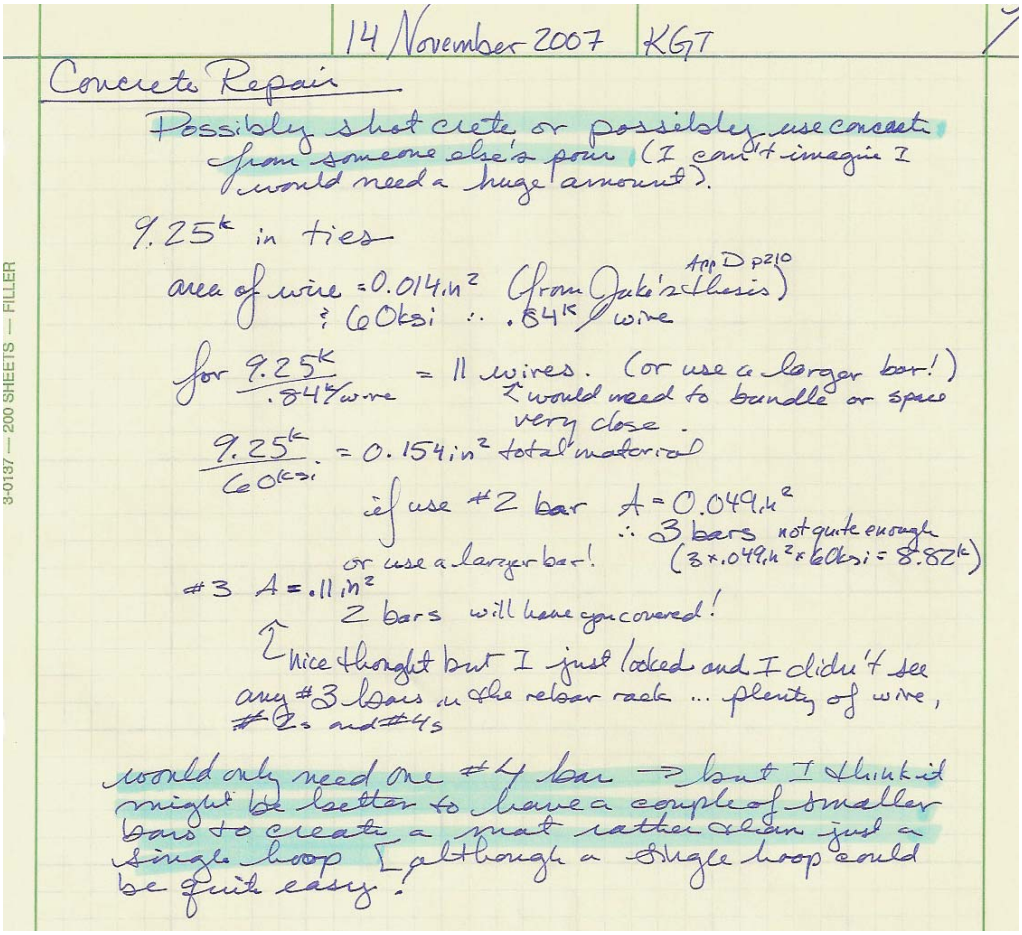

Figure B. 23: Concrete Jacket Repair Calculation

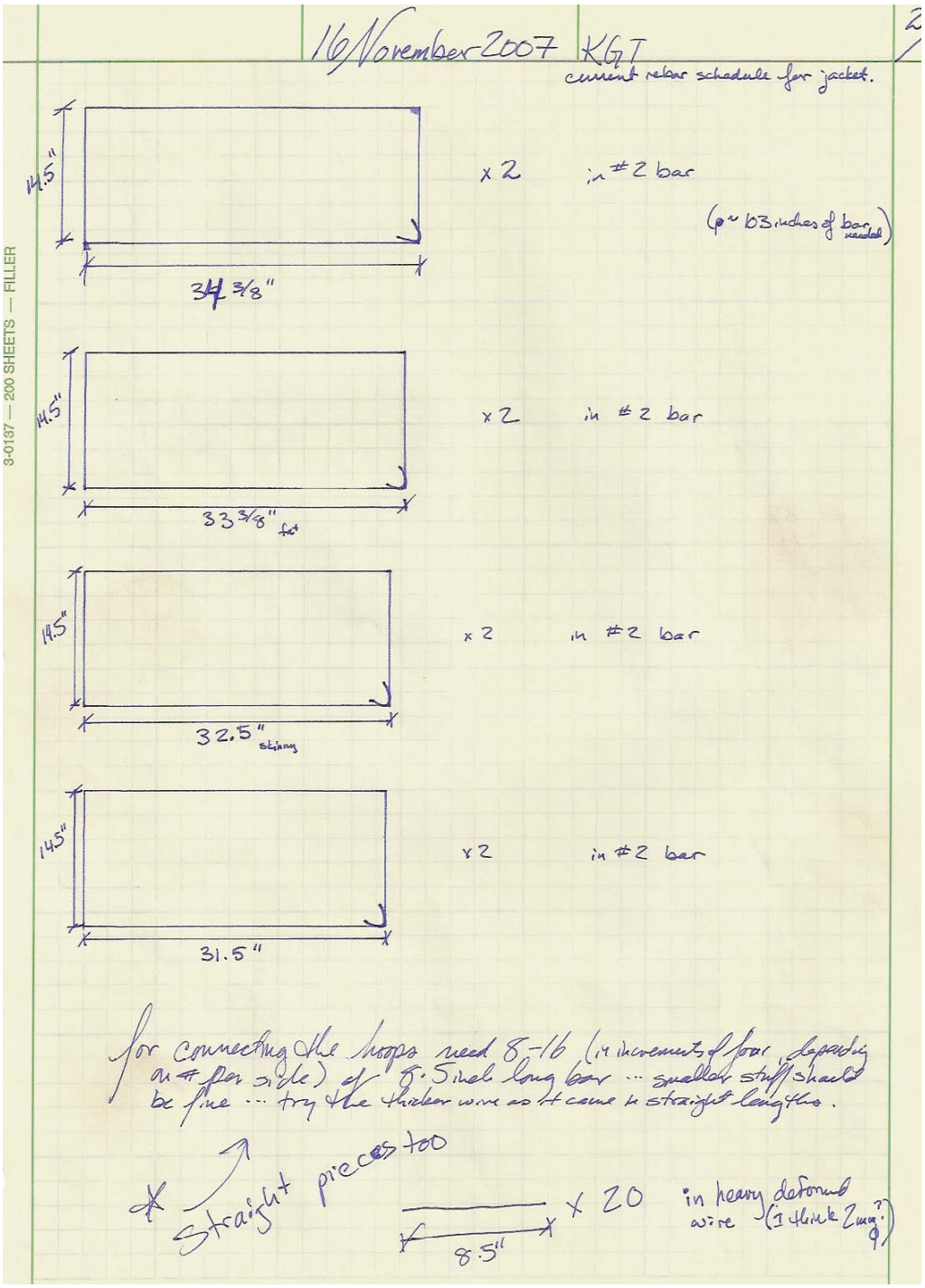

Figure B. 24: Concrete Jacket Repair Reinforcing

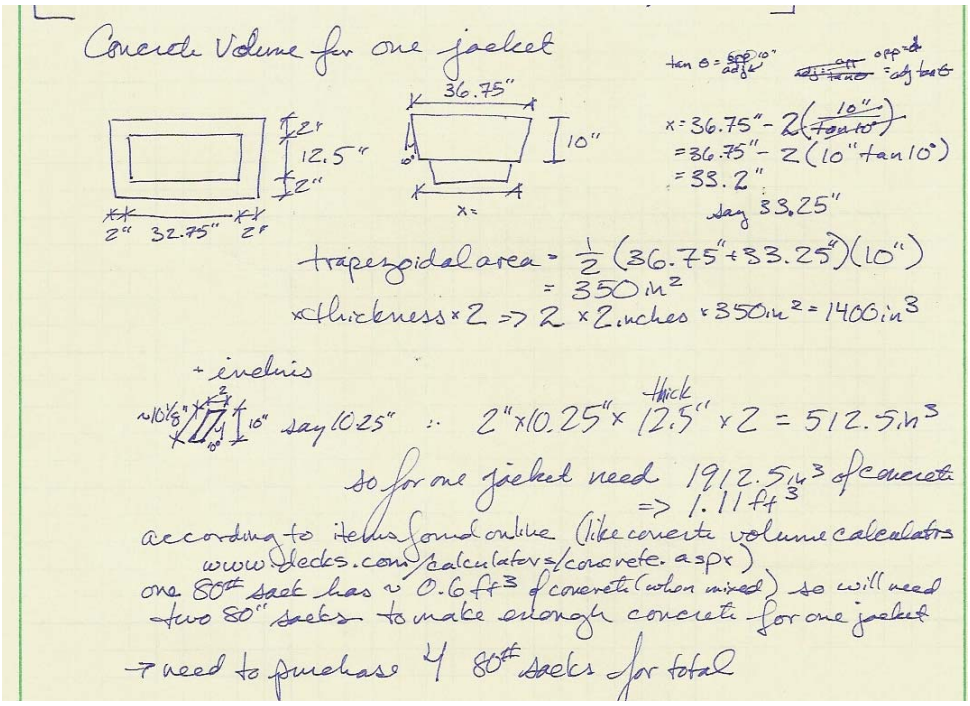

Figure B. 25: Concrete Volume Calculation for Concrete Jacket Repair

B.10 CALCULATION OF PLATEN PLATE SIZE

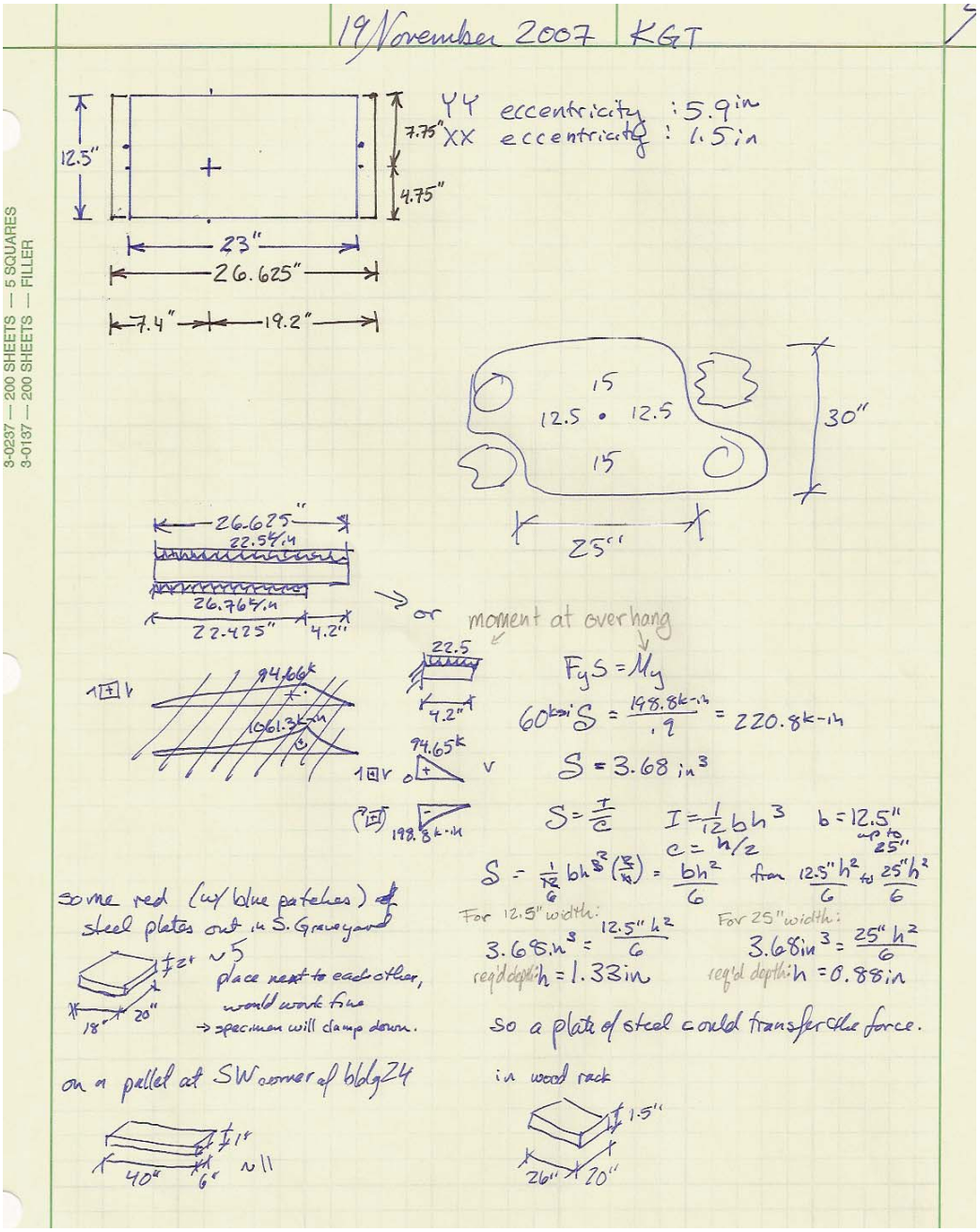

Figure B. 26: Calculation for Required Thickness of Plate for Platen Extension

APPENDIX C

Computer Program

C.1 SAMPLE CALCULATION OF ATENA VERTICAL LOAD

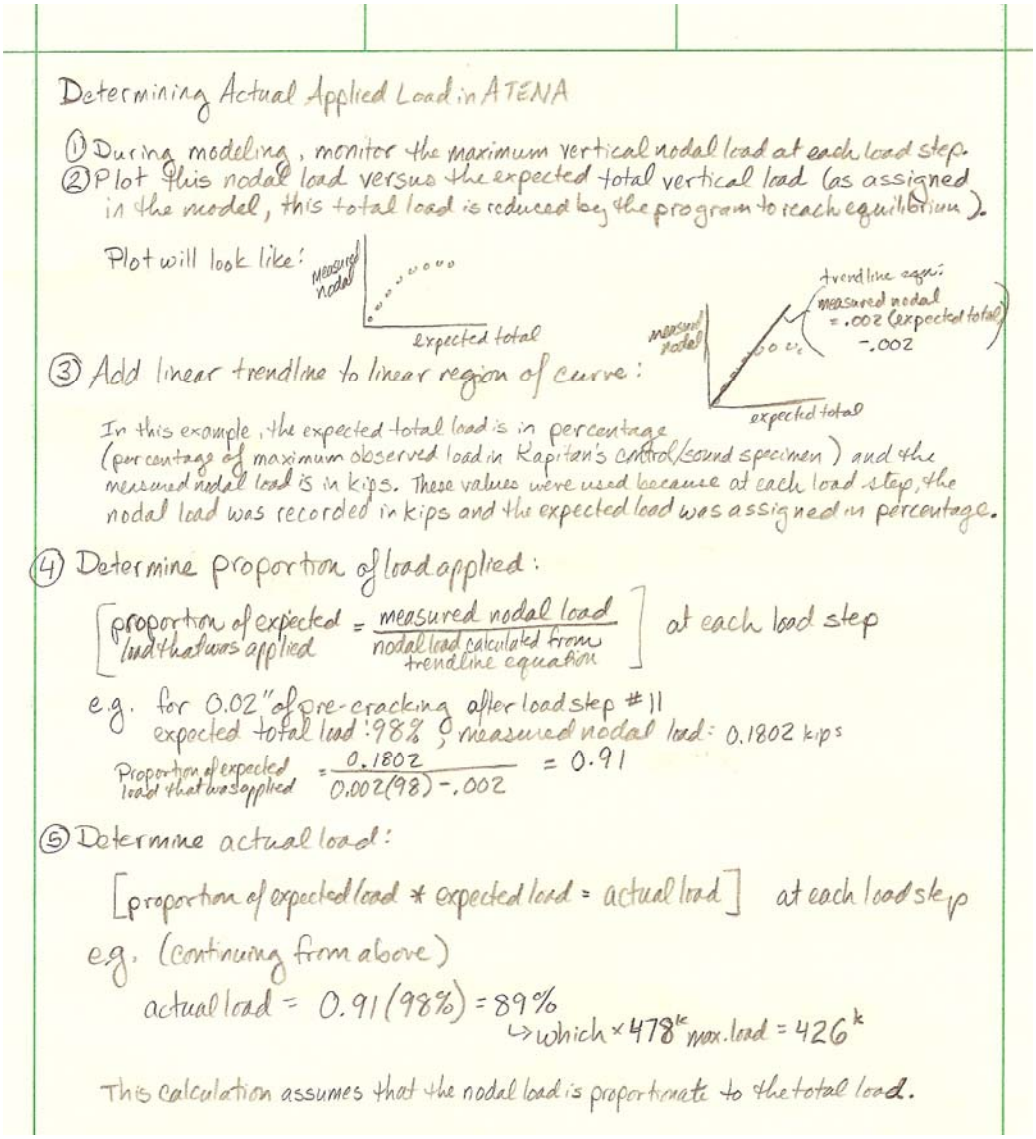

Figure C. 1: Sample Calculation of Actual Load

C.2 ATENA INPUT DATA

Description:	UT Grad model	Unit system:	Imperial	side 1
Note:	scaled version			

ANALYSIS INFORMATION

Property	Value
Description	UT Grad model
Note	scaled version
Unit system	Imperial
Solver type	standard
Run	geometrically nonlinear

MATERIALS

MATERIAL 1

Property	Value
Title	3D Nonlinear Cementitious 2
Type	CC3DNonLinCementitious2
Elastic modulus E [ksi]	4.341E+03
Poisson's ratio μ [–]	0.200
Specific material weight ρ [kci]	8.681E-05
Coefficient of thermal expansion α [1/°F]	6.667E-06
Tensile strength F_t [ksi]	5.712E-01
Compressive strength F_c [ksi]	-5.800E+00
Specfic fracture energy G_f [kip/in]	3.308E-04
Critical compressive displacement W_d [in]	-8.300E-03
Exc.,def. the shape of fail.surface e [–]	0.520
Multiplier for the direction of the pl.flow β [–]	0.000
Fixed crack model coefficient [–]	1.000
Plastic strain at compressive strength ε_{cp} [–]	-1.364E-03
Onset of non-linear behavior in compression F_{c0} [ksi]	-1.200E+00

MATERIAL 2

Property	Value
Title	Reinforcement
Type	CCReinforcement
Elastic modulus E [ksi]	3.046E+04
Specific material weight ρ [kci]	2.892E-04
Coefficient of thermal expansion α [1/°F]	6.667E-06
Reinf. type	Bilinear
σ_y [ksi]	60.000

MATERIAL 3

Property	Value
Title	3D Elastic Isotropic (wedge)
Type	CC3DElastIsotropic
Elastic modulus E [ksi]	3.000E+04
Poisson's ratio μ [–]	0.300
Specific material weight ρ [kci]	8.473E-05
Coefficient of thermal expansion α [1/°F]	6.667E-06

MATERIAL 4

Property	Value
Title	3D Elastic Isotropic-3ksi (wedge fill)

[Atena - 3D | version 1.2.14.0 | hardware key 325 / 1 | (c)Cervenka Consulting 2007 | www.cervenka.cz]

Figure C. 2: ATENA Input Data (1 of 9)

Description:	UT Grad model	Unit system:	Imperial	side 2
Note:	scaled version			

Type	CC3DElastIsotropic
Elastic modulus E [ksi]	3.000E+04
Poisson's ratio μ [–]	0.300
Specific material weight ρ [kci]	8.473E-05
Coefficient of thermal expansion α [1/°F]	6.667E-06

MATERIAL 5

Property	Value
Title	3D Elastic Isotropic
Type	CC3DElastIsotropic
Elastic modulus E [ksi]	6.000E+01
Poisson's ratio μ [–]	0.300
Specific material weight ρ [kci]	8.473E-05
Coefficient of thermal expansion α [1/°F]	6.667E-06

LC 1 - SUPPORTS

SURFACE SUPPORTS

Macro. / surface	Coordinate system	Support in dir. of the axis X	Y	Z
2/5	Global	fixed	fixed	fixed

LC 3 - TOP LOADS (GENERAL)

SURFACE FORCE LOADING

Macro. / surface	Loading type	Value [kip/in²]	Force direction Coord. system	Orientation
4/6	continuous constant - on surface	-6.650E-01	Global	Zg
5/6	continuous constant - on surface	-1.995E+00	Global	Zg
6/6	continuous constant - on surface	-2.217E+00	Global	Zg
7/6	continuous constant - on surface	-6.207E+00	Global	Zg

LC 4 - PRESCRIBED DEFORMATION - X DIR

LINE SUPPORTS AND PRESCRIBED DEFORMATIONS

Macro. / line	Coordinate system	Support and deformation in the direction of the axis X [in]	Y [in]	Z [in]
1/28	Global	fixed: -1.000E-02	free	free
1/34	Global	fixed: 1.000E-02	free	free
1/46	Global	fixed: -1.000E-02	free	free
1/52	Global	fixed: 1.000E-02	free	free
1/64	Global	fixed: -1.000E-02	free	free
1/70	Global	fixed: 1.000E-02	free	free
1/82	Global	fixed: -1.000E-02	free	free
1/88	Global	fixed: 1.000E-02	free	free
1/96	Global	fixed: 1.000E-02	free	free
1/102	Global	fixed: -1.000E-02	free	free
1/108	Global	fixed: 1.000E-02	free	free
1/200	Global	fixed: -1.000E-02	free	free
1/210	Global	fixed: 1.000E-02	free	free
1/212	Global	fixed: -1.000E-02	free	free
1/228	Global	fixed: -1.000E-02	free	free

Figure C. 3: ATENA Input Data (2 of 9)

1/230	Global	fixed: 1.000E-02	free	free
1/236	Global	fixed: 1.000E-02	free	free
1/238	Global	fixed: -1.000E-02	free	free
1/332	Global	fixed: -1.000E-02	free	free
1/333	Global	fixed: 1.000E-02	free	free
1/349	Global	fixed: 1.000E-02	free	free
1/352	Global	fixed: -1.000E-02	free	free
1/355	Global	fixed: 1.000E-02	free	free
1/358	Global	fixed: -1.000E-02	free	free
1/374	Global	fixed: 1.000E-02	free	free
1/376	Global	fixed: -1.000E-02	free	free
1/383	Global	fixed: 1.000E-02	free	free
1/386	Global	fixed: -1.000E-02	free	free
1/393	Global	fixed: 1.000E-02	free	free
1/396	Global	fixed: -1.000E-02	free	free

LC 5 - PRESCRIBED DEFORMATION - Y DIR

LINE SUPPORTS AND PRESCRIBED DEFORMATIONS

Macro. / line	Coordinate system	Support and deformation in the direction of the axis X [in]	Y [in]	Z [in]
1/118	Global	free	fixed: -1.000E-01	free
1/124	Global	free	fixed: 1.000E-01	free
1/136	Global	free	fixed: -1.000E-01	free
1/142	Global	free	fixed: 1.000E-01	free
1/154	Global	free	fixed: -1.000E-01	free
1/160	Global	free	fixed: 1.000E-01	free
1/172	Global	free	fixed: -1.000E-01	free
1/178	Global	free	fixed: 1.000E-01	free
1/190	Global	free	fixed: -1.000E-01	free
1/196	Global	free	fixed: 1.000E-01	free
1/244	Global	free	fixed: -1.000E-01	free
1/250	Global	free	fixed: 1.000E-01	free
1/262	Global	free	fixed: -1.000E-01	free
1/268	Global	free	fixed: 1.000E-01	free
1/280	Global	free	fixed: -1.000E-01	free
1/286	Global	free	fixed: 1.000E-01	free
1/298	Global	free	fixed: -1.000E-01	free
1/304	Global	free	fixed: 1.000E-01	free
1/316	Global	free	fixed: -1.000E-01	free
1/322	Global	free	fixed: 1.000E-01	free
1/344	Global	free	fixed: 1.000E-01	free
1/347	Global	free	fixed: -1.000E-01	free
1/362	Global	free	fixed: 1.000E-01	free
1/366	Global	free	fixed: -1.000E-01	free
1/367	Global	free	fixed: -1.000E-01	free
1/371	Global	free	fixed: 1.000E-01	free
1/377	Global	free	fixed: 1.000E-01	free
1/381	Global	free	fixed: -1.000E-01	free

Figure C. 4: ATENA Input Data (3 of 9)

1/387	Global	free	fixed: 1.000E-01	free
1/392	Global	free	fixed: -1.000E-01	free

SOLUTION PARAMETERS

SOLUTION PARAMETERS 1

Property	Value
Title	Standard Newton-Raphson
Method	Newton-Raphson (line search)
Iteration limit	40
Displacement Error	0.010000
Residual Error	0.010000
Absolute Residual Error	0.010000
Energy Error	0.000100
Optimize band-width	Sloan
Line Search	Yes
LS Type	With iterations
LS Unbalanced energy limit	0.800
LS Line search iteration limit	2
LS Minimum Eta	0.010
LS Maximum Eta	1.000
Update Stiffness	Each iteration
Stiffness Type	Tangent
Immediate Displacement Error Multiple	10000.0
After Step Displacement Error Multiple	1000.0
Immediate Residual Error Multiple	10000.0
After Step Residual Error Multiple	1000.0
Immediate Absolute Residual Error Multiple	10000.0
After Step Absolute Residual Error Multiple	1000.0
Immediate Energy Error Multiple	1000000.0
After Step Energy Error Multiple	10000.0

SOLUTION PARAMETERS 2

Property	Value
Title	Standard Arc Length
Method	Arc length (line search)
Arc Length Method	Consistently linearised
A-L Adjustment Method	Constant
A-L Load-Displacement Ratio	0.200
A-L Load-Displacement Method	Bergan constant
A-L Reference number of iterations	10
A-L Step-Length	Based on current load step
A-L Location	All nodes
Iteration limit	40
Displacement Error	0.010000
Residual Error	0.010000
Absolute Residual Error	0.010000
Energy Error	0.000100
Optimize band-width	Sloan
Line Search	Yes
LS Type	With iterations

Figure C. 5: ATENA Input Data (4 of 9)

LS Unbalanced energy limit	0.800
LS Line search iteration limit	2
LS Minimum Eta	0.010
LS Maximum Eta	1.000
Update Stiffness	Each iteration
Stiffness Type	Tangent
Immediate Displacement Error Multiple	10000.0
After Step Displacement Error Multiple	1000.0
Immediate Residual Error Multiple	10000.0
After Step Residual Error Multiple	1000.0
Immediate Absolute Residual Error Multiple	10000.0
After Step Absolute Residual Error Multiple	1000.0
Immediate Energy Error Multiple	1000000.0
After Step Energy Error Multiple	10000.0

SOLUTION PARAMETERS 3

Property	Value
Title	Newton_Raphson 100 iterations
Method	Newton-Raphson (line search)
Iteration limit	100
Displacement Error	0.010000
Residual Error	0.010000
Absolute Residual Error	0.010000
Energy Error	0.000100
Optimize band-width	Sloan
Line Search	Yes
LS Type	With iterations
LS Unbalanced energy limit	0.800
LS Line search iteration limit	2
LS Minimum Eta	0.010
LS Maximum Eta	1.000
Update Stiffness	Each iteration
Stiffness Type	Tangent
Immediate Displacement Error Multiple	10000.0
After Step Displacement Error Multiple	1000.0
Immediate Residual Error Multiple	10000.0
After Step Residual Error Multiple	1000.0
Immediate Absolute Residual Error Multiple	10000.0
After Step Absolute Residual Error Multiple	1000.0
Immediate Energy Error Multiple	1000000.0
After Step Energy Error Multiple	10000.0

SOLUTION PARAMETERS 4

Property	Value
Title	Arc length 100 iterations
Method	Arc length (line search)
Arc Length Method	Consistently linearised
A-L Adjustment Method	Constant
A-L Load-Displacement Ratio	0.200
A-L Load-Displacement Method	Bergan constant

Figure C. 6: ATENA Input Data (5 of 9)

Description:	UT Grad model	Unit system:	Imperial	side 6
Note:	scaled version			

A-L Reference number of iterations	5
A-L Step-Length	Based on current load step
A-L Location	All nodes
Iteration limit	100
Displacement Error	0.010000
Residual Error	0.010000
Absolute Residual Error	0.010000
Energy Error	0.000100
Optimize band-width	Sloan
Line Search	Yes
LS Type	With iterations
LS Unbalanced energy limit	0.500
LS Line search iteration limit	3
LS Minimum Eta	0.010
LS Maximum Eta	1.000
Update Stiffness	Each iteration
Stiffness Type	Tangent
Immediate Displacement Error Multiple	10000.0
After Step Displacement Error Multiple	1000.0
Immediate Residual Error Multiple	10000.0
After Step Residual Error Multiple	1000.0
Immediate Absolute Residual Error Multiple	10000.0
After Step Absolute Residual Error Multiple	1000.0
Immediate Energy Error Multiple	1000000.0
After Step Energy Error Multiple	10000.0

SOLUTION PARAMETERS 5

Property	Value
Title	Arc length 200 iterations
Method	Arc length (line search)
Arc Length Method	Consistently linearised
A-L Adjustment Method	Constant
A-L Load-Displacement Ratio	0.200
A-L Load-Displacement Method	Bergan constant
A-L Reference number of iterations	10
A-L Step-Length	Based on current load step
A-L Location	All nodes
Iteration limit	200
Displacement Error	0.010000
Residual Error	0.010000
Absolute Residual Error	0.010000
Energy Error	0.000100
Optimize band-width	Sloan
Line Search	Yes
LS Type	With iterations
LS Unbalanced energy limit	0.800
LS Line search iteration limit	2
LS Minimum Eta	0.010
LS Maximum Eta	1.000

Figure C. 7: ATENA Input Data (6 of 9)

Description:	UT Grad model	Unit system:	Imperial	side 7
Note:	scaled version			

Update Stiffness	Each iteration
Stiffness Type	Tangent
Immediate Displacement Error Multiple	10000.0
After Step Displacement Error Multiple	1000.0
Immediate Residual Error Multiple	10000.0
After Step Residual Error Multiple	1000.0
Immediate Absolute Residual Error Multiple	10000.0
After Step Absolute Residual Error Multiple	1000.0
Immediate Energy Error Multiple	1000000.0
After Step Energy Error Multiple	10000.0

SOLUTION PARAMETERS 6

Property	Value
Title	MyNR
Method	Newton-Raphson (line search)
Iteration limit	80
Displacement Error	0.010000
Residual Error	0.010000
Absolute Residual Error	0.010000
Energy Error	0.000100
Optimize band-width	Sloan
Line Search	Yes
LS Type	With iterations
LS Unbalanced energy limit	0.500
LS Line search iteration limit	2
LS Minimum Eta	0.010
LS Maximum Eta	1.000
Update Stiffness	Each iteration
Stiffness Type	Tangent
Immediate Displacement Error Multiple	10000.0
After Step Displacement Error Multiple	1000.0
Immediate Residual Error Multiple	10000.0
After Step Residual Error Multiple	1000.0
Immediate Absolute Residual Error Multiple	10000.0
After Step Absolute Residual Error Multiple	1000.0
Immediate Energy Error Multiple	1000000.0
After Step Energy Error Multiple	10000.0

ANALYSIS STEPS

Number	Load cases	Phase	Solution Parameters	Coefficient [–]
1	1,4-5	(1) Construction case 1	Newton_Raphson 100 iterations	0.800
2	1,4-5	(1) Construction case 1	Newton_Raphson 100 iterations	0.700
3	1,4-5	(1) Construction case 1	Newton_Raphson 100 iterations	0.800
4	1,4-5	(1) Construction case 1	Newton_Raphson 100 iterations	0.800
5	1,4-5	(1) Construction case 1	Newton_Raphson 100 iterations	0.800
6	1,4-5	(1) Construction case 1	Newton_Raphson 100 iterations	0.700
7	1,4-5	(1) Construction case 1	Newton_Raphson 100 iterations	0.400
8	1,4-5	(1) Construction case 1	Newton_Raphson 100 iterations	0.400
9	1,4-5	(1) Construction case 1	Newton_Raphson 100 iterations	0.400

Figure C. 8: ATENA Input Data (7 of 9)

	Description:	UT Grad model	Unit system:	Imperial	side 8
	Note:	scaled version			

10	1,4-5	(1) Construction case 1	Newton_Raphson 100 iterations	0.600
11	1,4-5	(1) Construction case 1	Newton_Raphson 100 iterations	0.200
12	1,4-5	(1) Construction case 1	Newton_Raphson 100 iterations	0.400
13	1,4-5	(1) Construction case 1	Newton_Raphson 100 iterations	0.300
14	1,4-5	(1) Construction case 1	Newton_Raphson 100 iterations	0.600
15	1,4-5	(1) Construction case 1	Newton_Raphson 100 iterations	0.500
16	1,4-5	(1) Construction case 1	Newton_Raphson 100 iterations	0.500
17	1,4-5	(1) Construction case 1	Newton_Raphson 100 iterations	0.500
18	1,4-5	(1) Construction case 1	Newton_Raphson 100 iterations	0.500
19	1,4-5	(1) Construction case 1	Newton_Raphson 100 iterations	0.500
20	1,4-5	(1) Construction case 1	Newton_Raphson 100 iterations	0.500
21	1,3	(1) Construction case 1	Arc length 100 iterations	0.100
22	1,3	(1) Construction case 1	Arc length 100 iterations	0.100
23	1,3	(1) Construction case 1	Arc length 100 iterations	0.100
24	1,3	(1) Construction case 1	Arc length 100 iterations	0.100
25	1,3	(1) Construction case 1	Arc length 100 iterations	0.100
26	1,3	(1) Construction case 1	Arc length 100 iterations	0.100
27	1,3	(1) Construction case 1	Arc length 100 iterations	0.100
28	1,3	(1) Construction case 1	Arc length 100 iterations	0.100
29	1,3	(1) Construction case 1	Arc length 100 iterations	0.100
30	1,3	(1) Construction case 1	Arc length 100 iterations	0.050
31	1,3	(1) Construction case 1	Arc length 100 iterations	0.030
32	1,3	(1) Construction case 1	Arc length 100 iterations	0.020
33	1,3	(1) Construction case 1	Arc length 100 iterations	0.040
34	1,3	(1) Construction case 1	Arc length 100 iterations	0.010
35	1,3	(1) Construction case 1	Arc length 100 iterations	0.050
36	1,3	(1) Construction case 1	Arc length 100 iterations	0.050
37	1,3	(1) Construction case 1	Arc length 100 iterations	0.050
38	1,3	(1) Construction case 1	Arc length 100 iterations	0.050
39	1,3	(1) Construction case 1	Arc length 100 iterations	0.025
40	1,3	(1) Construction case 1	Arc length 100 iterations	0.100
41	1,3	(1) Construction case 1	Arc length 100 iterations	0.025
42	1,3	(1) Construction case 1	Arc length 100 iterations	0.050
43	1,3	(1) Construction case 1	Arc length 100 iterations	0.050
44	1,3	(1) Construction case 1	Arc length 100 iterations	0.050

MONITORING POINTS

Number	Title	Type Location	Quantity - item
1	Displ 1	Value at node Macroelement 1, point (0.0000; 27.8750; 55.5000) [in]	Displacements - Component 1
2	Displ 2	Value at node Macroelement 1, point (0.0000; 27.8750; 55.5000) [in]	Displacements - Component 2
3	Displ 3	Value at node Macroelement 1, point (0.0000; 27.8750; 55.5000) [in]	Displacements - Component 3

Figure C. 9: ATENA Input Data (8 of 9)

	Description:	UT Grad model	Unit system:	Imperial	side 9
	Note:	scaled version			
4	Force 1	Maximum at nodes Macroelements (all)		External_Forces - Component 1	
5	Force 2	Maximum at nodes Macroelements (all)		External_Forces - Component 2	
6	Force 3	Maximum at nodes Macroelements (all)		External_Forces - Component 3	

Figure C. 10: ATENA Input Data (9 of 9)

C.3 LOAD DISPLACEMENT CURVES FOR ATENA MODELS

All of the following load versus displacement curves are from the movement of the most heavily loaded corner.

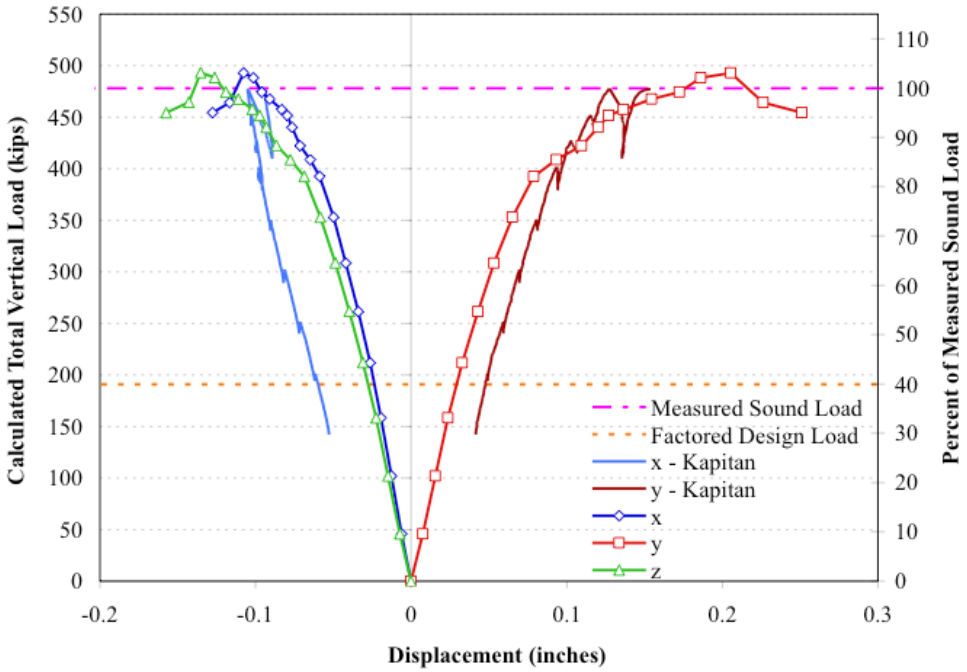

Figure C. 11: Load v. Displacement, Control (0.00” of Initial Cracking)

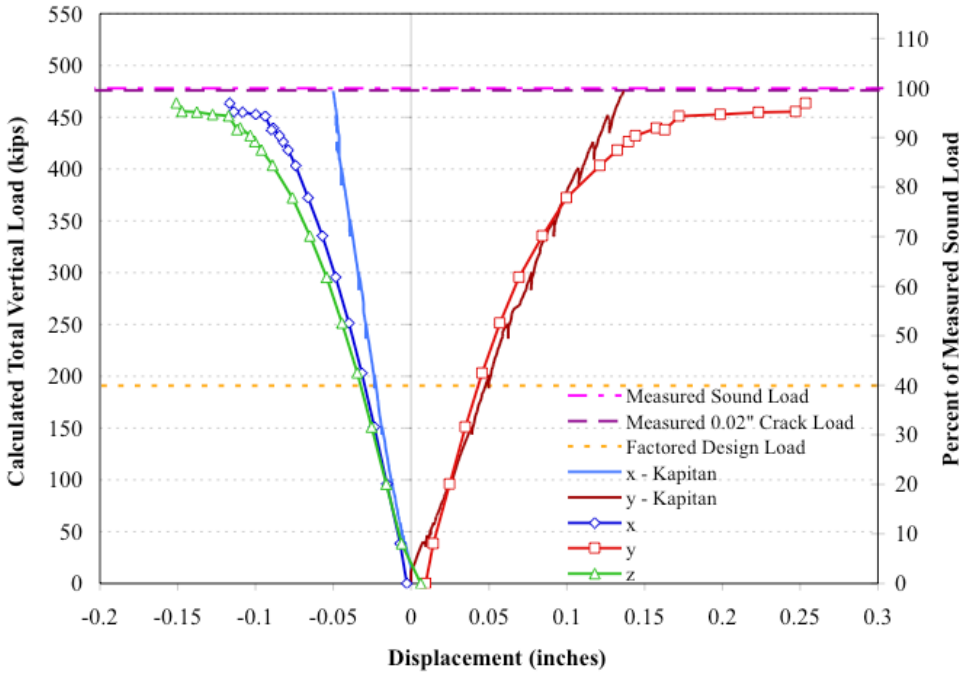

Figure C. 12: Load v. Displacement, 0.02” of Initial Cracking

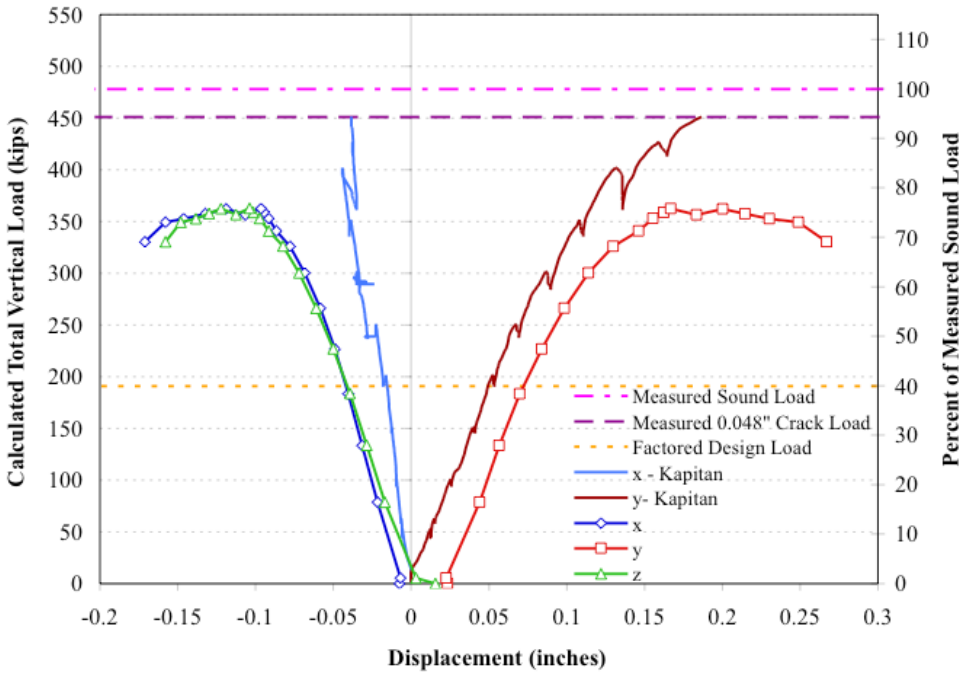

Figure C. 13: Load v. Displacement, 0.048” of Initial Cracking

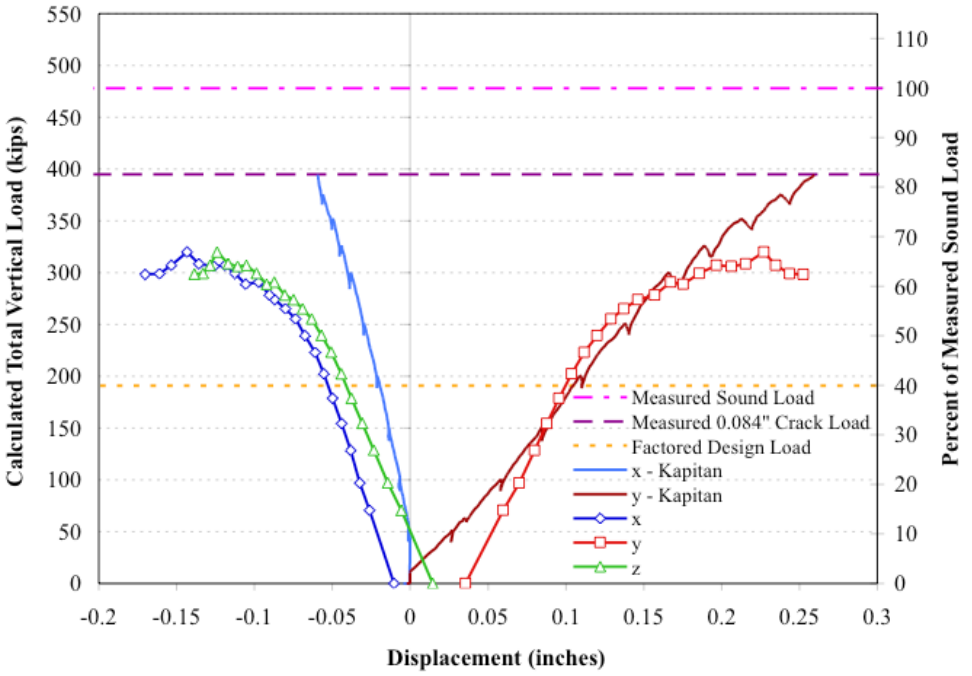

Figure C. 14: Load v. Displacement, 0.084” of Initial Cracking

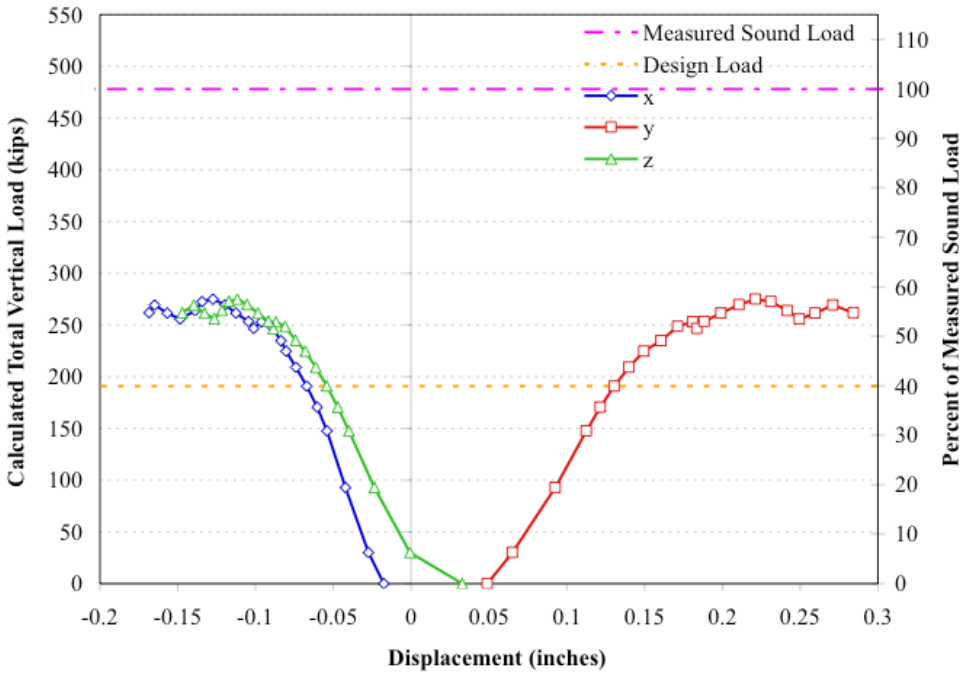

Figure C. 15: Load v. Displacement, 0.10” of Initial Cracking

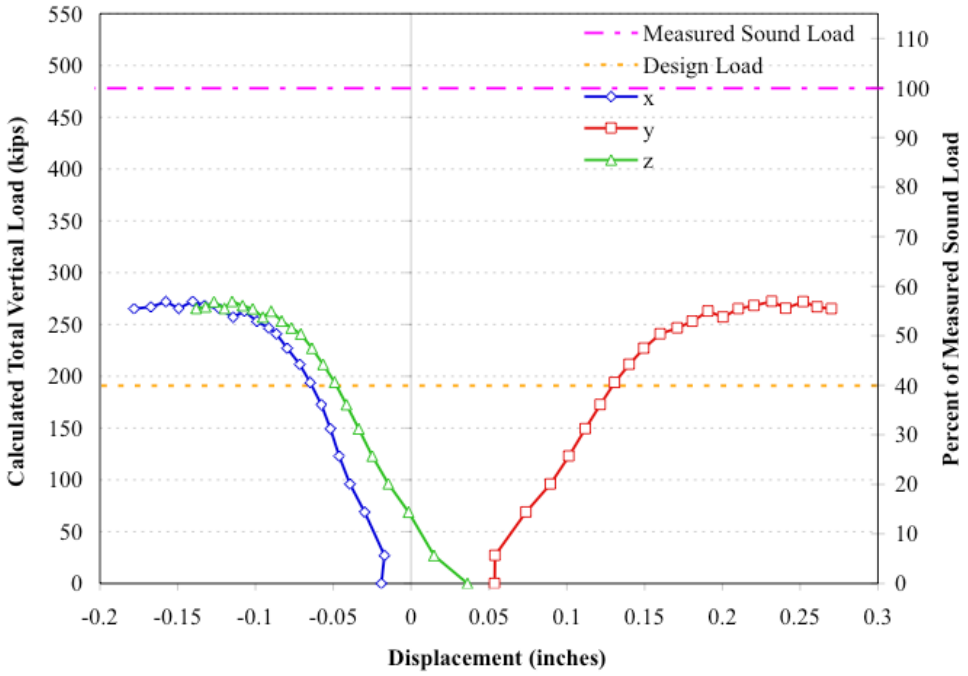

Figure C. 16: Load v. Displacement, 0.11" of Initial Cracking

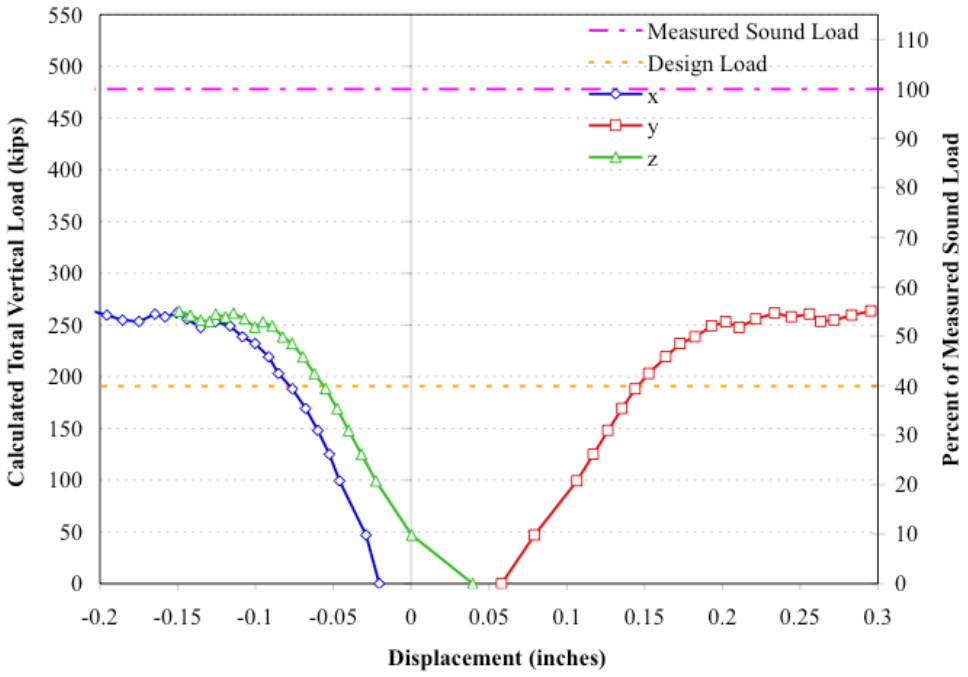

Figure C. 17: Load v. Displacement, 0.12" of Initial Cracking

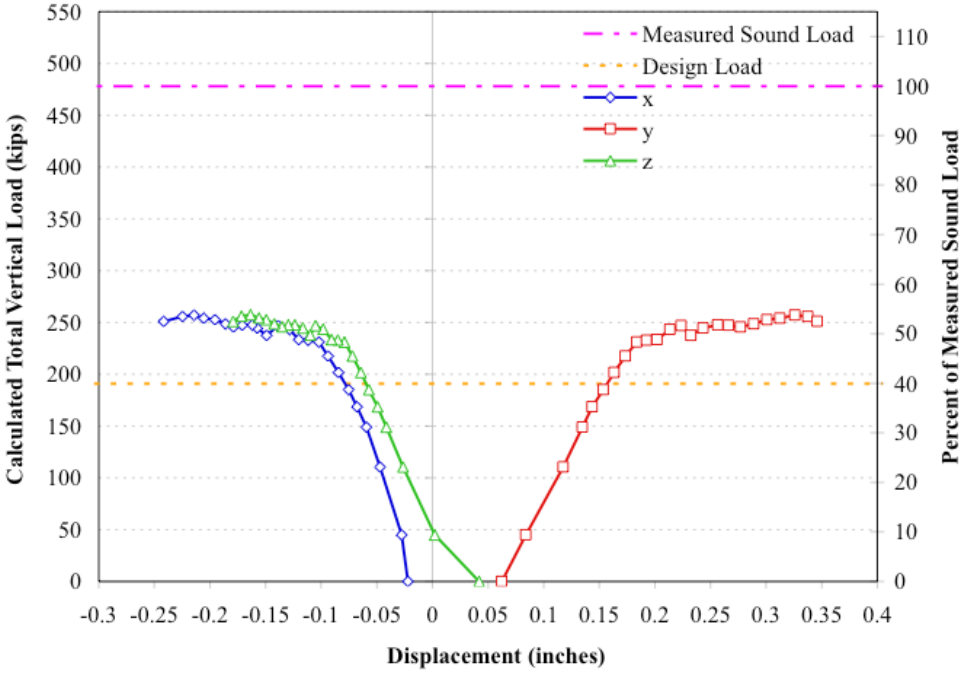

Figure C. 18: Load v. Displacement, 0.13” of Initial Cracking

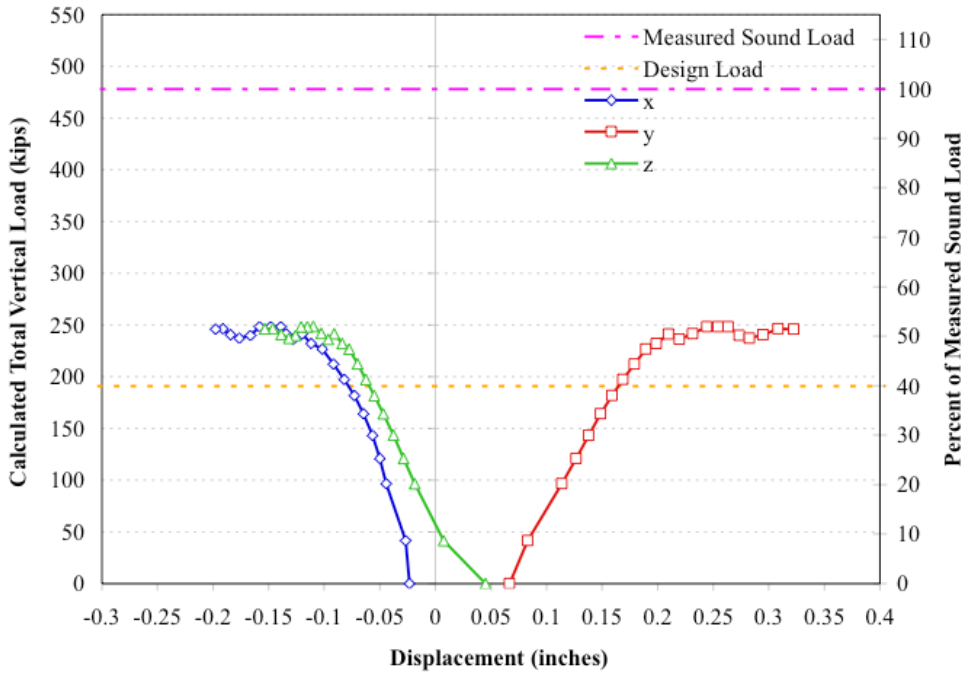

Figure C. 19: Load v. Displacement, 0.14” of Initial Cracking

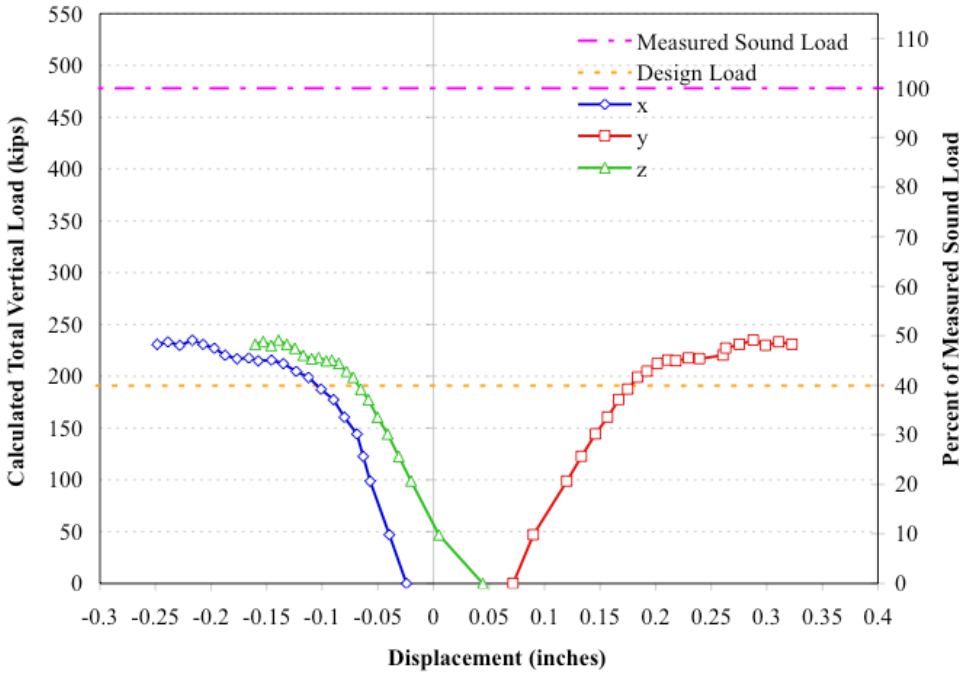

Figure C. 20: Load v. Displacement, 0.15” of Initial Cracking

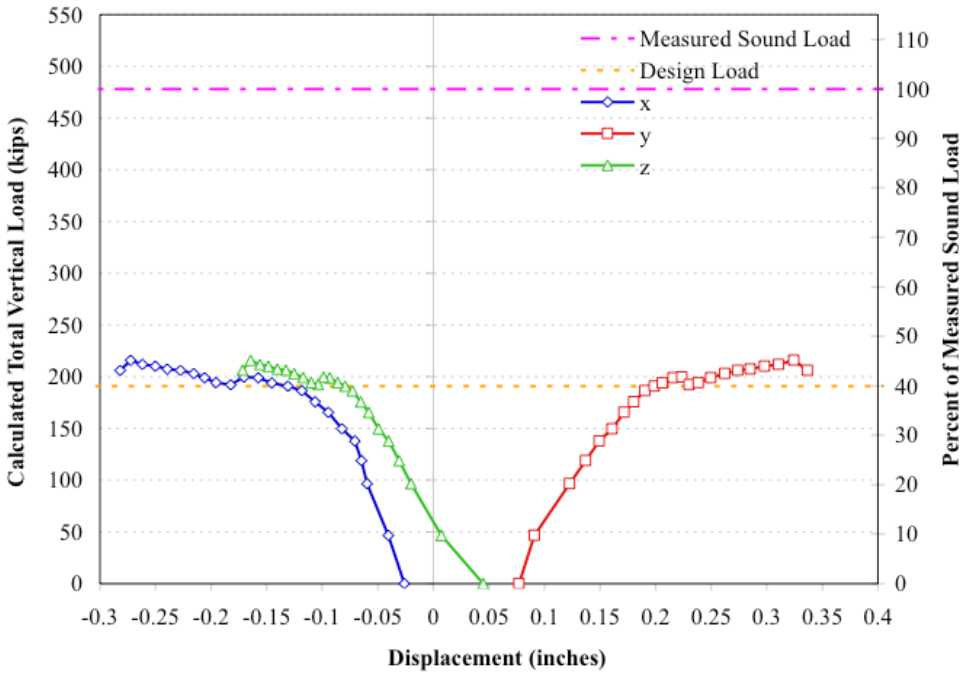

Figure C. 21: Load v. Displacement, 0.16” of Initial Cracking

REFERENCES

1. Folliard, K.J. "Extending Service Life of Large or Unusual Structures Affected by Premature Concrete Deterioration." Project Proposal, Center for Transportation Research, University of Texas at Austin, 2003.
2. Williams, S.A. "Structures Affected by Premature Concrete Deterioration: Diagnosis and Assessment of Deterioration Mechanisms." Master's Thesis, University of Texas at Austin, 2005.
3. Kapitan, J.G. "Examination and Evaluation of Bridge Piers Damaged by Alkali Silica Reaction and/or Delayed Ettringite Formation." Master's Thesis, University of Texas at Austin, 2006.
4. Hall, J.D. "Laboratory and Field Investigations of Alkali-Silica Reaction and Its Interaction with Delayed Ettringite Formation." Master's Thesis, University of Texas at Austin, 2003.
5. Folliard, K.J., B. Burgher, T. Ley, A. Thibonnier, and M.D.A. Thomas. "Extending Service Life of Large or Unusual Structures Affected by Premature Concrete Deterioration." Project 5218 Final Report, Center for Transportation Research, University of Texas at Austin, 2008.
6. Memberg, L., T. Fowler, and R. Klingner. "Bridges with Premature Concrete Deterioration: Damage Indices, Strand-Pullout Tests, and Field Observations." Project 1857-4 Report, Center for Transportation Research, University of Texas at Austin, 2002.
7. Folliard, K.J., R. Barborak, T. Drimalas, L. Du, S. Garber, J. Ideker, T. Ley, S. Williams, M. Juenger, M.D.A. Thomas, and B. Fournier. "Preventing Alkali-Silica Reaction and Delayed Ettringite Formation in New Concrete." Project 4085-S Report, Center for Transportation Research, University of Texas at Austin, 2006.
8. Fournier, B., M.A. Bérubé, M.D.A. Thomas, N. Smaoui, and K.J. Folliard. "Evaluation and Management of Concrete Structures Affected by Alkali-Silica Reaction – A Review." *Seventh CANMET/ACI International Conference on*

Recent Advances in Concrete Technology. Farmington Hills, Michigan: American Concrete Institute 2004.

9. Prezzi, M., P.J.M. Monteiro and G. Sposito. "The Alkali-Silica Reaction, Part 1: Use of the Double-Layer Theory to Explain the Behavior of Reaction-Product Gels." *ACI Materials Journal* 94, no. 1. Farmington Hills, Michigan: American Concrete Institute, 1997.
10. Monette, L., J. Gardner, and P. Grattan-Bellew. "Residual Strength of Reinforced Concrete Beams Damaged by Alkali-Silica reaction – Examination of Damage Rating Index Method." *ACI Materials Journal* 99, no. 1. Farmington Hills, Michigan: American Concrete Institute, 2002.
11. Collepardi, M. "A State-of-the-Art Review on Delayed Ettringite Attack on Concrete." *Cement and Concrete Composites* 25. Essex, England: Elsevier Science Publishers, 2003.
12. Diamond, S. "Delayed Ettringite Formation – Processes and Problems." *Cement and Concrete Composites* 18. Essex, England: Elsevier Science Publishers, 1996.
13. Fu, Y., P. Gu, P. Xie, and J. J. Beaudoin. "A Kinetic Study of Delayed Ettringite Formation in Hydrated Portland Cement Paste." *Cement and Concrete Research* 25. Essex, England: Elsevier Science Publishers, 1995.
14. Gillot, J.E. and C.A. Rogers. "The Behavior of Silicocarbonatite Aggregates from the Montreal Area." *Cement and Concrete Research* 33. Essex, England: Elsevier Science Publishers, 2003.
15. Idorn, G.M. "A Discussion of the Review Paper "Delayed Ettringite Formation" by H.F.W. Taylor, C. Famy, and K.L. Scrivener." *Cement and Concrete Research* 32. Essex, England: Elsevier Science Publishers, 2002.
16. Kuzel, H.J. "Initial Hydration Reactions and Mechanisms of Delayed Ettringite Formation in Portland Cements." *Cement and Concrete Composites* 18. Essex, England: Elsevier Science Limited, 1996.

17. Lawrence, C.D. “Mortar Expansions Due to Delayed Ettringite Formation: Effects of Curing Period and Temperature.” *Cement and Concrete Research* 25. Essex, England: Elsevier Science Ltd., 1995.

18. Lee, H., R.D. Cody, A.M. Cody, and P.G. Spry. “The Formation and Role of Ettringite in Iowa Highway Concrete Deterioration.” *Cement and Concrete Research* 35. Essex, England: Elsevier Science Publishers, 2005.

19. McDonald, D. “Delayed Ettringite Formation and Heat Curing – Implications of the Work of Kelham.” *Cement and Concrete Research* 28. Essex, England: Elsevier Science Ltd., 1998.

20. Shayan, A., and I. Ivanusec. “An Experimental Clarification of the Association of Delayed Ettringite Formation with Alkali-Aggregate Reaction.” *Cement and Concrete Composites* 18. Essex, England: Elsevier Science Limited, 1996.

21. Shimada, Y. and J.F. Young. “Thermal Stability of Ettringite in Alkaline Solutions at 80 ^{o}C.” *Cement and Concrete Research* 34. Essex, England: Elsevier Science Publishers, 2004.

22. Yan, P., F. Zheng, J. Peng, and X. Qin. “Relationship Between Delayed Ettringite Formation and Delayed Expansion in Massive Shrinkage-Compensating Concrete.” *Cement and Concrete Composites* 26. Essex, England: Elsevier Ltd., 2004.

23. Yang, R., C.D. Lawrence, and J.H. Sharp. “Delayed Ettringite Formation in 4-Year Old Cement Pastes.” *Cement and Concrete Research* 26. Essex, England: Elsevier Science Ltd., 1996.

24. Capra, B. and J. –P. Bournazel. “Modeling of Induced Mechanical Effects of Alkali Aggregate Reactions.” *Cement and Concrete Research* 28, no. 2. Essex, England: Elsevier Ltd., 1998.

25. Capra, B. and A. Sellier. “Orthotropic Modelling of Alkali-Aggregate Reaction in Concrete Structures: Numerical Simulations.” *Mechanics of Materials* 35, no. 8. Essex, England: Elsevier Science Publishers, 2003.

26. Diamond, S. “Alkali Silica Reactions – Some Paradoxes.” *Cement and Concrete Composites* 19. Essex, England: Elsevier Science Ltd., 1997.

27. Figg, J. “ASR – Inside Phenomena and Outside Effects (Crack Origin and Pattern).” *Proceedings from the 7th Conference on Concrete Alkali-Aggregate Reactions.* Ottawa, 1987.

28. Pantazopoulou, S.J. and M.D.A. Thomas. “Modeling Stress-Strain Behavior of Concrete Damaged by Alkali-Aggregate Reaction (AAR).” *ACI Structural Journal* 96, no. 5. Farmington Hills, Michigan: American Concrete Institute, 1999.

29. Thomas, M.D.A., Doug R. Hooton, and C.A. Rogers. “Prevention of Damage Due to Alkali-Aggregate Reaction (AAR) in Concrete Construction – Canadian Approach.” *Cement, Concrete, and Aggregates* 19, no. 1. American Society for Testing and Materials, 1997.

30. Bergol, L., G. DiPace, C. Rocco, S. Szteimberg, and L. Zitzer. “Use of Fracture Mechanics Parameters to Monitor Concrete Deterioration Due to Delayed Ettringite Formation” *Sixth CANMET/ACI International Conference on Durability of Concrete*. V.M. Malhotra, Ed. Farmington Hills, Michigan: American Concrete Institute, 2003.

31. Fu, Y. and J.J. Beaudoin. “Mechanisms of Delayed Ettringite Formation in Portland Cement Systems.” *ACI Materials Journal* 93. Farmington Hills, Michigan: American Concrete Institute, 1996.

32. Petrov, N. and A. Tagnit-Hamon. “Is Microcracking Really a Precursor to Delayed Ettringite Formation and Consequent Expansion.” *ACI Materials Journal* 101. Farmington Hills, Michigan: American Concrete Institute, 2004.

33. Tracy, S.L., S.R. Boyd, and J.D. Connolly. “Effect of Curing Temperature and Cement Chemistry of the Potential for Concrete Expansion Due to DEF.” *PCI Journal* 49. Chicago: The Institute, 2004.

34. Sahu, S. and N. Thaulow. “Delayed Ettringite Formation in Swedish Concrete Railroad Ties.” *Cement and Concrete Research* 34. Essex, England: Elsevier Science Publishers, 2004.

35. Brunetaud, X., L. Diret, and D. Damidot. “Delayed Ettringite Formation: Suggestion of a Global Mechanism in Order to Link Previous Hypothesis.” *Seventh CANMET/ACI International Conference on Durability of Concrete*. V.M. Malhotra, Ed.. Farmington Hills, Michigan: American Concrete Institute, 2004.

36. Cody, A.M., H. Lee, R.D. Cody, P.G. Spry, “The Effects of Chemical Environment on the Nucleation, Growth, and Stability of Ettringite $[Ca_3Al(OH)_6]_2(SO_4)_3$-$26H_2O$.” *Cement and Concrete Research* 34. Essex, England: Elsevier Science Publishers, 2004.

37. Institution of Structural Engineers. *Structural Effects of Alkali-Silica Reaction: Technical Guidance on the Appraisal of Existing Structures*. London: SETO Ltd, 1992.

38. *Guide to the Evaluation and Management of Concrete Structures Affected by Alkali-Aggregate Reaction*. M. Mortimer., Ed. Toronto: CSA International, 2000.

39. Corinaldesi, V. and G. Moriconi. “Diagnosis and Prognosis of Alkali-Aggregate Reactivity in Concrete Structures.” *Sixth CANMET/ACI International Conference on Durability of Concrete*. V.M. Malhotra, Ed.. Farmington Hills, Michigan: American Concrete Institute, 2003.

40. Farny, J.A. “Diagnosis and Control of Alkali-Aggregate Reactions in Concrete.” Portland Cement Association, 1996.

41. Class Notes from CE 397 “Concrete Durability” by Kevin Folliard, the University of Texas at Austin, February 1, 2005.

42. Zhang, Z., J. Olek, and S. Diamond. “Studies on Delayed Ettringite Formation in Early-Age, Heat-Cured Mortars: 1. Expansion Measurements, Changes in Dynamic Modulus of Elasticity, and Weight Gains.” *Cement and Concrete Research* 32. Essex, England: Elsevier Science Publishers, 2002.

43. Ahmed, T., E. Burley, and S. Rigden. “Effect of Alkali-Silica Reaction on Bearing Capacity of Plain and Reinforced Concrete.” *ACI Structural Journal*. Farmington Hills, Michigan: American Concrete Institute, 1999.

44. Ahmed, T., E. Burley, and S. Rigden. “Effect of Alkali-Silica Reaction on Tensile Bond Strength of Reinforcement in Concrete Tested under Static and Fatigue Loading.” *ACI Materials Journal.* Farmington Hills, Michigan: American Concrete Institute, 1999.

45. Monette, L., J. Gardner, and P. Grattan-Bellew. “Structural Effects of the Alkali-Silica Reaction on Non0loaded and Loaded Reinforced Concrete Beams.” *Eleventh International Conference on Alkali-Aggregate Reactions*. P.E. Grattan-Bellew, Ed. Park Ridge, New Jersey: Noyes Publications, 2000.

46. Poole, A.B., S. Rigden, and L. Wood. “The Strength of Model Columns Made with Alkali-Silica Reactive Concrete.” *Seventh International Conference on Alkali-Aggregate Reactions*. P.E. Grattan-Bellew, Ed. Park Ridge, New Jersey: Noyes Publications, 1987.

47. Wood, J.G.M. and P.J. Wickens. “Structural Effects of AAR on Reinforced Concrete and Consideration of Remedial Action.” *Sixth International Conference on Alkali-Aggregate Reactions*. P.E. Grattan-Bellew, Ed. Park Ridge, New Jersey: Noyes Publications, 1983.

48. Kubo, Y., O. Iketomi, T. Nakashima, and K. Torii. “Experimental Study of Fracture of Reinforced Steel Bar in Concrete Structures Due to Alkali-Silica Expansion.” *Sixth CANMET/ACI ACI International Conference on Durability of Concrete*. V.M. Malhotra, Ed. Farmington Hills, Michigan: American Concrete Institute, 2003.

49. Takemura, K., M. Ichitsubo, E. Tazawa, and A. Yonekura. “Mechanical Performance of ASR Affected Nearly Full-Scale Reinforced Concrete Columns.” *10^{th} International Conference on Alkali-Aggregate Reactions*. P.E. Grattan-Bellew, Ed.. Park Ridge, New Jersey: Noyes Publications, 1996.

50. Imai, H., T. Yamasaki, H. Maehara, and T. Miyagawa. "The Deterioration by Alkali-Silica Reaction of Hanshin Expressway Concrete Structures – Investigation and Repair." *7th International Conference on Alkali-Aggregate Reactions*. P.E. Grattan-Bellew, Ed. Park Ridge, New Jersey: Noyes Publications, 1987.
51. Ono, K. and M. Taguchi. "Long-Term Behavior of AAR Bridge Pier and the Internal Deterioration." *11th International Conference on Alkali-Aggregate Reactions*. P.E. Grattan-Bellew, Ed. Park Ridge, New Jersey: Noyes Publications, 2000.
52. Clayton, N. "Structural Performance of ASR Affected Concrete." *Eighth International Conference on Alkali-Aggregate Reactions*. P.E. Grattan-Bellew, Ed. Park Ridge, New Jersey: Noyes Publications, 1989.
53. Personal Communication from Lee Lawrence, WJE on September 26, 2007.
54. Construction Plans for San Antonio Y provided by TxDOT, sheet 429.
55. Photograph by Author, typical unless noted otherwise.
56. Doran, D.K. and J.F.A. Moore. "Appraisal of the Structural Effects of Alkali-Silica Reaction." *8th International Conference on Alkali-Aggregate Reactions*. P.E. Grattan-Bellew, Ed. Park Ridge, New Jersey: Noyes Publications, 1989.
57. Wood, J.G.M. "Physical Effects of AAR: Structures as a Laboratory." *CANMET International Workshop on AAR*. J.A. Soles, Ed. Halifax, Canada: CANMET, 1990.
58. Wood, J.G.M., R.A. Johnson, and R.J. Abbott. "Monitoring and Proof Load Testing to Determine the Rate of Deterioration and the Stiffness and Strength of Structures with AAR." *Structural Assessment: The Use of Full and Large Scale Testing,* Borough Green, Sevenoaks, Kent, England: Butterworths, 1987.
59. Wood, J.G.M., J.S. Young, and D.E. Ward. "The Structural Effects of Alkali-Aggregate Reaction on Reinforced Concrete." *8th International Conference on Alkali-Aggregate Reactions*. P.E. Grattan-Bellew, Ed. Park Ridge, New Jersey: Noyes Publications, 1989.
60. Baillemont, G, J.-B. Delaby, M. Brouxel, and P. Rémy. "Diagnosis, Treatment and Monitoring of a Bridge Damaged by AAR." *11th International Conference on*

Alkali-Aggregate Reactions. P.E. Grattan-Bellew, Ed. Park Ridge, New Jersey: Noyes Publications, 2000.

61. Deschenes, D. "Shear Capacity of Large-Scale Bridge Bent Specimens Subject to Alkali-Silica Reaction and Delayed Ettringite Formation." Master's Thesis, University of Texas at Austin, 2009.
62. Blight, G.E., M.G. Alexander, T.K. Ralph, and B.A. Lewis. "Effect of Alkali-Aggregate Reaction on the Performance of a Reinforced Concrete Structure over a Six-year Period." *Magazine of Concrete Research* 41, no 147. London: Cement and Concrete Association, 1989.
63. Alexander, M.G., G.E. Blight and B.J. Lampacher. "Pre-demolition Tests on Structural Concrete Damaged by AAR." *Proceedings of the 9th International Conference on Alkali-Aggregate Reaction in Concrete*, London, United Kingdom, 1992.
64. Blight, G.E., M.G. Alexander, W.K. Schutte, and T.K. Ralph. "The Effect of Alkali-Aggregate Reaction on the Strength and Deformation of a Reinforced Concrete Structure." *Proceedings of the 6th International Conference on Alkalis in Concrete*. Copenhagen, Denmark, 1983.
65. Jones, D.A. "11.5 Concrete." *Principles and Prevention of Corrosion*. 2nd Edition. Upper Saddle River, New Jersey: Prentice Hall, 1996.
66. Taylor, H.F.W., C. Famy, and K.L. Scrivener. "Delayed Ettringite Formation." *Cement and Concrete Research* 31, no. 5. Essex, England: Elsevier Ltd., 2001.
67. Katawaki, K. "Recent Diagnosis and Repair Techniques for Damaged Concrete Structure by ASR – A Guideline for Public Works Structure." *8th International Conference on Alkali-Aggregate Reaction*. P.E. Grattan-Bellew, Ed. Park Ridge, New Jersey: Noyes Publications, 1989.
68. Blight, G.E. and Y. Ballim. "Properties of AAR-Affected Concrete Studied Over 20 Years." *11th International Conference on Alkali-Aggregate Reaction*. P.E. Grattan-Bellew, Ed. Park Ridge, New Jersey: Noyes Publications, 2000.

69. Blight, G.E. and M.G. Alexander. "Assessment of AAR Damage to Concrete Structures." *Proceedings of the 7th International Conference on Alkalis in Concrete*. Ottawa, Canada, 1989.

70. Bae, S., O. Bayrak, J.O. Jirsa, and R.E. Klingner. "Structural Performance of Deep Anchor Bolts in Damaged Foundations." *Proceedings of the 2nd International Symposium on Connections Between Steel and Concrete* Vol. 1 of 2. R. Eligehausen, W. Fuchs, G. Gensio, and P. Grosser, Eds. Stuttgart, Germany: ibidem-Verlag, 2007.

71. Okada, K., S. Utoh, H. Imai, and K. Ono. "Concrete Structures Damaged by Alkali-Silica Reaction." *8th International Conference on Alkali-Aggregate Reaction*. P.E. Grattan-Bellew, Ed. Park Ridge, New Jersey: Noyes Publications, 1989

72. *Guide Manual for Condition Evaluation and Load and Resistance Factor Rating (LRFR)*. Washington, D.C.: American Association of State Highway and Transportation Officials, 2005.

73. *Standard Specifications for Highway Bridges.* 13th edition. Washington, D.C.: American Association for State Highway and Transportation Officials, 1983.

74. *AASHTO LRFD Bridge Design Specifications* 3rd edition, Washington, D.C.: American Association of State Highway and Transportation Officials, 2005.

75. Frangou, M., K. Pilakoutas, and S. Dritsos. "Structural Repair/Strengthening of RC Columns." *Construction and Building Materials* 9, no. 5. Essex, England: Elsevier Science Ltd, 1995.

76. Ramírez, J.L. "Ten Concrete Column Repair Methods." *Construction and Building Materials* 10, no 3. Essex, England: Elsevier Science Ltd., 1996.

77. Karbhari, V.M. and Y. Gao. "Composite Jacketed Concrete under Uniaxial Compression – Verification of Simple Design Equations." *Journal of Materials in Civil Engineering* 9, no. 4. New York: American Society of Civil Engineers, 1997.

78. Swamy, R.N. "Assessment and Rehabilitation of AAR-affected Structures." *Cement and Concrete Composites* 19. Essex, England: Elsevier Science Ltd., 1997.

79. El-Refaie, S.A., A.F. Ashour, and S.W. Garrity. "Flexural Strength of Continuous Reinforced Concrete Beams with Externally Bonded Carbon Fiber-Reinforced Polymer Reinforcement." *Proceedings from the 4th International Conference on Repair, Rehabilitation, and Maintenance of Concrete Structures, and Innovations in Design and Construction*. V.M. Malhotra, Ed. Farmington Hills, Michigan: American Concrete Institute, 2000.

80. Fukuyama, K., Y. Higashibata, and Y. Miyauchi. "Studies on Repair and Strengthening Methods of Damaged Reinforced Concrete Columns." *Cement and Concrete Composites* 22. Essex, England: Elsevier Science Ltd., 2000.

81. Lee, C., J.F. Bonacci, M.D.A. Thomas, M. Maalej, S. Khajehpour, N. Hearn, S. Pantazopoulou, and S. Sheikh. "Accelerated Corrosion and Repair of Reinforced Concrete Columns Using Carbon Fibre Reinforced Polymer Sheets." *Canadian Journal of Civil Engineering* 27. Ottawa: National Research Council of Canada, 2000.

82. Khaloo, A.R. "Shear Repair of Reinforced Concrete Beams Using Post-Tensioning." *Proceedings from the 4th International Conference on Repair, Rehabilitation, and Maintenance of Concrete Structures, and Innovations in Design and Construction*. V.M. Malhotra, Ed. Farmington Hills, Michigan: American Concrete Institute, 2000.

83. Rochette, P. and P. Labossière. "Axial Testing of Rectangular Column Models Confined with Composites." *Journal of Composites for Construction* 4, no. 3. New York: American Society of Civil Engineers, 2000.

84. Torii, K., Y. Kumagai, Y. Okuda, K. Ishii, and K. Sato. "Strengthening Method for ASR Affected Concrete Piers Using Prestressing Steel Wire." *11th International Conference on Alkali-Aggregate Reaction*. P.E. Grattan-Bellew, Ed. Park Ridge, New Jersey: Noyes Publications, 2000.

85. Pantazopoulou, S.J., J.F. Bonacci, S. Sheikh, M.D.A. Thomas, and N. Hearn. "Repair of Corrosion-Damaged Columns with FRP Wraps." *Journal of Composites for Construction* 5, no. 1. New York: American Society of Civil Engineers, 2001.

86. Esfahani, M.R. and M.R. Kianoush. "Axial Compressive Strength of Reinforced Concrete Columns Wrapped with FRP." *Proceedings First Conference on Application of FRP Composites in Construction and Rehabilitation of Structures*. Tehran, Iran, 2004

87. Haroun, M.A. and H.M. Elsanadedy. "Behavior of Cyclically Loaded Squat Reinforced Concrete Bridge Columns Upgraded with Advanced Composite-Material Jackets." *Journal of Bridge Engineering* 10, no. 6. New York: American Society of Civil Engineers, 2005.

88. Krauser, L. "Repairs, Modifications, and Strengthening with Post-Tensioning." *PTI Journal* 4, no. 3. Phoenix, Arizona: Post-Tensioning Institute, 2006.

89. Haddad, R.H., M.J. Shannag, and M.T. Al-Hambouth. "Repair of Reinforced Concrete Beams Damaged by Alkali-Silica Reaction." *ACI Structural Journal* 105, no. 2. Farmington Hills, Michigan: American Concrete Institute, 2008.

90. Klemens, T. "Beyond Crack Repair." *Concrete Construction*. Chicago: Hanley Wood, LLC., 2008

91. Orton, S.L. "Development of a CFRP System to Provide Continuity in Existing Reinforced Concrete Buildings Vulnerable to Progressive Collapse." Ph.D. Dissertation, University of Texas at Austin, 2007.

92. Kim, I.S. "Use of CFRP to Provide Continuity in Existing Reinforced Concrete Members Subjected to Extreme Loads." Ph.D. Dissertation, University of Texas at Austin, 2008.

93. Mirmiran, A., M. Shahawy, A. Nanni, V. Karbhari, B. Yalin, and A.S. Kalayci. "Recommended Construction Specifications and Process Control Manual for Repair and Retrofit of Concrete Structures Using Bonded FRP Composites." *NCHRP Repot 609*. Washington, D.C.: Transportation Research Board, 2008.

94. Photograph Courtesy of TxDOT

95. Zia, P., R.N. White, and D.A. Vanhorn. "Principles of Model Analysis." *Models for Concrete Structures ACI Publication SP-24.* Detroit, Michigan: American Concrete Institute, 1970.

96. Personal Communication from/Photograph by Tyler Ley
97. Stone, W.C. "Design Criteria for Post-tensioned Anchorage Zone Tensile Stresses." Ph.D. Dissertation, University of Texas at Austin, 1980.
98. Personal Communication from Ford Burgher
99. Photograph by Phillip Pesek
100. Drimalas, T. "Laboratory and Field Evaluations of External Sulfate Attack." Ph.D. Dissertation, University of Texas at Austin, 2007.
101. Hasler, H., P. Teichert, and D.R. Morgan. "Artistic Shotcrete for a Historic Auditorium." *Concrete International* 21, no. 3. Farmington Hills, Michigan: American Concrete Institute, 1999.
102. Personal Communication from I. Kim
103. ACI Committee 440. *Guide for the Design and Construction of Externally Bonded FRP Systems for Strengthening Concrete Structures*. Farmington Hills, Michigan: American Concrete Institute, 2002.
104. www.cervenka.cz
105. Cervenka Consulting. *ATENA User's Manual*., on disk with program.
106. www.ensoftinc.com
107. Talley, K. and J. Arrellaga, "Computational Modelling of ASR/DEF Affected Concrete Bridge Columns." *Proceedings 17th IABSE Congress.* Chicago, 2008.
108. Ford, J.S., D.C. Chang, and J.E. Breen. "Design Indications from Tests of Unbraced Mulitpanel Concrete Frames." *Concrete International* 3, no. 3. Detroit, Michigan: American Concrete Institute, 1981.
109. Based on Graphics by Ford Burgher
110. Predictions based upon J. Kapitan's capacity calculations.
111. Photograph by Jason Stith